


Saravanan Rajendran  
Hassan Karimi-Maleh  
Jiaqian Qin  
Eric Lichtfouse *Editors*

# Metal, Metal-Oxides and Metal Sulfides for Batteries, Fuel Cells, Solar Cells, Photocatalysis and Health Sensors

# Environmental Chemistry for a Sustainable World

Volume 62

## Series Editors

Eric Lichtfouse , Aix-Marseille University, CNRS, IRD, INRAE, Coll France, CEREGE, Aix-en-Provence, France

Jan Schwarzbauer, RWTH Aachen University, Aachen, Germany

Didier Robert, CNRS, European Laboratory for Catalysis and Surface Sciences, Saint-Avold, France

*Other Publications by the Editors*

**Books**

Environmental Chemistry

<http://www.springer.com/978-3-540-22860-8>

Organic Contaminants in Riverine and Groundwater Systems

<http://www.springer.com/978-3-540-31169-0>

Sustainable Agriculture

Volume 1: <http://www.springer.com/978-90-481-2665-1>

Volume 2: <http://www.springer.com/978-94-007-0393-3>

**Book series**

Environmental Chemistry for a Sustainable World

<http://www.springer.com/series/11480>

Sustainable Agriculture Reviews

<http://www.springer.com/series/8380>

**Journals**

Environmental Chemistry Letters

<http://www.springer.com/10311>

More information about this series at <http://www.springer.com/series/11480>

Saravanan Rajendran • Hassan Karimi-Maleh  
Jiaqian Qin • Eric Lichtfouse  
Editors

# Metal, Metal-Oxides and Metal Sulfides for Batteries, Fuel Cells, Solar Cells, Photocatalysis and Health Sensors

 Springer

*Editors*

Saravanan Rajendran  
Department of Mechanical Engineering  
University of Tarapacá  
Arica, Chile

Jiaqian Qin  
Metallurgy and Materials Science  
Research Institute  
Chulalongkorn University  
Bangkok, Thailand

Hassan Karimi-Maleh  
School of Resources and Environment  
University of Electronic Science and  
Technology of China  
Chengdu, China

Eric Lichtfouse   
Aix-Marseille University, CNRS, IRD, INRAE,  
Coll France, CEREGE  
Aix-en-Provence, France

ISSN 2213-7114

ISSN 2213-7122 (electronic)

Environmental Chemistry for a Sustainable World

ISBN 978-3-030-63790-3

ISBN 978-3-030-63791-0 (eBook)

<https://doi.org/10.1007/978-3-030-63791-0>

© The Editor(s) (if applicable) and The Author(s), under exclusive licence to Springer Nature Switzerland AG 2021

This work is subject to copyright. All rights are solely and exclusively licensed by the Publisher, whether the whole or part of the material is concerned, specifically the rights of translation, reprinting, reuse of illustrations, recitation, broadcasting, reproduction on microfilms or in any other physical way, and transmission or information storage and retrieval, electronic adaptation, computer software, or by similar or dissimilar methodology now known or hereafter developed.

The use of general descriptive names, registered names, trademarks, service marks, etc. in this publication does not imply, even in the absence of a specific statement, that such names are exempt from the relevant protective laws and regulations and therefore free for general use.

The publisher, the authors, and the editors are safe to assume that the advice and information in this book are believed to be true and accurate at the date of publication. Neither the publisher nor the authors or the editors give a warranty, expressed or implied, with respect to the material contained herein or for any errors or omissions that may have been made. The publisher remains neutral with regard to jurisdictional claims in published maps and institutional affiliations.

This Springer imprint is published by the registered company Springer Nature Switzerland AG  
The registered company address is: Gewerbestrasse 11, 6330 Cham, Switzerland

# Preface

*I happen to have discovered a direct relation between magnetism and light, also electricity and light, and the field it opens is so large and I think rich.*

– Michael Faraday

The discovery of electricity and electromagnetism opened unexplored research fields that led to many inventions of tremendous benefits for human life. The vision of Michael Faraday has highly inspired Allan Bard, the father of modern electrochemistry. Bard explained the concept of using electrochemistry to gather energy from nature in this way:

“You know, it’s easy to take electricity and make light – we do that all the time. What you really want to think about is using light to make electricity using solar energy.”

The vision of Bard is actually taking place in the fourth industrial revolution, where there is a high demand for sustainable energy. Here, recently developed nanomaterials are unique in terms of physical, chemical, electrical, and optical properties. This book reviews inorganic nanomaterials used in electrochemical applications for sustainable energy, environmental and biomedical. The chapters focus on batteries, fuel cells, supercapacitors, environmental monitoring, and bio-sensor applications.

In Chap. 1, Sanjay Nagarajan et al. discuss the potential of an advanced oxidation process such as photocatalysis (Fig. 1) for cellulose pre-treatment and conversion. Neethu et al. disclose the potential applications of lithium iron phosphate, a revolutionary material that will transform battery research, in Chap. 2. Chapter 3 by David et al. reviews the different types of hybrid supercapacitors. Precious and non-precious metals as catalysts for proton exchange membrane fuel cells and, alternatively, metal sulfides and metal oxides for composite proton membranes are presented by Hasan Ay et al. in Chap. 4. The contribution by Ananthi et al. in Chap. 5 provides a broad discussion about TiO<sub>2</sub> nanostructures and its hybrids for solar cell application.

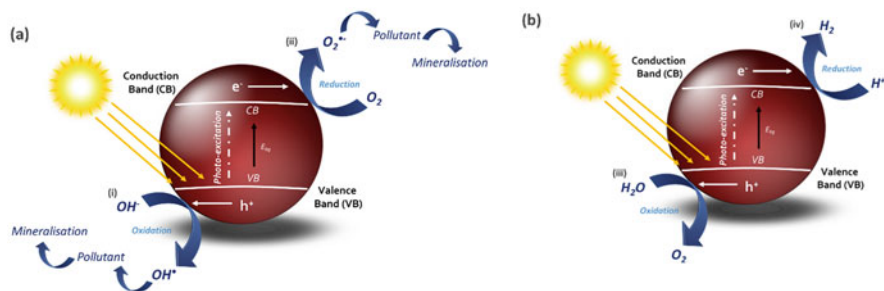


**Fig. 1** Schematic representation of the typical photocatalytic mechanism for its application towards (a) environmental remediation and (b) water splitting. (From Nagarajan et al. in Chap. 1)

Miyazaki et al. present designs of metal oxide and sulfide structures and the reaction mechanisms of glucose biosensing in Chap. 6. This chapter also reviews the role of hierarchical nanostructures to enable high sensitivity, rapid response, and detection of multicomponent elements, following an electronic tongue concept. Chapter 7 by Thiruppathi et al. describes electrochemical sensing and biosensing applications using metals, metal oxides, and metal sulfides. Chapter 8 by Chandrasekar et al. focuses on DNA biosensors and their applications for the detection of various biomolecules and clinical diagnosis. Recent developments in metal oxide and sulfide-based electrochemical sensors applied in differential pulse voltammetry, amperometry, and impedimetry are outlined by Suresh et al. in Chap. 9. In Chap. 10, Selvaraj Devi et al. present the fabrication methods of metal oxide-based optical waveguide sensors, optofluidic biosensors, electrochemical sensors, and their applications.

The main credit for this book is devoid to the contributing authors working in broad field of research related making materials related batteries, fuel cells, solar cells, photocatalysis and health sensors applications, this book would not have been possible without their generous participation.

Arica, Chile

Saravanan Rajendran

Chengdu, China

Hassan Karimi-Maleh

Bangkok, Thailand

Jiaqian Qin

Aix-en-Provence, France

Eric Lichtfouse

# Acknowledgments

First and foremost, we would like to thank Almighty **God** for giving us this opportunity and good strength to complete this book successfully.

We sincerely thank Springer and would like to convey our profound gratitude to all authors, reviewers, and series editors for contribution of chapters, evaluation, and accepting our book, *Metal, Metal-Oxides and Metal Sulfides for Batteries, Fuel Cells, Solar Cells, Photocatalysis and Health Sensors*, as a part of the series **Environmental Chemistry for a Sustainable World** and their continuous support to complete this hard task successfully. We feel great joy in acknowledging various publishers and authors for allowing us the copyright to use their figures and tables. However, we would still like to offer our sincere apologies to any copyright holder if unknowingly their right was infringed.

The editor, Dr. Saravanan Rajendran, would like to thank SERC – Chile (CONICYT/FONDAP/15110019) for the financial support. He expresses his sincere thanks to the Department of Mechanical Engineering at the University of Tarapacá, Arica, Chile.

One of the editors, Dr. Hassan Karimi-Maleh, would like to convey his gratitude to the Department of Chemical Engineering, Quchan University of Technology, Quchan, Iran; School of Resources and Environment, University of Electronic Science and Technology of China; and Department of Chemical Sciences, University of Johannesburg, South Africa.

One of the editors, Dr. Jiaqian Qin, would like to thank the support from Thailand Research Fund (RSA6080017), the Energy Conservation Promotion Fund, and the Energy Policy and Planning Office, Ministry of Energy, Thailand.

Editors

Saravanan Rajendran, Hassan Karimi-Maleh, Jiaqian Qin, and Eric Lichtfouse.



# Contents

<b>1</b>	<b>Cellulose Photocatalysis for Renewable Energy Production . . . . .</b>	<b>1</b>
	Sanjay Nagarajan, Nathan Skillen, Peter Robertson, and Linda Lawton	
<b>2</b>	<b>Lithium Iron Phosphate (LiFePO<sub>4</sub>) as High-Performance Cathode Material for Lithium Ion Batteries . . . . .</b>	<b>35</b>
	Neethu T. M. Balakrishnan, Asha Paul, M. A. Krishnan, Akhila Das, Leya Rose Raphael, Jou-Hyeon Ahn, M. J. Jabeen Fatima, and Raghavan Prasanth	
<b>3</b>	<b>Recent Advances in Hybrid Supercapacitors . . . . .</b>	<b>75</b>
	T. Manovah David and Tom Mathews	
<b>4</b>	<b>Metal, Metal Oxides, and Metal Sulfide Roles in Fuel Cell . . . . .</b>	<b>115</b>
	Hasan Ay and Fatih Sen	
<b>5</b>	<b>Role of TiO<sub>2</sub> in Highly Efficient Solar Cells . . . . .</b>	<b>147</b>
	Anandhi Sivaramalingam, Shyju Thankaraj Salammal, Ananthakumar Soosaimanickam, Tamilselvan Sakthivel, Samuel Paul David, and Balaji Sambandam	
<b>6</b>	<b>Metal Oxides and Sulfide-Based Biosensors for Monitoring and Health Control . . . . .</b>	<b>169</b>
	Celina M. Miyazaki, Nirav Joshi, Osvaldo N. Oliveira Jr., and Flavio M. Shimizu	
<b>7</b>	<b>Applications of Metals, Metal Oxides, and Metal Sulfides in Electrochemical Sensing and Biosensing . . . . .</b>	<b>209</b>
	Murugan Thirupathi, Natarajan Thiyagarajan, and Ja-an Annie Ho	
<b>8</b>	<b>Developing Trends in DNA Biosensor and Their Applications . . . .</b>	<b>245</b>
	Chandrasekar Selvaraj, Srinivas B.T.V, and Hai Xiong	

<b>9</b>	<b>Electrochemical Sensors Based on Metal Oxide and Sulfide Nanostructures</b> . . . . .	<b>285</b>
	R. Suresh, Claudio Sandoval, Eimmy Ramirez, K. Giribabu, R. V. Mangalaraja, and Jorge Yáñez	
<b>10</b>	<b>Biosensor Devices Based on Metal Oxide Materials</b> . . . . .	<b>311</b>
	Selvaraj Devi and Vairaperumal Tharmaraj	
	<b>Index</b> . . . . .	<b>335</b>

## About the Editors

**Saravanan Rajendran** received his Ph.D. in physics – material science in 2013 from the Department of Nuclear Physics, University of Madras, Chennai, India. He was awarded the University Research Fellowship (URF) during 2009–2011 by the University of Madras. After working as an assistant professor at Dhanalakshmi College of Engineering, Chennai, India, during the year 2013–2014, he was awarded SERC and CONICYT-FONDECYT postdoctoral fellowship, University of Chile, Santiago, from 2014 to 2017. He has worked (2017–2018) in the research group of Professor John Irvine, School of Chemistry, University of St Andrews, UK, as a postdoctoral research fellow within the framework of a EPSRC-Global Challenges Research Fund for the removal of blue-green algae and their toxins. Dr. Rajendran is currently working as an assistant professor in the Faculty of Engineering, Department of Mechanical Engineering, University of Tarapacá, Arica, Chile. Addition to this, he is also working as a Research Associate in SERC, Santiago, Chile. He is the associate editor for *International Journal of Environmental Science and Technology* (Springer). His research interests focus in the area of nanostructured functional materials, photophysics, surface chemistry, and nanocatalysts for renewable energy and waste water purification. Dr. Rajendran has published papers in several international peer-reviewed journals, eight book chapters, and seven books by renowned international publishers.

**Hassan Karimi-Maleh** was born in Sari, Iran (1982), and received his Ph.D. degree in chemistry from Isfahan University of Technology, Iran, in 2011. He is a highly cited researcher selected by Clarivate Analytics 2018 (cross field) and 2019 (agriculture field). Dr. Karimi-Maleh published more than 220 research papers with more than 11800 citations and H index = 66. He is working as full professor at the University of Electronic Science and Technology of China, at Quechan University of Technology, and also at the University of Johannesburg. He is member of the editorial boards of more than 20 international journals and active reviewer of many journals. Dr. Karimi-Maleh is an expert researcher in nanotechnology, biosensor, food analysis, and electrochemical sensors.

**Jiaqian Qin** is presently working as a researcher at the Metallurgy and Materials Science Research Institute, Chulalongkorn University, Thailand. He obtained his Ph. D. degree in physics from Sichuan University, China, in 2010. After graduation, Dr. Qin was awarded JSPS postdoctoral fellowship, Ehime University, Japan, in 2010–2012. His current research interest focuses on the development of advanced nanostructured materials for energy storage and conversion applications like batteries, supercapacitors, and nanocatalysts. He holds several Chinese patents and has over 90 publications in international journals of repute. Dr. Qin is the editor/editorial member of several reputed journals.

**Eric Lichtfouse** is geochemist and professor of scientific writing at Aix-Marseille University, France, and visiting professor at Xi'an Jiaotong University, China. He has discovered temporal pools of molecular substances in soils, invented carbon-13 dating, and published the book *Scientific Writing for Impact Factor Journals*. He is editor-in-chief and founder of the journal *Environmental Chemistry Letters* and the book series Sustainable Agriculture Reviews and Environmental Chemistry for a Sustainable World. Dr. Lichtfouse has awards in analytical chemistry and scientific editing. He is World XTerra Vice-Champion.

# Contributors

**Jou-Hyeon Ahn** Department of Chemical and Biological Engineering and Engineering Research Institute, Gyeongsang National University, Jinju-Daero, Republic of Korea

**Hasan Ay** Sen Research Group, Biochemistry Department, Faculty of Arts and Science, Dumlupınar University, Kütahya, Turkey

**Neethu T. M. Balakrishnan** Department of Polymer Science and Rubber Technology (PSRT), Cochin University of Science and Technology (CUSAT), Cochin, India

**Akhila Das** Department of Polymer Science and Rubber Technology (PSRT), Cochin University of Science and Technology (CUSAT), Cochin, India

**Samuel Paul David** HiLASE Centre, Institute of Physics of the Czech Academy of Sciences, Dolni Brezany, Czech Republic

Department of Physics, Kalasalingam Academy of Research and Education, Krishnankoil, Tamilnadu, India

**Selvaraj Devi** Department of Inorganic Chemistry, University of Madras, Chennai, Tamil Nadu, India

**K. Giribabu** Electrode and Electrocatalysis Division, Council of Scientific & Industrial Research-Central Electrochemical Research Institute, Karaikudi, India

**Ja-an Annie Ho** Bioanalytical Chemistry and Nanobiomedicine Laboratory, Department of Biochemical Science and Technology, National Taiwan University, Taipei, Taiwan

Center for Biotechnology, National Taiwan University, Taipei, Taiwan

**M. J. Jabeen Fatima** Department of Polymer Science and Rubber Technology (PSRT), Cochin University of Science and Technology (CUSAT), Cochin, India

**Nirav Joshi** São Carlos Institute of Physics, University of São Paulo, São Paulo, Brazil

**M. A. Krishnan** Department of Mechanical Engineering, Amrita Vishwa Vidyapeetham, Kollam, India

**Linda Lawton** School of pharmacy and life sciences, Sir Ian Wood Building, Robert Gordon University, Aberdeen, UK

**R. V. Mangalaraja** Department of Materials Engineering, Faculty of Engineering, University of Concepción, Concepción, Chile

Technological Development Unit (UDT), University of Concepción, Coronel Industrial Park, Coronel, Chile

**T. Manovah David** Thin Films and Coatings Section, Surface Nanoscience Division, Materials Science Group, Indira Gandhi Centre for Atomic Research, Kalpakkam, Tamil Nadu, India

**Tom Mathews** Thin Films and Coatings Section, Surface Nanoscience Division, Materials Science Group, Indira Gandhi Centre for Atomic Research, Kalpakkam, Tamil Nadu, India

**Celina M. Miyazaki** Universidade Federal de São Carlos, São Paulo, Brazil

**Sanjay Nagarajan** School of chemistry and chemical engineering, Queen's University Belfast, Belfast, UK

**Oswaldo N. Oliveira Jr.** São Carlos Institute of Physics, University of São Paulo, São Paulo, Brazil

**Asha Paul** Department of Polymer Science and Rubber Technology (PSRT), Cochin University of Science and Technology (CUSAT), Cochin, India

**Raghavan Prasanth** Department of Polymer Science and Rubber Technology (PSRT), Cochin University of Science and Technology (CUSAT), Cochin, India

**Eimmy Ramirez** Department of Analytical and Inorganic Chemistry, Faculty of Chemical Sciences, University of Concepción, Concepción, Chile

**Leya Rose Raphael** Department of Polymer Science and Rubber Technology (PSRT), Cochin University of Science and Technology (CUSAT), Cochin, India

**Peter Robertson** School of chemistry and chemical engineering, Queen's University Belfast, Belfast, UK

**Tamilselvan Sakthivel** Department of Materials Science and Engineering, University of Central Florida, Orlando, FL, USA

**Shyju Thankaraj Salammal** Centre for Nanoscience and Nanotechnology, Sathyabama Institute of Science and Technology, Chennai, Tamilnadu, India

Centre of Excellence for Energy Research, Sathyabama Institute of Science and Technology, Chennai, Tamilnadu, India

**Balaji Sambandam** Department of Materials Science and Engineering, Chonnam National University, Gwangju, South Korea

**Claudio Sandoval** Department of Analytical and Inorganic Chemistry, Faculty of Chemical Sciences, University of Concepción, Concepción, Chile

**Chandrasekar Selvaraj** Institute for Advanced Study, Shenzhen University, Shenzhen, China

**Fatih Sen** Sen Research Group, Biochemistry Department, Faculty of Arts and Science, Dumlupınar University, Kütahya, Turkey

**Flavio M. Shimizu** Department of Applied Physics, “Gleb Wataghin” Institute of Physics (IFGW), University of Campinas (UNICAMP), Campinas, SP, Brazil

**Anandhi Sivaramalingam** Department of Physics, School of Science and Humanities, Sathyabama Institute of Science and Technology, Chennai, Tamilnadu, India

**Nathan Skillen** School of chemistry and chemical engineering, Queen’s University Belfast, Belfast, UK

**Ananthakumar Soosaimanickam** Institute of Materials Science (ICMUV), University of Valencia, Valencia, Spain

**Srinivas B.T.V** Institute for Advanced Study, Shenzhen University, Shenzhen, China

**R. Suresh** Department of Chemistry, Easwari Engineering College (Autonomous), Chennai, India

**Vairaperumal Tharmaraj** Department of Analytical Chemistry, National Chung-Hsing University, Taichung, Taiwan

**Murugan Thiruppathi** Bioanalytical Chemistry and Nanobiomedicine Laboratory, Department of Biochemical Science and Technology, National Taiwan University, Taipei, Taiwan

**Natarajan Thiyagarajan** Institute of Chemistry, Academia Sinica, Taipei, Taiwan

**Hai Xiong** Institute for Advanced Study, Shenzhen University, Shenzhen, China

**Jorge Yáñez** Department of Analytical and Inorganic Chemistry, Faculty of Chemical Sciences, University of Concepción, Concepción, Chile

# Chapter 1

## Cellulose Photocatalysis for Renewable Energy Production



Sanjay Nagarajan, Nathan Skillen, Peter Robertson, and Linda Lawton

### Contents

1.1	Introduction .....	2
1.2	Cellulose Breakdown: Role of Potential of Advanced Oxidation Processes .....	6
1.3	Cellulose II for Energy Generation .....	8
1.3.1	Routes for Cellulose II Production .....	8
1.3.2	Cellulose II as Feedstock for Biofuel Production .....	13
1.4	Cellulose Photocatalysis and Renewable Energy .....	14
1.4.1	Photocatalysis of Cellulose I and Lignocellulosic Biomass .....	18
1.4.2	Photocatalysis of Cellulose II .....	23
1.5	Conclusion .....	25
	References .....	27

**Abstract** Renewable energy, especially biofuels, has the potential to supplement a part of the existing fossil-based transportation fuels. Biofuels such as bioethanol can be produced from established glucose fermentation processes; however, cheap and efficient glucose production is a hindering factor. Cellulose, the world's most abundant organic material, is a polymer of glucose and is locked within the lignocellulosic framework of plants. Pre-treatment is required to facilitate effective cellulose saccharification. Semiconductor photocatalysis, an advanced oxidation process, is a potential method for cellulose breakdown and the focus of this chapter will be on harnessing photocatalysis for cellulose-based renewable energy production.

We reviewed over 100 publications along the lines of structural properties of cellulose polymorphs, current pre-treatment strategies, conversion methods from

---

S. Nagarajan (✉) · N. Skillen · P. Robertson  
School of Chemistry and Chemical Engineering, Queen's University Belfast, Belfast, UK  
e-mail: [S.Nagarajan@qub.ac.uk](mailto:S.Nagarajan@qub.ac.uk)

L. Lawton  
School of Pharmacy and Life Sciences, Sir Ian Wood Building, Robert Gordon University,  
Aberdeen, UK

© The Editor(s) (if applicable) and The Author(s), under exclusive licence to Springer Nature Switzerland AG 2021

S. Rajendran et al. (eds.), *Metal, Metal-Oxides and Metal Sulfides for Batteries, Fuel Cells, Solar Cells, Photocatalysis and Health Sensors*, Environmental Chemistry for a Sustainable World 62, [https://doi.org/10.1007/978-3-030-63791-0\\_1](https://doi.org/10.1007/978-3-030-63791-0_1)



native cellulose I to an easily degradable polymorph cellulose II, and how semiconductor photocatalysis, an advanced oxidation process, can facilitate cellulose breakdown for saccharification and energy generation. Early reports in the 1980s utilized cellulose as sacrificial electron donor for the photocatalytic H<sub>2</sub> production over TiO<sub>2</sub> and noble metal co-catalysts; however, recently visible light activated photocatalysts have been used. An often-overlooked area with photocatalysis is cellulose saccharification. Only a handful of reports talk about saccharification over P25 TiO<sub>2</sub>, which is predominantly due to the lack of control over process conditions leading to undesired products. Addressing the recalcitrance of cellulose, by converting native cellulose I to cellulose II using a simple dissolution and regeneration technique, can be advantageous for enhancing valorization via semiconductor photocatalysis. For example, ~1.5-fold increase in photocatalytic cellulose saccharification was observed with cellulose II compared to cellulose I over P25 TiO<sub>2</sub>. A similar increase in photocatalytic H<sub>2</sub> production rate by over twofolds was also observed when cellulose II was used in suspension with Pt/TiO<sub>2</sub>. With advances in the development of semiconductor photocatalytic materials, especially in visible light activated materials such as CdS, reactor design, light emitting diode technology, and a novel “simple to produce” feedstock such as cellulose II, vast possibilities have opened up in this novel area of photocatalytic cellulose saccharification and H<sub>2</sub> production. Overall, the chapter aims to instil interest in the readers that combining cellulose II and semiconductor photocatalysis can be a feasible way forward to contribute toward renewable energy production.

**Keywords** Cellulose II · Renewable energy · Cellulose photocatalysis

## 1.1 Introduction

Anthropogenic activities combined with increased exploitation of fossil fuel stock has led to an increase in greenhouse gas emissions. Moreover, global politics also influences the movement of fossil fuel stocks and determines the fluctuating price of fuels. Assessments reported during the late 1990s highlighted that the seriousness of fossil fuel depletion will be experienced by the start of 2030 (Wigley et al. 1996). Furthermore, the International Energy Agency’s (IEA’s) World Energy Outlook Report from 2018 estimated that by 2040, 40% of the global power generation will be contributed by renewables, which is ~1.5 times higher than the current share (International Energy Agency). Consequently, there is a rise in global investments to boost the renewable-energy-based power generation (van der Hoeven 2013). Therefore, to increase the possibility of alternative energy production and to achieve the energy targets set nationally and internationally, sustainable renewable energy production is crucial. Brundtland’s commission defines sustainable development as “meeting the needs of the present without compromising the needs for the future” (Brundtland 1987). Although a variety of renewable energy alternatives in the form

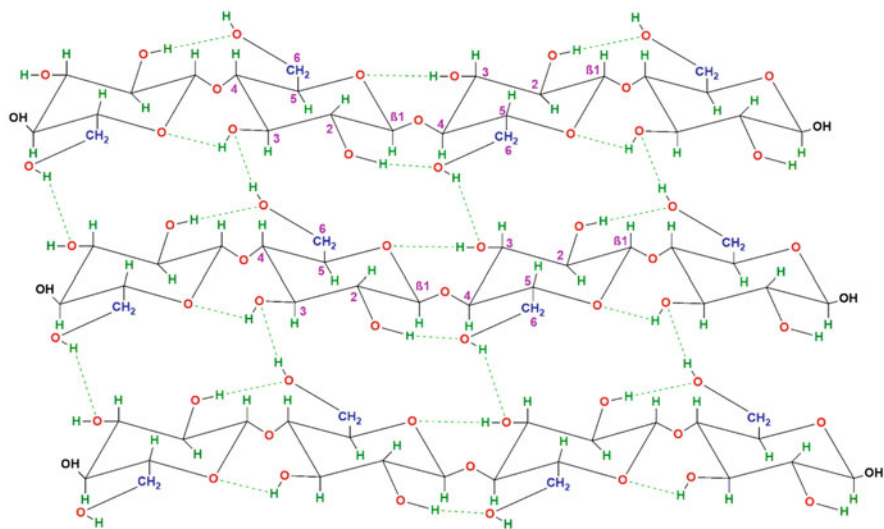


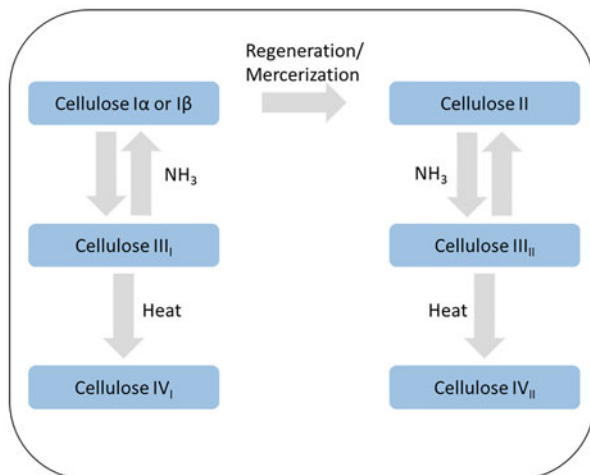
**Fig. 1.1** Structure of cellulose I with the intermolecular and intramolecular hydrogen bonds and  $\beta(1-4)$ -glycosidic bond between glucose monomers. (Reprinted with permission from Nagarajan et al. (2017a), Copyright (2017) Elsevier)

of solar, wind, geothermal, and tidal energies are available, sustainable renewable energy production is achievable via the utilization of waste biomass.

The primary component of waste biomass or lignocellulosic biomass in general is cellulose, which is the world's most abundant organic material (Lavoine et al. 2012). Cellulose is an amphiphilic homopolysaccharide compound (Lindman et al. 2010).  $\beta$ -D-glucose monomer units bonded by (1-4)-glycosidic bond as well as intermolecular and intramolecular hydrogen bonds present in the polymer leads to a rigid polymeric cellulose structure (Silverstein 2005). Highly ordered crystalline regions and disordered amorphous regions are found along the chain of cellulose (Sjöström 1993). Figure 1.1 represents the structure of cellulose with chair conformation and equatorial orientation of the glucose molecules. Intramolecular and intermolecular hydrogen bonds are represented by the green dotted lines.

In higher plants, native cellulose naturally exists in the cellulose I $\beta$  form, whereas microbes produce native cellulose I $\alpha$ . The only similarity between cellulose I $\alpha$  and I $\beta$  is the occurrence of parallel strands, whereas the lattice arrangement is different with I $\alpha$  exhibiting triclinic arrangement and I $\beta$  having a monoclinic structure. In addition to the native polymorphs, due to a variety of physico-chemical treatments, various cellulose polymorphs can be produced (O'Sullivan 1997) as shown in Fig. 1.2. Cellulose II is the most commonly produced man-made polymorph from both cellulose I $\alpha$  and I $\beta$  via alkali treatment known as mercerization or solubilizing and recrystallizing or regeneration, respectively, and has been extensively characterized (Sjöström 1993; Silverstein 2005; O'Sullivan 1997; Klemm et al. 1998). Naturally occurring cellulose II has also been isolated from bacterial cultures in a

**Fig. 1.2** Production of various cellulose polymorphs, namely cellulose I, cellulose II, cellulose III, and cellulose IV via a range of physico-chemical treatment methods



few cases (O'Sullivan 1997; Shibazaki et al. 1998; Kuga et al. 1993). Cellulose II has an antiparallel strand arrangement and monoclinic lattice arrangement and therefore differs from cellulose I. Other polymorphs, namely cellulose III<sub>I</sub> and III<sub>II</sub>, can be reversibly produced from cellulose I and II via ammonia treatment, respectively. Cellulose III polymorphs exhibit parallel strand arrangement and monoclinic crystal structure (Wada et al. 2004). Cellulose III<sub>I</sub> and III<sub>II</sub> materials, when further heat treated, give rise to cellulose IV<sub>I</sub> and IV<sub>II</sub>. A detailed understanding of the polymorphs' properties is necessary for determining end use.

Among the characteristics possessed by cellulose, intermolecular and intramolecular hydrogen bonding plays a central role in determining the supramolecular structure of polymorphs. The hydrogen bonding networks for cellulose I and II are shown along the a-c axis in Fig. 1.3, where the irreversible transformation of cellulose I to cellulose II leads to the formation of antiparallel chains affecting the hydrogen bonding patterns. In addition to the differences observed in hydrogen bonding, cellulose II has a higher surface area and porous volume compared to cellulose I, increased interplanar spacing or d-spacing, decreased crystallinity, increased hydrophilicity, and weak hydrophobic van der Waals interactions that make cellulose II a superior polymorph for use in renewable energy production (Boissou et al. 2014; Dadi et al. 2006; Yamane et al. 2006; Wada et al. 2010; Sakurada and Hutino 1936; Medronho and Lindman 2014, 2015; Lindman et al. 2010; Alves et al. 2015; Behrens et al. 2016).

The chapter so far has emphasized on the ever-growing need for renewable energy production and also highlighted that cellulose in waste biomass must be utilized to fulfil the needs. In addition to mentioning about the characteristics of native cellulose, the possibility of a superior cellulose polymorph being a better starting material based on the structure and molecular arrangement was highlighted. With the feedstock now being established, effective utilization must follow. The first step in the effective utilization of any feedstock for renewable energy production is

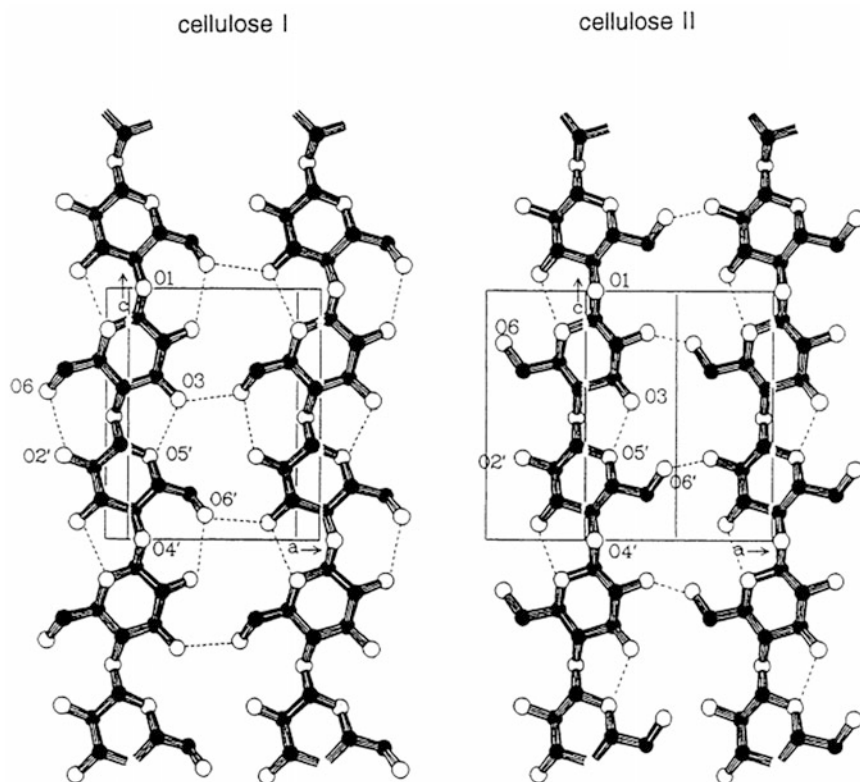


**Fig. 1.3** Intermolecular and intramolecular hydrogen bonding in cellulose I and II polymorphs. (Reprinted with permission from Klemm et al. (1998), Copyright (1998) Wiley-VCH Verlag GmbH)

pre-treatment. The following sections discuss the factors to consider when choosing a pre-treatment method and also briefly discuss the existing cellulose pre-treatment methods. The potential of heterogeneous photocatalysis as a novel pre-treatment alternative to produce fermentable sugars from cellulose as well as produce  $H_2$  directly by using cellulose as the sacrificial electron donor (SED) based on the limited reported literature is also discussed. Comprehensive discussion on the production of superior cellulose II polymorph for biofuel production is also provided and the potential of combining cellulose II and heterogeneous photocatalysis as a way forward is also emphasized.

## 1.2 Cellulose Breakdown: Role of Potential of Advanced Oxidation Processes

Effective and complete utilization of cellulose is hindered usually due to its amphiphilic and water insoluble properties. To ensure effective cellulose exploitation, an appropriate pre-treatment method should be in place to enhance utilization. To classify a method as a suitable pre-treatment technique, majority of the following requirements must be met, namely (Silverstein 2005):

- (i) Enable fermentable sugar release
- (ii) Minimal loss of fermentable sugars
- (iii) Minimal or no undesirable product formation
- (iv) Cost-effectiveness
- (v) Feasible scalability
- (vi) Energy efficiency

Considering the above-mentioned criteria, a variety of methods can be used for pre-treatment. Among available methods, steam explosion with dilute acid is commonly used. During steam explosion, biomass is treated with high-temperature and high-pressure steam followed by rapid depressurization to physico-chemically pre-treat biomass. Although preferable, inevitable loss of fermentable sugars due to degradation and formation of undesirable inhibitory by-products is a limitation (Sun and Cheng 2002). An overview of conventional pre-treatment processes highlighting the advantages and disadvantages of each of the processes can be found in Table 1.1. Numerous review articles are also available in the area of biomass pre-treatment, so that the reader can refer to those if interested (Silveira et al. 2015; Kumar and Sharma 2017; Alvira et al. 2010; Chen et al. 2017; Sun and Cheng 2002).

Although numerous established pre-treatment methods are available, contemporary processes still continue to emerge. An example would be the emergence of advanced oxidation processes (AOPs) as pre-treatment methods. AOPs are methods that generate highly oxidizing hydroxyl radicals in-situ and are often deployed in wastewater treatment applications to oxidize and completely mineralize pollutants (Oturán and Aaron 2014). The target for AOPs in cellulose pre-treatment would be to however reduce the crystallinity index and facilitate efficient saccharification to mediate subsequent fermentation. The in-situ non-specific OH radicals produced by AOPs may lead to saccharification of cellulose without affecting the crystallinity, and further microbial inhibitors such as acetic acid or 5-hydroxymethylfurfural may be formed in the highly oxidizing environment. Therefore, controlled AOPs are required for effective pre-treatment. The hypothesis behind AOPs as cellulose pre-treatment techniques has a firm base and therefore a range of AOPs have been identified to suit the purpose, namely degradation under ionizing radiation (von Sonntag and Schuchmann 2001; Ershov 1998), electrochemical saccharification (Meng et al. 2011; Wang et al. 2011), cavitation (Kojima et al. 2019; Zhang et al. 2016b), Fenton-based reactions (Hastrup et al. 2010, Arantes and Milagres 2006),

**Table 1.1** Advantages and disadvantage of conventional biomass pre-treatment methods

Pre-treatment category	Method	Advantages	Disadvantages	References
Physical	Mechanical grinding	Ease of handling the raw materials	High energy requirement	Fan et al. (1981), Miao et al. (2011) and Hiden et al. (2009)
	Pyrolysis	Rapid decomposition	High temperature requirement	
Physico-chemical	Steam explosion along with dilute acids	Less energy requirement when compared to mechanical grinding; cost-effective	Decomposition of monosaccharides	Sassner et al. (2008), Kumar and Wyman (2009), Chen et al. (2011), da Costa Sousa et al. (2016), Li et al. (2015), Gao et al. (2010) and Alinia et al. (2010)
	Ammonia fiber explosion	Relatively higher yield of monosaccharides than steam explosion	Cost involved in ammonia recovery to make the process environmentally friendly	
	CO <sub>2</sub> explosion	Cost-effective	Low yield of monosaccharides when compared to steam or ammonia explosion	
	Ozonolysis	Environmentally friendly; room temperature and pressure reactions	Large quantities of ozone required	
Chemical	Acid hydrolysis	Higher yield of monosaccharides	Toxic and corrosive; cost involved in acid recovery to make the process environmentally friendly; downstream pH adjustment is required	Saha et al. (2005), Scordia et al. (2011), Yang et al. (2012a) and Wu et al. (2011)
	Alkaline hydrolysis	Works well to remove lignin and hemicellulose	Salt formation and downstream pH adjustment is required	
Biological	White-rot and brown-rot fungi	Low energy requirements	Slow rate of hydrolysis	Ray et al. (2010), Sindhu et al. (2016), Saha et al. (2016) and Wan and Li (2012)
Enzymatic	Cellulases	High specificity for cellulose	Large quantities of enzyme required; expensive	

and photocatalysis (Kawai and Sakata 1980; Zhang et al. 2016a). Among the mentioned AOPs, heterogenous photocatalysis is least explored for cellulose pre-treatment due to the complexity involved. The limited literature available on photocatalytic cellulose conversion has predominantly focused on using cellulose as a sacrificial electron donor for H<sub>2</sub> production, which is understandable due to the non-specificity of the radicals. Recent articles have also started exploring the

possibilities of saccharification alternatively. A detailed discussion on the photocatalytic cellulose breakdown for fermentable sugar and H<sub>2</sub> production can be found in later sections of the chapter. Owing to the complexities surrounding scale-up of photocatalytic processes, heterogeneity of cellulose photocatalytic systems, and effective separation technique of sugars, photocatalysis is often least explored. A recent thesis submitted by Nagarajan in 2017 has, however, attempted to overcome these complexities by coupling effective reactor design with the use of cellulose II polymorph as feedstock and dialysis membranes to separate fermentable sugars (Nagarajan 2017). The nature of the feedstock, namely cellulose itself, being a key parameter is discussed in the next section. Especially, routes of cellulose II production, current use of cellulose II in biofuel production and how cellulose polymorphs can be used in conjunction with photocatalysis for effective valorization are discussed.

### 1.3 Cellulose II for Energy Generation

Bioethanol is an attractive biofuel that has the potential to contribute toward transportation fuel requirements. The precursor for bioethanol production is glucose, whose polymer cellulose is abundantly available and locked within lignocellulosic biomass in a highly crystalline cellulose I form. As mentioned in the previous sections, cellulose I is recalcitrant to hydrolysis; however, converting cellulose I to cellulose II—a more easily accessible polymorph of cellulose—can help in exploiting the substrate fully. The following subsection will give an overview of cellulose II production; however, a detailed discussion on the importance of cellulose II as an alternative feedstock to cellulose I for bioethanol has been reviewed and reported by Nagarajan et al. (2017a).

#### 1.3.1 Routes for Cellulose II Production

The two oldest-known cellulose II production processes are the viscose process and mercerization (Guenet 2008; Mercer 1850; Klemm et al. 2005; Cross et al. 1893a, b). Aqueous NaOH is used in both these techniques to dissolve cellulose I and precipitate cellulose II. Many variants of these processes have also been reported since, including dissolution of cellulose I in cold alkali (Wang and Deng 2009; Mittal et al. 2011; Dinand et al. 2002; Sharma et al. 2015; Halonen et al. 2012; Revol et al. 1987; Yu et al. 2014; Jin et al. 2016). An overview of other routes of cellulose II production is shown in Fig. 1.4 and briefed in Table 1.2, while the limits of cellulose I solubility in various solvents for cellulose II production are shown in Fig. 1.5.

Although aqueous alkali has the capability to dissolve cellulose I, complete molecular dissolution is not possible (Alves et al. 2015). To achieve a molecular dissolution, either anhydrous ionic liquids or aqueous onium hydroxides have to be

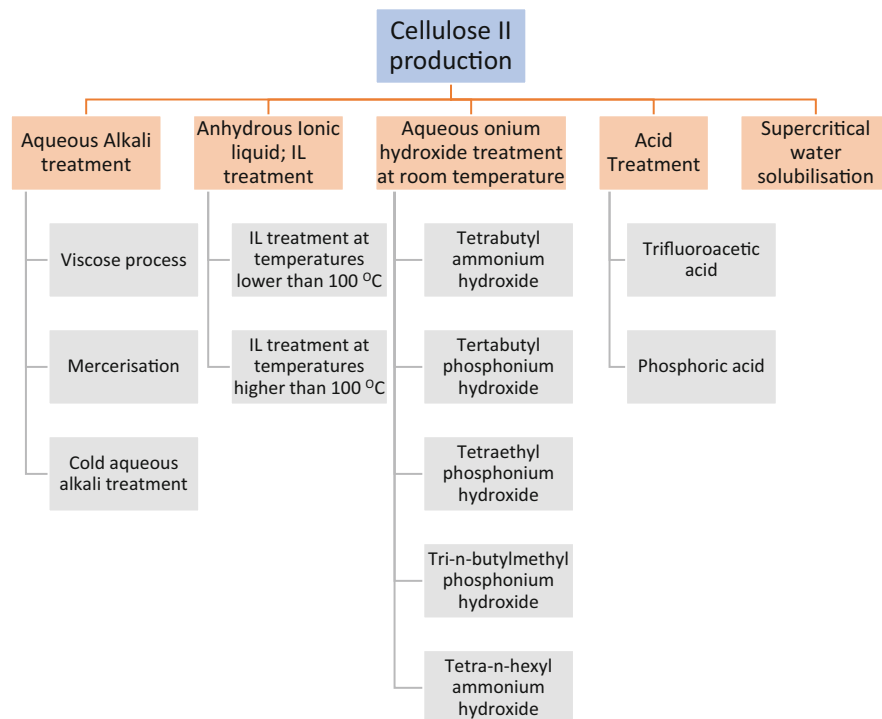


**Fig. 1.4** Various routes for cellulose II production from native cellulose or biomass. Note that ionic liquid or onium hydroxide treatments can achieve molecular dissolution and complete conversion to cellulose II and might be beneficial over other methods. (Figure based on Nagarajan et al. (2017a))

used (Abe et al. 2015). Salts with melting temperatures lower than 100 °C are known as ionic liquids. These are green solvents with negligible volatility and high flexibility. Due to the versatility possessed by ionic liquids, a range of cation–anion combinations could be made to effectively dissolve cellulose I. Swatloski et al. first reported a breakthrough research where methylimidazolium-based ionic liquid was used for the irreversible production of cellulose II from native cellulose (Swatloski et al. 2002). To date, methylimidazolium cations in combination with a variety of anions have been frequently reported as ionic liquids for cellulose dissolution (Dutta et al. 2012; Hou et al. 2012; Xiao et al. 2014; Park et al. 2012; Fu and Mazza 2011; Bokinsky et al. 2011; Cheng et al. 2011; Samayam et al. 2011; Dadi et al. 2006, 2007; Shafiei et al. 2013; Liu et al. 2015).

The nature of the constituting anion–cation mix determines the solubility of cellulose. Dissolution of cellulose II proceeds via the OH groups of C<sub>6</sub> and C<sub>3</sub> cellulose chains forming an electron acceptor–donor complex with the ionic liquids (Pinkert et al. 2009). Upon dissolution, water or alcohol can be used to precipitate cellulose II from the solution. Owing to high viscosity and anhydrous nature, the cellulose-dissolving capability of ionic liquids is limited. To overcome the limitation



**Table 1.2** Cellulose II production methods

Treatment type	Solvent used	Temperature	Method synopsis	References
Alkali treatment	Aqueous NaOH solution	–	Cellulose xanthogenate prepared from pulp is dissolved in aqueous NaOH and precipitated out of solution (viscose process).	Klemm et al. (2005) and Cross et al. (1893a, b)
	0–30% aqueous NaOH solution	70 °C/85 °C	Cellulose I was dissolved in NaOH aqueous solution followed by precipitation and purification (Mercerization); 9–15% NaOH aqueous solution was found to produce better cellulose II yields than other concentrations at 85 °C.	Mercer (1850) and Yu et al. (2014)
	6% aqueous NaOH solution	–8 °C to –20 °C	Cellulose I was dissolved at sub-zero temperatures and after 10 min of dissolution at –15 °C, cellulose II started to appear.	Wang and Deng (2009)
Ionic liquid treatment	1-ethyl-3-methylimidazolium acetate (EMIM-Ac)	120 °C/ 160 °C	Avicel, switchgrass, eucalyptus, and pine samples were dissolved in EMIM-Ac at 120 °C/160 °C and upon dissolution, cellulose II was precipitated out using hot water. Higher rate of cellulose II formation was observed with higher temperature.	Cheng et al. (2011)
	21 different ionic liquids	50 °C/80 °C	Avicel, $\alpha$ -cellulose, spruce wood, silver fir, common beech, and chestnut wood of 1–5 wt % were dissolved in 21 different ionic liquids at 50 °C and upon dissolution cellulose II was precipitated. EMIM-Ac was found to dissolve standard cellulose samples and 1-allyl-3-methylimidazolium-chloride (AMIM-Cl) dissolved the wood samples.	Zavrel et al. (2009)

	Imidazolium-based ionic liquids containing odd or even numbered alkyl side chains in combination with a range of anions	100 °C	8 wt% of Avicel PH 101 was dissolved in ionic liquids at 100 °C. Upon dissolution, excess methanol was used to precipitate cellulose II. It was determined that ionic liquids with shorter even-numbered side chains (2 or 4) combined with chloride anions showed good cellulose I dissolving properties.	Vitz et al. (2009)
Onium hydroxide treatment	Aqueous solutions of tetrabutylammonium hydroxide (TBAH) and tetrabutylphosphonium hydroxide (TBPH)	25 °C	Cellulose I was dissolved in 40–70 wt% aqueous TBAH and TBPH solution. Hot ethanol was added to the solutions to precipitate cellulose II. It was determined that concentration ranges of 50–60% TBAH and 50–70% TBPH in water were required for complete cellulose I dissolution at room temperature.	Abe et al. (2012)
	TBAH	16–28 °C	Cellulose I was dissolved in 40 and 60 wt% TBAH at different temperatures. Precipitation and regeneration of cellulose II were performed by the addition of hot water. It was determined that cellulose I dissolved better at 16 °C due to the stable ionic structure of TBAH at lower temperatures.	Wei et al. (2015)
	TBPH, tetraethylphosphonium hydroxide (TEPH), tri-n-hexylphosphine tetramethylammonium hydroxide (THTMAH), tetraethylammonium hydroxide (TEAH), TBAH, tri-n-butylmethylphosphonium hydroxide, and tetra-n-hexylammonium hydroxide	25 °C	Cellulose I was dissolved in various 40 wt% onium hydroxide aqueous solutions. A concentration of 15 wt% cellulose was found to be dissolved in all the onium hydroxides, whereas TBPH and TBAH dissolved 20 wt% cellulose. THTMAH and TEAH did not dissolve any cellulose.	Abe et al. (2015)

(continued)

Table 1.2 (continued)

Treatment type	Solvent used	Temperature	Method synopsis	References
Phosphoric acid treatment	77–85 wt% phosphoric acid	5–75 °C	0.5–3% wt/v cellulose was dissolved in 77–85 wt% phosphoric acid in the temperature range of 5–75 °C. Regeneration was performed with the addition of water. The investigators determined that a higher concentration of phosphoric acid ( $\geq 83$ wt%) was required to completely dissolve cellulose.	Jia et al. (2013)
Trifluoroacetic acid (TFA) treatment	99% trifluoroacetic acid	0–65 °C	Cotton linters were mixed in 99% TFA in mass ratios of 1:15 at different temperatures ranging from 0 to 65 °C for 3 h. The swollen samples were washed with water to recover cellulose II. Complete conversion to cellulose II was only observed at 0 °C.	Zhao et al. (2007)
Supercritical water solubilization	Supercritical water	320–400 °C	A 10 wt% cellulose I was mixed with water in a microreactor and rapidly heated for 0.02–0.6 s at 320–400 °C and 25–33 MPa pressure to obtain cellulose II. It was determined that at temperatures higher than 380 °C, cellulose conversion was constant and was independent of pressure.	Sasaki et al. (2003)

Reprinted with permission from Nagarajan et al. (2017a), Copyright (2017) Elsevier

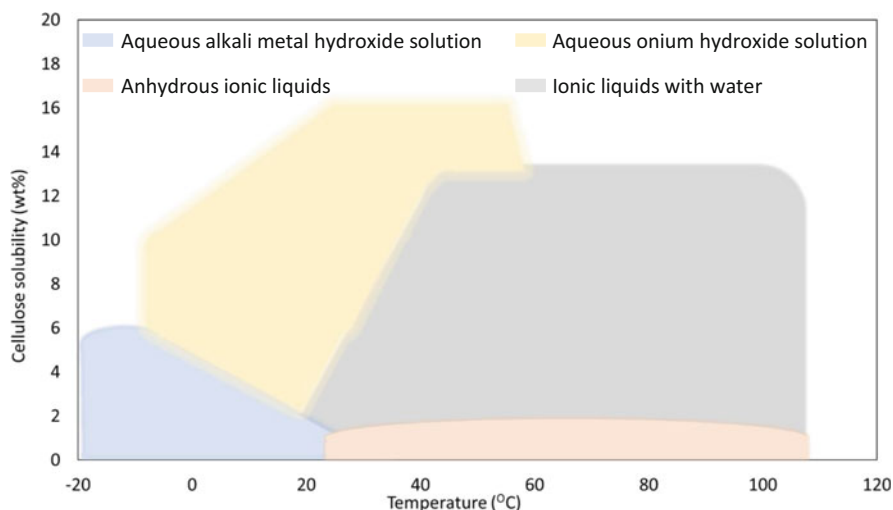


**Fig. 1.5** Representative solubilities of different cellulose I loading in various solvents such as alkali metal hydroxide aqueous solution in the blue-shaded region, ionic liquids with water in the orange-shaded region, anhydrous ionic liquids in the gray-shaded region, and aqueous onium hydroxide solution in the yellow-shaded region for cellulose II production. (Modified from Abe et al. (2015))

posed by the viscosity of ionic liquids, aqueous onium hydroxides can be used. Aqueous onium hydroxides are deep eutectic solvents and possess similar properties to ionic liquids and complement the amphiphilic property of cellulose thereby serving the purpose. Being an aqueous solution, onium hydroxides have a lower viscosity and higher cellulose-dissolving capability. The most commonly used onium hydroxides for cellulose II production are tetrabutylammonium hydroxide (TBAH) and tetrabutylphosphonium hydroxide (TBPH; Alves et al. 2015; Wei et al. 2015; Abe et al. 2012, 2015; Chang et al. 2019).

### 1.3.2 Cellulose II as Feedstock for Biofuel Production

There has been a lot of work lately on the use of cellulose II as feedstock for fermentable sugar and biofuel production. An overview of some of the reported work is shown in Table 1.3. As can be seen, when cellulose II was utilized as the feedstock, an enhanced yield of fermentable sugars or bioethanol was reported in all the cases. These reports established the importance of cellulose II as a renewable energy feedstock. Further sections in the chapter discuss the use of least-explored heterogeneous photocatalysis for fermentable sugar or  $H_2$  production from cellulose polymorphs.

**Table 1.3** Use of cellulose II for fermentable sugar and biofuel production

End use	Feedstock	Solvent used for cellulose II production	Key takeaway	References
Fermentable sugar production using Genencor GC220 cellulase enzyme preparation	Avicel PH-101, $\alpha$ -cellulose, cotton linters, and cellulose extracted from corn stover	16.5 wt% aqueous NaOH at 25 °C under a nitrogen atmosphere	Enzymatic hydrolysis rate of cellulose II was twice higher than cellulose I	Mittal et al. (2011)
Fermentable sugar production using commercial <i>Aspergillus niger</i> cellulase	Corn stalk	Pyrrolidonium-based ionic liquids at 90 °C	Higher fermentable sugar yield with cellulose II	Ma et al. (2016)
Fermentable sugar production using mixture of cellulase and $\beta$ -glucosidase enzymes and bioethanol production using <i>Saccharomyces cerevisiae</i> CCUG53310	Spruce wood chips or powder	Methylimidazolium-based ionic liquids and <i>N</i> -methylmorpholine- <i>N</i> -oxide at 120 °C	Significantly higher fermentable sugar and bioethanol yield from cellulose II produced from ionic liquids compared to other feedstocks	Shafiei et al. (2013)
Fermentable sugar production using enzymatic hydrolysis	Triticale straw	Anhydrous and aqueous 1-ethyl-3-methylimidazolium acetate with varying amounts of water	Increase in fermentable sugar yield with decrease in water content in the aqueous ionic liquid mixture	Fu and Mazza (2011)
Fermentable sugar production using a mixture of cellulase and $\beta$ -glucosidase	Microcrystalline cellulose	Aqueous TBPH and dimethyl sulfoxide (DMSO) mixture	Increasing rate of hydrolysis and fermentable sugar yield with decreasing crystallinity index of cellulose II	Pena et al. (2019)
Fermentable sugar and bioethanol production	Guinea grass	1-ethyl-3-methylimidazolium acetate	Improved fermentable sugar and bioethanol yield with cellulose II	Odorico et al. (2018)

## 1.4 Cellulose Photocatalysis and Renewable Energy

Photocatalysis and photocatalytic technology has developed significantly since the initial publications in the 1970s (Lyashenko and Gorokhovat-skii 1975; Inoue et al. 1979; Fujishima and Honda 1972) and, as a result, has now been deployed for a

range of applications (Daghrir et al. 2013; Matsuoka et al. 2007; Van Gerven et al. 2007; Zhao and Yang 2003). The most commonly reported applications are in environmental remediation, reactor design, chemical and materials synthesis, and energy production. In particular, photocatalytic water and air treatments have developed rapidly over the past four decades and now represent the most commercial and industrial application in the field. In contrast, photocatalytic energy production is yet to achieve the same level of development; however, it remains as one of the most desirable applications, which is primarily due to two key reasons. Firstly, one of the initial publications on photocatalysis was by Fujishima and Honda in 1972, which demonstrated water splitting over an irradiated  $\text{TiO}_2$  electrode (Fujishima and Honda 1972). In addition, achieving photocatalytic energy production could have significant impact on the global objective of increasing renewable fuel generation. As a result, photocatalytic research into energy conversion, renewable energy, and more recently bioenergy energy production has become extensive with the majority of publications focused on  $\text{H}_2$  generation (Matsuoka et al. 2007; Bahruji et al. 2010; Colón 2016; Liu et al. 2019a).

Regardless of the application, photocatalysis efficiency is dictated by the absorption of light at a suitable wavelength and subsequent generation of electron–hole pairs. In an aerobic-water system, typically, hydroxyl and superoxide radicals are formed, which drive the efficiency of environmental remediation applications such as water and air treatments (Fig. 1.6a). Photocatalytic  $\text{H}_2$  formation, however, is faced with several additional challenges in order to achieve the same level of efficiency. The primary challenges associated with a  $\text{H}_2$  evolving system include the selectivity of the process, electron–hole pair recombination and competition between the back-reactions of  $\text{H}_2$  and  $\text{O}_2$ . To discuss these further and to show how the field has evolved, photocatalytic  $\text{H}_2$  systems can be broadly divided into either water splitting (Fig. 1.6b) or sacrificial electron donor (SED) systems (Fig. 1.6c). In addition, Fig. 1.6d shows the equations that summarize the typical reactions taking place in photocatalytic systems for both environmental remediation and energy producing systems.

In water splitting, the key objective is for simultaneous photo-oxidation and reduction reactions to take place, generating  $\text{H}_2$  and  $\text{O}_2$  under ambient conditions. These systems, however, are often limited by both the rate of recombination and the back-reaction of  $\text{H}_2$  and  $\text{O}_2$  to form  $\text{H}_2\text{O}$ . In an attempt to suppress these limitations, researchers will often operate in an inert atmosphere and deploy a photocatalyst loaded with a metal co-catalyst, for example, Pt, Pd, Au, or Ni, to act as an electron trap (Skillen et al. 2015). Even under these conditions, however, the unfavorable thermodynamics of water splitting, due to a large change in the Gibbs free energy with  $\Delta G_o = -238 \text{ kJ mol}^{-1}$ , restricts the overall efficiency of the process. In an attempt to overcome the stringent requirements associated with water splitting, SED systems are often used. In a photocatalytic system, an SED can undergo an irreversible oxidation reaction that prevents recombination from occurring while also supplying electrons and protons for the subsequent reduction reaction. While a range of SEDs have been shown to be suitable, for example, alcohols and acids (Chen et al. 2018; Skillen et al. 2016), the development of the field has seen a shift in

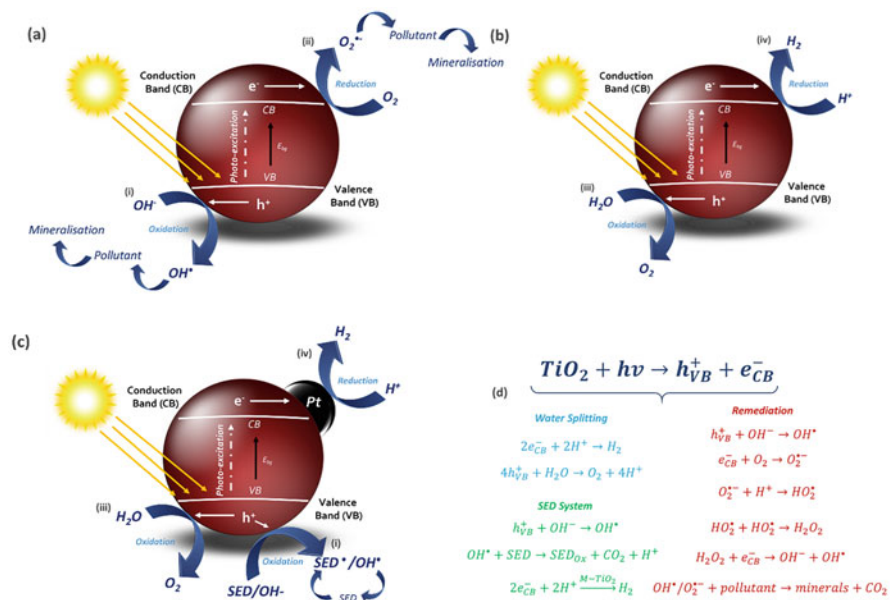


**Fig. 1.6** Typical photocatalytic mechanism that takes place in (a) environmental remediation, (b) water splitting, and (c) sacrificial electron donor (SED); SED-based systems along with (d) the equations that summarize the reactions. Processes shown include (i) formation of hydroxyl radicals ( $OH^{\cdot}$ ) for both (a) pollutant and (c) SED oxidation, (ii) formation of superoxide radicals ( $O_2^{\cdot -}$ ), (iii)  $O_2$  formation from water splitting, and (iv) proton reduction to form  $H_2$ . VB denotes valence band and CB denotes conduction band

focus toward using more sustainable and *green* compounds. As a result, an increase in papers reporting glycerol reforming to  $H_2$  has occurred (Luo et al. 2008; Slamet et al. 2017; Maurino et al. 2008; Bowker et al. 2008) and along with it, the use of biomass or biomass-derived substrates such as cellulose (Caravaca et al. 2016; Zhang et al. 2016a), lignin (Machado et al. 2000), and lignocellulose (Liu et al. 2019a; Kasap et al. 2018; Wakerley et al. 2017) has also increased. Recently, an extensive review was published by Liu et al., which highlighted the growth of photocatalytic conversion of lignocellulosic to  $H_2$  and value-added products (Liu et al. 2019a). Discussed in the subsequent sections are, what the authors feel, some of the key publications within the field in relation to  $H_2$  formation and biofuel generation. In addition, a more comprehensive overview of  $H_2$  formation from cellulose, lignocellulose, and raw biomass photocatalytic conversion has been tabulated in Table 1.4.

**Table 1.4** Cellulose, lignocellulose, and biomass conversion to H<sub>2</sub> via photocatalysis (UV denotes ultraviolet)

Substrate	Feedstock	Catalyst	Light source	Reaction solution	Hydrogen	Liquid phase products	References	
Cellulose	Filter paper	Ru/TiO <sub>2</sub> / Pt	500 W Hg ultra-high-pressure lamp	6 M NaOH	244 μmol		Kawai and Sakata (1980)	
	Micro crystal-line cellulose	Pt/TiO <sub>2</sub>	150 W Xe arc lamp	Water	~2.8 mL		Caravaca et al. (2016)	
	Fibrous long cellulose	Pt/TiO <sub>2</sub>	60 W UV-A lamps; natural irradiation	Water	54 μmol; 33 μmol		Speltini et al. (2014)	
	Cellulose (bound to TiO <sub>2</sub> )	Pt/TiO <sub>2</sub>	250 W iron-doped halide lamp	Water	195.2 μmol	Glucose, cellobiose, and formic acid	Zhang et al. (2016a)	
	α-Cellulose	CdS/ CdOx	100 mW cm <sup>-2</sup> solar light simulator	10 M KOH	~2.25 mmol g <sub>cat</sub> <sup>-1</sup> h <sup>-1</sup>		Wakerley et al. (2017)	
	Cellulose	Pt/TiO <sub>2</sub>	250 W iron-doped halide lamp	0.6 M H <sub>2</sub> SO <sub>4</sub>	123 μmol	5-hydroxymethylfurfural	Zou et al. (2018)	
	Cellulose	TiO <sub>2</sub> / NiO <sub>x</sub> @C <sub>g</sub>	500 W Xe lamp	Water	~270 μmol g <sub>cat</sub> <sup>-1</sup> h <sup>-1</sup>		Zhang et al. (2018)	
	Cellulose	TiO <sub>2</sub> / Ni <sub>x</sub> S <sub>y</sub>	500 W Xe lamp	Water	181.2 μmol		Hao et al. (2018)	
	Lignocellulosic biomass	Wooden branch	CdS/ CdOx	100 mW cm <sup>-2</sup> solar light simulator	10 M KOH	5.3 mmol g <sub>cat</sub> <sup>-1</sup> h <sup>-1</sup>		Wakerley et al. (2017)
		Grass	Pt/TiO <sub>2</sub>	150 W Xe arc lamp	Water	~0.6 mL		Caravaca et al. (2016)
Sawdust		<sup>NCN</sup> CN <sub>x</sub>	100 mW cm <sup>-2</sup> solar light simulator	0.1 M potassium phosphate	202 μmol g <sub>cat</sub> <sup>-1</sup> h <sup>-1</sup>		Kasap et al. (2018)	
Rice husk		Pt/TiO <sub>2</sub>	Natural irradiation	Water	16 μmol		Speltini et al. (2014)	
Alfalfa stems		Pt/TiO <sub>2</sub>	60 W UV-A lamps	Water	24 μmol			



### 1.4.1 Photocatalysis of Cellulose I and Lignocellulosic Biomass

While often described as an *emerging topic*, photocatalytic reforming of biomass to  $H_2$  was reported along with some of the earliest publications in the field (Lyashenko and Gorokhovat-skii 1975; Inoue et al. 1979; Fujishima and Honda 1972). In 1980, Kawai and Sakata demonstrated for the first time the evolution of  $H_2$  from sugar, starch, and cellulose using a  $RuO_2/TiO_2/Pt$  photocatalyst in a suspension of water (Kawai and Sakata 1980). Interestingly, rather than producing a system that mimicked natural photosynthesis, as is often done with photocatalysis, the authors developed one aimed at operating alongside it. The photocatalytic conversion of sugar, starch, and cellulose to  $H_2$  represented utilizing the carbohydrates produced during photosynthesis via  $CO_2$  fixation for the generation of a fuel. Furthermore, the authors also suggested any  $CO_2$  photocatalytically produced could be fed back into plants or alternatively captured by  $NaOH$  to form  $Na_2CO_3$  or  $NaHCO_3$ . The authors referred to the process as *photoinduced fermentation*, which was considered an alternative to traditional methods of fermenting sugar. Under optimum conditions of 6 M  $NaOH$  and  $\lambda = 380$  nm with a 500 W Xe lamp, quantum yields of 1.5%, 1.3%, and 1.0% were obtained for the photocatalytic conversion of sugar, starch, and cellulose to  $H_2$ , respectively. Moreover, a quantum yield of 0.02% was obtained when the photocatalyst was suspended in only water, to support that the formation of  $H_2$  was primarily occurring from the carbohydrates. Kawai and Sakata suggested that the carbon chains of the carbohydrates were oxidized at the valence band leading to  $H^+$  and  $CO_2$  formation, with  $H^+$  then being reduced by electrons to form  $H_2$  at the conduction band. While the operating conditions could be considered to be unfavorable with respect to the use of harsh chemicals and poor energy efficiency, the paper did highlight the potential of photocatalysis for biomass conversion.

Despite the early report by Kawai and Sakata on photocatalytic reforming of poly- and monosaccharides, it was a number of years before additional papers on biomass reforming were published. Even though a lack of photocatalytic cellulose reforming/degradation based papers in the literature were not seen, there was significant interest in photocatalytic glucose conversion (Kim et al. 2015; Zhou et al. 2017; Colmenares et al. 2011; Iervolino et al. 2018; Jin et al. 2017; Fu et al. 2008; Chong et al. 2014; Da Vià et al. 2017; Iervolino et al. 2016). The majority of these papers focused on photocatalysts in combination with typical metals such as Pt, Au, Ni, and Ru (Zhou et al. 2017; Iervolino et al. 2018; Da Vià et al. 2017) to monitor  $H_2$  formation, often as a comparison study to other SEDs. Given the structure of cellulose, there is obvious merit in investigating the photo-reforming of glucose as a model compound. Interestingly, however, very few of these papers looked at either the mechanism that may have occurred or a comparison between glucose, cellulose, and lignin. In this regard, Caravaca et al. (2016) looked at the formation of  $H_2$  via photocatalytic reforming of cellulose, glucose, and raw biomass. Using a 0.2% Pt- $TiO_2$  catalyst, the paper demonstrated that the evolution of  $H_2$  was occurring by initial in-situ hydrolysis via glucose. In a comparison study, the

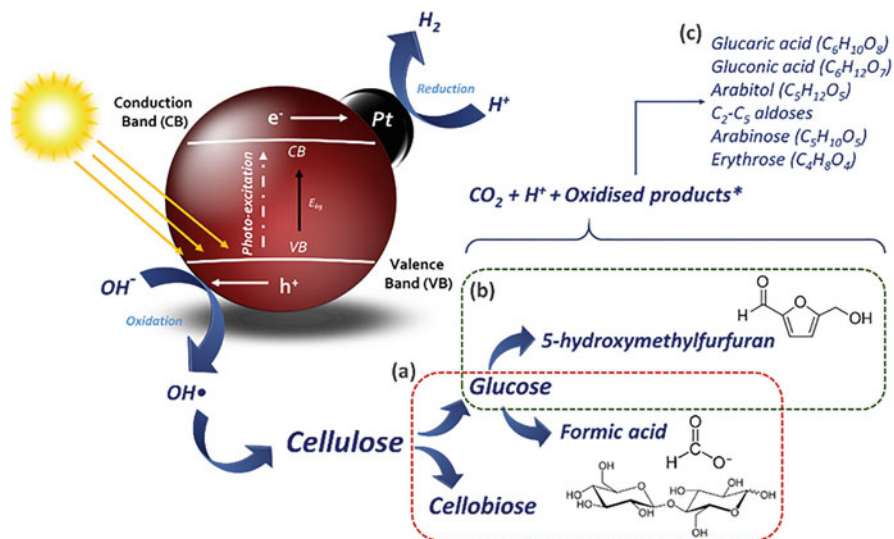


**Fig. 1.7** Proposed photocatalytic oxidation mechanism for cellulose conversion where (a) shows products such as glucose, cellobiose, and formic acid detected by Zhang et al. (2016a), (b) shows 5-hydroxymethylfuran from glucose as observed by Speltini et al. (2014), and (c) shows other typical oxidized products detected during glucose oxidation based on the literature (Kim et al. 2015; Zhou et al. 2017; Colmenares et al. 2011; Jin et al. 2017; Fu et al. 2008; Da Vià et al. 2017; Chong et al. 2014)

reaction orders for both glucose and cellulose were derived to be 0.24 and 0.2, respectively, which suggested that the initial stage of photocatalytic cellulose reforming was hydrolysis to glucose, which was followed by the reforming of glucose to eventually  $\text{H}_2$  and a range of oxidation products. Similar findings were also reported by Zhang et al. (2016a) and Speltini et al. (2014) in 2015 and 2014, respectively, who performed a systematic study of  $\text{H}_2$  evolution from cellulose. Speltini and colleagues confirmed that the initial stage in the conversion process was a  $\text{TiO}_2$ -mediated hydrolysis step followed by glucose reforming, which identified 5-hydroxymethylfurfural (5-HMF) as an intermediate in the mechanism. Figure 1.7 shows a potential mechanism and illustration for photocatalytic cellulose reforming based on the results obtained from literature.

Photocatalytic  $\text{H}_2$  production has often been coupled with attempts to utilize solar irradiation as a means to drive the process and achieve a sustainable method of clean energy production. While challenging, a number of papers have reported solar-driven photocatalysis across a range of applications including water disinfection (Malato et al. 2009), air treatment (Giménez et al. 1999),  $\text{CO}_2$  reduction (Varghese et al. 2009), and  $\text{H}_2$  production (Skillen et al. 2016). Achieving solar photocatalytic reforming of biomass-based materials, however, represents an extremely favorable approach to renewable energy production. Despite papers on photocatalytic biomass conversion to  $\text{H}_2$  being limited, many have already shown the potential to use solar light activated photocatalysts (Wakerley et al. 2017; Speltini et al. 2014; Zhang et al.

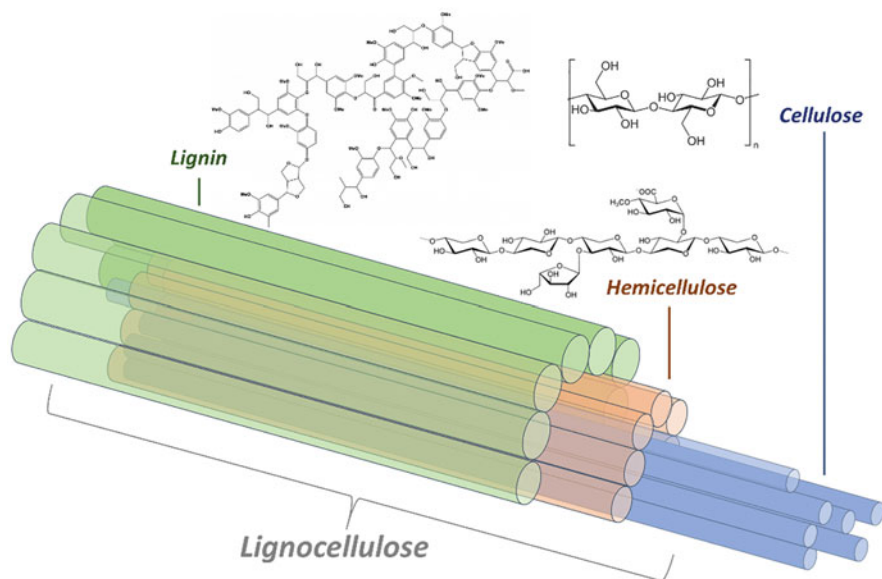


**Fig. 1.8** Simplified structure of lignocellulosic biomass with a cellulose core and subsequent layers of hemicellulose and lignin along with the representative chemical structure of each component

2016a). Work by Speltini et al. and Zhang et al. demonstrated the evolution of  $H_2$  from cellulose using Pt-TiO<sub>2</sub> under natural sunlight in Pavia, Italy (45°11'N, 9°09'E), and St Andrews, Scotland (56°20'N, 2°48'W), respectively. Both investigations exposed reaction solutions containing cellulose and a catalyst to natural unconcentrated light to achieve ~16  $\mu\text{mole } H_2$  formation over 6 h (Zhang et al. 2016a) and 33  $\mu\text{mole } H_2$  formation over 4 h (Speltini et al. 2014).

While solar-driven conversion of cellulose to  $H_2$  is a significant advancement, there is an argument to be made that using pure cellulose, that is,  $\alpha$ -cellulose for photocatalysis, is not a true representation of typical biomass composition. Lignocellulose composed of lignin, hemicellulose, and cellulose (Fig. 1.8) is the most abundant form of biomass and as such represents a compound that, if valorized, could significantly contribute toward renewable energy production. Therefore, there are now papers that have focused on the conversion of lignocellulosic material to  $H_2$  using typical visible light catalysts such as C<sub>3</sub>N<sub>4</sub> with a Ni co-catalyst (Kasap et al. 2018) and CdS (Wakerley et al. 2017). Wakerley et al. reported the conversion of lignocellulose to  $H_2$  using Cds/CdO<sub>x</sub>, which promoted both visible photon absorption via CdS and proton reduction and lignocellulose oxidation via CdO<sub>x</sub> (Wakerley et al. 2017). Prior to Wakerley et al.'s publication, the majority of photocatalytic cellulose reforming work focused on the use of TiO<sub>2</sub> and standard cellulose substrates such as  $\alpha$ -cellulose or microcrystalline cellulose, with only a few publications using alternative biomass substrates such as grass (Caravaca et al. 2016) and rice husks (Speltini et al. 2014; Lu et al. 2014). Alternatively, Wakerley and colleagues deployed CdS that was coated with CdOx as a photocatalyst along with  $\alpha$ -cellulose,

**Table 1.5** Tabulated results obtained by Wakerley et al. (2017) in their study on the photocatalytic reforming of lignocellulosic material

Substrate	Material	Substrate concentration	Hydrogen (mmol $\text{g}_{\text{cat}}^{-1} \text{h}^{-1}$ )
Standard feedstocks	$\alpha$ -Cellulose	50 mg $\text{mL}^{-1}$	$\sim 2.25$
	Hemicellulose–xylan from beech wood	25 mg $\text{mL}^{-1}$	$\sim 2.1$
	Lignin	0.25 mg $\text{mL}^{-1}$	$\sim 0.25$
Biomass feedstocks	Printer paper	50 mg $\text{mL}^{-1}$	$\sim 1.1$
	Cardboard		$\sim 0.75$
	Newspaper		$\sim 0.3$
	Wooden branch		$\sim 5.2$
	Bagasse		$\sim 0.3$
	Grass		$\sim 1.0$
	Sawdust		$\sim 0.75$

All reactions were performed using 0.5  $\mu\text{M}$  CdS/CdO<sub>x</sub> in 2 mL 10 M KOH at 25 °C in an anaerobic atmosphere and were irradiated for 24 h using a 100 mW  $\text{cm}^{-2}$  solar light simulator

hemicellulose, and lignin as standard starting materials and also a range of biomass substrates such as a printer paper, a wooden branch, and sawdust. The H<sub>2</sub> yields from each substrate have been summarized and are tabulated in Table 1.5, which shows activity under simulated solar light. While relatively low yields of H<sub>2</sub> were achieved, the impressive study did, for the first time, achieve photocatalytic conversion of raw biomass substrates under solar irradiation.

The use of CdS as the photocatalyst by Wakerley et al. was an interesting material choice. In the first instance, CdS is a favorable compound with a natural bandgap,  $E_{\text{bg}}$ , of 2.4 eV suitable for visible light activation, and has been proven to be active for H<sub>2</sub> production (Yang et al. 2012b) and is relatively inexpensive. Moreover, as lignin absorbs strongly in the UV region, typically around 300–400 nm, therefore lignin is unlikely to “block” visible photons from reaching CdS. In contrast, TiO<sub>2</sub>, which also absorbs strongly in the UV region, may have reduced activity due to competitive photon absorption. Incidentally, this is a limitation that has rarely been reported in the literature as to date there are limited examples of TiO<sub>2</sub> being used for photocatalytic lignin conversion. One of the few other examples, which used lignin as a feedstock, did so using a ZnO catalyst doped with C, N, and S to improve the visible light absorption properties of the material (Kadam et al. 2014). Kadam et al.’s study found that lignin degradation mildly enhanced the photocatalytic water splitting process. Despite the advantages of CdS, however, limitations associated with the stability and photo-corrosion of the compound have been well documented (Li et al. 2011; Fu et al. 2013). In addition, the valence band position of CdS, typically +1.9 V versus normal hydrogen electrode (NHE), does not support the formation of OH•. For OH• to be formed, the position of the valence band has to be more positive than +2.38 V versus NHE. OH• are important reactive oxygen species that have been suggested as the primary radicals responsible for cellulose oxidation. To overcome the limitations of CdS corrosion and valence band potentials,

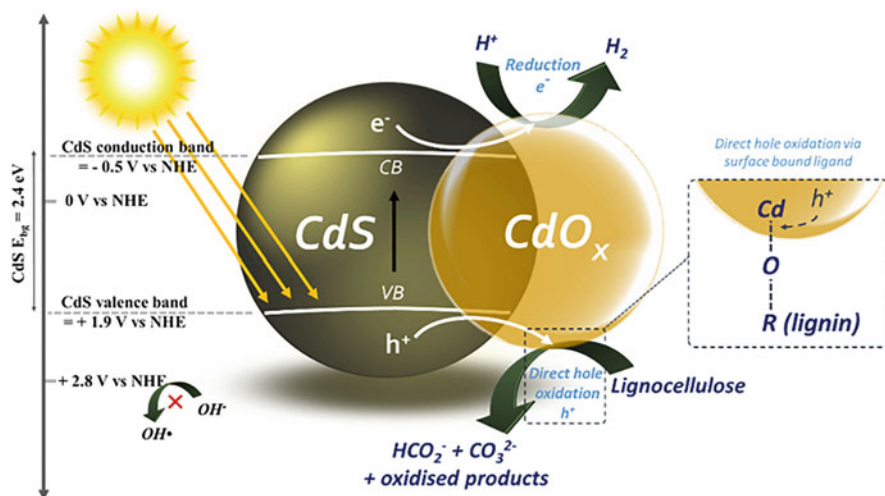


**Fig. 1.9** Mechanism suggested to be taking place in the work by Wakerley et al., which used CdS/CdO<sub>x</sub> to convert lignocellulose to both H<sub>2</sub> and oxidized product (Wakerley et al. 2017). (Illustration is based solely on information from the publication and is not a reprint)

Wakerley and colleagues performed reactions in a strong alkaline solution with 10 M KOH, which promoted the formation of Cd(OH)<sub>2</sub>/CdO, referred to as CdO<sub>x</sub>, on the CdS surface. The formation of Cd(OH)<sub>2</sub>/CdO structure suppressed photo-corrosion with the catalyst displaying activity for over 6 days of irradiation. Interestingly, however, the authors also suggested that in the absence of OH• production, the CdO<sub>x</sub> structure was responsible for the oxidation of lignocellulose material. An OH• probe molecule, namely terephthalic acid, was used to confirm that no OH radical formation occurred at pH 14 when CdS/CdO<sub>x</sub> was formed. Alternatively, direct hole oxidation at the surface of the catalyst was suggested as the dominant oxidation process. The presence of CdO<sub>x</sub> on the surface of CdS was suggested to promote effective binding between lignin and the catalyst via a Cd-O-R ligand, which would mirror the typical Ti-O-R bonds often reported during TiO<sub>2</sub> photocatalysis (Zhang et al. 2014, 2016a). Detection of products such as CO<sub>3</sub><sup>2-</sup> and HCO<sub>2</sub><sup>-</sup>, which were expected to form from the continued oxidation of alcohol and aldehydes, released from lignocellulose confirmed the hypothesis. An illustrative representation of the proposed mechanism is shown in Fig. 1.9.

In H<sub>2</sub> evolving photocatalytic SED systems, the role of the donor molecule is to undergo an irreversible oxidation, which subsequently supplies electrons/protons for the reduction reaction while suppressing the rate of recombination. In the case of cellulose, however, platform chemicals and biofuel feedstocks can potentially be produced from the oxidation pathway. To date, the work by Zhang et al., which demonstrated cellulose conversion under natural light, is one of the few publications to report H<sub>2</sub> production coupled with liquid phase product formation (Zhang et al. 2016a). Following irradiation in an anaerobic environment, high-performance liquid

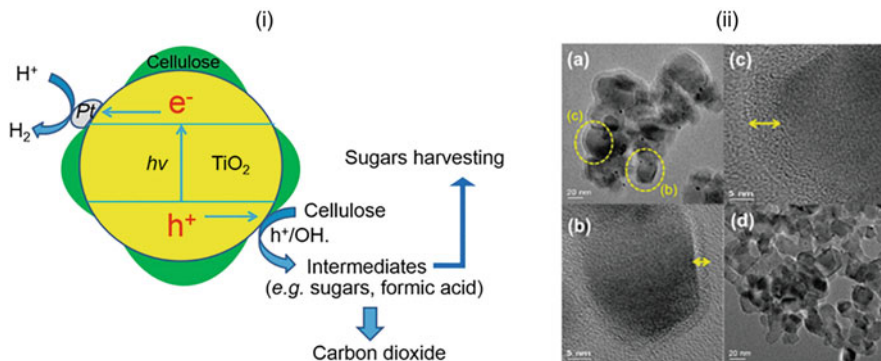


**Fig. 1.10** (i) Cellulose-TiO<sub>2</sub> composite material developed by Zhang et al. along with (ii) transmission electron microscopy (TEM) images showing a layer of cellulose around TiO<sub>2</sub> particles (a–c) and (d) bare Pt-TiO<sub>2</sub>. (Reprinted with permission from Zhang et al. (2016a), copyright (2016), The Royal Society of Chemistry)

chromatography (HPLC) analysis of the liquid phase showed the presence of glucose, cellobiose, and formic acid within the concentration range of 0.25 to ~1.2 μmol. Furthermore, over seven experimental cycles, glucose was detected in each, while cellobiose was only present in cycles 1–3 and formic acid only present in cycles 4–7. The presence of liquid phase compounds could be attributed to the method of deployment of cellulose in the study by Zhang and colleagues. In contrast to previous work, which typically used a cellulose–catalyst suspension in water (Speltini et al. 2014; Caravaca et al. 2016), Zhang et al.’s study developed a composite material, which consisted of a thin layer of cellulose grafted to the surface of TiO<sub>2</sub> particles (Fig. 1.10). The authors described the immobilization process as a two-step procedure involving condensation of surface hydroxyl groups and formation of intramolecular H-bonds between cellulose strands and TiO<sub>2</sub>. The approach of anchoring compounds to TiO<sub>2</sub> has been well documented and is ascribed to the formation of a “Ti-ligand” between the catalyst surface and compounds that have multiple hydroxyl groups (Zhang et al. 2014). The simultaneous production of H<sub>2</sub> and oxidation products by Zhang et al. was a significant achievement and demonstrated for the first time that photocatalytic cellulose reforming had a dual purpose—for renewable energy generation and as a pre-treatment method to release feedstocks for biofuel generation.

#### 1.4.2 Photocatalysis of Cellulose II

In a recent piece of work by Nagarajan, (via internal communication), cellulose II was produced from microcrystalline cellulose by dissolution in TBAH and precipitation with distilled water. Heterogeneous photocatalysis with suspended TiO<sub>2</sub> P25 photocatalyst and both cellulose I and II as feedstock was performed as a batch

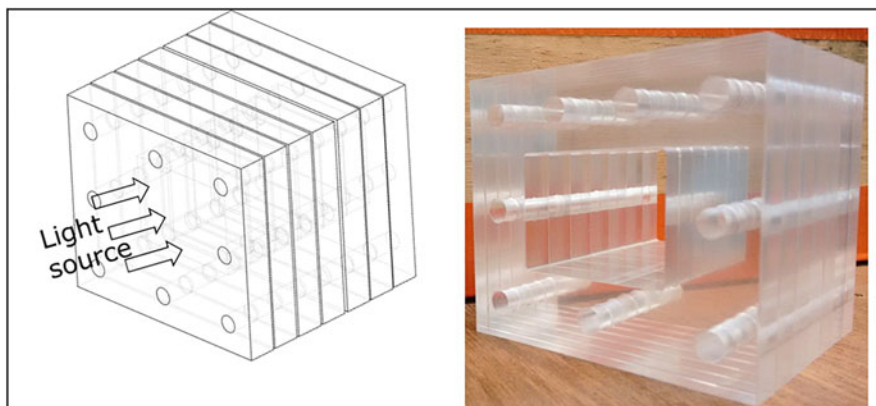


**Fig. 1.11** The stacked frame photocatalytic reactor used for fermentable sugar production from cellulose polymorphs

experiment in a beaker. In such a system, approximately fivefold increase in fermentable sugar production was observed upon photocatalysis of cellulose II when compared to cellulose I. With periodic separation of products using dialysis membrane bags, the cellulose II system produced 1.7 times higher fermentable sugars than the cellulose I system. Nagarajan's work was the first ever system to have observed and quantified fermentable sugars from cellulose II photocatalysis (Nagarajan 2017). The cellulose II production method used in the above process was similar to the one recently reported by Chang et al. (2019).

To further enhance the fermentable sugar yield, a stacked frame photocatalytic reactor (SFPR) was designed and used for the purpose. The design of the reactor has been reported by Nagarajan et al. (2017b). A schematic of the SFPR is shown in Fig. 1.11. With minor changes to the reported design, a separation chamber, separated by a dialysis membrane, was also included that aided in periodical removal of the produced fermentable sugars upon heterogeneous photocatalysis. The yield of fermentable sugars from cellulose II, upon photocatalysis, increased by  $\sim 3.5$  times when compared to the aforementioned beaker system using the same feedstock. Similarly, when the SFPR was operated with cellulose I as the feedstock, approximately four times improvement in yield was observed when compared to the beaker system. Comparing sugar yields from cellulose II and I in SFPR, fermentable sugar yields with the former was found to be  $\sim 1.5$  times higher than that observed with cellulose I feedstock. These results clearly indicate that cellulose II could be used as a superior feedstock for fermentable sugar production and thereby bioethanol production.

In the recent work by Chang et al., cellulose I and II were used as SEDs for photocatalytic  $H_2$  production (Chang et al. 2019). Pt loaded  $TiO_2$  was used as the photocatalyst and the reactions were performed in a novel propeller fluidized photo reactor (PFPR) irradiated with low power light emitting diodes (LEDs). The effect of type and concentration of starting cellulose polymorph, washed cellulose, and the

respective filtrate on the rates and yields of H<sub>2</sub> production was determined. The rate of photocatalytic H<sub>2</sub> production from cellulose II was 0.13 mmol min<sup>-1</sup> and was over twofolds higher than that achieved with cellulose I at 0.05 mmol min<sup>-1</sup>. The H<sub>2</sub> production with both the cases followed zero-order production kinetics. Lower crystallinity, particle size, and wettability possessed by cellulose II were established as reasons for higher H<sub>2</sub> yields. In addition to the previously mentioned study by Nagarajan in 2017, the study by Chang et al. has also shown that a novel process combining cellulose II and heterogeneous photocatalysis for fermentable sugars/energy production is possible. With further work focusing on photocatalytic reactor design and effective sugar separation, more exciting results could be achieved as well as new potentials could be unlocked to tweak the process toward sugar production or H<sub>2</sub> generation selectively.

## 1.5 Conclusion

While research on the utilization of cellulose as a feedstock for renewable fuel generation via photocatalysis has yielded some exciting and promising results, there are still some significant technical challenges that need to be overcome prior to the process being upscaled and commercially viable. While there has been much research on photoactive materials for photocatalysis for solar fuel generation, there has been significantly less activity on development of reactor technology for upscaling the process. Two of the key issues are the technical scalability and then the economic viability of the upscaled process.

To date, the photocatalytic yields of both H<sub>2</sub> and other fuel precursors have been low, at best in the μM range. For the first step in demonstrating a potentially viable process, a demonstrator unit capable of generating a minimum of between 1 and 5 m<sup>3</sup>h<sup>-1</sup> would need to be achieved. In designing a process that is both technically and economically viable, the following key factors are deemed important:

- Mode of photocatalyst deployment
- Photocatalyst distribution within the reactor
- Irradiation sources to activate the photocatalyst and light distribution characteristics within the reactor
- Mass transfer of cellulose within the photocatalytic reactor
- Reaction kinetics of the photocatalytic cellulose breakdown process
- Separation of the “fuel” precursors

The issue about cellulose solubility is a particular problem as the effective interaction of cellulose with the surface of the photocatalyst prior to reaction is greatly hindered. As detailed above, approaches such as ball milling prior to reaction have enhanced reaction yields but these are still relatively small. Other solvent systems will need to be investigated in detail; however, organic solvents also have problems as the photocatalyst may start preferentially reacting with the solvent rather than the cellulose. Effective visible light activated photocatalysts would probably be



a requirement for being economically viable. Over the past 25 years, there has been extensive research on visible light activated materials; however, to date the performance of visible light photocatalysts still falls short of UV-activated materials such as Evonik P25 TiO<sub>2</sub>. If UV materials are to be utilized, significant advances happening in UV LED technology over the past decade have to be exploited, which of course would require less power. Once the technical challenges of producing a large-scale reactor have been overcome, there are still issues that need to be addressed to demonstrate that the process is also economically viable. Energy balance needs to be established to demonstrate that there is more energy being generated from the process than is being put in to generate the fuel. In addition, demonstration of the cost per kWh of the fuel produced must be competitive with alternative systems. Finally, a practical life cycle analysis (LCA) model will have to be established for the photocatalytic process to provide an effective understanding of the economic and environmental impacts of the complete process for photocatalytic valorization cellulose. This is also not an inconsiderable challenge as there are currently a lack of LCA models for photocatalytic renewable energy production.

Systems for generating fuels based on semiconductor photocatalysis for renewable energy generation not utilizing cellulose also face these challenges despite being extensively researched for over the past 40 years for the reduction of water to H<sub>2</sub>. To date there are still no larger-scale commercial systems. One example of a larger-scale system that is being developed is the ARPChem project that involves Professor Domen's group at the University of Tokyo and a number of industrial partners including Mitsubishi Chemical, Mitsui Chemical, Sumitomo Chemical, Fuji Films, Inpex, and TOTO, which started in 2012 (Yamada and Domen 2018). The aim of the ARPChem project is to establish an artificial photosynthetic plant by 2030. Some further interesting examples of larger-scale applications of solar H<sub>2</sub> generation have been considered in a recent review by Liu and Xu (Liu et al. 2019b).

Overall, the chapter has emphasized on the growing interest within the research community on the utilization of cellulose and lignocellulosic materials as feedstock for photocatalytic fermentable sugar and H<sub>2</sub> generation. Furthermore, the authors believe that cellulose II utilization could provide a favorable way forward in combination with photocatalysis. The goal of the chapter is to instigate interest among the readers on the potential of heterogenous photocatalysis as a cellulose breakdown method. With huge gaps in the polymorph pre-processing, reactor design, challenges in light distribution, and product separation, there is scope for improvement in each of these areas with additional future research.

**Acknowledgments** Dr. Sanjay Nagarajan would like to acknowledge Queen's University Belfast (QUB) for funding his research while Dr. Nathan Skillen would like to acknowledge the Pioneering Research Program at QUB for funding his research. This work was supported by the Engineering and Physical Sciences Research Council, project number EP/K036769/1. The authors would also like to acknowledge the support of Professor John Irvine, University of St. Andrews, Fife, United Kingdom, and his research group for their valuable contribution and support throughout the project EP/K036769/1.

## References

- Abe M, Fukaya Y, Ohno H (2012) Fast and facile dissolution of cellulose with tetrabutylphosphonium hydroxide containing 40 wt% water. *Chem Commun* 48 (12):1808–1810. <https://doi.org/10.1039/C2CC16203B>
- Abe M, Kuroda K, Ohno H (2015) Maintenance-free cellulose solvents based on onium hydroxides. *ACS Sustain Chem Eng* 3(8):1771–1776. <https://doi.org/10.1021/acssuschemeng.5b00303>
- Alinia R, Zabihi S, Esmailzadeh F, Kalajahi JF (2010) Pretreatment of wheat straw by supercritical CO<sub>2</sub> and its enzymatic hydrolysis for sugar production. *Biosyst Eng* 107(1):61–66. <https://doi.org/10.1016/j.biosystemseng.2010.07.002>
- Alves L, Medronho BF, Antunes FE, Romano A, Miguel MG, Lindman B (2015) On the role of hydrophobic interactions in cellulose dissolution and regeneration: colloidal aggregates and molecular solutions. *Colloids Surf A Physicochem Eng Asp* 483:257–263. <https://doi.org/10.1016/j.colsurfa.2015.03.011>
- Alvira P, Tomás-Pejó E, Ballesteros M, Negro MJ (2010) Pretreatment technologies for an efficient bioethanol production process based on enzymatic hydrolysis: a review. *Bioresour Technol* 101 (13):4851–4861. <https://doi.org/10.1016/j.biortech.2009.11.093>
- Aranes V, Milagres AMF (2006) Degradation of cellulosic and hemicellulosic substrates using a chelator-mediated Fenton reaction. *J Chem Technol Biotechnol* 81(3):413–419. <https://doi.org/10.1002/jctb.1417>
- Bahruji H, Bowker M, Davies PR, Al-Mazroai LS, Dickinson A, Greaves J, James D, Millard L, Pedrono F (2010) Sustainable H<sub>2</sub> gas production by photocatalysis. *J Photochem Photobiol A Chem* 216(2):115–118. <https://doi.org/10.1016/j.jphotochem.2010.06.022>
- Behrens MA, Holdaway JA, Nosrati P, Olsson U (2016) On the dissolution state of cellulose in aqueous tetrabutylammonium hydroxide solutions. *RSC Adv* 6(36):30199–30204. <https://doi.org/10.1039/C6RA03547G>
- Boissou F, Muhlbauer A, De OV, Leclercq L, Kunz W, Marinkovic S, Estrine B, Nardello-Rataj V, Jerome F (2014) Transition of cellulose crystalline structure in biodegradable mixtures of renewably-sourced levulinic alkyl ammonium ionic liquids,  $\gamma$ -valerolactone and water. *Green Chem* 16(5):2463–2471. <https://doi.org/10.1039/C3GC42396D>
- Bokinsky G, Peralta-Yahya PP, George A, Holmes BM, Steen EJ, Dietrich J, Soon Lee T, Tullman-Ereck D, Voigt CA, Simmons BA, Keasling JD (2011) Synthesis of three advanced biofuels from ionic liquid-pretreated switchgrass using engineered *Escherichia coli*. *Proc Natl Acad Sci U S A* 108(50):19949–19954. <https://doi.org/10.1073/pnas.1106958108>
- Bowker M, Davies PR, Al-Mazroai L (2008) Photocatalytic reforming of glycerol over gold and palladium as an alternative fuel source. *Catal Lett* 128(3):253. <https://doi.org/10.1007/s10562-008-9781-1>
- Brundtland GH (1987) Our common future United Nations World Commission on Environment and Development. Available online at <http://www.un-documents.net/our-common-future.pdf>. Accessed Oct 2019
- Caravaca A, Jones W, Hardacre C, Bowker M (2016) H<sub>2</sub> production by the photocatalytic reforming of cellulose and raw biomass using Ni, Pd, Pt and Au on titania. *Proc R Soc A-Math Phys* 472(2191):20160054. <https://doi.org/10.1098/rspa.2016.0054>
- Chang C, Skillen N, Nagarajan S, Ralphs K, Irvine JTS, Lawton L, Robertson PKJ (2019) Using cellulose polymorphs for enhanced hydrogen production from photocatalytic reforming. *Sustain Energy Fuels* 3(8):1971–1975. <https://doi.org/10.1039/C9SE00377K>
- Chen W, Pen B, Yu C, Hwang W (2011) Pretreatment efficiency and structural characterization of rice straw by an integrated process of dilute-acid and steam explosion for bioethanol production. *Bioresour Technol* 102(3):2916–2924. <https://doi.org/10.1016/j.biortech.2010.11.052>
- Chen H, Liu J, Chang X, Chen D, Xue Y, Liu P, Lin H, Han S (2017) A review on the pretreatment of lignocellulose for high-value chemicals. *Fuel Process Technol* 160:196–206. <https://doi.org/10.1016/j.fuproc.2016.12.007>

- Chen W, Chan A, Sun-Waterhouse D, Llorca J, Idriss H, Waterhouse GIN (2018) Performance comparison of Ni/TiO<sub>2</sub> and Au/TiO<sub>2</sub> photocatalysts for H<sub>2</sub> production in different alcohol-water mixtures. *J Catal* 367:27–42. <https://doi.org/10.1016/j.jcat.2018.08.015>
- Cheng G, Varanasi P, Li C, Liu H, Melnichenko YB, Simmons BA, Kent MS, Singh S (2011) Transition of cellulose crystalline structure and surface morphology of biomass as a function of ionic liquid pretreatment and its relation to enzymatic hydrolysis. *Biomacromolecules* 12(4):933–941. <https://doi.org/10.1021/bm101240z>
- Chong R, Li J, Ma Y, Zhang B, Han H, Li C (2014) Selective conversion of aqueous glucose to value-added sugar aldose on TiO<sub>2</sub>-based photocatalysts. *J Catal* 314:101–108. <https://doi.org/10.1016/j.jcat.2014.03.009>
- Colmenares JC, Magdziarz A, Bielejewska A (2011) High-value chemicals obtained from selective photo-oxidation of glucose in the presence of nanostructured titanium photocatalysts. *Bioresour Technol* 102(24):11254–11257. <https://doi.org/10.1016/j.biortech.2011.09.101>
- Colón G (2016) Towards the hydrogen production by photocatalysis. *Appl Catal A* 518:48–59. <https://doi.org/10.1016/j.apcata.2015.11.042>
- Cross CF, Bevan EJ, Beadle C (1893a) Die Chemie der Pflanzenfasern. Cellulosen, Oxycellulosen, Lignocellulosen. *Ber Dtsch Chem Ges* 26(3):2520–2533. <https://doi.org/10.1002/cber.18930260348>
- Cross CF, Bevan ET, Beadle C (1893b) Thiokohlensäureester der Cellulose. *Ber Dtsch Chem Ges* 26(1):1090–1097. <https://doi.org/10.1002/cber.189302601230>
- da Costa Sousa L, Jin M, Chundawat SPS, Bokade V, Tang X, Azarpira A, Lu F, Avci U, Humpala J, Uppugundla N, Gunawan C, Pattathil S, Cheh AM, Kothari N, Kumar R, Ralph J, Hahn MG, Wyman CE, Singh S, Simmons BA et al (2016) Next-generation ammonia pretreatment enhances cellulosic biofuel production. *Energy Environ Sci* 9(4):1215–1223. <https://doi.org/10.1039/C5EE03051J>
- Da Vià L, Recchi C, Gonzalez-Yañez EO, Davies TE, Lopez-Sanchez JA (2017) Visible light selective photocatalytic conversion of glucose by TiO<sub>2</sub>. *Appl Catal B Environ* 202:281–288. <https://doi.org/10.1016/j.apcatb.2016.08.035>
- Dadi AP, Varanasi S, Schall CA (2006) Enhancement of cellulose saccharification kinetics using an ionic liquid pretreatment step. *Biotechnol Bioeng* 95(5):904–910. <https://doi.org/10.1002/bit.21047>
- Dadi AP, Schall CA, Varanasi S (2007) Mitigation of cellulose recalcitrance to enzymatic hydrolysis by ionic liquid pretreatment. *Appl Biochem Biotechnol* 137(1):407–421. <https://doi.org/10.1007/s12010-007-9068-9>
- Daghrir R, Drogui P, Robert D (2013) Modified TiO<sub>2</sub> for environmental photocatalytic applications: a review. *Ind Eng Chem Res* 52(10):3581–3599. <https://doi.org/10.1021/ie303468t>
- Dinand E, Vignon M, Chanzy H, Heux L (2002) Mercerization of primary wall cellulose and its implication for the conversion of cellulose I→cellulose II. *Cellulose* 9(1):7–18. <https://doi.org/10.1023/A:1015877021688>
- Dutta S, De S, Alam MI, Abu-Omar MM, Saha B (2012) Direct conversion of cellulose and lignocellulosic biomass into chemicals and biofuel with metal chloride catalysts. *J Catal* 288:8–15. <https://doi.org/10.1016/j.jcat.2011.12.017>
- Ershov BG (1998) Radiation-chemical degradation of cellulose and other polysaccharides. *Russ Chem Rev* 67(4):315–334. <https://doi.org/10.1070/RC1998v067n04ABEH000379>
- Fan LT, Lee Y, Beardmore DR (1981) The influence of major structural features of cellulose on rate of enzymatic hydrolysis. *Biotechnol Bioeng* 23(2):419–424. <https://doi.org/10.1002/bit.260230215>
- Fu D, Mazza G (2011) Aqueous ionic liquid pretreatment of straw. *Bioresour Technol* 102(13):7008–7011. <https://doi.org/10.1016/j.biortech.2011.04.049>
- Fu X, Long J, Wang X, Leung DYC, Ding Z, Wu L, Zhang Z, Li Z, Fu X (2008) Photocatalytic reforming of biomass: a systematic study of hydrogen evolution from glucose solution. *Int J Hydrog Energy* 33(22):6484–6491. <https://doi.org/10.1016/j.ijhydene.2008.07.068>

- Fu J, Chang B, Tian Y, Xi F, Dong X (2013) Novel C<sub>3</sub>N<sub>4</sub>-CdS composite photocatalysts with organic-inorganic heterojunctions: in situ synthesis, exceptional activity, high stability and photocatalytic mechanism. *J Mater Chem A* 1(9):3083-3090. <https://doi.org/10.1039/C2TA00672C>
- Fujishima A, Honda K (1972) Electrochemical photolysis of water at a semiconductor electrode. *Nature* 238(5358):37-38. <https://doi.org/10.1038/238037a0>
- Gao M, Xu F, Li S, Ji X, Chen S, Zhang D (2010) Effect of SC-CO<sub>2</sub> pretreatment in increasing rice straw biomass conversion. *Biosyst Eng* 106(4):470-475. <https://doi.org/10.1016/j.biosystemseng.2010.05.011>
- Giménez J, Curc6 D, Queral MA (1999) Photocatalytic treatment of phenol and 2,4-dichlorophenol in a solar plant in the way to scaling-up. *Catal Today* 54(2):229-243. [https://doi.org/10.1016/S0920-5861\(99\)00185-6](https://doi.org/10.1016/S0920-5861(99)00185-6)
- Guenet J (2008) Chapter 5 - cellulose. In: Guenet J (ed) *Polymer-solvent molecular compounds*. Elsevier, Amsterdam, pp 57-69
- Halonen H, Larsson PT, Iversen T (2012) Mercerized cellulose biocomposites: a study of influence of mercerization on cellulose supramolecular structure, water retention value and tensile properties. *Cellulose* 20(1):57-65. <https://doi.org/10.1007/s10570-012-9801-6>
- Hao H, Zhang L, Wang W, Zeng S (2018) Facile modification of titania with nickel sulfide and sulfate species for the photoreformation of cellulose into hydrogen. *ChemSusChem* 11(16):2810-2817. <https://doi.org/10.1002/cssc.201800743>
- Hastrup ACS, Jensen B, Green III F (2010) Chemical mediated depolymerization of cotton cellulose for the understanding of non-enzymatic fungal decay. In: Anonymous the International Research Group on Wood Protection, 9-13, May, Biarritz, France
- Hideno A, Inoue H, Tsukahara K, Fujimoto S, Minowa T, Inoue S, Endo T, Sawayama S (2009) Wet disk milling pretreatment without sulfuric acid for enzymatic hydrolysis of rice straw. *Bioresour Technol* 100(10):2706-2711. <https://doi.org/10.1016/j.biortech.2008.12.057>
- Hou X, Smith TJ, Li N, Zong M (2012) Novel renewable ionic liquids as highly effective solvents for pretreatment of rice straw biomass by selective removal of lignin. *Biotechnol Bioeng* 109(10):2484-2493. <https://doi.org/10.1002/bit.24522>
- Iervolino G, Vaiano V, Sannino D, Rizzo L, Ciambelli P (2016) Production of hydrogen from glucose by LaFeO<sub>3</sub> based photocatalytic process during water treatment. *Int J Hydrog Energy* 41(2):959-966. <https://doi.org/10.1016/j.ijhydene.2015.10.085>
- Iervolino G, Vaiano V, Sannino D, Rizzo L, Galluzzi A, Polichetti M, Pepe G, Campiglia P (2018) Hydrogen production from glucose degradation in water and wastewater treated by Ru-LaFeO<sub>3</sub>/Fe<sub>2</sub>O<sub>3</sub> magnetic particles photocatalysis and heterogeneous photo-Fenton. *Int J Hydrog Energy* 43(4):2184-2196. <https://doi.org/10.1016/j.ijhydene.2017.12.071>
- Inoue T, Fujishima A, Konishi S, Honda K (1979) Photoelectrocatalytic reduction of carbon dioxide in aqueous suspensions of semiconductor powders. *Nature* 277(5698):637-638. <https://doi.org/10.1038/277637a0>
- International Energy Agency World Energy Outlook (2018) Available online at <https://www.iea.org/weo2018/>. Accessed Aug 2019
- Jia X, Chen Y, Shi C, Ye Y, Wang P, Zeng X, Wu T (2013) Preparation and characterization of cellulose regenerated from phosphoric acid. *J Agric Food Chem* 61(50):12405-12414. <https://doi.org/10.1021/jf4042358>
- Jin E, Guo J, Yang F, Zhu Y, Song J, Jin Y, Rojas OJ (2016) On the polymorphic and morphological changes of cellulose nanocrystals (CNC-I) upon mercerization and conversion to CNC-II. *Carbohydr Polym* 143:327-335. <https://doi.org/10.1016/j.carbpol.2016.01.048>
- Jin B, Yao G, Wang X, Ding K, Jin F (2017) Photocatalytic oxidation of glucose into formate on nano TiO<sub>2</sub> catalyst. *ACS Sustain Chem Eng* 5(8):6377-6381. <https://doi.org/10.1021/acsuschemeng.7b00364>
- Kadam SR, Mate VR, Panmand RP, Nikam LK, Kulkarni MV, Sonawane RS, Kale BB (2014) A green process for efficient lignin (biomass) degradation and hydrogen production via water

- splitting using nanostructured C, N, S-doped ZnO under solar light. *RSC Adv* 4 (105):60626–60635. <https://doi.org/10.1039/C4RA10760H>
- Kasap H, Achilleos DS, Huang A, Reisner E (2018) Photoreforming of lignocellulose into H<sub>2</sub> using nanoengineered carbon nitride under benign conditions. *J Am Chem Soc* 140 (37):11604–11607. <https://doi.org/10.1021/jacs.8b07853>
- Kawai T, Sakata T (1980) Conversion of carbohydrate into hydrogen fuel by a photocatalytic process. *Nature* 286(5772):474–476. <https://doi.org/10.1038/286474a0>
- Kim G, Lee S, Choi W (2015) Glucose–TiO<sub>2</sub> charge transfer complex-mediated photocatalysis under visible light. *Appl Catal B Environ* 162:463–469. <https://doi.org/10.1016/j.apcatb.2014.07.027>
- Klemm D, Philipp B, Heinze T, Heinze U, Wagenknecht W (1998) General considerations on structure and reactivity of cellulose: section 2.1–2.1.4. In: Anonymous comprehensive cellulose chemistry. Wiley-VCH Verlag GmbH & Co. KGaA, pp 9–29
- Klemm D, Heublein B, Fink H, Bohn A (2005) Cellulose: fascinating biopolymer and sustainable raw material. *Angew Chem Int Ed* 44(22):3358–3393. <https://doi.org/10.1002/anie.200460587>
- Kojima Y, Takayasu M, Toma M, Koda S (2019) Degradation of cellulose in NaOH and NaOH/urea aqueous solutions by ultrasonic irradiation. *Ultrason Sonochem* 51:419–423. <https://doi.org/10.1016/j.ulsonch.2018.07.030>
- Kuga S, Takagi S, Brown RM (1993) Native folded-chain cellulose II. *Polymer* 34(15):3293–3297. [https://doi.org/10.1016/0032-3861\(93\)90404-X](https://doi.org/10.1016/0032-3861(93)90404-X)
- Kumar AK, Sharma S (2017) Recent updates on different methods of pretreatment of lignocellulosic feedstocks: a review. *Bioresour Bioprocess* 4(1):7. <https://doi.org/10.1186/s40643-017-0137-9>
- Kumar R, Wyman CE (2009) Effects of cellulase and xylanase enzymes on the deconstruction of solids from pretreatment of poplar by leading technologies. *Biotechnol Prog* 25(2):302–314. <https://doi.org/10.1002/btpr.102>
- Lavoine N, Desloges I, Dufresne A, Bras J (2012) Microfibrillated cellulose – its barrier properties and applications in cellulosic materials: a review. *Carbohydr Polym* 90(2):735–764. <https://doi.org/10.1016/j.carbpol.2012.05.026>
- Li Q, Guo B, Yu J, Ran J, Zhang B, Yan H, Gong JR (2011) Highly efficient visible-light-driven photocatalytic hydrogen production of CdS-cluster-decorated graphene nanosheets. *J Am Chem Soc* 133(28):10878–10884. <https://doi.org/10.1021/ja2025454>
- Li C, Wang L, Chen Z, Li Y, Wang R, Luo X, Cai G, Li Y, Yu Q, Lu J (2015) Ozonolysis pretreatment of maize stover: the interactive effect of sample particle size and moisture on ozonolysis process. *Bioresour Technol* 183:240–247
- Lindman B, Karlström G, Stigsson L (2010) On the mechanism of dissolution of cellulose. *J Mol Liq* 156(1):76–81. <https://doi.org/10.1016/j.molliq.2010.04.016>
- Liu W, Zhao S, Li L, Xin XZ (2015) Enhancement of cellulose reactivity using an ionic liquid pretreatment step. *Cellul Chem Technol* 49:397–403
- Liu X, Duan X, Wei W, Wang S, Ni B (2019a) Photocatalytic conversion of lignocellulosic biomass to valuable products. *Green Chem* 21(16):4266–4289. <https://doi.org/10.1039/C9GC01728C>
- Liu G, Sheng Y, Ager JW, Kraft M, Xu R (2019b) Research advances towards large-scale solar hydrogen production from water. *EnergyChem* 1(2):100014. <https://doi.org/10.1016/j.enchem.2019.100014>
- Lu Y, Wei X, Wen Z, Chen H, Lu Y, Zong Z, Cao J, Qi S, Wang S, Yu L, Zhao W, Fan X, Zhao Y (2014) Photocatalytic depolymerization of rice husk over TiO<sub>2</sub> with H<sub>2</sub>O<sub>2</sub>. *Fuel Process Technol* 117:8–16. <https://doi.org/10.1016/j.fuproc.2013.04.001>
- Luo N, Fu X, Cao F, Xiao T, Edwards PP (2008) Glycerol aqueous phase reforming for hydrogen generation over Pt catalyst – Effect of catalyst composition and reaction conditions. *Fuel* 87 (17):3483–3489. <https://doi.org/10.1016/j.fuel.2008.06.021>
- Lyashenko LV, Gorokhovat-skii Y (1975) Photocatalytic oxidation of carbon monoxide on metal oxides. *Theor Exp Chem* 10(2):138–142. <https://doi.org/10.1007/BF00524461>

- Ma H, Zhang B, Zhang P, Li S, Gao Y, Hu X (2016) An efficient process for lignin extraction and enzymatic hydrolysis of corn stalk by pyrrolidonium ionic liquids. *Fuel Process Technol* 148:138–145. <https://doi.org/10.1016/j.fuproc.2016.02.038>
- Machado AEH, Furuyama AM, Falone SZ, Ruggiero R, Perez DS, Castellan A (2000) Photocatalytic degradation of lignin and lignin models, using titanium dioxide: the role of the hydroxyl radical. *Chemosphere* 40(1):115–124. [https://doi.org/10.1016/S0045-6535\(99\)00269-6](https://doi.org/10.1016/S0045-6535(99)00269-6)
- Malato S, Fernández-Ibáñez P, Maldonado MI, Blanco J, Gernjak W (2009) Decontamination and disinfection of water by solar photocatalysis: recent overview and trends. *Catal Today* 147(1):1–59. <https://doi.org/10.1016/j.cattod.2009.06.018>
- Matsuoka M, Kitano M, Takeuchi M, Tsujimaru K, Anpo M, Thomas JM (2007) Photocatalysis for new energy production: recent advances in photocatalytic water splitting reactions for hydrogen production. *Catal Today* 122(1):51–61. <https://doi.org/10.1016/j.cattod.2007.01.042>
- Maurino V, Bedini A, Minella M, Rubertelli F, Pelizzetti E, Minero C (2008) Glycerol transformation through photocatalysis: a possible route to value added chemicals. *J Adv Oxid Technol* 11:184–192. <https://doi.org/10.1515/jaots-2008-0201>
- Medronho B, Lindman B (2014) Competing forces during cellulose dissolution: from solvents to mechanisms. *Curr Opin Colloid Interface Sci* 19(1):32–40. <https://doi.org/10.1016/j.cocis.2013.12.001>
- Medronho B, Lindman B (2015) Brief overview on cellulose dissolution/regeneration interactions and mechanisms. *Adv Colloid Interf Sci* 222:502–508. <https://doi.org/10.1016/j.cis.2014.05.004>
- Meng D, Li G, Liu Z, Yang F (2011) Study of depolymerization of cotton cellulose by Pb/PbO<sub>2</sub> anode electrochemical catalysis in sulfuric acid solution. *Polym Degrad Stab* 96(7):1173–1178. <https://doi.org/10.1016/j.polymdegradstab.2011.04.021>
- Mercer J (1850) Improvements in the preparation of cotton and other fabrics and other fibrous materials
- Miao Z, Grift TE, Hansen AC, Ting KC (2011) Energy requirement for comminution of biomass in relation to particle physical properties. *Ind Crop Prod* 33(2):504–513. <https://doi.org/10.1016/j.indcrop.2010.12.016>
- Mittal A, Katahira R, Himmel ME, Johnson DK (2011) Effects of alkaline or liquid-ammonia treatment on crystalline cellulose: changes in crystalline structure and effects on enzymatic digestibility. *Biotechnol Biofuels* 4(1):1–16. <https://doi.org/10.1186/1754-6834-4-41>
- Nagarajan S (2017) Development of photocatalytic reactor technology for the production of fermentable sugars. PhD, Queen's University Belfast. Available online at <https://pure.qub.ac.uk/en/studentTheses/development-of-photocatalytic-reactor-technology-for-the-producti>. Accessed Oct 2019
- Nagarajan S, Skillen NC, Irvine JTS, Lawton LA, Robertson PKJ (2017a) Cellulose II as bioethanol feedstock and its advantages over native cellulose. *Renew Sust Energ Rev* 77(Suppl C):182–192. <https://doi.org/10.1016/j.rser.2017.03.118>
- Nagarajan S, Stella L, Lawton LA, Irvine JTS, Robertson PKJ (2017b) Mixing regime simulation and cellulose particle tracing in a stacked frame photocatalytic reactor. *Chem Eng J* 313:301–308. <https://doi.org/10.1016/j.cej.2016.12.016>
- O'Sullivan A (1997) Cellulose: the structure slowly unravels. *Cellulose* 4(3):173–207. <https://doi.org/10.1023/A:1018431705579>
- Odorico FH, Morandim-Giannetti A, Lucarini AC, Torres RB (2018) Pretreatment of Guinea grass (*Panicum maximum*) with the ionic liquid 1-ethyl-3-methyl imidazolium acetate for efficient hydrolysis and bioethanol production. *Cellulose* 25(5):2997–3009. <https://doi.org/10.1007/s10570-018-1753-z>
- Oturan MA, Aaron J (2014) Advanced oxidation processes in water/wastewater treatment: principles and applications. A review. *Crit Rev Environ Sci Technol* 44(23):2577–2641. <https://doi.org/10.1080/10643389.2013.829765>

- Park JI, Steen EJ, Burd H, Evans SS, Redding-Johnson A, Bath T, Benke PI, D'haeseleer P, Sun N, Sale KL, Keasling JD, Lee TS, Petzold CJ, Mukhopadhyay A, Singer SW, Simmons BA, Gladden JM (2012) A thermophilic ionic liquid-tolerant cellulase cocktail for the production of cellulosic biofuels. *PLoS One* 7(5):e37010. <https://doi.org/10.1371/journal.pone.0037010>
- Pena CA, Soto A, King AWT, Rodríguez H (2019) Improved reactivity of cellulose via its crystallinity reduction by nondissolving pretreatment with an ionic liquid. *ACS Sustain Chem Eng* 7(10):9164–9171. <https://doi.org/10.1021/acssuschemeng.8b06357>
- Pinkert A, Marsh KN, Pang S, Staiger MP (2009) Ionic liquids and their interaction with cellulose. *Chem Rev* 109(12):6712–6728. <https://doi.org/10.1021/cr9001947>
- Ray MJ, Leak DJ, Spanu PD, Murphy RJ (2010) Brown rot fungal early stage decay mechanism as a biological pretreatment for softwood biomass in biofuel production. *Biomass Bioenergy* 34(8):1257–1262. <https://doi.org/10.1016/j.biombioe.2010.03.015>
- Revol JF, Dietrich A, Goring DAI (1987) Effect of mercerization on the crystallite size and crystallinity index in cellulose from different sources. *Can J Chem* 65(8):1724–1725. <https://doi.org/10.1139/v87-288>
- Saha BC, Iten LB, Cotta MA, Wu YV (2005) Dilute acid pretreatment, enzymatic saccharification and fermentation of wheat straw to ethanol. *Process Biochem* 40(12):3693–3700. <https://doi.org/10.1016/j.procbio.2005.04.006>
- Saha BC, Qureshi N, Kennedy GJ, Cotta MA (2016) Biological pretreatment of corn stover with white-rot fungus for improved enzymatic hydrolysis. *Int Biodeterior Biodegradation* 109:29–35. <https://doi.org/10.1016/j.ibiod.2015.12.020>
- Sakurada I, Hutino K (1936) Über die intrazelluläre Quellung der Zellulose durch Wasser. *Kolloid Z* 77(3):346–351. <https://doi.org/10.1007/BF01433526>
- Samayam IP, Hanson BL, Langan P, Schall CA (2011) Ionic-liquid induced changes in cellulose structure associated with enhanced biomass hydrolysis. *Biomacromolecules* 12(8):3091–3098. <https://doi.org/10.1021/bm200736a>
- Sasaki M, Adschiri T, Arai K (2003) Production of cellulose II from native cellulose by near- and supercritical water solubilization. *J Agric Food Chem* 51(18):5376–5381. <https://doi.org/10.1021/jf025989i>
- Sassner P, Mårtensson C, Galbe M, Zacchi G (2008) Steam pretreatment of H<sub>2</sub>SO<sub>4</sub>-impregnated *Salix* for the production of bioethanol. *Bioresour Technol* 99(1):137–145. <https://doi.org/10.1016/j.biortech.2006.11.039>
- Scordia D, Cosentino SL, Lee J, Jeffries TW (2011) Dilute oxalic acid pretreatment for biorefining giant reed (*Arundo donax* L.). *Biomass Bioenergy* 35(7):3018–3024. <https://doi.org/10.1016/j.biombioe.2011.03.046>
- Shafiei M, Zilouei H, Zamani A, Taherzadeh MJ, Karimi K (2013) Enhancement of ethanol production from spruce wood chips by ionic liquid pretreatment. *Appl Energy* 102:163–169. <https://doi.org/10.1016/j.apenergy.2012.05.060>
- Sharma S, Nair SS, Zhang Z, Ragauskas AJ, Deng Y (2015) Characterization of micro fibrillation process of cellulose and mercerized cellulose pulp. *RSC Adv* 5(77):63111–63122. <https://doi.org/10.1039/C5RA09068G>
- Shibazaki H, Saito M, Kuga S, Okano T (1998) Native cellulose II production by *Acetobacter Xylinum* under physical constraints. *Cellulose* 5(3):165–173. <https://doi.org/10.1023/A:1009277122329>
- Silveira MHL, Morais ARC, AMd L, Oleksyszyn DN, Bogel-Lukasik R, Andreau J, Ramos LP (2015) Current pretreatment technologies for the development of cellulosic ethanol and biorefineries. *ChemSusChem* 8(20):3366–3390. <https://doi.org/10.1002/cssc.201500282>
- Silverstein RA (2005) A comparison of chemical pretreatment methods for converting cotton stalks to ethanol. Master of Science, North Carolina State University
- Sindhu R, Binod P, Pandey A (2016) Biological pretreatment of lignocellulosic biomass – an overview. *Bioresour Technol* 199:76–82. <https://doi.org/10.1016/j.biortech.2015.08.030>
- Sjöström E (1993) *Wood chemistry: fundamentals and applications*. Academic, London

- Skillen N, McCullagh C, Adams M (2015) Photocatalytic splitting of water. In: Bahnemann DW, Robertson PKJ (eds) Environmental photochemistry part III. Springer Berlin Heidelberg, Berlin/Heidelberg, pp 45–86
- Skillen N, Adams M, McCullagh C, Ryu SY, Fina F, Hoffmann MR, Irvine JTS, Robertson PKJ (2016) The application of a novel fluidised photo reactor under UV–visible and natural solar irradiation in the photocatalytic generation of hydrogen. *Chem Eng J* 286:610–621. <https://doi.org/10.1016/j.cej.2015.10.101>
- Slamet, Ratnawati, Gunlazuardi J, Dewi EL (2017) Enhanced photocatalytic activity of Pt deposited on titania nanotube arrays for the hydrogen production with glycerol as a sacrificial agent. *Int J Hydrog Energy* 42(38):24014–24025. <https://doi.org/10.1016/j.ijhydene.2017.07.208>
- Speltini A, Sturini M, Dondi D, Annovazzi E, Maraschi F, Caratto V, Profumo A, Buttafava A (2014) Sunlight-promoted photocatalytic hydrogen gas evolution from water-suspended cellulose: a systematic study. *Photochem Photobiol Sci* 13(10):1410–1419. <https://doi.org/10.1039/C4PP00128A>
- Sun Y, Cheng J (2002) Hydrolysis of lignocellulosic materials for ethanol production: a review. *Bioresour Technol* 83(1):1–11. [https://doi.org/10.1016/S0960-8524\(01\)00212-7](https://doi.org/10.1016/S0960-8524(01)00212-7)
- Swatloski RP, Spear SK, Holbrey JD, Rogers RD (2002) Dissolution of cellulose with ionic liquids. *J Am Chem Soc* 124(18):4974–4975. <https://doi.org/10.1021/ja025790m>
- van der Hoeven M (2013) World energy outlook report. Available online at [http://www.worldenergyoutlook.org/media/weowebiste/factsheets/WEO2013\\_Factsheets.pdf](http://www.worldenergyoutlook.org/media/weowebiste/factsheets/WEO2013_Factsheets.pdf). Accessed Oct 2019
- Van Gerven T, Mul G, Moulijn J, Stankiewicz A (2007) A review of intensification of photocatalytic processes. *Chem Eng Process* 46(9):781–789. <https://doi.org/10.1016/j.cep.2007.05.012>
- Varghese OK, Paulose M, LaTempa TJ, Grimes CA (2009) High-rate solar photocatalytic conversion of CO<sub>2</sub> and water vapor to hydrocarbon fuels. *Nano Lett* 9(2):731–737. <https://doi.org/10.1021/nl803258p>
- Vitz J, Erdmenger T, Haensch C, Schubert US (2009) Extended dissolution studies of cellulose in imidazolium based ionic liquids. *Green Chem* 11(3):417–424. <https://doi.org/10.1039/B818061J>
- von Sonntag C, Schuchmann HP (2001) Carbohydrates. In: Charles DJ, Madhava Rao BS (eds) Radiation chemistry present status and future trends, vol 87. Elsevier, Amsterdam/New York, pp 481–511
- Wada M, Chanzy H, Nishiyama Y, Langan P (2004) Cellulose III crystal structure and hydrogen bonding by synchrotron X-ray and neutron fiber diffraction. *Macromolecules* 37(23):8548–8555. <https://doi.org/10.1021/ma0485585>
- Wada M, Ike M, Tokuyasu K (2010) Enzymatic hydrolysis of cellulose I is greatly accelerated via its conversion to the cellulose II hydrate form. *Polym Degrad Stab* 95(4):543–548. <https://doi.org/10.1016/j.polymdegradstab.2009.12.014>
- Wakerley DW, Kuehnel MF, Orchard KL, Ly KH, Rosser TE, Reisner E (2017) Solar-driven reforming of lignocellulose to H<sub>2</sub> with a CdS/CdO<sub>x</sub> photocatalyst. *Nat Energy* 2:17021. <https://doi.org/10.1038/nenergy.2017.21>
- Wan C, Li Y (2012) Fungal pretreatment of lignocellulosic biomass. *Biotechnol Adv* 30(6):1447–1457. <https://doi.org/10.1016/j.biotechadv.2012.03.003>
- Wang Y, Deng Y (2009) The kinetics of cellulose dissolution in sodium hydroxide solution at low temperatures. *Biotechnol Bioeng* 102(5):1398–1405. <https://doi.org/10.1002/bit.22160>
- Wang Z, Li G, Yang F, Chen Y, Gao P (2011) Electro-Fenton degradation of cellulose using graphite/PTFE electrodes modified by 2-ethylanthraquinone. *Carbohydr Polym* 86(4):1807–1813. <https://doi.org/10.1016/j.carbpol.2011.07.021>
- Wei W, Wei X, Gou G, Jiang M, Xu X, Wang Y, Hui D, Zhou Z (2015) Improved dissolution of cellulose in quaternary ammonium hydroxide by adjusting temperature. *RSC Adv* 5(49):39080–39083. <https://doi.org/10.1039/C5RA04247J>



- Wigley TML, Richels R, Edmonds JA (1996) Economic and environmental choices in the stabilization of atmospheric CO<sub>2</sub> concentrations. *Nature* 379(6562):240–243. <https://doi.org/10.1038/379240a0>
- Wu L, Arakane M, Ike M, Wada M, Takai T, Gau M, Tokuyasu K (2011) Low temperature alkali pretreatment for improving enzymatic digestibility of sweet sorghum bagasse for ethanol production. *Bioresour Technol* 102(7):4793–4799. <https://doi.org/10.1016/j.biortech.2011.01.023>
- Xiao S, Liu B, Wang Y, Fang Z, Zhang Z (2014) Efficient conversion of cellulose into biofuel precursor 5-hydroxymethylfurfural in dimethyl sulfoxide–ionic liquid mixtures. *Bioresour Technol* 151:361–366. <https://doi.org/10.1016/j.biortech.2013.10.095>
- Yamada T, Domen K (2018) Development of sunlight driven water splitting devices towards future artificial photosynthetic industry. *ChemEngineering* 2(3):36. <https://doi.org/10.3390/chemengineering2030036>
- Yamane C, Aoyagi T, Ago M, Sato K, Okajima K, Takahashi T (2006) Two different surface properties of regenerated cellulose due to structural anisotropy. *Polym J* 38(8):819–826. <https://doi.org/10.1295/polymj.PJ2005187>
- Yang L, Cao J, Jin Y, Chang H, Jameel H, Phillips R, Li Z (2012a) Effects of sodium carbonate pretreatment on the chemical compositions and enzymatic saccharification of rice straw. *Bioresour Technol* 124:283–291. <https://doi.org/10.1016/j.biortech.2012.08.041>
- Yang J, Yan H, Wang X, Wen F, Wang Z, Fan D, Shi J, Li C (2012b) Roles of cocatalysts in Pt–PdS/CdS with exceptionally high quantum efficiency for photocatalytic hydrogen production. *J Catal* 290:151–157. <https://doi.org/10.1016/j.jcat.2012.03.008>
- Yu L, Lin J, Tian F, Li X, Bian F, Wang J (2014) Cellulose nanofibrils generated from jute fibers with tunable polymorphs and crystallinity. *J Mater Chem A* 2(18):6402–6411. <https://doi.org/10.1039/C4TA00004H>
- Zavrel M, Bross D, Funke M, Büchs J, Spiess AC (2009) High-throughput screening for ionic liquids dissolving (ligno-)cellulose. *Bioresour Technol* 100(9):2580–2587. <https://doi.org/10.1016/j.biortech.2008.11.052>
- Zhang G, Kim G, Choi W (2014) Visible light driven photocatalysis mediated via ligand-to-metal charge transfer (LMCT): an alternative approach to solar activation of titania. *Energy Environ Sci* 7(3):954–966. <https://doi.org/10.1039/C3EE43147A>
- Zhang G, Ni C, Huang X, Welgamage A, Lawton LA, Robertson PKJ, Irvine JTS (2016a) Simultaneous cellulose conversion and hydrogen production assisted by cellulose decomposition under UV-light photocatalysis. *Chem Commun* 52:1673–1676. <https://doi.org/10.1039/C5CC09075J>
- Zhang M, Qin Y, Ma J, Yang L, Wu Z, Wang T, Wang W, Wang C (2016b) Depolymerization of microcrystalline cellulose by the combination of ultrasound and Fenton reagent. *Ultrason Sonochem* 31:404–408. <https://doi.org/10.1016/j.ultsonch.2016.01.027>
- Zhang L, Wang W, Zeng S, Su Y, Hao H (2018) Enhanced H<sub>2</sub> evolution from photocatalytic cellulose conversion based on graphitic carbon layers on TiO<sub>2</sub>/NiO<sub>x</sub>. *Green Chem* 20(13):3008–3013. <https://doi.org/10.1039/C8GC01398E>
- Zhao J, Yang X (2003) Photocatalytic oxidation for indoor air purification: a literature review. *Build Environ* 38(5):645–654. [https://doi.org/10.1016/S0360-1323\(02\)00212-3](https://doi.org/10.1016/S0360-1323(02)00212-3)
- Zhao H, Holladay JE, Kwak JH, Zhang ZC (2007) Inverse temperature-dependent pathway of cellulose decrystallization in trifluoroacetic acid. *J Phys Chem B* 111(19):5295–5300. <https://doi.org/10.1021/jp070253f>
- Zhou B, Song J, Zhang Z, Jiang Z, Zhang P, Han B (2017) Highly selective photocatalytic oxidation of biomass-derived chemicals to carboxyl compounds over Au/TiO<sub>2</sub>. *Green Chem* 19(4):1075–1081. <https://doi.org/10.1039/C6GC03022J>
- Zou J, Zhang G, Xu X (2018) One-pot photoreforming of cellulosic biomass waste to hydrogen by merging photocatalysis with acid hydrolysis. *Appl Catal A* 563:73–79. <https://doi.org/10.1016/j.apcata.2018.06.030>

# Chapter 2

## Lithium Iron Phosphate (LiFePO<sub>4</sub>) as High-Performance Cathode Material for Lithium Ion Batteries



Neethu T. M. Balakrishnan, Asha Paul, M. A. Krishnan, Akhila Das,  
Leya Rose Raphaez, Jou-Hyeon Ahn, M. J. Jabeen Fatima,  
and Raghavan Prasanth

### Contents

2.1	Introduction .....	38
2.1.1	Emergence of Lithium Iron Phosphate .....	40
2.2	Synthesis of Lithium Iron Phosphate .....	41
2.3	Approaches for Property Enhancement .....	43
2.3.1	Carbon Coating .....	43
2.3.2	Metal–Metal Oxide Coating .....	45
2.3.3	Composite Electrodes .....	48
2.3.4	Doping .....	63
2.3.5	Size and Morphology .....	65
2.4	Conclusion and Future Outlook .....	66
	References .....	67

**Abstract** As long as the energy consumption is intended to be more economical and more environment friendly, electrochemical energy production is under serious consideration as an alternative energy/power source. Among different energy/power storage devices, lithium-ion batteries (LIBs) are currently the best commercially available devices. However, there are safety issues to be investigated even when it is operating at room temperature since there have been various incidents

---

N. T. M. Balakrishnan · A. Paul · A. Das · L. R. Raphaez · M. J. Jabeen Fatima (✉) ·  
R. Prasanth (✉)

Department of Polymer Science and Rubber Technology (PSRT), Cochin University of Science  
and Technology (CUSAT), Cochin, India  
e-mail: [jabeen@cusat.ac.in](mailto:jabeen@cusat.ac.in); [prasanth@cusat.ac.in](mailto:prasanth@cusat.ac.in)

M. A. Krishnan

Department of Mechanical Engineering, Amrita Vishwa Vidyapeetham, Kollam, India

J.-H. Ahn

Department of Chemical and Biological Engineering and Engineering Research Institute,  
Gyeongsang National University, Jinju-Daero, Republic of Korea

© The Editor(s) (if applicable) and The Author(s), under exclusive licence to  
Springer Nature Switzerland AG 2021

S. Rajendran et al. (eds.), *Metal, Metal-Oxides and Metal Sulfides for Batteries, Fuel  
Cells, Solar Cells, Photocatalysis and Health Sensors*, Environmental Chemistry for  
a Sustainable World 62, [https://doi.org/10.1007/978-3-030-63791-0\\_2](https://doi.org/10.1007/978-3-030-63791-0_2)

reported. From that point of view, effective research has been going on to develop LIBs that are viable to operate safely at higher temperatures. In the search for better cathode materials for LIBs, researchers have been investigating a new class of iron-based compounds called polyanions such as  $(\text{SO}_4)^{2-}$ ,  $(\text{PO}_4)^{3-}$  or  $(\text{AsO}_4)^{3-}$ . Orthorhombic  $\text{LiFePO}_4$  (LFP), which has an ordered olivine structure, has attracted particular interest due to its high-power capability, non-toxicity, and thermal stability. This material has relatively high theoretical capacity of  $170 \text{ mAhg}^{-1}$  when compared with other cathode materials. The major drawbacks of the lithium iron phosphate (LFP) cathode include its relatively low average potential, weak electronic conductivity, poor rate capability, low  $\text{Li}^+$ -ion diffusion coefficient, and low volumetric specific capacity. Hence, this chapter clearly emphasizes the role and progress of LFP as efficient cathode material for LIBs and their ways to overcome the existing drawbacks which include the optimization of their synthesis methods, controlling the diffusion rate, and modification strategies. The use of conventional electrolytes with LFP caused iron dissolution on the cathode surface, which catalyzed the electrolyte decomposition, which then contributed to the formation of thick obstructive solid electrolyte interphase (SEI) films. Use of electrolyte additives is one of the most effective methods to protect against  $\text{LiFePO}_4$  dissolution. The thermal stability of these materials can be accounted by the high  $\text{Li}^+$  ion diffusion rate and the electron transfer activity. Even at elevated temperatures up to  $340^\circ\text{C}$ , charged LFP and electrolyte didn't show any kind of chemical reactions, which makes this material thermally more feasible than other cathode materials like  $\text{LiCoO}_2$ ,  $\text{LiNiO}_2$ , and  $\text{LiMn}_2\text{O}_4$ .

**Keywords** Lithium ion batteries · Lithium iron phosphate · Carbon nanotube · Graphene · Cathode materials · Charge–discharge · Cycling stability

### List of Symbols and Formulas

$(\text{AsO}_4)^{3-}$	arsenate ion
$(\text{PO}_4)^{3-}$	phosphate ion
$(\text{SO}_4)^{2-}$	sulfate ion
$\text{Al}_2\text{O}_3$	aluminum oxide
$\text{C}_2\text{H}_2$	acetylene
$\text{CH}_3\text{COOLi}$	lithium acetate
$\text{CuO}$	copper oxide
$\text{Fe}_2\text{P}$	iron phosphide
$\text{Fe}(\text{CH}_3\text{COO}_2)_2$	iron acetate
$\text{FeC}_2\text{O}_4$	ferrous oxalate
$\text{FeOCl}$	iron oxychloride
$\text{FeOOH}$	ferric oxyhydroxide
$\text{FePO}_4$	iron phosphate
$\text{FePO}_4(\text{H}_2\text{O})_2$	iron phosphate hydrate
$\text{FePS}_3$	iron phosphorus sulfide
$\text{HCl}$	hydrogen chloride
$\text{Li}_2\text{CO}_3$	lithium carbonate

Li <sub>4</sub> Ti <sub>5</sub> O <sub>12</sub>	lithium titanium oxide
LiCoO <sub>2</sub>	lithium cobalt oxide
LiF	lithium fluoride
LiFePO <sub>4</sub>	lithium iron phosphate
LiMn <sub>2</sub> O <sub>4</sub>	lithium manganese oxide
LiNi <sub>0.5</sub> Mn <sub>0.5</sub> O <sub>2</sub>	lithium nickel manganese oxide
LiNiMnCoO <sub>2</sub>	lithium nickel manganese cobalt oxide
LiOH	lithium hydroxide
MgO	magnesium oxide
NH <sub>4</sub> H <sub>2</sub> PO <sub>4</sub>	ammonium dihydrogen phosphate
SiO <sub>2</sub>	silicon oxide
ZrO <sub>2</sub>	zirconium oxide

### Abbreviations

1-D	one-dimensional
2-D	two-dimensional
3D	three-dimensional
CNS	carbon nanospheres
CNT	carbon nanotubes
CUO	copper oxide
CVD	chemical vapor deposition
EG	ethylene glycol
EV	electric vehicle
GNS	graphene nano sheets
GO	graphene oxide
HEV	hybrid electric vehicle
LCO	lithium cobalt oxide
LFP	lithium iron phosphate
LIB	lithium ion batteries
LTO	lithium titanium oxide
MWCNT	multi-walled carbon nanotubes
PAN	poly (acrylonitrile)
PEG	polyethylene glycol
Ppy	polyvinyl pyrrolidone
PVA	polyvinyl alcohol
PVDF	polyvinylidene difluoride
rGO	reduced graphene oxide
SEI	solid/electrolyte interphase
SEM	scanning electron microscope
SWCNT	single walled carbon nanotubes
TEM	tunneling electron microscope

## List of Units

A g <sup>-1</sup>	Ampere per gram
C	C- rate
cm <sup>2</sup> s <sup>-1</sup>	Centimeter square per second
°C	Degree Celsius
eV	Electron volt
g mol <sup>-1</sup>	Gram per mole
h	Hours
kW kg <sup>-1</sup>	Kilo watt per kilogram
m <sup>2</sup> g	Meter square gram
mAh g <sup>-1</sup>	Milli ampere hour per gram
mA g <sup>-1</sup>	Milli ampere per gram
nm	Nanometer
Ω	Ohm
S cm <sup>-1</sup>	Semen per centimeter
V	Volt
Wh kg <sup>-1</sup>	Watt hour per kilogram

## 2.1 Introduction

Today's world is at a turning point where there is a decline in resources that leads to a new scenario in energy consumption. It is essential to find a suitable substitute that can ensure the surveillance of our wealth and development on long-term basis in order to face the run out of fossil fuel energy sources. In spite of careful consideration given to renewable energy over the non-renewable energy, their production and efficiency cannot be guaranteed, so effective storage of energy from these sources is important. Fuel cells, supercapacitors, and batteries are some of the important energy storage systems under research. Among them, batteries attract greater interest due to their efficiency and portability. So, batteries have an indispensable role in our daily life. They can be connected in series to get high voltage and parallel to get high current, and that is the wonder behind the battery technology.

The range of current batteries extends from non-rechargeable alkaline batteries to rechargeable lithium ion batteries (LIBs) and among these LIB technology currently attracts great interest owing to the electric vehicle revolution, because compared to other energy storage devices Li<sup>+</sup>-ion technology could serve as most effective power source for the automotive vehicle that can replace most of the gasoline technology (Ruska and Kiviluoma 2011; Cano et al. 2018). LIBs have an excellent combination of power as well as energy density. The lowest reduction potential of Li<sup>+</sup>-ions that authorizes highest cell potential, gravimetric and volumetric capacity as well as power density are the direct results by of the light weight and smallest ionic radii. Apart from this, the low self-discharge and lack of memory effect make it promising

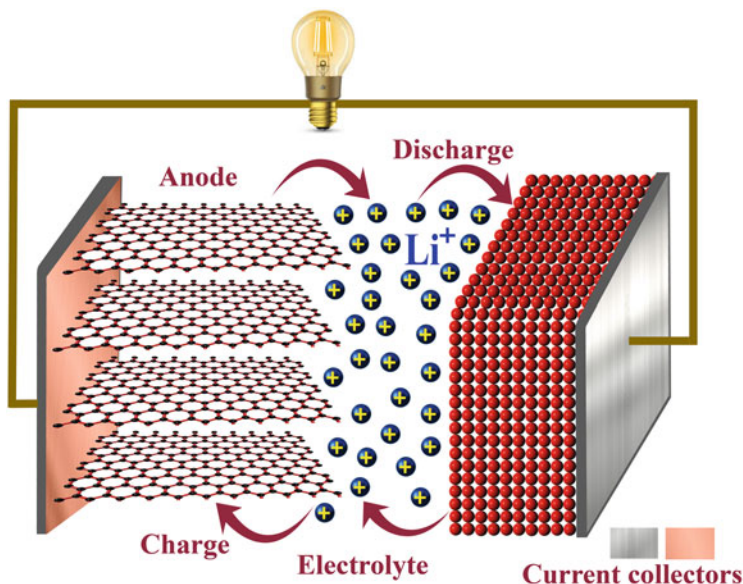


**Fig. 2.1** Schematic representation and operating principles of Li-ion batteries including the movement of ions between electrodes during charge and discharge states

candidate over other battery technologies such as lithium cadmium batteries (Li-Cd), nickel metal hydride battery (Ni-MH) (May et al. 2018). Also for these systems priming is not required. Low maintenance, low self-discharge (<5% for a month), and availability in varieties of shapes and sizes make LIBs superior over any other types of battery systems (Lu et al. 2013; Blomgren 2017).

An efficient and safer LIB was developed and commercialized after the successful safety test in 1985 by Akira Yoshino. At that time, he used lithium as the anode and vapor phase grown carbon fiber as the cathode material (Goodenough 2018). The typical schematic representation of lithium ion battery is given in Fig. 2.1. For efficient battery storage, an ideal cathode and anode are still remaining as a desire for the researchers. The first intercalation material discovered was titanium disulfide (TiS<sub>2</sub>) by Whittingham in 1975 (Whittingham 2012). But severe issues were related to cathode materials that produce lithium dendrite along with the metallic lithium anode and the titanium disulfide, which was expensive as well as forms hydrogen sulfide on exposure to air, which creates environmental issues (Whittingham and Gamble 1975). After that there comes the desire for an intercalation cathode material with higher intercalation potential of about >3 V.

The discovery of lithium cobalt oxide (LiCoO<sub>2</sub> simply LCO), the layered material as the cathode, by John Goodenough and Koichi Mizushima made a leap and it is known as the heart of LIBs. An intercalation compound is a type of material that is able to accommodate the guest Li<sup>+</sup>-ions in its layers and it can easily release the Li<sup>+</sup>-ions when needed. LCO was the most successful layered transition metal oxide cathode commercialized by SONY in 1991 and still it is used in many commercial

LIBs (Mizushima et al. 1981; Goodenough 2018). LCO exhibits high specific capacity ( $272 \text{ mAhg}^{-1}$ ) and high theoretical volumetric capacity ( $1363 \text{ mAhcm}^{-3}$ ). The high cost of cobalt made LCO expensive and as a toxic material it poses environmental issues. Low thermal stability and fast capacity fade are another issues associated with LCO. The major issue associated with the LIB is the thermal runaway during their application that is evident from the issue that led to the grounding of Boeing 787 airplanes in 2013, and explosion of electronic gadgets such as Samsung Note 7 (2017) and Samsung edge (2018) (Naoki et al. 2015). Several reports on electric vehicle explosion were reported worldwide. Chevrolet Volt was blasted while subjected to crash test in 2011. In 2013, Tesla Model S caught fire at Washington highway which was reported to be the worst case of explosion since the fire was inextinguishable with water. Later it was examined that dry fire extinguishers were found effective in putting out fire. In subsequent months, several incidents on explosion of Tesla model S were reported in Europe. This was also a reason for exploring new and efficient materials as cathodes. Lithium nickel oxide ( $\text{LiNiO}_2$  simply LNO) was considered as an alternative with similar structure of LCO, low cost but not efficient, because it has the tendency to replace  $\text{Li}^+$ -ion sites and thereby blocks the lithium diffusion. Continuous efforts led to the development of a new cathode material, lithium manganese oxide ( $\text{LiMn}_2\text{O}_4$ ,  $\text{Li}_2\text{MnO}_3$  simply LMO) in 1983, but still the tendency of the material to change structure from intercalation type to spinel during lithium extraction was a serious issue. This Jahn-Teller deformation reduces the capacity irreversibly on repeated cycling (Padhi 1997). After that, different intercalation type cathodes were developed, such as lithium nickel manganese oxide ( $\text{LiNi}_{0.5}\text{Mn}_{0.5}\text{O}_2$  simply NMO), lithium nickel cobalt manganese oxide ( $\text{LiNiMnCoO}_2$ , simply NMC), lithium titanate/lithium titanium oxide ( $\text{Li}_4\text{Ti}_5\text{O}_{12}$  simply LTO), that satisfactorily performed compared to the former.

### 2.1.1 Emergence of Lithium Iron Phosphate

The limitations of reported intercalation cathodes motivated the investigation for new type of cathode materials, out of which iron-based compounds were widely accepted owing to their properties. Initially studied compounds were iron phosphorus sulfide ( $\text{FePS}_3$ ), iron oxychloride ( $\text{FeOCl}$ ), and ferric oxyhydroxide ( $\text{FeOOH}$ ), which exhibited low discharge voltage, and they were found to be inadequate as cathode materials. The research was then focused on compounds containing polyanions such as  $(\text{SO}_4)^{2-}$ ,  $(\text{PO}_4)^{3-}$ , or  $(\text{AsO}_4)^{3-}$  (Padhi 1997; Takahashi et al. 2002). The use of lithium iron phosphate ( $\text{LiFePO}_4$  simply LFP) as cathode material in LIBs was first proposed by Akshaya Padhi, John Goodenough and his co-workers in 1996 (Padhi 1997; Rao 2015). It was the first ever reported cathode material with lower cost and abundance compared to LCO. It is olivine structured material with combination of plenty of Fe and covalent  $(\text{PO}_4)^{3-}$  units with fixed number of oxygen (Nishimura et al. 2010).

The major reason for the market acceptance of LFP is its superior properties such as thermal stability, safety, and specific capacity; however, it possesses certain drawbacks such as poor electronic conductivity and capacity retention under continuous charge–discharge cycling, especially at higher C-rate. While considering the safety aspects of LIBs, compared to small portable devices, the chances of catching fire is severe in electric vehicles (EVs), but the phosphate containing cathodes provide good thermal stability, so that it is able to withstand high temperatures and primarily stable during overcharged and short-circuiting conditions. Charging of LIB is also crucial above 4.7 V, since the formation of oxidative products or lithium deposition at high potential. So the choice of phosphate containing cathodes, such as olivine structured LFP, is completely safer even at high potential that it produces ferric oxide as the oxidative product, which is much more stable (Saw et al. 2014). Apart from this, LFP is the cathode material that provides low toxicity, flat potential during charge–discharge cycling process, and it provides high specific capacity. Also, LFP exhibits theoretical energy density of about 550 WhKg<sup>-1</sup>. It exhibits a theoretical specific capacity of 170 mAhg<sup>-1</sup>. So, the choice of LFP as the cathode material is even more satisfactory while considering the electrochemical performance as well as safety aspects of LIBs (Yang et al. 2002). Hence recent studies of cathode materials are mainly focused on LFP containing polyanions such as (SO<sub>4</sub>)<sup>2-</sup>, (PO<sub>4</sub>)<sup>3-</sup>, or (AsO<sub>4</sub>)<sup>3-</sup> (Padhi 1997). However, deterioration in capacity with cycle life and intolerance in high current is a problem with this material, so different studies are ongoing in order to meet excellent electrochemical properties and to reach extreme temperature performance (Dhindsa et al. 2013a; Lung-Hao Hu et al. 2013).

## 2.2 Synthesis of Lithium Iron Phosphate

Synthesis methods of LFP can be divided broadly into two types, mainly solid-state methods and solution phase methods. Solid state methods include solid phase synthesis, mechano-chemical activation, carbothermal reduction, and microwave heating, that usually results the formation of powder state LFP. Solid state synthesis is the conventional method for the synthesis of LFP. LiF, Li<sub>2</sub>CO<sub>3</sub>, LiOH·2H<sub>2</sub>O, CH<sub>3</sub>COOLi, etc. are used as lithium sources, FeC<sub>2</sub>O<sub>4</sub>·2H<sub>2</sub>O, Fe(CH<sub>3</sub>COO<sub>2</sub>)<sub>2</sub>, and FePO<sub>4</sub>(H<sub>2</sub>O)<sub>2</sub> are used as the iron sources, and NH<sub>4</sub>H<sub>2</sub>PO<sub>4</sub> and (NH<sub>4</sub>)<sub>2</sub>HPO<sub>4</sub> are used as the phosphorus sources. The process takes place at extreme condition that results in the formation of non-crystalline particle in non-crystalline form. Islam et al. (2015) synthesized LFP by solid state method using low cost material. In mechano-chemical activation method (Bağcı and Akyildiz 2018), as its name indicates, mechanical activation is done in order to enhance the chemical reaction and it results in the formation of smaller particles with high activation energy. In comparison with solid state methods, carbothermal reduction method produces fine LFP particles with uniform particle morphology and high capacity. Microwave heating (Park et al. 2003) includes heating of the material by making use of microwave



energy, hence it is more productive and less energy consuming process. Solution-based techniques get much attention compared to solid state method, because it results in small particle size, more uniform particle size distribution, higher purity, and better electrochemical performance. Hydrothermal synthesis, sol-gel synthesis, spray pyrolysis, and co-precipitation are the widely used solution techniques for the production of LFP.

During the hydrothermal synthesis of LFP (Qin et al. 2010), pure platelets are formed. It is the simple, clean, and low-cost method widely used, which involves the boiling of a solution of precursors above the boiling point of water, typically 150 °C. It is the synthesis method that enables more control over the particle size and particle size distribution. Normally hydrothermal synthesis is a high energy consuming process. Benedek et al. (2017) introduced a low temperature hydrothermal process with the use of high concentration of precursors. They produced LFP platelets with (010) dimension and practical capacity of 150 mAhg<sup>-1</sup>. For the preparation of nano LFP, a hydrothermal synthesis via solution stirring is employed, that results in cathodes with good capacity retention (Gariépy et al. 2012).

Sol-gel synthesis involves the formation of a sol, which get converted in to gel that consists of interconnected rigid skeleton with pores, made of colloidal particles. It is a low-cost process that doesn't require any high temperature conditions. It results in phase pure LFP with uniform morphology and good control over the particle size as well as it is possible to induce in situ carbon coating using suitable precursor or solvents (Yang and Xu 2004). LFP synthesized using a natural iron stone precursor along with Li<sub>2</sub>CO<sub>3</sub> powder and NH<sub>4</sub>H<sub>2</sub>PO<sub>4</sub> powder with dilute HCl as solvent exhibit an electronic conductivity of about 4.56 × 10<sup>-3</sup> Scm<sup>-1</sup>, which is six times greater than that of pure LFP (Angela et al. 2017).

Ultrasonic spray pyrolysis is the effective method that results in the formation of ultra-fine particles with narrow size distribution. It involves the formation of continuous droplets from a solution containing precursor colloids. The process starts with spraying of solution of mixed precursor in the form of droplets to the pyrolysis furnace followed by calcination at high temperature (Yang et al. 2006). LFP/C composite that is prepared by the same method exhibits a first discharge capacity of 140 mAh g<sup>-1</sup> at 0.1 C, and excellent cyclic performance (Konarova and Taniguchi 2008). Effect of carbon precursors on LFP/C composites shows that sucrose is one of the best carbon precursors for LFP in ultrasonic spray pyrolysis (Kashi et al. 2018).

Co-precipitation method forms LFP well-crystallized powders by mixing lithium and phosphate compounds in a mixed precursor solution. Co-precipitated slurries are then filtered, washed, and dried (Huang et al. 2013). Depending on the precursors and other processing conditions, the size of LFP can be varied from nano to micro size (Li et al. 2009; Ding et al. 2010). An environmentally benign co-precipitation method was introduced by Swider et al. (2014) by synthesizing technical grade reagent in ethylene glycol (EG) medium at an anhydrous environment that results in pure fine nano powder of LFP. But using ethylene glycol in aqueous solution for one step co-precipitation method results in the formation of LFP with excellent electrochemical properties (Wang et al. 2013).

## 2.3 Approaches for Property Enhancement

The major target of the research on LFP cathode was to improve the electronic conductivity of this active material. For achieving the required level of electronic conductivity several methods were chosen for modification of the structure and morphology of the LFP. Carbon coatings, doping with metallic impurities, constructing 3-D network frames with conducting materials such as carbon nanotubes, and graphene and particles size reduction or increase in the available active surface area for the electrochemical reaction are the important methods reported to improve the properties of LFP. The major refinements reported are discussed in detail. The enhancement of property is observed due to the formation of a conducting surface film, incorporation of the metallic impurities, addition of some metal dopants, formation of 3-D conducting channels, etc. But the problems with some of the dopants are that due to low solubility of dopant that they get located over the lithium site and they block the diffusion of Li<sup>+</sup>-ion (Fig. 2.2).

### 2.3.1 Carbon Coating

Carbon coating is considered as one of the simplest and powerful method to improve the electronic conductivity of LFP. The carbon coating was first proposed by Armand and his co-workers (Li and Zhou 2012). During the carbon coating, pyrolysis of an organic substance over the LFP occurs, which creates a reducing atmosphere that may result

in the formation of secondary phase, which enhances the electronic conductivity and enables to achieve a practical capacity value of 170 mAhg<sup>-1</sup> (Saroha and Panwar 2017). Carbon coating helps to inhibit the aggregation of nano particles and thereby provide the passage for Li<sup>+</sup>-ions, as well as the inter and intra particle

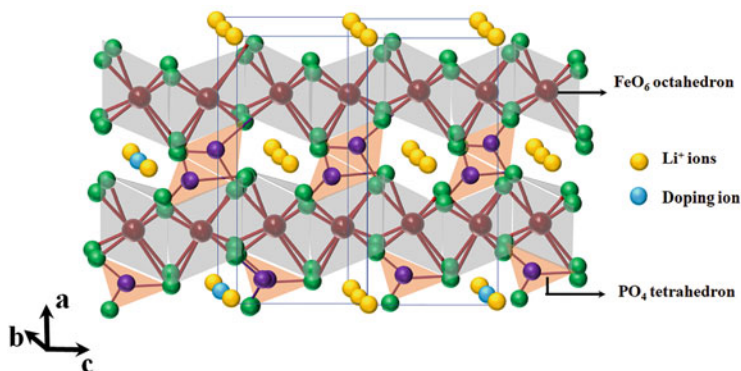


**Fig. 2.2** The schematic representation on diffusion of Li by obstruction of the channels, which degrades the electrochemical performance. (Modified after Julien 2017)

electronic conductivity. A thin layer of carbon was coated on nanosized LFP by pre-calcination and vacuum deposition process, which results into uniform particle size distribution, prevention of particle agglomeration, and inhibit the grain growth (Huang et al. 2017). In industrial scale, a high-performance carbon coating is achieved by coating 90 nm thick particle covering with 3 nm thick carbon coating. Carbon derived from different sources was used for coating process. Orange peel was introduced during the modified mechanical activation process. This carbon-coated LFP exhibits a high discharge capacity of about  $147.3 \text{ mAhg}^{-1}$ , which is 87% of the theoretical capacity at 0.5 C-rate (Kim et al. 2019).

A soft and hard carbon coating on LFP was prepared by using asphalt derived and glucose derived carbon and the electrochemical performances were evaluated. The variation study shows that the electrochemical property of soft carbon-coated LFP is greater than hard carbon-coated LFP. Asphalt is a good carbon precursor that could form uniform and denser carbon layer and thereby improve the  $\text{Li}^+$  diffusivity across the electrode–electrolyte interface as well as improve the electronic conductivity (Jiang et al. 2017). Acetylene gas is another precursor which is employed to introduce carbon coating on LFP via in situ pyrolysis. The  $\text{C}_2\text{H}_2$  treatment on LFP for 10 min shows excellent capacity at all C-rate studied (0.1–10 C) as well as superior rate performance (Saroja and Panwar 2017).

Among the different processes employed for the synthesis of carbon-coated LFP, an effective method for carbon coating was proposed by Wang et al. (2011). They produced nanosized LFP with carbon coating using  $\text{FePO}_4$  as the iron source and polyvinyl alcohol (PVA) gel as the carbon source. The best film forming property of PVA makes a uniform film coating over the LFP particle after it gets mixed with the  $\text{FePO}_4$  in ball mill, and during calcination it perfectly gets transferred into the uniform carbon coating. Electrospinning was also proposed as an effective method to grow LFP/C nanofibers. Poly (acrylonitrile) (PAN) is one of the carbon sources that provides the carbon coating during electrospinning. It offers a large surface area to volume ratio and provides a capacity value of  $162 \text{ mAhg}^{-1}$  at 0.1 C-rate. It is a better performance compared to other LFP/C nanofibers and the carbon content in the coating is found to be about 10 wt.% (Shao et al. 2013; Lin et al. 2014; Qiu et al. 2014a). The morphology of  $\text{LiFePO}_4/\text{C}$  composite synthesized at different mole ratio is depicted in Fig. 2.3. The variation in molar concentration was achieved by changing the precursor concentration in  $\text{LiH}_2\text{PO}_4/\text{FeC}_6\text{H}_5\text{O}_7$  of mole ratio 1.0–1.3 with regular increment of 0.1, out of which 1.3 mole ratio showed superior performance. Apart from this, the composite exhibits superior electrochemical performance than commercial LFP (Fig. 2.4) (Qiu et al. 2014b).

Hydrothermally synthesized LFP nano rods that are coated using sucrose precursor exhibit a capacity value of about  $173 \text{ mAhg}^{-1}$  at 0.1 C, which is greater than the theoretical value. This excellent improved property is due to the reduction of the lithium path along the (010) direction which is most favorable for  $\text{Li}^+$  diffusion (Bao et al. 2017). Solution deposition followed annealing is also employed for the formation of carbon-coated LFP nanostructures, which showed that annealing over  $700^\circ\text{C}$  results in the reduction of  $\text{LiFePO}_4$  to  $\text{FePO}_4$ . The reduction from  $\text{LiFePO}_4$  to  $\text{FePO}_4$  is favorable for the enhanced electronic conduction (Zhu et al. 2014). Apart

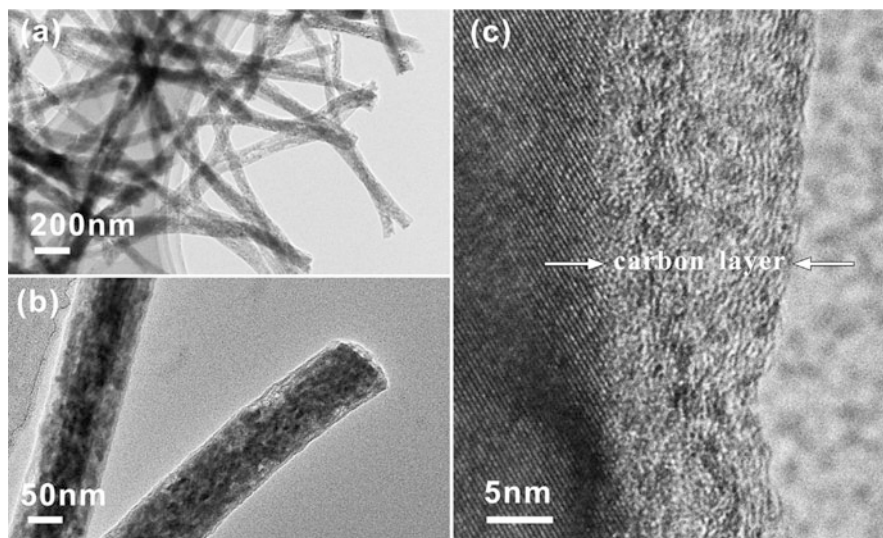


**Fig. 2.3** TEM images of LiFePO<sub>4</sub>/C composite nanofibers prepared using LiH<sub>2</sub>PO<sub>4</sub>/FeC<sub>6</sub>H<sub>5</sub>O<sub>7</sub> ratio of 1.3 with different magnifications. (Reprinted with permission of Elsevier from Qiu et al. 2014b)

from the effect of carbon layer formed on the active material (LFP) during carbon coating, the role of interface conductivity between carbon-coated LFP particle and carbon-coated current collector were studied. In this study, LFP prepared by sol-gel method and a nanosized thin layer of carbon was coated on the active materials and the electrode was fabricated on carbon-coated aluminum which produces highly distorted carbon at the interface. The sample containing more sp<sup>2</sup> hybridized carbon exhibits superior electrochemical properties over sp<sup>3</sup> hybridized carbon. This is due to the large polarization effect during the charge—discharge cycle (Swain et al. 2015).

### 2.3.2 Metal–Metal Oxide Coating

Among the different approaches introduced for the enhancement of rate capability and power density of LIBs, particle size reduction and carbon coating get much attention by the battery technologists; however, carbon coating cannot ensure a complete uniform coating on the active surface of LFP particles. When there is a barrier for the movement of electrons, the intercalated Li<sup>+</sup>-ions remain as such and it will create polarity in the electrode. For different active cathodic materials such as LCO and LTO, different metal coatings like MgO, ZrO<sub>2</sub>, Al<sub>2</sub>O<sub>3</sub>, and SiO<sub>2</sub> were effectively employed in order to improve the electronic conductivity (Zhao et al. 2017).

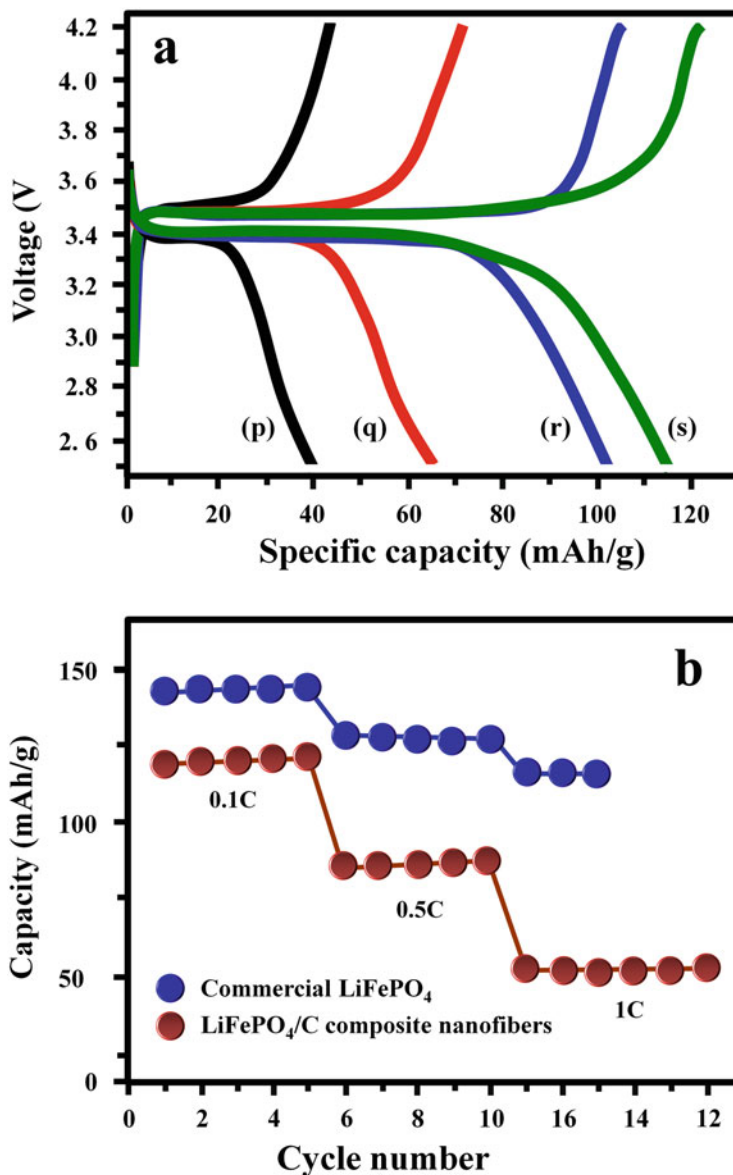


**Fig. 2.4** (a) Charge/discharge curves of  $\text{LiFePO}_4/\text{C}$  composite nanofiber samples prepared using different mole ratio of  $\text{LiH}_2\text{PO}_4/\text{FeC}_6\text{H}_5\text{O}_7$ : (p) 1.0; (q) 1.1; (r) 1.2; (s) 1.3. (b) Capacity of commercial  $\text{LiFePO}_4$  and  $\text{LiFePO}_4/\text{C}$  composite nanofibers at different discharge rate of 0.1, 0.5, and 1 C. (Cell configuration:  $\text{LiFePO}_4/\text{C}$  composite nanofibers/Li cells). (Reprinted with permission of Elsevier from Qiu et al. 2014b)

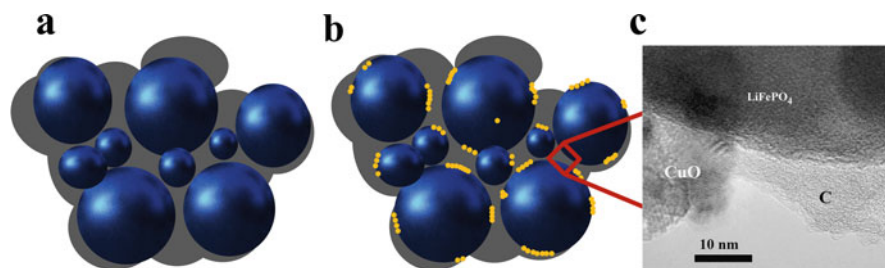


**Fig. 2.5** Schematic representation of LiFePO<sub>4</sub> particles: (a) partially coated with carbon, (b) designed ideal structure of LiFePO<sub>4</sub> particles coated with an integrate nanolayer, (c) HRTEM images of the CuO/C-LFP. (Reprinted with permission of Elsevier from Cui et al. 2010)

In LFP, nanosized CuO and carbon are together employed for coating, and this nano CuO cover up the incomplete carbon layer network and forms a metallic nano layer over the surface of LFP (Fig. 2.5). CuO coating was carried out with chemical vapor deposition and it results in the formation of an integrated and continuous conducting metallic layer on the active material. Compared to carbon-coated LFP, this system exhibits improved discharge capacity,  $125 \text{ mAhg}^{-1}$  (Cui et al. 2010). Another study of LTO modified carbon-coated LFP shows that compared to simply carbon-coated LFP, modified carbon-coated LFP exhibits high cyclic stability even when the cell was operating at a higher temperature like  $55^\circ\text{C}$ . A solid-state method is employed in order to synthesize LFP/C powder and 1–5% LTO was applied by using the spray drying process. Compared to LTO coated LFP, pristine LFP shows a decline in cycling stability and about 3 wt.% LTO was optimized for the best electrochemical properties of LFP (Yang et al. 2015).

In the carbon-coated LFP, a spherical phase growth is observed which completely differs from that of pure matrix phase and this growth was reported to be owing to the formation of a conducting Fe<sub>2</sub>P phase which was first reported by Herle et al. (2004). The report also examined the influence of carbon coating for the formation of Fe<sub>2</sub>P phase and the layer formed is controlled by the size, temperature, and annealing atmosphere of LFP (Liu et al. 2018).

Formation of a uniform carbon layer over LFP increases the Li<sup>+</sup> diffusion and electronic conductivity. SiO<sub>2</sub> is a non-metallic oxide that improves the structural stability of the LFP/C by insulating the LFP surface effectively from the electrolyte. An improved structural stability and reduced interfacial resistance increase the Li<sup>+</sup> diffusivity (Li et al. 2011). Similarly zinc oxide (ZnO) coating is also employed which greatly helps to attain the high reversible capacity (about 90% of that of theoretical capacity of the active material), when cycled between 2.5 and 4.2 V. ZnO coating by freeze drying method also showed an enhanced electrochemical performance of LFP, which is assigned to the semiconducting nature of ZnO.

### 2.3.3 Composite Electrodes

The fabrication of composite electrodes was another major modification approach carried out in LFP in order to enhance the conductivity and efficiency of the electrode in LIBs. It can be done by coating of the surface of LFP via chemical or physical route.

#### Lithium Iron Phosphate-Carbon Nanotube Composite Cathode

Discoveries of very stable nanometer size  $sp^2$  carbon bonded materials such as fullerenes, nanodiamonds, carbon nanotube (CNT), and graphene are enhanced the research in nanocomposites. A new era in carbon materials begins with the discovery of Buckminster Fullerene's family (Bucky Balls) (Kroto et al. 1985) at Rice University, United States in the mid of 1980s, followed by the discovery of Fullerene nanotubes (Bucky tubes by Sumio Iijima and Ajayan Pulickal) (Iijima et al. 1992), and large scale synthesis of carbon nanotubes by Ajayan and Ebbesen (1992). CNTs, the allotrope of carbon, having a seamless tubular structure, are dimensionally and structurally different from other allotrope of carbon like graphite, diamond, fullerene, and graphene. These are one-dimensional (1-D) materials having very high aspect ratio (length to diameter ratio) of up to 132,000,000:1, significantly larger than for any other nanostructured materials. They can be thought of as one atom thick flexible sheets of carbon called graphene, rolled up at specific and discrete (chiral) angles into a long and hollow structures basically categorized into two: (i) single walled carbon nanotubes (SWCNTs)—this can be visualized as cylinder composed of a rolled up graphene nanosheets around a central hollow core; (ii) multi-walled carbon nanotubes (MWCNTs). It consists of more than one graphene layers, that is held together by Van der Waals forces between adjacent layers and folded as hollow cylinders (Salem et al. 2003). The combination of rolling angle and radius decides the properties of CNTs, for instance, whether the individual nanotube shell is metallic, semiconducting, or insulating in nature (Fig. 2.6.).

The way graphene nanosheets are rolled can be described by a pair of indices  $(n, m)$ , where  $n$  and  $m$  represent number of unit vectors along the two directions of hexagonal crystal lattice of graphene. The chirality of CNTs is defined by chiral vector,  $C_h = na_1 + ma_2$  when  $m = 0$ , CNTs have zig-zag structure for  $n = m$  arm chair structure, and if both conditions are not satisfied, it is classified as chiral (Thostenson et al. 2001). The electronic property of CNTs greatly depends on the chirality. For a given pair of indices  $(n, m)$ , if  $(2n + m)$  is a multiple of 3, then the CNTs are metallic in nature, otherwise semiconductor. Figure 2.6 depicts (a) SWCNT, (b) MWCNT, and (c) their unit vectors. The  $(n, m)$  nanotube naming scheme can be thought as a vector ( $C_h$ ) in an infinite graphene sheet that describes how to "roll up" the graphene sheet to make the nanotube.  $T$  denotes the tube axis,  $a_1$  and  $a_2$  are the unit vectors of graphene in real space.

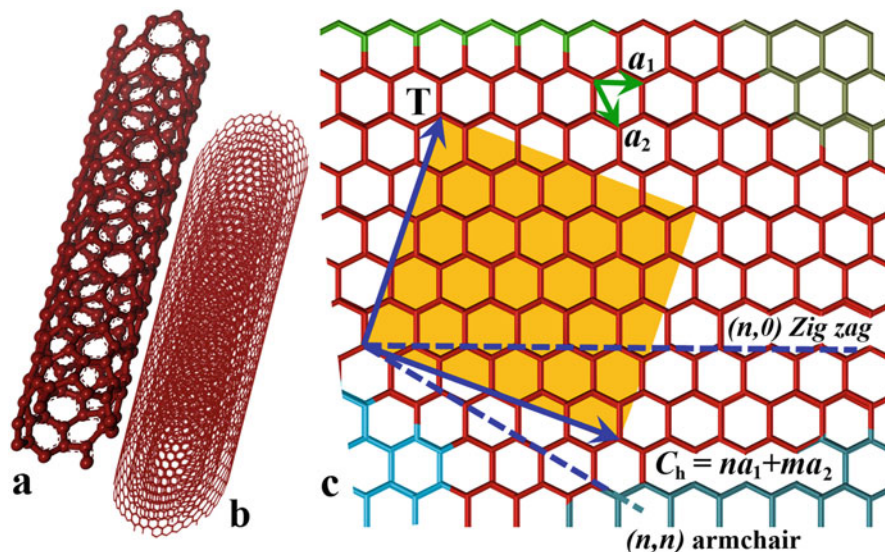


**Fig. 2.6** Schematic illustration of (a) SWCNT, (b) MWCNT, and (c) its unit vectors. The  $(n,m)$  nanotube naming scheme can be thought of as a vector ( $C_h$ ) in an infinite graphene sheet that describes how to “roll up” the graphene sheet to make the nanotube. T denotes the tube axis, and  $a_1$  and  $a_2$  are the unit vectors of graphene in real space. (Modified after Jabeen et al. 2015)

The characteristic electronic and electrochemical properties of CNTs are being identified as an ideal material for energy storage devices such as batteries, supercapacitors, and fuel cells. Among these devices, considerable number of efforts are being reported to make composite electrodes with lithium transition metal oxides such as LCO and LFP, for the development of high-performance LIBs. Due to the p-orbital overlap in metallic CNT chiralities, easy conduction of electrons can occur via ballistic transport (i.e., the electrons can transport with mean free path on the order of microns along the length of nanotube unless scattered by a defect). This type of property exceptionally improves the specific capacities, C-rate performance, and cyclic stability when used as an additive with active materials, particularly in conjunction with the poor transport inherent to cathode materials like LFP.

The large specific surface area, good transport properties, and cage like more accessible structure of CNTs for Li insertion are useful for the development of high performance and flexible electrodes for LIBs. Recent literature shows the ability to maintain about 10% improvement in reversible capacity at low rates up to 3 C-rate for LCO and 5 C-rate for LFP (Landi et al. 2009). For any cathode material, intercalation of ion and electron transport properties are very critical for high performance. Carbon nanotubes exhibit very high electrical conductivity in axial direction, and due to their particular structure, free electrons are distributed in the surface of CNTs, which help them displace randomly (Jin et al. 2008). A novel network made from LFP particles mixed with CNTs is being studied for high rate capabilities. The networks consisting of CNTs interconnect the LFP particles, which



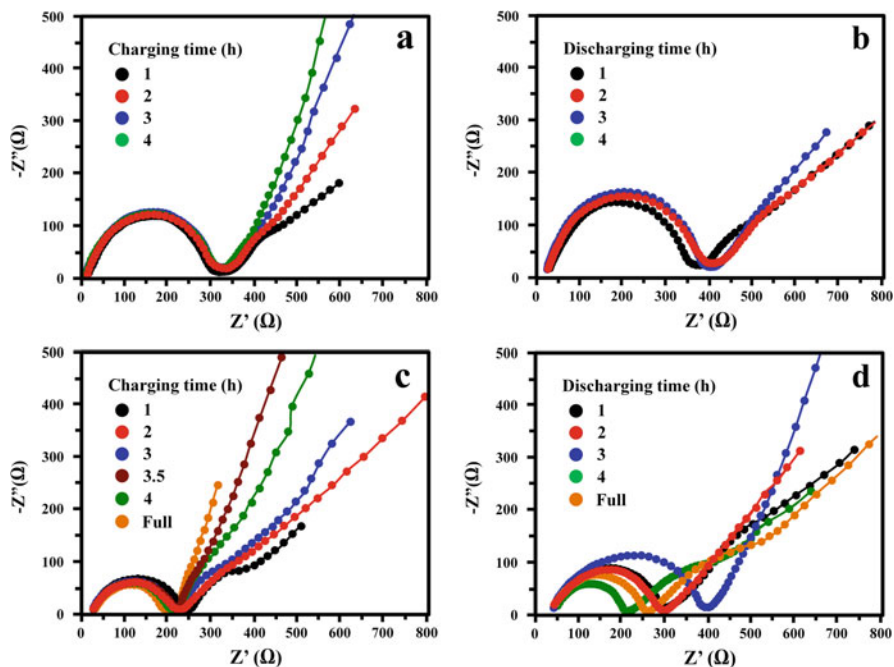


**Fig. 2.7** Electrochemical impedance spectra of cathodes: (a) Non- modified  $\text{LiFePO}_4$ , (b) Non modified  $\text{LiFePO}_4$ , (c) CNTs-modified  $\text{LiFePO}_4$ , (d) CNTs-modified  $\text{LiFePO}_4$ . (Reprinted with permission of Elsevier from Chen et al. 2010)

effectively enhance the electron transfer between the active material and current collector. The impedance slope of LFP/CNT composite studied by using electrochemical impedance microscope is very high, indicating enhanced electrochemical activity of LFP due to CNT network (Fig. 2.7). When comparing the non-modified LFP and CNTs-modified LFP, the resistance of charge transfers at high frequency drops sharply in all states. This shows that the state of charge has null effect on charge transfer resistance. From this, it can be concluded that CNTs have immense role in accelerating the charge transfer. There is a spontaneous increase in the charge transfer resistance from the state of charge to discharge. A substantial divergence is being perceived in the state of discharge. With this process of discharge, the resistance of charge transfer dwindles. This will be the reason for the enhancement of electronic conductivity and increase in contact efficiency between the particles of CNTs-modified LFP cathode that lessen the charge transfer resistance. The fall of resistance helps the improvement in performance, thus giving the major contribution for the excellent electrochemical performance of CNTs-modified LFP at high rate (Chen et al. 2010).

CNT-modified  $\text{LiFePO}_4$  evince exceptional performance in terms of both specific capacity and cycle life. The increase in electronic conductivity adversely increases the specific capacity and cyclic life of LFP. Both SWCNTs and MWCNTs are

effectively used in order to enhance the electrochemical performance of LFP. The modification of LFP with MWCNT evinces the electronic conductivity of LFP due to the formation of 3D network wiring. The addition of MWCNTs to LFP results in high capacity with fast rate and high efficiency. MWCNTs prepared by hydrogen arc discharge method in normal atmosphere and room temperature when incorporated with LFP showcased better charge-discharge cycling behaviors than LFP with acetylene black at the same amount of content respectively. The specific area of acetylene black is 92 m<sup>2</sup>/g, which is very much larger than that of MWCNTs, which have a surface area of 71 m<sup>2</sup>/g. The acetylene black has many oxo-functional groups and micropores on the surface that affect the electrochemical performance of LFP, which is being tackled by the introduction of CNTs- to LFPs (Li et al. 2007).

There are many methods of synthesis of CNT-modified LFP, like hydrothermal process, sol-gel synthesis, solid-state reactions, spray drying method, two step solution method, polyol process, electrospinning, and chemical vapor decomposition. In hydrothermal process, the CNTs are being coated with the help of high temperature in aqueous solution with high vapor pressure. Usually the construction of 3-D network of LFP/CNT, in which CNTs coat and connect the LFP nanoparticles, synthesized by hydrothermal process is being assisted by ethylene glycol. The presence of EG can limit the growth of LFP particles and help in the development of homogeneous structure. Very high initial discharge capacity, capacity retention, and rate capability are exhibited. The particle size of LFP, synthesized by hydrothermal method with the assistance of EG, is very small and thus improve the electronic conductivity performance of battery (Feng et al. 2017). This method of synthesis on large scale can enhance the manufacturing of batteries with higher rated capacity, which is useful for automotive industry for electric vehicles (Thanh et al. 2018). An attractive application of CNT-modified LFP proposed by adding a low fraction of graphene displays substantial increase in current density and Li<sup>+</sup> diffusion (Chen et al. 2018). Another study revealed that mesoporous 3-D CNT-modified LFP microsphere (Fig. 2.8) embedded homogeneously not only increase electronic conductivity, but also facilitate the penetration of electrolyte into the microstructure which was synthesized by polyethylene glycol (PEG)-assisted method using different molecular weight of PEG (400, 1500, and 20,000 gmol<sup>-1</sup>). The morphology of samples are displayed in Fig. 2.9 (Tan et al. 2014) Among the different samples the composite microsphere fabricated with 400 molg<sup>-1</sup> PEG showed enhanced electrochemical performance with a capacity retention of 95.7% even at 5 C after 100 cycles (Fig. 2.10).

Another method of synthesis for CNT composite is chemical vapor decomposition, where the CNTs-modified LFP synthesized by this method significantly enhances the electrochemical performance. By this method, CNT is coated uniformly on LFP grains and this improves the quality of the cathode (Tian et al. 2015). CNTs-modified LFP nanoplates composite cathode with graphene sheets (GS) by one-step polyol process under low temperature has been studied and found that CNTs are evenly distributed among LFP particles. Also the cross-linked CNTs penetrate through or embed into the LFP particles. In addition, the CNTs and GS inter-weaving tightly with each other thus form a 3-D network throughout the

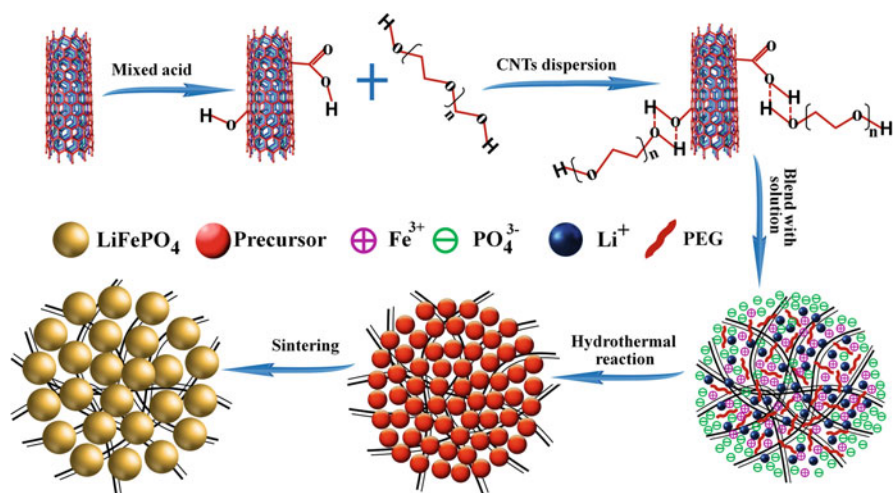


**Fig. 2.8** Schematic illustration of the formation process of the porous LFP/CNTs microsphere. (Reprinted with permission of Elsevier from Tan et al. 2014)

composite materials. This distinctively conductive network were successfully incorporated, which supply more paths and accelerate the speed of electron transfer and  $\text{Li}^+$ -ion diffusion in the composite. The electrochemical studies showed that the addition of CNTs led to the increase in specific capacity of LFP. The CNT-modified LFP synthesized by polyol process exhibit cycling profiles smoother than that of pristine LFP, indicating better cycling stability and superior reversibility of  $\text{Li}^+$ -ion insertion/extraction reactions of the composite (Wu et al. 2013a). CNT decorated with LFP and carbon has been reported by Wu et al. (2013b) in which they have obtained a low temperature performance at  $-25^\circ\text{C}$  and high temperature performance at  $120^\circ\text{C}$ . The morphological studies reveal that the carbon-coated LFP/CNT composite exhibits a single crystalline nature (Fig. 2.11) and show higher capacity retention at higher C-rate and cycling stability in both low and high temperatures (Fig. 2.12).

Carbon nanospheres (CNS)-modified LFP composite prepared by sol-gel route produced desirable structure of olivine composite. Compared to CNT; CNS exhibit novel characteristics such as greater diameter, high surface area, and electronic conductivity. During the sol-gel synthesis rather than a uniform coating, an agglomeration of CNS particles is formed over the LFP surface. This reveals that the simple mixing of CNS and LFP cannot ensure the formation of network. Similar is the case for CNTs (Liu et al. 2010). An innovative and environment friendly CNT-modified LFP composite cathode was synthesized by sonication of Na-carboxymethyl cellulose in aqueous medium, which not only delivers high electrochemical performance, excellent charge storage capability, and cycling stability but also creates sufficient space between CNT particles that facilitate the faster electrolyte permeability, thus easy to wet the electrode leads to early stabilization of the cell. This in turn decreases

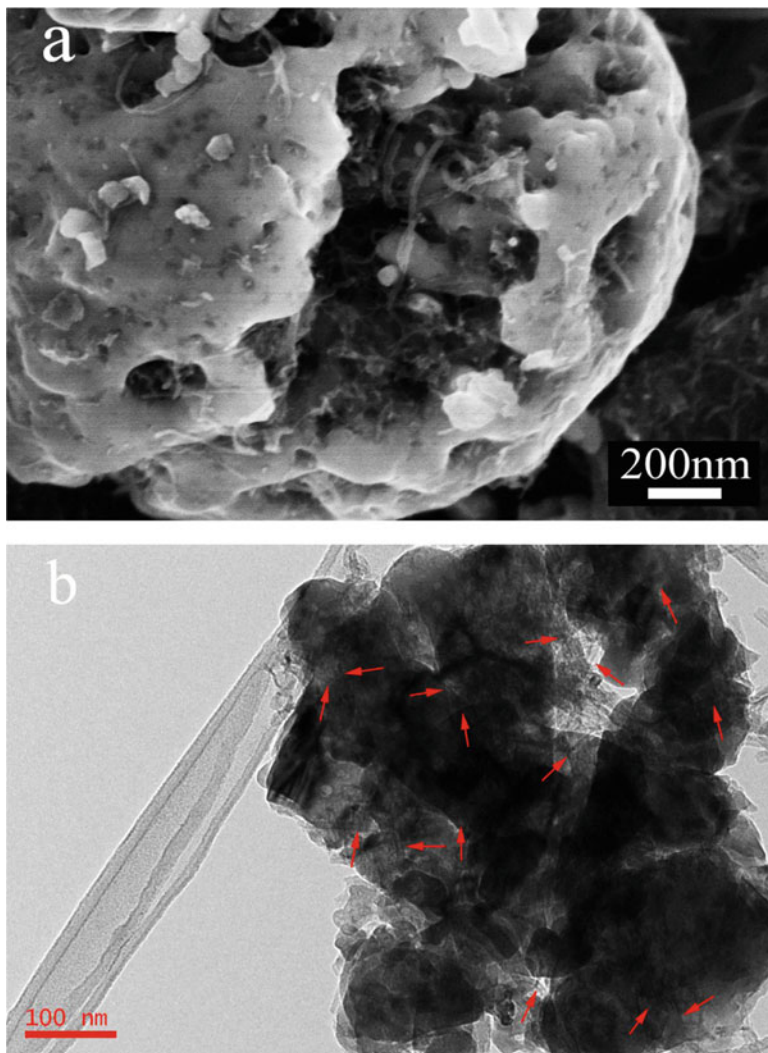


**Fig. 2.9** (a) SEM image, (b) TEM image of crushed M-LFP/CNTs-400 microsphere. (Reprinted with permission of Elsevier from Tan et al. 2014)

the concentration polarization when cathode is being subjected to high current loads. Besides the remarkable performance of battery, the great advantage of this is its environment friendly nature (Varzi et al. 2014). A hierarchical porous carbon-coated CNT-modified LFP microsphere composite is being experimented to enhance the properties of positive electrode. This method not only enhanced the electronic conductivity but also aimed to optimize the desired microstructure for accelerating mass transfer and enhance the tap density simultaneously. It has been found that the Li<sup>+</sup> transport in electrolyte toward the active site may also be limiting factor at high

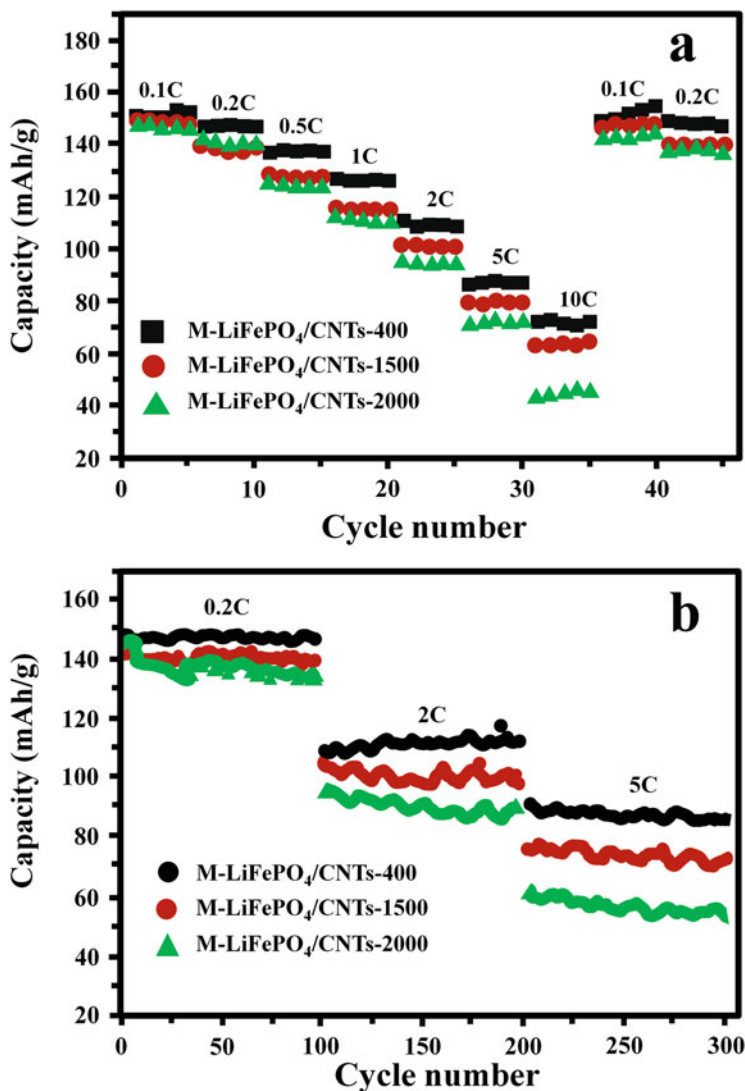
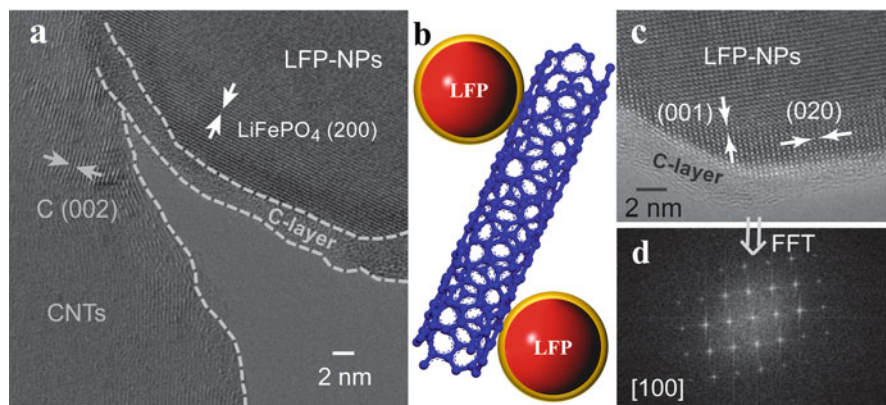


Fig. 2.10 (a) Rate capabilities and (b) cycling performances of the M-LFP/CNTs-x composites. (Reprinted with permission of Elsevier from Tan et al. 2014)

rates, and tap density directly influence the volumetric energy densities in LIBs, which is an essential feature for electric vehicles (EVs) and hybrid electric vehicles (HEVs) (Wang et al. 2016).

The electrochemical performance of carbon-coated LFP/MWCNT composite cathode having micron size of LFP (100–200 nm) (Qin et al. 2014b) and nanosized LFP (40–90 nm) (Zou et al. 2013) were reported. LFP have a carbon coating of thickness of 1–3 nm using poly(acrylonitrile) (PAN) (Qin et al. 2014a) or sucrose



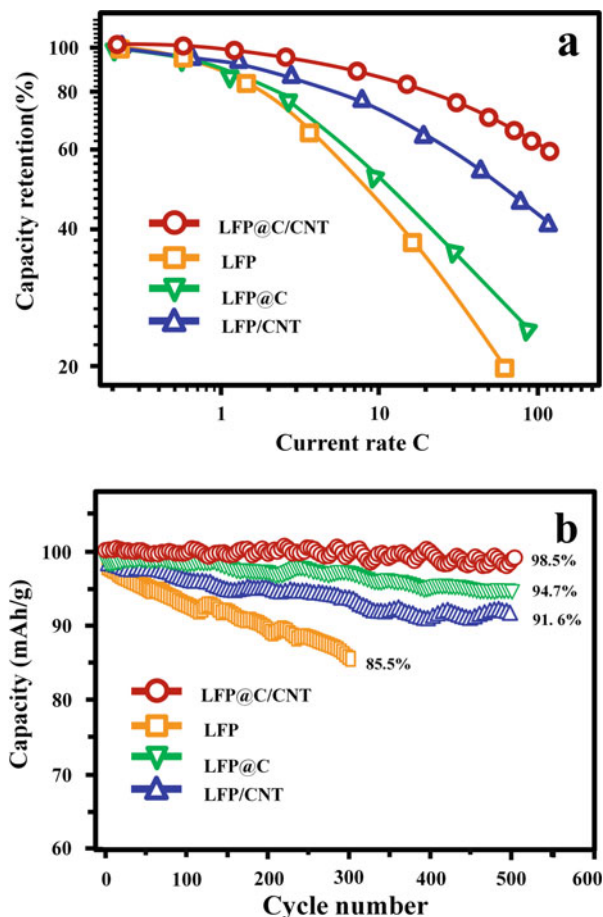
**Fig. 2.11** (a, c) HRTEM images of the prepared LFP@C/CNT nanocomposite; (b) schematic illustration of the prepared LFP@C/CNT nanocomposite; (d) the corresponding FFT pattern of the HRTEM in (c) (Reprinted with permission of John Wiley and Sons from Wu et al. 2013b)

(Wu et al. 2013c; Wang et al. 2016) as a carbon source. The electrical conductivity shown by C-LFP/MWCNT is  $2.3 \times 10^{-2} \text{ Scm}^{-1}$  (micron-sized LFP) and  $7.7 \times 10^{-2} \text{ Scm}^{-1}$  (nanosized LFP), which is much higher than the C-LFP or pristine LFP indicating that CNTs and amorphous carbon are the cause for the enhancement of electronic properties. The charge–discharge capacity of C-LFP/CNT is  $\sim 170 \text{ mAhg}^{-1}$  at a current density of 0.5 C and  $\sim 142 \text{ mAhg}^{-1}$  at 20 C with good capacity retention even at high C-rate (Qin et al. 2014a, b). The carbon-coated CNT-modified LFP exhibits superior electrochemical properties in terms of an ultra-high rate capability. For LIBs in electric vehicles, charging time is very important. It has been observed that the C-LFP/CNT cathode only took 142 s (20 C) for charging 76% of full charge capacity (Wang et al. 2016).

Qiao et al. (2017) reported LFP/CNT composite cathode exhibiting a high discharge capacity of  $123 \text{ mAhg}^{-1}$ . The LFP based composite cathode also evinced long cycling stability, which is prepared by using CNTs coated with polyvinylpyrrolidone (PVP). The composite cathodes obtained contain 3 wt. % CNT showed a high discharge capacity of  $123 \text{ mAhg}^{-1}$ . The cathode also exhibited a very low capacity fade of 1.6 and 20% up to 1000 and 3400 cycles respectively at a current density of 10 C. The loss in capacity in this study is four to eight times lower than that of previously reported LFP/CNT and LFP/graphene composite cathodes (Qiao et al. 2017). This superior rate capability and ultra-high cycling stability is accredited to the combined effect of the large  $\text{Li}^+$ -ion diffusion coefficient achieved in LFP nanoparticles by mixing with CNTs and the highly conductive 3-D framework of monodispersed CNTs, which is free from breaking and entangling effects (Qiao et al. 2017).

Electrospinning is an easy and versatile method of preparation of binder-free electrodes with fibrous morphology and controlled properties. The Fig. 2.13 shows schematic representation of an electrospinning set up for the preparation of metal

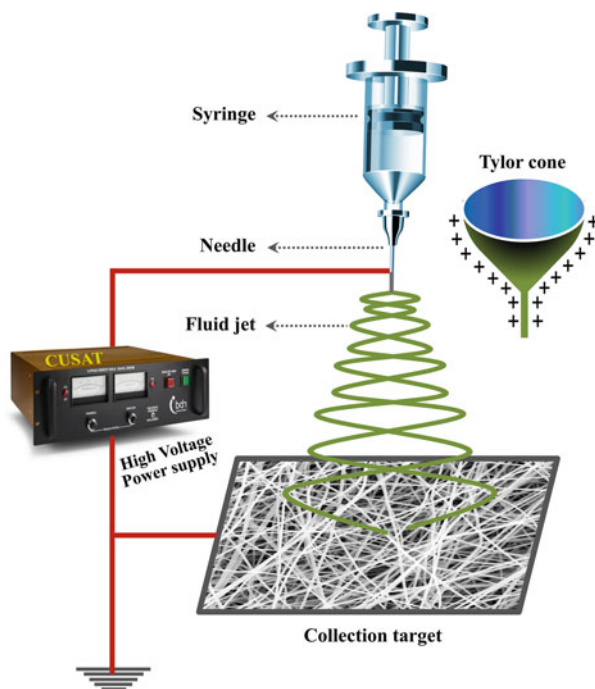
**Fig. 2.12** Comparisons of (a) rate capability and (b) cycling performances of LFP@C/CNT, LFP@C, LFP/CNT, and pristine LFP. (Reprinted with permission of John Wiley and Sons from Wu et al. 2013b)



oxide nanofibers. Toprakci et al. (2012) reported of the synthesis of LFP/CNT/C composite nanofibers by electrospinning and sol-gel method using CNT as functional filler and PAN as the medium for electrospinning and carbon source. The hybrid fibrous electrode evinces an initial reversible capacity of 150, 162, and 169  $\text{mAhg}^{-1}$  for pristine LFP powder LFP/C and LFP/CNT/C composite nanofibers respectively. The unique fibrous structure of LFP/CNT/C, high surface-volume ratio, complex porous structure, and shorter  $\text{Li}^+$ -ion diffusion pathway, enhance the electrode reaction kinetics and reduces the polarization, which in turn gives a good cycling stability, high reversible capacity, and high rate capabilities (Toprakci et al. 2012).

CNTs-modified LFP coated with carbonaceous materials (C/CNT-LFP) also received great attention as cathode materials in LIBs owing to their enhanced conductivity. C/CNT decorated LFP have been synthesized by polyol-based synthesis, which showed specific capacitance of  $160 \text{ mAhg}^{-1}$ . The samples also showed enhanced performance even at low temperature of  $-25^\circ\text{C}$  (Wu et al. 2013c). A 3D,

**Fig. 2.13** Schematic of typical electrospinning set up



porous, hierarchically modified C/LFP/MWCNT composite electrode was fabricated via in situ sol-gel method, showed enhanced electrochemical properties compared to the LFP and LFP/CNT electrodes. Modified C/LFP/MWCNT composite electrode delivers a power density of  $16.8 \text{ kWkg}^{-1}$  whereas for pristine LFP is  $12 \text{ kWkg}^{-1}$  and that of CNT/LFP is  $14 \text{ kWkg}^{-1}$ . Similarly, energy density of C/LFP/MWCNT composite electrode is much higher ( $84 \text{ Whkg}^{-1}$ ) compared to that of pristine LFP and CNT/LFP ( $60$  and  $70 \text{ Whkg}^{-1}$ ). The rate performance of C/LFP/MWCNT composite electrode was obtained about  $142 \text{ mAhg}^{-1}$  at  $20 \text{ C}$ -rate. At low C-rate C/10, it showed a capacitance of  $169.6 \text{ mAhg}^{-1}$ , which was almost equal to the theoretical capacity of LFP ( $170 \text{ mAhg}^{-1}$ ) (Qin et al. 2014a). The morphological studies (Fig. 2.14) showed a uniform carbon coating is formed over the porous LFP, which greatly contributes to the electrochemical properties (Fig. 2.15) and electronic conductivity of the composite material.

The electrodes in LIBs contain a large amount of inactive materials, which limit the specific capacity of LFP to  $120 \text{ mAhg}^{-1}$  from  $170 \text{ mAhg}^{-1}$ . There have been many attempts to eliminate these inactive components from LFP cathode by introducing a freestanding flexible cathode with super P and polyvinylidene difluoride (PVDF) binder and without super P or PVDF binder (Susantyoko et al. 2017). The freestanding electrode with 90 wt.% LFP at the current rate of  $170 \text{ mAg}^{-1}$  delivers a specific capacity of  $\sim 134 \text{ mAhg}^{-1}$  (Susantyoko et al. 2018), which is much higher than the specific capacity of  $\sim 79 \text{ mAhg}^{-1}$  at a current rate of  $127 \text{ mAg}^{-1}$  (about



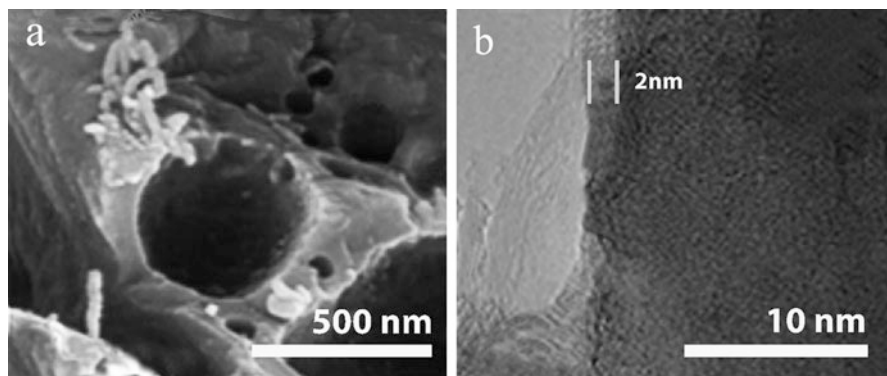
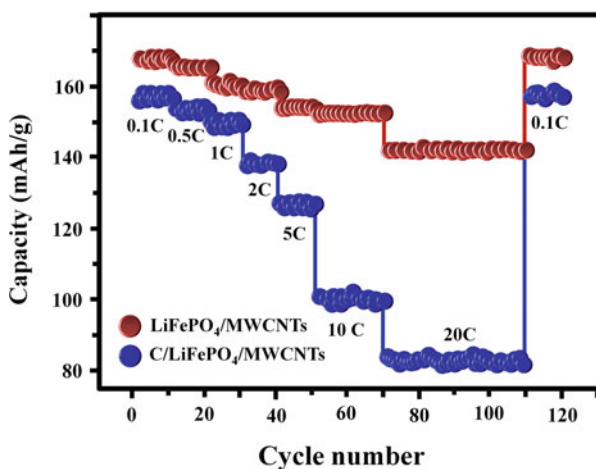


**Fig. 2.14** Morphology of LFP (a) SEM image of pure LFP, (b) HRTEM image of C/LiFePO<sub>4</sub>/MWCNT. (Reprinted with permission of Elsevier from Qin et al. 2014a)

**Fig. 2.15** The rate performance curves of MWCNTs modified LiFePO<sub>4</sub> materials at various current rates (0.1–20 C). Reprinted with permission of Elsevier from Qin et al. 2014a)



0.75 C-rate) reported in earlier study (Susantyoko et al. 2017). The difference in capacity is due to the different grade of MWCNT used in different studies.

### LiFePO<sub>4</sub>/Graphene Composite Electrode

The 2D sheets of carbon composed of sp<sup>2</sup> hybridized carbon atoms forming one atom thick planar sheet are known as graphene. It exhibits extraordinary properties such as high conductivity, mechanical stability, thermal stability and flexibility (Mao et al. 2012). It is the most strongest material which has been ever discovered (Papageorgiou et al. 2017). Incorporation of graphene with the metal oxides substantially enhances its electrochemical properties. The synergistic mechanism offered by this nanocomposite helps to deliver the properties of both graphene as

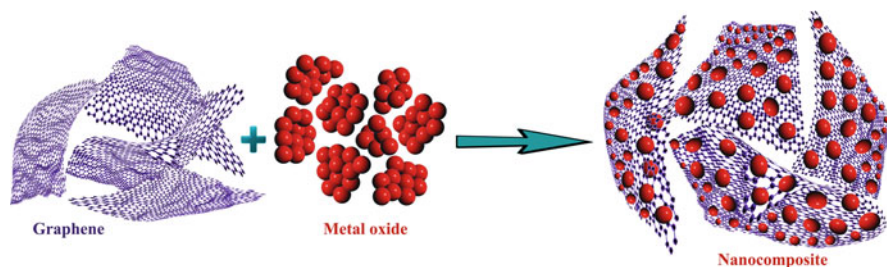


**Fig. 2.16** Schematic of the preparation of graphene/metal oxide composites with synergistic effects between graphene and metal oxides. (Modified after Wu et al. 2012)

well as the metal oxides (Fig. 2.16). This effect can be made use to enhance electrochemical properties of LFP, hence LFP/graphene composite electrode will substantially enhance the conductivity compared with pristine LFP electrode.

In recent past, a composite cathode of LFP with graphene and its nanostructures had been given much importance for its ability to enhance the electrochemical performance of LFP-based cathodes. The active material for use of cathode material is processed by the methods like, sol-gel, hydrothermal, or solid state reactions (Xu et al. 2007; Xiang et al. 2010). Until today, LFP/graphene composites are prepared by the simple methods such as sol-gel method (Yang et al. 2012), the solid state reactions (Wang et al. 2015b), the hydrothermal method (Wang et al. 2010; Zhang et al. 2012; Bo Wang et al. 2015a), co-precipitation method (Ding et al. 2010), and simple physical mixing. Ding et al. (2010) first reported a LFP/graphene composite having a specific capacity of  $160 \text{ mAhg}^{-1}$  as compared to  $113 \text{ mAhg}^{-1}$  for commercial LFP. Su et al. (2010) brought graphene into LFP as a planar conductive additive to give a flexible graphene based conductive network. These past studies conclude that even with a lower fraction of graphene additive (compared to commercial carbon-based additives such as CNT and CNF), the charge/discharge performance of the nanocomposite is superior to the pristine LFP. A conducting LFP/graphene composite was prepared using a facile hydrothermal method followed by heat treatment by Wang et al. (2010). and found that LFP particles attached to the surface of graphene or embedded in graphene nanosheets showed higher electronic conductivity and  $\text{Li}^+$ -ion diffusion due to the formation of uniformly interconnected 3D conducting network of graphene nanosheets (Wang et al. 2010). Similar charge-discharge and cycling properties were reported for LFP/graphene nanocomposite synthesized in the ratio of 92:8. The LFP/graphene nanocomposite exhibited a discharge capacity of  $160.3 \text{ mAhg}^{-1}$  at 0.1 C and  $81.5 \text{ mAhg}^{-1}$  at 10 C (Wang et al. 2010). For further improvement, Y. Wang et al. (2012) prepared LFP/graphene nanocomposite by solid-state synthesis, 3-D porous LFP/graphene composite via sol-gel process (Yang et al. 2012), and simple mechanical mixing methods (Tang et al. 2012). The specific capacity of  $161 \text{ mAhg}^{-1}$  at 0.1 C and  $70 \text{ mAhg}^{-1}$  at 50 C (Wang et al. 2012) were reported for composite prepared by solid-state synthesis, whereas porous LFP/graphene composites evinced a capacity values of 45–60 and 75–109  $\text{mAhg}^{-1}$  without and with graphene respectively for a high rate of 10 C

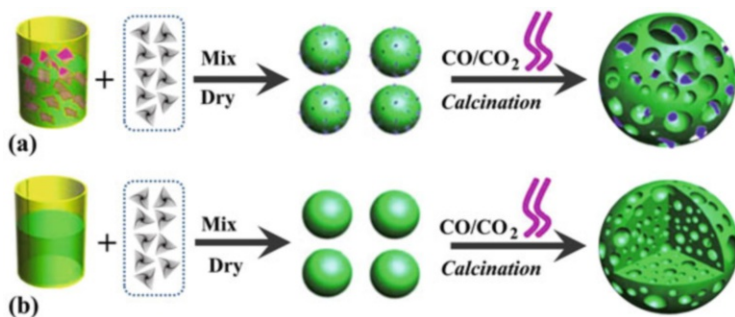


**Fig. 2.17** Schematic representation of formation of 3-D porous networks: (a) LFP/graphene and (b) LFP. (Reprinted with permission of Elsevier from Ma et al. 2013)

(Yang et al. 2012). The sol-gel method exhibited superior performance even at higher rates compared to other methods by mechanical mixing (Tang et al. 2012) and solid-state synthesis (Wang et al. 2012). Dhindsa et al. (2013b) used sol-gel method to prepare LFP/graphene nanocomposite to increase the electronic conductivity of LFP. Graphene oxide (GO) was mixed with LFP precursors for this study. The resulting composite improved the electron conductivity by six orders of magnitude compared to the pristine LFP (Dhindsa et al. 2013b). The uniformly sized LFP particles are covered by graphene nanosheet and form an interconnected 3-D conducting channel, which is responsible for high electronic conductivity. Additionally, a high specific capacity of  $160 \text{ mAhg}^{-1}$  was recorded, which is near to theoretical value limit, and excellent cycling stability was achieved. In order to reduce the distance of  $\text{Li}^+$  diffusion, three-dimensional nanoporous spheres within micron size regime are considered to be the optimal structure for LFP, capable of achieving high power capability without altering the packing density and facilitating the quick and efficient transport of ion and charge (Magasinski et al. 2010). LFP/graphene porous composites synthesized by a facile template-free sol-gel method (Yang et al. 2012) (Fig. 2.17) and facile precipitation method (Ma et al. 2013) were employed for two different studies. The reversible capacity of LFP/graphene ( $146 \text{ mAhg}^{-1}$  at  $17 \text{ mA} \text{g}^{-1}$ ) obtained is 1.4 times greater than that of porous LFP ( $104 \text{ mAhg}^{-1}$ ), demonstrating the incorporated graphene substantially enhances the specific capacity throughout the charge–discharge cycling process. It has also been noted that the porous LFP/graphene composite also shows a considerable tolerance to differing charge/discharge current densities. However, it is observed that the oversized holes fail to achieve the advantage of high tap density of porous structure, and no significant improvement on electrochemical performance is observed by the non-uniform distribution of graphene. Ma et al. (2013) prepared a  $\text{GO/Li}_3\text{PO}_4$  composite by precipitation process which was employed as a sacrificial template for the hydrothermal synthesis of porous graphene LFP composite. The LFP microspheres exhibited a uniform morphology, which are being wrapped by graphene nanosheets. The LFP/graphene cathodes deliver discharge capacities of 141, 130.9 and  $101.8 \text{ mAhg}^{-1}$  at current rates of 0.1, 1 and 10 C respectively due to

the formation of effective 3-D conducting network, formed by bridging of graphene nanosheets and the porous structure, which could absorb electrolyte to the interior of the LFP particles that help the easy diffusion of Li ions. The electrochemical studies showed that LFP/graphene nanocomposite material exhibits good rate capability, and displayed about 72% of the initial capacity at 10 C. The increase in performance is accredited to the porous LFP microsphere which exhibited a hierarchical structure assembled by nanoparticles, higher electronic conductivity, and chemical stability of graphene network in composite and porous structure in approval of Li ion diffusion (Ma et al. 2013).

By co-precipitation method of preparation of nanostructured LFP/graphene, composites in de-ionized water at room temperature was reported by Ding et al. (2010). In LFP/graphene composites, graphene nanosheets were used as scaffolds. There is a decrease in discharge capacity with higher C-rate, which is being accredited interfacial impedance offered to the Li<sup>+</sup>-ion diffusion at LFP and FePO<sub>4</sub> interface. The cycling stability and rate capability of LFP/graphene has been assured to the fact that nanosized particle with large surface area and improved electrical conductivity through the graphene nanosheets to increase the electronic conductivity and lowers the contact resistance between LFP and GNS (Ding et al. 2010; Chen et al. 2013). Yang et al. (2013) reported comparative study of electrochemical properties of folded and unfolded LFP/graphene nanocomposites. It is found that the composite electrode delivers good discharge capacity which is about 98% to the theoretical capacity (170 mAhg<sup>-1</sup>) and showcased a stable cycling behavior for 100 cycles. The composite electrode prepared with unfolded graphene was able to achieve high capacity due to efficient dispersion and restriction of size in nanoscale of LFP. The LFP particle easily attach with unfolded graphene and set a good interface between graphene nanosheets and LFP particles, thus increases the electronic conductivity (Yang et al. 2013). The LFP cathode with a specific capacity higher than theoretical value using carbon-coated LFP surface modified with 2 wt.% of electrochemically exfoliated graphene layer was reported by Hu et al. (Lung-Hao Hu et al. 2013). The composite cathode delivers a specific capacity of 208 mAhg<sup>-1</sup> without causing unfavorable voltage polarization. The composite cathode delivers a specific capacity of 208 mAhg<sup>-1</sup> without causing unfavorable voltage polarization. The enhanced conductivity exhibited by exfoliated graphene flakes wrapping around C-coated LFP helps fast electron transfer during the charge/discharge cycles, which in turn gives 100% Coulombic efficiency without fading at different current rates. The energy density is 686 Whkg<sup>-1</sup>, which is very much higher than the typical 500 Whkg<sup>-1</sup> of LFP. The graphene flakes which cover over the C-coated LFP exhibit high conductivity, diminishing the irreversible capacity at first cycle and thus giving ~100% Coulombic efficiency (Lung-Hao Hu et al. 2013). 3% graphene incorporated LFP composite cathode shows an initial discharge of 164 mAhg<sup>-1</sup> only owing to the grasping of Li<sup>+</sup>-ions by the multi-layer graphene films of LFP nanocomposite during the charge/discharge process (Wang et al. 2018). The synthesis of LFP/graphene composite was always found to be time consuming process. The motive behind this has always been to design an easy-to-use method and produced easily at low cost. Studies revealed that the best method for processing

LFP/graphene composite in terms of energy capacity is hydrothermal method with an efficiency of 97% of the theoretical value (Lei et al. 2014). The temperature in this method was being maintained at 180 °C for 10 h, the solution is cooled at room temperature, precipitated, centrifuged, washed in deionized water three times, dried under vacuum for 4 h, and finally sintered at 600 °C for 2 h under hydrogen/argon (5:95, v/v). This method also provided an easy pathway for electron transfer and Li<sup>+</sup> diffusion. Spray-drying is also an effective method for the preparation of LFP/graphene composite. Zhou et al. (Chem et al. 2011) studied the facile procedure by physical mixing of LFP and reduced graphene oxide (rGO) suspension when spray dried at 200 °C to be a solid LFP/graphene composite and annealed to form the LFP/graphene composite cathode. These LFP primary nanoparticles embedded in micron-sized spherical secondary nanoparticles were wrapped homogeneously and loosely with rGO sheets, thus forming a 3-D graphene network bridging between LFP. This structure is beneficial for fast electron transfer throughout the secondary particles, while the presence of ample voids between LFP nanoparticles and graphene sheets help for Li ion diffusion. This composite cathode exhibited high specific capacity and charging/discharging, cycling stability, and rate capability. The synergetic effect offered by the combination of nanosizing with organized conducting templates to provide an excellent electron transport for high power applications was being demonstrated by Sun et al. (Ha and Lee 2015). The study reported on a size-constrained in situ polymerization method to process core-shell C-coated LFP nanoparticles hybridized with rGO as a cathode for high-power LIBs. In order to prevent the spontaneous aggregation of hydrophobic graphene in a aqueous solution, hydrophilic graphene oxide was used as precursor during the formation of LFP/graphene composite via in situ polymerization of pyrrole. The fabrication of C-coated LFP/rGO hybrid cathode material is been accredited to three factors: (i) in situ polymerization of polypyrrole (Ppy) for constrained nanoparticle preparation of LFP, (ii) increase in dispersion of conducting 2-D networks endowed by colloidal stability of GO, and (iii) intimate film contact between the LFP and rGO nanosheets. The study evinced the importance of conducting template dispersion by different LFP/C-rGO composites in which an agglomerated rGO solution has been used as the starting template. The hybrid C-coated LFP/rGO cathodes exhibited superior rate capability and discharge capacity close to that of the theoretical capacity, thus increasing the electrochemical performance which is again accredited to the fast electron and Li<sup>+</sup>-ion transport through nanosized active materials (Ha and Lee 2015). Bi et al. (2013a) studied three methods to synthesize graphene by chemical vapor deposition (CVD), Wurtz-type reaction and chemical exfoliation (Bi et al. 2013a). The study claimed that the presence of graphene reduced the contact resistance between LFP particles, which enhanced the electronic conductivity of LFP. It also reported that LFP/graphene nanocomposite prepared with graphene by CVD is more efficient in terms of electronic conductivity, contact resistance, and electrochemical performance.

## LFP/Sulphur Cathodes

The performance of LFP can be enhanced by appropriate doping in the site of oxygen leading to anion doping (Liu et al. 2008). Sulfur being a same group element of oxygen with similar properties but with larger size makes the element suitable for anion doping in LFP to enhance the performance (Okada et al. 2018). The increase in size of the anion will enhance the rate de-intercalation owing to the lower dissociation energy of Li-S bond. Sulfur-lithium iron phosphate composites were synthesized by various processes such as solvothermal method (Okada et al. 2018), sol-gel method (Xu et al. 2016), mechano-fusion process (Seo et al. 2015), and solid state method (Yu et al. 2016). Apart from these common methods of synthesis, sulfur coated LiFePO<sub>4</sub> can be obtained by exposing the precursor with sulfur vapor at 400 °C followed by annealing at 400 °C in vacuum (Park et al. 2012). In 2012, Goodenough et al. (Park et al. 2012) proved the enhancement in the charge transfer ability of LFP cathode on nitrogen and sulfur substitution on the surface of anion. According to the theoretical studies reported, the non-coordinated ferrous and ferric ions on the surface of the LFP inhibit the charge transfer causing a decrease in the electrochemical performance of the electrode. On sulfur substitution, the sulfur stabilizes the antibonding 3-D states forming Fe-S bond. During intercalation Li<sup>+</sup> ion binds on the LFP with a binding energy of 0.18 eV (Park et al. 2012). The sulfur substitution is capable to influence the surface energy levels and the charge transfer kinetics. Later in 2015, experimental studies on the effect of sulfur substitution was proved by enhancement in the capacity retention and electrochemical properties (Seo et al. 2015). In 2016, Guan et al. (Yu et al. 2016) studied sulfur substituted LFP/C cathode to obtain a specific capacitance of 114 mAhg<sup>-1</sup> at current density of 0.2 Ag<sup>-1</sup>. Sulfur doped carbon decorated LFP was reported by Xu et al. (2016) obtaining a capacitance of 163.6 mAhg<sup>-1</sup> at a current rate of 0.1 Ag<sup>-1</sup> with a retention ratio of 99.6% after 20 cycles. Sulfur doping on to LFP in the ratio of Li: Fe: P: S is 2.7: 1: 1: 0.22 gave an optimum result with an enhancement of 131 mAhg<sup>-1</sup> at current density of 0.5 Ag<sup>-1</sup>, whereas undoped LFP was reported to have 120.6 mAhg<sup>-1</sup> (Okada et al. 2018). The electrochemical comparison of sulfur doped LFP and undoped LFP is depicted in Fig. 2.18.

### 2.3.4 Doping

Lattice substitution or doping is an alternative method to improve the electronic conductivity of the LFP. Lattice substitution can be done either in lithium site or in iron site. Doping at the lithium (Li) and iron (Fe) site leads to a reduction in the band gap that enhances the electronic conductivity, but the doping process is highly temperature dependent.

Fe site substitution can be done with Mn, Ni, or Co like species that results in the formation of LiMnPO<sub>4</sub>, LiNiPO<sub>4</sub>, LiCoPO<sub>4</sub> as well as partially substituted

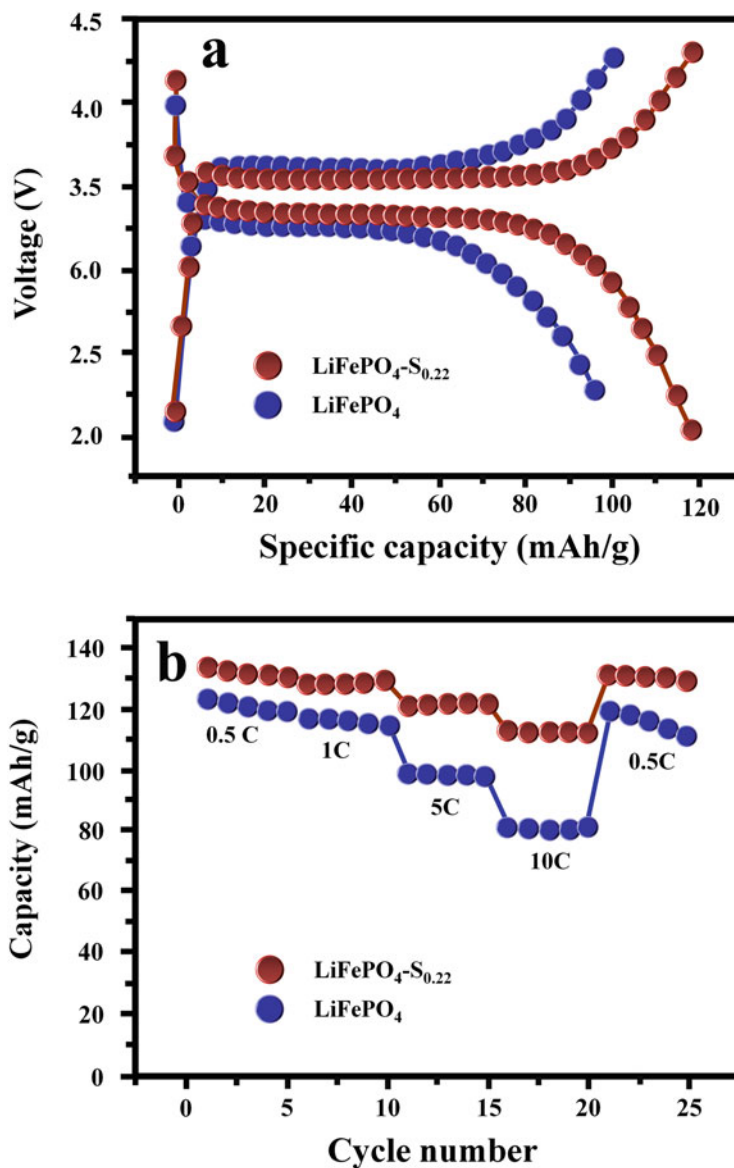


**Fig. 2.18** (a) Charge-discharge curves of LFP and LFP-S<sub>0.22</sub> at 5C, (b) rate performance of LFP and LFP-S<sub>0.22</sub>. (Reprinted with permission of Royal Society of Chemistry from Okada et al. 2018)

compound can also be formed. But due to the energy barrier for the movement of these compounds, the results show a poor property than  $\text{LiFePO}_4$ . The partial substitution of iron ion site is found to be effective in order to improve the bulk conductivity of the olivine compound. Doping with multi-valent cations such as

Al<sup>3+</sup>, Zr<sup>4+</sup>, and Nb<sup>5+</sup> provides an improvement in conductivity compared to that of the former. Compared to mono-valent dopant such as Na<sup>+</sup> at the Li<sup>+</sup>-ion site and M<sup>2+</sup> doping at the Fe<sup>2+</sup> site results in a low favorable energy for Li<sup>+</sup>-ion diffusion. At the same time substitution with the multi-valent cation at both the sites produce an improved conducting property (Fisher et al. 2008). It is found that the improved conductivity of doped olivine structures is not because of the bulk metallic property but due to the formation of a metallic iron phosphide at the surface. During its formation, reduction of LFP to iron phosphide (Fe<sub>2</sub>P) occurs, which induces a metallic conductivity over the LFP grains. Different methods are employed in order to form the dopant olivine structure; based on the synthesis method and temperature condition the effective property of the resultant olivine structure will get varied. Solid state reaction method and one step solid state methods are few of them (Fisher et al. 2008). Solid state reaction method is used for the preparation of Nb<sup>5+</sup> doped LFP and it shows that the ion dopant doesn't depend upon the structural property of LFP (Delacourt et al. 2006; Ban et al. 2012; Molenda et al. 2013).

Substitution of both lithium and iron sites depends strongly on variation in temperature since the solubility of doping decreases with increase in the temperature. Any of the divalent cations can be substituted for either Fe or Li-sites, however, according to the theoretical data multi-valent cations such as Al, Ga, Zr, Ti, Nb, Ta can't be substituted for either Li-site or Fe-site. But later studies show that multi-valent cations are capable to substitute both the Fe site and Li-site (Whittingham 2014). Croce et al. (2002) synthesized LFP with improved property by doping metals like silver and copper only about 1 wt.%. The doped metals improve the kinetics in terms of capacity and cycle life without affecting the structure of LFP.

### 2.3.5 *Size and Morphology*

Grain size and morphology of an electrode material is an important factor that determines its electrochemical performance. The morphology and particle size of LFP particles highly depend on the synthetic parameters such as volume ratio of solvent, reaction temperature, concentration, and feeding rate (Su et al. 2010). The nanosized cathode materials get more attention because of its better electrolyte contact and shorter transport length for both electrons and Li<sup>+</sup>-ions. Nanosized LFP crystals are found in different morphology as nano spindles, nano rods, urchins, nano particles, nano cuboids, and nano flowers (Fig. 2.19).

LFP nano flowers and nano rods reported exhibit superior electrochemical performance and specific capacity. LFP nano rods exhibit predominantly in (010) plane which provide short range pathway for Li<sup>+</sup>-ion transmission. In the case of nano flowers like morphology, diameter of each building block is less than 50 nm. So, the length of the pathway for Li<sup>+</sup>- ion transmission is different for different nano shapes (Nan et al. 2013). Different morphology helps to enhance the electrode–electrolyte interface which not only enhance the charge–discharge rate, but also improve the cycling performance (Bi et al. 2013b).



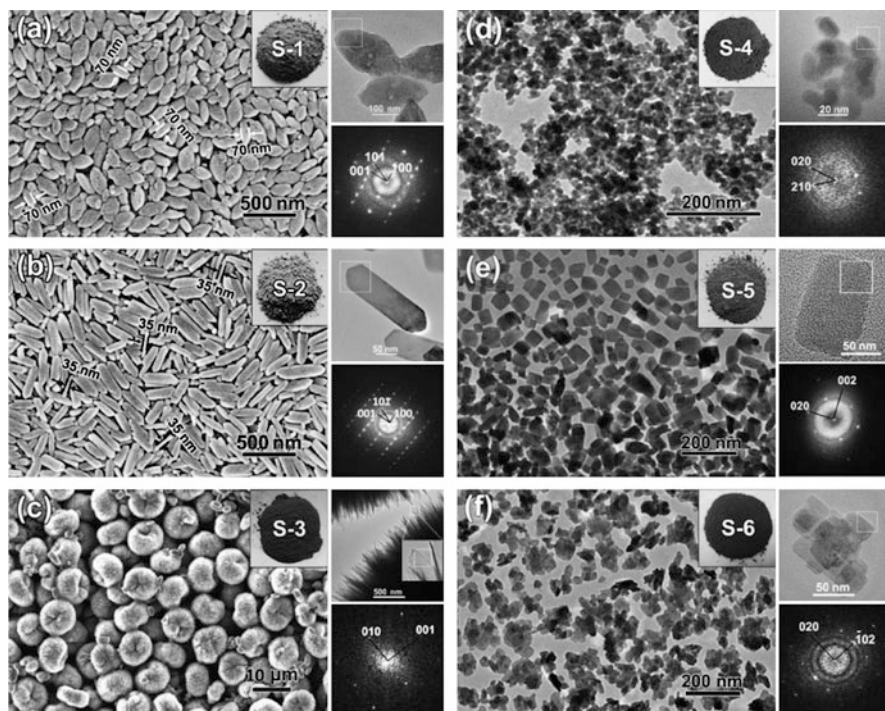


**Fig. 2.19** SEM (left), HRTEM (top-right), and FFT (bottom-right) images of; (a)  $\text{LiFePO}_4$  nanospindles, (b)  $\text{LiFePO}_4$  nanorods, (c)  $\text{LiFePO}_4$  urchins; TEM (left), HRTEM (top-right), and FFT (bottom-right) images of (d)  $\text{LiFePO}_4$  nanoparticles, (e)  $\text{LiFePO}_4$  nanocuboids, and (f)  $\text{LiFePO}_4$  nanoflowers. (Reprinted with permission of Springer Nature from Nan et al. 2013)

## 2.4 Conclusion and Future Outlook

LIBs are the systems that are potentially capable of changing the world. The revolutionary natures of LIBs lead to a huge transformation in battery world. However, some shortcomings make it a questionable technology for the future. The requirement of future batteries that are capable of working in extreme temperatures is important while considering military and space applications. Different research studies are carried out in order to enhance the extreme temperature properties. Being the best cathode, LFP can efficiently be used in variable temperatures with proper modification of the material. Performance of normal batteries appeared to be degrading below  $0^\circ\text{C}$ , but for LFP the electrochemical performance is observed to be efficient. For LFP, the insertion compounds such as  $\text{LiVOPO}_4$  exhibit extremely high temperature performance. While considering the low temperature performance, certain CNT-modified LFP exhibit improved low temperature properties. So, lithium iron phosphate batteries are going to be the future of energy storage

systems that are able to deliver high performance if it can be modified and can be efficiently used even at low and high temperatures.

**Acknowledgments** Author Dr. Jabeen Fatima M. J. would like to acknowledge the Kerala State Council for Science, Technology and Environment (KSCSTE) for financial assistance as post-doctoral research fellowship.

## References

- Ajayan PM, Ebbesen TW (1992) Large-scale synthesis of carbon nanotubes. *Nature* 358:220–222. <https://doi.org/10.1038/358220a0>
- Angela R, Islam H, Sari V et al (2017) Synthesis of LiFePO<sub>4</sub>/C composites based on natural iron stone using a sol gel method. *AIP Conf Proc* 1788:4–8. <https://doi.org/10.1063/1.4968355>
- Bağcı C, Akyıldız O (2018) Synthesis, characterization and electrochemical performance of Nb doped LiFePO<sub>4</sub>/C cathodes. *Hittite J Sci Eng* 5:49–55. <https://doi.org/10.17350/hjse19030000077>
- Ban C, Yin WJ, Tang H et al (2012) A novel codoping approach for enhancing the performance of liFePo 4 cathodes. *Adv Energy Mater* 2:1028–1032. <https://doi.org/10.1002/aenm.201200085>
- Bao L, Xu G, Sun X et al (2017) Mono-dispersed LiFePO<sub>4</sub>@C core-shell [001] nanorods for a high power Li-ion battery cathode. *J Alloys Compd* 708:685–693. <https://doi.org/10.1016/j.jallcom.2017.03.052>
- Benedek P, Wenzler N, Yarema M, Wood VC (2017) Low temperature hydrothermal synthesis of battery grade lithium iron phosphate. *RSC Adv* 7:17763–17767. <https://doi.org/10.1039/c7ra00463j>
- Bi H, Huang F, Tang Y et al (2013a) Study of LiFePO<sub>4</sub> cathode modified by graphene sheets for high-performance lithium ion batteries. *Electrochim Acta* 88:414–420. <https://doi.org/10.1016/j.electacta.2012.10.050>
- Bi Z, Zhang X, He W et al (2013b) Recent advances in LiFePO<sub>4</sub> nanoparticles with different morphology for high-performance lithium-ion batteries. *RSC Adv* 3:19744–19751
- Blomgren GE (2017) The development and future of Lithium ion batteries. *J Electrochem Soc* 164: A5019–A5025. <https://doi.org/10.1149/2.0251701jes>
- Cano ZP, Banham D, Ye S et al (2018) Batteries and fuel cells for emerging electric vehicle markets. *Nat Energy* 3:279–289. <https://doi.org/10.1038/s41560-018-0108-1>
- Chem JM, Zhou X, Wang F, Liu Z (2011) Graphene modified LiFePO<sub>4</sub> cathode materials for high power lithium ion. *J Mater Chem* 21:3353–3358. <https://doi.org/10.1039/c0jm03287e>
- Chen ZY, Zhu HL, Zhu W et al (2010) Electrochemical performance of carbon nanotube-modified LiFePO<sub>4</sub> cathodes for Li-ion batteries. *Trans Nonferrous Met Soc China. English Ed* 20:614–618
- Chen L, Zhang M, Wei W (2013) Graphene-based composites as cathode materials for Lithium ion batteries. *J Nanomater* 2013:8. <https://doi.org/10.1155/2013/940389>
- Chen YT, Zhang HY, Chen YM et al (2018) Graphene-carbon nanotubes-modified LiFePO<sub>4</sub> cathode materials for high-performance lithium-ion batteries. *Mater Sci Forum* 913:818–830. <https://doi.org/10.4028/www.scientific.net/msf.913.818>
- Croce F, D' Epifanio A, Hassoun J et al (2002) A novel concept for the synthesis of an improved LiFePO<sub>4</sub> lithium battery cathode. *Electrochem Solid-State Lett* 5:A47. <https://doi.org/10.1149/1.1449302>
- Cui Y, Zhao X, Guo R (2010) Enhanced electrochemical properties of LiFePO<sub>4</sub> cathode material by CuO and carbon co-coating. *J Alloys Compd* 490:236–240. <https://doi.org/10.1016/j.jallcom.2009.09.165>

- Delacourt C, Wurm C, Laffont L et al (2006) Electrochemical and electrical properties of Nb- and/or C-containing LiFePO<sub>4</sub> composites. *Solid State Ionics* 177:333–341. <https://doi.org/10.1016/j.ssi.2005.11.003>
- Dhindsa KS, Mandal BP, Bazzi K et al (2013a) Enhanced electrochemical performance of graphene modified LiFePO<sub>4</sub> cathode material for lithium ion batteries. *Solid State Ionics* 253:94–100. <https://doi.org/10.1016/j.ssi.2013.08.030>
- Dhindsa KS, Mandal BP, Bazzi K et al (2013b) Enhanced electrochemical performance of graphene modified LiFePO<sub>4</sub> cathode material for lithium ion batteries. *Solid State Ionics* 253:94–100. <https://doi.org/10.1016/j.ssi.2013.08.030>
- Ding Y, Jiang Y, Xu F et al (2010) Preparation of nano-structured LiFePO<sub>4</sub>/graphene composites by co-precipitation method. *Electrochem Commun* 12:10–13. <https://doi.org/10.1016/j.elecom.2009.10.023>
- Feng W, Cao Y, Zhao X et al (2017) Effect of carbon nanotubes on the electrochemical performance of LiFePO<sub>4</sub> particles in lithium ion batteries. *Int J Electrochem Sci* 12:5199–5207. <https://doi.org/10.20964/2017.06.07>
- Fisher CAJ, Prieto VMH, Islam MS (2008) Lithium battery materials LiMPO<sub>4</sub> (M = Mn, Fe, Co, and Ni): insights into defect association, transport mechanisms, and doping behavior. *Chem Mater* 20:5907–5915. <https://doi.org/10.1021/cm801262x>
- Gariépy V, Vediappan K, JT C, Gagnon F, Barray P, Hovington A, Guerfi K, Zaghbi A, Mauger CMJ (2012) Novel hydrothermal synthesis of Nano-LiFePO<sub>4</sub> via solution steering. *Electrochem Soc* 152:2199
- Goodenough JB (2018) How we made the Li-ion rechargeable battery. *Nat Electron* 1:204–204. <https://doi.org/10.1038/s41928-018-0048-6>
- Ha SH, Lee YJ (2015) Core-shell LiFePO<sub>4</sub>/carbon-coated reduced graphene oxide hybrids for high-power lithium-ion battery cathodes. *Chem A Eur J* 21:2132–2138. <https://doi.org/10.1002/chem.201404952>
- Herle PS, Ellis B, Coombs N, Nazar LF (2004) Nano-network electronic conduction in iron and nickel olivine phosphates. *Nat Mater* 3:147–152. <https://doi.org/10.1038/nmat1063>
- Huang C, Ai D, Wang L, He X (2013) Rapid synthesis of LiFePO<sub>4</sub> by Coprecipitation. *Chem Lett* 42:1191–1193. <https://doi.org/10.1246/cl.130436>
- Huang X, Du Y, Qu P et al (2017) Effect of carbon coating on the properties and electrochemical performance of LiFePO<sub>4</sub>/C composites by vacuum decomposition method. *Int J Electrochem Sci* 12:7183–7196. <https://doi.org/10.20964/2017.08.77>
- Iijima S, Ajayan PM, Ichihashi T (1992) Growth model for carbon nanotubes. *Phys Rev Lett* 69:3100–3103. <https://doi.org/10.1103/PhysRevLett.69.3100>
- Islam M, Yoon M, Min Y, Ur S (2015) Solid state synthesis of LiFePO<sub>4</sub>/C: using low cost materials. *J Ceram Process Res* 16:218–222. [https://doi.org/JCPR16-2/\\_082013-034\\_218-222](https://doi.org/JCPR16-2/_082013-034_218-222)
- Jabeen S, Kausar A, Muhammad B et al (2015) A review on polymeric Nanocomposites of Nanodiamond, carbon nanotube, and Nanobifiller: structure, preparation and properties. *Polym Plast Technol Eng* 54:1379–1409. <https://doi.org/10.1080/03602559.2015.1021489>
- Jiang W, Wu M, Liu F et al (2017) Variation of carbon coatings on the electrochemical performance of LiFePO<sub>4</sub> cathodes for lithium ionic batteries. *RSC Adv* 7:44296–44302. <https://doi.org/10.1039/c7ra08062j>
- Jin B, Jin EM, Park KH, Gu HB (2008) Electrochemical properties of LiFePO<sub>4</sub>-multiwalled carbon nanotubes composite cathode materials for lithium polymer battery. *Electrochem Commun* 10:1537–1540. <https://doi.org/10.1016/j.elecom.2008.08.001>
- Julien CM (2017) Lithium Iron phosphate: olivine material for high power Li-ion batteries. *Res Dev Mater Sci* 2:3–6. <https://doi.org/10.31031/rdms.2017.02.000545>
- Kashi R, Khosravi M, Mollazadeh M (2018) Effect of carbon precursor on electrochemical performance of LiFePO<sub>4</sub>-C nano composite synthesized by ultrasonic spray pyrolysis as cathode active material for Li ion battery. *Mater Chem Phys* 203:319–332. <https://doi.org/10.1016/j.matchemphys.2017.10.021>

- Kim HJ, Bae GH, Lee SM et al (2019) Properties of lithium iron phosphate prepared by biomass-derived carbon coating for flexible lithium ion batteries. *Electrochim Acta* 300:18–25. <https://doi.org/10.1016/j.electacta.2019.01.057>
- Konarova M, Taniguchi I (2008) Preparation of LiFePO<sub>4</sub>/C composite powders by ultrasonic spray pyrolysis followed by heat treatment and their electrochemical properties. *Mater Res Bull* 43:3305–3317. <https://doi.org/10.1016/j.materresbull.2008.02.014>
- Kroto HW, Heath JR, O'Brien SC, Curl RF, Smalley RE (1985) C<sub>60</sub>: Buckminsterfullerene. *Nature* 318:162–163. <https://doi.org/10.1038/318162a0>
- Landi BJ, Ganter MJ, Cress CD et al (2009) Carbon nanotubes for lithium ion batteries. *Energy Environ Sci* 2:638–654. <https://doi.org/10.1039/b904116h>
- Lei X, Zhang H, Chen Y, Wang W, Huang Z (2014) Hydrothermal synthesis and electrochemical performance of LiFePO<sub>4</sub> graphene composites for lithium-ion batteries. *Adv Mater Res* 900:242–246. <https://doi.org/10.4028/www.scientific.net/AMR.900.242>
- Li H, Zhou H (2012) Enhancing the performances of Li-ion batteries by carbon-coating: present and future. *Chem Commun* 48:1201–1217. <https://doi.org/10.1039/c1cc14764a>
- Li X, Kang F, Bai X, Shen W (2007) A novel network composite cathode of LiFePO<sub>4</sub>/multiwalled carbon nanotubes with high rate capability for lithium ion batteries. *Electrochem Commun* 9:663–666. <https://doi.org/10.1016/j.elecom.2006.10.050>
- Li L, Li X, Wang Z et al (2009) Stable cycle-life properties of Ti-doped LiFePO<sub>4</sub> compounds synthesized by co-precipitation and normal temperature reduction method. *J Phys Chem Solids* 70:238–242. <https://doi.org/10.1016/j.jpcs.2008.10.012>
- Li YD, Zhao SX, Nan CW, Li BH (2011) Electrochemical performance of SiO<sub>2</sub>-coated LiFePO<sub>4</sub> cathode materials for lithium ion battery. *J Alloys Compd* 509:957–960. <https://doi.org/10.1016/j.jallcom.2010.08.154>
- Lin HY, Yeh SM, Chen JS (2014) Physical and electrochemical properties of LiFePO<sub>4</sub>/C nanofibers synthesized by electrospinning. *Int J Electrochem Sci* 9:6936–6948
- Liu Z, Huang X, Wang D (2008) First-principle investigations of N doping in LiFePO<sub>4</sub>. *Solid State Commun* 147:505–509. <https://doi.org/10.1016/j.ssc.2008.06.013>
- Liu Y, Cao C, Li J (2010) Enhanced electrochemical performance of carbon nanospheres-LiFePO<sub>4</sub> composite by PEG based sol-gel synthesis. *Electrochim Acta* 55:3921–3926. <https://doi.org/10.1016/j.electacta.2010.02.032>
- Liu Y, Liu J, Wang J et al (2018) Formation of size-dependent and conductive phase on lithium iron phosphate during carbon coating. *Nat Commun* 9:1–8. <https://doi.org/10.1038/s41467-018-03324-7>
- Lu L, Han X, Li J et al (2013) A review on the key issues for lithium-ion battery management in electric vehicles. *J Power Sources* 226:272–288. <https://doi.org/10.1016/j.jpowsour.2012.10.060>
- Lung-Hao Hu B, Wu FY, Lin CT et al (2013) Graphene-modified LiFePO<sub>4</sub> cathode for lithium ion battery beyond theoretical capacity. *Nat Commun* 4:1687. <https://doi.org/10.1038/ncomms2705>
- Ma Y, Li X, Sun S et al (2013) Synthesize of graphene-LiFePO<sub>4</sub> composite porous microsphere with the enhanced rate performance. *Int J Electrochem Sci* 8:2842–2848
- Magasinski A, Dixon P, Hertzberg B et al (2010) High-performance lithium-ion anodes using a hierarchical bottom-up approach. *Nat Mater* 9:353–358. <https://doi.org/10.1038/nmat2725>
- Mao S, Pu H, Chen J (2012) Graphene oxide and its reduction: modeling and experimental progress. *RSC Adv* 2:2643–2662. <https://doi.org/10.1039/c2ra00663d>
- May GJ, Davidson A, Monahov B (2018) Lead batteries for utility energy storage: a review. *J Energy Storage* 15:145–157. <https://doi.org/10.1016/j.est.2017.11.008>
- Mizushima K, Jones PC, Wiseman PJ, Goodenough JB (1981) Li<sub>x</sub>CoO<sub>2</sub> (0 < x ≤ 1): a new cathode material for batteries of high energy density. *Solid State Ionics* 3–4:171–174. [https://doi.org/10.1016/0167-2738\(81\)90077-1](https://doi.org/10.1016/0167-2738(81)90077-1)
- Molenda J, Kulka A, Milewska A et al (2013) Structural, transport and electrochemical properties of liFePO<sub>4</sub> substituted in lithium and iron sublattices (Al, Zr, W, Mn, Co and Ni). *Materials (Basel)* 6:1656–1687. <https://doi.org/10.3390/ma6051656>

- Nan C, Lu J, Li L et al (2013) Size and shape control of LiFePO<sub>4</sub> nanocrystals for better lithium ion battery cathode materials. *Nano Res* 6:469–477. <https://doi.org/10.1007/s12274-013-0324-8>
- Naoki N, Feixiang W, Tae LJ, Gleb Y (2015) A new cathode material for batteries of high-energy density. *Mater Today* 18:252–264. <https://doi.org/10.1016/j.mattod.2014.10.040>
- Nishimura SI, Nakamura M, Natsui R, Yamada A (2010) New lithium iron pyrophosphate as 3.5 V class cathode material for lithium ion battery. *J Am Chem Soc* 132:13596–13597. <https://doi.org/10.1021/ja106297a>
- Okada K, Kimura I, Machida K (2018) High rate capability by sulfur-doping into LiFePO<sub>4</sub> matrix. *RSC Adv* 8:5848–5853. <https://doi.org/10.1039/c7ra12740e>
- Padhi AK (1997) Phospho-olivines as positive-electrode materials for rechargeable Lithium batteries. *J Electrochem Soc* 144:1188. <https://doi.org/10.1149/1.1837571>
- Papageorgiou DG, Kinloch IA, Young RJ (2017) Mechanical properties of graphene and graphene-based nanocomposites. *Prog Mater Sci* 90:75–127. <https://doi.org/10.1016/j.pmatsci.2017.07.004>
- Park KS, Son JT, Chung HT et al (2003) Synthesis of LiFePO<sub>4</sub> by co-precipitation and microwave heating. *Electrochem Commun* 5:839–842. <https://doi.org/10.1016/j.elecom.2003.08.005>
- Park KS, Xiao P, Kim SY et al (2012) Enhanced charge-transfer kinetics by anion surface modification of LiFePO<sub>4</sub>. *Chem Mater* 24:3212–3218. <https://doi.org/10.1021/cm301569m>
- Qiao YQ, Feng WL, Li J, Shen TD (2017) Ultralong cycling stability of carbon-nanotube/LiFePO<sub>4</sub> nanocomposites as electrode materials for lithium-ion batteries. *Electrochim Acta* 232:323–331. <https://doi.org/10.1016/j.electacta.2017.02.161>
- Qin X, Wang X, Xiang H et al (2010) Mechanism for hydrothermal synthesis of LiFePO<sub>4</sub> platelets as cathode material for lithium-ion batteries. *J Phys Chem C* 114:16806–16812. <https://doi.org/10.1021/jp104466e>
- Qin G, Ma Q, Wang C (2014a) A porous C/LiFePO<sub>4</sub>/multiwalled carbon nanotubes cathode material for lithium ion batteries. *Electrochim Acta* 115:407–415. <https://doi.org/10.1016/j.electacta.2013.10.177>
- Qin G, Wu Q, Zhao J et al (2014b) C/LiFePO<sub>4</sub>/multi-walled carbon nanotube cathode material with enhanced electrochemical performance for lithium-ion batteries. *J Power Sources* 248:588–595. <https://doi.org/10.1016/j.jpowsour.2013.06.070>
- Qiu Y, Geng Y, Li N et al (2014a) Nonstoichiometric LiFePO<sub>4</sub>/C nano fibers by electrospinning as cathode materials for lithium-ion battery. *Mater Chem Phys* 144:226–229. <https://doi.org/10.1016/j.matchemphys.2013.12.027>
- Qiu Y, Geng Y, Li N et al (2014b) Nonstoichiometric LiFePO<sub>4</sub>/C nanofibers by electrospinning as cathode materials for lithium-ion battery. *Mater Chem Phys* 144:226–229. <https://doi.org/10.1016/j.matchemphys.2013.12.027>
- Rao MC (2015) Novel cathode materials for rechargeable batteries. *Int J Sci Res* 172:637–671. [https://doi.org/10.1007/978-3-319-15458-9\\_23](https://doi.org/10.1007/978-3-319-15458-9_23)
- Ruska M, Kiviluoma J (2011) Challenges in the development of advanced Liion batteries: a review. *Energy Environ Sci*:1–72. <https://doi.org/10.1039/c1ee01598b>
- Salem JR, de Vries MS, Bethune DS et al (2003) Atoms in carbon cages: the structure and properties of endohedral fullerenes. *Nature* 366:123–128. <https://doi.org/10.1038/366123a0>
- Saroha R, Panwar AK (2017) Effect of in situ pyrolysis of acetylene (C<sub>2</sub>H<sub>2</sub>) gas as a carbon source on the electrochemical performance of LiFePO<sub>4</sub> for rechargeable lithium-ion batteries. *J Phys D Appl Phys* 50. <https://doi.org/10.1088/1361-6463/aa708c>
- Saw LH, Somasundaram K, Ye Y, Tay AAO (2014) Electro-thermal analysis of Lithium Iron Phosphate battery for electric vehicles. *J Power Sources* 249:231–238. <https://doi.org/10.1016/j.jpowsour.2013.10.052>
- Seo J, Sankarasubramanian S, Kim CS et al (2015) Thermal characterization of Li/sulfur, Li/S-LiFePO<sub>4</sub> and Li/S-LiV<sub>3</sub>O<sub>8</sub> cells using isothermal micro-calorimetry and accelerating rate calorimetry. *J Power Sources* 289:1–7. <https://doi.org/10.1016/j.jpowsour.2015.04.149>

- Shao D, Wang J, Dong X et al (2013) Electrospinning fabrication and electrochemical properties of LiFePO<sub>4</sub>/C composite nanofibers. *J Mater Sci Mater Electron* 24:4263–4269. <https://doi.org/10.1007/s10854-013-1395-8>
- Su FY, You C, He YB et al (2010) Flexible and planar graphene conductive additives for lithium-ion batteries. *J Mater Chem* 20:9644–9650. <https://doi.org/10.1039/c0jm01633k>
- Susantyoko RA, Karam Z, Alkhoori S et al (2017) A surface-engineered tape-casting fabrication technique toward the commercialisation of freestanding carbon nanotube sheets. *J Mater Chem A* 5:19255–19266. <https://doi.org/10.1039/c7ta04999d>
- Susantyoko RA, Alkindi TS, Kanagaraj AB et al (2018) Performance optimization of freestanding MWCNT-LiFePO<sub>4</sub> sheets as cathodes for improved specific capacity of lithium-ion batteries. *RSC Adv* 8:16566–16573. <https://doi.org/10.1039/c8ra01461b>
- Swain P, Viji M, Mocherla PSV, Sudakar C (2015) Carbon coating on the current collector and LiFePO<sub>4</sub> nanoparticles – influence of sp<sup>2</sup> and sp<sup>3</sup>-like disordered carbon on the electrochemical properties. *J Power Sources* 293:613–625. <https://doi.org/10.1016/j.jpowsour.2015.05.110>
- Świder J, Świątosławski M, Molenda M, Dziembaj R (2014) A novel concept for the synthesis of nanometric LiFePO<sub>4</sub> by co-precipitation method in an anhydrous environment. *Procedia Eng* 98:36–41. <https://doi.org/10.1016/j.proeng.2014.12.484>
- Takahashi M, Tobishima S, Takei K, Sakurai Y (2002) Reaction behavior of LiFePO<sub>4</sub> as a cathode material for rechargeable lithium batteries. *Solid State Ionics* 148:283–289. [https://doi.org/10.1016/S0167-2738\(02\)00064-4](https://doi.org/10.1016/S0167-2738(02)00064-4)
- Tan L, Tang Q, Chen X et al (2014) Mesoporous LiFePO<sub>4</sub> microspheres embedded homogeneously with 3D CNT conductive networks for enhanced electrochemical performance. *Electrochim Acta* 137:344–351. <https://doi.org/10.1016/j.electacta.2014.06.015>
- Tang Y, Huang F, Bi H et al (2012) Highly conductive three-dimensional graphene for enhancing the rate performance of LiFePO<sub>4</sub> cathode. *J Power Sources* 203:130–134. <https://doi.org/10.1016/j.jpowsour.2011.12.011>
- Thanh L, Huynh N, Thuy T et al (2018) Carbon – coated LiFePO<sub>4</sub>– carbon nanotube electrodes for high-rate Li-ion battery. *J Solid State Electrochem* 22:2247–2254. <https://doi.org/10.1007/s10008-018-3934-y>
- Thostenson ET, Ren Z, Chou T (2001) Advances in the science and technology of carbon nanotubes and their composites: a review. *Compos Sci Technol* 61:1899–1912. [https://doi.org/10.1016/S0266-3538\(01\)00094-X](https://doi.org/10.1016/S0266-3538(01)00094-X)
- Tian R, Liu H, Jiang Y et al (2015) Drastically enhanced high-rate performance of carbon-coated LiFePO<sub>4</sub> nanorods using a green chemical vapor deposition (CVD) method for lithium ion battery: a selective carbon coating process. *ACS Appl Mater Interfaces* 7:11377–11386. <https://doi.org/10.1021/acsami.5b01891>
- Toprakci O, Toprakci HAK, Ji L et al (2012) Carbon nanotube-loaded electrospun LiFePO<sub>4</sub>/carbon composite nanofibers as stable and binder-free cathodes for rechargeable lithium-ion batteries. *ACS Appl Mater Interfaces* 4:1273–1280. <https://doi.org/10.1021/am201527r>
- Varzi A, Bresser D, Von Zamory J et al (2014) ZnFe<sub>2</sub>O<sub>4</sub>-C/LiFePO<sub>4</sub>-CNT: a novel high-power lithium-ion battery with excellent cycling performance. *Adv Energy Mater* 4. <https://doi.org/10.1002/aenm.201400054>
- Wang L, Wang H, Liu Z et al (2010) A facile method of preparing mixed conducting LiFePO<sub>4</sub>/graphene composites for lithium-ion batteries. *Solid State Ionics* 181:1685–1689. <https://doi.org/10.1016/j.ssi.2010.09.056>
- Wang Y, Liu Z, Zhou S (2011) An effective method for preparing uniform carbon coated nano-sized LiFePO<sub>4</sub> particles. *Electrochim Acta* 58:359–363. <https://doi.org/10.1016/j.electacta.2011.09.053>
- Wang Y, Feng ZS, Chen JJ, Zhang C (2012) Synthesis and electrochemical performance of LiFePO<sub>4</sub>/graphene composites by solid-state reaction. *Mater Lett* 71:54–56. <https://doi.org/10.1016/j.matlet.2011.12.034>

- Wang S, Yang H, Feng L et al (2013) A simple and inexpensive synthesis route for LiFePO<sub>4</sub>/C nanoparticles by co-precipitation. *J Power Sources* 233:43–46. <https://doi.org/10.1016/j.jpowsour.2013.01.124>
- Wang B, Abdulla WA, Wang D, Zhao XS (2015a) Three-dimensional porous LiFePO<sub>4</sub> cathode material modified with nitrogen-doped graphene aerogel for high-power lithium ion batteries. *Energy Environ Sci* 8:869–875. <https://doi.org/10.1039/b000000x>
- Wang Y, Lv L, Wang J et al (2015b) Influence of microstructure on electrochemical properties of Si/C multilayer thin-film anodes deposited using a sputtering method. *Mater Lett* 160:210–212. <https://doi.org/10.1016/j.matlet.2015.07.084>
- Wang B, Liu T, Liu A et al (2016) A hierarchical porous C@LiFePO<sub>4</sub>/carbon nanotubes microsphere composite for high-rate lithium-ion batteries: combined experimental and theoretical study. *Adv Energy Mater* 6:1600426. <https://doi.org/10.1002/aenm.201600426>
- Wang X, Feng Z, Huang J et al (2018) Graphene-decorated carbon-coated LiFePO<sub>4</sub> nanospheres as a high-performance cathode material for lithium-ion batteries. *Carbon N Y* 127:149–157. <https://doi.org/10.1016/j.carbon.2017.10.101>
- Whittingham MS (2012) History, evolution, and future status of energy storage. *Proc IEEE* 100:1518–1534. <https://doi.org/10.1109/JPROC.2012.2190170>
- Whittingham MS (2014) Ultimate limits to intercalation reactions for Lithium batteries. *Chem Rev* 114:11414–11443. <https://doi.org/10.1021/cr5003003>
- Whittingham MS, Gamble FR (1975) The lithium intercalates of the transition metal dichalcogenides. *Mater Res Bull* 10:363–371. [https://doi.org/10.1016/0025-5408\(75\)90006-9](https://doi.org/10.1016/0025-5408(75)90006-9)
- Wu ZS, Zhou G, Yin LC et al (2012) Graphene/metal oxide composite electrode materials for energy storage. *Nano Energy* 1:107–131. <https://doi.org/10.1016/j.nanoen.2011.11.001>
- Wu G, Zhou Y, Shao Z (2013a) Carbon nanotube and graphene nanosheet co-modified LiFePO<sub>4</sub> nanoplate composite cathode material by a facile polyol process. *Appl Surf Sci* 283:999–1005. <https://doi.org/10.1016/j.apsusc.2013.07.059>
- Wu XL, Guo YG, Su J et al (2013b) Carbonnanotube decorated nano-LiFePO<sub>4</sub> @c cathode material with superior high-rate and low-temperature performances for lithium-ion batteries. *Adv Energy Mater* 3:1155–1160. <https://doi.org/10.1002/aenm.201300159>
- Wu XL, Guo YG, Su J et al (2013c) Carbon-nanotube-decorated nano-LiFePO<sub>4</sub>@C cathode material with superior high-rate and low-temperature performances for lithium-ion batteries. *Adv Energy Mater* 3:1155–1160. <https://doi.org/10.1002/aenm.201300159>
- Xiang JY, Tu JP, Zhang L et al (2010) Improved electrochemical performances of 9LiFePO<sub>4</sub>·Li<sub>3</sub>V<sub>2</sub>(PO<sub>4</sub>)<sub>3</sub>/C composite prepared by a simple solid-state method. *J Power Sources* 195:8331–8335. <https://doi.org/10.1016/j.jpowsour.2010.06.070>
- Xu Z, Xu L, Lai Q, Ji X (2007) A PEG assisted sol-gel synthesis of LiFePO<sub>4</sub> as cathodic material for lithium ion cells. *Mater Res Bull* 42:883–891. <https://doi.org/10.1016/j.materresbull.2006.08.018>
- Xu D, Wang P, Shen B (2016) Synthesis and characterization of sulfur-doped carbon decorated LiFePO<sub>4</sub> nanocomposite as high performance cathode material for lithium-ion batteries. *Ceram Int* 42:5331–5338. <https://doi.org/10.1016/j.ceramint.2015.12.064>
- Yang J, Xu JJ (2004) Nonaqueous sol-gel synthesis of high-performance LiFePO<sub>4</sub>. *Electrochem Solid-State Lett* 7:A515. <https://doi.org/10.1149/1.1819893>
- Yang S, Song Y, Zavalij PY, Stanley Whittingham M (2002) Reactivity, stability and electrochemical behavior of lithium iron phosphates. *Electrochem Commun* 4:239–244. [https://doi.org/10.1016/S1388-2481\(01\)00298-3](https://doi.org/10.1016/S1388-2481(01)00298-3)
- Yang MR, Teng TH, Wu SH (2006) LiFePO<sub>4</sub>/carbon cathode materials prepared by ultrasonic spray pyrolysis. *J Power Sources* 159:307–311. <https://doi.org/10.1016/j.jpowsour.2006.04.113>
- Yang J, Wang J, Wang D et al (2012) 3D porous LiFePO<sub>4</sub> graphene hybrid cathodes with enhanced performance for Li-ion batteries. *J Power Sources* 208:340–344. <https://doi.org/10.1016/j.jpowsour.2012.02.032>
- Yang J, Wang J, Tang Y, Wang D, Li X, Hu Y, Li R, Liang G, Shamb T-K, Sun X (2013) LiFePO<sub>4</sub>-graphene as a superior cathode material for rechargeable lithium batteries: impact of stacked

- graphene and unfolded graphene. *Energy Environ Sci* 6:1521–1528. <https://doi.org/10.1039/C3EE24163G>
- Yang CC, Jang JH, Jiang JR (2015) Preparation of carbon and oxide co-modified LiFePO<sub>4</sub> cathode material for high performance lithium-ion battery. *Mater Chem Phys* 165:196–206. <https://doi.org/10.1016/j.matchemphys.2015.09.018>
- Yu T, Wang Z, Fu Y et al (2016) Sulfur substituted LiFePO<sub>4</sub>/C with improved rate performance for lithium ion batteries. *Int J Electrochem Sci* 11:5999–6008. <https://doi.org/10.20964/2016.07.47>
- Zhang Y, Wang W, Li P et al (2012) A simple solvothermal route to synthesize graphene-modified LiFePO<sub>4</sub> cathode for high power lithium ion batteries. *J Power Sources* 210:47–53. <https://doi.org/10.1016/j.jpowsour.2012.03.007>
- Zhao Y, Li J, Dahn JR (2017) Interdiffusion of Cations from metal oxide surface coatings into LiCoO<sub>2</sub> during sintering. *Chem Mater* 29:5239–5248. <https://doi.org/10.1021/acs.chemmater.7b01219>
- Zhu J, Yoo K, El-Halees I, Kisailus D (2014) Solution deposition of thin carbon coatings on LiFePO<sub>4</sub>. *ACS Appl Mater Interfaces* 6:21550–21557. <https://doi.org/10.1021/am506498p>
- Zou B, Wang Y, Zhou S (2013) Spray drying-assisted synthesis of LiFePO<sub>4</sub>/C composite microspheres with high performance for lithium-ion batteries. *Mater Lett* 92:300–303. <https://doi.org/10.1016/j.matlet.2012.10.111>



# Chapter 3

## Recent Advances in Hybrid Supercapacitors



T. Manovah David and Tom Mathews

### Contents

3.1	Introduction .....	76
3.2	Construction of a Supercapacitor Cell .....	78
3.3	Electrical Energy Storage in Different Types of Supercapacitors .....	80
3.3.1	Electric Double Layer Capacitor .....	80
3.3.2	Pseudocapacitor .....	82
3.3.3	Hybrid Supercapacitor .....	83
3.3.4	Electrochemical Characteristics of Capacitor, Battery, and Hybrid Systems ....	85
3.4	Symmetric Hybrid Supercapacitors .....	86
3.5	Asymmetric Hybrid Supercapacitors .....	87
3.6	Supercapacitor—Battery Hybrid (Supercapattery) .....	89
3.6.1	Li-Ion Capacitor .....	91
3.6.2	Na-Ion Capacitor .....	93
3.6.3	K-Ion Capacitor .....	96
3.6.4	Al-Ion Capacitor .....	98
3.6.5	Pseudocapacitor—Battery Hybrid .....	98
3.6.6	Pb-Based Supercapacitor—Battery Hybrid [Acidic] .....	101
3.6.7	Ni-Based Supercapacitor Battery Hybrid [Alkaline] .....	104
3.6.8	Effectiveness of Supercapattery Systems .....	106
3.7	Conclusion .....	107
	References .....	107

**Abstract** Research on electrochemical storage systems are persistently on the rise especially in the fields of supercapacitors and batteries. Several modifications are made continuously in supercapacitors with an intention to retain its excellent power density and to improve the inherently poor energy density. Initially, changes were made to these systems by introducing new electrodes, then new materials such as pseudocapacitors were launched and recently the formation of ‘hybrid’ systems.

T. M. David · T. Mathews (✉)

Thin Films and Coatings Section, Surface Nanoscience Division, Materials Science Group,  
Indira Gandhi Centre for Atomic Research, Kalpakkam, Tamil Nadu, India  
e-mail: [tom@igcar.gov.in](mailto:tom@igcar.gov.in)

© The Editor(s) (if applicable) and The Author(s), under exclusive licence to  
Springer Nature Switzerland AG 2021

75

S. Rajendran et al. (eds.), *Metal, Metal-Oxides and Metal Sulfides for Batteries, Fuel Cells, Solar Cells, Photocatalysis and Health Sensors*, Environmental Chemistry for a Sustainable World 62, [https://doi.org/10.1007/978-3-030-63791-0\\_3](https://doi.org/10.1007/978-3-030-63791-0_3)

Three predominant supercapacitor hybrid systems are reported so far viz. symmetric, asymmetric, and supercapacitor-battery hybrid (SBH) systems. Each amendment in the hybrid systems revolutionized the electrochemical storage systems; however, the SBH systems dominated all the forms of hybrid devices. Several battery electrodes are introduced in hybrid cell along with a supercapacitor electrode and they exhibit excellent energy densities at high power densities. This chapter briefly reviews all forms of hybrid supercapacitors.

**Keywords** Hybrid supercapacitor · Symmetric electrodes · Asymmetric electrodes · Supercapattery · EDLC · Pseudocapacitance

### 3.1 Introduction

One of the greatest concerns for the global society is materials for high performance energy storage in unique devices. Several energy storage materials are well known to the scientific and the commercial community. Some have excellent energy densities viz., nickel-metal hydride batteries, nickel-cadmium batteries and lithium-ion batteries (LIBs). On the other hand, some have superior power densities, such as supercapacitors. Interestingly, both forms of energy storage systems are novel, eco-friendly, economic, and exhibit greater performance. Also, they have the ability to meet the need of the ever-increasing global demand. The comparison of the energy densities and power densities of both batteries and capacitors are given in Table 3.1. In spite of all the grand and impending abilities of these materials, they are yet incompetent and fall short of their expectations, when they are used as batteries and supercapacitors individually, with the possibility of non-monotonic consumption of energy occurring as a result of frequent modifications during the battery discharging processes (Kouchachvili et al. 2018). With these hitches, several modifications in the energy components have been tried to make the balance right, that is, to improve both the densities (energy and power) without compromising each other.

Major work is going on in the sectors of batteries and supercapacitors. Especially, in the supercapacitor sector the scientists are looking forward to harness its power density along with improvement in the energy density. For this purpose, several electrode materials have been tested such as having electrical double layer capacitance (EDLC) electrodes and pseudocapacitance with improved energy density with innate power density. But the progress was stalled after a certain limit without the possibility of moving any further. Therefore, the researchers have implemented the

**Table 3.1** Comparison of lithium-ion batteries and supercapacitors

Devices	Parameters		
	Energy density (Wh kg <sup>-1</sup> )	Power density (kW kg <sup>-1</sup> )	Cycles
Supercapacitor	5–10	10	>1 × 10 <sup>5</sup>
Li-ion battery	150–200	1	<1000

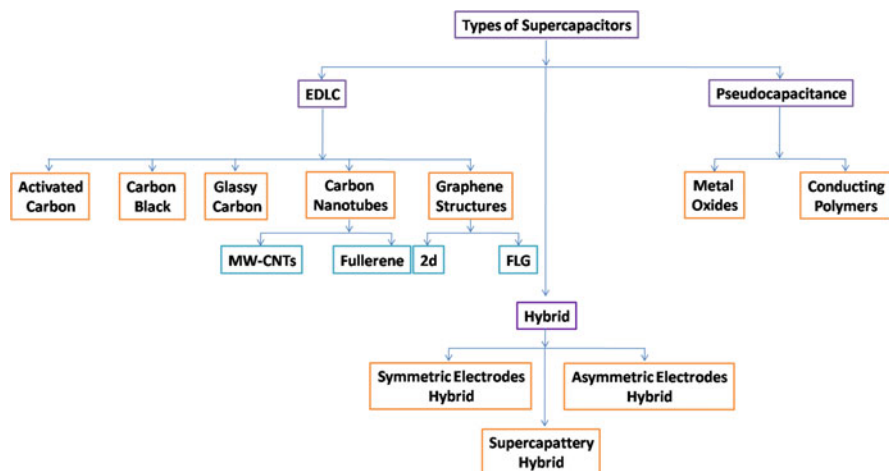


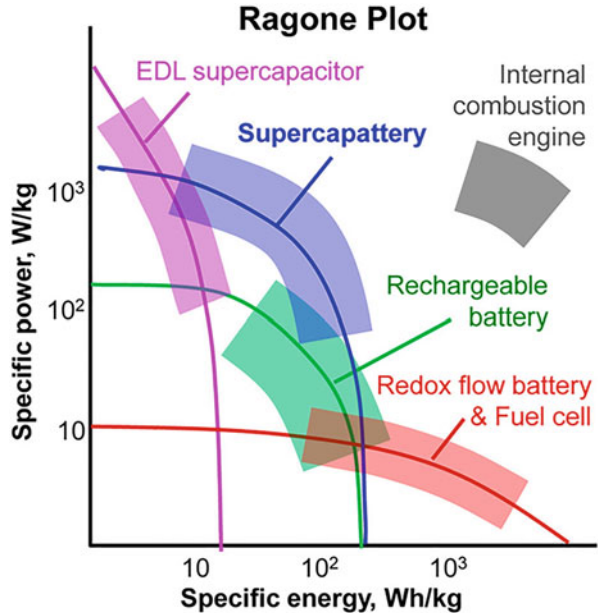
**Fig. 3.1** Classifications of the supercapacitors. Electric double layer capacitance (EDLC), multiwall carbon nanotubes (MW-CNTs), two dimensional (2d), few layer graphene (FLG)

idea of combining two different electrodes to fabricate a supercapacitor with enhanced energy density. The classification of supercapacitors is given in Fig. 3.1.

The combination of two distinct electrodes in a single unit has led to the formation of hybrid supercapacitors. Hybrid supercapacitors are systems with enhanced energy density along with improved power density. Three different types of hybrid supercapacitors are now reported viz.: (a) symmetric hybrid supercapacitors, (b) asymmetric hybrid supercapacitors, and (c) supercapacitor-battery hybrid (SBH). A simple definition of a hybrid capacitor is that it may be two different electrodes (asymmetric) or same electrodes made with hybrid composites (symmetric) or a combination of a supercapacitor electrode and a battery electrode (Chen et al. 2010). The electrodes can be exhibiting electric double layer capacitance (EDLC) or pseudocapacitance behavior or can also be a battery electrode. In other words, one half is constituted of EDLC and the other half with pseudocapacitance electrode or one of these supercapacitor electrodes on one side and the battery electrode on the other (Muzaffar et al. 2019). The combined properties are said to have a positive effect on the assembled hybrid supercapacitor. For example, in a EDLC and pseudocapacitance hybrid, the former electrode displays intrinsic charge storage based on double layer formation depending on the atomic charge partition length and the later is based on repetitive redox reactions (Lu et al. 2011). The amalgamation of these electrodes as anodes and cathodes constitutes a hybrid capacitor.

The energy storage ability of hybrid supercapacitors is better as identified in the Ragone plot (power density [ $\text{W kg}^{-1}$ ] vs. energy density [ $\text{Wh kg}^{-1}$ ]) when compared with other such similar devices such fuel cells, batteries, non-hybrid supercapacitors such as EDLC and pseudocapacitor and conventional capacitors (Fig. 3.2). The hybrid supercapacitors have an edge over other energy storage

**Fig. 3.2** Ragone plot for different energy storage devices. The plot compares the specific energy and power of electrical double layer (EDL) supercapacitor, supercapattery, internal combustion engine, rechargeable battery and redox flow battery and fuel cell. (Reprinted with permission of Taylor and Francis from Chen 2017)



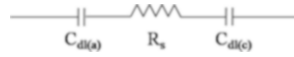
systems. The plot also gives information that all the types of supercapacitors have better power density over the present rechargeable batteries. This phenomenon of large power density is largely possible because only the outer surface of the supercapacitors is used whereas in batteries, processes like intercalation and de-intercalation takes place (Lee et al. 2011). On the other hand, hybrid supercapacitors exhibit large storage ability with superior power rates. This capability of hybrid supercapacitors makes them a suitable choice to replace portable batteries used in mobile phones where both high energy and power densities could be utilized along with improvement in the net cell voltage (Jorio et al. 2001; Plitz et al. 2006). This unique combination of higher power density along with higher specific energy defines the possibility of using the hybrid supercapacitor as a complement to most of the other power sources (Pandolfo and Hollenkamp 2006).

The credentials of hybrid supercapacitors are found to be superior. A good understanding in every aspect of this is required and this chapter reviews the basic construction of a supercapacitor cell, type of electrical energy storage in supercapacitors, hybrid supercapacitors and their various forms.

### 3.2 Construction of a Supercapacitor Cell

The supercapacitor assembly is very much similar to that of a conventional battery system where both the electrodes are inserted into an electrolyte. The major difference of supercapacitors from that of batteries is that both the electrodes are separated

by an ion-permeable membrane, meaning that the electrodes are separated by a membrane. However, the electrodes of a battery are not separated by an ion-permeable membrane. For better understating the electrode/electrolyte *interface* is considered to be one *capacitor*. Therefore, when a supercapacitor cell is constructed, it means that two capacitors (each electrode) in series separated by an electrolyte resistance. The general equivalent electrical circuit for a symmetrical capacitor cell is given as,



where, the  $C_{dl(a)}$  and  $C_{dl(c)}$  are double layer capacitance of anode and cathode, respectively, and  $R_s$  is the electrolyte resistance exerted.

The capacitance of the supercapacitor cell ( $C_{cell}$ ) is given as (Winter and Brodd 2004),

$$1/C_{cell} = 1/C_{dl(a)} + 1/C_{dl(c)} \quad (3.1)$$

If  $C_{dl(a)} = C_{dl(c)}$ , then eq. (3.1) could be written as

$$C_{cell} = C_{dl(a)}/2 \quad (3.2)$$

Then, the double layer capacitor is given to be as,

$$C_{dl} = \epsilon A/4\pi d \quad (3.3)$$

where  $\epsilon$  is the dielectric constant of the electrical double layer formed,  $A$  denotes the surface area, and  $d$  is thickness of the double layer (Qu and Shi 1998). Higher capacitance can be achieved based on the formulae, when the charge separation is thin and surface area is large. The information helps in deriving the energy and power densities of the capacitor,

$$E = CV^2/2 \text{ or } QV/2 \quad (3.4)$$

$$P = V^2/4R \quad (3.5)$$

where  $E$  is energy,  $C$  is capacitance,  $V$  is applied voltage,  $Q$  is charge,  $P$  is power density, and  $R$  is resistance (Conway 2013).

Apart from the formulae, two other factors are involved in deciding the efficacy of a supercapacitor material viz. (a) the pore-size distribution and (b) operating voltage. The pore-size distribution plays a pivotal role in directing the ion movement in the electrode within the pores since ions cannot travel in solids as in liquids. The ionic movement is largely hindered if the pore-size is extremely small and, therefore, can never contribute to the capacitance. If the size of pores is very less, then the

capacitance achieved and the specific surface area will not match (Sharma and Bhatti 2010). Moreover, another important factor determining the capacitance is the size of the ions. Smaller the ions in the electrolyte greater the capacitance. Also, a pivotal role is played by the operating voltage that is determined by the electrolyte. It is a deciding factor for the specific energy and power density of the supercapacitors. Usually aqueous electrolytes such as acidic or basic solutions  $\text{H}_2\text{SO}_4$  or  $\text{KOH}$ , respectively, have a poor decomposition voltage of around  $\sim 1.23$  V (Fernández et al. 2008). Non-aqueous electrolytes or organic electrolytes such as acetonitrile and propylene carbonate improve the operating voltage up to 2.5 V (Du et al. 2013).

### 3.3 Electrical Energy Storage in Different Types of Supercapacitors

Generally, the supercapacitors involve two different types of energy storage mechanisms. They are electrical double layer capacitance (EDLC) and the pseudocapacitance involving redox reactions. The EDLC type does not have electrochemically active electrodes and, therefore, no transfer of electrons take place at the electrode–electrolyte interface. The charges are stored in EDLC electrostatically and this type is also known as non-Faradaic charge storage. An example for EDLC type charge storage electrode is Carbon. On the other hand, electrode materials with electrochemically active (transferring electrons) property display pseudocapacitance. In this type, the electrons are transferred across the interface and this process is known as *Faradaic* charge storage. For better understanding all the major classification of supercapacitors is described here viz. EDLC, pseudocapacitance, and hybrid supercapacitor.

#### 3.3.1 Electric Double Layer Capacitor

As a charged material such as carbon electrode is dipped into an electrolyte, electric double layer capacitance (EDLC) arises. When the electrode is dipped a swift arrangement of a double layer takes place. The accumulation of charges is like electrons or holes in the electrode and the respective counter-ions in the electrolyte. In other words, there is adsorption of ion on the surface of the electrode. The EDLC type charge storage is very common and several theories have been put forward to explain the double layer formation as shown in Fig. 3.3. The very simple model is called the Helmholtz model (Fig. 3.3a), where the charges are accumulated continuously along the electrode. Here the theory considers the formation of rigid layer, which counterbalances the charges formed in the solid (Endo et al. 2001). This is also called approximation modeling. Thereafter, Gouy-Chapman (Fig. 3.3b) came up with another theory with the introduction of diffuse layer. This theory states that

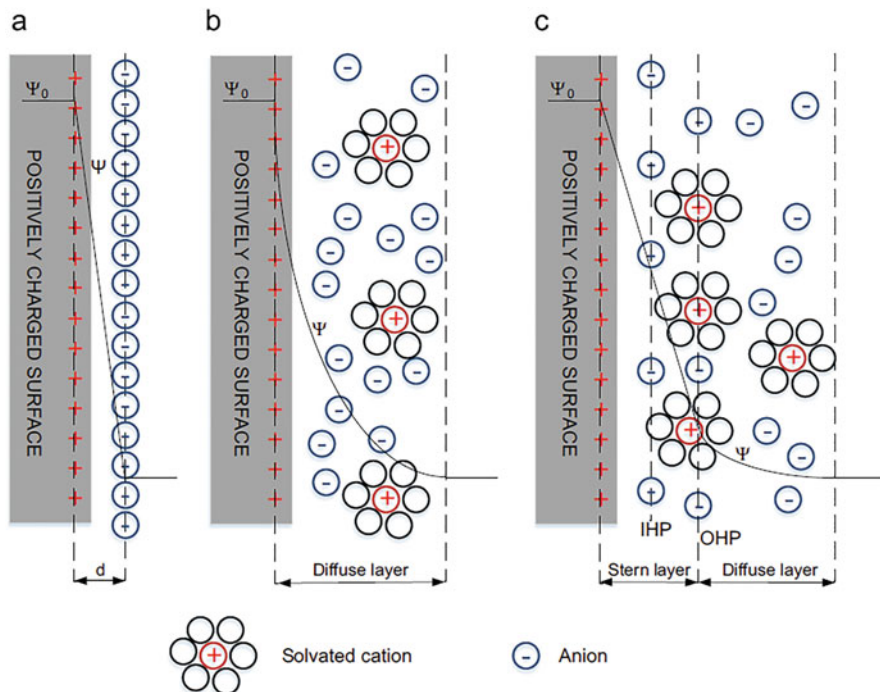


**Fig. 3.3** Electrical double layer capacitance (EDLC) models (a) Helmholtz model, (b) Gouy-Chapman model and (c) Stern model. (Reprinted with permission of Elsevier from González et al. 2016). The terms IHP and OHP in the image indicates inner Helmholtz layer and outer Helmholtz layer, respectively

the ions in the solution tend to diffuse into the liquid phase until a counter potential is set. In addition, the kinetics of movement of the ions will also determine the diffusion of the ions (González et al. 2016). The theory could not explain much as the diffusion layer was thicker than the theoretically devised one. Finally, Stern devised another theory (Fig. 3.3c) with two adjacent layers in one diffusion layer. That is, one of the layers is compact and it is closer to the electrode known as inner Helmholtz layer. The layer away from the electrode is known as outer Helmholtz layer [or Gouy-Chapman layer] (Zhang and Zhao 2009). This theory clarified the formation of EDLC in supercapacitors.

In this type of supercapacitors, when a cell is constructed, both the electrodes contribute individually to the formation of electric double layer capacitance (EDLC). One of the electrodes will have an excess of electrons and other will have a deficiency of electrons (Fig. 3.4). The applied potential between the anode and cathode strictly direct the accumulation and withdrawal of electrons over electrodes. The arrangement takes place in such a manner that the status of the electrode is maintained at electroneutrality at the interface. Therefore, this process involved only the surface of the electrode for charge storage, and hence it is called as physical

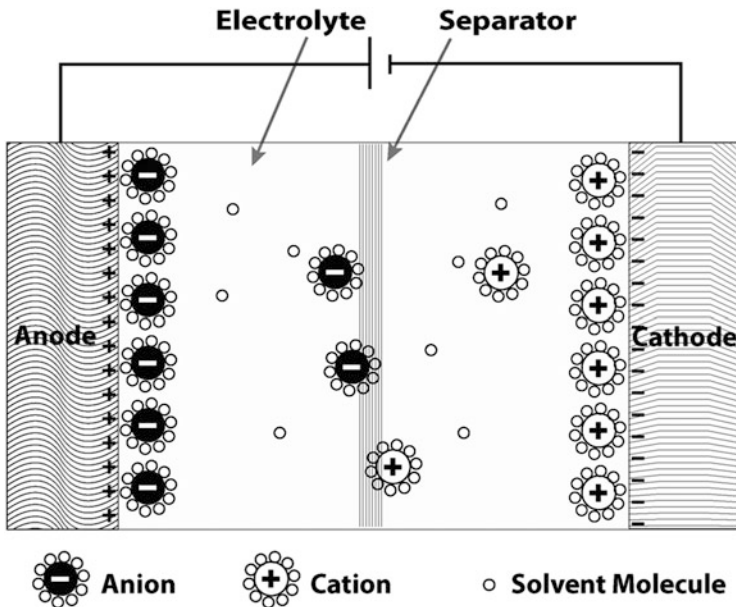


**Fig. 3.4** Electric double layer capacitance (EDLC) based supercapacitor is denoted in this image. At the anode the positive charges in the electrode and the hydrated anions in the electrolyte align as a double layer at the electrode–electrolyte interface. On the other hand, the electrons in the cathode and the hydrated cations align as double layer at the electrode–electrolyte interface

charge storage. The double layer thickness at the interface is around 5–10 Å, which strongly depends on the size of the ions being accumulated and the electric field at interface is anticipated to be as high as  $10^6$  V cm<sup>-1</sup> (Faraji and Ani 2015). For effective operation of the EDLC supercapacitor the following 5 points have to be satisfied: (a) large surface area (b) better electrical conduction, (c) superior pore size distribution, (d) interconnecting pores, and (e) high wettability (Pandolfo and Hollenkamp 2006).

### 3.3.2 Pseudocapacitor

Pseudocapacitance is exhibited usually by all non-carbonaceous substances such as conducting polymers and metal oxides. Unlike electric double layer capacitance (EDLC), these materials undergo Faradaic charge-transfer processes resulting in redox reactions (Fig. 3.5). The capacitance in this type is by the swift redox reactions that occur ‘near the surface’ of the electrode. However, the electrical response of this type of materials is similar to that of EDLC (Pandolfo and Hollenkamp 2006). Pseudocapacitance involves different mechanisms in charge storage such as transition metal oxide based redox reactions, underpotential deposition of ‘H’ adatoms,



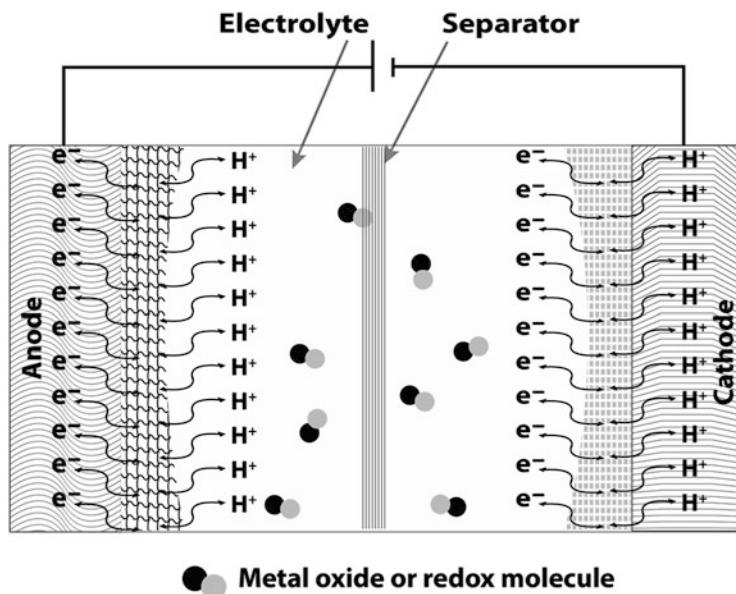


**Fig. 3.5** Schematic representation of pseudocapacitance based supercapacitor. Charge crossover at the electrode-electrolyte boundaries occurs through a few layers in the respective electrodes

intercalation reactions in porous materials and doping/de-doping in conducting polymers (Conway and Pell 2003). Comparing the performance based on power burst it is evident that the EDLC type materials have higher power densities compared with that of pseudocapacitance type materials and this is due to the involvement of rate-determining step in Faradaic processes. Moreover, the electrode stability of pseudocapacitance type capacitors are slightly less stable owing to the expansion and contraction of electrode phases during the cycling process and it also leads to poor mechanical stability and retarded cycle life. These types of capacitors display capacitance about 10 to 100 times more than that of EDLC (Chuang et al. 2010).

### 3.3.3 Hybrid Supercapacitor

The term hybrid supercapacitor was first coined by Amatucci et al. (Amatucci et al. 2001). This group first formed an asymmetric hybrid supercapacitor with activated carbon capacitor electrode as cathode and  $\text{Li}_4\text{Ti}_5\text{O}_{12}$  as anode in an organic electrolyte. The idea of forming a hybrid supercapacitor formulated when researchers across the globe looked forward to improve the energy density in a supercapacitor. It is well known that the energy density of supercapacitors range between 5 and 10  $\text{Wh kg}^{-1}$ . But as the result of hybridization the energy density elevated up to

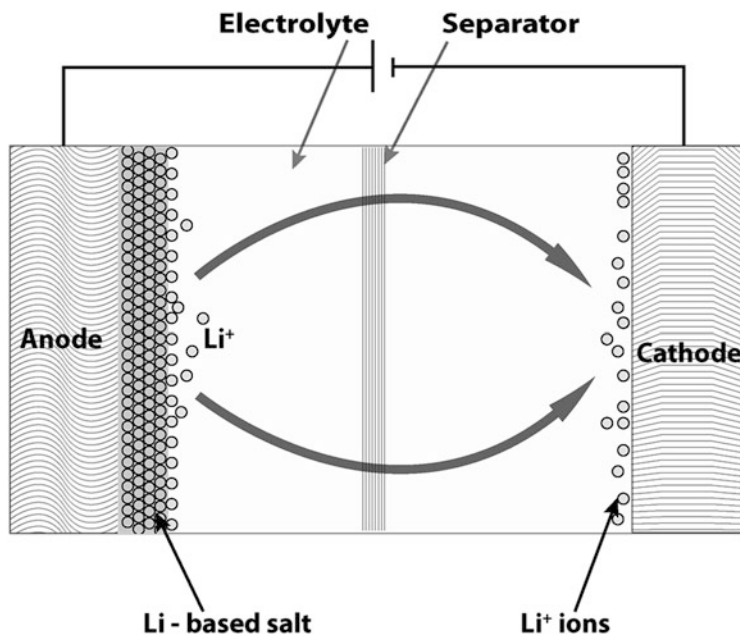


**Fig. 3.6** Supercapacitor battery hybrid (SBH) is illustrated in this diagram, battery electrode at the anode has a complete crossover of charge across the electrode–electrolyte interface and the supercapacitor electrode at the cathode has an electrical double layer formation

20 Wh kg<sup>-1</sup> (Amatucci et al. 2001). Hybrid supercapacitors can be of two major types' viz. external hybrid and internal hybrid. External hybrid is manual connection of readily available supercapacitor to a battery. If they are connected in series, the hybrid would be called external series hybrid or if connected in parallel mode, then the hybrid would be called external parallel hybrid (Cericola and Kötz 2012). If the hybridization of electrodes is made at electrode level it is then called internal hybrid supercapacitor. Even in this case the hybrids could be connected in series or in parallel mode. The scope of this chapter is to deal only with the 'internal hybrid supercapacitor' systems.

The hybrid supercapacitors could also be formed by coupling electric double layer capacitance (EDLC) and pseudocapacitance material in one electrode. This combination provides higher working potential and as a result the capacitance is reported to enhance by two to three times (Wang et al. 2016e). The hybrid capacitors can be either symmetric or asymmetric based on the electrode assembly. Symmetric supercapacitors are assembled through the same type of combined electrodes on both the ends. For instance, combining EDLC and pseudocapacitive components as one hybrid material to be used as both ends of supercapacitor. On the other hand, asymmetric supercapacitors are made of two different electrodes in the following combination, either EDLC and pseudocapacitance electrodes or EDLC and battery type electrodes as shown in Fig. 3.6 (Cericola and Kötz 2012). Hybrid

**Table 3.2** Comparison of symmetric, asymmetric and supercapattery hybrid Systems

Parameter	Symmetric Hybrid supercapacitor	Asymmetric hybrid supercapacitor	Supercapacitor battery hybrid (SBH)
Electrode	Same materials	Dissimilar materials	Supercapacitor and Battery type electrode
Energy Density (W h kg <sup>-1</sup> )	1.13–3.74	5–30	> 30
Power Density (kW kg <sup>-1</sup> )	10–20	0.1–5	> 20
Operational Voltage	Individual characteristics of an electrode are observed	Restricts individual characteristics of the electrode	Restricts individual characteristics of the electrode
Example	Co-Al-MWCNTs// Co-Al-MWCNTs	AC//MnO <sub>2</sub>	AC//LiCoO <sub>2</sub>
Charge Storages	Either Non-Faradaic or Faradaic system	Both Faradaic and Non-Faradaic	Both Faradaic and Non-Faradaic

MWCNTs multi-walled carbon nanotubes, AC activated carbon

supercapacitors can be either symmetric or asymmetric depending on the exhibition of their supercapacitor behavior. It is to be noted that the symmetric hybrid supercapacitors display better supercapacitive properties than conventional faradaic (pseudocapacitive) or non-faradaic (EDLC) supercapacitors. However, asymmetric supercapacitor-battery hybrids are remarkably efficient than all the other forms of supercapacitors. The comparison on symmetric, asymmetric and a supercapacitor-battery hybrid system are given in Table 3.2. The chapter will briefly discuss each type of the hybrid supercapacitors.

### 3.3.4 Electrochemical Characteristics of Capacitor, Battery, and Hybrid Systems

The electrochemical characteristics for capacitor, battery, and hybrid systems vary, though the basic construction of all these devices is similar (Conway 2013). The change in the characteristic behavior is graphically represented in Fig. 3.7.

Cyclic voltammetry: The ideal voltammogram of each system has a unique pattern viz. for in a battery, both the electrodes positive and negative, the redox peaks are clearly seen (Fig. 3.7a and b), for in a supercapacitor, it is like a rectangle (Fig. 3.7d and e) and in a hybrid, the voltammogram corresponding to one electrode has redox peaks (Fig. 3.7f) and the other has a rectangle (Fig. 3.7g). In a supercapacitor, the voltage is independent of the current and for a battery the phase changes of a redox reaction are visible. Charge-discharge (CD) curves: the ideal charge-discharge profile for supercapacitor is linear with respect to time (Fig. 3.7f). However, in a battery charge-discharge profile a plateau is observed in

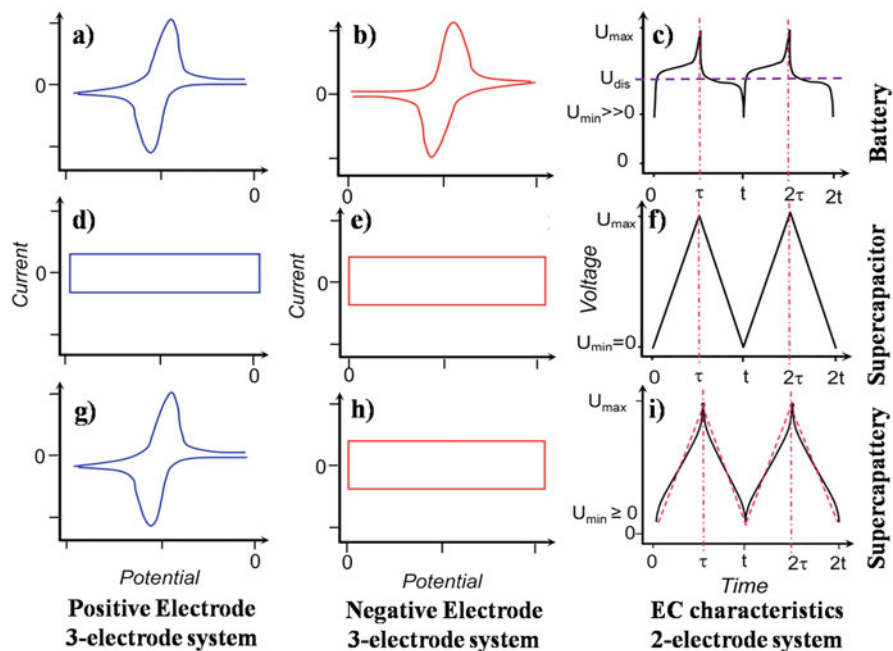


**Fig. 3.7** Electrochemical characteristics of **a, b** and **c**) battery, **d, e** and **f**) supercapacitor and **g, h** and **i**) supercapattery systems. Reprinted with permission of Taylor and Francis from (Chen 2017).  $U_{\max}$  (maximum voltage),  $U_{\min}$  (minimum voltage),  $U_{\text{dis}}$  (discharge voltage)

both charging and discharging trend owing to the phase transformation in the redox reactions (Fig. 3.7c). In a hybrid system, the charge-discharge profile is linear with a small curvature in the linearity (Fig. 3.7i). Thus, indicating the incorporation of both the characteristics (Chen 2017).

### 3.4 Symmetric Hybrid Supercapacitors

In this class of hybrid supercapacitors, both the electrodes are identical in terms of material and composition. However, each electrode is a hybrid in itself. In an investigation, multiwalled carbon nanotubes (MWCNT) were mixed with Co-Al double hydroxides to make it into a composite of active material. Thereafter, the composite material was constructed into two individual electrodes and was assembled as a symmetric hybrid capacitor. Since the process of making a hybrid is related to individual electrodes it is also termed as self-hybrid. The electrolyte used in the process is 1 M KOH. The composite hybridization process largely improved the energy density and power density when compared with normal symmetric supercapacitors with  $13.2 \text{ Wh kg}^{-1}$  and  $6400 \text{ W kg}^{-1}$ , respectively (Su et al.

2008). Likewise, all-solid-state symmetric supercapacitors were prepared by Dubal et al. In this work, reduced graphene oxide was coupled with phosphomolybdate (rGO-PMo<sub>12</sub>). A polymer gel electrolyte was used to assemble the system. The energy density displayed by the device was 1.7 mWh cm<sup>-3</sup> and a maximum power density of 188 mW cm<sup>-3</sup> was exhibited (Dubal et al. 2015b). In another work, fern-like BiVO<sub>4</sub> was made composite with reduced graphene oxide (rGO) to design the supercapacitor electrode with 6 M KOH as the electrolyte. The system is reported to exhibit volumetric energy density of 1.6 mWh cm<sup>-3</sup> at 391 mW cm<sup>-3</sup> (Patil et al. 2016). Purushothaman et al. prepared an active composite of CuO/rGO in a simple low-cost hydrothermal method. This combination is reported to address the issue of poor electrode kinetics with a strategy of combining a transition metal oxide with a carbon-based material. This symmetric hybrid capacitor exhibited energy density of 65.7 Wh kg<sup>-1</sup> at a power density of 302 W kg<sup>-1</sup> (Purushothaman et al. 2014). The electrochemical features of the symmetric capacitors are given in Table 3.3.

### 3.5 Asymmetric Hybrid Supercapacitors

Asymmetric hybrid systems have two different electrodes at both the ends. They may be electric double layer capacitance (EDLC)//pseudocapacitance (vice versa) or pseudocapacitance//pseudocapacitance combinations. But the negative electrode material is different from that of the positive electrode material. These combinations are made to improve the energy and the power density of the system. The pseudocapacitive materials combined with EDLC type materials are expected to contribute with the following features, viz. a) effective faradaic capacitance at the electrode surface providing superior capacitance (surface redox reaction) and b) high power density (above 10<sup>3</sup> W kg<sup>-1</sup>) along with fast charge-discharge process. Though intercalation may take place at the surface level, they do not behave as batteries (Zuo et al. 2017). They majorly have a CV plot as pseudo-rectangular similar to that of EDLC type materials. Therefore, the combinatorial effect of EDLC and pseudocapacitive materials leaves no big difference in the voltammogram of the hybrid. The combinations of pseudocapacitance//pseudocapacitance also displays voltammogram exhibiting the capacitive behavior.

The prime aim is to improve the energy density of a supercapacitor when an asymmetric supercapacitor is built. However, most of the asymmetric supercapacitor hybrid use carbon type capacitive electrodes as these have electrostatic origin along with high power density, high surface area, superior cycle life and could be used in both aqueous and non-aqueous media (Laforgue et al. 2003). An asymmetric hybrid supercapacitor was assembled with mixed metal Ni, Co hydroxide over reduced graphene oxide (rGO) as the positive electrode (Ni, Co-OH/rGO) and hierarchical porous carbon as the negative electrode. The system exhibited 37.5 Wh kg<sup>-1</sup> at 7120 W kg<sup>-1</sup> with a capacitance retention of about 80% for 17,000 cycles (Ma et al. 2016). In another report, graphene foam and carbon nanotubes (CNTs) were made into composite hybrid film (graphene foam/CNTs) with high flexibility and perfect

**Table 3.3** Symmetric hybrid supercapacitors

Electrode material	Specific capacitance ( $F g^{-1}$ )	Power density ( $W kg^{-1}$ )	Energy density ( $Wh kg^{-1}$ )	Electrolyte	Working voltage (V)	Cycle performance	References
MWCNTs and Co–Al layered double hydroxide	15.2	6400	13.2	1 M KOH	1.6	>1000	Su et al. (2008)
CuO/rGO	326	302	65.7	0.5MK <sub>2</sub> SO <sub>4</sub>	1.2	1500	Purushothaman et al. (2014)
rGO–PMo <sub>12</sub>	3.18 F cm <sup>-3</sup>	188 mW cm <sup>-3</sup>	1.7 mW h cm <sup>-3</sup>	PVA/ H <sub>2</sub> SO <sub>4</sub> gel	1.6	5000	Dubal et al. (2015b)
rGO/BIVO <sub>4</sub>	151	8000	33.7	6 M KOH	1.6	2000	Patil et al. (2016)

MWCNTs multi-walled carbon nanotubes, rGO reduced graphene oxide, PVA polyvinyl alcohol

robustness as ideal supporters of holding large quantity of electrochemically active materials. To this support material  $\text{MnO}_2$  and polypyrrole (PPy) was individually mixed to form grapheme foam/CNT/ $\text{MnO}_2$  and grapheme foam/CNT/PPy, respectively, and were correspondingly made as positive and negative electrodes in an aqueous electrolyte. The system had an output voltage of 1.6 V delivering a  $10.3 \text{ kW kg}^{-1}$  at  $10.9 \text{ Wh kg}^{-1}$  (Liu et al. 2014). Capacitance of mixed metal oxide (Co and Ni) nanostructured arrays interconnected with 3D carbon (C/ $\text{CoNi}_3\text{O}_4$  NA) over stainless steel to be made as positive electrode for the asymmetric system. The negative electrode of the system was activated carbon. The asymmetric hybrid capacitor exhibited cycling at a high potential of 1.8 V and was efficient upto  $19.2 \text{ Wh kg}^{-1}$  at a power density of  $13 \text{ kW kg}^{-1}$  (Zhu et al. 2014).

An asymmetric hybrid supercapacitor was fabricated with  $\text{NiSe}@\text{MoSe}_2$  nanoarrays and nitrogen-doped pamelo mesocarps based carbon nanosheet as positive and negative electrodes, respectively. The interconnection in the sheets of nanoarrays and carbon cause the system to exhibit high specific capacity ( $128 \text{ mAh g}^{-1}$ ) and capacitance ( $223 \text{ F g}^{-1}$ ). This asymmetric assembly operated at high voltage of 1.6 V displaying an energy density of  $0.55 \text{ mWh cm}^{-3}$  at  $139.1 \text{ mW cm}^{-3}$  (Peng et al. 2017). Multidimensional poly (3,4-ethylenedioxythiophene) nanotubes (mPNTs) were prepared by J.E. Lee et al. to investigated the contribution of the morphological features to the electrochemical characteristics of the system. The group built an asymmetric hybrid supercapacitor with  $\text{MnO}_2$  loaded mPNTs as the positive electrode and rGO-carbon nanofibers as the negative electrode in an optimized weight ratio of 1:1 leading to superior specific capacitance. The report, however, did not include the energy and power densities (Lee et al. 2014). Yang et al. fabricated a flexible solid-state asymmetric hybrid supercapacitor with  $\alpha\text{-MnO}_2$  nanowires and  $\text{Fe}_2\text{O}_3$  nanotubes grown individually on flexible carbon fabric with a gel electrolyte. The system showed extended response up to 1.6 V and displayed energy density of about  $0.55 \text{ mWh cm}^{-3}$  at  $139.1 \text{ mW cm}^{-3}$  (Yang et al. 2014). The electrochemical features of the asymmetric capacitors are given in Table 3.4.

### 3.6 Supercapacitor—Battery Hybrid (Supercapattery)

Thereafter, the researchers came up with a unique design configuration consisting of a battery electrode and a supercapacitor electrode, termed as supercapacitor—battery hybrid (SBH) or supercapattery hybrid (Fig. 3.6). This is also an asymmetric hybrid system. However, in the previous section, the asymmetric system contained two different electrodes, yet ultimately both the electrodes exhibited supercapacitive behavior only. In the present case of SBH, one electrode exhibits supercapacitive behavior and the other battery type behavior. Notably, though the electrochemical characteristics of both battery and supercapacitor are completely different, the striking similarity between the both is their configurations. Since, both the systems have electrodes such as anode and cathode, electrolyte and a separator. These

**Table 3.4** Asymmetric hybrid supercapacitors

Electrode 1 (Positive)	Electrode 2 (Negative)	Specific capacitance ( $F g^{-1}$ )	Power density ( $W kg^{-1}$ )	Energy density ( $Wh kg^{-1}$ )	Working voltage	Cycle performance	References
$Co(OH)_2$	urchin-like VN	429	15,900	22	1.6	4000	Wang et al. (2014b)
GF/CNTs/ $MnO_2$	GF/CNTs/PPy	215	860	22.8	1.6	10,000	Liu et al. (2014)
Ni, Co-OH/rGO	Porous carbon	1691	7120	56.1	1.6	17,000	Ma et al. (2016)
$MnO_2$ -mPNTs <sup>a</sup>	rGO-CNFs <sup>a</sup>	153	–	–	1.2	1000	Lee et al. (2014)
C/CoNi <sub>3</sub> O <sub>4</sub>	Activated carbon	1299	13,000	19.2	1.8	5000	Zhu et al. (2014)
CF-Co(OH) <sub>2</sub>	CF-WO <sub>3</sub> @PPy	2.85	0.12 $W cm^{-3}$	1.02 $mWh cm^{-3}$	1.6	5000	Wang et al. (2015b)
NiSe@MoSe <sub>2</sub>	N-PMCN	223	415	32.6	1.65	5000	Peng et al. (2017)
$\alpha$ -MnO <sub>2</sub> nanowires	Fe <sub>2</sub> O <sub>3</sub> nanotubes	–	139.1 $mW cm^{-3}$	0.55 $mWh cm^{-3}$	1.6	6000	Yang et al. (2014)

<sup>a</sup>PNTs poly(3,4-ethylenedioxythiophene), CNFs Carbon nanofibers, N-PMCN nitrogen-doped pomelo mesocarps-based carbon nanosheet, GF graphene foam, rGO reduced graphene oxide, PPy Polypyrrole



features make the combination or hybridization of two different systems highly feasible. Interesting attribute of this combination is that the direct link between the energy and power components of the system (Zuo et al. 2017). In addition, the system offers ecofriendly trait and safety.

From the previous section we are aware that electric double layer capacitance (EDLC) and pseudocapacitive materials can form a hybrid. Likewise, in this section EDLC (or pseudocapacitive) electrode and battery electrode can form a hybrid. Pseudocapacitive material might be mistakenly understood as a battery material since it also involves ‘surface redox reaction’. But the major change is that the battery electrode involves the ‘bulk redox reaction’. Here in this hybrid system, the charge separation takes place in a battery electrode, and the electrons flow through the external circuit. The charge separation leads to the movement of anions and cations in the electrolyte. The advantage of this combination over other hybrid systems like symmetric and asymmetric supercapacitive system is that battery component largely improves the energy density and the supercapacitor component largely enhances power density. Notably, each component compensates the other in which the other component is lacking and the final outcome is effectively positive. That is the combinatorial effect is improved in two factors: (i) capacity and (ii) operational voltage (Choi and Park 2014; Khomenko et al. 2008). The capacitance of the SBH is largely improved by about twofold and the operational voltage improves by 1 or 2 V. The battery electrodes involved in the SBHs are Li-ion, Na-ion electrodes, and other ion-based electrodes.

The supercapacitor electrodes utilized could exhibit EDLC or pseudocapacitance properties. So based on these two combinations the following can be derived: a) EDLC—battery hybrids and b) pseudocapacitance—battery hybrid. The battery-supercapacitor system is believed to link two different types of storage mechanisms, the physical and chemical type charge storage. Also, the combinatorial effect of SBHs is expected to be useful in two different ways: a) to possess the excellent features of both a battery and a supercapacitor and b) this combination has the potential to reduce the non-monotonic energy consumption in the batteries (Kouchachvili et al. 2018).

### ***3.6.1 Li-Ion Capacitor***

The first ever supercapacitor-battery hybrid (SBH) system was made with Li-ion as the battery component (Amatucci et al. 2001). The combination is also known as Li-ion capacitor or Li-ion hybrid capacitor. Among the materials used for electrochemical storage, it is understood that Li-ion is widely used, in the form of Li-ion batteries and it is extensively employed in portable devices. These capacitors combine the energy storage mechanism of both batteries and supercapacitors. That is, in one of the electrodes, the anions (or cations) adsorb or desorb forming double layer charge storage mechanism. On the other hand, Li-ions are intercalated and deintercalated, where the energy storage follows bulk electrochemical redox

reactions (Wang et al. 2017b). In this system, the Li-ions are reversibly consumed in the charge storage ‘rocking chair’ process similar to that of in the Li-ion batteries. It is to be noted that the individual electrodes as half cells have to be tested for their charge storage performance before the construction of a whole hybrid system. This is to be done to evaluate the mass loading since one of the electrodes undergoes Faradaic mechanism and the other non-Faradaic mechanism. The mass accumulation balance is one of the prerequisites to be achieved to tap excellent energy density (Mhamane et al. 2016). The total mass loadings are added to calculate the energy density and the power density. The hybrid system is flexible to the usage of both aqueous and non-aqueous electrolytes. However, the advantages of non-aqueous organic electrolyte have been tapped in most of the hybrid systems that include wide voltage window, which largely contributes to better energy density than aqueous electrolyte system.

Amatucci et al. assembled the first SBH with  $\text{Li}_4\text{Ti}_5\text{O}_{12}$  as the anode and activated carbon as the cathode. The energy density reported was as high as  $20 \text{ Wh kg}^{-1}$  in this system (Amatucci et al. 2001). Thereafter, several electrodes were tested for their Li-ion SBH such as, metal oxides  $\text{TiO}_2$  (Kim et al. 2013),  $\text{MnO}$  (Wang et al. 2014a),  $\text{Nb}_2\text{O}_5$  (Lim et al. 2015),  $\text{Fe}_3\text{O}_4$  (Zhang et al. 2013), and  $\text{Si}$  (Liu et al. 2013a), intercalated carbonaceous materials (activated carbon, carbon nanotubes, and graphene) (Wang et al. 2017b) and  $\text{MnNCN}$  (Liu et al. 2017) as anodes. Moreover, Li metal oxides were used as cathodes viz.  $\text{LiMn}_2\text{O}_4$  (Hu et al. 2009),  $\text{Li}_2\text{CoPO}_4\text{F}$  (Karthikeyan et al. 2013),  $\text{LiNi}_{0.5}\text{Mn}_{1.5}\text{O}_4$  (Arun et al. 2015), and  $\text{Li}_3\text{V}_2(\text{PO})_4$  (Satish et al. 2015). One of the most commonly used electrodes in this hybrid system is the prelithiated carbon anode, especially of the graphite owing to its low Li-ion intercalation potential and highest cycling stability. Prelithiated carbon electrode can be utilized to harvest energy density of up to  $15 \text{ Wh kg}^{-1}$  with a cell voltage up to 3.8 V (Zhang et al. 2014a). This system also contributes in preventing the consumption of electrolyte at the anode side and high output voltage. However, the overall specific capacity of the device is lower than that of the batteries and the specific capacitance of the device is higher than the supercapacitors. Activated carbon is another material that plays a pivotal role as electrode in the Li-ion SBH as it is cost effective and has large surface area (Cherusseri et al. 2019). Commercial activated carbon can be utilized as anode and the counter electrode was of mesocarbon microbeads with energy density of  $92.3 \text{ Wh kg}^{-1}$  and power density of  $5.5 \text{ kW kg}^{-1}$  (Zhang et al. 2014a). However, a major drawback in this anode is the easy formation of lithium dendrites at the electrode–electrolyte interface. This phenomenon decomposes the electrolyte, poor cycling ability and has safety hazard, thereby preventing a superior performance.

Another section of the EDLC-Li-ion battery hybrid is the use of aqueous electrolytes. The use of aqueous-based electrolytes is deemed superior in terms of safety and ionic conductivity compared with the non-aqueous systems that provide high energy density and extended operational voltage. Aqueous electrolytes are normally nontoxic, nonvolatile, and nonflammable (Luo and Xia 2009). The aqueous salt solutions are neutral viz.  $\text{Li}_2\text{SO}_4$ ,  $\text{LiCl}$ , and  $\text{LiNO}_3$ . The major limitations of the aqueous electrolyte Li-ion SBHs are the poor energy density ( $< 40 \text{ Wh kg}^{-1}$ ) and

restrained power density ( $< 900 \text{ W kg}^{-1}$ ) (Wang et al. 2006). Apart from these modifications, metal oxides such as  $\text{CuBiO}_4$  (Yuvaraj et al. 2016),  $\text{TiO}_2$ ,  $\text{MnO}$ , and  $\text{Nb}_2\text{O}_5$  also contribute effectively to the Li-ion SBH system. In general, the metal oxide system provides lower  $\text{CuBiO}_4$  used as negative electrode that has the tendency to exchange its Bi ions for Li-ion through redox reactions or in other words through reversible intercalation. The specific capacitance of this is much lower from the expected value with  $26.5 \text{ F g}^{-1}$  and low energy density with  $24 \text{ Wh kg}^{-1}$ . Similarly,  $\text{TiO}_2$  along with its composites were examined for negative electrodes in Li-ion capacitors. However, due to their semiconductive nature, they exhibit poor electron conductivity. The limitation can be overcome by reducing the particle size to the nanoscale level, treating with hydrogen and overlaying with a conducting layer. Thereafter, with these changes the  $\text{TiO}_2$  produced better results on performance (Kim et al. 2016; Wang et al. 2017b). X. Zhao et al. reported the asymmetric hybrid combination with multi-walled carbon nanotubes (MWCNTs) as the cathode and  $\alpha\text{-Fe}_2\text{O}_3/\text{MWCNTs}$  composite as the anode with the Li-ion as the electrolyte. The system exhibited a specific energy density of  $50 \text{ Wh kg}^{-1}$  and a power density of  $1000 \text{ W kg}^{-1}$  (Zhao et al. 2009). Metal nitrides also contributed to the formation of Li-ion capacitor and they possess excellent electronic conductivity.  $\text{NbN}$  has the ability to exhibit power density upto  $45 \text{ kW kg}^{-1}$  (Wang et al. 2016d). The summary of the electrochemical performances of Li-ion SBH is presented in Table 3.5.

### 3.6.2 Na-Ion Capacitor

After the successful experimentation with Li-ion electrodes, Na-ion electrodes were tested to form the Na-ion capacitor (or Na-ion supercapacitor battery hybrid [SBH]). The latter was tested for its ability as a battery electrode due to its enormous abundance on the planet earth up to 4–5 orders above Li availability (Wang et al. 2017b). In addition, both Li and Na share common physiochemical properties. The merits of Na in terms of abundance and similar physiochemical property like that of Li make it to be a better choice to replace Li (Yabuuchi et al. 2014). Similar to Li-ion capacitors, in this class of SBHs Na-ion electrodes are mostly used as negative electrodes and the supercapacitive-based materials are used as positive electrodes. Obvious difference between the Li-ion battery electrodes and Na-ion electrodes is that the former has voltammogram as that of a battery, whereas the later is like of capacitive electrode (Ma et al. 2011). One of the main disadvantages of Na in the charge storage device is that it is not compatible with aqueous electrolyte. Therefore, no major work has been reported with Na-ion capacitor using aqueous electrolytes.

In general, the negative electrodes of the Na-ion capacitor includes activated carbon (Kuratani et al. 2012; Wang et al. 2016c),  $\text{Na}_2\text{Ti}_3\text{O}_7$  (Yin et al. 2012),  $\text{Na}_3\text{V}_2(\text{PO}_4)_3$  (Wang et al. 2015a),  $\text{Nb}_2\text{O}_5$  (Lim et al. 2016),  $\text{NiCo}_2\text{O}_4$  (Ding et al. 2013), and  $\text{V}_2\text{O}_5$  (Chen et al. 2012). Likewise, the positive electrodes include,  $\text{NaMnO}_2$  (Ma et al. 2011),  $\text{Na}_{0.44}\text{MnO}_2$  (Wang et al. 2015d),  $\text{Na}_x[\text{Fe}_{1/2}\text{Mn}_{1/2}]\text{O}_2$

**Table 3.5** Performance of Li-ion capacitors

Supercapacitor electrode	Battery electrode	Specific capacitance (F g <sup>-1</sup> )	Power density (kW kg <sup>-1</sup> )	Energy density (Wh kg <sup>-1</sup> )	Electrolyte	Working voltage (V)	Cycle performance/capacitance retention	References
Activated carbon	Li <sub>4</sub> Ti <sub>5</sub> O <sub>12</sub>	120	4.3	57	1 M LiPF <sub>6</sub> in 1:1 EC <sup>a</sup> and DMC <sup>a</sup>	1–3	2000 / 92%	Babu et al. (2016)
Activated carbon	Li-CuBi <sub>2</sub> O <sub>4</sub>	26.5	0.3	24	1 M LiPF <sub>6</sub> in 1:1 EC, DEC <sup>u</sup> and DMC	0–3	1500 / 86%	Yuvaraj et al. (2016)
Activated carbon	LiTi <sub>2</sub> (PO <sub>4</sub> ) <sub>3</sub> /Carbon	30	1.0	27	1 M Li <sub>2</sub> SO <sub>4</sub>	0.3–1.5	1000 / 85%	Luo and Xia (2009)
Activated carbon	Li <sub>3</sub> V <sub>2</sub> (PO <sub>4</sub> ) <sub>3</sub> /C	–	0.2	27	1 M LiPF <sub>6</sub> in 1:1 EC and DMC	3–5	1000 / 66%	Satish et al. (2015)
Activated carbon	MnO/Carbon	387.7	2.952	227	1 M LiPF <sub>6</sub> in 1:1 EC, DEC and DMC	0.1–4	5000 / 76%	Liu et al. (2016)
Graphene	Fe <sub>3</sub> O <sub>4</sub> /Graphene	–	0.055–4.6	204–65	1 M LiPF <sub>6</sub> in 1:1 EC, DEC and DMC	0.01–3	1000 / 70%	Zhang et al. (2013)
Activated carbon	Li <sub>4</sub> Ti <sub>5</sub> O <sub>12</sub> (LTO)	165.6	–	20	1 M LiPF <sub>6</sub> in 1:1 EC and DMC	1.5–3	5000 / 85%	Amatucci et al. (2001)
Graphene	Li <sub>3</sub> VO <sub>4</sub>	206–33	–	110	1 M LiClO <sub>4</sub>	–	2400 / 86%	Wang et al. (2017a)
Activated carbon	MnO	30	2.608	220	1 M LiPF <sub>6</sub> in 1:1 EC, DEC and DMC	0–3.5	3600 / 95.3	Liu et al. (2017)
N-doped Graphene	Li <sub>4</sub> Ti <sub>5</sub> O <sub>12</sub> (LTO)	–	0.2	70	1 M LiPF <sub>6</sub> in 1:1 EC, DEC and DMC	1–3	10,000 / 64%	Fan et al. (2016)

Activated 1,2,4,5-benzene tetra carboxylic acid derived carbon	$\text{Li}_4\text{Ti}_5\text{O}_{12}$ (LTO)	225	0.5 0.5	43.9 63	(1) 1 M TEA·BF <sub>4</sub> in ACN (2) 1 M LiPF <sub>6</sub> in 1:1 EC and DMC	0–3	6000 / 97%	Mhamane et al. (2016)
Activated carbon	$\text{LiNi}_{0.5}\text{Mn}_{1.5}\text{O}_4$	–	–	19	1 M LiPF <sub>6</sub> in 1:1 EC and DMC	0–3	3000 / 81%	Arun et al. (2015)
Activated carbon	Hydrogen titanate	–	15	33.3	1 M LiPF <sub>6</sub> in 1:1 EC and DMC	0–3	3000 / 78.8%	Que et al. (2016)
Graphene	TiO <sub>2</sub> /Graphene	205	–	72	Li-ion conducting gel polymer	1–2.5	1000 / 90%	Wang et al. (2015a)
MWCNT	$\text{Li}_4\text{Ti}_5\text{O}_{12}$ (LTO)	109	565 mW/cm <sup>3</sup>	4.38 mWh/cm <sup>3</sup>	1 M LiPF <sub>6</sub> in 1:1 EC and DMC	0–3	3000 / 92%	Zuo et al. (2017)
Activated carbon	Porous NbN	–	45	149	1 M LiPF <sub>6</sub> in 1:1 EC and DMC	0–4	15,000 / 95%	Wang et al. (2016d)

<sup>a</sup>EC Ethylene carbonate, DMC Dimethyl carbonate, DEC Diethyl carbonate, MWCNT multi-walled carbon nanotubes, DMC Dimethyl carbonate

(Yabuuchi et al. 2012), and  $\text{Na}_{0.85}\text{Li}_{0.17}\text{Ni}_{0.21}\text{Mn}_{0.64}\text{O}_2$  (Kim et al. 2011). In the recent years, the intercalation hard carbon anode and capacitive carbon cathode was studied for the Na-ion SBH. In this case, the intercalated hard carbon displayed poor performance owing to its poor electrochemical behavior in Na-ion based electrolyte. It is to be noted that fast kinetics for Na intercalation in hard carbon and large surface area for capacitive carbon is basically essential for superior performance of the assembled Na-ion capacitor. The condition to improve the working ability of the electrode is to make the electrode highly porous (Kuratani et al. 2012). The required modifications were done in one of the subsequent works where the carbon electrode was constructed using peanut derived activated carbon made as thin flakes and with high porosity. This alteration supported the swift Na-ion intercalation and largely supported the redox reaction. Thereafter, the Na-ion SBH produced energy density of up to  $200 \text{ Wh kg}^{-1}$  with a power density of up to  $16.5 \text{ kW kg}^{-1}$  (Ding et al. 2015). The electrochemical performances of Na-ion SBH are presented in Table 3.6.

### 3.6.3 K-Ion Capacitor

Next element in group 1 of the periodic table that is suitable to be used in supercapacitor battery hybrid (SBH) is K-ion. Notably, like Na, K is also found in abundance across the planet and the redox potential of K ( $-2.93 \text{ V [K}^+/\text{K]}$  vs standard hydrogen electrode [SHE]) is lower than that of Na ( $-2.71 \text{ V [Na}^+/\text{Na]}$ ).

The atomic size of K does not hinder the gravimetric capacity of the K-ion capacitor. In general, hard carbon is utilized in the K-ion capacitor as the negative electrode. The electrolyte generally used for this section of SBH is 1 M potassium bis (fluorosulfonyl) imide (KFSI) dissolved in ethylene carbonate and diethyl carbonate. Interestingly, ionic conductivity of 1 M KFSI with  $10.7 \text{ mS cm}^{-1}$  is observed to be superior compared with LiFSI and NaFSI with  $9.3$  and  $9.7 \text{ mS cm}^{-1}$ , respectively. This phenomenon largely aids the fast kinetics of metal ion in the electrolyte. However, this capacitor works at a lower working potential, which lies around  $0.2 \text{ V}$  closer to  $0 \text{ V}$  and this aids the formation of dendrites at the electrode–electrolyte interface. Moreover, the melting point of potassium ( $337.15 \text{ K}$ ) is much lower than that of sodium ( $371 \text{ K}$ ) and lithium ( $453.7 \text{ K}$ ), which is a safety hazard to the fabricated device.

In order to surmount the demerits displayed by K-ion capacitors several steps have been taken. One of the modifications tested by L. Fan et al. was to replace hard carbon negative electrode with soft carbon. They also replaced the common electrolyte with bis(fluoro-sulfonyl)imide dissolved in dimethyl ether as the electrolyte. This SBH exhibited an energy density of about  $120 \text{ Wh kg}^{-1}$  and a power density of about  $600 \text{ W kg}^{-1}$ . The investigation also provided the long desired fast charging and slow discharging behavior (Fan et al. 2018). In another work, the active electrode was replaced with  $\text{K}_{0.27}\text{MnO}_2$  with  $\text{K}_2\text{SO}_4$  as the electrolyte. This combination has an operational voltage between  $0$  and  $1.9 \text{ V}$  displaying an energy density of  $25.3 \text{ Wh kg}^{-1}$  and power density of  $140 \text{ W kg}^{-1}$  (Qu et al. 2010). Also, cubic

**Table 3.6** Performance of Na-ion capacitors

Supercapacitor electrode	Battery electrode	Power density (kW kg <sup>-1</sup> )	Energy density (Wh kg <sup>-1</sup> )	Electrolyte	Working voltage (V)	Cycle performance / capacitance retention	References
Activated carbon	Spinel NiCo <sub>2</sub> O <sub>4</sub>	0.308	13.8	1.5 M NaClO <sub>4</sub> PC:DMC <sup>a</sup> (1:2)	0–3	2000	Ding et al. (2013)
NaMnO <sub>2</sub>	Activated carbon	0.13	19.5	0.5 M Na <sub>2</sub> SO <sub>4</sub>	0–1.9	10,000	Qu et al. (2009)
Activated carbon	Nb <sub>2</sub> O <sub>5</sub> @C/rGO-50	20.8	76	1.0 M NaPF <sub>6</sub> + other	1.0–4.3	3000	Lim et al. (2016)
Carbon mesoporous	Macroporous graphene	0.501	168	Na <sup>+</sup> ion conducting gel	0–4.2	1200	Wang et al. (2015a)
Peanut Shell Hybrid Sodium Ion	Peanut Shell Hybrid Sodium Ion	16.5	201	1 M NaClO <sub>4</sub> in 1:1 EC:DEC	1.57–3.5	100,000	Ding et al. (2015)
Activate carbon	V <sub>2</sub> O <sub>5</sub> /CNT	45	48	1 M NaClO <sub>4</sub> in PC	0–2.8	900	Chen et al. (2012)
Peanut shell carbon	Nb <sub>2</sub> O <sub>5</sub>	5.72	43.2	1 M NaClO <sub>4</sub> EC: PC (1:1)	1–3	3000/	Li et al. (2016)
Na-ion active carbon	Na <sub>4</sub> Mn <sub>9</sub> O <sub>18</sub>	21.0	377.4	1 M Na <sub>2</sub> SO <sub>4</sub> aqueous	0–1.7	4000/	Liu et al. (2013b)
Carbon	Peanut skin derived carbon nanosheets	12	45	1.0 M NaClO <sub>4</sub> in 1:1 EC:DEC	0–4	3000	Wang et al. (2016b)
Activated carbon	Porous carbon and NaTiO <sub>3</sub> nanotubes	889	34	1.5 M NaClO <sub>4</sub> in PC and DMC	0.1–2	1000	Yin et al. (2012)
Na metallic foil	Na <sub>4</sub> Mn <sub>9</sub> O <sub>18</sub>	–	–	Polymer Gel	2–4	–	Zhu et al. (2017)

<sup>a</sup>EC Ethylene carbonate, DEC Diethyl carbonate, PC: Propylene carbonate, DMC Dimethyl carbonate, DEC diethyl carbonate, rGO: Reduced graphene oxide, CNTs: Carbon nanotubes

Prussian blue crystals ( $C_{18}Fe_7N_{18}$ ) were utilized as the active electrode in  $K_2SO_4$  and this K-ion capacitor showed energy and power densities as  $28 \text{ Wh kg}^{-1}$  and  $214 \text{ W kg}^{-1}$ , respectively (Zhou et al. 2017). The summary of the K-ion SBHs electrochemical performances are presented in Table 3.7.

### 3.6.4 Al-Ion Capacitor

So far, the discussion was on monovalent alkali elements and their role in the supercapacitor battery hybrid (SBH) system. Aluminum is a trivalent ion and the 3-electron transfer during the charge storage offers high efficiency than the monovalent counterparts (Li et al. 2017). Also, Al is highly economical and one of the most abundant metal on the earth's crust. Conductive polypyrrole coated  $MoO_3$  was employed as the negative electrode for the intercalation/deintercalation of  $Al^{3+}$  ions in aqueous solution with activated carbon as the positive electrode (Wang et al. 2016a). The energy and power density exhibited by this device was about  $28 \text{ Wh kg}^{-1}$  and  $460 \text{ W kg}^{-1}$ , respectively. This system also has ability to exhibit an energy density of  $20 \text{ Wh kg}^{-1}$  at a power density of  $2840 \text{ W kg}^{-1}$ . The capacitance of the device was around  $693 \text{ F g}^{-1}$ , which is thrice than that of the Na-ion capacitor (Wang et al. 2016a). In another work the reversible  $Al^{3+}$  ion intercalation in Prussian blue analogs were studied and the energy density of the system was observed to be  $13 \text{ Wh kg}^{-1}$  (Li et al. 2015). The summary of the Al-ion SBHs electrochemical performances are presented in Table 3.8.

### 3.6.5 Pseudocapacitor-Battery Hybrid

In general, most of the supercapacitor battery hybrid (SBH) systems employ EDLC type electrodes usually made of carbon. Alternatively, another concept was developed by replacing the double layer capacitive electrodes with pseudocapacitive electrodes. The combination was expected to largely improve the energy density of the SBH devices. It is to be noted that several metal oxides (as discussed here) such as  $Nb_2O_5$  (Lim et al. 2015),  $MnO_2$  and its associates (Ma et al. 2011; Qu et al. 2010; Wang et al. 2015d),  $MoO_3$  (Wang et al. 2016a),  $TiO_2$  (Kim et al. 2013) contribute to the pseudocapacitive behavior. In addition, conducting polymers PANI (polyaniline) and PPy (polypyrrole) also exhibit pseudocapacitive property. However, other electrode materials such as MXenes and  $MoS_2$  are also involved. Advantages of MXenes are that they are two-dimensional (2D) metal carbides that have superior volumetric capacitance compared with all other carbon materials (Zhao et al. 2015b).

Surfaces of MXenes are terminated with O, OH, and F groups and in common they are represented as  $M_{n-1}X_nT_x$ , where M is the transition metal, X is C or N and T is the terminal groups, and n can be 1, 2 or 3 and x denote the number of terminating



**Table 3.7** Performance of K-ion capacitors

Supercapacitor electrode	Battery electrode	Power density (kW kg <sup>-1</sup> )	Energy density (Wh kg <sup>-1</sup> )	Electrolyte	Working voltage (V)	Cycle performance / capacitance retention	References
Activated carbon	K <sub>0.27</sub> MnO <sub>2.0</sub> ·6H <sub>2</sub> O	140	25.3	K <sub>2</sub> SO <sub>4</sub>	0–1.8	10,000 / 98%	Qu et al. (2010)
Graphite	Polyacrylate	–	–	1 M KN(SO <sub>2</sub> F) <sub>2</sub> in 1:1 EC:DEC	0–3	–	Komaba et al. (2015)
Activated carbon	Prussian Blue	214	28	0.5 M K <sub>2</sub> SO <sub>4</sub>	1–3	1200 / 98%	Zhou et al. (2017)
Soft carbon	Activated carbon	0.599	120	1 M KN(SO <sub>2</sub> F) <sub>2</sub> in DME*	1–4	1500 / 97.5%	Fan et al. (2018)

\*DME Dimethoxy ethane, EC ethylene carbonate, DEC diethyl carbonate

**Table 3.8** Performance of Al-ion capacitors

Supercapacitor electrode	Battery electrode	Specific capacitance (F g <sup>-1</sup> )	Power density (kW kg <sup>-1</sup> )	Energy density (Wh kg <sup>-1</sup> )	Electrolyte	Working voltage (V)	Cycle performance / capacitance retention	References
Activated carbon	PPy@MoO <sub>3</sub>	693	0.46	30	0.5 M Al <sub>2</sub> (SO <sub>4</sub> ) <sub>3</sub>	0–1.5	1800 / 93%	Wang et al. (2016a)
Activated carbon	W <sub>18</sub> O <sub>49</sub> NWs @ SWCNTs	459	0.000295	19	Al <sup>3+</sup>	0–1.8	5000 / 99.3%	Li et al. (2017)
Activated carbon	Al-0.2 CuFe-PBA	–	–	13	1 M Al (NO <sub>3</sub> ) <sub>3</sub>	0.2–0.7	1000 /	Li et al. (2015)

SWCNTs single wall carbon nanotubes, PPy polypyrrole, PBA Prussian blue analogs NWs nano-walls.

groups in the given system. These systems can support the intercalation and deintercalation of ions such as  $\text{Na}^+$ ,  $\text{K}^+$ ,  $\text{NH}_4^+$ ,  $\text{Mg}^{2+}$ , and  $\text{Al}^{3+}$  provided space for higher capacitance up to  $300 \text{ F cm}^{-3}$  (Lukatskaya et al. 2013). As understood, the system has more provision for pseudocapacitance. The expected volumetric capacitance of these groups could be up to  $450 \text{ F cm}^{-3}$  at the scan rate of  $2 \text{ mV cm}^{-2}$  (Zhao et al. 2015b). MXene  $\text{Ti}_2\text{C}$  employed as a negative electrode with  $\text{Na}_2\text{Fe}_2(\text{SO}_4)_3$  as the positive electrode displayed excellent current density. The specific capacitance was several fold above the double layer capacitance (Wang et al. 2015c). Likewise,  $\text{MoS}_2$  intercalation and deintercalation with Na-ions are observed to deliver higher capacity to fabricate an effective Na-ion capacitor (Wang et al. 2014c). The electrochemical performances of pseudocapacitor-battery hybrid are presented in Table 3.9.

### 3.6.6 Pb-Based Supercapacitor-Battery Hybrid [Acidic]

Lead acid batteries are safe, economical, and oldest energy storage devices. This system works under the partial state of charge storage, which causes irreversible sulfation of negative electrode leading to its lessened lifespan (Lam et al. 2004). At this juncture, it can be well understood that carbon-based supercapacitors as negative electrode has a superior role to play as they are not easily corroded or evaded (Moseley et al. 2006). This triggered the amalgamation of  $\text{PbO}_2$ -based battery electrode and activated carbon-based supercapacitor electrodes.  $\text{PbO}_2$ -based SBHs are the only systems that use highly acidic electrolytes compared with all such similar systems. The system is also known as the lead-carbon capacitors and acidic SBHs. Moreover, this is one of the systems that are successfully commercialized as SBH. The device with  $\text{PbO}_2$ /activated carbon showed excellent energy density of about  $49.4 \text{ Wh kg}^{-1}$  and power density of  $433.2 \text{ W kg}^{-1}$  (Lam et al. 2004). The system could work up to a power density of  $2078 \text{ W kg}^{-1}$  to render an energy density of  $30 \text{ Wh kg}^{-1}$ . In another work,  $\text{PbO}_2$  thin film and activated carbon was used as the positive and negative electrodes, respectively, in methanesulfonic acid electrolyte. The system exhibited an energy density of about  $29 \text{ Wh kg}^{-1}$  (Perret et al. 2011).  $\text{PbO}_2$  electrodeposited on to graphite was fabricated as SBH along with activated carbon. Operational voltage of this system ranged between 1.88 and 0.65 V. This SBH delivered an energy density of  $27 \text{ Wh kg}^{-1}$  at a power density of  $691 \text{ W kg}^{-1}$  (Ni et al. 2013). In another work,  $\text{PbO}_2$  thin films were synthesized on  $\text{Ti/SnO}_2$  substrates via galvanostatic electrodeposition technique. The device had  $\text{PbO}_2$  as the positive electrode and the activated carbon as the negative electrode with  $\text{H}_2\text{SO}_4$  as the electrolyte. The system displayed energy density of  $7.8 \text{ Wh kg}^{-1}$  and power density of  $258 \text{ W kg}^{-1}$  (Yu et al. 2009). Table 3.10 provides the electrochemical performances of acidic SBHs.

**Table 3.9** Performance of pseudocapacitor-battery hybrid

Supercapacitor electrode	Battery electrode	Specific capacitance (F g <sup>-1</sup> )	Power density (kW kg <sup>-1</sup> )	Energy density (Wh kg <sup>-1</sup> )	Electrolyte	Working voltage (V)	Cycle performance/ capacitance retention	References
Na foil	MoS <sub>2</sub> /G	50	–	–	1 M NaClO <sub>4</sub> 1:1 PC; EC 5% FEC*	0.1–2.5	2000 / 81%	Wang et al. (2014c)
Activated carbon	MXene Ti <sub>3</sub> C <sub>2</sub> T <sub>x</sub> / MWCNT	150	–	–	1 M MgSO <sub>4</sub>	–0.8–0.1	10,000	Zhao et al. (2015a)
Activated carbon	MXene Ti <sub>3</sub> C <sub>2</sub> T <sub>x</sub>	81	2.23	3.4	1 M KOH	–0.5–1.0	10,000	Lukatskaya et al. (2013)
Na <sub>2</sub> Fe <sub>2</sub> (SO <sub>4</sub> ) <sub>3</sub>	MXene Ti <sub>2</sub> C T <sub>x</sub>	245	1.4	260	1 M NaPF <sub>6</sub> in 1:1 EC and DEC	0.1–3	100 / 99.7%	Wang et al. (2015c)
Poly aniline derived porous carbon	MoS <sub>2</sub> /Carbon	–	12	111.4	1 M NaClO <sub>4</sub> in 1:1:0.05 EC, DEC and FEC	0.4–3	10,000 / 77.3%	Wang et al. (2017c)

\*PC propylene carbonate, EC ethylene carbonate, FEC fluoroethylene carbonate, DEC diethyl carbonate

**Table 3.10** Performance of Pb-based supercapacitor-battery hybrids [acidic]

Supercapacitor electrode	Battery electrode	Specific capacitance ( $F\ g^{-1}$ )	Power density ( $kW\ kg^{-1}$ )	Energy density ( $Wh\ kg^{-1}$ )	Electrolyte	Working voltage (V)	Cycle performance/capacitance retention	References
Activated carbon	PbO <sub>2</sub>	34		29	Pb salt in CH <sub>4</sub> O <sub>3</sub> S	0.7–1.7	3000 / 83%	Perret et al. (2011)
Activated carbon	3D-Ti/PbO <sub>2</sub>	135.2	0.433	49.4	1 M H <sub>2</sub> SO <sub>4</sub>	1–3	1000 / 99.2%	Zhang et al. (2014b)
Activated carbon	Graphite-PbO <sub>2</sub>	63.2	0.152	27	5.3 M H <sub>2</sub> SO <sub>4</sub>	0.65–1.88	3000 / 80%	Ni et al. (2013)

### 3.6.7 Ni-Based Supercapacitor Battery Hybrid [Alkaline]

Soon after the invention of Pb acid batteries, the Ni–Cd batteries were also found and unlike the former, the later majorly works in the alkaline electrolytes. In this class, electrospun NiO nanofibers with high aspect ratio and the activated carbon were used as the battery type cathode material and anode material, respectively. The system used 6 M KOH as the electrolyte and had an operating potential of 1.5 V. The setup displayed an energy density of about 43.75 Wh kg<sup>-1</sup> in a power density of 7500 W kg<sup>-1</sup> (Kolathodi et al. 2015). In another work, honeycomb-like mesoporous NiO microspheres were used as a cathode material and reduced graphene oxide as anode material. This SBH produced an energy density of 23.25 Wh kg<sup>-1</sup> and a power density of 9.3 kW kg<sup>-1</sup> (Ren et al. 2015). Ni(OH)<sub>2</sub> is an additional material, which is majorly employed in Ni-based alkaline supercapacitor battery hybrid (SBH) systems.

Hierarchical flower like Ni(OH)<sub>2</sub> decorated graphene sheets were coupled with porous graphene as the positive and negative electrodes, respectively. The working voltage of this SBH was noted to be in the region 0–1.6 V with it displaying an energy density of 77.8 Wh kg<sup>-1</sup> at a power density of 174.7 W kg<sup>-1</sup> (Yan et al. 2012). Al-substituted  $\alpha$ -Ni(OH)<sub>2</sub> as positive electrode and activated carbon as the negative electrode was formed as SBH in an alkaline medium. The energy density displayed by the system was 26.9 Wh kg<sup>-1</sup> at a power density of 1100 W kg<sup>-1</sup> and it increased upto 42.3 Wh kg<sup>-1</sup> at 1100 W kg<sup>-1</sup> (Lang et al. 2010). Furthermore, Ni(OH)<sub>2</sub>/CNT composite electrode was built on Ni foams to be used as the anode and the activated carbon was employed as the cathode. This combination of SBH displayed an energy density of 50.6 Wh kg<sup>-1</sup> at a power density of at 95 W kg<sup>-1</sup> (Tang et al. 2012). Moreover, nanoporous Ni(OH)<sub>2</sub> thin film was grown over ultrathin graphite foam (UGF) to be used as positive electrode. Activated microwave exfoliated graphite oxide was used as the negative electrode. An effective power density of 44 kW kg<sup>-1</sup> was exhibited with an energy density of 13.4 Wh kg<sup>-1</sup> (Ji et al. 2013).

Additive free NiMoO<sub>4</sub> nanosheets or nanorods were synthesized to be used as the positive electrode and activated carbon was used as the negative electrode. The SBH formed had an extended operating voltage of 0–1.7 V with excellent electrochemical performance of 60.9 Wh kg<sup>-1</sup> energy density at a power density of 850 W kg<sup>-1</sup> (Peng et al. 2015). Another Ni-based electrode, Ni<sub>3</sub>S<sub>2</sub> loaded onto multi-walled carbon nanotubes was employed as cathode and activated carbon as the anode with 2 M KOH as the electrolyte operating reversibly in the voltage range between 0 and 1.6 V. The system delivered maximum energy density of 19.8 Wh kg<sup>-1</sup> at 798 W kg<sup>-1</sup> (Dai et al. 2013). Hierarchical Mn<sub>0.4</sub>Ni<sub>0.6</sub>Co<sub>2</sub>O<sub>4</sub> nanowires were fabricated as positive electrode and activated carbon as the negative electrode with KOH as the electrolyte. The system cycled reversibly at 1.5 V displaying a superior high energy density of 35.2 Wh kg<sup>-1</sup> (Tamboli et al. 2017). The electrochemical performances displayed by alkaline SBHs are presented in Table 3.11.

**Table 3.11** Performance of Ni-based supercapacitor battery hybrid [alkaline]

Supercapacitor electrode	Battery electrode	Specific capacitance ( $F\ g^{-1}$ )	Power density ( $W\ kg^{-1}$ )	Energy density ( $Wh\ kg^{-1}$ )	Electrolyte	Working voltage (V)	Cycle performance/capacitance retention	References
Activated carbon	Ni(OH) <sub>2</sub> /CNT/NF	3300	95	50.6	6 M KOH	1.8	3000 / 87%	Tang et al. (2012)
Porous graphene	Ni(OH) <sub>2</sub> /graphene	218.4	174.7	77.8	1 M KOH	1.6	300 / 94.3%	Yan et al. (2012)
Activated carbon	NiMoO <sub>4</sub>	1221	850	60.9	2 M KOH	1.7	10,000 / 85.7%	Peng et al. (2015)
rGO	NiO microspheres	945	9300	23.25	6 M KOH	1.5	3500 / 88.4%	Ren et al. (2015)
Activated carbon	Ni <sub>3</sub> S <sub>2</sub> and MWCNTs	800	798	19.8	2 M KOH	1.6	5000 / 90%	Dai et al. (2013)
Activated carbon	$\alpha$ -Ni(OH) <sub>2</sub>	127	1100	46	2 M KOH	1.6	1000 / 82%	Lang et al. (2010)
Activated carbon	Mn <sub>1-x</sub> Ni <sub>x</sub> Co <sub>2</sub> O <sub>4</sub>	1762	–	35.2	2 M KOH	1.5	2000 / 83.2%	Tamboli et al. (2017)
Activated carbon	NiO nanofibers	141	7500	43.75	6 M KOH	1.5	5000 / 88%	Kolathodi et al. (2015)
Activated carbon	Graphene–nickel cobaltite	618	5600	19.5	6 M KOH	1.4	10,000 / 102%	Wang et al. (2012)
a-MEGO <sup>a</sup>	Ni(OH) <sub>2</sub> /UGF <sup>a</sup>	166	44,000	13.4	6 M KOH	1.8	10,000 / 63.2%	Ji et al. (2013)

<sup>a</sup>a-MEGO activated microwave exfoliated graphite oxide, UGF Ultrathin graphene foam, CNTs carbon nanotubes, MWCNTs multi-wall carbon nanotubes, NF Nickel Foam

### 3.6.8 Effectiveness of Supercapattery Systems

The hybridization of a capacitor and a battery into a single system has innate advantages and it could be explained with the charging potential profiles as illustrated in Fig. 3.8. The primary change witnessed is in the voltage limit expansion: the charging potential for a supercapacitor (Fig. 3.8a) is linear with respect to time in a given voltage limits ( $\Delta V_c$ ). Likewise, the charging potential of the battery system (Fig. 3.8b) is in parabolic form, which includes a redox phase change in a given voltage limit ( $\Delta V_b$ ). In a supercapacitor battery hybrid (SBH) system, a combinatorial effect (Fig. 3.8c) takes place with an increase in the voltage limits ( $\Delta V$ ) with the final equation (Dubal et al. 2015a) being,

$$\Delta V = \Delta V_c + \Delta V_b \quad (3.6)$$

Thus, the increase in voltage is obvious. Thereafter, the SBH exhibits an expansion in the energy storage: the supercapacitors render high power density and the battery render high energy density. The amalgamation of two such components in SBHs improves the energy storage with a contribution from both (Chen 2017). Energy stored in a battery and supercapacitor is given as below, respectively,

$$E_b = Q_b \cdot \Delta V_b \quad (3.7)$$

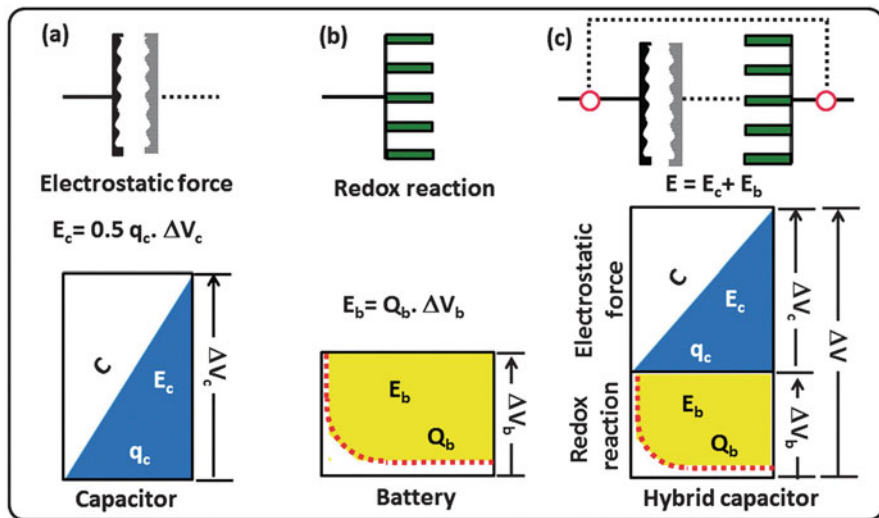


**Fig. 3.8** Electrode systems (a) capacitor (b) battery, and (c) an asymmetric supercapacitor-battery hybrid. (Reprinted with permission of RSC from Dubal et al. 2015a)



$$E_c = 0.5q_c \cdot \Delta V_c \quad (3.8)$$

where  $E_b$  and  $E_c$  are energy stored in battery and supercapacitor, respectively.  $Q_b$  and  $q_c$  are the charges stored in battery and supercapacitor, respectively. It is to be noted that the energy stored in a capacitor is half than that of the battery. The total energy stored (Fig. 3.8c) in a SBH system (Dubal et al. 2015a) is given as,

$$E_{SBH} = E_b + E_c \quad (3.9)$$

Apart from these fundamental changes, the supercapacitor and battery components compensate each other with the lacking energy density and power density, respectively.

### 3.7 Conclusion

This chapter provides an outline to understand the improvements in the supercapacitor sector. The hybrid supercapacitor systems are in the line of current electrochemical energy storage systems. Earlier, it was development only in the EDLC or pseudocapacitance systems. Now, it is a combination of both and the addition of battery electrodes in supercapacitor devices. The supercapacitor-battery hybrid has brought in excellent energy density rendering devices at a superior power density and is still prone to advancement. The field is swiftly expanding and advanced outputs are anticipated.

**Acknowledgment** T. Manovah David gratefully acknowledges the award of ‘Research Associate-ship’ received from Indira Gandhi Centre for Atomic Research, Kalpakkam, Department of Atomic Energy (DAE), Government of India. The authors wish to thank Rebeca Gopu, Jayanthi Karthikeyan, and Edward Joshua for their timely help and inputs.

### References

- Amatucci GG, Badway F, Du Pasquier A, Zheng T (2001) An asymmetric hybrid nonaqueous energy storage cell. *J Electrochem Soc* 148:A930–A939. <https://doi.org/10.1149/1.1383553>
- Arun N, Jain A, Aravindan V, Jayaraman S, Ling WC, Srinivasan MP, Madhavi S (2015) Nanostructured spinel  $\text{LiNi}_{0.5}\text{Mn}_{1.5}\text{O}_4$  as new insertion anode for advanced Li-ion capacitors with high power capability. *Nano Energ* 12:69–75. <https://doi.org/10.1016/j.nanoen.2014.12.006>
- Babu B, Lashmi P, Shaijumon M (2016) Li-ion capacitor based on activated rice husk derived porous carbon with improved electrochemical performance. *Electrochim Acta* 211:289–296. <https://doi.org/10.1016/j.electacta.2016.06.055>
- Cericola D, Kötzer R (2012) Hybridization of rechargeable batteries and electrochemical capacitors: principles and limits. *Electrochim Acta* 72:1–17. <https://doi.org/10.1016/j.electacta.2012.03.151>

- Chen GZ (2017) Supercapacitor and supercapattery as emerging electrochemical energy stores. *Int Mater Rev* 62:173–202. <https://doi.org/10.1080/09506608.2016.1240914>
- Chen PC, Shen G, Shi Y, Chen H, Zhou C (2010) Preparation and characterization of flexible asymmetric supercapacitors based on transition-metal-oxide nanowire/single-walled carbon nanotube hybrid thin-film electrodes. *ACS Nano* 4:4403–4411. <https://doi.org/10.1021/nn100856y>
- Chen Z, Augustyn V, Jia X, Xiao Q, Dunn B, Lu Y (2012) High-performance sodium-ion pseudocapacitors based on hierarchically porous nanowire composites. *ACS Nano* 6:4319–4327. <https://doi.org/10.1021/nn300920e>
- Cherusseri J, Kumar KS, Choudhary N, Nagaiah N, Jung Y, Roy T, Thomas J (2019) Novel mesoporous electrode materials for symmetric, asymmetric and hybrid supercapacitors. *Nanotechnol* 30:202001. <https://doi.org/10.1088/1361-6528/ab0685>
- Choi HS, Park CR (2014) Theoretical guidelines to designing high performance energy storage device based on hybridization of lithium-ion battery and supercapacitor. *J Power Sources* 259:1–14. <https://doi.org/10.1016/j.jpowsour.2014.02.001>
- Chuang CM, Huang CW, Teng H, Ting JM (2010) Effects of carbon nanotube grafting on the performance of electric double layer capacitors. *Energ Fuel* 24:6476–6482. <https://doi.org/10.1021/ef101208x>
- Conway BE (2013) *Electrochemical supercapacitors: scientific fundamentals and technological applications*. Springer. <https://doi.org/10.1007/978-1-4757-3058-6>
- Conway B, Pell W (2003) Double-layer and pseudocapacitance types of electrochemical capacitors and their applications to the development of hybrid devices. *J Solid State Electrochem* 7:637–644. <https://doi.org/10.1007/s10008-003-0395-7>
- Dai C-S et al (2013) Hierarchically structured Ni<sub>3</sub>S<sub>2</sub>/carbon nanotube composites as high performance cathode materials for asymmetric supercapacitors. *ACS Appl Mater Interfaces* 5:12168–12174. <https://doi.org/10.1021/am404196s>
- Ding R, Qi L, Wang H (2013) An investigation of spinel NiCo<sub>2</sub>O<sub>4</sub> as anode for Na-ion capacitors. *Electrochim Acta* 114:726–735. <https://doi.org/10.1016/j.electacta.2013.10.113>
- Ding J et al (2015) Peanut shell hybrid sodium ion capacitor with extreme energy–power rivals lithium ion capacitors. *Energy Environ Sci* 8:941–955. <https://doi.org/10.1039/C4EE02986K>
- Du X et al (2013) Preparation of activated carbon hollow fibers from ramie at low temperature for electric double-layer capacitor applications. *Bioresour Technol* 149:31–37. <https://doi.org/10.1016/j.biortech.2013.09.026>
- Dubal DP, Ayyad O, Ruiz V, Gomez-Romero P (2015a) Hybrid energy storage: the merging of battery and supercapacitor chemistries. *Chem Soc Rev* 44:1777–1790. <https://doi.org/10.1039/C4CS00266K>
- Dubal DP, Suarez-Guevara J, Tonti D, Enciso E, Gomez-Romero P (2015b) A high voltage solid state symmetric supercapacitor based on graphene–polyoxometalate hybrid electrodes with a hydroquinone doped hybrid gel-electrolyte. *J Mater Chem A* 3:23483–23492. <https://doi.org/10.1039/c5ta05660h>
- Endo M, Takeda T, Kim Y, Koshiba K, Ishii K (2001) High power electric double layer capacitor (EDLC's); from operating principle to pore size control in advanced activated carbons. *Carbon* 1:117–128
- Fan Q, Yang M, Meng Q, Cao B, Yu Y (2016) Activated-nitrogen-doped graphene-based aerogel composites as cathode materials for high energy density lithium-ion supercapacitor. *J Electrochem Soc* 163:A1736–A1742. <https://doi.org/10.1149/2.1271608jes>
- Fan L, Lin K, Wang J, Ma R, Lu B (2018) A nonaqueous potassium-based battery–Supercapacitor hybrid device. *Adv Mater* 30:1800804. <https://doi.org/10.1002/adma.201800804>
- Faraji S, Ani FN (2015) The development supercapacitor from activated carbon by electroless plating—a review. *Renew Sust Energ Rev* 42:823–834. <https://doi.org/10.1016/j.rser.2014.10.068>

- Fernández J, Morishita T, Toyoda M, Inagaki M, Stoeckli F, Centeno TA (2008) Performance of mesoporous carbons derived from poly (vinyl alcohol) in electrochemical capacitors. *J Power Sources* 175:675–679. <https://doi.org/10.1016/j.jpowsour.2007.09.042>
- González A, Goikolea E, Barrena JA, Mysyk R (2016) Review on supercapacitors: technologies and materials. *Renew Sust Energ Rev* 58:1189–1206. <https://doi.org/10.1016/j.rser.2015.12.249>
- Hu X, Deng Z, Suo J, Pan Z (2009) A high rate, high capacity and long life (LiMn<sub>2</sub>O<sub>4</sub>+ AC)/Li<sub>4</sub>Ti<sub>5</sub>O<sub>12</sub> hybrid battery–supercapacitor. *J Power Sources* 187:635–639. <https://doi.org/10.1016/j.jpowsour.2008.11.033>
- Ji J et al (2013) Nanoporous Ni(OH)<sub>2</sub> thin film on 3D ultrathin-graphite foam for asymmetric supercapacitor. *ACS Nano* 7:6237–6243. <https://doi.org/10.1021/nm4021955>
- Jorio A et al (2001) Structural (n, m) determination of isolated single-wall carbon nanotubes by resonant Raman scattering. *Phys Rev Lett* 86:1118. <https://doi.org/10.1103/PhysRevLett.86.1118>
- Karthikeyan K, Amaresh S, Kim K, Kim S, Chung K, Cho B, Lee Y (2013) A high performance hybrid capacitor with Li<sub>2</sub>CoPO<sub>4</sub>F cathode and activated carbon anode. *Nanoscale* 5:5958–5964. <https://doi.org/10.1039/C3NR00760J>
- Khomenko V, Raymundo-Piñero E, Béguin F (2008) High-energy density graphite/AC capacitor in organic electrolyte. *J Power Sources* 177:643–651. <https://doi.org/10.1016/j.jpowsour.2007.11.101>
- Kim D et al (2011) Enabling sodium batteries using lithium-substituted sodium layered transition metal oxide cathodes. *Adv Energ Mater* 1:333–336. <https://doi.org/10.1002/aenm.201000061>
- Kim H et al (2013) A novel high-energy hybrid supercapacitor with an anatase TiO<sub>2</sub>-reduced graphene oxide anode and an activated carbon cathode. *Adv Energ Mater* 3:1500–1506. <https://doi.org/10.1002/aenm.201300467>
- Kim H-K et al (2016) TiO<sub>2</sub>-reduced graphene oxide nanocomposites by microwave-assisted forced hydrolysis as excellent insertion anode for Li-ion battery and capacitor. *J Power Sources* 327:171–177. <https://doi.org/10.1016/j.jpowsour.2016.07.053>
- Kolathodi MS, Palei M, Natarajan TS (2015) Electrospun NiO nanofibers as cathode materials for high performance asymmetric supercapacitors. *J Mater Chem A* 3:7513–7522. <https://doi.org/10.1039/C4TA07075E>
- Komaba S, Hasegawa T, Dahbi M, Kubota K (2015) Potassium intercalation into graphite to realize high-voltage/high-power potassium-ion batteries and potassium-ion capacitors. *Electrochem Commun* 60:172–175. <https://doi.org/10.1016/j.elecom.2015.09.002>
- Kouchachvili L, Yaïci W, Entchev E (2018) Hybrid battery/supercapacitor energy storage system for the electric vehicles. *J Power Sources* 374:237–248. <https://doi.org/10.1016/j.jpowsour.2017.11.040>
- Kuratani K, Yao M, Senoh H, Takeichi N, Sakai T, Kiyobayashi T (2012) Na-ion capacitor using sodium pre-doped hard carbon and activated carbon. *Electrochim Acta* 76:320–325. <https://doi.org/10.1016/j.electacta.2012.05.040>
- Laforge A et al (2003) Activated carbon/conducting polymer hybrid supercapacitors. *J Electrochem Soc* 150:A645–A651. <https://doi.org/10.1149/1.1566411>
- Lam L, Haigh N, Phyland C, Urban A (2004) Failure mode of valve-regulated lead-acid batteries under high-rate partial-state-of-charge operation. *J Power Sources* 133:126–134. <https://doi.org/10.1016/j.jpowsour.2003.11.048>
- Lang J-W, Kong L-B, Liu M, Luo Y-C, Kang L (2010) Asymmetric supercapacitors based on stabilized α-Ni(OH)<sub>2</sub> and activated carbon. *J Solid State Electr* 14:1533–1539. <https://doi.org/10.1007/s10008-009-0984-1>
- Lee SW, Gallant BM, Byon HR, Hammond PT, Shao-Horn Y (2011) Nanostructured carbon-based electrodes: bridging the gap between thin-film lithium-ion batteries and electrochemical capacitors. *Energy Environ Sci* 4:1972–1985. <https://doi.org/10.1039/C0EE00642D>

- Lee JE, Park SJ, Kwon OS, Shim HW, Jang J, Yoon H (2014) Systematic investigation on charge storage behaviour of multidimensional poly(3, 4-ethylenedioxythiophene) nanostructures. *RSC Adv* 4:37529–37535. <https://doi.org/10.1039/C4RA06161F>
- Li Z, Xiang K, Xing W, Carter WC, Chiang Y-M (2015) Reversible aluminum-ion intercalation in prussian blue analogs and demonstration of a high-power aluminum-ion asymmetric capacitor. *Adv Energy Mater* 5:1401410. <https://doi.org/10.1002/aenm.201401410>
- Li H, Zhu Y, Dong S, Shen L, Chen Z, Zhang X, Yu G (2016) Self-assembled Nb<sub>2</sub>O<sub>5</sub> nanosheets for high energy–high power sodium ion capacitors. *Chem Mater* 28:5753–5760. <https://doi.org/10.1021/acs.chemmater.6b01988>
- Li K, Shao Y, Liu S, Zhang Q, Wang H, Li Y, Kaner RB (2017) Aluminum-ion-intercalation supercapacitors with ultrahigh areal capacitance and highly enhanced cycling stability: power supply for flexible Electrochromic devices. *Small* 13:1700380. <https://doi.org/10.1002/sml.201700380>
- Lim E et al (2015) Facile synthesis of Nb<sub>2</sub>O<sub>5</sub>@ carbon core–shell nanocrystals with controlled crystalline structure for high-power anodes in hybrid supercapacitors. *ACS Nano* 9:7497–7505. <https://doi.org/10.1021/acs.nano.5b02601>
- Lim E et al (2016) High-performance sodium-ion hybrid supercapacitor based on Nb<sub>2</sub>O<sub>5</sub>@ carbon core–shell nanoparticles and reduced graphene oxide nanocomposites. *Adv Funct Mater* 26:3711–3719. <https://doi.org/10.1002/adfm.201505548>
- Liu X, Jung H-G, Kim S-O, Choi H-S, Lee S, Moon JH, Lee JK (2013a) Silicon/copper dome-patterned electrodes for high-performance hybrid supercapacitors. *Sci Rep* 3:3183. <https://doi.org/10.1038/srep03183>
- Liu X, Zhang N, Ni J, Gao L (2013b) Improved electrochemical performance of sol–gel method prepared Na<sub>4</sub>Mn<sub>9</sub>O<sub>18</sub> in aqueous hybrid Na-ion supercapacitor. *J Sol State Electrochem* 17:1939–1944. <https://doi.org/10.1007/s10008-013-2044-0>
- Liu J, Zhang L, Wu HB, Lin J, Shen Z, Lou XWD (2014) High-performance flexible asymmetric supercapacitors based on a new graphene foam/carbon nanotube hybrid film. *Energy Environ Sci* 7:3709–3719. <https://doi.org/10.1039/C4EE01475H>
- Liu C, Zhang C, Song H, Zhang C, Liu Y, Nan X, Cao G (2016) Mesocrystal MnO cubes as anode for Li-ion capacitors. *Nano Energy* 22:290–300. <https://doi.org/10.1016/j.nanoen.2016.02.035>
- Liu C, Zhang C, Fu H, Nan X, Cao G (2017) Exploiting high-performance anode through tuning the character of chemical bonds for Li-ion batteries and capacitors. *Adv Energy Mater* 7:1601127. <https://doi.org/10.1002/aenm.201601127>
- Lu Z, Chang Z, Zhu W, Sun X (2011) Beta-phased Ni(OH)<sub>2</sub> nanowall film with reversible capacitance higher than theoretical faradic capacitance. *Chem Commun* 47:9651–9653. <https://doi.org/10.1039/C1CC13796D>
- Lukatskaya MR et al (2013) Cation intercalation and high volumetric capacitance of two-dimensional titanium carbide. *Science* 341:1502–1505. <https://doi.org/10.1126/science.1241488>
- Luo J-Y, Xia Y-Y (2009) Electrochemical profile of an asymmetric supercapacitor using carbon-coated LiTi<sub>2</sub>(PO<sub>4</sub>)<sub>3</sub> and active carbon electrodes. *J Power Sources* 186:224–227. <https://doi.org/10.1016/j.jpowsour.2008.09.063>
- Ma X, Chen H, Ceder G (2011) Electrochemical properties of monoclinic NaMnO<sub>2</sub>. *J Electrochem Soc* 158:A1307–A1312. <https://doi.org/10.1149/2.035112jes>
- Ma H, He J, Xiong D-B, Wu J, Li Q, Dravid V, Zhao Y (2016) Nickel cobalt hydroxide@reduced graphene oxide hybrid nanolayers for high performance asymmetric supercapacitors with remarkable cycling stability. *ACS Appl Mater Interfaces* 8:1992–2000. <https://doi.org/10.1021/acsami.5b10280>
- Mhamane D et al (2016) Silica-assisted bottom-up synthesis of graphene-like high surface area carbon for highly efficient ultracapacitor and Li-ion hybrid capacitor applications. *J Mater Chem A* 4:5578–5591. <https://doi.org/10.1039/C6TA00868B>
- Moseley P, Nelson R, Hollenkamp A (2006) The role of carbon in valve-regulated lead–acid battery technology. *J Power Sources* 157:3–10. <https://doi.org/10.1016/j.jpowsour.2006.02.031>

- Muzaffar A, Ahamed MB, Deshmukh K, Thirumalai J (2019) A review on recent advances in hybrid supercapacitors: design, fabrication and applications. *Renew Sust Energ Rev* 101:123–145. <https://doi.org/10.1016/j.rser.2018.10.026>
- Ni J, Wang H, Qu Y, Gao L (2013) PbO<sub>2</sub> electrodeposited on graphite for hybrid supercapacitor applications. *Phys Scr* 87:045802. <https://doi.org/10.1088/0031-8949/87/04/045802>
- Pandolfo A, Hollenkamp A (2006) Carbon properties and their role in supercapacitors. *J Power Sources* 157:11–27. <https://doi.org/10.1016/j.jpowsour.2006.02.065>
- Patil SS et al (2016) Fern-like rGO/BiVO<sub>4</sub> hybrid nanostructures for high-energy symmetric supercapacitor. *ACS Appl Mater Interfaces* 8:31602–31610. <https://doi.org/10.1021/acsami.6b08165>
- Peng S, Li L, Wu HB, Madhavi S, Lou XW (2015) Controlled growth of NiMoO<sub>4</sub> nanosheet and nanorod arrays on various conductive substrates as advanced electrodes for asymmetric supercapacitors. *Adv Energ Mater* 5:1401172. <https://doi.org/10.1002/aenm.201401172>
- Peng H, Zhou J, Sun K, Ma G, Zhang Z, Feng E, Lei Z (2017) High-performance asymmetric supercapacitor designed with a novel NiSe@ MoSe<sub>2</sub> nanosheet array and nitrogen-doped carbon nanosheet. *ACS Sust Chem Engg* 5:5951–5963. <https://doi.org/10.1021/acssuschemeng.7b00729>
- Perret P, Khani Z, Brousse T, Bélanger D, Guay D (2011) Carbon/PbO<sub>2</sub> asymmetric electrochemical capacitor based on methanesulfonic acid electrolyte. *Electrochim Acta* 56:8122–8128. <https://doi.org/10.1016/j.electacta.2011.05.125>
- Plitz I, DuPasquier A, Badway F, Gural J, Pereira N, Gmitter A, Amatucci G (2006) The design of alternative nonaqueous high power chemistries. *Appl Phys A Mater Sci Process* 82:615–626. <https://doi.org/10.1007/s00339-005-3420-0>
- Purushothaman KK, Saravanakumar B, Babu IM, Sethuraman B, Muralidharan G (2014) Nanostructured CuO/reduced graphene oxide composite for hybrid supercapacitors. *RSC Adv* 4:23485–23491. <https://doi.org/10.1039/C4RA02107J>
- Qu D, Shi H (1998) Studies of activated carbons used in double-layer capacitors. *J Power Sources* 74:99–107. [https://doi.org/10.1016/S0378-7753\(98\)00038-X](https://doi.org/10.1016/S0378-7753(98)00038-X)
- Qu Q, Shi Y, Tian S, Chen Y, Wu Y, Holze R (2009) A new cheap asymmetric aqueous supercapacitor: activated carbon//NaMnO<sub>2</sub>. *J Power Sources* 194:1222–1225. <https://doi.org/10.1016/j.jpowsour.2009.06.068>
- Qu Q, Li L, Tian S, Guo W, Wu Y, Holze R (2010) A cheap asymmetric supercapacitor with high energy at high power: activated carbon//K<sub>0.27</sub>MnO<sub>2</sub>·0.6H<sub>2</sub>O. *J Power Sources* 195:2789–2794. <https://doi.org/10.1016/j.jpowsour.2009.10.108>
- Que L, Wang Z, Yu F, Gu D (2016) 3D ultralong nanowire arrays with a tailored hydrogen titanate phase as binder-free anodes for Li-ion capacitors. *J Mater Chem A* 4:8716–8723. <https://doi.org/10.1039/C6TA02413K>
- Ren X, Guo C, Xu L, Li T, Hou L, Wei Y (2015) Facile synthesis of hierarchical mesoporous honeycomb-like NiO for aqueous asymmetric supercapacitors. *ACS Appl Mater Interfaces* 7:19930–19940. <https://doi.org/10.1021/acsami.5b04094>
- Satish R, Aravindan V, Ling WC, Madhavi S (2015) Carbon-coated Li<sub>3</sub>V<sub>2</sub>(PO<sub>4</sub>)<sub>3</sub> as insertion type electrode for lithium-ion hybrid electrochemical capacitors: an evaluation of anode and cathodic performance. *J Power Sources* 281:310–317. <https://doi.org/10.1016/j.jpowsour.2015.01.190>
- Sharma P, Bhatti T (2010) A review on electrochemical double-layer capacitors. *Energ Convers Manage* 51:2901–2912. <https://doi.org/10.1016/j.enconman.2010.06.031>
- Su L, Zhang X, Yuan C, Gao B (2008) Symmetric self-hybrid supercapacitor consisting of multiwall carbon nanotubes and Co–Al layered double hydroxides. *J Electrochem Soc* 155: A110–A114. <https://doi.org/10.1149/1.2806844>
- Tamboli MS et al (2017) Mimics of microstructures of Ni substituted Mn<sub>1-x</sub>Ni<sub>x</sub>Co<sub>2</sub>O<sub>4</sub> for high energy density asymmetric capacitors. *Chem Engg J* 307:300–310. <https://doi.org/10.1016/j.cej.2016.08.086>

- Tang Z, Tang C-h, Gong H (2012) A high energy density asymmetric supercapacitor from nano-architected Ni(OH)<sub>2</sub>/Carbon nanotube electrodes. *Adv Funct Mater* 22:1272–1278. <https://doi.org/10.1002/adfm.201102796>
- Wang Y-G, Luo J-Y, Wang C-X, Xia Y-Y (2006) Hybrid Aqueous Energy Storage Cells Using Activated Carbon and Lithium-Ion Intercalated Compounds II. Comparison of LiMn<sub>2</sub>O<sub>4</sub>, LiCo<sub>1/3</sub>Ni<sub>1/3</sub>Mn<sub>1/3</sub>O<sub>2</sub>, and LiCoO<sub>2</sub> Positive Electrodes. *J Electrochem Soc* 153:A1425–A1431
- Wang H et al (2012) Graphene-nickel cobaltite nanocomposite asymmetrical supercapacitor with commercial level mass loading. *Nano Res* 5:605–617. <https://doi.org/10.1007/s12274-012-0246-x>
- Wang H et al (2014a) Hybrid device employing three-dimensional arrays of MnO in carbon nanosheets bridges battery–supercapacitor divide. *Nano Lett* 14:1987–1994. <https://doi.org/10.1021/nl500011d>
- Wang R, Yan X, Lang J, Zheng Z, Zhang P (2014b) A hybrid supercapacitor based on flower-like Co(OH)<sub>2</sub> and urchin-like VN electrode materials. *J Mater Chem A* 2:12724–12732. <https://doi.org/10.1039/C4TA01296H>
- Wang Y-X, Chou S-L, Wexler D, Liu H-K, Dou S-X (2014c) High-performance sodium-ion batteries and sodium-ion Pseudocapacitors based on MoS<sub>2</sub>/graphene composites. *Chem Eur J* 20:9607–9612. <https://doi.org/10.1002/chem.201402563>
- Wang F et al (2015a) A quasi-solid-state sodium-ion capacitor with high energy density. *Adv Mater* 27:6962–6968. <https://doi.org/10.1002/adma.201503097>
- Wang F et al (2015b) Tungsten oxide@polypyrrole core–shell nanowire arrays as novel negative electrodes for asymmetric supercapacitors. *Small* 11:749–755. <https://doi.org/10.1002/smll.201402340>
- Wang X et al (2015c) Pseudocapacitance of MXene nanosheets for high-power sodium-ion hybrid capacitors. *Nat Commun* 6:6544. <https://doi.org/10.1038/ncomms7544>
- Wang Y et al (2015d) Ti-substituted tunnel-type Na<sub>0.44</sub>MnO<sub>2</sub> oxide as a negative electrode for aqueous sodium-ion batteries. *Nat Commun* 6:6401. <https://doi.org/10.1038/ncomms7401>
- Wang F et al (2016a) A conductive polymer coated MoO<sub>3</sub> anode enables an Al-ion capacitor with high performance. *J Mater Chem A* 4:5115–5123. <https://doi.org/10.1039/C6TA01398H>
- Wang H, Mitlin D, Ding J, Li Z, Cui K (2016b) Excellent energy–power characteristics from a hybrid sodium ion capacitor based on identical carbon nanosheets in both electrodes. *J Mater Chem A* 4:5149–5158. <https://doi.org/10.1039/C6TA01392A>
- Wang H, Mitlin D, Ding J, Li Z, Cui K (2016c) Excellent energy–power characteristics from a hybrid sodium ion capacitor based on identical carbon nanosheets in both electrodes. *J Mater Chem A* 4:5149–5158. <https://doi.org/10.1039/C6TA01392A>
- Wang P, Wang R, Lang J, Zhang X, Chen Z, Yan X (2016d) Porous niobium nitride as a capacitive anode material for advanced Li-ion hybrid capacitors with superior cycling stability. *J Mater Chem A* 4:9760–9766. <https://doi.org/10.1039/C6TA02971J>
- Wang Q, Nie YF, Chen XY, Xiao ZH, Zhang ZJ (2016e) Controllable synthesis of 2D amorphous carbon and partially graphitic carbon materials: large improvement of electrochemical performance by the redox additive of sulfanilic acid azochromotrop in KOH electrolyte. *Electrochim Acta* 200:247–258. <https://doi.org/10.1016/j.electacta.2016.03.183>
- Wang F et al (2017a) A quasi-solid-state Li-ion capacitor with high energy density based on Li<sub>3</sub>VO<sub>4</sub>/carbon nanofibers and electrochemically-exfoliated graphene sheets. *J Mater Chem A* 5:14922–14929. <https://doi.org/10.1039/C7TA03920D>
- Wang F et al (2017b) Latest advances in supercapacitors: from new electrode materials to novel device designs. *Chem Soc Rev* 46:6816–6854. <https://doi.org/10.1039/C7CS00205J>
- Wang R, Wang S, Peng X, Zhang Y, Jin D, Chu PK, Zhang L (2017c) Elucidating the intercalation pseudocapacitance mechanism of MoS<sub>2</sub>–carbon monolayer interoverlapped superstructure: toward high-performance sodium-ion-based hybrid supercapacitor. *ACS Appl Mater Interfaces* 9:32745–32755. <https://doi.org/10.1021/acsami.7b09813>
- Winter M, Brodd RJ (2004) What are batteries, fuel cells, and supercapacitors? *Chem Rev* 104:4245–4269. <https://doi.org/10.1021/cr020730k>

- Yabuuchi N et al (2012) P2-type  $\text{Na}_x[\text{Fe}_{1/2}\text{Mn}_{1/2}]\text{O}_2$  made from earth-abundant elements for rechargeable Na batteries. *Nat Mater* 11:512. <https://doi.org/10.1038/nmat3309>
- Yabuuchi N, Kubota K, Dahbi M, Komaba S (2014) Research development on sodium-ion batteries. *Chem Rev* 114:11636–11682. <https://doi.org/10.1021/cr500192f>
- Yan J et al (2012) Advanced asymmetric supercapacitors based on  $\text{Ni}(\text{OH})_2$ /graphene and porous graphene electrodes with high energy density. *Adv Funct Mater* 22:2632–2641. <https://doi.org/10.1002/adfm.201102839>
- Yang P et al (2014) Low-cost high-performance solid-state asymmetric supercapacitors based on  $\text{MnO}_2$  nanowires and  $\text{Fe}_2\text{O}_3$  nanotubes. *Nano Lett* 14:731–736. <https://doi.org/10.1021/nl404008e>
- Yin J, Qi L, Wang H (2012) Sodium titanate nanotubes as negative electrode materials for sodium-ion capacitors. *ACS Appl Mater Interface* 4:2762–2768. <https://doi.org/10.1021/am300385r>
- Yu N, Gao L, Zhao S, Wang Z (2009) Electrodeposited  $\text{PbO}_2$  thin film as positive electrode in  $\text{PbO}_2/\text{AC}$  hybrid capacitor. *Electrochim Acta* 54:3835–3841. <https://doi.org/10.1016/j.electacta.2009.01.086>
- Yuvaraj S, Karthikeyan K, Kalpana D, Lee YS, Selvan RK (2016) Surfactant-free hydrothermal synthesis of hierarchically structured spherical  $\text{CuBi}_2\text{O}_4$  as negative electrodes for Li-ion hybrid capacitors. *J Colloid Interface Sci* 469:47–56. <https://doi.org/10.1016/j.jcis.2016.01.060>
- Zhang LL, Zhao X (2009) Carbon-based materials as supercapacitor electrodes. *Chem Soc Rev* 38:2520–2531. <https://doi.org/10.1039/B813846J>
- Zhang F, Zhang T, Yang X, Zhang L, Leng K, Huang Y, Chen Y (2013) A high-performance supercapacitor-battery hybrid energy storage device based on graphene-enhanced electrode materials with ultrahigh energy density. *Energy Environ Sci* 6:1623–1632. <https://doi.org/10.1039/C3EE40509E>
- Zhang J, Shi Z, Wang C (2014a) Effect of pre-lithiation degrees of mesocarbon microbeads anode on the electrochemical performance of lithium-ion capacitors. *Electrochim Acta* 125:22–28. <https://doi.org/10.1016/j.electacta.2014.01.040>
- Zhang W, Lin H, Kong H, Lu H, Yang Z, Liu T (2014b) High energy density  $\text{PbO}_2$ /activated carbon asymmetric electrochemical capacitor based on lead dioxide electrode with three-dimensional porous titanium substrate. *Int J Hydrogen Energ* 39:17153–17161. <https://doi.org/10.1016/j.ijhydene.2014.08.039>
- Zhao X, Johnston C, Grant PS (2009) A novel hybrid supercapacitor with a carbon nanotube cathode and an iron oxide/carbon nanotube composite anode. *J Mater Chem* 19:8755–8760. <https://doi.org/10.1039/B909779A>
- Zhao M-Q et al (2015a) Flexible MXene/carbon nanotube composite paper with high volumetric capacitance. *Adv Mater* 27:339–345. <https://doi.org/10.1002/adma.201404140>
- Zhao MQ et al (2015b) Flexible MXene/carbon nanotube composite paper with high volumetric capacitance. *Adv Mater* 27:339–345. <https://doi.org/10.1002/adma.201404140>
- Zhou L et al (2017) Cubic Prussian blue crystals from a facile one-step synthesis as positive electrode material for superior potassium-ion capacitors. *Electrochim Acta* 232:106–113. <https://doi.org/10.1016/j.electacta.2017.02.096>
- Zhu J et al (2014) 3D carbon/cobalt-nickel mixed-oxide hybrid nanostructured arrays for asymmetric supercapacitors. *Small* 10:2937–2945. <https://doi.org/10.1002/smll.201302937>
- Zhu Y, Yang Y, Fu L, Wu Y (2017) A porous gel-type composite membrane reinforced by nonwoven: promising polymer electrolyte with high performance for sodium ion batteries. *Electrochim Acta* 224:405–411. <https://doi.org/10.1016/j.electacta.2016.12.030>
- Zuo W, Li R, Zhou C, Li Y, Xia J, Liu J (2017) Battery-supercapacitor hybrid devices: recent progress and future prospects. *Adv Sci* 4:1600539. <https://doi.org/10.1002/advs.201600539>

# Chapter 4

## Metal, Metal Oxides, and Metal Sulfide Roles in Fuel Cell



Hasan Ay and Fatih Sen

### Contents

4.1	Introduction .....	116
4.2	Fuel Cell .....	118
4.2.1	Fuel Cell Origins .....	120
4.2.2	Types of Fuel Cells .....	121
4.3	Metal Catalysts .....	122
4.3.1	Non-precious Metals .....	124
4.3.2	Precious Metal Catalysts .....	125
4.4	Function and Performance of Metal Oxide in the Proton Exchange Membrane Fuel Cells .....	127
4.4.1	Proton Exchange Membrane for the Fuel Cell Applications .....	128
4.4.2	Fuel-Cell Performance of SiO <sub>2</sub> and TiO <sub>2</sub> Composites .....	130
4.4.3	Performance of Nafion Membranes with Zirconia and Alumina Doped .....	133
4.5	Reduction of Sulfide Electrocatalysis, Metal Sulfides (NiS <sub>2</sub> , FeS <sub>2</sub> , CoS <sub>2</sub> ) .....	136
4.6	Conclusion .....	139
	References .....	140

**Abstract** Today, energy generation is the most challenging issue for scientists and engineers, since their goal to produce energy via economic, efficient, clean, and environmentally friendly processes. Fuel cells have turned chemical energy which is obtained from fuel gas directly into electrical energy that is both efficient and environmentally clean because of being a lack of combustion in years. The proton exchange membrane (PEM) fuel cell technology has developed rapidly in recent years. This advancement leads to conduct new researches in this area that is related to fuel converter catalysts for the production of H<sub>2</sub>. The primary objective is to obtain fuel cells that are catalytically more active, which increases fuel processing speed and reduces to ergonomic dimensions. In fuel cells, the H<sub>2</sub> production flow

---

H. Ay · F. Sen (✉)

Sen Research Group, Biochemistry Department, Faculty of Arts and Science, Dumlupınar University, Kütahya, Turkey  
e-mail: [fatih.sen@dpu.edu.tr](mailto:fatih.sen@dpu.edu.tr)

© The Editor(s) (if applicable) and The Author(s), under exclusive licence to Springer Nature Switzerland AG 2021

115

S. Rajendran et al. (eds.), *Metal, Metal-Oxides and Metal Sulfides for Batteries, Fuel Cells, Solar Cells, Photocatalysis and Health Sensors*, Environmental Chemistry for a Sustainable World 62, [https://doi.org/10.1007/978-3-030-63791-0\\_4](https://doi.org/10.1007/978-3-030-63791-0_4)



can be achieved by allowing very small amounts of CO to be released by the efficient operation of the catalysts of each part. In this paper, the use of precious and non-precious metals as catalysts for proton exchange membrane fuel cell (PEMFC), alternatively metal sulfides and metal oxides for composite proton membranes is reviewed.

**Keywords** Fuel cell · Proton exchange membrane · Alkaline fuel cells · Metal · Metal oxide · Nanomaterials

### Abbreviations

AFC	alkaline fuel cells
DMFC	direct methanol fuel cells
HER	hydrogen reaction
ICE	internal combustion engine
LHV	smaller value of heating
LPG	liquid propane gas
MCFC	molten carbonate fuel cells
MEA	membrane electrode assembly
MOFs	metal-organic frameworks
NG	natural gas
PAFC	phosphoric acid fuel cells
PEM	proton exchange membrane
PEMFC	proton exchange membrane fuel cell
PFSA	perfluorosulfonic acid
PTFE	polytetrafluorethylene
QDSSCs	quantum dot-sensitized
SO	solid oxide
SOFC	solid oxide fuel cells
SPFC	solid polymer fuel cells
TWC	three-way catalysts
WGS	water gas exchange

## 4.1 Introduction

One of the many alternatives for clean energy is fuel cells (Acres et al. 1997; Andreeva et al. 1998, 1999; Basińska et al. 1999; Antonucci et al. 1999; Adjemian et al. 2002a, b; Ahmad et al. 2006; Ay et al. 2019). The largest commercial sectors of fuel cells are private transport, public transport, and public housing. Their applications allow use in many different areas, from portable micropower to stationary buildings and distributed production areas (Gray and Frost 1998; Docter and Lamm 1999; Carpenter et al. 1999). Recently, automotive companies and fuel cell

companies have announced some prototype vehicles and new technologies using fuel cells to reduce air pollution. There are no alternatives to fuel cells for other practices at a necessary level (Acres et al. 1997; Society of Chemical Industry (Great Britain) 1998; Services 2000). Proton exchange membrane (PEM), known as solid polymer fuel cells (SPFC) working at 80 °C, alkaline fuel cells (AFC) working at 100 °C, phosphoric acid fuel cells (PAFC) working at 200 °C, molten carbonate fuel cells (MCFC) at 650 °C, solid oxide fuel cells (SOFC) works at higher temperature 800–1100 °C. SPFC fuel cells have many positive characteristics that give them permission for candidates for the practices of mobile power or small portable power units; long piling life, convenient for discontinuous practices at lower practicing temperatures and sustaining practices at higher current density, start-ups, compactness, and low weight.

For PEM, the optimum fuel is the pure H<sub>2</sub> with a smaller value than 50 ppm carbon monoxide except for direct methanol fuel cells (DMFC), since it is the poisoning limit of Pt fuel cell catalyst. Weight, size, technical, and cost limitations lead to the problematic storage process of H<sub>2</sub> in a required amount and density, so the H<sub>2</sub> gas is produced on-site and requisition, by changing reachable fuels such as gasoline, natural gas (NG), propane (LPG), and methanol. The efficiencies only life usage of existing changer or fuel cell systems depend on the Low Heating Value (LHV) of the fuel that is between 35% and 50%. It can be inferred from that it is a smaller priority on the theoretical efficiency of the internal combustion engine (ICE), the net priority on internal combustion engine is to release the smaller amount of pollutants to the environment. If it is operated with pure H<sub>2</sub>, the regional emissions will be zero. In the case of the generation of H<sub>2</sub> from hydrocarbon fuels, the emission may be restricted with CO<sub>2</sub> and maybe the minimum amount of hydrocarbons obtained at the beginning. Because of the lower temperatures in the process of fuel on active catalysts, it is necessary to avoid some pollutants such as NO<sub>x</sub> and particulates. There are some other advantageous sides over internal combustion engine such as quiet energy production without moving parts and load-independent efficiency.

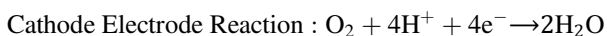
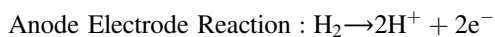
One of the most important factors in determining the method of obtaining hydrogen in fuel cells is the design of catalysts. By thermal process; the endothermic reaction to obtain hydrogen in the fuel cell leads to very high temperatures (Clarke et al. 1997). In contrast, proton exchange membranes (PEMs), designed to operate at lower temperatures, operate using air, steam and/or both, and use hydrogen generated by the catalysis of fuels. It contains H<sub>2</sub>, CO<sub>2</sub>, and 3–10% CO in the output depending on the fuel, working conditions, and catalyst. In series, these catalytic processes produce a high output of hydrogen-containing 35–75% H<sub>2</sub>, 13–26% CO<sub>2</sub>, up to 1% CO, 0–25% N<sub>2</sub>, and 15–30% H<sub>2</sub>O. The system has a cleaning system so that the amount of CO formed is less than 50 ppm.

Catalysis in the fuel cell: It has some difficulties such as large footprint catalytic volumes, long starting times, stable and inactive structures, and the need to develop poison resistant structures.

In the following sections, the roles of fuel cells of different groups of catalysts in different sections will be examined.

## 4.2 Fuel Cell

Fuel cells, which have begun to create a huge change in the field of electrical energy; we can define the fuel input as an electrochemical unit cell that converts from chemical energy to electrical energy without any combustion process. Consequently, an electrochemical reaction occurs with the oxidant in the fuel cell to convert the fuel into electricity, water, and heat. Commonly used fuel types are ethanol, methanol, and  $H_2$  and the like. In general, we can describe the reactions taking place in the fuel cell as follows: Hydrogen gas supplied to the anode part of the fuel cell is converted to an ion and electrons are flowing from the anode to the cathode (Peighambardoust et al. 2010a).



The essential elements and the most important parts of the fuel cell consist of two parts, the electrocatalyst and the membrane electrode assembly (MEA). The task of the membrane in the fuel cells is to ensure that the occurred protons pass from the anode to the cathode between the electrodes (Ahmad et al. 2006). With the transmission of these ions through the membrane, the free electrons remaining in the anode create a voltage while the cathode flows through the anode, producing heat, electricity, and water. Figure 4.1 shows a fuel cell operating by the PEM method. The advantages of fuel cells compared to the systems used to obtain energy can be listed as follows: it does not contain moving parts, and therefore quiet operation, high efficiency, and the absence of polluting gas emissions such as  $NO_x$ ,  $SO_x$ ,  $CO$ , and  $CO_2$ . Despite these advantages, their only disadvantage is the high costs of solving them with new technological developments and the ability to produce these cells in series.

Fuel cells can be classified depending on their operating structure and based on different criteria such as operating conditions. Fuel cells operate pressure and temperature, the target ion of the electrolyte, and the type of electrode and the type of fuels (oxidants or primary fuels). However, fuel cells are generally classified according to the electrolyte types used within the cell, the classification of which will be further examined.

Membranes are already used in many different industrial processes according to the ion exchange principle. In these areas, as a separator for electrolysis, in the treatment of brine, separation of ionic materials with non-ionic materials, and such other examples can be given (Kariduraganavar et al. 2006). On the other hand, a solid and polymer-based proton exchange membrane capable of selectively proton transfer is used in fuel cells. These ionic electrolytes, which contain gel-like and swollen polymer matrices, carry constant negative and positive charges. Proton transfer capabilities are absent in the dry state, and if they are moist and in direct

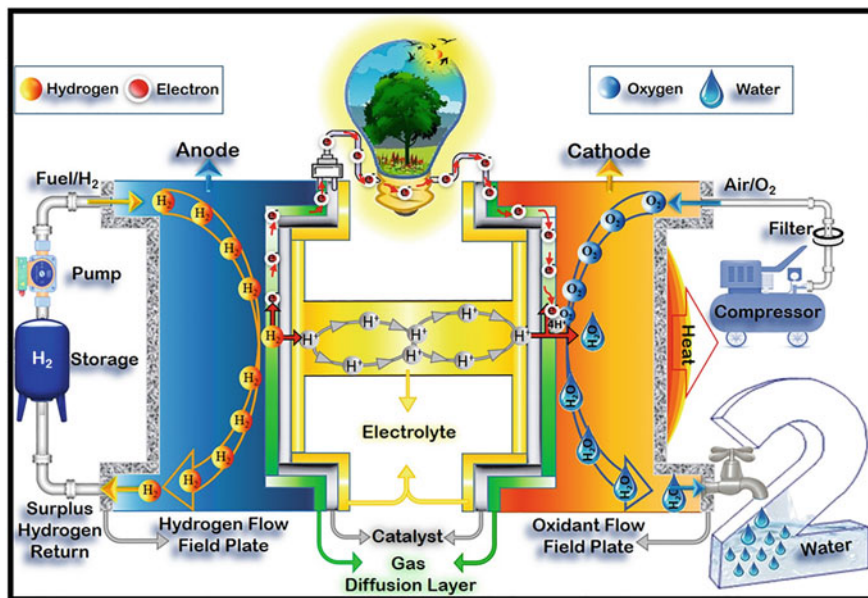


**Fig. 4.1** Working principle of proton exchange membrane fuel cell. The schematic part of the hydrogen or hydrogen source fuels separated into protons and electrons by the catalyst effect is shown in the anode section of the fuel cell. Thanks to the membrane that selectively permits only proton passage, electrons flow from anode to cathode, thereby generating electrical energy. In the cathode section, there is a reaction that results with a hydrogen proton and electrons and an externally fed oxygen source and a water product

proportion to the increase in moisture content, the ion permeability increases. The so-called Nafion, which developed chemically based on sulfonated polytetrafluoroethylene by DuPont in the 1980s, was the first stable material and was thus widely used in energy conversion and storage with Chlor-alkali production applications (Grot 1973). For polymer-based proton exchange membranes, DuPont's (Nafion) fluorinated sulfonic acid membrane is standardized and is an ideal material for fuel cells. The historical development of these types of ion exchange membranes and its variants are shown in Table 4.1.

Generally, selectively ion-permeable membranes are classified into two groups as cation and anion exchange membranes according to the type of ionic groups present in the matrix structure. In the structures of selective anion permeable membranes ( $-\text{SO}_3^-$ ,  $-\text{PO}_3^{2-}$ ,  $-\text{COO}^-$ ,  $-\text{C}_6\text{H}_4\text{O}^-$ ,  $-\text{PO}_3\text{H}^-$ , etc.), there are components which do not let the transition of cations, such as selective cation-transmitting membranes in their structures ( $-\text{NH}_3^+$ ,  $-\text{PR}_3^+$ ,  $-\text{NR}_3^+$ ,  $-\text{SR}_2^+$ ,  $-\text{NRH}_2^+$ , etc.). There are also some components which do not allow the passage of anions and only cations containing positive and negative groups (Finch 1993; Strathmann 1995). Membranes selectively ion-permeable according to their structure may also be classified as heterogeneous and homogeneous membranes, depending on the chemical bonding or the

**Table 4.1** The historical development of these types of ion exchange membranes and its variants (Peighambaroust et al. 2010b)

Years	Historical development stages
1890	First electro-membrane process
1910	Donnan exclusion potential
1925	First synthesis of ion exchange membrane
1932	First mosaic membrane, amphoteric membrane
1940	First industrial application of electro-membrane
1950	First commercial ion exchange membranes and electrodeposition
1962	First sea salt production (Asahi)
1970	First electrodialysis reversal, first continuous electrodeionization
1978	Nafion: Chlor-alkali electrolysis; first bipolar membrane
1988–2003	Novel ion exchange membrane process; Coupling/hybrid electrodeposition process; Comprehensively industrial applications; Hybrid ion exchange membranes, etc.

physical loading of the charged groups in the matrix and depending on their binding patterns. The advantage of membranes formed by homogeneous groups exhibits excellent electrochemical properties compared to heterogeneous membranes, whereas on the contrary, they exhibit low mechanical strength compared to membranes formed by heterogeneous groups (Feng and Alonso-Vante 2008). The difference between heterogeneous and homogeneous groups of these selective ion filtration membranes is that heterogeneous groups have much better dimensional stability (Xu 2005).

Many developments have become a current issue recently; however, in the commercialization of fuel cells, there are many economic and/or technical drawbacks. In that context, it is necessary to have the care to advance a membrane for PEMFC with developed durability and performance. In this respect, studies are continuing for PEMFCs in terms of efficiency, performance, strength, and cost. Although these studies contain hope, it seems that it will take more time in terms of commercialization and therefore may be the next-generation energy source. Therefore, today's technology depends on the materials that make the commercialization of fuel cell accessible and prevalent.

#### 4.2.1 Fuel Cell Origins

Despite the high technology and promising future, more than a century and a half of the scientifically known fuel cells have gained intense interest and intensive work in the 1940s. Alessandro Volta was the first scientist to observe electricity and form a scientific basis. The phenomenon and understanding of electrochemistry was with the help of the scientist J. W. Ritter, who was also regarded as the founder of electrochemistry. The (C/H<sub>2</sub>O,NH<sub>3</sub>/O<sub>2</sub>/C) compound, Sir Humphrey Davy, who created a low electric current and created a single fuel cell. However, the basic

principle of the fuel cell is based on the work of Christian Friedrich Schönbein, which lasted 39 years, until 1868. Sir William Grove, a British lawyer has renowned his thermal cell battery design, the so-called Grove Cell and whose principle is based on reversible hydrolysis of water (Bezerra et al. 2007). Ceramic fuel cells, which began with the discovery of solid oxides by Nernst (Feng and Alonso-Vante 2008), emerged much later than these developments. Ludwig Mond announced a hydrogen-oxygen-based fuel cell with a yield of  $1/6 \text{ m}^2/\text{A}$  with a 0.73 V voltage related to the surface area of the electrode. Friedrich Wilhelm Ostwald, the founder of the physical-chemistry field, explained most of the working principles of fuel cells. Since the early 1900s, Emil Baur has conducted long investigations for different types of fuel cells and has worked on high-temperature devices using solid electrolytes, metal oxides, and clays. Francis Thomas Bacon, who succeeded in manufacturing the first fuel cell in 1939, worked on devices using alkaline groups as electrolytes. NASA has successfully spent millions of dollars on hydrogen fuel cells to power all the electrical devices that this shuttle will use on its Apollo moon trip. As the 1990s approached, Japan, Canada, and the US government agencies increased their research and development funds and fuel cell funds considerably. Nowadays, while the fuel cells are becoming widespread in space flights, it also means that they can be used in areas ranging from portable and stationary power plants to home electricity.

#### 4.2.2 *Types of Fuel Cells*

Fuel cells are usually assorted by the characteristics of its electrolyte's chemical utilized for the ionic conductor in the cell, as shown in Table 4.2. The first five kinds on the table have classified by its low to the average temperature of operation (50–210 °C), their comparatively low electrical generation efficiencies (40–50% when worked on readily available fuels like methanol and hydrocarbons, 50% when utilizing pure  $\text{H}_2$  fuel). The last three groups in the table have an operating range of 600–1000 °C so that fuels such as methane can be directly recycled in the fuel cell and can operate at high efficiencies (45–60%). This efficiency can be increased to approximately 90% by recovering the heat generated by the process temperature.

Other kinds of fuel cells are also used today, but they are less employed so that they can be used for a special application later. Currently, there are also different types of fuel cells that are used less frequently than these types and have the potential to be used in specific applications in the future. Inorganic redox cells, alkali metal-halogen cells, air-depolarized cells, inorganic redox cells, sodium amalgam cells, regenerative cells, biochemical fuel cells are good examples for this situation. Actual material science makes the fuel cells can be applied for many special areas. Up to now, the most significant investigation conducted on this topic is the proton exchange membrane and solid oxide cell stacks throughout the world. Proton exchange membranes are the well-designed kinds of fuel cells that are convenient for both cars and public transportation.

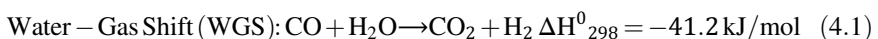
**Table 4.2** Application and operating characteristics of the basic five different types of fuel cells

Types of fuel cell	Electrolyte	Operating temp. (°C)	Fuel	Oxidant	Efficiency (%)
Alkaline (AFC)	Potassium hydroxide (KOH)	500–200	O <sub>2</sub> /Air	Pure hydrogen or hydrazine	50–55
Direct methanol (DMFC)	Polymer	60–200	O <sub>2</sub> /Air	Liquid methanol	40–55
Phosphoric acid (SAFC)	Phosphoric acid	160–210	O <sub>2</sub> /Air	Hydrogen from hydrocarbons and alcohol	40–50
Sulfuric acid (SAFC)	Sulfuric acid	80–90	O <sub>2</sub> /Air	Alcohol or impure hydrogen	40–50
Proton exchange membrane (PEMFC)	Polymer, proton exchange membrane	50–80	O <sub>2</sub> /Air	Less pure hydrogen from hydrocarbons or methanol	40–50
Molten carbonate (MCFC)	Molten salt such as nitrate, sulfate, carbonates. . .	630–650	CO <sub>2</sub> /O <sub>2</sub> /Air	Hydrogen, carbon monoxide, naturel gas, propane, marine diesel	50–60
Solid oxide (SOFC)	Ceramic as stabilized zirconia and doped perovskite	600–1000	O <sub>2</sub> /Air	Naturel gas, propane	45–60
Protonic ceramic (PCFC)	Thin membrane of barium cerium oxide	600–700	O <sub>2</sub> /Air	Hydrocarbons	45–60

Adapted with permission from Adjemian et al. (2006). Copyright (2006) American Chemical Society

### 4.3 Metal Catalysts

During the process of oxidation and methanation in fuel cells, water gas exchange (WGS) is a crucial step, especially in order to reduce the amount of CO formed in the environment and provide extra hydrogen sources, mainly caused by alloy-based catalysts. In the flow direction shown in Eq. 4.1, the water gas exchange units are conveniently placed to increase hydrogen efficiency and reduce the CO concentration. The ideal performance of the water gas exchange system should ensure that at low temperatures, such as 180–280 °C, the CO level does not exceed 5000 ppm and draw as low as possible, depending on the feed density of the fuel (Ridler 1996). Since it contains CO<sub>2</sub>, CO, H<sub>2</sub>, and H<sub>2</sub>O in the flow here, reactions such as equality two at high temperatures according to the ratio of water and carbon monoxide (Xue et al. 1996) can also work (Ridler 1996).



There are many publications about the classical water gas shift catalysts, applied mainly on the reaction or kinetics mechanism (Rhodes et al. 1995; Ridler 1996; Ovesen et al. 1996) and catalyst preparation (Schneider et al. 1986; Hu and Wagner 1999). Some debates are done in the mechanization step and especially for the Cu-ZnO catalyst, on whether the reaction mechanism relatedly happens through intermediate like formates, and the occurrence of relatedly surface species like carbonates or hydroxy carbonates of which participate in the mechanism is just not answered.

A usually desired mechanism for water gas shift is not just found, so it is necessary to select the more various types of catalytic surfaces having various crystal constructions between the ranges of experimental conditions selected for such works. It may be seen as probably of combined mechanism (Rhodes et al. 1995) based on the conditions of reactions or reconstruction of induced surface in many cases (Peppley et al. 1999). Raney Cu-ZnO (Wainwright and Trimm 1995) formulations or as in the methanol changing catalysts, to modify zirconium or titanium (Hu and Wagner 1999; Velu et al. 2001) seem to have more durable and active under stable state circumstances. The developed activity of the formulations of Cu-ZnO has revealed that alkali has promoted (Klier et al. 1991; Campbell 1993), but Cu-ZnO catalysts have a difficulty of being pyrophoric and higher vulnerable to poisons for all cases (Ridler 1996; Twigg and Spencer 2001).

The usage of Cu-ZnO and Fe-Cr formulas in fuel processors has many drawbacks; high temperature shift catalysts' low activity and their thermodynamically restrains at higher temperatures and also the sensation of the Cu-ZnO catalysts to temperature or air excursions. The length preconditions of some catalysts for intermittent processes (pre-reduction/passivation) or the large volume of reactor directed by the slow WGS kinetics of the Cu-ZnO catalyst at lower temperatures. Fe-Cr merged with Cu-ZnO setting is not convenient to usage in either automotive or residential applications that quick drives which lower catalyst volume (fewer steps) and pyrophoric catalysts are utilized.

While alternative catalyst formulations are currently being evaluated as an alternative, high temperature shift–low temperature shift standard catalyst formulations are used in early and experimental fuel processors with step cooling in adiabatic reactors. Commercially available water gas exchange systems bring about a 25–50% load in terms of weight of fuel processor and volume of catalyst. For a standard reactor, the high temperature shift first reduces at about 400 °C (CO input up to about 10% and in a wet environment) to less than about 5% in stable operation. At low temperature (low temperature shift/180–240 °C), this ratio is reduced to below 1% (% CO) according to the amount of catalyst and process step in the system. The aim of Cu-ZnO-based water gas exchange systems is: It is important for CO reduction and size reduction of reactors by providing air to the tail medium of the reactor.

The designs of the water gas exchange catalysts to be used in the fuel cells should be designed to eliminate the shortcomings indicated above. The features expected from an ideal WGS killer can be listed as follows: High efficiency at temperatures not exceeding 300 °C, minimum catalyst size by volume, and constant concentration for CO output. In the modification and development of water gas exchange catalysts,



economic and productivity in order to keep the balance, the new and not prophylactic issues are two different trends. These non-precious metals with activity at high temperatures, except for some alloys reported, and gold or PGM matrix precious metals have a wider operating temperature range than activity rates.

When it is aimed to find the best assent between cost and activity, two ways may be selected for the advancement of new, non-pyrophoric water gas shift catalysts for fuel cell processors; invaluable metal catalyst generally is active at rising temperatures with many formulations, but having been reported as owning lower temperature activity and also valuable metal formulations depending on platinum group *metals* or gold, having high activity on the intervals of rising temperature.

In addition, many important developments in the field of nanotechnology have led to the emergence of new materials by pushing the boundaries in engineering and especially in materials science. In this context, metal-based metal-organic frameworks (MOFs) have been found to play an important role in fuel cells in many fields including wastewater treatment and efficient, environmentally friendly energy conversion (Ren et al. 2013; Ay et al. 2019).

### 4.3.1 Non-precious Metals

For water gas shift, formulations of non-precious metals are desired for their lower prices, because platinum group *metals* have a higher price for the catalysts. An alkaline-promoted, sulfur resistant basic oxide high temperature shift formulation depends on Ce, Pr, Nd, Mg, Mn, La, Co-MgAl<sub>2</sub>O<sub>4</sub>, Al (Mg aluminate spinel), Mg-ZrO<sub>2</sub> series have been advanced by Haldor-Topsoe recently (Schiodt et al. 2001). The catalyst formulations are active above 400 °C and at lower CO conversion (25–30%), but the determined positive sides on other formulations at a higher temperature such as Co- or Ni-promoted Mo. V. W oxides (119) is the lack of methanation. Cobalt-molybdenum or nickel-molybdenum sulfide (Newsome 1980) catalysts or their alkaline-promoted types are active, sulfur tolerant high temperature shift formulations; in a feed including only H<sub>2</sub>O and CO, they are being specified to give equitable CO conversions above 40% at low space velocities (lower than 8000 h<sup>-1</sup>) (Andreev et al. 1999).

At high temperatures, the activity of the formulations mentioned above and their equitable CO conversions at lower velocities (lower than 20.000 h<sup>-1</sup>) mention that additional application in fuel processor, additional downstream water gas shift reactors will charge with the active catalyst for their application in fuel processors at lower temperatures for the operation.

To develop for different types of commercial Cu-ZnO, Argonne National Laboratory has invented a series of vanadium-cobalt binary oxides; the materials' surface area is relatively lower so that show special activities (normalized to surface area) bigger than Cu-ZnO. Patt et al. (2000) searching the usefulness of high surface area molybdenum carbide for the reactions of WGS, specified that Mo<sub>2</sub>C has an active

formulation of low temperature shift with an activity commensurable or higher than Cu-ZnO-AlO<sub>3</sub>. The mentioned materials of nanocrystalline, named as active hydrotreating catalysts, are sensitive to oxygen and their performance is under real fuel processing circumstances, which has just to be searched. Engelhard has clarified the non-pyrophoric, base metal water gas shift catalysts without methanation activity (Ruettinger et al. 2003). The formulations of cerium oxide-including water gas shift have gain attention on the oxygen storage capacity of ceria (Trovarelli 1996) and depend on the total effect of ceria-metal results in higher active sites. Despite the fact that formulations of ceria and ceria-promoted are generally being related with precious metals, non-platinum group *metals*—ceria water gas shift catalysts have been promoted as an excellent alternative to Cu-ZnO. Li et al. showed that nickel or copper deposited on the high surface area Ce(La)Ox helps to prepare by urea precipitation-gelation (Li et al. 2000) shows good low temperature shift activity at high space velocities when checked under low CO concentrations (2%). The enhanced reducibility of ceria in the presence of metal depends on the high activity. There are no durability performances for the formulations mentioned above.

### 4.3.2 Precious Metal Catalysts

Since the 1980s, the interest for water gas shift has increased by the Pt/CeO<sub>2</sub>, when it is related to the advancement of the three-way catalysts. It was founded that the best non-noble metal oxide promoter is ceria for a typical Pt-Pd-Rh three-way catalysts that is supported on alumina mostly since it promotes the water-gas shift reactions' (Trovarelli 1996). The methanation reaction and WGS activity of Pt/CeO<sub>2</sub> have been stated by Mendelovich and Steinberg in 1985 (Mendelovici 1985a, b). A Pt/CeO<sub>2</sub> catalyst is developed by NexTech Materials that are already studied at higher temperatures for the reactions of water gas shift for many years (Swartz et al. 2001). A formulation of Pt/CO<sub>2</sub> is a potential candidate for the usage in fuel processor water gas shift reactors since it is an active and non-pyrophoric with activity higher than that of conventional water gas shift catalysts in the medium range 300–400 °C.

Academic studies applied on Pd, Pt, Ni, Rh, Co, Fe-ceria for water gas shift triggered the mechanistic works (Bunluesin et al. 1998; Hilaire et al. 2001) and the effects of oxygen storage capacity on water gas shift activity. The mechanism of regenerative (redox) and a high OSC are usually stated to be operative and liable to the high activity when metal-ceria relationships are specified, respectively. The water gas shift activity is stated to be based on both platinum group *metals*-supported relations and on the degree of surface hydration (Iwasawa 1993) or CO, coverage (Hilaire et al. 2001). The method of preparation has an essential effect on establishing the metal-support interaction, with an effect on the low-temperature activity (SE et al. 1995; Golunski et al. 2002). In precious and non-pyrophoric metal—high temperature shift catalysts have further increased to hold down methanation are also stated by Engelhard (Ruettinger et al. 2003). It is stated that Ru is

collected on a  $\text{Fe}_2\text{O}_3$ , and has been reported in the literature since it supplies promises for water gas shift conversion with the lack of methanation activity (Basińska et al. 1999).

Johnson Matthey has worked on Pt-CeO, catalysts mentioned that although it has higher initial activity taken at the medium-high temperature range (325–400 °C, Fig. 4.2.), the catalyst deceives its activity under real and synthetic reformation tests. Many reaction mechanisms can lead to explain deactivation, containing the coverage of surface within the situated form of carbonate-like species and also partially deceiving of re-oxidizing ability in the mainly reducing CO/H<sub>2</sub> environment. The first decrease in the dispersion of metal and total surface area of BET ((Brunauer–Emmett–Teller) is one of the theories that deals about the physical adsorption of gas molecules on a solid surface) is seen after the operations' initial hours. Ceria crystallite size is gradually rising at an extended time-on-stream in reformation, so it results in a future gradual decline at the total surface area of BET and to the slugging of Pt particles in support. This characteristic may lead to indicate the multiple operative mechanisms; also, the process of redox is usually asserted, based on the inlet concentrations and temperature. As a result, deactivation multi-paths can be reached easily. The partial deception of WGS activity to levels that need over-designing of water gas shift reactors for long-term operation systems from the complete deactivation, utilizing the routine reformation tests, as stated by others

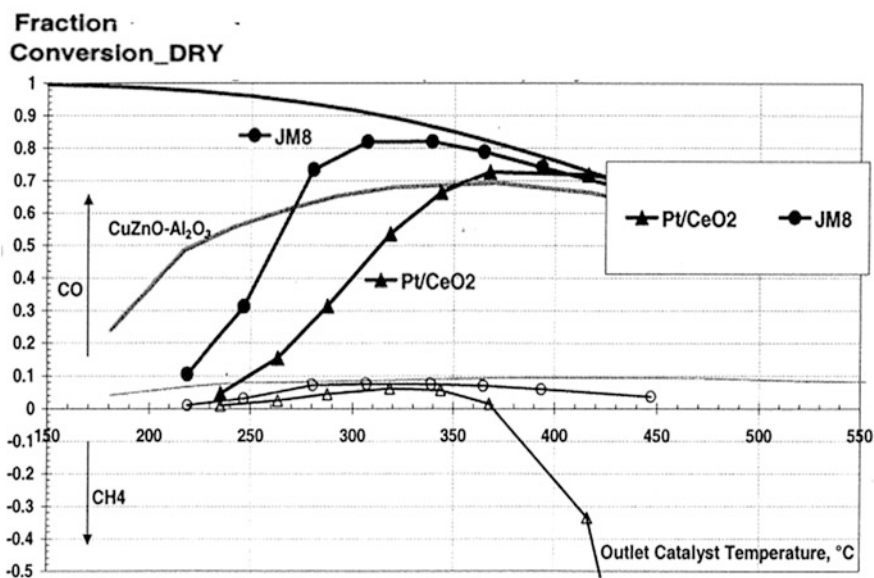


**Fig. 4.2** Performance of the water gas shift that Pt-including catalysts and metal construction as the Pt-CeO<sub>2</sub> catalyst. Pt-containing WGS formulations 67.500 cc/g cat/h, 11.4% CO (mol DRY) in synthetic reformat. The water gas shifting process is that it interacts with the Johnson Matthey fuel processor single stage and means a large decrease in the reactor volume compared to if commercially used Cu-ZnO (Ghenciu 2002)

(Zalc et al. 2002). Moreover, the reaction of methanation occurs on Pt/CeO<sub>2</sub> (Mendelovici 1985a), seen in Fig. 4.2 at higher temperatures than 375 °C.

Johnson Matthey has found a new water gas shift catalyst, which contains non-pyrophoric platinum group *metals* formulations with advanced durability and also lack of activity of methanation over a larger range of temperature (200–500 °C Fig. 4.2 states the performance of one of the Pt-including catalysts that own the same metal construction as the Pt- CeO<sub>2</sub> catalyst stated as in the same graph). As it is specified in Fig. 4.2, the formulation (JM8) has higher activity of WGS while there is no production of methane over the whole temperature range of interest (the methanation conversion in Fig. 4.2 is determined according to the 1.4% CH<sub>4</sub>, (mol, DRY (in dry conditions) inlet concentration)). Also, non-pyrophoric platinum group *metals* catalysts with a lack of methanation activity are being developed for even low-temperature operations. Under both a stable state and temporary circumstances, with any reducing activity at 250–260 °C for more than 1500 k with the durability and performance, a new catalyst is being tested in Johnson Matthey's fuel processor for the immobile applications at 2–10 kW load (electric) with reformation of produced from methane utilizing one of the new formulations of autothermal reforming. The Johnson Matthey's fuel processor of water gas shift operation is now be interacted with a single-stage and translates into a large decreasing agent in reactor volume when it is compared with the case of using Cu-ZnO commercially.

Gold catalysts state the increasing interest of WGS, depending on their higher activities for the oxidation of CO at lower temperatures rapidly (Haruta and Daté 2001; Bond 2002; Golunski et al. 2002). Metal oxides are supported by gold particles such as CeO<sub>2</sub> (Fu et al. 2001; Andreeva et al. 2002), TiO<sub>2</sub> (Bocuzzi et al. 2002), Fe<sub>2</sub>O<sub>3</sub> (Andreeva et al. 1998) are being clarified as active for water gas shift, with an advanced activity at lower temperatures that are being clarified as due to the synergism of gold-metal oxide. However, gold catalysts are sensitive to the circumstances when they are prepared, since the desired properties of the last material based on gold particle size, dispersion, and intimate metal-support contact (Golunski et al. 2002). During the reaction and high impact on activity leads to change the gold particle size easily, also improved stability is being reported recently (Fu et al. 2001). On the other hand, it is thought that more development is required for the mentioned catalysts to be a candidate for meeting the need for conditions in fuel cell processing applications.

#### 4.4 Function and Performance of Metal Oxide in the Proton Exchange Membrane Fuel Cells

By replacing the perfluorosulfonic acid membranes that are used today, hydrogen-oxygen proton exchange membrane in addition to carbon monoxide poisoning eliminates the problems in the water-thermal management of the fuel cell. As an example of perfluorosulfonic acid, Nafion can make fuel cells conductive when

operating at temperatures of 90 °C and above, Adjemian et al. as well as how metal oxide particles added to perfluorosulfonic acid are useful in forming a composite membrane, a proton exchange membrane fuel cell of Nafion, which is a perfluorosulfonic acid at 130 °C water retention capabilities were evaluated. In this study, metal oxide particles such as zirconia, alumina, titania, and silica were studied. In the previous (Watanabe 1996; Antonucci et al. 1999) experiments, metal oxide particles, such as SiO<sub>2</sub>, were incorporated into the membranes and Nafion, yielding very successful water retention capacities (Adjemian et al. 2006) 0.4 V 600 mA cm<sup>-2</sup> and the structure of the silica composite membrane, Antonucci et al. studied the methanol fuel cell (Antonucci et al. 1999).

The performance of the reinforced composite membrane was attributed to the hygroscopic properties of silica by Antonucci. Minimum external humidification and Nafion composite membranes impregnated with titania and silica in H<sub>2</sub>/O<sub>2</sub> PEMFC operating at 100 °C were investigated by Watanabe (1996). It was also noted by Watanabe et al. that the titania particles were less than the silica particles when the water retention capacity in the Nafion membrane was evaluated, and that the reason was that the titania had less water absorption. Since sol-gel silica produced for particle composites is homogeneously distributed on the angstrom scale against the lower micrometer scale, the sol-gel method has been proposed by Mauritz et al. to add silica to the Nafion membrane, which can perform better than the particles (Deng et al. 1995). In this part, a summary of metal oxide particles with beneficial effects on high-temperature PEMFC is presented. Improved cell behavior has been suggested to be unrelated to the acidity or water holding capacity of the metal oxide compounds. However, metal oxide particles are considered to have an effect depending on the temperature of the polymer matrix. Special attention is paid to the physicochemical properties of various metal oxide composites under investigation. Specifically, an understanding of the interface chemistry between the Nafion membrane and metal oxide particles and how this interface affects the fuel cell at high temperatures are discussed.

#### ***4.4.1 Proton Exchange Membrane for the Fuel Cell Applications***

As seen above, the membrane, in general, is the core of proton exchange membrane fuel cells. To prevent electron passage, the electronic insulator, separation of reactive gases, and charge carriers (for protons) are the triple roles of the polymeric membrane in the PEMFCs. Nafion, which was perfluorosulfonic acid in the 70s, was developed by DuPont. This not only prolongs the life of the membrane by approximately 400% but also increases its conductivity by an average of 200%. (104–105 h). Later, Nafion has since become the standard for PEMFCs. The improved perfluorosulfonic acid membrane with high SO<sub>3</sub>H content and CF<sub>2</sub> and short side chains was synthesized by Asahi Chemical Company and Dow Chemical

**Table 4.3** Characteristics of some commercial proton exchange membranes

Membrane	Membrane type	IEC (mequiv./gr)	Thickness (mm)	Gel water (%)	Conductivity (S/cm) at 30 °C and 100% R.H.
K 101	Sulfonated polyarylene	1.4	0.24	24	0.0114
CMV	Sulfonated polyarylene	2.4	0.15	25	0.0051
DMV	Sulfonated polyarylene	–	0.15	–	0.0071
Flemion	Perfluorinated	–	0.15	–	–
MC 3470	–	1.5	0.6	35	0.0075
MC 3142	–	1.1	0.8	–	0.0114
61 AZL 386	–	2.3	0.5	46	0.0081
61 AZL 389	–	2.6	1.2	48	–
61 CZL 386	–	2.7	0.6	40	0.0067
N 117	Perfluorinated	0.9	0.2	16	0.0133
N 901	Perfluorinated	1.1	0.4	5	0.0105
R-1010	Perfluorinated	1.2	0.1	20	0.0333

Adapted with permission from Adjemian et al. (2006). Copyright (2006) American Chemical Society

Company (Costamagna and Srinivasan 2001). Table 4.3 shows the comparison of cation exchange membranes (some commercial products) (Smitha et al. 2005).

The Nafion membrane has a construction of copolymer from fluoro 3,6-dioxo 4,6-octane sulfonic acid with polytetrafluorethylene (PTFE) that is known as Teflon backbone of this construct supplies the hydrophobic nature for membrane and hydrophilic sulfonic acid groups ( $\text{HSO}_3^-$ ) have been implanted to chemically into the backbone. The ionic groups lead to the absorption of huge amount of water by polymer and so results in polymer hydration. The level of hydration and thickness factors are affecting the performance of the appropriate proton exchange membrane. These factors have a critical role in determining their convenience for applying in fuel cells (Appleby and Foulkes 1989). The proton exchange membrane performance links to the extension of its conductivity of proton. The proton conductivity is indeed associated with the membrane humidity. The higher extent of humidity leads to higher proton conductivity. There are some ways to refrain from conductivity of water drag, or water crossover is to decrease the membrane thickness thereby supplying an improvement in the fuel cell performance. Other positive sides are decreased thickness containing lower membrane resistance, rapid hydration and lower cost. On the other hand, it is limited to extent to which membrane thickness may be decreased since it has drawbacks about durability and fuel bypass. To reach high yield in fuel cell applications, the polymer electrolyte (membrane) has to own these characteristics such as high proton conductivity to give high current with

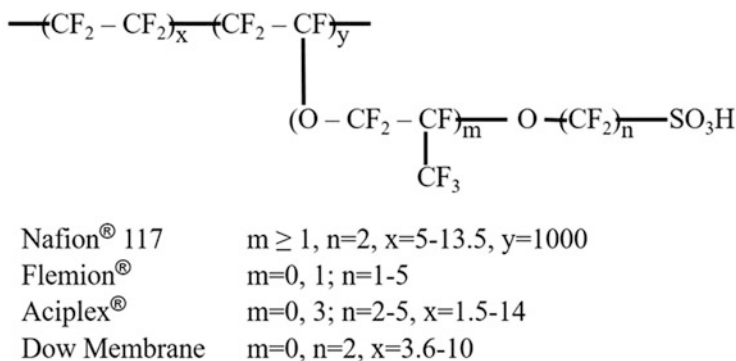


**Fig. 4.3** Basic chemical structure of Nafion and other famous proton membranes

minimal resistive losses, lack of electronic conductivity and appropriate mechanical stability and strength, electrochemical and chemical stability under the convenient circumstances, controlling moist in stack, and very low fuel or oxygen by-pass to extent columbic yield and cost of generation appropriate with intended applications (Smitha et al. 2005). Figure 4.3 states Nafion's construction chemically and other famous perfluorinated electrolyte membranes (Rikukawa and Sanui 2000).

#### 4.4.2 Fuel-Cell Performance of $\text{SiO}_2$ and $\text{TiO}_2$ Composites

The metal oxides physical properties are used to prepare the composite membranes which are shown in Table 4.4 at 100% RH; there is no important difference in fuel cell performance based on the metal oxide impregnation, with the exception of Alfa-Aeser titania-impregnated membranes, which stated a rising R-value (see Table 4.5 and Fig. 4.4a). This variety is not intrinsic to  $\text{TiO}_2$ -impregnated membranes, since the usage of Degussa-Huls titania does not supply a general high cell resistivity, and its effect is taken into consideration later in this study.

$\text{SiO}_2$  and  $\text{TiO}_2$  composite membranes produced current–voltage properties that outperformed control recast Nafion membranes, as stated in Fig. 4.4b. The new approach from the smallest resistance and highest cell potential at a given current density at 88% humidity relatively is as follows where DH and AA show Alfa-Aeser and Degussa-Huls metal oxides, respectively.

$$\text{DH SiO}_2 \sim \text{AA SiO}_2 \sim \text{DH TiO}_2 > \text{AA TiO}_2 \gg \text{Plain Recast}$$

The titania and silica composite performances at 75% RH and 130 °C are stated in Fig. 4.4c, in which it is examined that output parameters of the recast Nafion-based cell maintain to be worse (0.9 cm<sup>2</sup> cell resistivity); however, the systems of

**Table 4.4** Metal oxides physical composition

Metal oxide	Particle size	Surface area (m <sup>2</sup> /g)
SiO <sub>2</sub> (AA)	0.2–0.3μm	90
SiO <sub>2</sub> (DH)	20 nm	90
Al <sub>2</sub> O <sub>3</sub> (AA)	1μm	6–8
Al <sub>2</sub> O <sub>3</sub> (AA)	25μm	6
Al <sub>2</sub> O <sub>3</sub> (DH)	13 nm	100
TiO <sub>2</sub> (AA)	1–2μm	3–6
TiO <sub>2</sub> (AA)-Acid Treated/Degreased	1–2μm	3–6
TiO <sub>2</sub> (AA)-Silylated	1–2μm	3–6
TiO <sub>2</sub> (DH)	21 nm	50
ZrO <sub>2</sub> (AA)	7.5μm	–
ZrO <sub>2</sub> (GFS)	44μm	–
ZrO <sub>2</sub> (Aldrich)	1.5μm	0.38

Adapted with permission from Adjemian et al. (2006). Copyright (2006) American Chemical Society

AA Alfa-Aesar, DH Degussa-Huls, GFS GFS Chemicals

**Table 4.5** Electrode kinetic parameters of SiO<sub>2</sub> and TiO<sub>2</sub> composite membranes at 130 °C, 30 psig, and various calculated relative humidities in PEMFCs with H<sub>2</sub>/O<sub>2</sub> reactant gases

Relative humidity (%)	$E_0$ (mV)	$b$ (mV/decade)	$R$ (ohm cm <sup>2</sup> )	Cell potential at 600 mA/cm <sup>2</sup> (mV)	
Plain recast	100	961	65	0.26	632
	94	960	59	0.52	491
	88	935	50	0.65	435
	75	940	54	0.9	–
SiO <sub>2</sub> (AA)	100	950	60	0.23	648
	94	950	60	0.27	624
	88	957	67	0.27	611
	75	975	82	0.29	573
SiO <sub>2</sub> (DH)	100	954	54	0.25	659
	94	954	53	0.27	648
	88	955	54	0.29	636
	75	967	65	0.33	587
TiO <sub>2</sub> (AA)	100	948	49	0.41	580
	94	965	57	0.42	564
	88	974	65	0.45	526
	75	976	68	0.58	424
TiO <sub>2</sub> (DH)	100	960	54	0.25	662
	94	959	53	0.28	648
	88	959	54	0.31	633
	75	980	70	0.35	582
TiO <sub>2</sub> (degreased)	75	908	65	0.33	590
TiO <sub>2</sub> (silylated)	75	897	77	0.36	400

Adapted with permission from Adjemian et al. (2006). Copyright (2006) American Chemical Society

AA Alfa-Aesar, DH Degussa-Huls



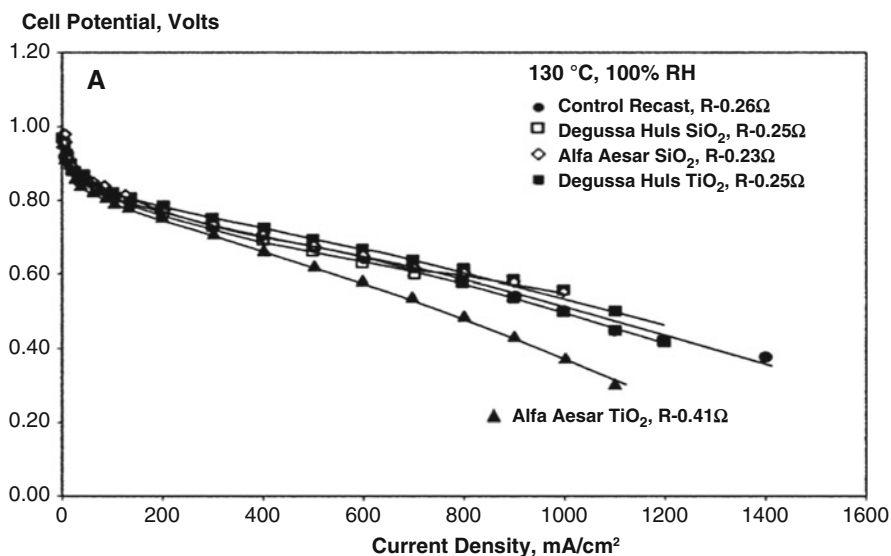


**Fig. 4.4a** Current–voltage profiles for membrane electrode assemblies containing SiO<sub>2</sub> and TiO<sub>2</sub> composite membranes with 100% relative humidity. Depending on the content rates of the commercial membranes using titanium oxide and silicon oxide (100%) in the working environment; current–voltage variation comparisons were evaluated

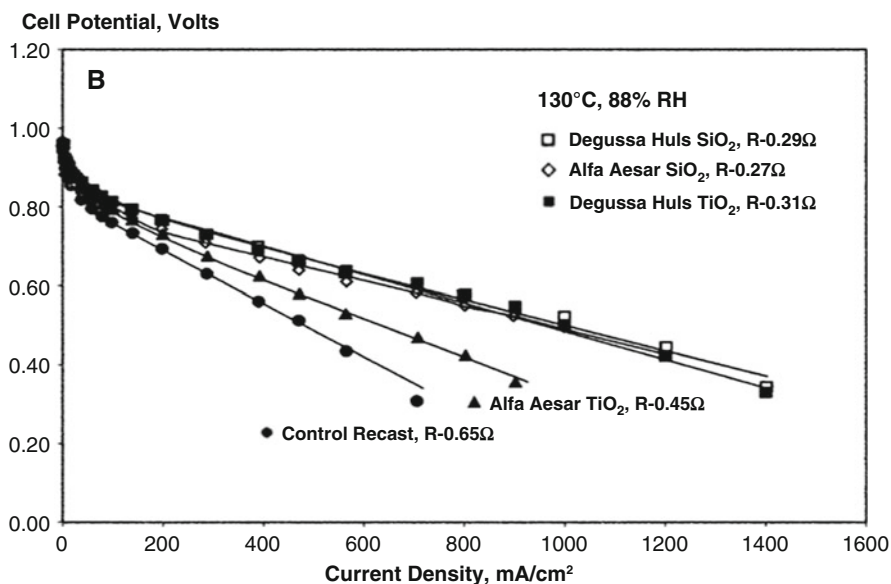


**Fig. 4.4b** Current–voltage profiles for membrane electrode assemblies containing SiO<sub>2</sub> and TiO<sub>2</sub> composite membranes with 88% relative humidity. Depending on the content rates of the commercial membranes using titanium oxide and silicon oxide (88%) in the working environment; current–voltage variation comparisons were evaluated. It is observed that the efficiency of the current–voltage values decreases due to the decrease in the humidity in the working environment

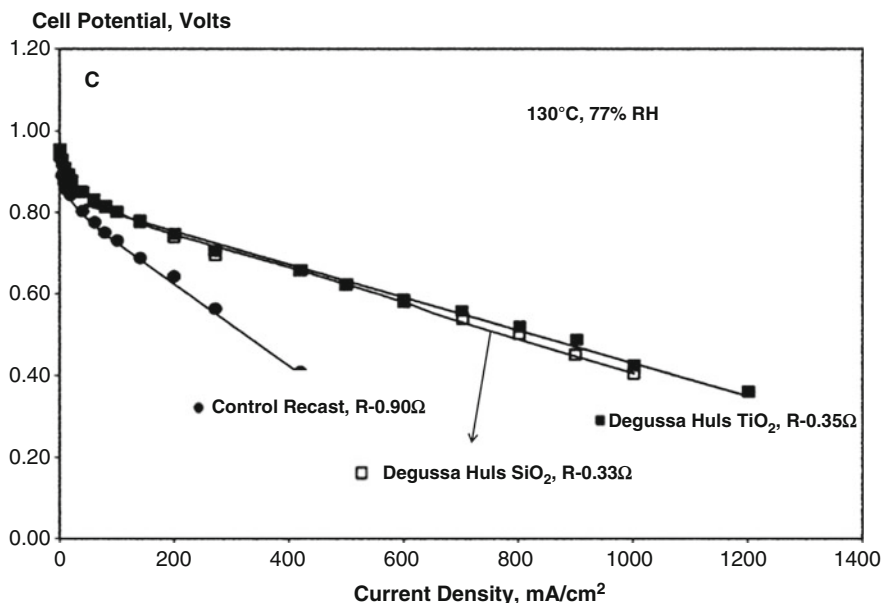


**Fig. 4.4c** Current–voltage profiles for membrane electrode assemblies containing SiO<sub>2</sub> and TiO<sub>2</sub> composite membranes with 75% relative humidity. The lowest efficiency of the current–voltage values was determined due to the decrease in the humidity of the working medium up to 75%

composite membrane supply a fundamentally relative humidity variance of the cell conductivity.

As a result, under the circumstances of saturation, the recast Nafion and Nafion-metal oxide composite membranes produce similar proton conductivities, just the vapor phase of water pressure partially is under its saturation value, the composite MEA shows more proton conductivity. This proposes constructional differences in the composite membrane that modify the water included when compared with a recast Nafion at reduced relative humidity and high temperatures. The findings are appropriate with the other reports (Adjemian et al. 2002a, b) stated before that show to embody in silicon oxide via sol-gel processing rises the water management properties of a Nafion membrane in a PEMFC operating higher than 100 °C.

#### 4.4.3 Performance of Nafion Membranes with Zirconia and Alumina Doped

The advanced search of the potential position of an interaction chemically between groups of Nafion sulfonate and interface of metal oxide, membranes that have composite construction has been structured including alumina (Al<sub>2</sub>O<sub>3</sub>) particles.

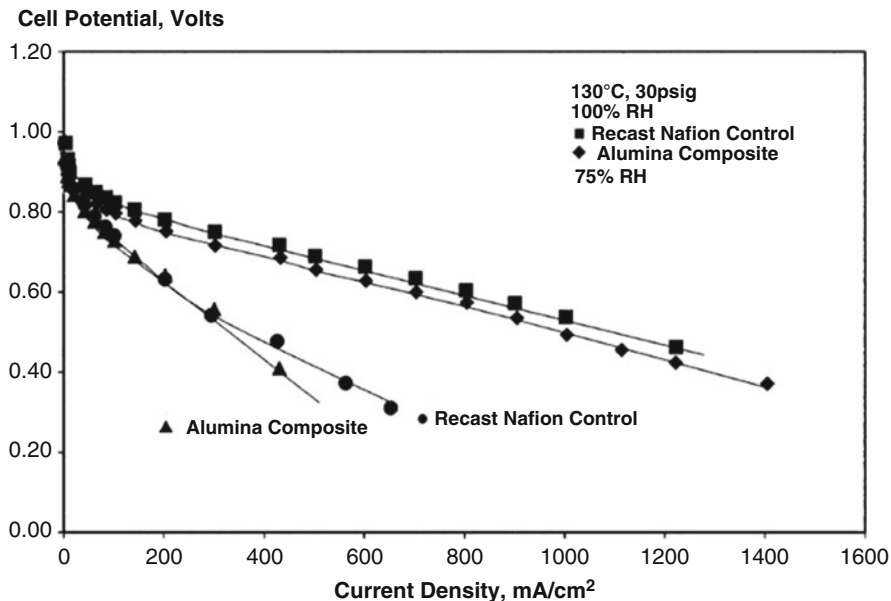


**Fig. 4.5** Current–voltage profiles for a membrane electrode assembly including a membrane of alumina composite. Temperature of the cell was 130 °C, humidity rate is 100% and 75% and 30 psig of reactant gas of H<sub>2</sub>/O<sub>2</sub>. In the cell, the humidity rate is obtained from the vapor pressure of saturation of water, temperatures of cathode, and anode humidifiers

The material is chosen since it has a great level of chemical reactivity and superior to titania. As it was stated in Fig. 4.5, at 100% RH and 130 °C where purified recast membranes of Nafion and composites of titania represent equal characteristics, a composite of Degussa-Huls alumina is fatal to performance of PEM fuel cell.

The surface kinds of advancing examined in the first part do not bear advanced materials. In Table 4.5, electrode kinetic parameter values are seen for different composites stated an excellent achievement which is a good comparison with a stagnate changing membrane at 75% humidity rate. There is a justification for the obtained declination at advancement is to release of Al<sup>3+</sup> ions into the membrane. The progression makes it simpler for acidic pK<sub>a</sub> of Nafion. It is soaked of alumina from Alfa-Aeser and Degussa-Huls in 0.5 M concentration of H<sub>2</sub>SO<sub>4</sub> at 1 h to check this proposal. The recipe is too partial neutralization of sodium carbonate at the acidity of pH 5.5, and the colorimetric indicator of Al<sup>3+</sup> Alizarin S is supplemented. These solutions are prepared for changing to red color, showing an occurrence of a considerable solubility of concentration of Al (Snell 1921). The discharging of Al<sup>3+</sup> into the Nafion matrix may change the proportion of the motile protons from sulfonate parts or crosslink sulfonate parts, transferring to morphology of polymer partially and potential proton having parts that cannot be reached for ion exchange. Metal-oxide-incorporated titration of membranes has been shown in Table 4.5 and does not supply proof of depletion of proton on alumina impregnation.

So, proven membranes answer the alumina occurrence that is thought to associate with the conductivity of limited proton as in the association with  $\text{Al}^{3+}$  decreases in changing the microstructure of Nafion.

To have an idea about the alumina composite, it is also amalgamated membranes including a zirconia agent. As it is understood that parameters of electrochemistry have shown in Table 4.6, and the systems act as a composite of alumina-based, usually synthesizing cells that have elevated-resistance, that cannot tolerate to circumstances at the lower rate of humid. As in the alumina, the composites do not waste extra protons, but the zirconium's nature of oxophilicity paves the way for generating of oxysulfate of zirconium in the medium own higher acidity level at the environment of Nafion, also decomposing a sulfonate parts fraction. As in the alumina example, the typical reactivity rate is needed to up-to-date of topology of membrane, limiting of proton diffusion powerfully.

**Table 4.6** At 130 °C, the parameters of electrode kinetic of  $\text{ZrO}_2$  and  $\text{Al}_2\text{O}_3$  composite membranes, at 30 psig, different calculations in proportional humidity rates in PEMFCs with reactant gases  $\text{H}_2/\text{O}_2$

Relative humidity (%)	$E_0$ (mV)	$b$ (mV/decade)	$R$ (ohm $\text{cm}^2$ )	Cell potential at 600 mA/ $\text{cm}^2$ (mV)	
Plain recast	100	961	65	0.26	632
	94	960	59	0.52	491
	88	935	50	0.65	435
	75	940	54	0.9	–
$\text{Al}_2\text{O}_3$ , 1 $\mu\text{m}$ (AA)	100	940	52	0.32	625
	94	960	74	0.48	462
	88	968	77	0.55	426
	75	970	84	0.79	406
$\text{Al}_2\text{O}_3$ , 25 $\mu\text{m}$ (AA)	100	953	45	0.29	664
	94	960	69	0.4	538
	88	954	61	0.54	458
	75	970	57	0.7	344
$\text{ZrO}_2$ , 6 $\mu\text{m}$ (AA)	100	958	51	0.29	645
	94	964	57	0.32	617
	88	962	54	0.4	575
	75	965	72	0.54	458
$\text{ZrO}_2$ , 1 $\mu\text{m}$ (AA)	100	960	55	0.32	620
	94	970	62	0.41	568
	88	953	60	0.58	449
	75	970	83	0.7	400
$\text{ZrO}_2$ , (Aldrich)	~100	944	57	0.25	646
	78	964	64	0.62	442
$\text{ZrO}_2$ , (GFS)	~100	939	52	0.57	454
	78	986	105	0.85	–

Adapted with permission from Adjemian et al. (2006). Copyright (2006) American Chemical Society

AA Alfa-Aesar, DH Degussa-Huls

## 4.5 Reduction of Sulfide Electrocatalysis, Metal Sulfides (NiS<sub>2</sub>, FeS<sub>2</sub>, CoS<sub>2</sub>)

There are many materials invented as possible enhancement of hydrogen reaction (HER) electrocatalysts to produce a clean fuel that sources from hydrogen via water electrolysis, however, none of them encounter with high yields and superior metals stability, but they have repressive costs. As in a similar example, noble metals generally exceed the counter electrode materials electro-catalytically in reproducible solar cells of liquid-junction photoelectrochemically, such as solar cells with quantum dot-sensitized (QDSSCs) which maintain polysulfide or sulfide electrolyte redox as a hole mediator. Now it is searched systematically on thin films of the transition of earth-abundant pyrite-phase disulfides of metals (e.g., CoS<sub>2</sub>, NiS<sub>2</sub>, FeS<sub>2</sub>) as agreed in a choice of electrocatalysts for the reduction of polysulfide and HER. The activity of their electrocatalytic through the HER is closely related to the morphology and composition of them. The new methods for performances of them propose that cobalt has a crucial position in advancing the HER with CoS<sub>2</sub> showing the whole max performance. Moreover, it has shown the highest transition activity metal pyrites through the reduction of polysulfide, also underlines the especially high activity of intrinsic of NiS<sub>2</sub>, that may supply developed QDSSC advancement. In addition, the disorders in terms of construction that are interfaced with alloying several pyrites of transition metals can rise catalysts' active side of areal density, give rises to advancements of performs.

It is vital to develop hydrogen gas inexpensively and efficiently to adopt its asserted process as security, sustainable, clean, and alternative next-generation energy carrier (Turner 2004; Lewis and Nocera 2006). There are several ways to synthesize H<sub>2</sub> fuel (Turner 2004), however electrolysis of water, which is the most attractive ones of ideally yielded by solar energy (Gray 2009; Cook et al. 2010; Chen et al. 2010; Walter et al. 2010; Nocera 2012) is the most attractive one. There are no detrimental fallouts that are released by the water-splitting electrocatalytically to get clean H<sub>2</sub> fuel, and then only energy and water are synthesized by their exhaustion in air, only water and energy are generated (Cook et al. 2010). Several inorganic materials are searched for a source of the reaction of potential H<sub>2</sub> enhancement (HER) electrocatalysts (Faber and Jin 2014), however there is no matching with the stability level and performance of noble metals, especially Pt (Nørskov et al. 2005). On the other side, the higher price and scarcity of them prevent the large range of deployment of conversion in energy technologies which use the noble metal electrolysts (Vesborg and Jaramillo 2012). By altering these valuable metal electrocatalysts with high-performance substituents that are constructed wholly of elements (McKone et al. 2011, 2013; Merki et al. 2011; Benck et al. 2012; Cao et al. 2013; Popczun et al. 2013, 2014; Wang et al. 2013a; Xu et al. 2013; Kong et al. 2013, 2014; Lukowski et al. 2013, 2014; Voiry et al. 2013; Sun et al. 2013; Ding et al. 2014; Faber and Jin 2014; Faber et al. 2014) of earth-abundant. Although the electrochemical and photochemical prices of synthesizing of hydrogen are substantially decreased.

As though main (and sustaining) efforts on investigation, a quantity of materials of earth-abundant have been clarified as an affirmative candidate of electrocatalysts of HER (Faber and Jin 2014) containing  $WS_2$  (Voiry et al. 2013; Lukowski et al. 2014),  $MoS_2$  (Lukowski et al. 2013; Wang et al. 2013a; Ding et al. 2014), Co-S (Sun et al. 2013), amorphous  $MoS_x$  (Merki et al. 2011; Benck et al. 2012), CoP (Popczun et al. 2014), FeP (Xu et al. 2013),  $Ni_2P$  (Popczun et al. 2013), the Ni-Mo alloys (McKone et al. 2011, 2013), and  $Co_{0.6}Mo_{1.4}N_2$  (Cao et al. 2013) in other ones. The pyrite-phase cubic transition metal dichalcogenides (with the general formula  $MX_2$ , where characteristically  $M = Ni, Fe, \text{ and } Co$ , and also  $X = Se \text{ or } S$ ) have justly emerged as effective electrocatalysts of HER (Kong et al. 2013, 2014; Ivanovskaya et al. 2013; Faber et al. 2014), they can catalyze the HER over 20 years ago (Jaegermann and Tributsch 1988) within the pyrites family of transition metals such as disulfide of iron ( $FeS_2$ ; pyrite of iron, “fool’s gold”), disulfide of cobalt ( $CoS_2$ ; cobalt pyrite, catterite), and disulfide of nickel ( $NiS_2$ , pyrite of nickel, vaesite). These pyrites have several minerals that are usual and well-examined.

The synthesized rock-forming chalcogens and 1st-row transition metals, the pyrites of transition metal are so abundant and cheaper that make them especially charming for changing of energy applications of materials. For instance, semiconducting  $FeS_2$  is now investigating enormous for a solar light absorber with earth-abundance (Cabán-Acevedo et al. 2012, 2013; Seefeld et al. 2013). The features of electrocatalysis of  $FeS_2$  is ascendant in solar cells with dye-sensitized (DSSCs) (Hagfeldt et al. 2010), with nanorod array (Huang et al. 2013) and electrodes with thin-film get from a nanocrystal ink (Wang et al. 2013b) supplying tool performance competitive with that reached utilizing platinum counter electrodes. As in similar examples,  $(Fe, Co)S_2$  and  $FeS_2$  alloys are being searched for the reduction of oxygen reaction (ORR) electrocatalysts (Susac et al. 2007).  $CoS_2$  (Wang et al. 2011) and  $FeS_2$  (Li et al. 2014) are both give promises for materials of electrode for batteries that work with lithium-ion principle. On the contrary, the pyrites of semiconductors, as though,  $CoS_2$  is a metal that has conductivity intrinsically that permits for the usage of an electrode material directly. It is shown for usage of thin films of  $CoS_2$  synthesized on glass directly as higher effect on inverse electrodes (Faber et al. 2013) in solar cells of quantum dot-sensitized (QDSSCs) (Kamat 2013; Selinsky et al. 2013) that use either polysulfide or sulfide electrolytic redox as the medium of hole-transporting. Composite electrodes that are based on graphene are incorporating  $CoS_2$  nanoparticles that have tested for effectiveness in DSSCs for decreasing triiodide, showing higher advancement than platinum (Duan et al. 2013). It has worked on strategies of nanostructure recently to advance rising in the  $CoS_2$  electrode activity toward reduction of polysulfide and triiodide (Faber et al. 2014). At the study, thin films, microwires, and nanowires of  $CoS_2$  prepared closely on applying support of graphite are presented for showing the perfect activity electrocatalytically through HER, with micro- and nanostructure of  $CoS_2$  material modifying synergistically both stability of states and performing (Faber et al. 2014). As  $FeS_2$  and  $CoS_2$  nanocrystals and thin films also are examined for ORR electrocatalysts (Zhu et al. 2008; Jirkovský et al. 2012; Zhao et al. 2013) as a well-performed electrocatalyst.  $CoS_2$  and  $NiS_2$  hollow spheres have been utilized for supercapacitors (Peng et al.

2014) as having NiS<sub>2</sub> nanocubes recently (Pang et al. 2014). These NiS<sub>2</sub> nanocubes are thought of as effective Co-catalysts for the H<sub>2</sub> production photocatalytically (Pang et al. 2014).

It is reported that investigation in HER systematically and polysulfide reduction of electrocatalytic activity of various disulfides of pyrite-phase transition metals known as CoS<sub>2</sub>, NiS<sub>2</sub>, FeS<sub>2</sub> with alloys of them. It is stated that performances of them which evaluated as ability to obtain high density of catalytic current at lower high-potential, akin to rise with elevated cobalt content, CoS<sub>2</sub> is better, proposing a vital role for cobalt in modifying the HER, when pyrites of each transition metals specified, shows the activity through the HER, approving common pyrites' electrocatalytic features. It is similar to the reduction of polysulfide activity of NiS<sub>2</sub>, FeS<sub>2</sub>, and their alloys; as a result, NiS<sub>2</sub> and CoS<sub>2</sub> as owning higher activity especially. So, it is proposed for preparing alloy is an effective and usual way of modifying the transition metal pyrites of electrocatalytic activities depending on introducing constructional disorders that may raise its active parts' areal density of catalysis.

In sum, it specifies that alloyed and binary disulfides of pyrite-phase transition metals' thin films may be obtained easily on the glass or graphite particles for the facile thermal sulfidation films of metal indicator, and pyrites of transition metal thin films are very effective in hydrogen reaction and polysulfide reduction of electrocatalysis. Voltage characterization and pyrites' current density phases of electrocatalyst thin films present the beginning of H<sub>2</sub> (g) changing at lower overpotentials being rival with different electrocatalysts with earth-abundance. The new methods in their performances have found that cobalt may have a crucial position in advancing hydrogen reaction electrocatalytic development. In addition, Raman spectrometry characterization of alloy thin films has approved their elevated constructional disarray of which may support the advanced electrocatalytic development. Moreover, thin films of PyS<sub>2</sub>, NiS<sub>2</sub>, and FeS<sub>2</sub> are determined as an effective reduction of catalyzes of polysulfides, with an activity of intrinsic of NiS<sub>2</sub> surpassing that of CoS<sub>2</sub>. The usual activity of electrocatalysis of the pyrite-phase transition metal disulfides refers to the common property may disclose this type of activity. Additionally, the effect of the transition metals on electrocatalytic activity presented here, the anions of disulfide (S<sub>2</sub><sup>2-</sup>) shown in whole pyrite structures are crucial for their higher electrocatalytic activity through hydrogen reaction.

Edges of disulfide-terminated of MoS<sub>2</sub> and other transition layered metal dichalcogenides have been identified experimentally (Jaramillo et al. 2007) and followed in mimics of molecules (Karunadasa et al. 2012; Kibsgaard et al. 2014) as the active sites of hydrogen reaction electrocatalysis, proposing a role for catalytic disulfide. Disulfide-terminated surface sites' abundance in crystal of pyrite construction can help to an excellent and common activity of electrocatalysis, the metal disulfides of pyrite-phase transitions; but supplementary mechanistic works are needed for setting up a connection. However, new methods are developed for activity of electrocatalysis of the pyrite-phase thin films through the hydrogen reaction and decreasing of polysulfide proposes to several ways for advanced rising

in their performances of these and potentially other renewable energies of electrocatalysis and applications.

## 4.6 Conclusion

For humanity, many studies have been carried out to replace fossil fuels to solve environmental pollution and energy crises which have become the biggest problem. Due to the specific properties of the fuel cells, it has the potential to make a huge transformation in the electric field. Solid polymer electrodes with proton transfer capability were used as membranes in PEMFCs. In recent years, selective and active catalysts containing valuable metals have been developed which are reliable and result in small PROX, WGS, or ATR units due to the difficulties in producing hydrogen in PEMFCs. In the development of cost-effective catalytic systems, governments, industrial and academic sectors are making great efforts. A large part of the work is aimed at solving problems such as durability encountered during the fuel process and understanding the catalysts used in this field under stable, real, and transient conditions. In proton exchange membrane fuel cell electrodes, ion exchange membranes (especially proton exchange membranes) play an essential role in proton transfer.

Chemical stability, good mechanical properties, proper proton conductivity, and high permeability and high selectivity are among the required properties of the desired ion exchange membrane. Anion exchange membranes are obtained by binding alkali functional groups to the polymer backbone of the membrane, while cation exchange membranes are obtained by binding acidic functional groups. Membranes of low thickness have increased fuel pass through the membrane simultaneously, although an increase in proton conductivity has been observed. There is a homogeneous distribution of metal oxide in Nafion structure, metal oxide composite Nafion membrane preparation technique using different metal oxide and dissolved Nafion particles. At low relative humidity and low temperatures, the use of metal oxides such as silica and titania obtained from Degussa-Huls and Alfa-Aesar to the PEMFCs provided self-resistance to the membrane. The chemical interaction between the Nafion membrane and the metal oxide surface plays a critical role in the performance of the PEMFCs. PEMFCs operating in a low relative humidity environment exhibited the best performance of silica composite from Alfa-Aesar and titania and silica metal oxides from Degussa-Huls. In summary, many studies have been conducted on the effects of metals, metal oxides, and metal sulfides in fuel cells, in different regions and elements for each process, and studies are still ongoing.

**Acknowledgments** The author(s) declare no competing interests.



## References

- Acres GJK, Frost JC, Hards GA et al (1997) Electrocatalysts for fuel cells. *Catal Today* 38:393–400. [https://doi.org/10.1016/S0920-5861\(97\)00050-3](https://doi.org/10.1016/S0920-5861(97)00050-3)
- Adjemian KT, Lee SJ, Srinivasan S et al (2002a) Silicon oxide nafion composite membranes for proton-exchange membrane fuel cell operation at 80–140°C. *J Electrochem Soc* 149:A256. <https://doi.org/10.1149/1.1445431>
- Adjemian KT, Srinivasan S, Benziger J, Bocarsly AB (2002b) Investigation of PEMFC operation above 100 C employing perfluorosulfonic acid silicon oxide composite membranes. *J Power Sources* 109:356–364
- Adjemian KT, Dominey R, Krishnan L et al (2006) Function and characterization of metal oxide–nafion composite membranes for elevated-temperature H<sub>2</sub>/O<sub>2</sub> PEM fuel cells. *Chem Mater* 18(9):2238–2248. <https://doi.org/10.1021/CM051781B>
- Ahmad MI, Zaidi SMJ, Rahman SU (2006) Proton conductivity and characterization of novel composite membranes for medium-temperature fuel cells. *Desalination* 193:387–397. <https://doi.org/10.1016/j.desal.2005.06.069>
- Andreev AA, Kafedjiysky VJ, Edreva-Kardjieva RM (1999) Active forms for water-gas shift reaction on NiMo-sulfide catalysts. *Appl Catal A Gen* 179:223–228. [https://doi.org/10.1016/S0926-860X\(98\)00321-4](https://doi.org/10.1016/S0926-860X(98)00321-4)
- Andreeva D, Tabakova T, Idakiev V et al (1998) Au/ $\alpha$ -Fe<sub>2</sub>O<sub>3</sub> catalyst for water–gas shift reaction prepared by deposition–precipitation. *Appl Catal A Gen* 169:9–14. [https://doi.org/10.1016/S0926-860X\(97\)00302-5](https://doi.org/10.1016/S0926-860X(97)00302-5)
- Andreeva D, Idakiev V, Tabakova T et al (2002) Low-temperature water-gas shift reaction over Au/CeO<sub>2</sub> catalysts. *Catal Today* 72:51–57. [https://doi.org/10.1016/S0920-5861\(01\)00477-1](https://doi.org/10.1016/S0920-5861(01)00477-1)
- Antonucci P, Aricò A, Cretì P et al (1999) Investigation of a direct methanol fuel cell based on a composite Nafion®-silica electrolyte for high temperature operation. *Solid State Ionics* 125:431–437. [https://doi.org/10.1016/S0167-2738\(99\)00206-4](https://doi.org/10.1016/S0167-2738(99)00206-4)
- Appleby AJ, Foulkes FR (1989) *Fuel cell handbook*. Van Nostrand Reinhold, New York
- Ay H, Karakus S, Burhan H et al (2019) Metal-organic-framework (MOFs) and environmental application. In: *Metal-organic framework composites: volume I*. Materials Research Forum LLC, Millersville, pp 73–104
- Basińska A, Kępiński L, Domka F (1999) The effect of support on WGS activity of ruthenium catalysts. *Appl Catal A Gen* 183:143–153. [https://doi.org/10.1016/S0926-860X\(99\)00049-6](https://doi.org/10.1016/S0926-860X(99)00049-6)
- Benck JD, Chen Z, Kuritzky LY et al (2012) Amorphous molybdenum sulfide catalysts for electrochemical hydrogen production: insights into the origin of their catalytic activity. *ACS Catal* 2:1916–1923. <https://doi.org/10.1021/cs300451q>
- Bezerra CWB, Zhang L, Liu H et al (2007) A review of heat-treatment effects on activity and stability of PEM fuel cell catalysts for oxygen reduction reaction. *J Power Sources* 173:891–908. <https://doi.org/10.1016/J.JPOWSOUR.2007.08.028>
- Bocuzzi F, Chiorino A, Manzoli M et al (2002) Gold, silver and copper catalysts supported on TiO<sub>2</sub> for pure hydrogen production. *Catal Today* 75:169–175. [https://doi.org/10.1016/S0920-5861\(02\)00060-3](https://doi.org/10.1016/S0920-5861(02)00060-3)
- Bond GC (2002) Gold: a relatively new catalyst. *Catal Today* 72:5–9. [https://doi.org/10.1016/S0920-5861\(01\)00522-3](https://doi.org/10.1016/S0920-5861(01)00522-3)
- Bunluesin T, Gorte RJ, Graham GW (1998) Studies of the water-gas-shift reaction on ceria-supported Pt, Pd, and Rh: implications for oxygen-storage properties. *Appl Catal B Environ* 15:107–114. [https://doi.org/10.1016/S0926-3373\(97\)00040-4](https://doi.org/10.1016/S0926-3373(97)00040-4)
- Cabán-Acevedo M, Faber MS, Tan Y et al (2012) Synthesis and properties of semiconducting iron pyrite (FeS<sub>2</sub>) nanowires. *Nano Lett* 12:1977–1982. <https://doi.org/10.1021/nl2045364>
- Cabán-Acevedo M, Liang D, Chew KS et al (2013) Synthesis, characterization, and variable range hopping transport of pyrite (FeS<sub>2</sub>) nanorods, nanobelts, and nanoplates. *ACS Nano* 7:1731–1739. <https://doi.org/10.1021/nn305833u>

- Campbell CT (1993) Promoters and poisons in the water-gas shift reaction. In: Chemical physics of solid surfaces. Elsevier, Amsterdam, pp 287–310
- Cao B, Veith GM, Neuefeind JC et al (2013) Mixed close-packed cobalt molybdenum nitrides as non-noble metal electrocatalysts for the hydrogen evolution reaction. *J Am Chem Soc* 135 (51):19186–19192. <https://doi.org/10.1021/ja4081056>
- Carpenter I, Edwards N, Ellis S et al (1999) On-board hydrogen generation for PEM fuel cells in automotive applications. *J PowerSources* 84:194–200
- Chen X, Shen S, Guo L, Mao SS (2010) Semiconductor-based photocatalytic hydrogen generation. *Chem Rev* 110:6503–6570. <https://doi.org/10.1021/cr1001645>
- Clarke SH, Dicks AL, Pointon K et al (1997) Catalytic aspects of the steam reforming of hydrocarbons in internal reforming fuel cells. *Catal Today* 38:411–423. [https://doi.org/10.1016/S0920-5861\(97\)00052-7](https://doi.org/10.1016/S0920-5861(97)00052-7)
- Cook TR, Dogutan DK, Reece SY et al (2010) Solar energy supply and storage for the legacy and nonlegacy worlds. *Chem Rev* 110(11):6474–6502. <https://doi.org/10.1021/cr100246c>
- Costamagna P, Srinivasan S (2001) Quantum jumps in the PEMFC science and technology from the 1960s to the year 2000. *J Power Sources* 102:242–252. [https://doi.org/10.1016/S0378-7753\(01\)00807-2](https://doi.org/10.1016/S0378-7753(01)00807-2)
- Deng Q, Moore RB, Mauritz KA (1995) Novel Nafion/ORMOSIL hybrids via in situ sol-gel reactions. 1. Probe of ORMOSIL phase nanostructures by infrared spectroscopy. *Chem Mater* 7:2259–2268. <https://doi.org/10.1021/cm00060a012>
- Ding Q, Meng F, English CR et al (2014) Efficient photoelectrochemical hydrogen generation using heterostructures of Si and chemically exfoliated metallic MoS<sub>2</sub>. *J Am Chem Soc* 136 (24):8504–8507. <https://doi.org/10.1021/ja5025673>
- Docter A, Lamm A (1999) Gasoline fuel cell systems. *J Power Sources* 84(2):194–200. [https://doi.org/10.1016/S0378-7753\(99\)00317-1](https://doi.org/10.1016/S0378-7753(99)00317-1)
- Duan X, Gao Z, Chang J et al (2013) CoS<sub>2</sub>–graphene composite as efficient catalytic counter electrode for dye-sensitized solar cell. *Electrochim Acta* 114:173–179. <https://doi.org/10.1016/j.electacta.2013.10.045>
- Faber MS, Jin S (2014) Earth-abundant inorganic electrocatalysts and their nanostructures for energy conversion applications. *Energy Environ Sci* 7:3519–3542
- Faber MS, Park K, Cabán-Acevedo M et al (2013) Earth-abundant cobalt pyrite (CoS<sub>2</sub>) thin film on glass as a robust, high-performance counter electrode for quantum dot-sensitized solar cells. *J Phys Chem Lett* 4:1843–1849. <https://doi.org/10.1021/jz400642e>
- Faber MS, Dziedzic R, Lukowski MA et al (2014) High-performance electrocatalysis using metallic cobalt pyrite (CoS<sub>2</sub>) micro- and nanostructures. *J Am Chem Soc* 136:10053–10061. <https://doi.org/10.1021/ja504099w>
- Feng Y, Alonso-Vante N (2008) Nonprecious metal catalysts for the molecular oxygen-reduction reaction. *Phys Status Solidi* 245:1792–1806. <https://doi.org/10.1002/pssb.200879537>
- Finch CA (1993) Ion exchangers Edited by K. Dorfner Walter de Gruyter & Co., Berlin & New York, 1991. pp. xxxi + 1495, price DM680. ISBN 0-89925-31 1-3 (USA) 3-1 1-010341-9 (Germany). *Polym Int* 30:282–282. <https://doi.org/10.1002/pi.4990300225>
- Fu Q, Weber A, Flytzani-Stephanopoulos M (2001) Nanostructured Au-CeO<sub>2</sub> catalysts for low-temperature water-gas shift. *Catal Lett* 77(1–3):87–95. <https://doi.org/10.1023/A:1012666128812>
- Ghenciu AF (2002) Review of fuel processing catalysts for hydrogen production in PEM fuel cell systems. *Curr Opin Solid State Mater Sci* 6:389–399. [https://doi.org/10.1016/S1359-0286\(02\)00108-0](https://doi.org/10.1016/S1359-0286(02)00108-0)
- Golunski S, Rajaram R, Hodge N et al (2002) Low-temperature redox activity in co-precipitated catalysts: a comparison between gold and platinum-group metals. *Catal Today* 72:107–113. [https://doi.org/10.1016/S0920-5861\(01\)00484-9](https://doi.org/10.1016/S0920-5861(01)00484-9)
- Gray HB (2009) Powering the planet with solar fuel. *Nat Chem* 1:7–7. <https://doi.org/10.1038/nchem.141>

- Gray PG, Frost JC (1998) Impact of catalysis on clean energy in road transportation. *Energy Fuel* 12:1121–1129. <https://doi.org/10.1021/ef980110f>
- Grot WG (1973) Laminates of support material and fluorinated polymer containing pendant side chains containing sulfonfyl groups
- Hagfeldt A, Boschloo G, Sun L et al (2010) Dye-sensitized solar cells. *Chem Rev* 110:6595–6663. <https://doi.org/10.1021/cr900356p>
- Haruta M, Daté M (2001) Advances in the catalysis of Au nanoparticles. *Appl Catal A Gen* 222:427–437. [https://doi.org/10.1016/S0926-860X\(01\)00847-X](https://doi.org/10.1016/S0926-860X(01)00847-X)
- Hilaire S, Wang X, Luo T et al (2001) A comparative study of water-gas-shift reaction over ceria supported metallic catalysts. *Appl Catal A Gen* 215:271–278. [https://doi.org/10.1016/S0926-860X\(01\)00535-X](https://doi.org/10.1016/S0926-860X(01)00535-X)
- Hu XD, Wagner JP (1999) Promoted and stabilized copper oxide and zinc oxide catalyst and preparation
- Huang Q-H, Ling T, Qiao S-Z, Du X-W (2013) Pyrite nanorod arrays as an efficient counter electrode for dye-sensitized solar cells. *J Mater Chem A* 1:11828. <https://doi.org/10.1039/c3ta12347b>
- Ivanovskaya A, Singh N, Liu R-F et al (2013) Transition metal sulfide hydrogen evolution catalysts for hydrobromic acid electrolysis. *Langmuir* 29:480–492. <https://doi.org/10.1021/la3032489>
- Iwasawa Y (1993) The effects of coadsorbates on the behaviour of surface species and sites in catalysis by means of EXAFS and FTIR. In: *Elementary reaction steps in heterogeneous catalysis*. Springer Netherlands, Dordrecht, pp 287–304
- Jaegermann W, Tributsch H (1988) Interfacial properties of semiconducting transition metal chalcogenides. *Prog Surf Sci* 29:1
- Jaramillo TF, Jørgensen KP, Bonde J et al (2007) Identification of active edge sites for electrochemical H<sub>2</sub> evolution from MoS<sub>2</sub> nanocatalysts. *Science* (80- ) 317(5834):100–102. <https://doi.org/10.1126/science.1141483>
- Jirkovský JS, Björling A, Ahlberg E (2012) Reduction of oxygen on dispersed nanocrystalline CoS 2. *J Phys Chem C* 116:24436–24444. <https://doi.org/10.1021/jp307669k>
- Kamat PV (2013) Quantum dot solar cells. The next big thing in photovoltaics. *J Phys Chem Lett* 4 (6):908–918
- Kariduraganavar MY, Nagarale RK, Kittur AA, Kulkarni SS (2006) Ion-exchange membranes: preparative methods for electrodialysis and fuel cell applications. *Desalination* 197:225–246. <https://doi.org/10.1016/j.desal.2006.01.019>
- Karunadasa HI, Montalvo E, Sun Y et al (2012) A molecular MoS<sub>2</sub> edge site mimic for catalytic hydrogen generation. *Science* (80- ) 335(6069):698–702. <https://doi.org/10.1126/science.1215868>
- Kibsgaard J, Jaramillo TF, Besenbacher F (2014) Building an appropriate active-site motif into a hydrogen-evolution catalyst with thiomolybdate [Mo<sub>3</sub>S<sub>13</sub>]<sub>2</sub>– clusters. *Nat Chem* 6:248–253. <https://doi.org/10.1038/nchem.1853>
- Klier K, Herman RG, Vedage GA (1991) Water gas shift reaction with alkali-doped catalyst
- Kong D, Cha JJ, Wang H et al (2013) First-row transition metal dichalcogenide catalysts for hydrogen evolution reaction. *Energy Environ Sci* 6(12):3553. <https://doi.org/10.1039/c3ee42413h>
- Kong D, Wang H, Lu Z, Cui Y (2014) CoSe<sub>2</sub> nanoparticles grown on carbon fiber paper: an efficient and stable electrocatalyst for hydrogen evolution reaction. *J Am Chem Soc* 136:4897–4900. <https://doi.org/10.1021/ja501497n>
- Lewis NS, Nocera DG (2006) Powering the planet: chemical challenges in solar energy utilization. *Proc Natl Acad Sci* 103:15729–15735. <https://doi.org/10.1073/pnas.0603395103>
- Li Y, Fu Q, Flytzani-Stephanopoulos M (2000) Low-temperature water-gas shift reaction over Cu- and Ni-loaded cerium oxide catalysts. *Appl Catal B Environ* 27:179–191. [https://doi.org/10.1016/S0926-3373\(00\)00147-8](https://doi.org/10.1016/S0926-3373(00)00147-8)

- Li L, Cabán-Acevedo M, Girard SN, Jin S (2014) High-purity iron pyrite (FeS<sub>2</sub>) nanowires as high-capacity nanostructured cathodes for lithium-ion batteries. *Nanoscale* 6:2112–2118. <https://doi.org/10.1039/C3NR05851D>
- Lukowski MA, Daniel AS, Meng F et al (2013) Enhanced hydrogen evolution catalysis from chemically exfoliated metallic MoS<sub>2</sub> nanosheets. *J Am Chem Soc* 135(28):10274–10277. <https://doi.org/10.1021/ja404523s>
- Lukowski MA, Daniel AS, English CR et al (2014) Highly active hydrogen evolution catalysis from metallic WS<sub>2</sub> nanosheets. *Energy Environ Sci* 7:2608–2613. <https://doi.org/10.1039/C4EE01329H>
- McKone JR, Warren EL, Bierman MJ et al (2011) Evaluation of Pt, Ni, and Ni-Mo electrocatalysts for hydrogen evolution on crystalline Si electrodes. *Energy Environ Sci* 4:3573–3583. <https://doi.org/10.1039/c1ee01488a>
- McKone JR, Sadtler BF, Werlang CA et al (2013) Ni-Mo nanopowders for efficient electrochemical hydrogen evolution. *ACS Catal* 3(2):166–169. <https://doi.org/10.1021/cs300691m>
- Mendelovici L (1985a) Methanation and water-gas shift reactions over Pt/CeO<sub>2</sub>. *J Catal* 96:285–287. [https://doi.org/10.1016/0021-9517\(85\)90381-1](https://doi.org/10.1016/0021-9517(85)90381-1)
- Mendelovici L (1985b) Reaction of ethylene with oxygen on a Pt/CeO<sub>2</sub> catalyst. *J Catal* 93:353–359. [https://doi.org/10.1016/0021-9517\(85\)90182-4](https://doi.org/10.1016/0021-9517(85)90182-4)
- Merki D, Fierro S, Vruble H, Hu X (2011) Amorphous molybdenum sulfide films as catalysts for electrochemical hydrogen production in water. *Chem Sci* 2:1262–1267. <https://doi.org/10.1039/C1SC00117E>
- Newsome DS (1980) The water-gas shift reaction. *Catal Rev* 21:275–318. <https://doi.org/10.1080/03602458008067535>
- Nocera DG (2012) The artificial leaf. *Acc Chem Res* 45(5):767–776. <https://doi.org/10.1021/ar2003013>
- Nørskov JK, Bligaard T, Logadottir A et al (2005) Trends in the exchange current for hydrogen evolution. *J Electrochem Soc* 152:J23. <https://doi.org/10.1149/1.1856988>
- Ovesen CV, Clausen BS, Hammershøi BS et al (1996) A microkinetic analysis of the water–gas shift reaction under industrial conditions. *J Catal* 158:170–180. <https://doi.org/10.1006/jcat.1996.0016>
- Pang H, Wei C, Li X et al (2014) Microwave-assisted synthesis of NiS<sub>2</sub> nanostructures for supercapacitors and cocatalytic enhancing photocatalytic H<sub>2</sub> production. *Sci Rep* 4:3577. <https://doi.org/10.1038/srep03577>
- Patt J, Moon DJ, Phillips C, Thompson L (2000) Molybdenum carbide catalysts for water–gas shift. *Catal Lett* 65:193–195. <https://doi.org/10.1023/A:1019098112056>
- Peighambaroust SJ, Rowshanzamir S, Amjadi M (2010a) Review of the proton exchange membranes for fuel cell applications. Elsevier Ltd
- Peighambaroust SJ, Rowshanzamir S, Amjadi M (2010b) Review of the proton exchange membranes for fuel cell applications. In: *Int J Hydrog Energy*. Pergamon, pp 9349–9384
- Peng S, Li L, Tan H et al (2014) MS<sub>2</sub> (M = Co and Ni) hollow spheres with tunable interiors for high-performance supercapacitors and photovoltaics. *Adv Funct Mater* 24:2155–2162. <https://doi.org/10.1002/adfm.201303273>
- Peppley BA, Amphlett JC, Kearns LM, Mann RF (1999) Methanol–steam reforming on Cu/ZnO/Al<sub>2</sub>O<sub>3</sub> catalysts. Part 2. A comprehensive kinetic model. *Appl Catal A Gen* 179:31–49. [https://doi.org/10.1016/S0926-860X\(98\)00299-3](https://doi.org/10.1016/S0926-860X(98)00299-3)
- Popczun EJ, McKone JR, Read CG et al (2013) Nanostructured nickel phosphide as an electrocatalyst for the hydrogen evolution reaction. *J Am Chem Soc* 135(25):9267–9270. <https://doi.org/10.1021/ja403440e>
- Popczun EJ, Read CG, Roske CW et al (2014) Highly active electrocatalysis of the hydrogen evolution reaction by cobalt phosphide nanoparticles. *Angew Chem Int Ed* 53(21):5427–5430. <https://doi.org/10.1002/anie.201402646>
- (1985) Process for the conversion of carbon monoxide by steam using a thioresistant catalyst

- Ren Y, Chia GH, Gao Z (2013) Metal–organic frameworks in fuel cell technologies. *Nano Today* 8:577–597. <https://doi.org/10.1016/J.NANTOD.2013.11.004>
- Rhodes C, Hutchings GJ, Ward AM (1995) Water-gas shift reaction: finding the mechanistic boundary. *Catal Today* 23:43–58. [https://doi.org/10.1016/0920-5861\(94\)00135-O](https://doi.org/10.1016/0920-5861(94)00135-O)
- Ridler DE (1996) *Catalyst handbook* (Twigg MV ed). Version details, Trove
- Rikukawa M, Sanui K (2000) Proton-conducting polymer electrolyte membranes based on hydrocarbon polymers. *Prog Polym Sci* 25:1463–1502. [https://doi.org/10.1016/S0079-6700\(00\)00032-0](https://doi.org/10.1016/S0079-6700(00)00032-0)
- Ruettinger W, Ilinich O, Farrauto RJ (2003) A new generation of water gas shift catalysts for fuel cell applications. *J Power Sources* 118:61–65. [https://doi.org/10.1016/S0378-7753\(03\)00062-4](https://doi.org/10.1016/S0378-7753(03)00062-4)
- Schiodt NC, Nielsen PE, Lehrmann P, Aasberg-petersen K (2001) Process for the production of a hydrogen rich gas
- Schneider M, Pohl J, Kochloeff K, Bock O (1986) Iron oxide-chromium oxide catalyst and process for high temperature water-gas shift reaction
- SE G, JM G, AF, JW J (1995) Metal oxide catalyst and use thereof in chemical reactions
- Seefeld S, Limpinsel M, Liu Y et al (2013) Iron pyrite thin films synthesized from an Fe(acac) 3 ink. *J Am Chem Soc* 135:4412–4424. <https://doi.org/10.1021/ja311974n>
- Selinsky RS, Ding Q, Faber MS et al (2013) Quantum dot nanoscale heterostructures for solar energy conversion. *Chem Soc Rev* 42:2963
- Services E (2000) *Fuel cell handbook*, 5th edn. EG&G Services Parsons, Morgantown
- Smitha B, Sridhar S, Khan AA (2005) Solid polymer electrolyte membranes for fuel cell applications—a review. *J Membr Sci* 259:10–26. <https://doi.org/10.1016/j.memsci.2005.01.035>
- Snell FD (1921) *Snell\_colorimetric analysis*. Von Norstrand Co, New York. <https://www2.humboldt.edu/scimus/Instruments/Color-Snell/ColorAnal.html>. Accessed 5 Sept 2019
- Society of Chemical Industry (Great Britain) (1998) *Chemistry and industry*. Society of Chemical Industry
- Strathmann H (1995) Chapter 6: electro dialysis and related processes. In: *Membrane science and technology*. Elsevier, Amsterdam, pp 213–281
- Sun Y, Liu C, Grauer DC et al (2013) Electrodeposited cobalt-sulfide catalyst for electrochemical and photoelectrochemical hydrogen generation from water. *J Am Chem Soc* 135:17699–17702. <https://doi.org/10.1021/ja4094764>
- Susac D, Zhu L, Teo M et al (2007) Characterization of FeS 2 -based thin films as model catalysts for the oxygen reduction reaction. *J Phys Chem C* 111:18715–18723. <https://doi.org/10.1021/jp073395i>
- Swartz BSL, Holt T, Dawson WJ (2001) Fuel processing catalysts based on nanoscale ceria. *Fuel Cells Bull* 4:7–10
- TROVARELLI A (1996) Catalytic properties of ceria and CeO 2 -containing materials. *Catal Rev* 38:439–520. <https://doi.org/10.1080/01614949608006464>
- Turner JA (2004) Sustainable hydrogen production. *Science* (80- ) 305:972–974. <https://doi.org/10.1126/science.1103197>
- Twigg MV, Spencer MS (2001) Deactivation of supported copper metal catalysts for hydrogenation reactions. *Appl Catal A Gen* 212:161–174. [https://doi.org/10.1016/S0926-860X\(00\)00854-1](https://doi.org/10.1016/S0926-860X(00)00854-1)
- Velu S, Suzuki K, Kapoor M et al (2001) Selective production of hydrogen for fuel cells via oxidative steam reforming of methanol over CuZnAl(Zr)-oxide catalysts. *Appl Catal A Gen* 213:47–63. [https://doi.org/10.1016/S0926-860X\(00\)00879-6](https://doi.org/10.1016/S0926-860X(00)00879-6)
- Vesborg PCK, Jaramillo TF (2012) Addressing the terawatt challenge: scalability in the supply of chemical elements for renewable energy. *RSC Adv* 2(21):7933–7947
- Voiry D, Yamaguchi H, Li J et al (2013) Enhanced catalytic activity in strained chemically exfoliated WS2 nanosheets for hydrogen evolution. *Nat Mater* 12:850–855. <https://doi.org/10.1038/nmat3700>
- Wainwright MS, Trimm DL (1995) Methanol synthesis and water-gas shift reactions on Raney copper catalysts. *Catal Today* 23:29–42. [https://doi.org/10.1016/0920-5861\(94\)00137-Q](https://doi.org/10.1016/0920-5861(94)00137-Q)

- Walter MG, Warren EL, McKone JR et al (2010) Solar water splitting cells. *Chem Rev* 110:6446–6473. <https://doi.org/10.1021/cr1002326>
- Wang Q, Jiao L, Han Y et al (2011) CoS<sub>2</sub> hollow spheres: fabrication and their application in lithium-ion batteries. *J Phys Chem C* 115:8300–8304. <https://doi.org/10.1021/jp111626a>
- Wang H, Lu Z, Xu S et al (2013a) Electrochemical tuning of vertically aligned MoS<sub>2</sub> nanofilms and its application in improving hydrogen evolution reaction. *Proc Natl Acad Sci U S A* 110:19701–19706. <https://doi.org/10.1073/pnas.1316792110>
- Wang YC, Wang DY, Jiang YT et al (2013b) FeS<sub>2</sub> nanocrystal ink as a catalytic electrode for dye-sensitized solar cells. *Angew Chem Int Ed* 52(26):6694–6698. <https://doi.org/10.1002/anie.201300401>
- Watanabe M (1996) Self-humidifying polymer electrolyte membranes for fuel cells. *J Electrochem Soc* 143:3847. <https://doi.org/10.1149/1.1837307>
- Xu T (2005) Ion exchange membranes: state of their development and perspective. *J Membr Sci* 263:1–29. <https://doi.org/10.1016/j.memsci.2005.05.002>
- Xu Y, Wu R, Zhang J et al (2013) Anion-exchange synthesis of nanoporous FeP nanosheets as electrocatalysts for hydrogen evolution reaction. *Chem Commun* 49(59):6656–6658. <https://doi.org/10.1039/c3cc43107j>
- Xue E, O’Keeffe M, Ross JRH (1996) Water-gas shift conversion using a feed with a low steam to carbon monoxide ratio and containing sulphur. *Catal Today* 30:107–118. [https://doi.org/10.1016/0920-5861\(95\)00323-1](https://doi.org/10.1016/0920-5861(95)00323-1)
- Zalc JM, Sokolovskii V, Löffler DG (2002) Are noble metal-based water–gas shift catalysts practical for automotive fuel processing? *J Catal* 206:169–171. <https://doi.org/10.1006/jcat.2001.3465>
- Zhao C, Li D, Feng Y (2013) Size-controlled hydrothermal synthesis and high electrocatalytic performance of CoS<sub>2</sub> nanocatalysts as non-precious metal cathode materials for fuel cells. *J Mater Chem A* 1:5741. <https://doi.org/10.1039/c3ta10296c>
- ZHU L, SUSAC D, TEO M et al (2008) Investigation of CoS<sub>2</sub>-based thin films as model catalysts for the oxygen reduction reaction. *J Catal* 258:235–242. <https://doi.org/10.1016/j.jcat.2008.06.016>

# Chapter 5

## Role of TiO<sub>2</sub> in Highly Efficient Solar Cells



**Anandhi Sivaramalingam, Shyju Thankaraj Salammal,  
Ananthakumar Soosaimanickam, Tamilselvan Sakthivel,  
Samuel Paul David, and Balaji Sambandam**

### Contents

5.1	Introduction to Thin-Film Solar Cells and Titania .....	148
5.1.1	How Do Solar Cells Work? .....	149
5.1.2	Various Forms of TiO <sub>2</sub> .....	150
5.2	Importance of Mesoporous TiO <sub>2</sub> in Photovoltaics and Its Mechanism in Photoanodes .....	151
5.3	Role of TiO <sub>2</sub> in Solar Cells .....	151
5.4	Role of TiO <sub>2</sub> in Highly Efficient DSSC .....	154
5.5	Role of TiO <sub>2</sub> in Highly Efficient Perovskite Solar Cells .....	157
5.6	Role of TiO <sub>2</sub> in Highly Efficient Metal Oxide Solar Cells .....	159

---

A. Sivaramalingam (✉)

Department of Physics, School of Science and Humanities, Sathyabama Institute of Science and Technology, Chennai, Tamilnadu, India

S. Thankaraj Salammal

Centre for Nanoscience and Nanotechnology, Sathyabama Institute of Science and Technology, Chennai, Tamilnadu, India

Centre of Excellence for Energy Research, Sathyabama Institute of Science and Technology, Chennai, Tamilnadu, India

A. Soosaimanickam

Institute of Materials Science (ICMUV), University of Valencia, Valencia, Spain

T. Sakthivel

Department of Materials Science and Engineering, University of Central Florida, Orlando, FL, USA

S. Paul David

HiLASE Centre, Institute of Physics of the Czech Academy of Sciences, Dolni Brezany, Czech Republic

Department of Physics, Kalasalingam Academy of Research and Education, Krishnankoil, Tamilnadu, India

B. Sambandam

Department of Materials Science and Engineering, Chonnam National University, Gwangju, South Korea

© The Editor(s) (if applicable) and The Author(s), under exclusive licence to Springer Nature Switzerland AG 2021

147

S. Rajendran et al. (eds.), *Metal, Metal-Oxides and Metal Sulfides for Batteries, Fuel Cells, Solar Cells, Photocatalysis and Health Sensors*, Environmental Chemistry for a Sustainable World 62, [https://doi.org/10.1007/978-3-030-63791-0\\_5](https://doi.org/10.1007/978-3-030-63791-0_5)

5.7	Role of TiO <sub>2</sub> in Highly Efficient Quantum Dot Solar Cells .....	161
5.8	Role of TiO <sub>2</sub> in Highly Efficient Tandem Solar Cells .....	162
5.9	Summary and Conclusion .....	163
	References .....	164

**Abstract** Titanium dioxide (TiO<sub>2</sub>) is a naturally occurring oxide of titanium. It has a wide range of applications. It has three metastable phases, which can be synthesized easily by chemical routes. Usage of TiO<sub>2</sub> in thin-film solar cells has gained much attention in increasing the performance of the cell. The objectives are to harvest the freely available earth's energy and to gain expertise in yielding a maximum conversion efficiency. Various strategies are employed to face the challenges in improving the efficiency of solar cells. This study provides a broad view of the usage of different forms of TiO<sub>2</sub> layers, like nanochannel, porous, nanotubes, and mesoporous layers, in enhancing electron injection between the layers. Various types include photoanodes in thin-film solar cells, perovskite cells, dye-sensitized solar cells, metal oxide solar cells, quantum dot solar cells, and tandem solar cells.

**Keywords** Perovskite solar cells · Mesopores · Titanium dioxide · Efficiency · Photovoltaics

## 5.1 Introduction to Thin-Film Solar Cells and Titania

Silicon-based solar cells are widely used in photovoltaic (PV) technology. Nanosized materials exhibit a much greater surface area for a given mass or volume compared to conventional particles (Chopra et al. 1983). Therefore, all applications involving surfaces and interfaces will benefit from nanosized particles, enhancing catalytic reactions and increasing interactions with surrounding media. In addition, new physical and chemical properties emerge when the size of the material is reduced to the nanometer scale, leading to quantum confinement effects, affecting the charge transport or causing bandgap energy shifts. Direct bandgap materials are attractive candidates for receiving maximum solar spectrum. Solar cells have hole-transporting layer and electron-transporting layer that aid in the movement of electrons in the cell. One of the main objectives is to produce cost-effective photovoltaic technology (Chopra et al. 2004). Due to its favorable electronic and optoelectrochemical properties of TiO<sub>2</sub>, it has been widely applied to solar cells, photocatalysts, lithium ion battery electrodes, smart coatings, etc. (Reyes et al. 2008).

Titanium dioxide, an n-type semiconductor, is one of those materials that have been applied to heterojunction solar cells as an electron transport layer because of its high efficiency, low cost, chemical inertness, and thermal- and photo-stability.

To enhance the conversion efficiency, many research works were undertaken by varying the methods and the potential raw materials. Figure 5.1 shows a view of p-n solar cell and its working principle. Recently, scientific and research communities have shown great interest in synthesizing titanium dioxide (TiO<sub>2</sub>) for device-grade



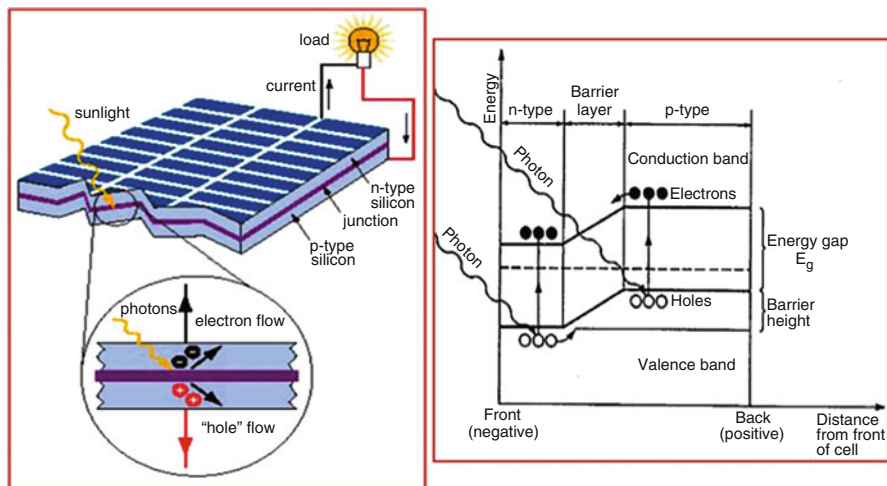


**Fig. 5.1** TiO<sub>2</sub> in dye-sensitized solar cells (DSSC) (Reprinted with permission from Varma 2015)

applications because of its excellent properties such as easy availability, nontoxicity, safety, and being environmentally friendly and cheap. Several excellent properties of TiO<sub>2</sub> are known, such as its chemical inertness, superior light-scattering characteristics, thermodynamic stability, better charge transport, lower conduction band (CB) edge position, large bandgap, easy processing in laboratory, etc.

TiO<sub>2</sub> exists in three crystal phases: anatase, rutile, and brookite. The anatase and rutile phases are well known and many studies on their synthesis, photocatalysis, and application as catalyst supports have been reported. Synthesized brookite TiO<sub>2</sub> was successfully used as a catalyst material. A photovoltaic (PV) cell is a device that converts sunlight into electricity using semiconductor materials. Solar-cell structures that employ TiO<sub>2</sub> as mesopores change the concept of two distinctive p and n layers conventionally used to form p–n junction devices (Rath 2003; Kuwahara and Yamashita 2011).

### 5.1.1 How Do Solar Cells Work?

A photovoltaic cell is a device that converts sunlight into electricity using semiconductor materials. Semiconductor materials enable electron flow when photons from sunlight are absorbed and eject electrons, leaving a hole that is filled by surrounding electrons. This phenomenon of electron flow by photon absorption is called the photovoltaic effect. The PV cell directs the electrons in one direction, which forms a current. The amount of current is proportional to the number of absorbed photons, which means that PV solar cells are a variable current source. Silicon was the first material used for the fabrication of solar cells. The semiconductor material, such as silicon, has the property to eject electrons when sunlight is absorbed; the PV cell then

direct the electrons in one direction. The challenges that are faced by photovoltaic cells are cost, efficiency, and operating lifetime. Monocrystalline PV cells are efficient and expensive than Si. The third-generation solar cells include concentrators and organic solar cells such as dye-sensitized solar cells (DSSC) (Andrew Stapleton 2017).

### 5.1.2 Various Forms of $TiO_2$

The three common phases of titanium dioxide are rutile (tetragonal), anatase (tetragonal), and brookite (orthorhombic). Rutile is the most stable form of titanium dioxide. Anatase and brookite are stable at normal temperatures but slowly convert to rutile upon heating to temperatures above 550 and 750 °C, respectively. All three forms of titanium dioxide have six coordinated titanium atoms in their unit cells. Both the more stable rutile and the metastable anatase structures are tetragonal. The anatase unit cell is more elongated. In the rutile form, the atoms occupy the least space. This makes the rutile form the most stable at higher temperatures (Lim et al. 2009; Kominami et al. 2000).

At very small particle dimensions, the surface energy of anatase is lower than those of rutile and brookite. The crystal structure stability has been explained on the basis of a molecular picture, where the nucleation and growth of the different polymorphs exist. The nanoparticle dimensions of phase-pure anatase, rutile, and brookite can be controlled over the synthesis methods (Hanaor and Sorrell 2011).

Table 5.1 shows a comparative study of the existing three forms. The conversion of one phase into another depends upon the synthesis procedure. Brookite is the least-studied titania phase, with experimental bandgap energies ranging from 3.1 to 3.4 eV. The bandgap increases in the order of rutile (1.44 eV), anatase (1.68 eV), and brookite (1.86 eV), and anatase is the only indirect semiconductor (Sun et al. 2019; Wu et al. 2014). In hydrothermal treatment, the anatase nanoparticles show a well-faceted crystal habit. The ordering of rutile nanomaterial has a complex morphology.

**Table 5.1** Comparative data of various forms of titania and their properties

Compound	Rutile	Anatase	Brookite
Molecules per unit cell (Z)	2	4	8
Crystal structure	Tetragonal	Tetragonal	Orthorhombic
Unit cell parameters			
a (Å)	4.58	3.78	9.184
b (Å)	4.58	3.78	5.447
c (Å)	2.95	9.78	5.145
Unit cell volume Å <sup>3</sup>	62.07	136.25	257.38
Density, g/m <sup>3</sup>	4.273	3.895	4.123
Bandgap(eV)	3.02	3.2	3.1
Mobility of electrons in thin film	0.1 cm <sup>2</sup> /Vs	0.1–0.4 cm <sup>2</sup> /Vs	–

A short-range ordering in amorphous material is observed in the vicinity of brookite nanoparticles obtained by a very different synthesis route. The anatase and brookite nanomaterials consist of porous aggregates, and are suitable for application in photocatalysis, sensors, and dye-sensitized solar cells (Kranz et al. 2015).

## 5.2 Importance of Mesoporous TiO<sub>2</sub> in Photovoltaics and Its Mechanism in Photoanodes

TiO<sub>2</sub> acts as a mesoporous photoanode, which has a micron thickness and acts as a light-scattering layer in the form of electrodes. In quantum dot (QD) solar cells, the usage of metal with TiO<sub>2</sub> acts as a photoanode (Zhang et al. 2017; Zhou et al. 2014). To increase the performance of solar cells, Ti photoanodes are implemented by immersing in CdSe-CH<sub>2</sub>Cl<sub>2</sub>, due to which the photoanodes get passivated (Baraton 2011). The combination of ligands and photoanodes improves the photoluminescence (PL) quantum yield of semiconductor particles by remediating nonradiative recombination centers located on particle surface. After loading quantum dot over the photoanodes, reducing the tunneling distance and energy barrier thereby promotes a good charge collection yield. The charge recombination at the interface of Ti/QD tends to be lower. The change of photoanode material should not induce a shift in the energy levels (Kuwahara and Yamashita 2011; Shen et al. 2018). When quantum dots are loaded over Ti substrate instead of Si substrate, there is an extra relaxation time. The mesoporous TiO<sub>2</sub> films increase the absorption of QDs (Khalid et al. 2017; Kominami et al. 2000). Pretreatment of TiO<sub>2</sub> photoanodes increases the loading of Quantum dots, which increases the performance of cell. QD agglomeration weakens the photovoltaic parameters (Ghicov and Schmuki 2009; Ali et al. 2018).

## 5.3 Role of TiO<sub>2</sub> in Solar Cells

TiO<sub>2</sub> is an n-type semiconductor used in solar cells. It acts as a photoanode (Szindler et al. 2017). The other forms, anatase and brookite nanomaterials, consist of porous aggregates and are suitable for application in photocatalysis, sensors, and dye-sensitized solar cells (Pushpa 2015; Govindasamy et al. 2016). Compared to other metal oxides, TiO<sub>2</sub> is a suitable candidate for optical applications because of its high chemical and optical stability, mechanical durability, nontoxicity, low cost, and corrosion resistance. Out of all other phases, the anatase structure is preferred over other polymorphs for solar applications due to its potential higher conduction band edge energy and lower recombination rate of electron–hole pairs. The physical and chemical properties of TiO<sub>2</sub> depend on size, shape, interfacial energy, and surface properties. TiO<sub>2</sub> has a high refractive index, which is suitable in antireflective

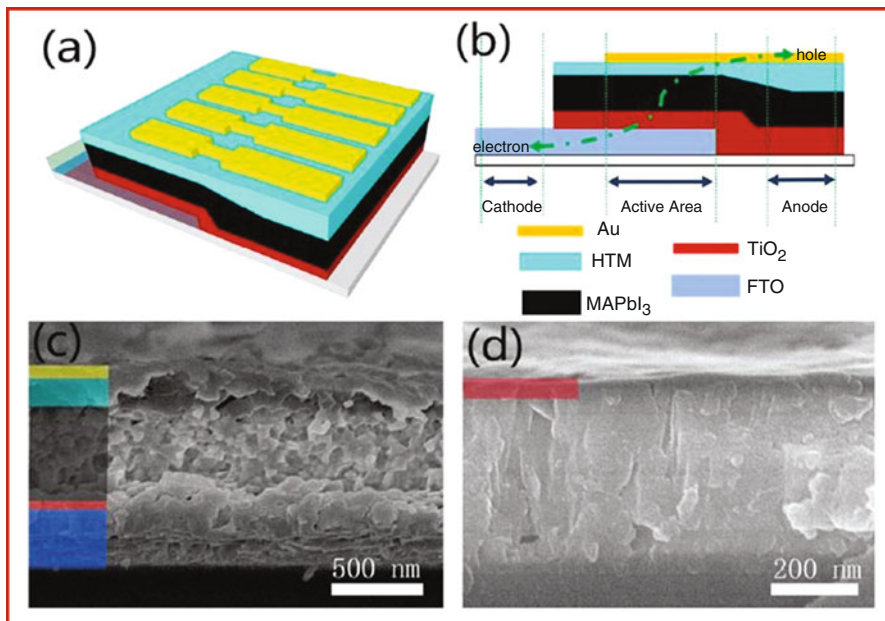


**Fig. 5.2** (a) Top view of a perovskite solar cell. (b) Schematic architecture of perovskite solar cell with  $\text{TiO}_2$  electron transport layer. (c, d) SEM images of the fabricated solar cell and the interface between  $\text{TiO}_2$  and FTO layer. (Reprinted with permission from Chen et al. 2015)

coatings for optical devices.  $\text{TiO}_2$  absorbs photons of nearly ultraviolet (UV) wavelengths to produce electron–hole pairs (Shriwastava and Singh 2016).

The perovskite solar cells have reached remarkable high efficiency of 19% for both mesoporous metal oxide scaffolds and planar heterojunction architectures. It acts as a potential light-harvesting material, with the desirable characteristics such as large absorption coefficient, high charge carrier mobility, and long diffusion length. Methods such as spray pyrolysis and spin-coating are implemented to fabricate the electron-collecting compact layer for planar heterojunction perovskite solar cells. Atomic layer deposition (ALD) has been used to fabricate compact layers for perovskite solar cells, but it requires a relatively long time and high cost for the thin film preparation. A one-step or two-step solution-processing method used to control crystallinity, morphology, and film uniformity. A planar heterojunction perovskite solar cells based on compact layer  $\text{TiO}_2$  electron transport layer results 12.1% with an open-circuit voltage ( $V_{\text{OC}}$ ) of 1.09 V was achieved. An average of 10.9% was obtained. Figure 5.2 (a, b) shows the schematic architecture of perovskite solar cells consisting of fluorine-doped tin oxide (FTO) transparent conductive anode, compact layer  $\text{TiO}_2$  electron transport layer. Figure 5.2(c) shows the cross-sectional scanning electronic microscopy (SEM) image of a well-constructed perovskite solar cell. Figure 5.2(d) shows the SEM image of the interface between  $\text{TiO}_2$  and FTO manifesting the infiltration of  $\text{TiO}_2$  into the FTO layer.

Chen et al. (2015) reported about the coating of TiO<sub>2</sub> on FTO substrate. The process was carried out using different sputtering time. The uneven surface prepared by spray pyrolysis or spin-coating with precursor solution may be due to the diffusibility and surface tension. The devices without the compact TiO<sub>2</sub> electron transport layer can be fabricated exhibits a low value as output. The short-circuit current density ( $J_{sc}$ ) and open-circuit voltage ( $V_{oc}$ ) values for perovskite solar cells are mainly based on TiO<sub>2</sub> and the hole-transporting polymer, spiro-OMeTAD. The estimated incident photon-to-current conversion efficiency measurement was also carried out for the devices based on TiO<sub>2</sub> with different thickness. TiO<sub>2</sub> electron transport layers were also deposited on PET/ITO substrate by different techniques to fabricate flexible perovskite solar cells. In the assembly of the perovskite solar cells, TiO<sub>2</sub> target was sputtered and spin coated, monitored by the film-thickness meter.

The mesoporous scaffold of a metal oxide such as TiO<sub>2</sub> can be deposited on a perovskite layer which forms a good photovoltaic (PV) structure. The presence of these metal oxides confines the charge carriers within the layers. On fabrication, these metal oxides over the perovskite layer act as a good electron-hole transporting layer for efficient organic photovoltaics cell. Figure 5.2 (b) illustrates electron-hole pair formation and its transport. The perovskite film has remarkably low energetic disorder which favors the efficient performance in PV devices. The pattern yielded reasonable power conversion efficiency ( $\eta$ ) of 8%. The observation of low electroluminescence (EL) is due to non-confinement of charge carriers. The reports clearly picturize the presence of spiral metal oxide layer with perovskite-polymer heterointerface which provides a promising path for future enhancement. Under forward bias, electrons are injected from the cathode and holes are injected from the MoO<sub>x</sub>-coated ITO anode, and the device yields emission of the injected electrons from the LUMO to the conduction band of perovskite. The transfer of injected holes from the valence band of perovskite to the HOMO results in electron-hole recombination at the perovskite interface, followed by energy transfer results in spectral overlap of emission was reported by Aditya Sadhanala et al. (2015).

The observations provide a thorough investigation of electron-hole recombination dynamics in perovskite materials interfaced with metal oxide and its usage in heterointerface of multilayer optoelectronic devices. Figure 5.3 shows the schematic of perovskite device and energy level diagram of perovskite solar cells (a, b). Together with this, SEM image of the cross section of the fabricated device is given (Fig. 5.3 (c)). Infrared emission from a single perovskite conjugated polymer PV diodes, with a control of the recombination between the perovskite and the hole transport polymer layer. This work clearly depicts the electroluminescent recombination zone near the perovskite polymer heterointerface and the charge carrier recombination mechanism inside PVs and LEDs. The process of tuning the optical bandgap of perovskite-metal oxide-based material are considered as a promising future materials in the field of PV.

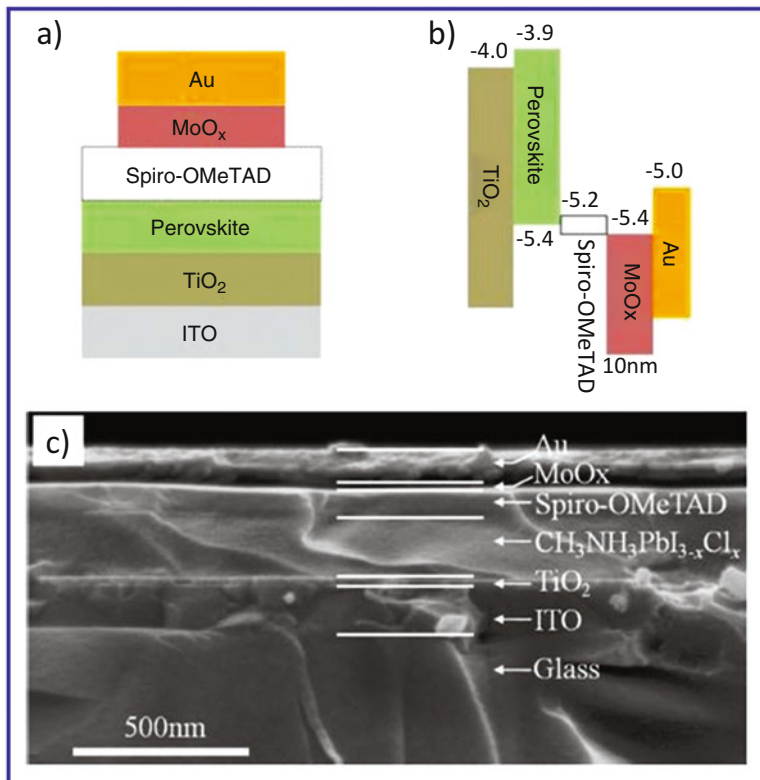


**Fig. 5.3** (a) The schematic of PV device. (b) Energy level diagram. (c) SEM micrograph. (Reprinted with permission from Sadhanala et al. 2015)

#### 5.4 Role of $\text{TiO}_2$ in Highly Efficient DSSC

The dye-sensitized solar cells (DSSC) provide an alternative concept to a normal, present-day p-n junction photovoltaic devices. DSSC is convenient to fabricate, has low cost, and has high power-conversion efficiency (Sun et al. 2018; Nair et al. 2011). DSSC contains a combination of dye-sensitized transparent conducting substrate, semiconductor film (such as titanium dioxide [ $\text{TiO}_2$ ], zinc oxide [ $\text{ZnO}$ ], tin dioxide [ $\text{SnO}_2$ ], Niobium pentoxide [ $\text{Nb}_2\text{O}_5$ ]), electrolyte, and counter electrode (Fan et al. 2017; Li et al. 2013). The heart of the DSSC is the mesoporous oxide containing  $\text{TiO}_2$  nanoparticles as a roadway for the electrons to cross from the cathode to the anode; it is doped with a dye for absorbing the photons (Salman et al. 2017; Opara Krasovec et al. 2009). The oxide layer allows electronic conduction to take place.  $\text{TiO}_2$  semiconductivity is as electrode in dye-sensitized solar cells (DSSCs) in which the high surface-to-volume ratio of the nanostructured semiconductor is required to obtain an acceptable power-conversion efficiency. Attached to

the oxide monolayer is the charge transfer dye (Jo et al. 2019). Photo excitation results in the injection of electron into the conduction band of the oxide. A photon-induced electron–hole pair has been observed at the junction (Mao et al. 2016).

TiO<sub>2</sub> in DSSC has achieved efficiency of the order of 11%. In the case of inorganic solid-state photovoltaics, the approach of host-guest is attractive, TiO host with CdTe guest. It results in smaller voids and higher diffusion.



The rate of light harvesting and electron transport is more efficient in DSSC when compared to other types of cells. The performance of solar cell is greatly influenced by electron transport. The dye molecules attach to the oxide monolayer and involves in the charge transfer process (Mnu et al. 2019).

Photo excitation of dye results in the injection of electron into the conduction band of the oxide. Consequently, a photon-induced electron-hole pair has been observed at the junction (Xiaoli et al. 2016).

$$\eta_{\text{overall}} = (J_{\text{sc}} \times V_{\text{oc}} \times \text{FF}) / (I_s) \quad (5.3)$$

A modern type of DSSC cell is the Gratzel cell that has a porous layer of titanium dioxide covered with a dye, which absorbs sunlight. When sunlight passes through the dye layer, it excites electrons that flow toward TiO<sub>2</sub> electrode is later collected by load. In the dye-sensitized solar cell, a nanometer dye molecule present captures a reasonable amount of incoming sunlight.

Dye-sensitized solar cells based on titanium dioxide (TiO<sub>2</sub>) offer high conversion efficiency but suffer from durability; to overcome that, an organic liquid electrolyte has been substituted. Figure 5.4 shows the usage of TiO<sub>2</sub> in DSSC. It leads to corrosion effects. Replacement of electrodes results in lower efficiency in DSSC cells. In a typical dye-sensitized solar cell CsSnI<sub>3</sub> with a nanoporous TiO<sub>2</sub>, N719 dye with a tunable bandgap of 1.3 eV is used to a produce a conversion efficiency of 10.2%. CsSnI<sub>3</sub> is soluble in polar organic solvents, such as acetonitrile, *N,N*-dimethylformamide, and methoxy acetonitrile, which acts as a good hole producer in the liquid electrolyte (Li et al. 2013). On further doping of CsSnI<sub>3</sub> with F and SnF<sub>2</sub>, it dramatically improves the photocurrent density ( $J_{\text{sc}}$ ) and power-conversion efficiency ( $\eta$ ). The dye-sensitized solar cells (DSSCs) were assembled by using natural dyes extracted from black rice, capsicum, *Erythrina variegata* flower, *Rosa xanthina*, and kelp as sensitizers. They have a better interaction with the surface of TiO<sub>2</sub> film (Fan et al. 2017; Khalid et al. 2017).

The photocurrent from natural dye-sensitized solar cell *Monascus* yellow extracted from *Monascus* fermentations (red yeast rice) is effective and yields an energy-conversion efficiency of 2.3% (Hayat et al. 2018; Zie and Zainab 2017). To have high-efficiency DSSCs, TiO<sub>2</sub> layer is essential for harvesting large amount of sun's source. To have high-efficiency DSSCs, a high surface area of TiO<sub>2</sub>

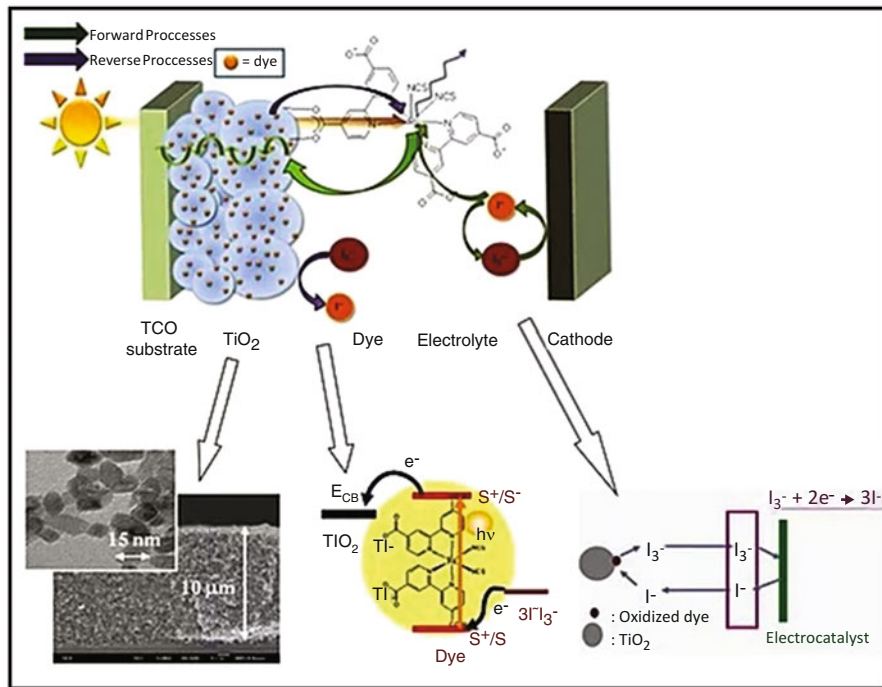


**Fig. 5.4** TiO<sub>2</sub> in dye-sensitized solar cells (DSSC). (Reprinted with permission from [http://freeopt.wixsite.com/skang/dssc\(2014\)](http://freeopt.wixsite.com/skang/dssc(2014)))

nanostructure is essential. It supports harvesting light radiation on a large scale. Besides, a good connection between the TiO<sub>2</sub> grains and a good adhesion transparent conducting oxide (TCO) assure good electrical conductivity. The optimization of the morphology of TiO<sub>2</sub> layer is a prerequisite for the efficiency of solar cells. TCO is treated with aqueous solution of TiCl<sub>4</sub>, to form a compact layer of nanoparticles TiO<sub>2</sub>. Even TiO<sub>2</sub> is used as a paste followed by annealing, which also shows an effective efficiency in DSSC. The efficiency of DSSC depends on the mixture of electrolytes and improved electron transport due to TiO<sub>2</sub>. The TiO<sub>2</sub> paste was prepared by mixing the TiO<sub>2</sub> powder and sol in mortar grinder for 1 h. Later, the paste was deposited on transparent conduction electrode.

Then, it is immersed in dye for the sensitization under a fixed period of time, and the device structure is completed with an electrolyte and the counter electrode, which is usually a platinum electrode. Figure 5.5 shows the usage of different metal oxides and its efficiency. The usage of dye with various metal oxide and its efficiency has been reported by Kim and Kwon (2011). The overall conversion efficiencies of DSSCs increased when CdO, ZnO, NiO, and CuO were used as the blocking layer material.



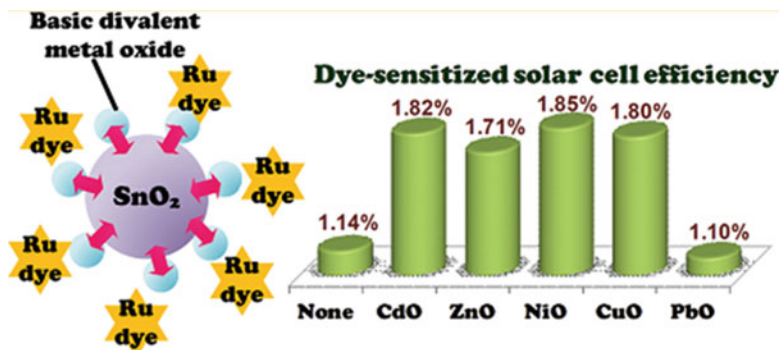


Fig. 5.5 Various metal oxides used for the DSSC and its efficiency. (Reprinted with permission from Kim and Kwon 2011)

## 5.5 Role of TiO<sub>2</sub> in Highly Efficient Perovskite Solar Cells

Perovskite solar cells nowadays are an interesting topic of research in the field of photovoltaics (Zheng et al. 2017; Kanhere and Chen 2014). Their fascinating attractive properties are broad absorption spectrum, fast charge separation, long transport distance of electrons and holes, and long carrier separation lifetime (Ganguly et al. 2015). Perovskite PVs are constantly undergoing research and improvement, going from just 2% in 2006 to over 20.1% in 2015. Also, it offers additional attributes like flexibility, semi-transparency, thin-film, light-weight, and low processing costs (Lee et al. 2017). Perovskite solar cells were fabricated using mesoporous TiO<sub>2</sub> layer (Etgar et al. 2012; Varma 2015; Xia et al. 2016) as a hole-transporting layer (Cheng and Lin 2010). Perovskite structure has the general structure as ABO<sub>3</sub>, where A and B are of cations with different sizes and O is the anion (Govindasamy et al. 2016). The A site cation is slightly larger than the B cation. The B atom has sixfold coordination number and the A atom has 12-fold coordination number perovskite solar cells (Yamada et al. 2014; Yin et al. 2016; Su et al. 2017).

The perovskite layer made up of methylammonium lead triiodide acts as a good absorber. The nanometer-sized methylammonium lead bromide (MAPbBr<sub>3</sub>) was tailored over a mesoporous TiO<sub>2</sub> layer, which results in hybrid perovskite solar cells; plus, they extract the electrons from the light-absorbing layer, which transports to the electrode (Murugadoss et al. 2014). Titanate perovskite shows excellent photocatalytic properties under UV radiation. Certain titanate perovskites have negative conduction band (CB) potential, which is useful for hydrogen reduction. Titanates offer good photostability and corrosion resistance. TiO<sub>2</sub> is a good mediator for carrier transport. When photoexcited the electrons will move to the CB of TiO<sub>2</sub>, while the holes will move to the valence band (VB) of the hole transport material (HTM) layer. For perovskite solar cells, a mesoporous TiO<sub>2</sub> network is essential for transporting charges to the collecting electrode (Xia et al. 2016). TiO<sub>2</sub> is an n-type

semiconductor with suitable electronic band levels that increase the ability of electron injection. The tasks of an mp-TiO<sub>2</sub> layer in the perovskite cells are: (i) to separate electrons and holes in the perovskite layer by electron injection to the TiO<sub>2</sub> layer, and (ii) to transport the injected electrons to the electrode. Optimizing the mp-TiO<sub>2</sub> thickness, the output voltage varies by changing the charge injection (Wu et al. 2014; Lee et al. 2017).

The typical device structure of a perovskite solar cell consists of ITO/p-type material/perovskite/n-type material/metal electrode. Here, TiO<sub>2</sub> is mainly used due to the chemical stability, low-cost and high charge transportability. An electron can be effectively transported from perovskite absorber to TiO<sub>2</sub> due to the presence of minimum conduction band of TiO<sub>2</sub>. Furthermore, TiO<sub>2</sub> results in blocking hole capability due to the presence of valence band maximum is lower than perovskite absorber. Presence of TiO<sub>2</sub> in perovskite solar cells can be subdivided as mesoporous-structured TiO<sub>2</sub> layer and TiO<sub>2</sub> compact layer. By pulsed laser deposition, TiO<sub>2</sub> can be deposited to fabricate the perovskite solar cells at low temperature. Table 5.2 lists out the properties of TiO<sub>2</sub>-electron extraction/transporting layer deposited at low temperature (Xia et al. 2016; Chen et al. 2016).

By using laser, sublimation occurs resulting in the deposition of TiO<sub>2</sub> layers. The formation of TiO<sub>2</sub> array can be obtained by chemical bath deposition method. The light-harvesting efficiency of the perovskite-coated TiO<sub>2</sub> array increases with increasing chemical bath deposition, reaction time, and rate. The formation of TiO<sub>2</sub> nanorods in anatase phase results in a higher rate of light-harvesting property.

The mesoporous TiO<sub>2</sub> layer is fabricated by spin-coating method followed by UV treatment. It yields a satisfied efficiency of 18.2%. The presence of trap states at perovskite absorber and the interface can hinder the photovoltaic performance. On passivating the perovskite absorber/electron extraction layer interface can proficiently suppress deep trap states. This type of planar perovskite solar cells has exhibited an efficiency of 20%. Researchers are exploiting alternate materials to replace TiO<sub>2</sub> using ZnO and SnO<sub>2</sub> as an electron extraction layer for PSC due to its electron mobility, suitable energy structure, and high conductivity.

**Table 5.2** List of the properties of TiO<sub>2</sub>-electron extraction layer deposited at low temperature

Device structure	EEL	temp. (°C)	Deposition method	J <sub>sc</sub>	V <sub>oc</sub>	FF	PCE %	References
n-i-p	TiO <sub>2</sub>	80	Chemical bath deposition	22	0.99	72.0	15.7	Chen et al., 2016
		120	Thermal Evaporation	21.3	1.07	84.0	19.1	Schulze et al., 2017
		150	Spin-Coating	22.3	1.19	80.6	21.4	Tan et al., 2017
		200	Pulse laser Deposition	20.1	1.01	69.0	14.1	Yang et al., 2016

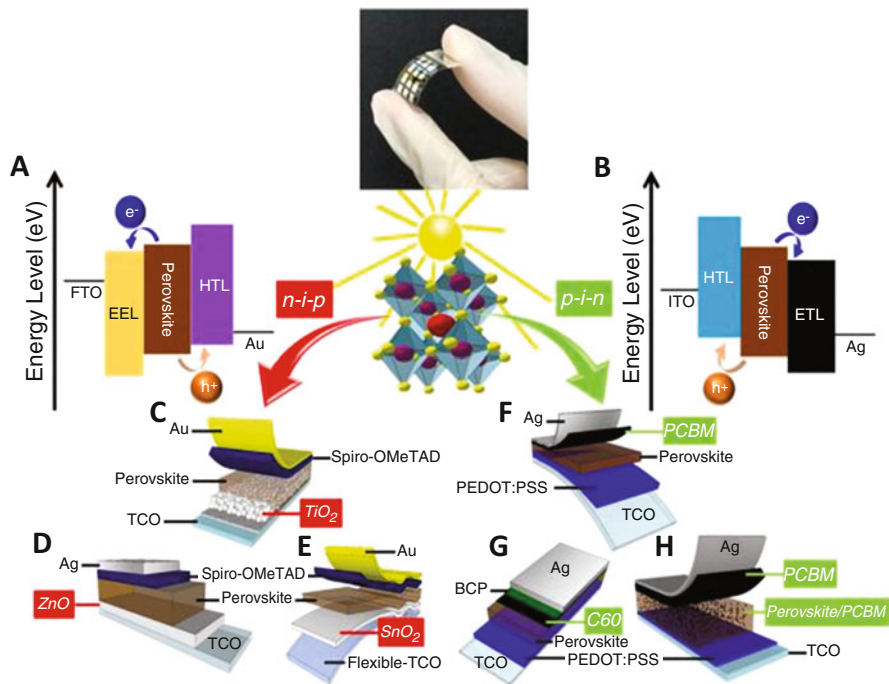


**Fig. 5.6** Schematic diagram of (a, b) energy level and (c–h) device structure of perovskite solar cells prepared by low-temperature process (Chan et al. 2019)

## 5.6 Role of TiO<sub>2</sub> in Highly Efficient Metal Oxide Solar Cells

TiO<sub>2</sub> is used in metal oxide solar cell, which acts as a source of energy-harvesting system. The device, which is made of conventional semiconductor with narrow bandgap, absorbs a broad wavelength (Bai et al. 2014). The porous TiO<sub>2</sub> acts as photoanode with large surface area causing good absorption. Photovoltaic cells built using nonporous TiO<sub>2</sub> with heterostructure II–VI semiconductors have increased an efficiency of 3.37%. Figure 5.7 (A & B) shows TiO<sub>2</sub> in solar cell and the mechanism of increased photoconductivity.

Among other new materials, TiO<sub>2</sub> is preferred due to its chemical inertness, eco-friendliness, photostability, thermodynamic stability, better charge transport (Diguna et al. 2007), lower conduction band edge position, and large bandgap (Su and Zhou 2011; Etggar 2013).

All devices with metal oxides show improved efficiencies like the parameters, the short circuit current ( $J_{sc}$ ), the open-circuit voltage ( $V_{oc}$ ) and the fill-factor (FF) are increased, resulting in higher efficiency. Well dispersed, probably, on the surfaces of the TiO<sub>2</sub> nanoparticles modifies all the parameters. The presence of metal oxide

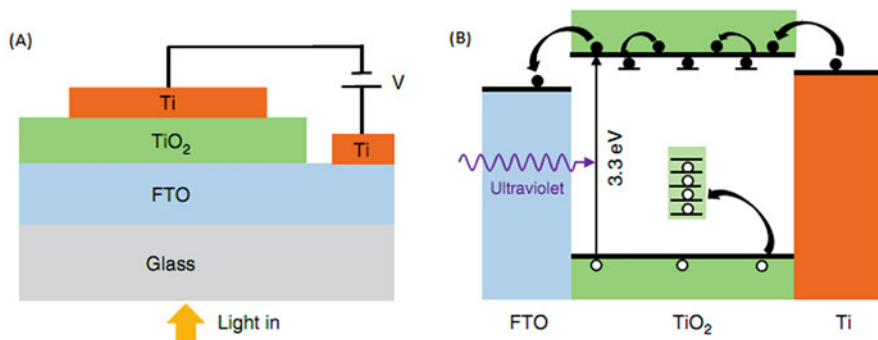


**Fig. 5.7** (A) Schematic of  $\text{TiO}_2$  thin film. (B) A schematic of the mechanism of photoconductivity in the  $\text{TiO}_2$  thin film. (Reprinted with permission from Yanbo Li et al. 2016)

enhances protonation and deprotonation, which effects the surface properties (Kim and Kwon 2011, Yanbo Li et al. 2016).

Figure 5.5 shows the usage of various metal oxides in perovskite solar cells at different configurations such as n-i-p and p-i-n with different energy levels.

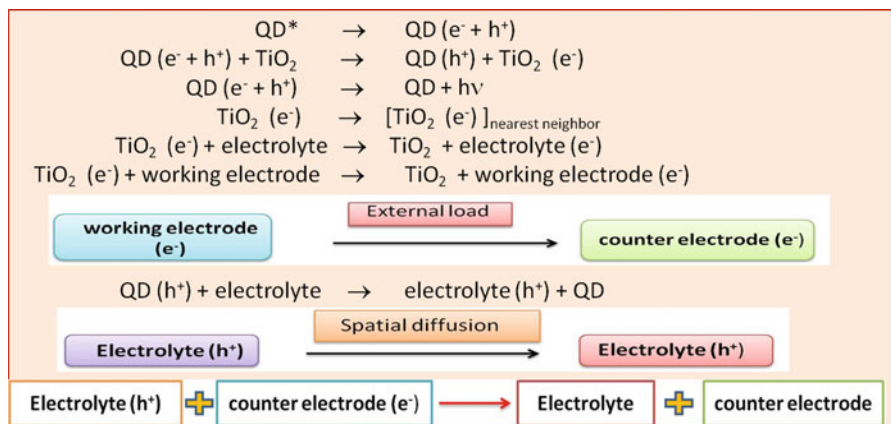
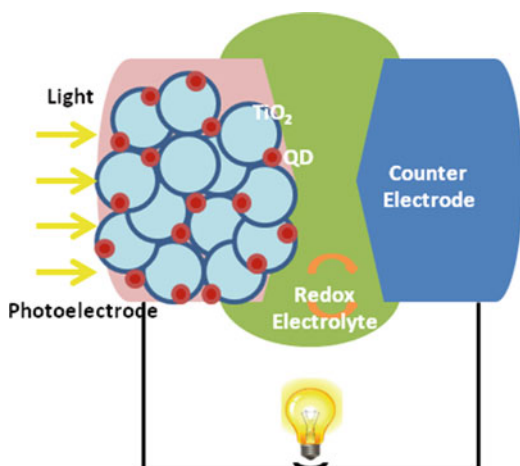
The effect of metal oxide layers on the recombination dynamics open-circuit voltages after turning off the light. In other words, the presence of metal oxides is a direct measure of the recombination reaction rate. The life time of these cells are also longer. The charge-transfer resistance at the interface of electrolyte depends upon the electron lifetime for the recombination. The presence of metal oxide with semiconducting nature acting as an electron transporting layer. The possibility of the presence of trap sites at the pn junction creates resistance at the interface thereby increasing the fill factor. The usage of various metal oxide and its efficiency has been reported by Kim and Kwon (2011). The overall conversion efficiencies of DSSCs increased when CdO, ZnO, NiO, and CuO were used as the blocking layer material.

The transparent photovoltaic is also possible by using  $\text{TiO}_2$  layer. p-type and n-type form a heterojunction. Ultrathin layer of embedded  $\text{TiO}_2$  results in highly transparent solar cell. Under UV illumination, transparent solar cells provide a conversion efficiency of 6.1% (Hoye et al. 2013). Transparent photovoltaics are mainly applied in electronic devices and photoelectronic devices. Insertion of ultrathin  $\text{TiO}_2$  at the back contact of all types of oxide based transparent photovoltaic solar cells. All types of metal oxide junction absorb abundant amount of light produces electric power from the Sun. The presence of  $\text{TiO}_2$  enhances the performance like high photovoltage in the case of transparent metal oxide solar cells.

## 5.7 Role of TiO<sub>2</sub> in Highly Efficient Quantum Dot Solar Cells

Quantum dot solar cells have a similar structure and working principles as DSSC; the size of quantum dot is larger than a dye molecule (Nadrah et al. 2015; Guijarro et al. 2009). The dye molecules get fixed with Ti, which acts as a substrate. QD deposited on Ti electrodes increases the injection rate through different approaches such as chemical bath deposition (CBD), successive ionic layer absorption and SILAR. A linker has been used between Ti and QD, which increases the driving force between the ligands. The metal ions in association with TiO<sub>2</sub> promote the efficiency of the solar cells. The working of quantum dot solar cells is very similar to DSSC. Figure 5.8 shows a TiO<sub>2</sub> quantum dot solar cell. The electron transfer kinetics

**Fig. 5.8** Structure of a quantum dot solar cell



between Ti and QD leads to a better cell performance (Yaacob et al. 2013; Das and Baruah 2018).

Quantum dots are less at risk to photodegradation than organic dyes; hence, it is more favorable than other types. The mechanism involved in the working of all types of DSSC.

Mechanism of a QD solar cell quantum dots exhibit higher photoconversion efficiency. It maximizes the capturing ability of the incident light and transmits electrons through network. The network enable faster electron injection rate through the small-sized particles with greater absorption rate (Nguyena et al. 2019).

## 5.8 Role of TiO<sub>2</sub> in Highly Efficient Tandem Solar Cells

Tandem solar cells have two sections, one with a wide bandgap and other with a narrow bandgap acting as an absorber layer. When light pass through the wide bandgap layer, photons with energy greater than the energy gap  $E_{g1}$  would be absorbed. The remaining photons less than  $E_{g1}$  would be transmitted. Again the second segment absorbs photons with energy greater than  $E_{g2}$ . The presence of two segments utilizes maximum solar energy thereby reducing thermalization loss. In general, there are two-terminal (2T) and four-terminal (4T) tandem devices. In four-terminal configuration, the presence of two subcells is complete solar cells simply stacked together with a transparent back contact. In the case to two terminal tandem cells, the presence of two subcells is stacked electrically. The four-terminal tandem solar cells fabricated independently there is no difference between the junctions. It is optically coupled provided with a transparent back contact. In the case of 2T tandem solar cells, the two subcells are connected electrically and optically without any back contact. Improving better light coupling property with reduced loss improves the use of the choice of wide or narrow bandgap.

The potential of spectrum splitting for ultrahigh performance using Si solar cells has been observed in tandem solar cells (Shen et al. 2018). Aim is to increase absorption coefficient of TiO<sub>2</sub>, which acts as a top layer that enhances the rate of absorption (Sheng et al. 2015; Kao et al. 2015). Figure 5.9 shows the structure of a tandem solar cell. Tandem solar cells can have more than two electrically coupled junctions, in which each junction has different  $E_g$ . With two junctions, it has high  $E_g$  of anode and cathode. The charge carriers move from top to bottom and maintain the charge neutrality. Here, band-to-band tunneling occurs at the recombination region (Kanda et al. 2016).

In the case of perovskite-polymer-based tandem solar cells, perovskite serves as a wide bandgap absorber and polymer acts as a narrow bandgap absorber with active layers from solution-solvent precursor. The deposition strategies also involve the formation of interfacial layers by spin coating technique with different solvents. The role of TiO<sub>2</sub> in tandem solar cells, The perovskite subcell has a top layer of TiO<sub>2</sub> by atomic layer deposition followed by the formation of mesoporous TiO<sub>2</sub> layer. The electrons generated are extracted by TiO<sub>2</sub> and transported which recombines with

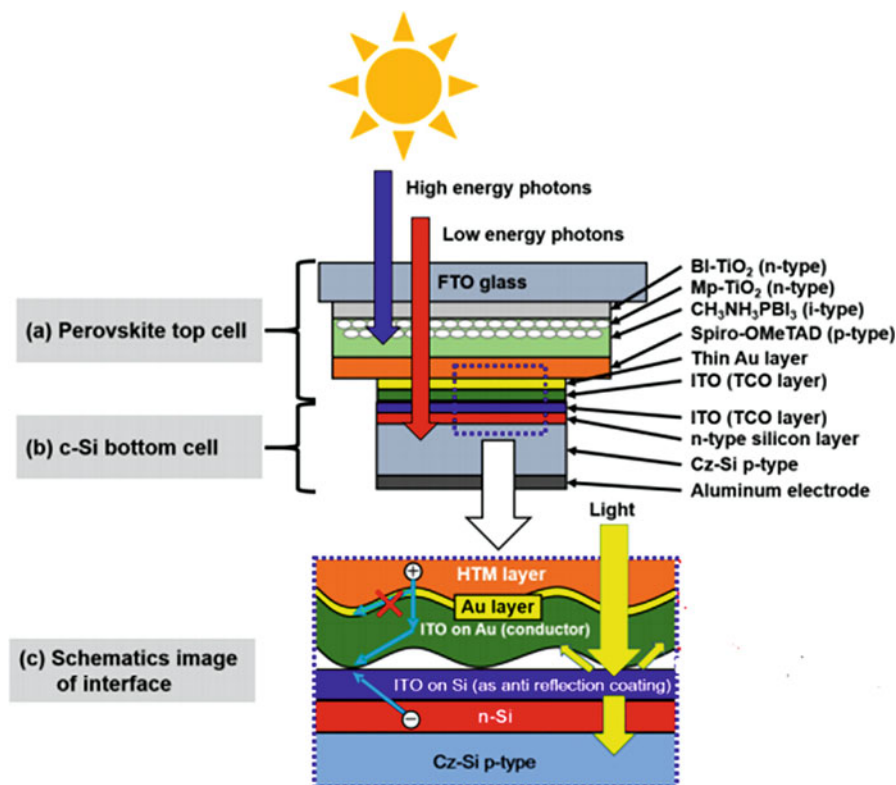


**Fig. 5.9** Tandem solar cell structure with TiO<sub>2</sub> thin film. (Reprinted with permission from Kanda et al. 2016)

the holes in the subcell. In the case of perovskite-polymer-based (2T) tandem solar cells, generates a power conversion efficiency of 13.7%. Can and co-workers demonstrated perovskite-nanocrystalline silicon tandem solar cells. The generated electrons in the perovskite subcell recombine with holes in the tunnel junction generates the current flow in the tandem cell (Cao et al. 2020). The reports reveal the gain of power conversion efficiency of 22.7% on 0.25 cm<sup>2</sup>.

## 5.9 Summary and Conclusion

Titanium dioxide or titania (TiO<sub>2</sub>) occurs in three phases. Mostly it exists as rutile and anatase phases; nanostructured layers of TiO<sub>2</sub> help in the formation of photo-generated electrons that enhance light harvesting. To date, numerous materials show excellent properties to satisfy the need. TiO<sub>2</sub> as an electron transporter at the semiconductor interface offers excellent property to enable maximum light

absorption resulting in photo-generated charge carriers. Titanate perovskite shows a potential photostability useful for visible light photocatalysis. In the case of metal oxide semiconductors, the usage of titanium dioxide increases the photocurrent with good performance of the fabricated solar cell. It acts as an efficient electron-transporting layer in the case of quantum dot solar cells.  $\text{TiO}_2$  acts as a photoanode layer that enhances faster electron injection rate, which results in the better performance of quantum dot semiconductor solar cells. DSSCs using natural pigments have  $\text{TiO}_2$  as a conducting layer. When semiconductor of suitable bandgap combines with this, it results in high electron injection rate. It helps to reduce the defect state thereby leading to attractive light-harvesting property. It increases the photocurrent by improving the cell efficiency. Hybrid perovskite solar cells possess  $\text{TiO}_2$  as a mesoporous layer. The electron injection and transport properties of the above-said layer influence the photovoltaic property of the cell. The pores over the Ti matrix improve the performance of perovskite solar cells. Tandem solar cells show higher conversion efficiency when compared to other types. It has different junctions that act as its own anode and cathode. Improving single junction solar cell, we go for tandem solar cells provided with suitable energy bandgap. As of today, commercialization of solar cells with new organic/inorganic species is a challenging task to obtain an increased solar cell efficiency. Remarkable progress occurs every day in the processing techniques, optimizing the bandgap, and formation of nano multi-layers over the substrate. It has been proved that  $\text{TiO}_2$  is as one of the potential candidates that is used as electron injection layer, good light harvester, etc. More advantageous analysis of  $\text{TiO}_2$  for the future-generation solar cells will be beneficial for improving the efficiency in this field.

**Acknowledgment** One of the authors (Anandhi) greatly acknowledges the support given by the management members of Sathyabama Institute of Science and Technology during this course of work.

## References

- Ali AK, Ela SE, Hassoon KI, Ela C, Ahmed DS (2018) Design of high-efficiency tandem dye-sensitized solar cell with two-photoanodes toward the broader light harvesting. *Dig J Nanomater Biostruct* 13(1):299–305
- Bai Y, Mora-Sero I, De Angelis F, Bisquert J, Wang P (2014) Titanium dioxide nanomaterials for photovoltaic applications. *Chem. Rev* 114(19):10095–10130. <https://doi.org/10.1021/cr400606n>
- Baraton M-I (2011) Nano- $\text{TiO}_2$  for solar cells and photocatalytic water splitting: scientific and technological challenges for commercialization. *Open Nanosci J* 5:64–77
- Bett AJ, Schulze PSC, Winkler K, Gasparetto J, Ndione PF, Bivour M, Hinsch A, Kohlstä M, Lee S, Mastroianni S, Mundt LE, Mundus M, Reichel C, Richter A, Veit C, Wienands K, Würfel U, Veurmana W, Glunz SW, Hermle M, Goldschmit JC (2017) Low temperature perovskite solar cells with an evaporated  $\text{TiO}_2$  compact layer for perovskite silicon tandem solar cells. *Energy Procedia* 124:567–576



- Cao Z, Li C, Deng X, Wang S, Yuan Y, Chen Y, Wang Z, Liu Y, Ding L, Hao F (2020) Metal oxides alternatives for efficient electron transport in perovskite solar cells: beyond TiO<sub>2</sub> and SnO<sub>2</sub>. *J Mater Chem A*. <https://doi.org/10.1039/D0TA07282F>
- Chan S-H, Chang Y-H, Wu M-C (2019) High-performance perovskite solar cells based on low-temperature processed electron extraction layer. 6:57. <https://doi.org/10.3389/fmats.2019.00057>
- Chen C, Yu C, Dai Q, Song H (2015) Radio frequency magnetron sputtering deposition of TiO<sub>2</sub> thin films and their perovskite solar cell applications. *Sci Rep* 5:17684. <https://doi.org/10.1038/srep17684>
- Chen X, Tang LJ, Yang S, Hou Y, Yang HG (2016) A low temperature processed flower-like TiO<sub>2</sub> array as an electron transport layer for high-performance perovskite solar cells. *J Mater Chem A* 4:6521–6526. <https://doi.org/10.1039/C6TA00893C>
- Cheng Z, Lin J (2010) Layered organic–inorganic hybrid perovskites: structure, optical properties, film preparation, patterning and templating engineering. *Cryst Eng Comm* 12:2646–2662
- Chopra KL, Major S, Pandya DK (1983) Transparent conductors—a status review. *Thin Solid Films* 102(1):1–46
- Chopra KL, Paulson PD, Dutta V (2004) Progress in photovoltaics: research and applications. *Prog Photovolt Res Appl* 12:69–92. <https://doi.org/10.1002/pip.541>
- Das K, Baruah S (2018) Quantum dots for solar energy harvesting. *Curr Sci* 115(4):25
- Diguna LJ, Shen Q, Kobayashi J, Toyoda T (2007) High efficiency of CdSe quantum-dot-sensitized TiO<sub>2</sub> inverse opal solar cells. *Appl Phys Lett* 91:023116. <https://doi.org/10.1063/1.2757130>
- Etgar L (2013) Semiconductor nanocrystals as light harvesters in solar cells. *Materials* 6 (2):445–459. <https://doi.org/10.3390/ma6020445>
- Etgar L, Gao P, Xue Z, Peng Q, Chandiran AK, Liu B, Nazeeruddin MK, Grätzel M (2012) Mesoscopic CH<sub>3</sub>NH<sub>3</sub>PbI<sub>3</sub>/TiO<sub>2</sub> heterojunction solar cells. *J Am Chem Soc* 13442:17396–17399. <https://doi.org/10.1021/ja307789s>
- Fan Y-H, Ho C-Y, Chang Y-J (2017) Enhancement of dye-sensitized solar cells efficiency using mixed-phase TiO<sub>2</sub> nanoparticles as photoanode. *Scanning* 7. <https://doi.org/10.1155/2017/9152973>
- Ganguly A, Anjaneyulu O, Ojha K, Ganguli AK (2015) Oxide based nanostructures for photocatalytic and electrocatalytic applications. *Cryst Eng Comm* 17:8978. <https://doi.org/10.1039/C5CE01343G>
- Ghicov A, Schmuki P (2009) Self-ordering electrochemistry: a review on growth and functionality of TiO<sub>2</sub> nanotubes and other self-aligned MOx structures. *Chem Commun*:2791–2808. <https://doi.org/10.1039/b822726h>
- Govindasamy G, Murugasen P, Sagadevan S (2016) Investigations on the synthesis, optical and electrical properties of TiO<sub>2</sub> thin films by Chemical Bath Deposition (CBD) method. *Materials Research* 19(2):413–419. <https://doi.org/10.1590/1980-5373-MR-2015-0411>
- Guijarro N, LanaVillarreal T, MoraSeró I, Bisquert J, Gómez R (2009) CdSe quantum dot sensitized TiO<sub>2</sub> electrodes: effect of quantum dot coverage and mode of attachment. *J Phys Chem C* 113:4208–4214
- Hanaor DAH, Sorrell CC (2011) Review of the anatase to rutile phase transformation. *J Mater Sci* 46:855–874. <https://doi.org/10.1007/s10853-010-5113-0>
- Hayat A, Erwin A, Putra E, Amaliyah N, Hayase S, Pandey SS (2018) Piper Ornatum and Piper Betle organic dyes for TiO<sub>2</sub> and SnO<sub>2</sub> dye sensitized solar cells. *IOP Conf. Series: Journal of Physics: Conf. Series* 979:012062. <https://doi.org/10.1088/1742-6596/979/1/012062>
- Hoye RLZ, Musselman KP, MacManus-Driscoll JL (2013) Research update: doping ZnO and TiO<sub>2</sub> for solar cells. *Apl Materials* 1:060701
- Jo MS, Cho JS, Wang XL, Jin EM, Jeong SM, Kang D-W (2019) Improving of the photovoltaic characteristics of dye-sensitized solar cells using a photoelectrode with electrospun porous TiO<sub>2</sub> nanofibers. *Nanomaterials* 9:95. <https://doi.org/10.3390/nano9010095>
- Kanda H, Uzum A, Nishino H, Umeyama T, Imahori H, Ishikawa Y, Uraoka Y, Ito S (2016) Interface optoelectronics engineering for mechanically stacked tandem solar cells based on

- perovskite and silicon. *ACS Appl Mater Interfaces* 8:33553–33561. <https://doi.org/10.1021/acscami.6b07781>
- Kanhere P, Chen Z (2014) A review on visible light active perovskite-based photocatalysts. *Molecules* 19:19995–20022. <https://doi.org/10.3390/molecules191219995>
- Kao LC, Liou YHS, Dong C-L, Yeh P-H, Chen CL (2015) The tandem structure of QD co-sensitized TiO<sub>2</sub> nanorod arrays for solar light driven hydrogen generation. *ACS Sustain Chem Eng*. <https://doi.org/10.1021/acssuschemeng.5b01010>
- Khalid HM, Pervez MF, Mia MNH, Tayyaba S, Jalal uddin M, Ahamed R, Khan RA, Hoq M, Khan MA, Ahmed F (2017) Annealing temperature effect on structural, morphological and optical parameters of mesoporous TiO<sub>2</sub> film photoanode for dye-sensitized solar cell application. *Mater Sci-Poland* 35(4):868–877. <https://doi.org/10.1515/msp-2017-0082>
- Kim M-H, Kwon Y-U (2011) Semiconducting divalent metal oxides as blocking layer material for SnO<sub>2</sub>-based dye-sensitized solar cells. *J Phys Chem C* 115:23120–23125. <https://doi.org/10.1021/jp2069978>
- Kominami H, Kohno M, Kera Y (2000) Synthesis of brookite-type titanium oxide nano-crystals in organic media. *J Mater Chem* 10:1151–1156. <https://doi.org/10.1039/a9085281>
- Kranz L, Abate A, Feurer T, Fan F, Avancini E, Loeckinger J, Reinhard P, Zakeeruddin SM, Grätzel M, Buecheler S, Tiwari AN (2015) High-efficiency polycrystalline thin film tandem solar cells. *J Phys Chem Lett* 6:2676. <https://doi.org/10.1021/acs.jpcllett.5b01108>
- Kuwahara Y, Yamashita H (2011) Efficient photocatalytic degradation of organics diluted in water and air using TiO<sub>2</sub> designed with zeolites and mesoporous silica materials. *J Mater Chem* 21:2407–2416. <https://doi.org/10.1039/c0jm02741c>
- Lee J-W, Hsieh Y-T, De Marco N, Bae S-H, Han Q, Yang Y (2017) Halide Perovskites for tandem solar cells. *J Phys Chem Lett* 8:1999–2011. <https://doi.org/10.1021/acs.jpcllett.7b00374>
- Li Y, Wang H, Feng Q, Zhou G, Wang Z-S (2013) Gold nanoparticles inlaid TiO<sub>2</sub> photoanodes: a superior candidate for high-efficiency dye-sensitized solar cells. *Energy Environ Sci* 6:2156. <https://doi.org/10.1039/c3ee23971c>
- Li Y, Cooper JK, Liu W, Sutter-Fella CM, Amani M, Beeman JW, Javey A, Ager JW, Liu Y, Toma FM, Sharp ID (2016) *Nat Commun* 7:12446. <https://doi.org/10.1038/ncomms12446>
- Lim SH, Ritter C, Ping Y, Schreyer M, White TJ (2009) Nonstoichiometry, amorphicity and microstructural evolution during phase transformations of photocatalytic titania powders. *J Appl Crystallogr* 42:917–924. <https://doi.org/10.1107/S0021889809031021>
- Mao X, Zhou R, Zhang S, Ding L, Wan L, Qin S, Chen Z, Xu J, Miao S (2016) High efficiency dye-sensitized solar cells constructed with composites of TiO<sub>2</sub> and the hot-bubbling synthesized ultra-small SnO<sub>2</sub> nanocrystals. *Sci Rep* 6:19390. <https://doi.org/10.1038/srep19390>
- Murugadoss G, Mizuta G, Tanaka S, Nishino H, Umeyama T, Imahori H, Ito S (2014) Double functions of porous TiO<sub>2</sub> electrodes on CH<sub>3</sub>NH<sub>3</sub>PbI<sub>3</sub> perovskite solar cells: enhancement of perovskite crystal transformation and prohibition of short circuiting. *APL Mater* 2:081511. <https://doi.org/10.1063/1.4891597>
- Nadrah W, Amin M, Zaina Z, Talib ZA, Lim HN, Chang SK (2015) Quantum dot-sensitized solar cell based on nano-TiO<sub>2</sub> electrodes. *PJSRR* 1(1):67–81
- Nair S, Peining Z, Babu VJ, Shengyuanc Y, Ramakrishna S (2011) Anisotropic TiO<sub>2</sub> nanomaterials in dye-sensitized solar cells. *Phys Chem Chem Phys* 13:21248–21261. <https://doi.org/10.1039/c1cp23085a>
- Nguyena TT, Patel M, Kim J-W, Lee W, Kim J (2019) Functional TiO<sub>2</sub> interlayer for all-transparent metal-oxide photovoltaics. *J Alloys Compd*. <https://doi.org/10.1016/j.jallcom.2019.152602>
- Opara Krasovec U, Berginc M, Hocevar M, Topic M (2009) Unique TiO<sub>2</sub> paste for high efficiency dye-sensitized solar cells. *Sol Energy Mater Sol Cells* 93:379–381. <https://doi.org/10.1016/j.solmat.2008.11.012>
- Persson K (2016) Materials data on TiO<sub>2</sub> (SG:15) by materials project. United States. <https://doi.org/10.17188/1206871>

- Preparation of Quantum Dot Solar Cell – QDs (2019). <https://bohatala.com/preparation-of-quantum-dot-solar-cell-qds/>
- Pushpa (2015) A study on the role of titanium oxide for solar cell applications. *Int J Chem Stud* 4 (1):134–137
- Rath JK (2003) Low temperature polycrystalline silicon: a review on deposition, physical properties and solar cell applications. *Sol Energy Mater Sol Cells* 76(4):431–487
- Reyes-Coronado D, Rodriguez-Gattorno G, Espinosa-Pesqueira ME, Cab C, de Coss R, Oskam G (2008) Phase-pure TiO<sub>2</sub> nanoparticles: anatase, brookite and rutile. *Nanotechnology* 19:145605. <https://doi.org/10.1088/0957-4484/19/14/145605>
- Sadhanala A, Kumar A, Pathak S, Rao A, Steiner U, Greenham NC, Snaith HJ, Friend RH (2015) Electroluminescence from organometallic lead halide perovskite-conjugated polymer diodes. *Adv Electron Mater* 1:1500008. <https://doi.org/10.1002/aelm.201500008>
- Salman ON, Agoor IR, Ismail MM (2017) Preparation of the scattering layer based on TiO<sub>2</sub> nanotube and their dye sensitized solar cell applications. *Appl Phys A Mater Sci Process* 123:402. <https://doi.org/10.1007/s00339-017-1012-4>
- Shen H, Omelchenko ST, Jacobs DA, Yalamanchil S, Di Yan YW, Phang P, Duong T, Wu Y, Yin Y, Samundsett C, Peng J, Wu N, White TP, Andersson GG, Lewis NS, Catchpole KR (2018) In situ recombination junction between p-Si and TiO<sub>2</sub> enables high-efficiency monolithic perovskite/Si tandem cells. *Sci Adv* 4:eaau9711
- Sheng R, Ho-Baillie AWY, Huang S, Keevers M, Hao X, Jiang L, Cheng Y-B, Green MA (2015) Four-terminal tandem solar cells using CH<sub>3</sub>NH<sub>3</sub>PbBr<sub>3</sub> by spectrum splitting. *J Phys Chem Lett* 6:3931–3934. <https://doi.org/10.1021/acs.jpcllett.5b01608>
- Shrivastava SK, Singh S (2016) Effect & growth of TiO<sub>2</sub> thin films for solar cell applications. *Int J Hybrid Inf Technol* 9(2):267–274. <https://doi.org/10.14257/ijhit.2016.9.2.24>
- Stapleton A (2017) Technology. <https://cosmosmagazine.com/technology/how-solar-cells-turn-sunlight-into-electricity>
- Su Z, Zhou W (2011) Formation, morphology control and applications of anodic TiO<sub>2</sub> nanotube arrays. *J Mater Chem* 21:8955–8970. <https://doi.org/10.1039/c0jm04587j>
- Su P, Fu W, Yao H, Liu L, Ding D, Feng F, Feng S, Xue Y, Liu X, Yang H (2017) Enhanced photovoltaic properties of perovskite solar cells by TiO<sub>2</sub> homogeneous hybrid structure. *R Soc Open Sci* 4:170942. <https://doi.org/10.1098/rsos.170942>
- Sun Q, Hong Y, Zang T, Liu Q, Yu L, Dong L (2018) The application of heterostructured SrTiO<sub>3</sub>-TiO<sub>2</sub> nanotube arrays in dye-sensitized solar cells. *J Electrochem Soc* 165(4):H3069–H3075
- Sun P-P, Bai L, Kripalani DR, Zhou K (2019) A new carbon phase with direct bandgap and high carrier mobility as electron transport material for perovskite solar cells. *npj Comput Mater* 9:5
- Szindler M, Szindler MM, Boryło P, Jung T (2017) Structure and optical properties of TiO<sub>2</sub> thin films deposited by ALD method. *Open Phys* 15:1067–1071
- Varma M (2015) Infrared plastic solar cell: seminar report. Jawaharlal Nehru Technological University, Hyderabad
- Wu Y, Yang X, Chen H, Zhang K, Qin C, Liu J, Peng W, Islam A, Bi E, Ye F, Yin M, Zhang P, Han L (2014) Highly compact TiO<sub>2</sub> layer for efficient hole-blocking in perovskite solar cells. *Appl Phys Express* 7:052301. <https://doi.org/10.7567/APEX.7.052301>
- Xia X, Ku Z, Zhou D, Zhong Y, Zhang Y, Wang Y, Huang MJ, Tu J, Fan HJ (2016) Perovskite solar cell powered electrochromic batteries for smart windows. *Mater Horiz*. <https://doi.org/10.1039/c6mh00159a>
- Yaacob KA, Ishak MN, Alias NN (2013) Quantum dots sensitized solar cell: effect of CdSe nanoparticles purification procedure of QD sensitized photoanodes. *J Phys Conf Ser* 431:012019. <https://doi.org/10.1088/1742-6596/431/1/012019>
- Yamada Y, Nakamura T, Endo M, Wakamiya A, Kanemitsu Y (2014) Near-band-edge optical responses of solution-processed organic–inorganic hybrid perovskite CH<sub>3</sub>NH<sub>3</sub>PbI<sub>3</sub> on mesoporous TiO<sub>2</sub> electrodes. *Appl Phys Express* 7:032302. <https://doi.org/10.7567/APEX.7.032302>

- Yin X, Xu Z, Guo Y, Xu P, He M (2016) Ternary oxides in the  $\text{TiO}_2$ –ZnO system as efficient electron-transport layers for perovskite solar cells with efficiency over 15%. *ACS Appl Mater Interfaces* 8:29580–29587. <https://doi.org/10.1021/acsami.6b09326>
- Zhang Q, Zhang G, Sun X, Yin K, Li H (2017) Improving the power conversion efficiency of carbon quantum dot-sensitized solar cells by growing the dots on a  $\text{TiO}_2$  photoanode in situ. *Nano* 7:130. <https://doi.org/10.3390/nano7060130>
- Zheng YM, Wang Y, Xiao L, Zhang F, Yang H (2017) Hole blocking layer-free perovskite solar cells with over 15% efficiency. *Energy Procedia* 105:188–193
- Zhou R, Zhang Q, Uchaker E, Yang L, Yin N, Chen Y, Yin M, Cao G (2014) Photoanodes with mesoporous  $\text{TiO}_2$  beads and nanoparticles for enhanced performance of CdS/CdSe quantum dot co-sensitized solar cells. *Electrochim Acta* 135:284–292
- Zie CWS, Zainab N (2017) Incorporation of kojic acid-azo dyes on  $\text{TiO}_2$  thin films for dye sensitized solar cells applications. *J Solar Energy*:Article ID 2760301. <https://doi.org/10.1155/2017/276030>
- Zulkefly MYB (2014) A thesis on “Titanium Dioxide ( $\text{TiO}_2$ ) as buffer layer in organic solar cell device”

# Chapter 6

## Metal Oxides and Sulfide-Based Biosensors for Monitoring and Health Control



Celina M. Miyazaki, Nirav Joshi, Osvaldo N. Oliveira Jr.,  
and Flavio M. Shimizu

### Contents

6.1	Introduction .....	170
6.2	Sulfide-Based Biosensors .....	172
6.2.1	Copper Sulfides .....	173
6.2.2	Nickel Sulfides .....	179
6.2.3	Molybdenum Sulfide .....	183
6.2.4	Other Sulfides .....	189
6.3	Metal Oxide Biosensors .....	193
6.4	Conclusion .....	198
	References .....	199

**Abstract** Monitoring health conditions with low-cost, portable devices is a target for diseases such as diabetes, which is now performed by detecting the glucose level in blood samples. Since commercial biosensors suffer with limited enzyme stability and shelf-life problems, novel materials have been exploited, including metal oxides and sulfide nanostructures. These materials are suitable for detection with electrochemical methods owing to their high surface area-to-volume ratio, selectivity, sensitivity, and fast response properties. In this chapter, we discuss some of these nanostructures to detect glucose through nonenzymatic reactions, which are advantageous to increase robustness and shelf-life of biosensors. Furthermore, the work on metal oxides and sulfide-based biosensors is being extended with the design of hierarchical nanostructures to enable high sensitivity, rapid response, and detection

---

C. M. Miyazaki  
Universidade Federal de São Carlos, São Paulo, Brazil

N. Joshi · O. N. Oliveira Jr.  
São Carlos Institute of Physics, University of São Paulo, São Paulo, Brazil

F. M. Shimizu (✉)  
Department of Applied Physics, “Gleb Wataghin” Institute of Physics (IFGW), University of Campinas (UNICAMP), Campinas, SP, Brazil

© The Editor(s) (if applicable) and The Author(s), under exclusive licence to  
Springer Nature Switzerland AG 2021

169

S. Rajendran et al. (eds.), *Metal, Metal-Oxides and Metal Sulfides for Batteries, Fuel Cells, Solar Cells, Photocatalysis and Health Sensors*, Environmental Chemistry for a Sustainable World 62, [https://doi.org/10.1007/978-3-030-63791-0\\_6](https://doi.org/10.1007/978-3-030-63791-0_6)

of multicomponent elements following the electronic tongue concept. The challenges and prospects for glucose biosensing are also highlighted.

**Keywords** Biosensor · Metal oxide · Sulfides · Glucose

## 6.1 Introduction

Biosensors are highly selective devices comprising basically two parts: biological recognition elements such as enzymes, antibodies, DNA, and cells, which interact selectively in a complex medium with the substance of interest (analyte), and a transducer to convert the biochemical response into an appropriate signal (Bohunicky and Mousa 2011). Biosensors can be classified in different ways, for example, according to the transduction process or the biological recognition element (Soper et al. 2006). Biosensors can be applied to a variety of samples including cell cultures, food samples, body fluids, and wastewater (Hasan et al. 2014; Srivastava et al. 2018; Brindha et al. 2018; Kuswandi 2019). To obtain a sensitive and reliable detection system, the sensor surface must permit immobilization of biorecognition elements, also avoiding nonspecific binding that may interfere with the biological activity of the biomolecule. In principle, the molecules may be immobilized on the surface or in a 3D matrix, which generally provides a greater number of binding sites (Welch et al. 2017). Nanotechnology has been applied in several fields, including clinical diagnosis, agriculture, water quality management, food quality analysis, and mainly in the creation sensory tools through novel thrilling film architectures that act as sensing units (Kumar et al. 2017; Dasgupta et al. 2017; Villaseñor and Ríos 2018; Raymundo-Pereira et al. 2019; Kuswandi 2019).

Diabetes is a metabolic disease identified by chronic *hyperglycemia* and characterized by elevated levels of blood glucose. This occurs due to pancreas deficiency that produces insufficient insulin to regulate blood glucose, or when the body tolerance is low and cannot effectively use the insulin it produces. Diabetes leads over time to serious damage to the heart, blood vessels, eyes, kidneys, nerves, and may cause deaths and disabilities (WHO 2016, 2019). More than 400 million people in the world have diabetes and the early diagnosis of diabetes has important implications on society, not only for their health, but it may also affect their employment, health and life insurance, driving status, social opportunities, and carry other cultural, ethical, and human rights consequences (WHO 2019).

Various technologies developed to detect glucose level include the application of high-performance liquid chromatography, optical methods, and electrochemical biosensors. However, the main challenge for the diagnosis of diabetes is to create devices for daily use by patients in personalized monitoring (Bruen et al. 2017). Within all technologies, electrochemical biosensors can fulfill most of these requirements concerning sensitivity, specificity, portability, cost-effectiveness, and the possibilities for miniaturization and point-of-care diagnostic testing (Wang et al.

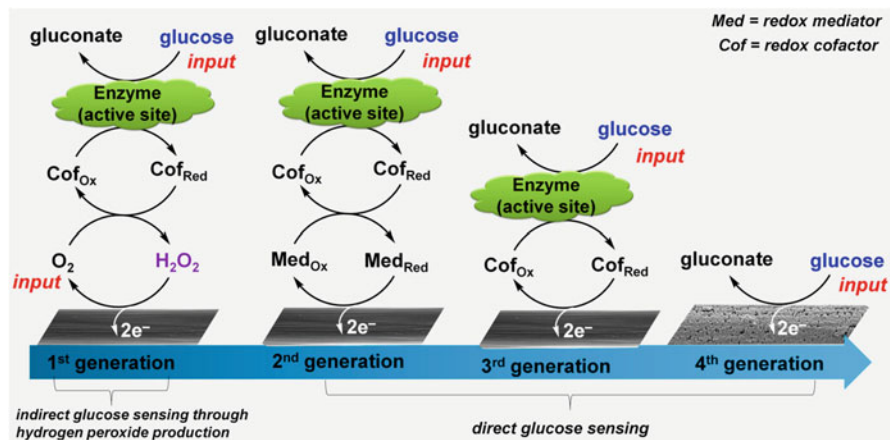


**Fig. 6.1** Biosensors classification according to its reaction mechanism exemplified in a glucose detection model: the first generation with a co-substrate/co-product (hydrogen peroxide, H<sub>2</sub>O<sub>2</sub>) as the redox indicator; the second generation, when a redox mediator (Med<sub>Ox</sub>-Med<sub>Red</sub>) is used to relay the electrons; the third generation encompasses the direct electron transfer between the enzyme and the electrode; and the fourth generation sensor described by the glucose direct oxidation in a nonenzymatic system. (Reproduced with permission from (Holade et al. 2017) Copyright MDPI 2017)

2018a; Nguyen et al. 2019). Different techniques such as voltammetric, conductometric, potentiometric, and amperometric have been used to detect such analytes for electrochemical biosensors. Within the topic of glucose biosensors, there is a classification according to its reaction mechanism, as schematically summarized in Fig. 6.1. In the first generation, enzymatic reaction with glucose consumes oxygen and produces hydrogen peroxide. The last one diffuses to the transducer; it is oxidized and generates a measurable electrical response. In the second-generation sensors, electroactive molecules are applied as electrochemical mediators to shuttle electrons between the enzymatic reaction and transducer. In the absence of the mediator, the thick protein layer hampers the direct electron transfer between the inner redox center and flat conventional electrodes. The third generation is independent of oxygen or mediator and directly transfers electrons from the enzyme to the transducer and is usually based on the excellent conductivity properties of novel nanostructured materials. In the last decades, nonenzymatic glucose biosensors have attracted attention, being referred to as the fourth generation type, and can directly catalyze biomolecules (glucose) with no need for specific enzymes (Holade et al. 2017).

Notwithstanding the advantages of electrochemical biosensors, some challenges remain to be overcome. They include matrix effects, for example, in biofluids, there is a difference in pH and ionic strength that affects the response. In addition, there are the challenges of lack of selectivity and poor sensitivity depending on the target analyte and the need of miniaturization technology for portable devices for daily use.

In this chapter, we describe novel materials based on sulfides and metal oxides to develop biosensors that can address the drawbacks mentioned.

## 6.2 Sulfide-Based Biosensors

Metal sulfides are relevant for electronics and optoelectronics because of their excellent physical and chemical properties, with impressive results in photothermal conversion, supercapacitors, sensors, batteries, and solar cells. Sulfides can assume various forms, such as monosulfides, disulfides, or even polysulfides (Atkins et al. 2008). Properties of these materials can vary from insulating  $\text{HfS}_2$ , semiconductors such as  $\text{MoS}_2$  up to metal-like materials such as  $\text{NbS}_2$  (Chhowalla et al. 2013). Special attention has been given to disulfides that fall into the metal dichalcogenide groups with the general formula  $\text{MX}_2$ , where M is a transition metal (groups 4–10) and X is a chalcogen. They belong to a 2D material class with a lamellar structure and are potential substitute materials to gapless graphene.  $\text{MX}_2$  exhibits semiconducting behavior with bandgap between 1 and 2 eV (Wang et al. 2012; Chhowalla et al. 2013; Jariwala et al. 2014), which is attractive for optoelectronics.

Another advantage of metal sulfide is its abundance. Various metals are naturally present in sulfide form in ores, which is blown in the air to form oxides or soluble sulfates for further metal extraction (Atkins et al. 2008). Examples are heazlewoodite ( $\text{Ni}_3\text{S}_2$ ), chalcocite ( $\text{Cu}_2\text{S}$ ), and pyrite ( $\text{FeS}_2$ ). Metal sulfides can also be synthesized in the laboratory with diverse structural configurations. The possibility to control composition and form has great advantages for controlling the sensor parameters. Composition and stoichiometry depend on the metal and sulfur atoms ratio, pH, and other experimental conditions. For example, star-shaped PbS with eight symmetric arms was synthesized with controlled release of sulfide ions at 80 °C and appropriate pH. Otherwise, nanorods and nanocubes are obtained using similar synthetic procedures (Ma et al. 2004). Copper sulfides exhibit possibilities for many stoichiometric compositions, nanocrystal morphologies, and valence states. For instance, covellite copper sulfide, formed by alternating layers of CuS and  $\text{Cu}_2\text{S}_2$ , shows semiconductor or metallic conductivity (Qin et al. 2005), or even superconductor behavior at 1.6 K (Liang and Whangbo 1993). Variations in the experimental conditions can lead to ball-like, rod-like, spaghetti-like, and chrysanthemum-shaped covellite structures (Gorai et al. 2005; Qin et al. 2005).

Concerning electrochemical sensing applications, sulfides can be synthesized by physical or chemical methods, and further immobilized on the sensing surface, or can be grown in situ directly on the surface, for example, by electrodeposition. The most traditional methods encompass (i) hydrothermal/solvothermal method, (ii) chemical and physical vapor depositions, and (iii) solution-phase chemistry like evaporation, recrystallization, and diffusion (Lai et al. 2012; Xiong et al. 2014).

Various sensing applications have been developed, including gas sensors (Sagade and Sharma 2008; Cho et al. 2015; Qin et al. 2018), immunosensors (Kima et al. 2010; Zhang et al. 2016b), DNA sensors (Hansen et al. 2006), and aptasensors (Liu



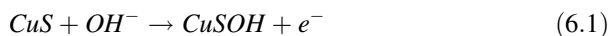
et al. 2014). Glucose has been the main target because of diabetes monitoring, and it is a model for new sensing concepts. Hydrogen peroxide ( $\text{H}_2\text{O}_2$ ) sensors have also been popular owing to their wide applications in pharmaceutical, industrial, and clinical research.  $\text{H}_2\text{O}_2$  is a by-product of reactions catalyzed by many oxidase enzymes, and therefore its quantification is important for many biomedical applications, especially for biosensors. As glucose and hydrogen peroxide are two good representatives of health control and monitoring, we describe in this section some outstanding biosensors made with metal sulfides that are divided into four main groups: copper, molybdenum and nickel sulfides, and other sulfides.

### 6.2.1 Copper Sulfides

Copper sulfides adopt different stoichiometric compositions, crystal morphologies, complex structures, and valence states (Qin et al. 2005). The form  $\text{Cu}_2\text{S}$  (chalcocite) and  $\text{CuS}$  (covellite) are the most common, but there are several nonstoichiometric stable and metastable species ranging between them (Qin et al. 2005). Other interesting applications of copper sulfides include photothermal ablation for tumor cells (Li et al. 2010b), gas sensors (Sagade and Sharma 2008), supercapacitors (Naveed et al. 2019), and as electrode materials for batteries (Kravchik et al. 2019; Zhang et al. 2019).

Copper sulfide-based biosensors for glucose quantification are attractive because of the redox pair  $\text{Cu}^{2+}/\text{Cu}^{3+}$ , which is an effective mediator for the electrocatalytic oxidation of glucose in alkaline solution (Zhao et al. 2006). Qian et al. fabricated a fourth-generation glucose biosensor with  $\text{CuS}$  nanotubes deposited onto  $\text{Cu}$  electrode. Figure 6.2a, b show the cyclic voltammetry (CV) plots of  $\text{CuS}$  nanotubes/ $\text{Cu}$ - and bare  $\text{Cu}$ -electrodes, respectively, in 0.15 M sodium hydroxide solution (dashed curve). They established that peak 1, at  $-0.45$  V, is assigned to the  $\text{Cu}^0/\text{Cu}^+$  transition, while peak 2, at  $-0.15$  V, indicates the  $\text{Cu}^0/\text{Cu}^{2+}$  and  $\text{Cu}^+/\text{Cu}^{2+}$  transitions. Peaks 4, 5, and 6 are assigned to the reduction of  $\text{Cu}^{3+}/\text{Cu}^{2+}$ ,  $\text{Cu}^{2+}/\text{Cu}^+$ , and  $\text{Cu}^+/\text{Cu}^0$ , respectively (Qian et al. 2013). After the addition of glucose (solid curve), the current of peak 2 decreased, and a new peak, 3, appeared due to glucose oxidation, at  $+0.5$  V, with higher intensity for modified than the bare  $\text{Cu}$  electrode (Qian et al. 2013).

The reaction mechanism of glucose for copper sulfide-based electrodes is similar to that for copper only in alkaline medium (Marioli and Kuwana 1992). The glucose oxidation peak is associated with Eq. 6.1, with the oxidation of  $\text{CuS}$  into  $\text{CuSOH}$  (Radhakrishnan et al. 2016).



Qian et al. described the above mechanism in detail. Glucose initially loses one proton forming enediol in an alkaline medium. Then, enediol complexes with  $\text{Cu}^{2+}$  producing an intermediate compound, Eq. 6.2, which explains the decrease in

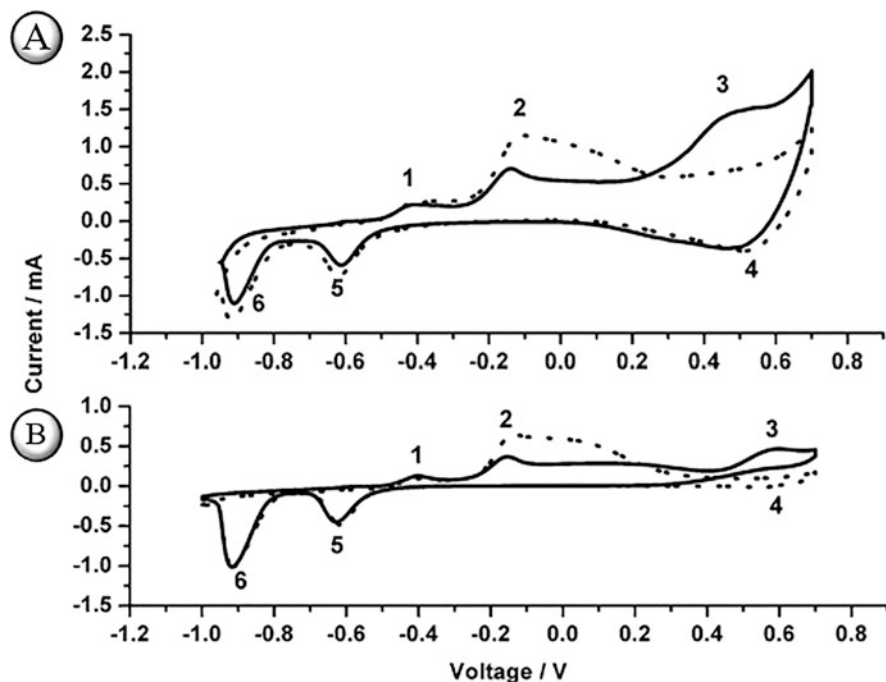
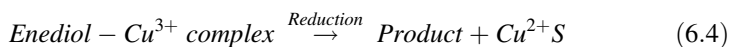
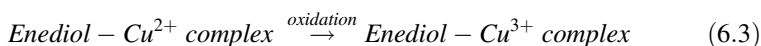
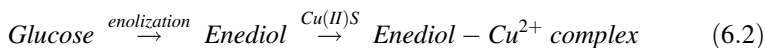


**Fig. 6.2** Cyclic voltammetry plots of (a) CuS nanotubes/Cu and (b) bare Cu electrodes in 0.15 M NaOH collected using saturated calomel electrode as reference. Dotted and solid lines represent the cyclic voltammetry collected in the absence and presence of 2 mM glucose. Peak 1:  $\text{Cu}^0/\text{Cu}^+$  transition; peak 2:  $\text{Cu}^0/\text{Cu}^{2+}$  and  $\text{Cu}^+/\text{Cu}^{2+}$  transitions; peaks 4, 5, and 6 are assigned to the reduction of  $\text{Cu}^{3+}/\text{Cu}^{2+}$ ,  $\text{Cu}^{2+}/\text{Cu}^+$ , and  $\text{Cu}^+/\text{Cu}^0$ , respectively. After the addition of glucose, note a reduction in peak 2 intensity and the appearance of a new peak, 3, due to the glucose oxidation. (Reproduced with permission from (Qian et al. 2013). Copyright Elsevier 2013)

peak 2. Third, the complex intermediate is electro-oxidized to an enediol-complex- $\text{Cu}^{3+}$  form, Eq. 6.3, for further reduction and generation of a product and  $\text{Cu}^{2+}\text{S}$ , Eq. 6.4 (Qian et al. 2013).



Based on the reaction mechanism proposed above, many nonenzymatic, fourth generation, glucose biosensors have been developed using as principle of detection the chronoamperometric technique; the measurements were taken between +0.45 and +0.55 V, related to glucose oxidation, as depicted in Table 6.1, which summarizes the copper sulfide-based glucose biosensors found in literature. A wide

**Table 6.1** Copper sulfide-based glucose and hydrogen peroxide amperometric biosensors

Glucose sensors		Electrode	Range	Sensitivity	Detection limit ( $\mu\text{M}$ )	Working potential (V)	Response time (s)	References
		Cu rod— $\text{Cu}_2\text{S}$	2 $\mu\text{M}$ –8.1 mM	361.58 $\mu\text{A mM}^{-1}$	0.1	–0.10 vs. SCE	10	Zhang et al. (2012)
		CuS nanotubes/Cu	0.2 $\mu\text{M}$ –2.5 mM	3135 $\mu\text{A mM}^{-1} \text{cm}^{-2}$	0.045	+0.45 vs. SCE	2	Qian et al. (2013)
		CuS nanoflowers/GCE	2.5–6.0 mM	2205 $\mu\text{A mM}^{-1} \text{cm}^{-2}$	0.3	+0.46 vs. SCE	3	Yang et al. (2014c)
		CuS microflowers/GCE	10 $\mu\text{M}$ –10 mM	$5.86 \times 10^{-3} \mu\text{A M}^{-1}$	2.0	+0.50 vs. Ag/AgCl	4	Radhakrishnan et al. (2016)
		$\text{Cu}_2\text{O}/\text{Cu}_2\text{S}/\text{GCE}$	20 $\mu\text{M}$ –5.4 mM	1007 $\mu\text{A mM}^{-1} \text{cm}^{-2}$	10	+0.45 vs. SCE	–	Xu et al. (2016)
		CuS/Ni foam electrode	0.001–4.9 mM	8337 $\mu\text{A mM}^{-1} \text{cm}^{-2}$	0.05	+0.55 vs. Ag/AgCl	10	Kim et al. (2016)
		S-rGO/CuS/RDE	0.1 $\mu\text{M}$ –3.88 mM	429.4 $\mu\text{A mM}^{-1} \text{cm}^{-2}$	0.032	+0.48 vs. Ag/AgCl	0.8	Karikalan et al. (2017)
		rGO/CuS nanoflakes/GCE	3.88–20.17 mM	76.27 $\mu\text{A mM}^{-1} \text{cm}^{-2}$	0.19	+0.4 vs. SCE	6	Yan et al. (2018)
		Cu– $\text{Cu}_2\text{S}/\text{GCE}$	1–2000 $\mu\text{M}$	53.5 $\mu\text{A mM}^{-1} \text{cm}^{-2}$	0.33	+0.55 vs. Ag/AgCl	5	Xu et al. (2019a)
		Cu– $\text{S}_4$ hollow nanospheres/GCE	0.1 $\mu\text{M}$ –0.5 mM	5020 $\mu\text{A mM}^{-1} \text{cm}^{-2}$	0.023	+0.50 vs. Ag/AgCl	2	Cao et al. (2019)

(continued)

Table 6.1 (continued)

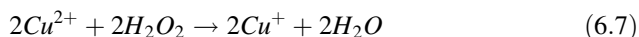
Glucose sensors						
Electrode	Range	Sensitivity	Detection limit ( $\mu\text{M}$ )	Working potential (V)	Response time (s)	References
<i>Hydrogen peroxide sensors</i>						
Cu <sub>2</sub> S-MWCNT/Nafion/GCE	50 nM–10 $\mu\text{M}$	125 nA mM <sup>-1</sup>	0.050	+0.55 vs. Ag/AgCl	3	Lee et al. (2007)
Cu <sub>2</sub> S/OMC/GCE	1–3030 $\mu\text{M}$	36.8 $\mu\text{A mM}^{-1}$ cm <sup>-2</sup>	0.2	-0.1 vs. Ag/AgCl	3.6	Bo et al. (2010)
Cu <sub>2</sub> S nanoplates/GCE	10 $\mu\text{M}$ –3.75 mM	64.27 $\mu\text{A mM}^{-1}$	1.1	-0.35 vs. Ag/AgCl	5	Maji et al. (2013)
CuS/rGO/GCE	1 $\mu\text{M}$ –1 mM	821.13 $\mu\text{A mM}^{-1}$ cm <sup>-2</sup>	0.1	-0.2 vs. SCE	3	Yang et al. (2014b)
CuS nanoflowers/CS/GCE	1 $\mu\text{M}$ –100 $\mu\text{M}$	3.64·10 <sup>4</sup> $\mu\text{A M}^{-1}$	0.3	-0.1 vs. SCE	3	Yang et al. (2014c)

CS chitosan, GCE glass carbon electrode, MWCNT multiwalled carbon nanotube, NT nanotubes, OMC ordered mesoporous carbon, RDE rotatory disk electrode, rGO reduced graphene oxide, S-rGO sulfur-doped reduced graphene oxide. The working potentials are given versus the respective reference electrode employed in the experiments, which are saturated calomel electrode (SCE) and silver/silver chloride (Ag/AgCl)

detection range and a fast response have been achieved in recent works, as Karikalan et al. reported a range of 0.0001–3.88 mM, detection limit of 32 nM and response time of 0.8 s, using a rotatory disk electrode, modified with sulfur-doped reduced graphene oxide and copper sulfide (Karikalan et al. 2017). Another remarkable result was achieved by Kim et al. that synthesized dendritic CuS structures by electrodeposition on nickel foam electrode by hydrogen gas bubbling and further treatment with vapor-phase sulfurization. The large surface area of dendritic structures led to fast electron transport, with excellent performance in detecting glucose with a sensitivity of 8337  $\mu\text{A mM}^{-1} \text{cm}^{-2}$ , detection range of 0.001–4.9 mM, and detection limit of 0.05  $\mu\text{M}$  (Kim et al. 2016).

Copper sulfide-based glucose sensors have also presented good anti-interference property against other carbohydrates and common electroactive compounds such as uric acid, ascorbic acid, and dopamine (Bo et al. 2010; Yang et al. 2014c; Karikalan et al. 2017). Due to the great selectivity of biosensors, we can find in literature some examples of real sample analysis with excellent recovery property varying from 93 to 107% (Qian et al. 2013; Kim et al. 2016; Xu et al. 2019b). Sensing reproducibility is another important parameter investigated where the lowest relative standard deviation was obtained by Qian et al. (2013) that tested seven independent sensors obtaining a deviation of 3.7%, followed by Xu et al. (2019a) that determined 4.3% in a test with five independent sensors.

Decreasing the oxidation/reduction overpotentials is the key point on developing electrochemical hydrogen peroxide sensors. Based on their excellent catalytic ability, sulfides have decreased the reduction potential in the same way that graphene-based materials. Glassy carbon electrodes were modified with flower-like CuS nanoparticles and chitosan, as shown in Fig. 6.3a, and their electrochemical response to the solution with and without hydrogen peroxide are depicted in Fig. 6.3b. In the absence of hydrogen peroxide, a pair of redox peaks assigned to  $\text{Cu}_2\text{S}/\text{CuS}$  is observed (Eq. 6.5). With the addition of peroxide, a broad cathodic peak at  $-0.1$  V appears due to the hydrogen peroxide ( $\text{H}_2\text{O}_2$ ) reduction (Eq. 6.6). An increase in the anodic peak current was observed, probably because of a parallel catalytic reaction in which  $\text{Cu}^{2+}$  is reduced to  $\text{Cu}^+$  by hydrogen peroxide according to Eq. 6.7. This produces  $\text{Cu}^+$  that is electro-oxidized back to  $\text{Cu}^{2+}$ , causing the increase in the anodic peak (Yang et al. 2014c).



The amperometric response of the CuS and chitosan-modified glassy carbon electrode at  $-0.1$  V working potential and the corresponding calibration curve are shown in Fig. 6.3c, d, respectively. A dynamic range of 1–100  $\mu\text{M}$  and detection limit of 0.3  $\mu\text{M}$  were achieved (Yang et al. 2014c). A comparison of some recent copper sulfide-based hydrogen peroxide sensors is presented in Table 6.1. It is worth

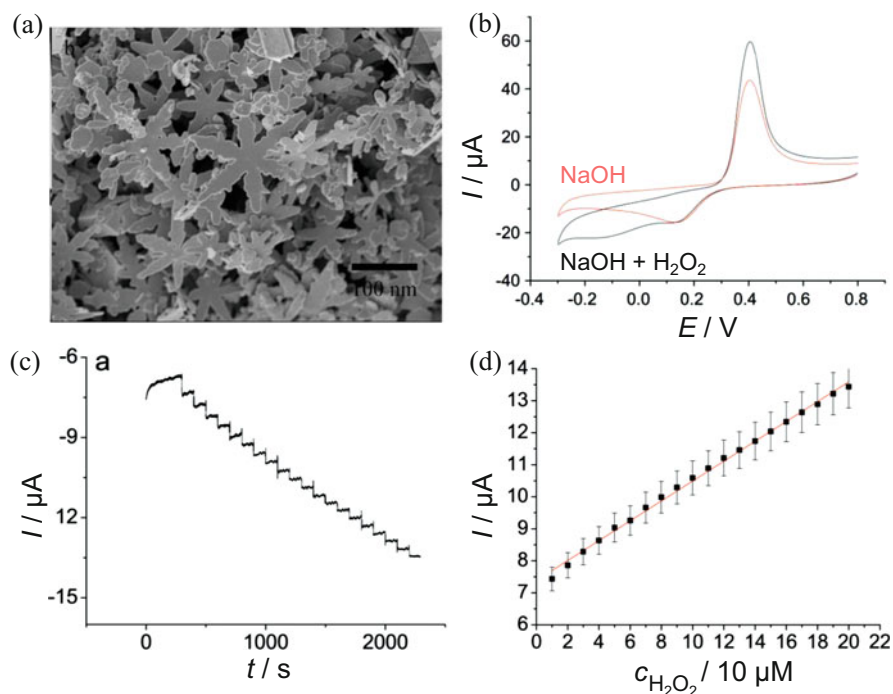
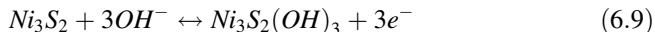
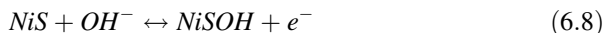


**Fig. 6.3** (a) Scanning electron microscopy image of the flower-like CuS nanoparticles and chitosan-modified glassy carbon electrode. (b) Cyclic voltammograms in 0.1 M phosphate buffer solution (pH 7.2) in the absence (red colored) and presence of 0.5 mM hydrogen peroxide (H<sub>2</sub>O<sub>2</sub>, black colored). Note the cathodic peak at  $-0.1$  V due to the hydrogen peroxide reduction. Scan rate:  $100 \text{ mV s}^{-1}$ . (c) Dynamic current responses to successive additions of hydrogen peroxide. Injections of  $20 \mu\text{L}$ ,  $5 \times 10^{-2} \text{ M}$  hydrogen peroxide solution into  $10 \text{ mL}$  phosphate buffer. Applied potential:  $-0.1 \text{ V}$ . (d) Calibration curve of the hydrogen peroxide amperometric sensor. The analytical performance of sensor demonstrated a dynamic range of  $1\text{--}100 \mu\text{M}$  and a detection limit of  $0.3 \mu\text{M}$ . Electrochemical measurements were taken using a saturated calomel electrode as reference. (Reproduced with permission from (Yang et al. 2014c). Copyright Elsevier 2014)

mentioning that Maji et al. achieved in an amperometric detection, a wide range detection from  $10 \mu\text{M}$  to  $3.75 \text{ mM}$  with detection limit of  $1.1 \mu\text{M}$  (signal–noise ratio = 3) by using a glassy carbon electrode modified with Cu<sub>2</sub>S nanoplates synthesized via one-step solvothermal decomposition. With the quantification of hydrogen peroxide arising from glucose oxidation catalyzed by glucose oxidase (GOD), the glucose was quantified in an enzymatic biosensor in a range of  $10 \mu\text{M}$ – $3.1 \text{ mM}$ , with detection limit of  $1.3 \mu\text{M}$ . The sensor exhibited selectivity and anti-interference ability against uric acid, ascorbic acid, L-cysteine, acetaminophen, and glutathione (Maji et al. 2013). However, the analytical performance falls below most of the nonenzymatic glucose biosensors in Table 6.1.

## 6.2.2 Nickel Sulfides

Nickel sulfides ( $\text{NiS}_x$ ) have attracted interest because of the low cost, abundance, easy preparation, and catalytic activity. The atomic ratio can vary with  $x$  increasing from 0.5 to 2.0, that is,  $\text{NiS}$ ,  $\text{NiS}_2$ ,  $\text{Ni}_3\text{S}_2$ ,  $\text{Ni}_3\text{S}_4$ ,  $\text{Ni}_7\text{S}_{10}$ , and  $\text{Ni}_9\text{S}_8$ , in distinct phases and morphologies. For instance,  $\text{NiS}$  exhibits two phases, the low-temperature rhombohedral ( $\beta$ - $\text{NiS}$ , millerite) and the high-temperature hexagonal ( $\alpha$ - $\text{NiS}$ ) (Ghezelbash et al. 2004). This opens the possibility of tuning properties by varying the phase and morphology, and they can coexist as a combination of two or more phases, though getting a single phase is difficult (Theerthagiri et al. 2018; Zheng et al. 2019). Nickel sulfides have been used in supercapacitors (Yang et al. 2014a; Yu et al. 2015), lithium-ions batteries (Lai et al. 2009; Li et al. 2017), and catalysis for oxygen and hydrogen evolution reactions in water splitting (Jiang et al. 2016; Luo et al. 2017; Zheng et al. 2019). Ni compounds have also been utilized for detecting glucose because of their ability to catalyze the glucose oxidation. Biosensors have been made with conventional glassy carbon electrode and in Ni foam as a 3D supporting electrode with larger exposed area and faster electron transfer (Huo et al. 2014; Lin et al. 2014; Kim et al. 2016). The reversible redox reaction of  $\text{NiS}$  (Kannan and Rout 2015; Lin et al. 2018) and  $\text{Ni}_3\text{S}_2$  (Huo et al. 2014) in alkaline medium is represented in Eqs. 6.8 and 6.9.



During the anodic scan,  $\text{Ni}^{2+}$  is oxidized to  $\text{Ni}^{3+}$  (Eq. 6.10). In the presence of glucose,  $\text{Ni}^{3+}$  species oxidizes glucose to gluconolactone (Eq. 6.11) (Kannan and Rout 2015).



$\text{Ni}_3\text{S}_2$  is one of the most investigated due to its high conductivity (with resistivity  $\sim 1.8 \times 10^{-5} \Omega$  at room temperature (Kim et al. 2016)), abundance (in minerals as hazelwoodite) (Huo et al. 2014), and simple synthesis route (Theerthagiri et al. 2018). Figure 6.4a–d shows scanning electron microscopy topographic images for the  $\text{Ni}_3\text{S}_2$  synthesized by hydrothermal process on Ni foam electrode using different media (water, ethanol, and ethanol/water mixture), thus giving rise to different morphologies.

Figure 6.5a shows the oxidation and reduction peaks at  $\sim +0.6$  and  $\sim +0.35$  V of a voltammogram plot, respectively, attributed to the reversible  $\text{Ni}^{2+}/\text{Ni}^{3+}$  and  $\text{OH}^-$  in an alkaline electrolyte (Kim et al. 2016). The electrode produced in a mixture of ethanol and water ( $\text{Ni}_3\text{S}_2$ -ethanol/water) denoted as cauliflower-like structure exhibited the highest current density and area under the cyclic voltammetry. In the

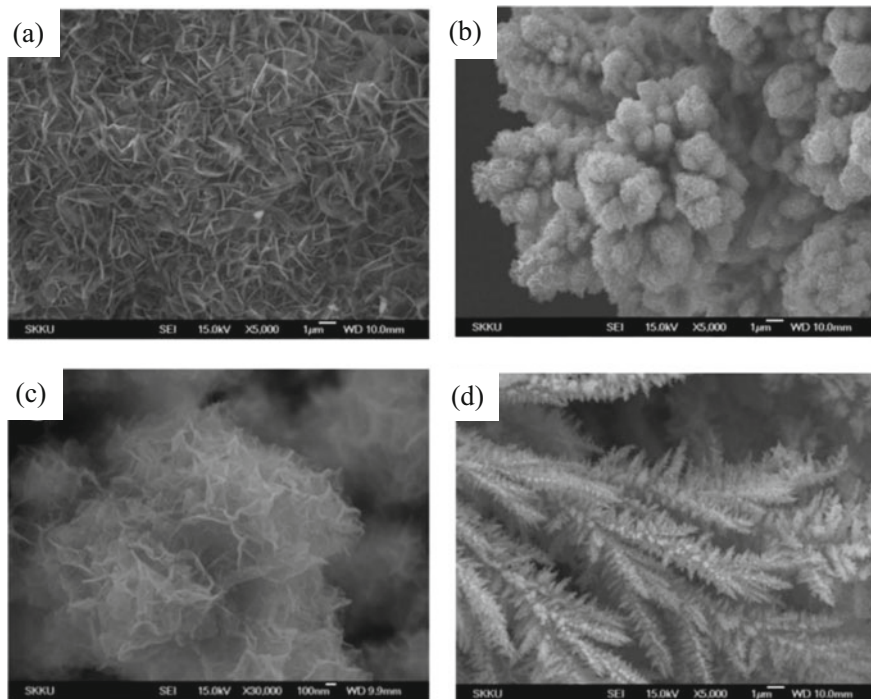


**Fig. 6.4** Scanning electron microscopy images of nickel sulfide by various reaction media: (a)  $\text{Ni}_3\text{S}_2$ -ethanol, (b and c)  $\text{Ni}_3\text{S}_2$ -ethanol/water in two magnifications, and (d)  $\text{Ni}_3\text{S}_2$ -water. (Reproduced with permission from (Kim et al. 2016). Copyright Elsevier 2016)

presence of 1 mM glucose solution, this electrode demonstrated an increased oxidation peak current as shown in Fig. 6.5b. Based on Eq. 6.11,  $\text{Ni}^{3+}$  oxidizes the glucose to gluconolactone, generating  $\text{Ni}^{2+}$  and sacrificing  $\text{Ni}^{3+}$  leading to an increase in anodic peak current (Kim et al. 2016). The increase in the anodic peak current was monitored by chronoamperometric measurements at +0.55 V working potential (Fig. 6.5c), and their calibration curves are shown in Fig. 6.5d. The sensing performance of this sensor is compared to others in the literature in Table 6.2.

To exemplify the influence of different phases in the sensing performance, Wei et al. developed glucose sensors with  $\alpha$ -NiS and  $\beta$ -NiS forms. Amperometric measurements at +0.60 V working potential revealed the superior detection range and sensitivity of  $\alpha$  form (comparison of the analytical parameters can be done in Table 6.2). This higher performance was ascribed to: (i)  $\alpha$ -NiS offered a larger accessible surface area and efficient pathways for ion and electron transport; (ii)  $\alpha$ -NiS is polycrystalline by nature, which shortens the diffusion path for ions and electrons; (iii) the crystal structure at the atomic scale favors the  $\alpha$ -NiS form with more surface exposed Ni atoms (Wei et al. 2015).

Some hybrid nickel sulfides/oxides have been investigated as well. Kannan et al. observed that Ni-Ni<sub>3</sub>S<sub>3</sub>/NiMoO<sub>4</sub> nanowire-based electrode has a low onset oxidation



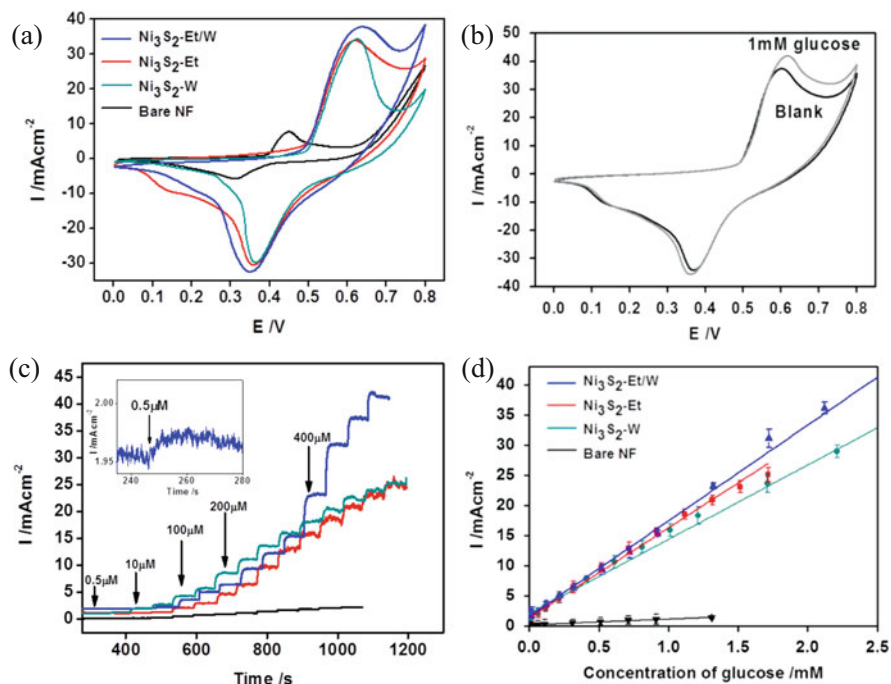


**Fig. 6.5** (a) Cyclic voltammetry of the different  $\text{Ni}_3\text{S}_2$  structures on Ni foam electrodes in 0.5 M NaOH solution at  $10 \text{ mV s}^{-1}$ . The oxidation and reduction peaks are attributed to the reversible  $\text{Ni}^{2+}/\text{Ni}^{3+}$  reaction in an alkaline electrolyte. Bare NF refers to bare Ni foam,  $\text{Ni}_3\text{S}_2\text{-Et}$ ,  $\text{Ni}_3\text{S}_2\text{-W}$ , and  $\text{Ni}_3\text{S}_2\text{-Et/W}$  refers to the  $\text{Ni}_3\text{S}_2\text{-ethanol}$ ,  $\text{Ni}_3\text{S}_2\text{-water}$ , and  $\text{Ni}_3\text{S}_2\text{-ethanol/water}$ . (b) Cyclic voltammetry of  $\text{Ni}_3\text{S}_2\text{-ethanol/water}$ -composed electrode in 1 mM glucose/0.5 M sodium hydroxide aqueous solution at  $20 \text{ mV s}^{-1}$ . The sensor response is based on the glucose oxidation to gluconolactone by  $\text{Ni}^{3+}$  and consequent generation and increase of  $\text{Ni}^{2+}$  concentration, which leads to an increased  $\text{Ni}^{2+}$  oxidation anodic peak current. (c) Amperometric responses of bare Ni foam electrode (black colored), and the modified ones with  $\text{Ni}_3\text{S}_2\text{-ethanol}$  (green colored),  $\text{Ni}_3\text{S}_2\text{-ethanol/water}$  (blue colored), and  $\text{Ni}_3\text{S}_2\text{-water}$  (red colored) to successive addition of glucose at +0.55 V. Inset: magnification of  $\text{Ni}_3\text{S}_2\text{-ethanol/water}$  response during addition of 0.5  $\mu\text{M}$  of glucose. (d) Calibration curves from amperometric responses. Electrochemical measurements were taken using a silver/silver chloride electrode as reference (Reproduced with permission from (Kim et al. 2016). Copyright Elsevier 2016)

potential and an enhanced catalytic response toward glucose oxidation when compared to the electrodes made with the individual materials, that is, Ni- $\text{Ni}_3\text{S}_2$  and Ni- $\text{NiMoO}_4$  (Kannan et al. 2019). The sensitivities were  $5.72$  and  $1.32 \mu\text{A } \mu\text{M cm}^{-2}$  for the Ni- $\text{Ni}_3\text{S}_2$  and Ni- $\text{NiMoO}_4$  electrodes, respectively, and  $10.49 \mu\text{A } \mu\text{M cm}^{-2}$  for the nanocomposite electrode. The best performance was attributed to the large specific surface area with an interconnected  $\text{NiMoO}_4$  thin sheet-like configuration on the 3D Ni- $\text{Ni}_3\text{S}_2$  nanowires enabling good electronic conductivity and providing consistent electrical connections to access a large number of glucose molecules.

**Table 6.2** Nickel sulfides-based glucose amperometric sensors

Electrode	Sensitivity	Range	Detection limit ( $\mu\text{M}$ )	Working potential (V)	Response time (s)	References
NiS/ITO	$7430 \mu\text{A mM}^{-1} \text{cm}^{-2}$	$5\text{--}45 \mu\text{M}$	0.32	+0.5 vs. Ag/AgCl	8	Kamran and Rout (2015)
$\text{Ni}_3\text{S}_2/\text{MWCNT}/\text{NiF}$	$3345 \mu\text{A mM}^{-1}$	30–500	1.0	+0.54 vs. Ag/AgCl	–	Lin et al. (2014)
3D $\text{Ni}_3\text{S}_2/\text{NiF}$	$6148.02 \mu\text{A mM}^{-1} \text{cm}^{-2}$	0.005–3.0 mM	1.2	+0.55 vs. Hg/HgO	2	Huo et al. (2014)
NiS-rGO/GCE	–	0.05–1.7 mM	10	+0.5 vs. Ag/AgCl	2	Radhakrishnan et al. (2016)
$\text{Ni}_3\text{S}_2$ nanocauliflower nanosheets/NiF	$16,460 \mu\text{A mM}^{-1} \text{cm}^{-2}$	$0.5 \mu\text{M}$ – 3.0 mM	0.82	+0.55 vs. Ag/AgCl	–	Kim et al. (2016)
3D $\text{Ni}_7\text{S}_6/\text{GCE}$	$271.80 \mu\text{A mM}^{-1} \text{cm}^{-2}$	0.005–3.7 mM	0.15	+0.45 vs. Ag/AgCl	–	Wu et al. (2016)
Hollow $\alpha\text{-NiS}/\text{GCE}$	$155 \mu\text{A mM}^{-1} \text{cm}^{-2}$	$0.125 \mu\text{M}$ – 2.0 mM	0.125	+0.60 vs. Ag/AgCl	–	Wei et al. (2015)
Hollow $\beta\text{-NiS}/\text{GCE}$	$3.6 \mu\text{A mM}^{-1} \text{cm}^{-2}$	0.24–2.0 mM	20	+0.60 vs. Ag/AgCl	–	Wei et al. (2015)
f-CB/NiS/GCE	$1223 \mu\text{A mM}^{-1} \text{cm}^{-2}$	$0.125\text{--}268 \mu\text{M}$	0.022	+0.47 vs. Ag/AgCl	–	Kubendhiran et al. (2018a)
		268–1781 $\mu\text{M}$				
$\text{Ni}_7\text{S}_6/\text{NiO}/\text{GCE}$	$7.10 \mu\text{A mM}^{-1} \text{cm}^{-2}$	0.09–3.12 mM	0.3	+0.50 vs. Hg/HgO	–	Tan et al. (2019)
$\text{Ni}_3\text{S}_2/\text{NiMoO}_4/\text{NiF}$	$10.49 \mu\text{A mM}^{-1} \text{cm}^{-2}$	0–240 $\mu\text{M}$	0.055	+0.50 vs. Ag/AgCl	1	Kamran et al. (2019)

*f*-CB functionalized-carbon black, *GCE* glassy carbon electrode, *ITO* indium tin oxide, *NiF* nickel foam, *rGO* reduced graphene oxide, *MWCNT* multiwalled carbon nanotubes, *3D* three-dimensional

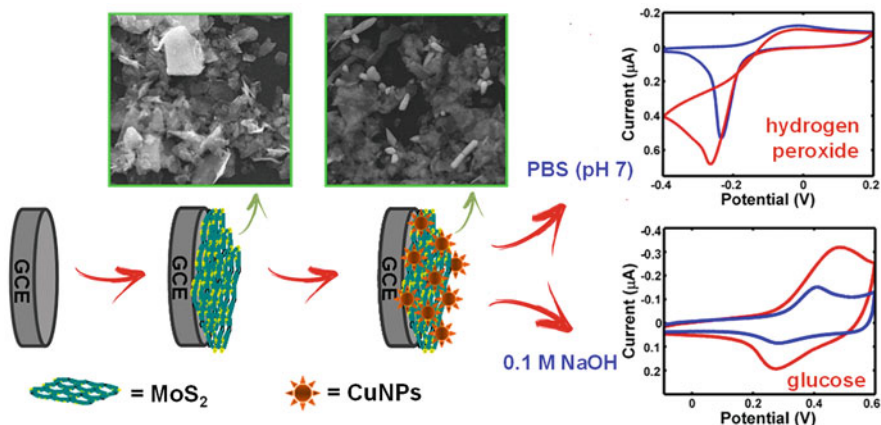
The working potentials are given versus the respective reference electrode employed in the experiments, which are silver/silver chloride (Ag/AgCl) or mercury/mercury oxide (Hg/HgO).

### 6.2.3 Molybdenum Sulfide

Molybdenum sulfides ( $\text{MoS}_x$ ) are promising as alternative materials to Pt for electrochemical generation of hydrogen from water (Laursen et al. 2012; Yan et al. 2014). The most studied molybdenum disulfide ( $\text{MoS}_2$ ) is a 2D material with S–Mo–S layers constituted by atomic planes of Mo sandwiched between atomic planes of S (Li and Zhu 2015; Wang et al. 2015). The direct bandgap of 1.8 eV makes  $\text{MoS}_2$  layers as a complement or even surpass graphene in optoelectronics (Bo et al. 2010; Li and Zhu 2015). It is also interesting for (bio)/sensing applications owing to the large surface area, biocompatibility, high conductivity, electrochemical activity, and structural versatility. As S–Mo–S layers are stacked together by van der Waals interactions, topdown approaches have been proposed for obtaining single and few-layer  $\text{MoS}_2$ , by mechanical and chemical exfoliation methods (Joensen et al. 1986; Gan et al. 2017). The popular chemical exfoliation uses the intercalation method with lithium-ion and further reaction with water (Joensen et al. 1986; Su et al. 2014). Bottom-up methodologies can be utilized as well, as solvothermal and hydrothermal methods (Peng et al. 2001; Mani et al. 2016), and chemical vapor deposition (Lee et al. 2012). Solvothermal and hydrothermal paths are simple and scalable, but usually require high temperature and pressure, and need special organic reagents (Gan et al. 2017).

Among the diverse applications,  $\text{MoS}_2$  has been explored as gas sensors due to its high surface area and because the electron transport through the exposed surface atoms is sensitive to the adsorbed molecules (Zhang et al. 2014; Cho et al. 2015; Park et al. 2018; Qin et al. 2018). Additionally, its catalytic activity (Wang et al. 2015; Gan et al. 2017; Sinha et al. 2018) has been exploited toward pollutants like nitrite and *m*-nitrophenol (Wang et al. 2016; Zhang et al. 2016a, 2017; Chen et al. 2017).

$\text{MoS}_2$  has been used in electrochemical sensors, normally combined with other nanomaterials such as gold nanoparticles (Su et al. 2013; Sun et al. 2014), carbon nanotubes, and graphene (Mani et al. 2016; Park et al. 2018). This applies to  $\text{MoS}_2$ -based glucose biosensors (Kibsgaard et al. 2012). For example, a composite of Cu-based materials and  $\text{MoS}_2$  exploited the sensing signal derived from the  $\text{Cu}^{2+}/\text{Cu}^{3+}$  redox pair (Huang et al. 2013; Fang et al. 2017), while a similar approach was employed with Ni-based materials where the signal derived from the  $\text{Ni}^{2+}/\text{Ni}^{3+}$  redox pair (Huang et al. 2014; Geng et al. 2017). Furthermore,  $\text{MoS}_2$  was combined with graphene (Jeong et al. 2017) and gold nanoparticles (Dai et al. 2009; Su et al. 2014; Parlak et al. 2017; Ma et al. 2019). Lin et al. developed a 3D Cu nanoflowers/layered  $\text{MoS}_2$  composite on glassy carbon electrode (3D CuNFs- $\text{MoS}_2$ /GCE) capable to detect glucose and hydrogen peroxide, as schematically represented in

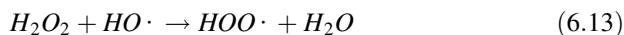


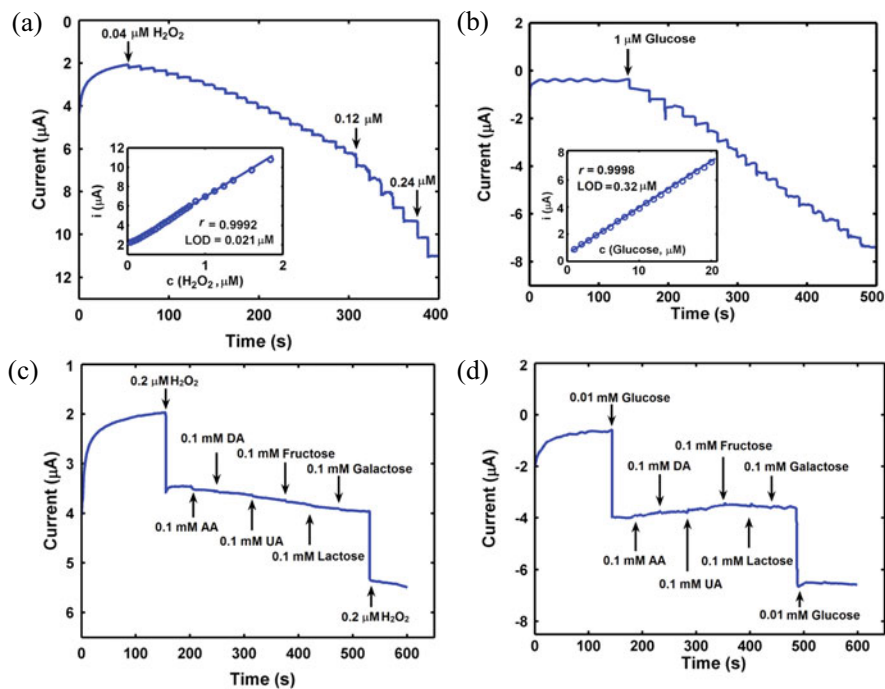
**Fig. 6.6** Schematic representation of 3D Cu nanoflowers-MoS<sub>2</sub>-modified glassy carbon electrode fabrication and the detection of 2.0 μM hydrogen peroxide and 20 μM glucose (red colored) by cyclic voltammetry in 0.1 M phosphate buffer saline solution (pH 7.0) and 0.1 M sodium hydroxide (NaOH, blue colored), respectively, at 0.10 V s<sup>-1</sup> (Reproduced with permission from (Lin et al. 2016). Copyright Elsevier 2016)

Fig. 6.6. The cyclic voltammety plots indicate that the presence of the hydrogen peroxide in 0.1 M phosphate buffer saline solution (PBS, pH 7) causes an enhanced reduction in the peak current at -0.3 V, differently from the glucose addition, in 0.1 M sodium hydroxide solution, which makes an anodic peak current appear at +0.50 V. Both reaction were catalyzed by Cu<sup>2+</sup>/Cu<sup>3+</sup> redox pair.

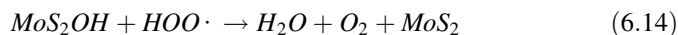
Since the working potential for detecting hydrogen peroxide and glucose solution was established by cyclic voltammetry experiments, further analytical studies were performed by amperometric technique. The response to successive addition of hydrogen peroxide and glucose, monitored at -0.30 and +0.50 V, respectively, is shown in Fig. 6.7a, b, and the analytical parameters are depicted in the insets and compared in Table 6.3. Moreover, Cu nanoflowers/layered MoS<sub>2</sub>-modified glassy carbon electrode exhibits selectivity toward different chemicals such as ascorbic acid (AA), dopamine (DA), uric acid (UA), fructose, lactose, and galactose, because negligible changes are observed in Fig. 6.7c, d. Significant decrease is observed only with hydrogen peroxide and glucose addition. The performance of this sensor and others in the literature is compared in Table 6.3.

The possible reaction mechanism is based on the oxidation of MoS<sub>2</sub> to MoS<sub>2</sub>OH, as shown in Eq. 6.12. HOO is produced by the reaction of H<sub>2</sub>O<sub>2</sub> and HO (Eq. 6.13), and O<sub>2</sub> is eventually produced according to the reaction in Eq. 6.14 (Lin et al. 2016).





**Fig. 6.7** Amperometric response of the modified electrode to successive additions of (a) hydrogen peroxide ( $\text{H}_2\text{O}_2$ ) to 0.1 M phosphate-buffered saline solution (pH 7.0) at  $-0.30$  V, and (b) glucose to 0.1 sodium hydroxide at  $+0.50$  V. Inset: Analytical curve. Amperometric response for some interferent compounds, ascorbic acid (AA), dopamine (DA), uric acid (UA), fructose, lactose, and galactose in the presence of (c) hydrogen peroxide and (d) glucose. Electrochemical measurements were taken using a saturated calomel as reference electrode (Reproduced with permission from (Lin et al. 2016). Copyright Elsevier 2016)



Wang et al. incorporated few-layer MoS<sub>2</sub> nanosheets on NiCo<sub>2</sub>O<sub>4</sub> nanoplates using the hydrothermal method to inhibit NiCo<sub>2</sub>O<sub>4</sub> natural self-aggregation and promote conductive chains to accelerate charge transfer. They take advantage of MoS<sub>2</sub> basal surfaces nanoplates to connect dispersed NiCo<sub>2</sub>O<sub>4</sub> and obtain polycrystalline MoS<sub>2</sub>-NiCo<sub>2</sub>O<sub>4</sub> hybrid, as shown in Fig. 6.8a. MoS<sub>2</sub>-NiCo<sub>2</sub>O<sub>4</sub> had an enhanced electrocatalytic activity toward glucose oxidation, compared to pristine MoS<sub>2</sub> and NiCo<sub>2</sub>O<sub>4</sub>, as shown in Fig. 6.8b. The amperometric signal was monitored at a constant potential of  $+0.418$  V, as shown in Fig. 6.8c, with the analytical parameters described in Table 6.3. Negligible signal changes were observed in interferent experiments when ascorbic acid, uric acid, dopamine, chloride ion, fructose, galactose, and mannose were added to an alkaline solution. Reproducibility and stability of signals were monitored for 15 days and kept down to 3.82% of the standard deviation. Real samples were also assessed in blood serum matrix and a

**Table 6.3** Molybdenum sulfides-based glucose and hydrogen peroxide electrochemical sensors

Glucose sensors										
Electrode	Sensitivity	Range	Detection limit ( $\mu\text{M}$ )	Working potential (V)	Response time (s)	Reference				
Cu-MoS <sub>2</sub> /GCE	1055 $\mu\text{A mM}^{-1} \text{cm}^{-2}$	0–4 mM	–	+0.65 vs. Ag/AgCl	–	Huang et al. (2013)				
GOx-AuNP@MoS <sub>2</sub> /GCE	–	10–300 $\mu\text{M}$	2.8	–0.50 vs. SCE	–	Su et al. (2014)				
NiNP-MoS <sub>2</sub> /GCE	1824 $\mu\text{A mM}^{-1} \text{cm}^{-2}$	0–4 mM	0.31	+0.50 vs. Ag/AgCl	2	Huang et al. (2014)				
Cu NF/MoS <sub>2</sub> /GCE	–	1–20 $\mu\text{M}$	0.32	+0.50 vs. SCE	–	Lin et al. (2016)				
		20–70 $\mu\text{M}$								
MoS <sub>2</sub> MF/GCE	570.71 $\mu\text{A mM}^{-1}$	0–30 $\mu\text{M}$	–	~ + 0.55 vs. Ag/AgCl	–	Zhai et al. (2016)				
Ni-MoS <sub>2</sub> /rGO/GCE	256.1 $\mu\text{A mM}^{-1} \text{cm}^{-2}$	0.005–8.2 mM	2.7	+0.55 vs. Ag/AgCl	2	Geng et al. (2017)				
MoS <sub>2</sub> /AuNP/GOx	13.80 $\mu\text{A mM}^{-1} \text{cm}^{-2}$	0.25–13.2 mM	0.042	+0.35 vs. Ag/AgCl	3	Parlak et al. (2017)				
GOx/3D MoS <sub>2</sub> -graphene aerogel/GCE	3.36 $\mu\text{A mM}^{-1}$	2–20 mM	290	–0.45 vs. Ag/AgCl	4	Jeong et al. (2017)				
Cu <sub>2</sub> O/MoS <sub>2</sub> /GCE	3108.87 $\mu\text{A mM}^{-1} \text{cm}^{-2}$	0.01–4.0 mM	1.0	+0.70 vs. SCE	3	Fang et al. (2017)				
Au-Pd/MoS <sub>2</sub> /GCE	–	0.5–20 mM	400	–0.10 vs. SCE	–	Li and Du (2017)				
MoS <sub>2</sub> -NiCo <sub>2</sub> O <sub>4</sub>	1748.58 $\mu\text{A mM}^{-1} \text{cm}^{-2}$	1–11,100 $\mu\text{M}$	0.152	–0.418 vs. SCE	5	Wang et al. (2018a)				
MoS <sub>2</sub> -Ppy-AuNP/GCE	37.35 $\mu\text{A mM}^{-1} \text{cm}^{-2}$	0.1–80 nM	0.0008	+0.45 vs. SCE	–	Ma et al. (2019)				

Hydrogen peroxide sensors								
MoS <sub>2</sub> NP	2580 $\mu\text{A mM}^{-1} \text{cm}^{-2}$	5–100 nM	0.0025	–0.25 vs. SCE	5	Wang et al. (2013)		
	160 $\mu\text{A mM}^{-1} \text{cm}^{-2}$	100 nM– 100 $\mu\text{M}$						
Cu NF/MoS <sub>2</sub> /GCE	–	0.04–1.88 $\mu\text{M}$ 1.88–35.6 $\mu\text{M}$	0.021	–0.30 vs. SCE	–	Lin et al. (2016)		
Au-Pd/MoS <sub>2</sub> /GCE	184.9 $\mu\text{A mM}^{-1} \text{cm}^{-2}$	0.8 $\mu\text{M}$ – 10 mM	0.16	~ – 0.04 vs. SCE	–	Li and Du (2017)		
MoS <sub>2</sub> -ICPC/GCE	370 $\mu\text{A mM}^{-1}$	20–300 $\mu\text{M}$	11.8	–0.38 vs. Ag/AgCl	3	Mutyala et al. (2018)		
O-MoS <sub>2</sub> /graphene/GCE	269.7 $\mu\text{A mM}^{-1} \text{cm}^{-2}$	0.25–16 mM	0.12	–0.38 vs. Hg/HgO	5	Xue et al. (2018)		

3D three-dimensional, AuNP gold nanoparticles, GCE glassy carbon electrodes, GOx glucose oxidase, NF nanoflowers, rGO reduced graphene oxide, MF microflowers, Ppy poly(pyrrrole), NP nanoparticles, ICPC interconnected porous carbon, O-MoS<sub>2</sub> oxygen implanted MoS<sub>2</sub>

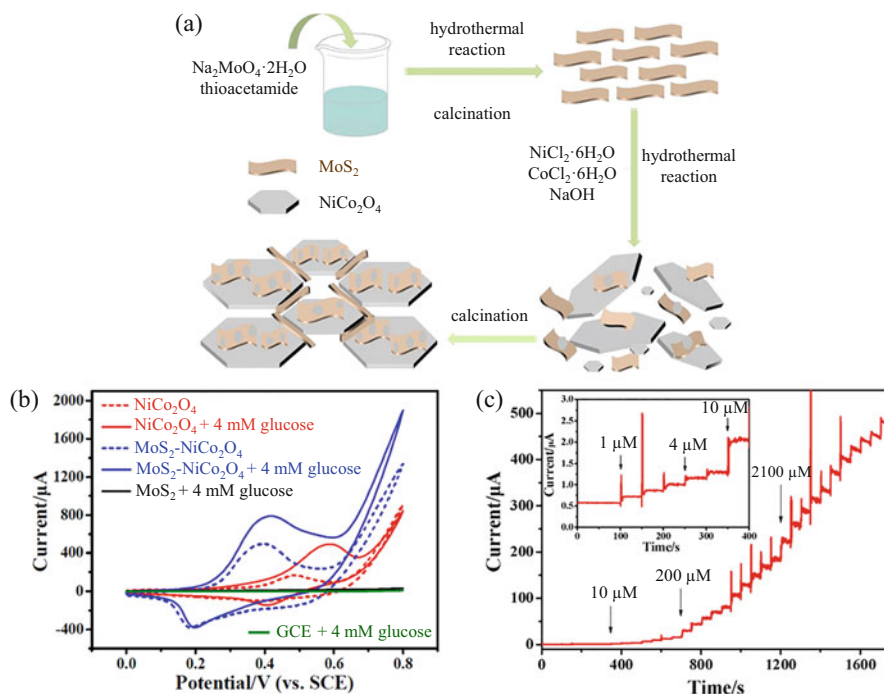
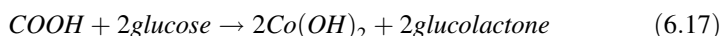
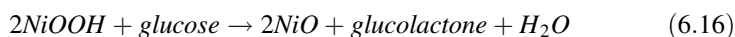


**Fig. 6.8** (a) The fabrication process of the MoS<sub>2</sub>-NiCo<sub>2</sub>O<sub>4</sub> hybrid. (b) Cyclic voltammograms indicating the enhanced electrocatalytic activity toward the glucose oxidation by the MoS<sub>2</sub>-NiCo<sub>2</sub>O<sub>4</sub>/GCE compared to pristine MoS<sub>2</sub> and NiCo<sub>2</sub>O<sub>4</sub> and the bare glassy carbon electrode (GCE). Dotted and solid lines represent, respectively, the measurements in the absence and presence of 4 mM glucose in 0.1 M NaOH at a scan rate of 50 mV s<sup>-1</sup>. (vs. SCE) indicates that the reference electrode employed is a saturated calomel electrode. (c) Amperometric curve of MoS<sub>2</sub>-NiCo<sub>2</sub>O<sub>4</sub> toward successive additions of glucose from 1 µM to 11.1 mM at the applied potential of +0.418 V. Amperometric response from 0 to 400 s (inset). (Reproduced with permission from (Wang et al. 2018a). Copyright Elsevier 2018)

recovery around 98.7 and 104.1% was achieved (Wang et al. 2018a). The reaction mechanism includes generation of Ni<sup>3+</sup> and Co<sup>3+</sup>, Eq. 6.15), as key catalytic intermediates to transform glucose to gluconolactone and then convert back to Ni<sup>2+</sup> and Co<sup>2+</sup> at the same time, Eqs. 6.16 and 6.17.



The working potential refers to the chronoamperometric measurements, otherwise specified as CV (cyclic voltammetry) or DPV (differential pulse voltammetry)



using the saturated calomel (SCE), silver/silver chloride (Ag/AgCl), and mercury/mercury oxide (Hg/HgO) as reference electrode.

The use of MoS<sub>2</sub> in dopamine detection (Su et al. 2013; Sun et al. 2014; Mani et al. 2016) should be highlighted. Abnormal levels of dopamine are related to disorders such as schizophrenia, Parkinson's disease, and attention deficit hyperactivity disorder (Sun et al. 2014). Su et al. synthesized MoS<sub>2</sub> nanosheets by Li intercalation exfoliation and decorated then with gold nanoparticles by microwave-assisted hydrothermal method. The product gold nanoparticles@MoS<sub>2</sub> suspension was drop cast on glassy carbon electrodes for differential pulse voltammetry detection of dopamine. A wide detection range was achieved, from 0.1 to 200 μM, with a limit of detection of 80 nM ( $S/N = 3$ ). The interference of uric acid and ascorbic acid, common interferents in dopamine detection due to similar oxidation potentials, was tested proving the selectivity of the sensor toward dopamine (Su et al. 2013). Another gold nanoparticles@MoS<sub>2</sub>-based sensor was developed by Sun et al. that detected ascorbic acid, dopamine, and uric acid simultaneously, as the oxidation peaks were distinct, with a detection limit of 100, 0.05, and 10 μM, respectively. The MoS<sub>2</sub> solution was drop cast on the glassy carbon electrodes surface for further electrodeposition of gold nanoparticles. The sensor was applied for dopamine quantification in human serum, with recovery varying from 98.03% to 102.08% (Sun et al. 2014). A composite material made of graphene, carbon nanotubes, and MoS<sub>2</sub> microflowers could detect dopamine with a linear range of 0.1–100 μM and a detection limit of 0.05 μM, in addition to the detection in serum samples of rat brain and pharmaceutical was performed with recovery from 97 to 102% (Mani et al. 2016).

The superior sensing performance of composites when compared to single Cu nanoflowers and MoS<sub>2</sub> is not the only advantage, as materials combination allows one to identify two different analytes working under different reaction mechanisms. This may drive future studies for multisensory systems such as electronic tongues (Raymundo-Pereira et al. 2019) that are capable of analyzing multicomponent aqueous solutions, overcoming the single response of each sensor.

### 6.2.4 Other Sulfides

Various other metal sulfides have been applied in sensing, including cadmium sulfides (Maji et al. 2012b), Co sulfides (Zhang et al. 2015; Wu et al. 2017; Kubendhiran et al. 2018b), and Fe sulfides (Dai et al. 2009; Maji et al. 2012a), as summarized in Table 6.4. Also used in electrochemical sensing were bimetallic sulfides and hybrid sulfide/oxide composites. The bimetallic Ni-S and Ni-Mn-S films were electrodeposited on Ti mesh, with the inclusion of Mn in Ni-Mn-S structure enhancing the conductivity fourfold. The electrochemically active surface area (ECSA) for Ni-S/titanium mesh and Ni-Mn-S/titanium mesh as 4.75 and 6.5 cm<sup>2</sup> per geometry area of 1 cm<sup>2</sup>, respectively. Scanning electron microscopy images indicated that in the absence of Mn the surface was smooth while it assumed

**Table 6.4** Other sulfides-based glucose and hydrogen peroxide electrochemical sensors

<i>Glucose sensors</i>						
Electrode	Sensitivity	Range	Detection limit ( $\mu\text{M}$ )	Working potential (V)	Response time (s)	References
CoS NF@C/GCE	$697 \mu\text{A mM}^{-1} \text{cm}^{-2}$	10–960 $\mu\text{M}$	2.0	+0.45 vs. SCE	3	Qu et al. (2015)
Hollow Co <sub>9</sub> S <sub>8</sub> /GCE	$33.0.3 \text{ mA M}^{-1} \text{cm}^{-2}$	0.02–3.96 mM	6.67	+0.50 vs. Ag/AgCl	–	Zhang et al. (2015)
	$15 \text{ mA M}^{-1} \text{cm}^{-2}$	3.96–23.96 mM				
Ni-co-S/TM	$3291.5 \mu\text{A mM}^{-1} \text{cm}^{-2}$	0.001–3 mM	0.12	+0.55 vs. Hg/HgO	5	Cao et al. (2016)
CoS/GCE	$139.35 \mu\text{A mM}^{-1} \text{cm}^{-2}$	0.005–1.10	1.5	+0.20 vs. Ag/AgCl	–	Wu et al. (2017)
	$28.44 \mu\text{A mM}^{-1} \text{cm}^{-2}$	1.20–10.20				
CoS/GCE	$17.4 \mu\text{A mM}^{-1} \text{cm}^{-2}$	0.005–14.82 mM	1.5	–0.35 vs. Ag/AgCl	3	Wu et al. (2017)
NiCo <sub>2</sub> S <sub>4</sub> /Ni/CFP	$283 \mu\text{A mM}^{-1} \text{cm}^{-2}$	0.0005–6.0 mM	0.05	+0.45 vs. Ag/AgCl	8	Babu et al. (2018)
VS <sub>2</sub> NP/GCE	$41.96 \mu\text{A } \mu\text{M}^{-1}$	0.5 $\mu\text{M}$ –3.0 mM	0.211	–0.75 vs. SCE	5	Sarkar et al. (2018)
Ni-co-S/Ppy/NiF	$2.819 \text{ mA mM}^{-1} \text{cm}^{-2}$	2–140 $\mu\text{M}$	0.82	+0.5 vs. SCE	15	Dai et al. (2018a)
	$0.125 \text{ mA mM}^{-1} \text{cm}^{-2}$	0.14–2 mM				
CuCo <sub>2</sub> S <sub>4</sub> /CFT	$3852.7 \mu\text{A mM}^{-1} \text{cm}^{-2}$	2.5 $\mu\text{M}$ –3.67 mM	1.01	+0.35 vs. Ag/AgCl	–	Xu et al. (2018)
Ni-Ms-S/TM	$860.8 \mu\text{A } \mu\text{M}^{-1} \text{cm}^{-2}$	12 $\mu\text{M}$ –3.5 mM	4.8	+0.75 vs. Ag/AgCl	5	Wang et al. (2019b)

*Hydrogen peroxide sensors*

FeS/GCE	0.5–150 $\mu\text{M}$	0.092	–0.40 vs. SCE	10	Dai et al. (2009)
CdNPs/GCE	1.0 $\mu\text{M}$ –1.9 mM	0.28	–0.6 V vs. Ag/AgCl	7	Maji et al. (2012b)
FeS/FTO	0.5–1300 $\mu\text{M}$	0.12	–0.4 vs. Ag/AgCl	3	Maji et al. (2012a)
Hollow $\text{Co}_9\text{S}_8$ /GCE	0.0001–11.11 mM	0.02	–0.4 vs. Ag/AgCl	–	Zhang et al. (2015)
$\text{MoS}_2$ -CuS/GCE	1.0–100 $\mu\text{M}$	0.3	+0.18 vs. Ag/AgCl	3	Gao et al. (2017)
CoS/rGO/GCE	0.1–2542.4 $\mu\text{M}$	0.042	–0.19 vs. Ag/AgCl	3	Kubendhiran et al. (2018b)
$\text{VS}_2$ NP/GCE	0.5 $\mu\text{M}$ –2.5 mM	0.244	–0.75 vs. SCE	–	Sarkar et al. (2018)
$\text{FeS}_2$ electrode	10 $\mu\text{M}$ –10 mM	8.6	–0.2 vs. Ag/AgCl	3	Wang et al. (2018b)
Cu $\text{FeS}_2$ electrode	100 $\mu\text{M}$ –30 mM	52	–0.4 vs. Ag/AgCl	4	Wang et al. (2018b)
$\text{FeS}_2$ /CVD-graphene	~0.5 nm–5 mM	0.0005	–0.5 vs. Ag/AgCl (LSV)	–	Ebrahimi et al. (2019)
Ni $\text{Co}_2\text{S}_4$ /rGO/GCE	0.025–11.25 mM	0.19	–0.45 vs. Ag/AgCl	5	Wang et al. (2019a)

GCE glassy carbon electrode,  $\text{CoSNF@C}$  nanoflowers-like CoS decorated 3D porous carbon skeleton of rose,  $\text{TM Ti}$  mesh,  $\text{FTO}$  fluorine-doped tin oxide,  $r\text{GO}$  reduced graphene oxide, NP nanoparticles, CFP cellulose filter paper, LSV linear sweep voltammetry,  $\text{FeS}_x$  composed by FeS and  $\text{FeS}_2$ , Ppy poly(pyrole), CFP carbon fiber textile,  $\text{CoS}_2@C$  carbon-coated cobalt sulfide core–shell nanoparticles, CVD chemical vapor deposition

a flower-like morphology in the presence of Mn (Wang et al. 2019b). Composite materials formed by two sulfides also had higher catalytic activity than electrodes composed by individual sulfides. MoS<sub>2</sub>-CuS-modified glassy carbon electrode exhibited stronger catalytic behavior toward glucose oxidation when compared to the MoS<sub>2</sub>- and CuS-modified glassy carbon electrodes (Gao et al. 2017), which was attributed to the high surface-to-volume ratio of Mo<sub>2</sub>S. Additionally, MoS<sub>2</sub>-CuS serves as a good matrix to favor electron transport.

An impressive analytical performance for glucose detection was attained by Babu et al. whose detection limit and linear range were 50 nM and 0.0005–6 mM, respectively. Flexible electrodes were fabricated by first modifying cellulose filter paper (CFP) with nickel film by electroless deposition method. The Ni/cellulose filter paper electrode was modified with three different nanocomposites NiCo<sub>2</sub>S<sub>4</sub>, Co(OH)<sub>2</sub>, and CoS by electrodeposition technique as schematically depicted in Fig. 6.9a. The electrode fabrication was further monitored by scanning electron microscopy and the different morphologies of (i) Ni, (ii) Co(OH)<sub>2</sub>/Ni, (iii) CoS/Ni, and (iv) NiCo<sub>2</sub>S<sub>4</sub>/Ni deposited on cellulose filter paper can be observed in Fig. 6.9b. Cyclic voltammetry experiments were performed for all-step deposition in the presence of 2 mM glucose dissolved in 0.1 M sodium hydroxide solution as shown in Fig. 6.9c. The bare cellulose filter paper has an electrochemically inactive behavior. Ni/cellulose filter paper exhibited the well-defined Ni<sup>3+</sup>/Ni<sup>2+</sup> redox couple for glucose oxidation, whereas an increased anodic peak at ~0.58 V due to the Co<sup>4+</sup>/Co<sup>3+</sup> redox couple was observed for Co(OH)<sub>2</sub>/Ni/cellulose filter paper. After replacing oxygen with sulfur, the peak current at +0.52 V increased for CoS/Ni/cellulose filter paper. NiCo<sub>2</sub>S<sub>4</sub>/Ni/cellulose filter paper had the highest glucose oxidation peak current at +0.45 V due to the participation of both Ni and Co active centers, as depicted in the electro-oxidation mechanism of Fig. 6.9c.

The chronoamperometric response to the addition of glucose and the calibration plot are shown in Fig. 6.10a, b, respectively. The inset image shows that NiCo<sub>2</sub>S<sub>4</sub>/Ni-cellulose filter paper biosensor is capable to measure even 0.5 μM of glucose. This outstanding performance is attributed to the collective promotion of electrical conductivity and abundant active reaction sites in the porous NiCo<sub>2</sub>S<sub>4</sub> nanostructures (Babu et al. 2018). The anti-interference ability against chloride and different substances such as ascorbic acid (AA), uric acid (UA) dopamine (DA), urea (U), acetaminophen (AP), lactose (CA), potassium chloride (KCl), sodium chloride (NaCl), sucrose (Suc), fructose (Fru), mannose (Man), xylose (Xyl), and maltose (Mal) at concentration of 0.1 mM is depicted in Fig. 6.10c, d. It was observed that negligible changes occur when interferent reagents are added to the solution against the apparent increase in the current when 1 mM of glucose (Glu) is present. Finally, in further experiments, the capability to detect glucose in human serum samples was demonstrated with a recovery varying from 98.2 to 102.1%.

The working potential refers to the chronoamperometric experiments, otherwise specified as LSV (linear sweep voltammetry), measured using saturated calomel (SCE), silver/silver chloride (Ag/AgCl), and mercury/mercury oxide (Hg/HgO) reference electrodes.

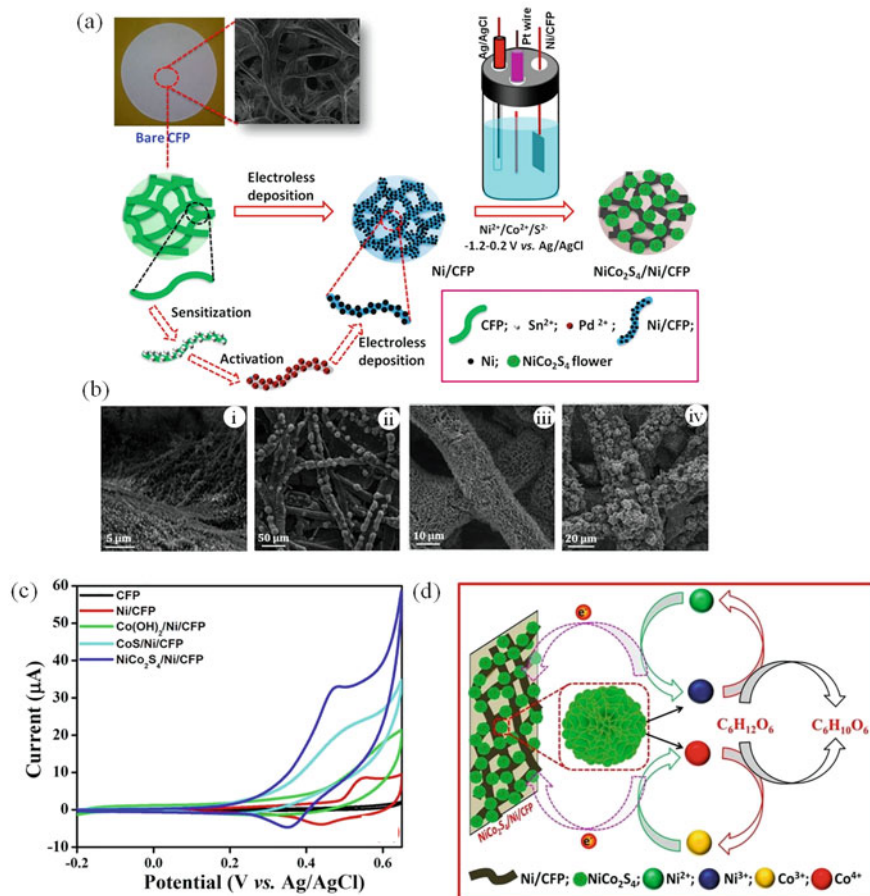


**Fig. 6.9** (a) Preparation of electrodeposited NiCo<sub>2</sub>S<sub>4</sub> on Ni/cellulose filter paper (CFP). (b) Topographic images of scanning electron microscopy of (i) Ni, (ii) Co(OH)<sub>2</sub>/Ni, (iii) CoS/Ni, and (iv) NiCo<sub>2</sub>S<sub>4</sub>/Ni on cellulose filter paper. (c) Cyclic voltammetry of cellulose filter paper, and deposited Ni, Co(OH)<sub>2</sub>/Ni, CoS/Ni, NiCo<sub>2</sub>S<sub>4</sub>/Ni on cellulose filter paper in the presence of 2 mM glucose in 0.1 M sodium hydroxide solution at 20 mV s<sup>-1</sup>. (d) Proposed mechanism in the electrooxidation of glucose at NiCo<sub>2</sub>S<sub>4</sub>/Ni/cellulose filter paper. (Reproduced with permission from (Babu et al. 2018). Copyright American Chemical Society 2018)

### 6.3 Metal Oxide Biosensors

Functional nanomaterials have been exploited in sensing and biosensing (Joshi et al. 2018b; Wongkaew et al. 2019), including metal semiconducting oxides (Malik et al. 2018; Joshi et al. 2019; Tomer et al. 2019) that are also used in UV light-emitting diodes (Yan et al. 2016), dye-sensitized solar cells, and industrial nanodevices (Turkdogan and Kilic 2017; Garcia et al. 2017). Metal semiconducting oxides are advantageous due to their surface reaction activity and ability to immobilize

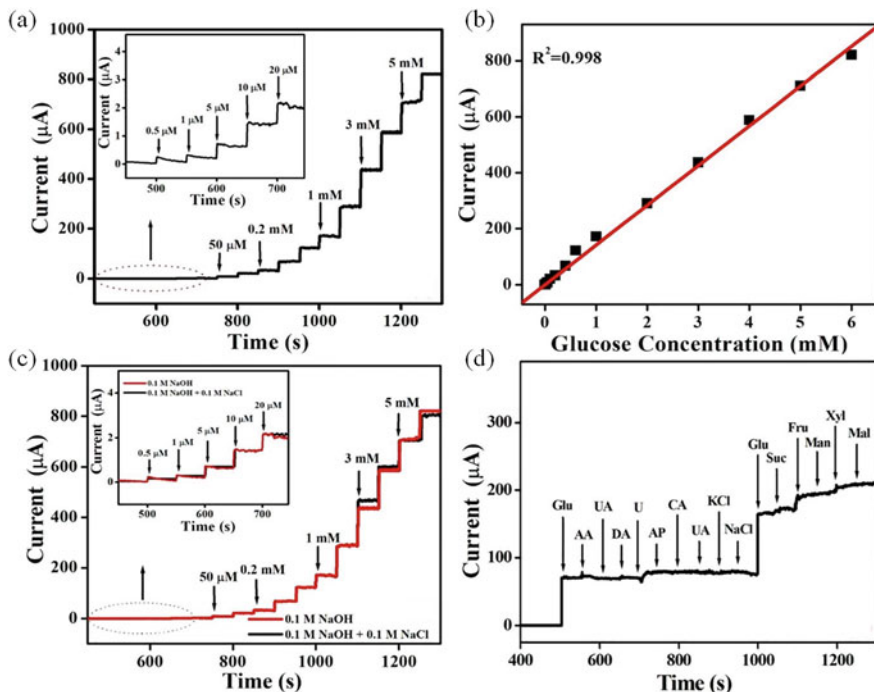


**Fig. 6.10** (a) Amperometric response of NiCo<sub>2</sub>S<sub>4</sub>/Ni/cellulose filter paper upon successive injection of glucose at +0.45 V. Inset: injection interval between 0.5 and 20 μM of glucose. (b) Analytical curve. (c) Chloride poisoning experiment and (d) selectivity experiment of NiCo<sub>2</sub>S<sub>4</sub>/Ni/cellulose filter paper upon exposure to glucose (Glu), ascorbic acid (AA), uric acid (UA), dopamine (DA), urea (U), acetaminophen (AP), lactose (CA), potassium chloride (KCl), sodium chloride (NaCl), sucrose (Suc), fructose (Fru), mannose (Man), xylose (Xyl), and maltose (Mal)

biomolecules (Dakshayini et al. 2019), in addition to their chemical stability, cost-effectiveness, sensitivity, and rapid response. They can be tailored into nanostructures like nanowires, nanotubes, nanorods, nanoparticles, and nanofibers (Pinna and Niederberger 2008; Wu et al. 2012; Sun et al. 2017). Due to their high isoelectric points (IEP), glucose oxidase can be easily immobilized (Aini et al. 2015). Many oxide nanostructures have been used to enhance the selectivity and sensitivity of electrochemical biosensors, as indicated in recent review articles. Xu et al. (Xu and Wang 2012) outlined the application of magnetic nanoparticles in biosensors containing DNA, antibody–antigen, enzyme, and aptamer. Similarly, Haun et al. reviewed the detection of biomolecules and cells based on magnetic resonance effects using magnetic nanoparticles (Haun et al. 2010). Table 6.5 shows the details of sensors made with metal oxide nanostructures and their composites.

In this section, we provide a comprehensive and critical review of the progress and perspectives of metal oxide-based biosensors, like those made with nanostructured ZnO, NiO, SnO<sub>2</sub>, CuO (Yang et al. 2013; Vabbina et al. 2015; Kaur et al. 2016;

**Table 6.5** Nanostructured metal oxide-based biosensors

<i>Glucose sensors</i>						
Electrode	Sensitivity	Range	Detection limit ( $\mu\text{M}$ )	Working potential (V)	Response time (s)	Reference
ZnO nanowire	$30.85 \mu\text{AmM}^{-1} \text{cm}^{-1}$	0.5–4.0	10	+0.8 vs. Ag/AgCl	5	Shukla et al. (2017)
ZnO nanotube	$30.85 \mu\text{AmM}^{-1} \text{cm}^{-1}$	0.1–4.2	10	+0.8 vs. SCE	< 6	Yang et al. (2009)
CuO nanowire	$0.49 \mu\text{A} \mu\text{mol}^{-1} \text{dm}^{-3}$	0.4–2.0	0.049	+0.33 vs. Ag/AgCl	< 1	Zhuang et al. (2008)
CuO nanospheres	$404.85 \mu\text{AmM}^{-1} \text{cm}^{-1}$	0–20.0	1	+0.6 vs. Ag/AgCl	–	Reitz et al. (2008)
CuO-graphene	$1065 \mu\text{AmM}^{-1} \text{cm}^{-1}$	0.001–8.0	1	+0.6 vs. Ag/AgCl	1	Hsu et al. (2012)
MWCNT/CuO nanoparticles	$2596 \mu\text{AmM}^{-1} \text{cm}^{-1}$	0.0004–1.2	0.2	+0.4 vs. Ag/AgCl	1	Jiang and Zhang (2010)
CeO <sub>2</sub> nanorods	$0.165 \mu\text{AmM}^{-1} \text{cm}^{-1}$	2.0–26.0	100	+0.8 vs. Ag/AgCl	1–2	Patil et al. (2012)
CeO <sub>2</sub> nanoparticles	$0.00287 \mu\text{Amg}^{-1} \text{dL}^{-1} \text{cm}^{-1}$	N.A.	12	–	–	Ansari et al. (2008)
TiO <sub>2</sub> -graphene	$6.2 \mu\text{AmA}^{-1} \text{cm}^{-1}$	0–8.0	–	+0.6 vs. SCE	5	Jang et al. (2012)
Ni-cu/TiO <sub>2</sub>	$1590.9 \mu\text{AmA}^{-1} \text{cm}^{-1}$	0.001–3.2	5	+0.6 vs. Ag/AgCl	5	Li et al. (2013)
Fe <sub>3</sub> O <sub>4</sub> @SiO <sub>2</sub> -MWCNT	$58.9 \mu\text{AmM}^{-1} \text{cm}^{-1}$	0.001–30	0.8	0.2	3–6	Baby and Ramaprabhu (2010)
ZrO <sub>2</sub> nanostructures	$111 \mu\text{AmM}^{-1} \text{cm}^{-1}$	0.29–14	130	–0.4 V	–	Viliani et al. (2014)
<i>Hydrogen peroxide sensors</i>						
CeO <sub>2</sub> porous nanostructures	$5.4 \mu\text{AmM}^{-1} \text{cm}^{-1}$	–	0.6	–0.3 vs. Ag/AgCl	8	Yagati et al. (2013)
MnO <sub>2</sub> -graphene	$38.2 \mu\text{AmM}^{-1} \text{cm}^{-1}$	0.0005–0.6	0.8	–0.3 vs. SCE	5	Li et al. (2010a)

MWCNT multiwalled carbon nanotube. The working potential refers to the chronoamperometric measurements, otherwise specified as CV (cyclic voltammetry) or DPV (differential pulse voltammetry), and are given vs SCE, versus saturated calomel electrode, or vs Ag/AgCl, versus silver/silver chloride electrode.

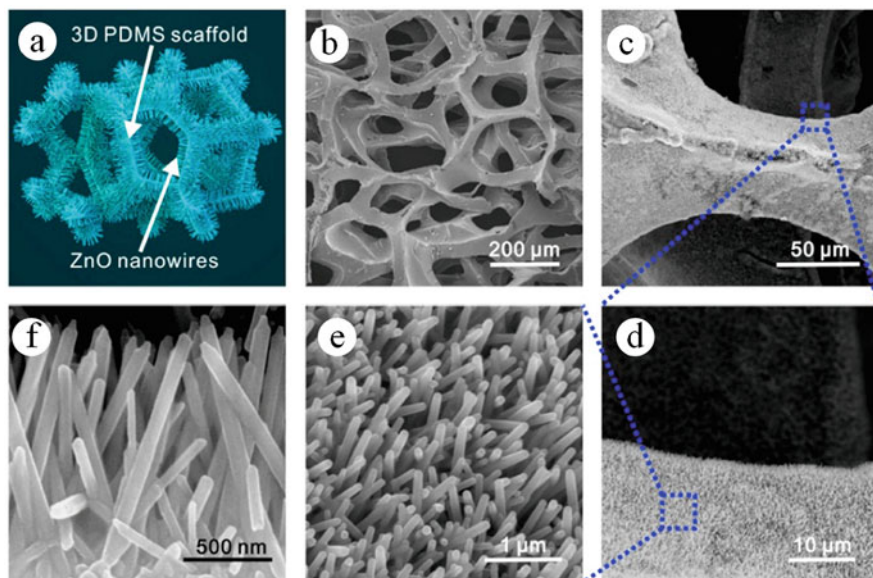


**Fig. 6.11** (a) Illustration of ZnO nanowires-coated 3D polydimethylsiloxane (PDMS) scaffold. Scanning electron microscopy image of (b) ZnO nanowires-coated 3D scaffold. (c–e) ZnO nanowires on the 3D scaffold with different magnifications. (f) The height of the ZnO nanowires. (Reproduced with permission from (Chen et al. 2018). Copyright Elsevier 2018)

Hu et al. 2017). Efforts have been made to synthesize nanostructured metal oxides with porous morphology, including sol–gel method, hydrothermal method, and thermal evaporation. These strategies were aimed at growing oxide nanostructures for solar cells, gas sensors, and photocatalysis. As described in Table 6.5, these oxide nanostructures provide a versatile platform for biomolecules loading that makes them prominent for biosensing. In this regard, an effective immunocapture was developed for colorimetric detection of exosomes using ZnO nanowires coating 3D chip devices (Chen et al. 2018). Figure 6.11a shows the ZnO nanowires coating 3D scaffolds with a microporous size distribution of 40–250  $\mu\text{m}$  (Fig. 6.11b, d). The vertically aligned ZnO nanowires had a diameter ranging from 150 to 200 nm (Fig. 6.11e) and  $\sim 1 \mu\text{m}$  in height (Fig. 6.11f). These nanowires did not affect the porous size of PDMS but made the surface rougher. The captured exosomes are detected by horseradish peroxidase labeled antibody, and quantitative readout of exosomes can be analyzed by UV–Vis spectrometry. The lowest detectable concentration of ZnO-chip device was  $2.2 \times 10^4$  particles  $\mu\text{L}^{-1}$  with a relative standard deviation of  $<7.5\%$ .

A nonenzymatic hydrogen peroxide electrochemical biosensor made with Au@C-Co<sub>3</sub>O<sub>4</sub> porous hierarchical heterostructures presented large active sites and excellent conductivity (Dai et al. 2018b). Figure 6.12a shows the field emission scanning electron microscopy of gold@zeolitic imidazole framework 67 (Au@ZIF-67) wide crystals ( $\sim 450$  nm) of rhombic dodecahedral shapes with multiple gold



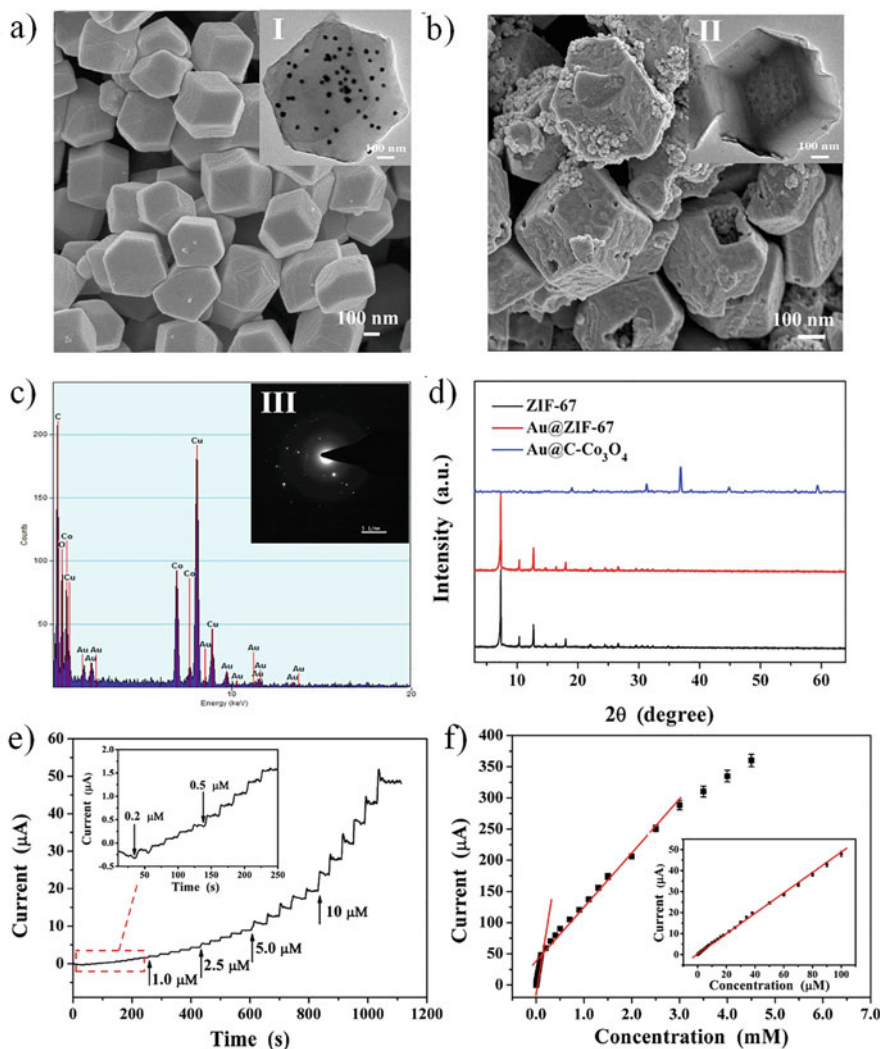


**Fig. 6.12** Field emission-scanning electron microscopy image of (a) Au@ZIF-67, (b) Au@C-Co<sub>3</sub>O<sub>4</sub>, (c) elemental analysis by energy dispersion X-ray spectroscopy (EDS) of Au@C-Co<sub>3</sub>O<sub>4</sub>, An (d) diffraction pattern of ZIF-67, Au@ZIF-67, and Au@C-Co<sub>3</sub>O<sub>4</sub>. (e) Amperometric current–time curves of Au@C-Co<sub>3</sub>O<sub>4</sub>/GCE with different concentrations of hydrogen peroxide. Inset: high magnification of the current–time curve. (f) Calibration curve for hydrogen peroxide sensing (Reproduced with permission from (Dai et al. 2018b). Copyright Elsevier 2018)

nanoparticles that are fully encapsulated and well dispersed by zeolitic imidazole framework 67 (Inset I, Fig. 6.12a). After calcination, the black fluffy powder was obtained that preserved the uniform size and shape (Fig. 6.12b). All these particles were integrated with gold nanoparticles (Inset II, Fig. 6.12b). The gold nanoparticles are well dispersed without agglomeration (Fig. 6.12c), which is crucial for

improving electrochemical performance. The polycrystalline structure of the materials was confirmed using selected-area electron diffraction (Inset III, Fig. 6.12b), while the diffraction peaks of Au@ZIF-67 match those of the crystalline structure of ZIF-67 in Fig. 6.12d. After calcination, the diffraction peaks match with pure cubic spinel  $\text{Co}_3\text{O}_4$  (JCPDS 42-1467), and the gold nanoparticles peaks were too weak to be observed in the diffraction pattern because of their low contents and small size. Figure 6.12e shows the amperometric response of hydrogen peroxide with a steady-state current reached within 4 s at the Au@C- $\text{Co}_3\text{O}_4$ /glassy carbon electrode. The calibration curve shows linearity with a detection limit of 19 nM. The sensitivity is  $7553 \mu\text{A mM}^{-1}$ , which is much higher than reported electrochemical sensors based on  $\text{Co}_3\text{O}_4$  composites (Fig. 6.12f).

Although great advances in metal oxide-based electrochemical biosensors have been achieved, there are many challenges to obtaining good performance for real sample analysis. Up to now, most of the research has been done in the laboratory and few biosensors appear to be commercially feasible except for some blood glucose and handheld immunosensors. Therefore, to commercialize metal oxide-based biosensors (Li et al. 2014; Han et al. 2015), efforts should be made to break some key technical barriers such as controlling the morphology, realizing efficient immobilization, and improving data analysis with artificial intelligence and machine learning. In the last decade, some hierarchical porous nanostructures, binary metal oxides (Joshi et al. 2016, 2018a), porous carbon nanostructures (Eranna et al. 2004; Liu et al. 2018; Materón et al. 2018; Wu et al. 2019), and 2D materials (Liu et al. 2018; Materón et al. 2018) have been used owing to their outstanding properties, such as large surface area, high electron mobility, excellent electron conductivity, and thermal conductivity suitable for sensors and biosensors.

## 6.4 Conclusion

In this chapter, we have reviewed a range of metal oxide and sulfide structures for glucose biosensing through electrochemical methods. Nonenzymatic glucose biosensors are a promising solution with reduced cost-production and increased shelf-life since no biological component is required. As is well-known, enzymes naturally lose biological activity or even denature along time. Higher performance was obtained with sulfide-based devices achieving a limit of detection at nM with an average response time around 3–5 s. Albeit metal oxide biosensors presented a detection limit around  $\mu\text{M}$ , they presented the fastest response, 1 s, to glucose. Exciting hierarchical nanostructures are being designed to enable detection of multicomponent analytes as in the work of electronic tongues. They can be combined with miniaturization technology to develop portable devices for daily use, for example, with wearable sensors to monitor continuously and in a noninvasive manner the levels of glucose and other biomarkers. Knowledge in nanotechnology and electrochemistry can be leveraged with integrated circuit silicon technology and

data processing, in order to produce off a new generation of selective, sensitive microsensors (Jothi and Nageswaran 2019).

**Acknowledgments** This work was carried out with financial assistance from the Brazilian funding agencies: São Paulo Research Foundation-FAPESP (2013/14262-7, 2014/23546-1, 2016/23474-6) and National council for scientific and technological development – CNPq.

**Author Contributions** All the authors have contributed equally to this work.

**Conflicts of Interest** The authors declare no conflict of interest.

## References

- Aini BN, Siddiquee S, Ampon K et al (2015) Development of glucose biosensor based on ZnO nanoparticles film and glucose oxidase-immobilized eggshell membrane. *Sens Bio-Sensing Res* 4:46–56. <https://doi.org/10.1016/j.sbsr.2015.03.004>
- Ansari AA, Solanki PR, Malhotra BD (2008) Sol-gel derived nanostructured cerium oxide film for glucose sensor. *Appl Phys Lett* 92. <https://doi.org/10.1063/1.2953686>
- Atkins P, Overton T, Rourke J et al (2008) Shriver & Atkins Química Inorgânica, 4th edn. Bookman, Porto Alegre
- Babu KJ, Kumar RT, Yoo DJ et al (2018) Electrodeposited nickel cobalt sulfide flowerlike architectures on disposable cellulose filter paper for enzyme-free glucose sensor applications. *ACS Sustain Chem Eng* 6:16982–16989. <https://doi.org/10.1021/acssuschemeng.8b04340>
- Baby TT, Ramaprabhu S (2010) SiO<sub>2</sub> coated Fe<sub>3</sub>O<sub>4</sub> magnetic nanoparticle dispersed multiwalled carbon nanotubes based amperometric glucose biosensor. *Talanta* 80:2016–2022. <https://doi.org/10.1016/j.talanta.2009.11.010>
- Bo X, Bai J, Wang L, Guo L (2010) In situ growth of copper sulfide nanoparticles on ordered mesoporous carbon and their application as nonenzymatic amperometric sensor of hydrogen peroxide. *Talanta* 81:339–345. <https://doi.org/10.1016/j.talanta.2009.12.007>
- Bohuniccky B, Mousa SA (2011) Biosensors: the new wave in cancer diagnosis. *Nanotechnol Sci Appl* 4:1–10. <https://doi.org/10.2147/NSA.S13465>
- Brindha J, Chanda K, Balamurali MM (2018) Biosensors for pathogen surveillance. *Environ Chem Lett* 16:1325–1337. <https://doi.org/10.1007/s10311-018-0759-y>
- Bruen D, Delaney C, Florea L, Diamond D (2017) Glucose sensing for diabetes monitoring: recent developments. *Sensors (Switzerland)* 17:1–21. <https://doi.org/10.3390/s17081866>
- Cao X, Wang K, Du G et al (2016) One-step electrodeposition of a nickel cobalt sulfide nanosheet film as a highly sensitive nonenzymatic glucose sensor. *J Mater Chem B* 4:7540–7544. <https://doi.org/10.1039/c6tb01736c>
- Cao M, Wang H, Kannan P et al (2019) Highly efficient non-enzymatic glucose sensor based on Cu<sub>2</sub>S hollow nanospheres. *Appl Surf Sci* 492:407–416. <https://doi.org/10.1016/j.apsusc.2019.06.248>
- Chen L, Ji L, Zhao J et al (2017) Facile exfoliation of molybdenum disulfide nanosheets as highly efficient electrocatalyst for detection of m-nitrophenol. *J Electroanal Chem* 801:300–305. <https://doi.org/10.1016/j.jelechem.2017.08.013>
- Chen Z, Cheng SB, Cao P et al (2018) Detection of exosomes by ZnO nanowires coated three-dimensional scaffold chip device. *Biosens Bioelectron* 122:211–216. <https://doi.org/10.1016/j.bios.2018.09.033>
- Chhowalla M, Shin HS, Eda G et al (2013) The chemistry of two-dimensional layered transition metal dichalcogenide nanosheets. *Nat Chem* 5:263–275. <https://doi.org/10.1038/nchem.1589>

- Cho SY, Kim SJ, Lee Y et al (2015) Highly enhanced gas adsorption properties in vertically aligned MoS<sub>2</sub> layers. *ACS Nano* 9:9314–9321. <https://doi.org/10.1021/acsnano.5b04504>
- Dai Z, Liu S, Bao J, Ju H (2009) Nanostructured FeS as a mimic peroxidase for biocatalysis and biosensing. *Chem – A Eur J* 15:4321–4326. <https://doi.org/10.1002/chem.200802158>
- Dai H, Cao P, Chen D et al (2018a) Ni-Co-S/PPy core-shell nanohybrid on nickel foam as a non-enzymatic electrochemical glucose sensor. *Synth Met* 235:97–102. <https://doi.org/10.1016/j.synthmet.2017.12.004>
- Dai H, Chen Y, Niu X et al (2018b) High-performance electrochemical biosensor for nonenzymatic H<sub>2</sub>O<sub>2</sub> sensing based on Au@C-Co<sub>3</sub>O<sub>4</sub> heterostructures. *Biosens Bioelectron* 118:36–43. <https://doi.org/10.1016/j.bios.2018.07.022>
- Dakshayini BS, Reddy KR, Mishra A et al (2019) Role of conducting polymer and metal oxide-based hybrids for applications in amperometric sensors and biosensors. *Microchem J* 147:7–24. <https://doi.org/10.1016/j.microc.2019.02.061>
- Dasgupta N, Ranjan S, Ramalingam C (2017) Applications of nanotechnology in agriculture and water quality management. *Environ Chem Lett* 15:591–605. <https://doi.org/10.1007/s10311-017-0648-9>
- Ebrahimi A, Zhang K, Dong C et al (2019) FeS<sub>x</sub>-graphene heterostructures: nanofabrication-compatible catalysts for ultra-sensitive electrochemical detection of hydrogen peroxide. *Sensors Actuators B Chem* 285:631–638. <https://doi.org/10.1016/j.snb.2018.12.033>
- Eranna G, Joshi BC, Runthala DP, Gupta RP (2004) Oxide materials for development of integrated gas sensors – a comprehensive review. *Crit Rev Solid State Mater Sci* 29:111–188. <https://doi.org/10.1080/10408430490888977>
- Fang L, Wang F, Chen Z et al (2017) Flower-like MoS<sub>2</sub> decorated with Cu<sub>2</sub>O nanoparticles for non-enzymatic amperometric sensing of glucose. *Talanta* 167:593–599. <https://doi.org/10.1016/j.talanta.2017.03.008>
- Gan X, Zhao H, Quan X (2017) Two-dimensional MoS<sub>2</sub>: a promising building block for biosensors. *Biosens Bioelectron* 89:56–71. <https://doi.org/10.1016/j.bios.2016.03.042>
- Gao Z, Lin Y, He Y, Tang D (2017) Enzyme-free amperometric glucose sensor using a glassy carbon electrode modified with poly(vinyl butyral) incorporating a hybrid nanostructure composed of molybdenum disulfide and copper sulfide. *Microchim Acta* 184:807–814. <https://doi.org/10.1007/s00604-016-2061-7>
- Garcia A, Eastlake A, Topmiller JL et al (2017) Nano-metal oxides: exposure and engineering control assessment. *J Occup Environ Hyg* 14:727–737. <https://doi.org/10.1080/15459624.2017.1326699>
- Geng D, Bo X, Guo L (2017) Ni-doped molybdenum disulfide nanoparticles anchored on reduced graphene oxide as novel electroactive material for a non-enzymatic glucose sensor. *Sensors Actuators B Chem* 244:131–141. <https://doi.org/10.1016/j.snb.2016.12.122>
- Ghezlbash A, Sigman MB, Korgel BA (2004) Solventless synthesis of nickel sulfide nanorods and triangular nanoprisms. *Nano Lett* 4:537–542. <https://doi.org/10.1021/nl035067+>
- Grorai S, Ganguli D, Chaudhuri S (2005) Synthesis of copper sulfides of varying morphologies and stoichiometries controlled by chelating and nonchelating solvents in a solvothermal process. *Cryst Growth Des* 5:875–877. <https://doi.org/10.1021/cg0496787>
- Han L, Yang DP, Liu A (2015) Leaf-templated synthesis of 3D hierarchical porous cobalt oxide nanostructure as direct electrochemical biosensing interface with enhanced electrocatalysis. *Biosens Bioelectron* 63:145–152. <https://doi.org/10.1016/j.bios.2014.07.031>
- Hansen JA, Mukhopadhyay R, Hansen J, Gothelf KV (2006) Femtomolar electrochemical detection of DNA targets using metal sulfide nanoparticles. *J Am Chem Soc* 128:3860–3861. <https://doi.org/10.1021/ja0574116>
- Hasan A, Nurunnabi M, Morshed M et al (2014) Recent advances in application of biosensors in tissue engineering. *Biomed Res Int* 2014. <https://doi.org/10.1155/2014/307519>
- Haun JB, Yoon TJ, Lee H, Weissleder R (2010) Magnetic nanoparticle biosensors. *Wiley Interdiscip Rev Nanomed Nanobiotechnol* 2:291–304. <https://doi.org/10.1002/wnan.84>

- Holade Y, Tingry S, Servat K et al (2017) Nanostructured inorganic materials at work in electrochemical sensing and biofuel cells. *Catalysts* 7:31. <https://doi.org/10.3390/catal7010031>
- Hsu YW, Hsu TK, Sun CL et al (2012) Synthesis of CuO/graphene nanocomposites for nonenzymatic electrochemical glucose biosensor applications. *Electrochim Acta* 82:152–157. <https://doi.org/10.1016/j.electacta.2012.03.094>
- Hu Y, Huang Y, Tan C et al (2017) Two-dimensional transition metal dichalcogenide nanomaterials for biosensing applications. *Mater Chem Front* 1:24–36. <https://doi.org/10.1039/C6QM00195E>
- Huang J, Dong Z, Li Y et al (2013) MoS<sub>2</sub> nanosheet functionalized with Cu nanoparticles and its application for glucose detection. *Mater Res Bull* 48:4544–4547. <https://doi.org/10.1016/j.materresbull.2013.07.060>
- Huang J, He Y, Jin J et al (2014) A novel glucose sensor based on MoS<sub>2</sub> nanosheet functionalized with Ni nanoparticles. *Electrochim Acta* 136:41–46. <https://doi.org/10.1016/j.electacta.2014.05.070>
- Huo H, Zhao Y, Xu C (2014) 3D Ni<sub>3</sub>S<sub>2</sub> nanosheet arrays supported on Ni foam for high-performance supercapacitor and non-enzymatic glucose detection. *J Mater Chem A* 2:15111–15117. <https://doi.org/10.1039/c4ta02857k>
- Jang HD, Kim SK, Chang H et al (2012) A glucose biosensor based on TiO<sub>2</sub>-graphene composite. *Biosens Bioelectron* 38:184–188. <https://doi.org/10.1016/j.bios.2012.05.033>
- Jariwala D, Sangwan VK, Lauhon LJ et al (2014) Emerging device applications for semiconducting two-dimensional transition metal dichalcogenides. *ACS Nano* 8:1102–1120. <https://doi.org/10.1021/nn500064s>
- Jeong JM, Yang MH, Kim DS et al (2017) High performance electrochemical glucose sensor based on three-dimensional MoS<sub>2</sub>/graphene aerogel. *J Colloid Interface Sci* 506:379–385. <https://doi.org/10.1016/j.jcis.2017.07.061>
- Jiang LC, De Zhang W (2010) A highly sensitive nonenzymatic glucose sensor based on CuO nanoparticles-modified carbon nanotube electrode. *Biosens Bioelectron* 25:1402–1407. <https://doi.org/10.1016/j.bios.2009.10.038>
- Jiang N, Tang Q, Sheng M et al (2016) Nickel sulfides for electrocatalytic hydrogen evolution under alkaline conditions: a case study of crystalline NiS, NiS<sub>2</sub>, and Ni<sub>3</sub>S<sub>2</sub> nanoparticles. *Cat Sci Technol* 6:1077–1084. <https://doi.org/10.1039/c5cy01111f>
- Joensen P, Frindt RF, Morrison SR (1986) Single-layer MoS<sub>2</sub>. *Mater Res Bull* 21:457–461. [https://doi.org/10.1016/0025-5408\(86\)90011-5](https://doi.org/10.1016/0025-5408(86)90011-5)
- Joshi N, Shimizu FM, Awan IT, et al (2016) Ozone sensing properties of nickel phthalocyanine: ZnO nanorod heterostructures. In: 2016 IEEE Sensors pp 1–3
- Joshi N, da Silva LF, Jadhav HS et al (2018a) Yolk-shelled ZnCo<sub>2</sub>O<sub>4</sub> microspheres: surface properties and gas sensing application. *Sensors Actuators B Chem* 257:906–915. <https://doi.org/10.1016/j.SNB.2017.11.041>
- Joshi N, Hayasaka T, Liu Y et al (2018b) A review on chemiresistive room temperature gas sensors based on metal oxide nanostructures, graphene and 2D transition metal dichalcogenides. *Microchim Acta* 185:213. <https://doi.org/10.1007/s00604-018-2750-5>
- Joshi N, da Silva LF, Shimizu FM et al (2019) UV-assisted chemiresistors made with gold-modified ZnO nanorods to detect ozone gas at room temperature. *Microchim Acta* 186:418. <https://doi.org/10.1007/s00604-019-3532-4>
- Jothi L, Nageswaran G (2019) Plasma modified polymeric materials for biosensors/biodevice applications. In: Thomas S, Mozetič M, Cvelbar U et al (eds) *Non-thermal plasma technology for polymeric materials*. Elsevier, pp 409–437
- Kannan PK, Rout CS (2015) High performance non-enzymatic glucose sensor based on one-step electrodeposited nickel sulfide. *Chem – A Eur J* 21:9355–9359. <https://doi.org/10.1002/chem.201500851>
- Kannan P, Chen F, Jiang H et al (2019) Hierarchical core-shell structured Ni<sub>3</sub>S<sub>2</sub>/NiMoO<sub>4</sub> nanowires: a high-performance and reusable electrochemical sensor for glucose detection. *Analyst* 144:4925–4934. <https://doi.org/10.1039/c9an00917e>

- Karikalan N, Karthik R, Chen SM et al (2017) Sonochemical synthesis of sulfur doped reduced graphene oxide supported CuS nanoparticles for the non-enzymatic glucose sensor applications. *Sci Rep* 7:1–10. <https://doi.org/10.1038/s41598-017-02479-5>
- Kaur G, Tomar M, Gupta V (2016) Realization of a label-free electrochemical immunosensor for detection of low density lipoprotein using NiO thin film. *Biosens Bioelectron*. <https://doi.org/10.1016/j.bios.2016.01.071>
- Kibsgaard J, Chen Z, Reinecke BN, Jaramillo TF (2012) Engineering the surface structure of MoS<sub>2</sub> to preferentially expose active edge sites for electrocatalysis. *Nat Mater* 11:963–969. <https://doi.org/10.1038/nmat3439>
- Kim S, Lee SH, Cho M, Lee Y (2016) Solvent-assisted morphology confinement of a nickel sulfide nanostructure and its application for non-enzymatic glucose sensor. *Biosens Bioelectron* 85:587–595. <https://doi.org/10.1016/j.bios.2016.05.062>
- Kima DM, Rahmanb MA, Do MH et al (2010) An amperometric chloramphenicol immunosensor based on cadmium sulfide nanoparticles modified-dendrimer bonded conducting polymer. *Biosens Bioelectron* 25:1781–1788. <https://doi.org/10.1016/j.bios.2009.12.024>
- Kravchik KV, Widmer R, Erni R et al (2019) Copper sulfide nanoparticles as high-performance cathode materials for Mg-ion batteries. *Sci Rep* 9:1–8. <https://doi.org/10.1038/s41598-019-43639-z>
- Kubendhiran S, Sakthivel R, Chen S, Mutharani B (2018a) Functionalized-carbon black as a conductive matrix for nickel sulfide Nanospheres and its application to non-enzymatic glucose sensor. *J Electrochem Soc* 165:B96–B102. <https://doi.org/10.1149/2.0451803jes>
- Kubendhiran S, Thirumalraj B, Chen SM, Karuppiah C (2018b) Electrochemical co-preparation of cobalt sulfide/reduced graphene oxide composite for electrocatalytic activity and determination of H<sub>2</sub>O<sub>2</sub> in biological samples. *J Colloid Interface Sci* 509:153–162. <https://doi.org/10.1016/j.jcis.2017.08.087>
- Kumar V, Guleria P, Mehta SK (2017) Nanosensors for food quality and safety assessment. *Environ Chem Lett* 15:165–177. <https://doi.org/10.1007/s10311-017-0616-4>
- Kuswandi B (2019) Nanobiosensor approaches for pollutant monitoring. *Environ Chem Lett* 17:975–990. <https://doi.org/10.1007/s10311-018-00853-x>
- Lai CH, Huang KW, Cheng JH et al (2009) Oriented growth of large-scale nickel sulfide nanowire arrays via a general solution route for lithium-ion battery cathode applications. *J Mater Chem* 19:7277–7283. <https://doi.org/10.1039/b909261g>
- Lai CH, Lu MY, Chen LJ (2012) Metal sulfide nanostructures: synthesis, properties and applications in energy conversion and storage. *J Mater Chem* 22:19–30. <https://doi.org/10.1039/c1jm13879k>
- Laursen AB, Kegnaes S, Dahl S, Chorkendorff I (2012) Molybdenum sulfides – efficient and viable materials for electro – and photoelectrocatalytic hydrogen evolution. *Energy Environ Sci* 5:5577–5591. <https://doi.org/10.1039/c2ee02618j>
- Lee H, Yoon SW, Kim EJ, Park J (2007) In-situ growth of copper sulfide nanocrystals on multiwalled carbon nanotubes and their application as novel solar cell and amperometric glucose sensor materials. *Nano Lett* 7:778–784. <https://doi.org/10.1021/nl0630539>
- Lee YH, Zhang XQ, Zhang W et al (2012) Synthesis of large-area MoS<sub>2</sub> atomic layers with chemical vapor deposition. *Adv Mater* 24:2320–2325. <https://doi.org/10.1002/adma.201104798>
- Li X, Du X (2017) Molybdenum disulfide nanosheets supported au-Pd bimetallic nanoparticles for non-enzymatic electrochemical sensing of hydrogen peroxide and glucose. *Sensors Actuators B Chem* 239:536–543. <https://doi.org/10.1016/j.snb.2016.08.048>
- Li X, Zhu H (2015) Two-dimensional MoS<sub>2</sub>: properties, preparation, and applications. *J Mater* 1:33–44. <https://doi.org/10.1016/j.jmat.2015.03.003>
- Li L, Du Z, Liu S et al (2010a) A novel nonenzymatic hydrogen peroxide sensor based on MnO<sub>2</sub>/graphene oxide nanocomposite. *Talanta* 82:1637–1641. <https://doi.org/10.1016/j.talanta.2010.07.020>

- Li Y, Lu W, Huang Q et al (2010b) Copper sulfide nanoparticles for photothermal ablation of tumor cells. *Nanomedicine* 5:1161–1171. <https://doi.org/10.2217/nmm.10.85>
- Li X, Yao J, Liu F et al (2013) Nickel/copper nanoparticles modified TiO<sub>2</sub> nanotubes for non-enzymatic glucose biosensors. *Sensors Actuators B Chem* 181:501–508. <https://doi.org/10.1016/j.snb.2013.02.035>
- Li Y, Xu C, Li H et al (2014) Nonenzymatic immunosensor for detection of carbohydrate antigen 15-3 based on hierarchical nanoporous PtFe alloy. *Biosens Bioelectron* 56:295–299. <https://doi.org/10.1016/j.bios.2014.01.020>
- Li H, Wang Y, Huang J et al (2017) Microwave-assisted synthesis of CuS/graphene composite for enhanced Lithium storage properties. *Electrochim Acta* 225:443–451. <https://doi.org/10.1016/j.electacta.2016.12.117>
- Liang W, Whangbo MH (1993) Conductivity anisotropy and structural phase transition in Covellite CuS. *Solid State Commun* 85:405–408. [https://doi.org/10.1016/0038-1098\(93\)90689-K](https://doi.org/10.1016/0038-1098(93)90689-K)
- Lin TW, Liu CJ, Dai CS (2014) Ni<sub>3</sub>S<sub>2</sub>/carbon nanotube nanocomposite as electrode material for hydrogen evolution reaction in alkaline electrolyte and enzyme-free glucose detection. *Appl Catal B Environ* 154–155:213–220. <https://doi.org/10.1016/j.apcatb.2014.02.017>
- Lin X, Ni Y, Kokot S (2016) Electrochemical and bio-sensing platform based on a novel 3D Cu nano-flowers/layered MoS<sub>2</sub> composite. *Biosens Bioelectron* 79:685–692. <https://doi.org/10.1016/j.bios.2015.12.072>
- Lin HS, Bin SJ, Peng CM et al (2018) Manipulating the temperature of sulfurization to synthesize  $\alpha$ -nis nanosphere film for long-term preservation of non-enzymatic glucose sensors. *Nanoscale Res Lett* 13. <https://doi.org/10.1186/s11671-018-2511-8>
- Liu YM, Shi GF, Zhang JJ et al (2014) A novel label-free electrochemiluminescence aptasensor based on layered flowerlike molybdenum sulfide-graphene nanocomposites as matrix. *Colloids Surf B Biointerfaces* 122:287–293. <https://doi.org/10.1016/j.colsurfb.2014.07.011>
- Liu H, Chu Y, Liu Y, et al (2018) Selective sensing of chemical vapors using phase spectra detection on CVD graphene fet. In: Proceedings of the IEEE international conference on Micro Electro Mechanical Systems (MEMS), pp 210–213
- Luo P, Zhang H, Liu L et al (2017) Targeted synthesis of unique nickel sulfide (NiS, NiS<sub>2</sub>) microarchitectures and the applications for the enhanced water splitting system. *ACS Appl Mater Interfaces* 9:2500–2508. <https://doi.org/10.1021/acsami.6b13984>
- Ma Y, Qi L, Ma J, Cheng H (2004) Hierarchical, star-shaped PbS crystals formed by a simple solution route. *Cryst Growth Des* 4:351–354. <https://doi.org/10.1021/cg034174e>
- Ma K, Sinha A, Dang X, Zhao H (2019) Electrochemical preparation of gold nanoparticles-Polypyrrole co-decorated 2D MoS<sub>2</sub> nanocomposite sensor for sensitive detection of glucose. *J Electrochem Soc* 166:B147–B154. <https://doi.org/10.1149/2.1231902jes>
- Maji SK, Dutta AK, Biswas P et al (2012a) Nanocrystalline FeS thin film used as an anode in photo-electrochemical solar cell and as hydrogen peroxide sensor. *Sensors Actuators B Chem* 166–167:726–732. <https://doi.org/10.1016/j.snb.2012.03.048>
- Maji SK, Dutta AK, Srivastava DN et al (2012b) Peroxidase-like behavior, amperometric biosensing of hydrogen peroxide and photocatalytic activity by cadmium sulfide nanoparticles. *J Mol Catal A Chem* 358:1–9. <https://doi.org/10.1016/j.molcata.2012.03.007>
- Maji SK, Dutta AK, Bhadu GR et al (2013) A novel amperometric biosensor for hydrogen peroxide and glucose based on cuprous sulfide nanoplates. *J Mater Chem B* 1:4127–4134. <https://doi.org/10.1039/c3tb20846j>
- Malik R, Tomer VK, Joshi N et al (2018) Au-TiO<sub>2</sub>-loaded cubic g-C<sub>3</sub>N<sub>4</sub> Nanohybrids for photocatalytic and volatile organic amine sensing applications. *ACS Appl Mater Interfaces* 10:34087–34097. <https://doi.org/10.1021/acsami.8b08091>
- Mani V, Govindasamy M, Chen SM et al (2016) Determination of dopamine using a glassy carbon electrode modified with a graphene and carbon nanotube hybrid decorated with molybdenum disulfide flowers. *Microchim Acta* 183:2267–2275. <https://doi.org/10.1007/s00604-016-1864-x>
- Marioli JM, Kuwana T (1992) Electrochemical characterization of carbohydrate oxidation at copper electrodes. *Electrochim Acta* 37:1187–1197. [https://doi.org/10.1016/0013-4686\(92\)85055-P](https://doi.org/10.1016/0013-4686(92)85055-P)

- Materón EM, Lima RS, Joshi N, et al (2018) Graphene-containing microfluidic and chip-based sensor devices for biomolecules. In: Pandikumar A, Rameshkumar PBT-G-BES for B (eds) Graphene-based electrochemical sensors for biomolecules: a volume in micro and nano technologies. Elsevier, pp 321–336
- Mutyala S, Kinsly J, Sharma GVR et al (2018) Non-enzymatic electrochemical hydrogen peroxide detection using MoS<sub>2</sub>- interconnected porous carbon heterostructure. *J Electroanal Chem* 823:429–436. <https://doi.org/10.1016/j.jelechem.2018.06.038>
- Naveed M, Younas W, Zhu Y et al (2019) Template free and facile microwave-assisted synthesis method to prepare mesoporous copper sulfide nanosheets for high-performance hybrid supercapacitor. *Electrochim Acta* 319:49–60. <https://doi.org/10.1016/j.electacta.2019.06.169>
- Nguyen HH, Lee SH, Lee UJ et al (2019) Immobilized enzymes in biosensor applications. *Materials (Basel)* 12:1–34. <https://doi.org/10.3390/ma12010121>
- Park SY, Lee JE, Kim YH et al (2018) Room temperature humidity sensors based on rGO/MoS<sub>2</sub> hybrid composites synthesized by hydrothermal method. *Sensors Actuators B Chem* 258:775–782. <https://doi.org/10.1016/j.snb.2017.11.176>
- Parlak O, Incel A, Uzun L et al (2017) Structuring Au nanoparticles on two-dimensional MoS<sub>2</sub> nanosheets for electrochemical glucose biosensors. *Biosens Bioelectron* 89:545–550. <https://doi.org/10.1016/j.bios.2016.03.024>
- Patil D, Dung NQ, Jung H et al (2012) Enzymatic glucose biosensor based on CeO<sub>2</sub> nanorods synthesized by non-isothermal precipitation. *Biosens Bioelectron* 31:176–181. <https://doi.org/10.1016/j.bios.2011.10.013>
- Peng Y, Meng Z, Zhong C et al (2001) Hydrothermal synthesis of MoS<sub>2</sub> and its pressure-related crystallization. *J Solid State Chem* 159:170–173. <https://doi.org/10.1006/jssc.2001.9146>
- Pinna N, Niederberger M (2008) Surfactant-free nonaqueous synthesis of metal oxide nanostructures. *Angew Chem Int Ed*. <https://doi.org/10.1002/anie.200704541>
- Qian L, Mao J, Tian X et al (2013) In situ synthesis of CuS nanotubes on Cu electrode for sensitive nonenzymatic glucose sensor. *Sensors Actuators B Chem* 176:952–959. <https://doi.org/10.1016/j.snb.2012.09.076>
- Qin AM, Fang YP, Ou HD et al (2005) Formation of various morphologies of covellite copper sulfide submicron crystals by a hydrothermal method without surfactant. *Cryst Growth Des* 5:855–860. <https://doi.org/10.1021/cg049736o>
- Qin X, Feng W, Yang X et al (2018) Molybdenum sulfide/citric acid composite membrane-coated long period fiber grating sensor for measuring trace hydrogen sulfide gas. *Sensors Actuators B Chem* 272:60–68. <https://doi.org/10.1016/j.snb.2018.05.152>
- Qu P, Gong Z, Cheng H et al (2015) Nanoflower-like CoS-decorated 3D porous carbon skeleton derived from rose for a high performance nonenzymatic glucose sensor. *RSC Adv* 5:106661–106667. <https://doi.org/10.1039/c5ra22495k>
- Radhakrishnan S, Kim HY, Kim BS (2016) A novel CuS microflower superstructure based sensitive and selective nonenzymatic glucose detection. *Sensors Actuators B Chem* 233:93–99. <https://doi.org/10.1016/j.snb.2016.04.056>
- Raymundo-Pereira PA, Shimizu FM, Lima RS, Oliveira ON (2019) Nanoarchitectonics in microfluidic devices for sensing and biosensing. *Adv Supramol Nanoarchitectonics*:231–252. <https://doi.org/10.1016/B978-0-12-813341-5.00009-7>
- Reitz E, Jia W, Gentile M et al (2008) CuO nanospheres based nonenzymatic glucose sensor. *Electroanalysis* 20:2482–2486. <https://doi.org/10.1002/elan.200804327>
- Sagade AA, Sharma R (2008) Copper sulphide (Cu<sub>2</sub>S) as an ammonia gas sensor working at room temperature. *Sensors Actuators B Chem* 133:135–143. <https://doi.org/10.1016/j.snb.2008.02.015>
- Sarkar A, Ghosh AB, Saha N et al (2018) Newly designed Amperometric biosensor for hydrogen peroxide and glucose based on vanadium sulfide nanoparticles. *ACS Appl Nano Mater* 1:1339–1347. <https://doi.org/10.1021/acsanm.8b00076>



- Shukla M, Pramila DT et al (2017) Influence of aspect ratio and surface defect density on hydrothermally grown ZnO nanorods towards amperometric glucose biosensing applications. *Appl Surf Sci* 422:798–808. <https://doi.org/10.1016/j.apsusc.2017.06.119>
- Sinha A, Dhanjai TB et al (2018) MoS<sub>2</sub> nanostructures for electrochemical sensing of multidisciplinary targets: a review. *TrAC – Trends Anal Chem* 102:75–90. <https://doi.org/10.1016/j.trac.2018.01.008>
- Soper SA, Brown K, Ellington A et al (2006) Point-of-care biosensor systems for cancer diagnostics/prognostics. *Biosens Bioelectron* 21:1932–1942. <https://doi.org/10.1016/j.bios.2006.01.006>
- Srivastava AK, Dev A, Karmakar S (2018) Nanosensors and nanobiosensors in food and agriculture. *Environ Chem Lett* 16:161–182. <https://doi.org/10.1007/s10311-017-0674-7>
- Su S, Sun H, Xu F et al (2013) Highly sensitive and selective determination of dopamine in the presence of ascorbic acid using gold nanoparticles-decorated MoS<sub>2</sub> Nanosheets modified electrode. *Electroanalysis* 25:2523–2529. <https://doi.org/10.1002/elan.201300332>
- Su S, Sun H, Xu F et al (2014) Direct electrochemistry of glucose oxidase and a biosensor for glucose based on a glass carbon electrode modified with MoS<sub>2</sub> nanosheets decorated with gold nanoparticles. *Microchim Acta* 181:1497–1503. <https://doi.org/10.1007/s00604-014-1178-9>
- Sun H, Chao J, Zuo X et al (2014) Gold nanoparticle-decorated MoS<sub>2</sub> nanosheets for simultaneous detection of ascorbic acid, dopamine and uric acid. *RSC Adv* 4:27625–27629. <https://doi.org/10.1039/c4ra04046e>
- Sun Z, Liao T, Kou L (2017) Strategies for designing metal oxide nanostructures. *Sci China Mater* 60. <https://doi.org/10.1007/s40843-016-5117-0>
- Tan Z, Huang Y, Wang S et al (2019) Production of Ni<sub>7</sub>S<sub>6</sub>/NiO hybrids as a highly sensitive amperometric sensor for glucose. *Ionics (Kiel)* 25:3961–3969. <https://doi.org/10.1007/s11581-019-02926-5>
- Theerthagiri J, Karuppasamy K, Durai G et al (2018) Recent advances in metal chalcogenides (MX; X = S, Se) nanostructures for electrochemical supercapacitor applications: a brief review. *Nano* 8:256. <https://doi.org/10.3390/nano8040256>
- Tomer VK, Malik R, Joshi N (2019) A special section on applications of 2D/3D materials in sensing and Photocatalysis. *J Nanosci Nanotechnol* 19:5052–5053. <https://doi.org/10.1166/jnn.2019.16841>
- Turkdogan S, Kilic B (2017) Metal oxide sandwiched dye-sensitized solar cells with enhanced power conversion efficiency fabricated by a facile and cost effective method. *Mater Sci Semicond Process* 71:382–388. <https://doi.org/10.1016/j.mssp.2017.08.036>
- Vabbina PK, Kaushik A, Pokhrel N et al (2015) Electrochemical cortisol immunosensors based on sonochemically synthesized zinc oxide 1D nanorods and 2D nanoflakes. *Biosens Bioelectron* 63:124–130. <https://doi.org/10.1016/j.bios.2014.07.026>
- Vilian ATE, Chen SM, Ali MA, Al-Hemaid FMA (2014) Direct electrochemistry of glucose oxidase immobilized on ZrO<sub>2</sub> nanoparticles-decorated reduced graphene oxide sheets for a glucose biosensor. *RSC Adv* 4:30358–30367. <https://doi.org/10.1039/c4ra04350b>
- Villaseñor MJ, Ríos Á (2018) Nanomaterials for water cleaning and desalination, energy production, disinfection, agriculture and green chemistry. *Environ Chem Lett* 16:11–34. <https://doi.org/10.1007/s10311-017-0656-9>
- Wang QH, Kalantar-Zadeh K, Kis A et al (2012) Electronics and optoelectronics of two-dimensional transition metal dichalcogenides. *Nat Nanotechnol* 7. <https://doi.org/10.1038/nnano.2012.193>
- Wang T, Zhu H, Zhuo J et al (2013) Biosensor based on ultrasmall MoS<sub>2</sub> nanoparticles for electrochemical detection of H<sub>2</sub>O<sub>2</sub> released by cells at the nanomolar level. *Anal Chem* 85:10289–10295. <https://doi.org/10.1021/ac402114c>
- Wang T, Du K, Liu W et al (2015) Electrochemical sensors based on molybdenum disulfide nanomaterials. *Electroanalysis* 27:2091–2097. <https://doi.org/10.1002/elan.201500117>

- Wang H, Wen F, Chen Y et al (2016) Electrocatalytic determination of nitrite based on straw cellulose/molybdenum sulfide nanocomposite. *Biosens Bioelectron* 85:692–697. <https://doi.org/10.1016/j.bios.2016.05.078>
- Wang S, Zhang S, Liu M et al (2018a) MoS<sub>2</sub> as connector inspired high electrocatalytic performance of NiCo<sub>2</sub>O<sub>4</sub> nanoplates towards glucose. *Sensors Actuators B Chem* 254:1101–1109. <https://doi.org/10.1016/j.snb.2017.08.011>
- Wang Y, Zhao KJ, Tao DP et al (2018b) Application of pyrite and chalcopyrite as sensor electrode for amperometric detection and measurement of hydrogen peroxide. *RSC Adv* 8:5013–5019. <https://doi.org/10.1039/c7ra13628e>
- Wang M, Ma J, Guan X et al (2019a) A novel H<sub>2</sub>O<sub>2</sub> electrochemical sensor based on NiCo<sub>2</sub>S<sub>4</sub> functionalized reduced graphene oxide. *J Alloys Compd* 784:827–833. <https://doi.org/10.1016/j.jallcom.2019.01.043>
- Wang Y, Wang J, Xie T et al (2019b) Three-dimensional flower-like Ni-Mn-S on Ti mesh: a monolithic electrochemical platform for detecting glucose. *New J Chem* 43:7866–7873. <https://doi.org/10.1039/c9nj00970a>
- Wei C, Cheng C, Zhao J et al (2015) NiS hollow spheres for high-performance supercapacitors and non-enzymatic glucose sensors. *Chem – An Asian J* 10:679–686. <https://doi.org/10.1002/asia.201403198>
- Welch NG, Scoble JA, Muir BW, Pigram PJ (2017) Orientation and characterization of immobilized antibodies for improved immunoassays (review). *Biointerphases* 12:02D301. <https://doi.org/10.1116/1.4978435>
- WHO (2016) Global report on diabetes. In: World Health Organ
- WHO (2019) Classification of diabetes mellitus. In: World Health Organ
- Wongkaew N, Simsek M, Griesche C, Baeumner AJ (2019) Functional nanomaterials and nanostructures enhancing electrochemical biosensors and lab-on-a-Chip performances: recent Progress, applications, and future perspective. *Chem Rev* 119:120–194. <https://doi.org/10.1021/acs.chemrev.8b00172>
- Wu J, Cao J, Han WQ et al (2012) Functional metal oxide nanostructures. Springer, New York
- Wu W, Li Y, Jin J et al (2016) A novel nonenzymatic electrochemical sensor based on 3D flower-like Ni<sub>7</sub>S<sub>6</sub> for hydrogen peroxide and glucose. *Sensors Actuators B Chem* 232:633–641. <https://doi.org/10.1016/j.snb.2016.04.006>
- Wu W, Yu B, Wu H et al (2017) Synthesis of tremella-like CoS and its application in sensing of hydrogen peroxide and glucose. *Mater Sci Eng C* 70:430–437. <https://doi.org/10.1016/j.msec.2016.08.084>
- Wu Y, Huang Q, Nie J et al (2019) All-carbon based flexible humidity sensor. *J Nanosci Nanotechnol* 19:5310–5316
- Xiong WW, Zhang G, Zhang Q (2014) New strategies to prepare crystalline chalcogenides. *Inorg Chem Front* 1:292–301. <https://doi.org/10.1039/c4qi00013g>
- Xu Y, Wang E (2012) Electrochemical biosensors based on magnetic micro/nano particles. *Electrochim Acta* 84:62–73. <https://doi.org/10.1016/j.electacta.2012.03.147>
- Xu X, Jin H, Ren Q et al (2016) Electrochemical synthesis of Cu<sub>x</sub>O/Cu<sub>2</sub>S nanocomposites as nonenzymatic glucose sensor. *Int J Electrochem Sci* 14:5637–5645. <https://doi.org/10.20964/2019.06.38>
- Xu W, Lu J, Huo W et al (2018) Direct growth of CuCo<sub>2</sub>S<sub>4</sub> nanosheets on carbon fiber textile with enhanced electrochemical pseudocapacitive properties and electrocatalytic properties towards glucose oxidation. *Nanoscale* 10:14304–14313. <https://doi.org/10.1039/c8nr04519d>
- Xu GR, Ge C, Liu D et al (2019a) In-situ electrochemical deposition of dendritic Cu-Cu<sub>2</sub>S nanocomposites onto glassy carbon electrode for sensitive and non-enzymatic detection of glucose. *J Electroanal Chem* 847:113177. <https://doi.org/10.1016/j.jelechem.2019.05.059>
- Xu X, Jin H, Ren Q et al (2019b) Electrochemical synthesis of Cu<sub>x</sub>O/Cu<sub>2</sub>S nanocomposites as nonenzymatic glucose sensor. *Int J Electrochem Sci* 14:5637–5645. <https://doi.org/10.20964/2019.06.38>

- Xue Y, Maduraiveeran G, Wang M et al (2018) Hierarchical oxygen-implanted MoS<sub>2</sub> nanoparticle decorated graphene for the non-enzymatic electrochemical sensing of hydrogen peroxide in alkaline media. *Talanta* 176:397–405. <https://doi.org/10.1016/j.talanta.2017.08.060>
- Yagati AK, Lee T, Min J, Choi JW (2013) An enzymatic biosensor for hydrogen peroxide based on CeO<sub>2</sub> nanostructure electrodeposited on ITO surface. *Biosens Bioelectron* 47:385–390. <https://doi.org/10.1016/j.bios.2013.03.035>
- Yan Y, Xia B, Xu Z, Wang X (2014) Recent development of molybdenum sulfides as advanced electrocatalysts for hydrogen evolution reaction. *ACS Catal* 4:1693–1705. <https://doi.org/10.1021/cs500070x>
- Yan X, Ma J, Xu H et al (2016) Fabrication of silver nanowires and metal oxide composite transparent electrodes and their application in UV light-emitting diodes. *J Phys D Appl Phys* 49. <https://doi.org/10.1088/0022-3727/49/32/325103>
- Yan X, Gu Y, Li C et al (2018) A non-enzymatic glucose sensor based on the CuS nanoflakes-reduced graphene oxide nanocomposite. *Anal Methods* 10:381–388. <https://doi.org/10.1039/c7ay02290e>
- Yang K, She GW, Wang H et al (2009) ZnO nanotube arrays as biosensors for glucose. *J Phys Chem C* 113:20169–20172. <https://doi.org/10.1021/jp901894j>
- Yang L, Zhou Q, Wang G, Yang Y (2013) Acetylcholinesterase biosensor based on SnO<sub>2</sub> nanoparticles-carboxylic graphene-nafion modified electrode for detection of pesticides. *Biosens Bioelectron* 49:25–31. <https://doi.org/10.1016/j.bios.2013.04.037>
- Yang J, Duan X, Guo W et al (2014a) Electrochemical performances investigation of NiS/rGO composite as electrode material for supercapacitors. *Nano Energy* 5:74–81. <https://doi.org/10.1016/j.nanoen.2014.02.006>
- Yang YJ, Li W, Wu X (2014b) Copper sulfidelreduced graphene oxide nanocomposite for detection of hydrazine and hydrogen peroxide at low potential in neutral medium. *Electrochim Acta* 123:260–267. <https://doi.org/10.1016/j.electacta.2014.01.046>
- Yang YJ, Zi J, Li W (2014c) Enzyme-free sensing of hydrogen peroxide and glucose at a CuS nanoflowers modified glassy carbon electrode. *Electrochim Acta* 115:126–130. <https://doi.org/10.1016/j.electacta.2013.10.168>
- Yu L, Yang B, Liu Q et al (2015) Interconnected NiS nanosheets supported by nickel foam: soaking fabrication and supercapacitors application. *J Electroanal Chem* 739:156–163. <https://doi.org/10.1016/j.jelechem.2014.12.031>
- Zhai YJ, Li JH, Chu XY et al (2016) MoS<sub>2</sub>microflowers based electrochemical sensing platform for non-enzymatic glucose detection. *J Alloys Compd* 672:600–608. <https://doi.org/10.1016/j.jallcom.2016.02.130>
- Zhang X, Wang L, Ji R et al (2012) Nonenzymatic glucose sensor based on Cu-Cu 2S nanocomposite electrode. *Electrochem Commun* 24:53–56. <https://doi.org/10.1016/j.elecom.2012.08.014>
- Zhang SL, Choi HH, Yue HY, Yang WC (2014) Controlled exfoliation of molybdenum disulfide for developing thin film humidity sensor. *Curr Appl Phys* 14:264–268. <https://doi.org/10.1016/j.cap.2013.11.031>
- Zhang B, Zhang X, Huang D et al (2015) Co<sub>9</sub>S<sub>8</sub> hollow spheres for enhanced electrochemical detection of hydrogen peroxide. *Talanta* 141:73–79. <https://doi.org/10.1016/j.talanta.2015.03.048>
- Zhang Y, Chen P, Wen F et al (2016a) Construction of polyaniline/molybdenum sulfide nanocomposite: characterization and its electrocatalytic performance on nitrite. *Ionics (Kiel)* 22:1095–1102. <https://doi.org/10.1007/s11581-015-1634-5>
- Zhang Z, Duan F, He L et al (2016b) Electrochemical clenbuterol immunosensor based on a gold electrode modified with zinc sulfide quantum dots and polyaniline. *Microchim Acta* 183:1089–1097. <https://doi.org/10.1007/s00604-015-1730-2>
- Zhang Y, Wen F, Tan J et al (2017) Highly efficient electrocatalytic oxidation of nitrite by electrodeposition of Au nanoparticles on molybdenum sulfide and multi-walled carbon nanotubes. *J Electroanal Chem* 786:43–49. <https://doi.org/10.1016/j.jelechem.2017.01.007>

- Zhang Y, Li Y, Wang Y et al (2019) A flexible copper sulfide @ multi-walled carbon nanotubes cathode for advanced magnesium-lithium-ion batteries. *J Colloid Interface Sci* 553:239–246. <https://doi.org/10.1016/j.jcis.2019.06.027>
- Zhao J, Wang F, Yu J, Hu S (2006) Electro-oxidation of glucose at self-assembled monolayers incorporated by copper particles. *Talanta* 70:449–454. <https://doi.org/10.1016/j.talanta.2006.03.004>
- Zheng X, Han X, Zhang Y et al (2019) Controllable synthesis of nickel sulfide nanocatalysts and their phase-dependent performance for overall water splitting. *Nanoscale* 11:5646–5654. <https://doi.org/10.1039/c8nr09902b>
- Zhuang Z, Su X, Yuan H et al (2008) An improved sensitivity non-enzymatic glucose sensor based on a CuO nanowire modified Cu electrode. *Analyst* 133:126–132. <https://doi.org/10.1039/b712970j>

# Chapter 7

## Applications of Metals, Metal Oxides, and Metal Sulfides in Electrochemical Sensing and Biosensing



Murugan Thiruppathi, Natarajan Thiyagarajan, and Ja-an Annie Ho

### Contents

7.1	Introduction .....	210
7.1.1	Modification of Nanomaterials on Electrode Surface .....	212
7.1.2	Operational Stages of the Electrochemical Sensor (Fig. 7.3) .....	214
7.2	Non-noble Metals .....	214
7.2.1	Titanium (Ti) .....	214
7.2.2	Vanadium (V) .....	216
7.2.3	Manganese (Mn) .....	216
7.2.4	Iron (Fe) .....	217
7.2.5	Cobalt (Co) .....	217
7.2.6	Nickel (Ni) .....	220
7.2.7	Molybdenum (Mo) .....	221
7.2.8	Copper (Cu) .....	224
7.3	Precious/Noble Metal Electrodes (Pd, Ag, Au, Pt) .....	229
7.3.1	Palladium (Pd) .....	229
7.3.2	Silver (Ag) .....	230
7.3.3	Gold (Au) .....	230
7.3.4	Platinum (Pt) .....	234
7.4	Conclusion .....	237
	References .....	239

---

M. Thiruppathi

Bioanalytical Chemistry and Nanobiomedicine Laboratory, Department of Biochemical Science and Technology, National Taiwan University, Taipei, Taiwan

N. Thiyagarajan

Institute of Chemistry, Academia Sinica, Taipei, Taiwan

J.-a. A. Ho (✉)

Bioanalytical Chemistry and Nanobiomedicine Laboratory, Department of Biochemical Science and Technology, National Taiwan University, Taipei, Taiwan

Center for Biotechnology, National Taiwan University, Taipei, Taiwan

e-mail: [jaho@ntu.edu.tw](mailto:jaho@ntu.edu.tw)

© The Editor(s) (if applicable) and The Author(s), under exclusive licence to Springer Nature Switzerland AG 2021

209

S. Rajendran et al. (eds.), *Metal, Metal-Oxides and Metal Sulfides for Batteries, Fuel Cells, Solar Cells, Photocatalysis and Health Sensors*, Environmental Chemistry for a Sustainable World 62, [https://doi.org/10.1007/978-3-030-63791-0\\_7](https://doi.org/10.1007/978-3-030-63791-0_7)

**Abstract** Conventional working electrodes encounter several drawbacks, such as requirement of high overpotential, poor selectivity and sensitivity, and surface fouling or poisoning of the electrode surface due to adsorption of the oxidized/reduced products of molecules under investigation. Surface modifications indeed play a catalytic role in determining the sensitivity of measurement in electroanalytical applications. Particularly, the use of metal nanoparticles in electroanalytical chemistry is an area of research, which is continually expanding. Taking advantage of exceptional attributes, such as being easy to handle, cost effectiveness, user friendliness, maintenance free electroanalytical devices have been utilized for the development of environmental sensors, chemical sensors, and biosensors. This chapter represents a comprehensive attempt to summarize and discuss various electrochemical sensing and biosensing applications using metals, metal oxides, and metal sulfides. These materials have been widely used as working electrodes, due to their good conductivity, large surface area, fast diffusion kinetics, low resistance, ease of functionalization, offering the versatile option of controllable adjustment with proper choice of materials. In this review, we have concentrated on widely used metal electrodes with specific application.

**Keywords** Metals · Metal oxides · Metal sulfides · Electrochemical sensor · Biosensor

## 7.1 Introduction

There is no doubt that electrochemical sensors provide quick response, require low-power, and are easy to use, compact, cost-effective, and portable than other analytical tools (Thiruppathi et al. 2019; Thiyagarajan et al. 2014). Electrochemical sensors offer timely results for samples with complex matrices even outside of laboratories. Glucose meter, pH meter, and the other ion-selective meter exemplify the potential real-time applications of electrochemical sensors (Gooding 2008). According to the current IUPAC's definition (Devi and Tharmaraj 2019), a chemical or bio-sensor is a device that transforms chemical information, ranging from the concentration of a specific sample component to total composition analysis, into an analytically useful signal. There are different electrochemical techniques available for sensing important chemical and biochemical targets, including, voltammetry, amperometry, potentiometry, and electrochemiluminescence. Among the various electrochemical techniques, voltammetry is one of the most widely employed electrochemical techniques, which includes cyclic voltammetry (CV), linear sweep voltammetry (LSV), square wave voltammetry (SWV), and differential pulse voltammetry (DPV) (Fig. 7.1). Basically, it is used to get electrochemical information of analyte by measuring the current response of analyte as the function of potential and/or time. In the voltammetric methods, variety of electrode substrates are used to improve sensing performance of electrodes. Metals, metal oxides, and

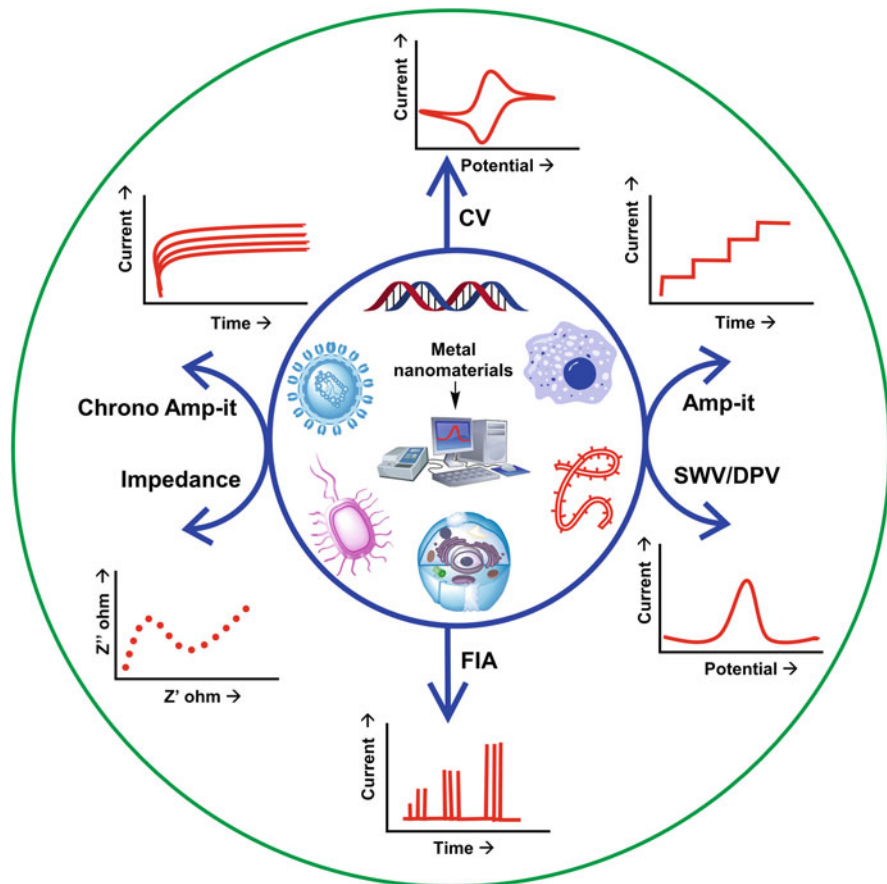


**Fig. 7.1** Various available electrochemical techniques for sensing important chemical and biochemical targets (*CV* cyclic voltammetry, *SWV* square wave voltammetry, *DPV* differential pulse voltammetry, and *FIA* flow injection analysis)

metal sulfides are one of such substrates, and are widely used as electrode materials in electrochemical sensor field that transforms chemical signal of analyte into electrical signal (Alves et al. 2011). The following characteristics may be deemed necessary to be a good electrode material for sensing: (i) good conductivity, (ii) chemical inertness, (iii) high surface area, (iv) low resistance, (v) fast diffusion kinetics, and (vi) extraction and accumulation of an analyte at the electrode. More than half of the elements known today in the periodic tables are metals (Fig. 7.2).

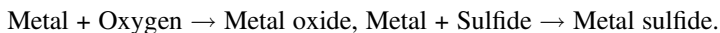
Among the metals, d-block transition metals have been widely used in electrochemical analysis due to their good conductivity and a great range of catalytic activity (Gates 1993). Utilization of metal oxide nanoparticles in electrochemical sensing and biosensing has drawn a lot of attention and explored in the recent review (George et al. 2018). In this chapter, we highlight the widely employed transition

H	Non metals																He
Li	Be	Metalloids										B	C	N	O	F	Ne
Na	Mg	Metals										Al	Si	P	S	Cl	Ar
		← d-Block Transition Elements →															
K	Ca	Sc	Ti	V	Cr	Mn	Fe	Co	Ni	Cu	Zn	Ga	Ge	As	Se	Br	Kr
Rb	Sr	Y	Zr	Nb	Mo	Tc	Ru	Rh	Pd	Ag	Cd	Id	Sn	Sb	Te	I	Xe
Cs	Ba	La-Lu	Hf	Ta	W	Re	Os	Ir	Pt	Au	Hg	Tl	Pb	Bi	Po	At	Rn
Fr	Ra	Ac-Lr	Rf	Db	Sg	Bh	Hs	Mt	Ds	Rg							

Fig. 7.2 Classifications of metals, nonmetals, and metalloid elements in the modern periodic table

metals/metal oxide/metal sulfide electrode properties along with their advanced applications in chemical and biological electro-sensing.

Though, metal-based electrodes are used for sensing analytes, they were largely restricted by poor kinetics and limited surface area. Surface modification for those oxides/sulfides of metals may be the solution to improve. Metal oxides are usually formed by the reaction of metal with oxygen, whereas metal sulfides, one of the broadly accepted and employed nanomaterials, are produced by the reaction of a metal and sulfide (Velmurugan and Incharoensakdi 2018).



### 7.1.1 Modification of Nanomaterials on Electrode Surface

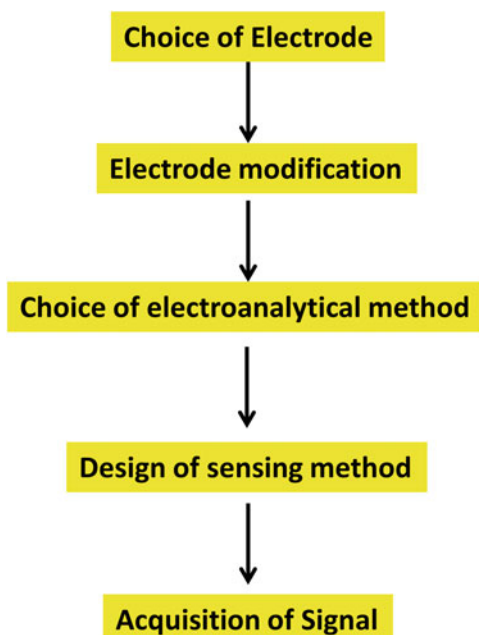
Surface modification is employed for two main purposes, either to protect an electrode that is not corrosion resistant under operating conditions or to incorporate specific properties to the surface. Conventional working electrodes encounter several drawbacks, such as requirement of high overpotential, poor selectivity and sensitivity, and surface fouling or poisoning of the electrode surface due to adsorption of the oxidized/reduced products of molecules under investigation. The concept of chemically modified electrodes (CMEs) was introduced to overcome aforementioned problems.



CMEs consist of a conductive substrate modified with electrochemically active, functional moieties; metals, metal oxides, metal sulfides, and polymers. CMEs are fabricated for a specific application that may not be feasible with a bare/unmodified metal electrode. Modification of the nano-metal oxide and sulfides onto the electrode surface may result in enhanced electron transfer kinetics, improved sensitivity, and reduced overpotential. These modifications involved irreversible adsorption (Thirupathi et al. 2016), self-assembled layers, covalent bonding, electropolymerization (Thirupathi et al. 2017), and others (Lane and Hubbard 1973; Murray 1980; Zen et al. 2003b). Surface modifications indeed played a catalytic role in determining the sensitivity of measurement in electroanalytical applications. Such surface modifications endowed the surface with new properties independent of those of the unmodified electrode. Modified electrodes in general led to the following:

1. Endowing with physicochemical properties of the modifier for the electrode
2. Improved sensitivity and electrocatalytic ability
3. High selectivity toward analyte due to special functional moieties and pores
4. Improved diffusion kinetics
5. Extraction and accumulation of an analyte at the electrode

**Fig. 7.3** Operational stages of the electrochemical sensor



### 7.1.2 Operational Stages of the Electrochemical Sensor (Fig. 7.3)

Overall, this chapter is divided into two parts (i) non-noble and (ii) noble metal-based sensors.

## 7.2 Non-noble Metals

### 7.2.1 Titanium (Ti)

Titanium is the strongest pure metal on earth. It is also an attractive material used in electrochemical analysis and mostly utilized in chemical sensors. Bukkitgar et al. 2016 have investigated the electrochemical oxidation of nimesulide at TiO<sub>2</sub> nanoparticles-modified glassy carbon electrode (Bukkitgar et al. 2016). Furthermore, Ti is largely used as a base substrate for deposition/immobilization of active catalyst materials. Kang et al. 2008 decorated a Gold–Platinum nanoparticle onto a highly oriented titania nanotube array surface by electrochemical method that was used for amperometric detection of H<sub>2</sub>O<sub>2</sub> (Figs. 7.4 and 7.5) (Kang et al. 2008). A modified titanium electrode of nanoporous gold particles (Yi and Yu 2009) and silver nanoparticles (Yi et al. 2008) was utilized for the detection of hydrazine. Kubota and co-workers have tried to immobilize Meldola's Blue on titanium, and employed it for electrocatalytic oxidation of reduced nicotinamide adenine dinucleotide (NADH) (Kubota et al. 1996). Noble nanomaterials (Ag, Pt, Au) have been commonly seen in modifying Ti electrode, and subsequently utilized for chemical sensing. Some examples for the Titanium (Ti) electrode-based sensors are listed in Table 7.1.

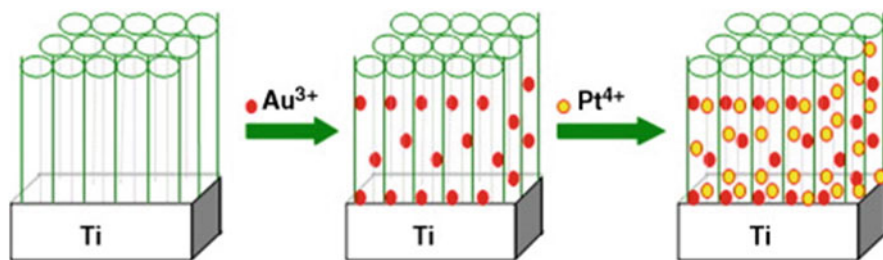


**Fig. 7.4** Deposition process of Au and Pt nanoparticles (Reproduced with permission from Kang et al. 2008)

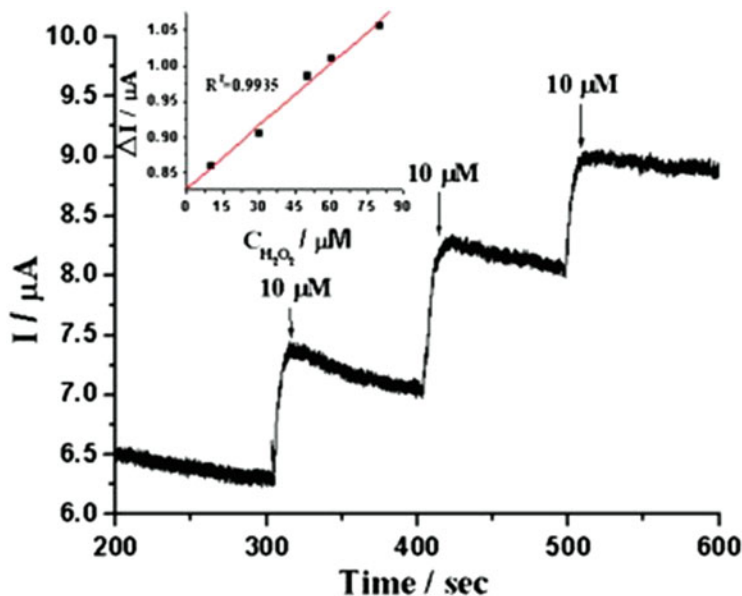


**Fig. 7.5** Amperometric responses of the Pt–Au/TiO<sub>x</sub> NT electrode upon adding continuously 10 μM H<sub>2</sub>O<sub>2</sub> in 10 mM PBS (pH 7.3) containing 0.1 M NaCl at –0.2 V vs Ag/AgCl (saturated by KCl). 10 μM H<sub>2</sub>O<sub>2</sub> is the final concentration. The inset shows the calibration curve. (Reproduced with permission from Kang et al. 2008)

**Table 7.1** List of Titanium (Ti) electrode-based sensors

Electrode material	Detection method	Analyte	Electrolyte	Linear range	Detection limit	Reference
GCE–TiO <sub>2</sub>	DPV	Nimesulide	pH 2, PBS	40–100 μM	3.37 nM	Bukkitgar et al. (2016)
Pt–Au/TiO <sub>x</sub> NT	Amperometry	H <sub>2</sub> O <sub>2</sub>	pH 7.3, PBS	0–1.8 mM	0.1 mM	Kang et al. (2008)
nanoAg/Ti	Amperometry	Hydrazine	NaOH	0–60 mM	–	Yi et al. (2008)
Au/Ti	Amperometry	Hydrazine	NaOH	5–40 mM	0.042 mM	Yi and Yu (2009)
Meldola’s Blue/Ti	Amperometry	NADH	pH 7.4, PBS	10–50 μM	–	Kubota et al. (1996)

*GCE–TiO<sub>2</sub>* titanium oxide modified glassy carbon electrode, *Pt–Au/TiO<sub>x</sub> NT* gold-platinum nanoparticle modified onto a highly oriented titania nanotube array, *nanoAg/Ti* nano-silver-titanium electrode, *Au/Ti* gold titanium electrode, *DPV* differential pulse voltammetry, *PBS* phosphate buffer saline, *H<sub>2</sub>O<sub>2</sub>* hydrogen peroxide, *NaOH* sodium hydroxide, and *NADH* nicotinamide adenine dinucleotide

### 7.2.2 Vanadium (V)

Vanadium is the lightest, corrosion-resistant d-block transition metal, which exists in oxidation states ranging from  $-1$  to  $+5$  (Barceloux and Barceloux 1999b; Privman and Hepel 1995). Vanadium electrodes have been widely used in capacitors and batteries, only a little amount of success has been achieved in the sensor field. Cyclic voltammetric behavior of vanadium electrodes has been summarized by Privman and Hepel (1995) (Privman and Hepel 1995). A VO-polypropylene carbonate modified glassy carbon electrode prepared by casting method was described by Tian et al. (2006) and used for amperometric detection of ascorbic acid (AA) (Tian et al. 2006). Huang group developed a novel electrochemical biosensor for the determination of  $17\beta$ -estradiol using  $VS_2$  nanoflowers-gold nanoparticles modified glassy carbon electrode (Huang et al. 2014). Tsiafoulis et al. 2005 prepared vanadium hexacyanoferrate and casted onto the glassy carbon electrode, which was subsequently used as electro catalyst for  $H_2O_2$  sensing (Tsiafoulis et al. 2005). Some examples for the Vanadium (V) electrode-based sensors are listed in Table 7.2.

### 7.2.3 Manganese (Mn)

Reports show that MnS can be utilized as one of promising active materials for pseudocapacitor and battery applications (Li et al. 2015; Zhang et al. 2008). Manganese oxide ( $MnO_2$ ), however, was extensively used for electrochemical sensors than Mn and MnS. Several kinds of  $MnO_2$  nanomaterials were employed to construct chemical sensors or biosensors in recent years (Bai et al. 2009). The reactivity of thiol group toward  $MnO_2$  is higher than those of amine and carboxylic functional groups (Eremenko et al. 2012). Therefore, Bai and co-workers developed a sensing

**Table 7.2** List of Vanadium (V) electrode-based sensors

Electrode material	Detection method	Analyte	Electrolyte	Linear range	Detection limit	Reference
VO( $OC_3H_7$ ) <sub>3</sub> -PPC/GCE	Amperometry	Ascorbic acid	pH 8.06, BRS	40 nM–0.1 mM	15 nM	Tian et al. (2006)
AuNPs/ $VS_2$ /GCE	DPV	$17\beta$ -estradiol	pH 7, PBS	10 pM–10 nM	1 pM	Huang et al. (2014)
VHCF/GCE	Amperometry	$H_2O_2$	pH 7, Tris buffer	0.01–3 mM	4 $\mu$ M	Tsiafoulis et al. (2005)

VO( $OC_3H_7$ )<sub>3</sub>-PPC/GCE vanadium tri (isopropoxide) oxide and polypropylene carbonate glassy carbon electrode, AuNPs/ $VS_2$ /GCE vanadium sulfide nanoflowers-gold nanoparticles modified glassy carbon electrode, VHCF/GCE vanadium hexacyanoferrate and casted onto the glassy carbon electrode, BRS Britton–Robinson solution, PBS phosphate buffer saline,  $H_2O_2$  hydrogen peroxide, DPV differential pulse voltammetry

method for cysteine using  $\beta$ - $\text{MnO}_2$  nanowires modified glassy carbon (GC) electrode (Bai et al. 2009), a manganese dioxide-carbon ( $\text{MnO}_2$ -C) nanocomposite was also applied in the development of sensors to detect cysteine (Xiao et al. 2011).  $\text{MnO}_2$  was also used to prepare screen printed electrodes (Šljukić et al. 2011), enabling the development of point of care sensors. Additionally, the electrocatalytic behavior of  $\text{MnO}_2$  was also adopted for non-enzymatic  $\text{H}_2\text{O}_2$  sensor (Chinnasamy et al. 2015; Dontsova et al. 2008; Šljukić et al. 2011; Wang et al. 2013; Zhang et al. 2014). Hierarchical  $\text{MnO}_2$  microspheres composed of nanodisks were once used for nitrite sensing (Xia et al. 2009). Moreover, Revathi and Kumar (2017) hydrothermally prepared polymorphs of alpha ( $\alpha$ ), beta ( $\beta$ ), gamma ( $\gamma$ ), epsilon ( $\epsilon$ )  $\text{MnO}_2$  and  $\text{MnOOH}$  under different conditions for  $\text{H}_2\text{O}_2$  sensing (Revathi and Kumar 2017). Some examples for the Manganese (Mn) electrode-based sensors are listed in Table 7.3.

### 7.2.4 Iron (Fe)

Iron is the fourth most common element in the Earth's crust (Anderson 1989). A few review articles were highlighted below, showing how iron is useful for electrochemical sensor applications. The development of electrochemical biosensors based on Fe and Fe-oxide nanomaterials has been well summarized in the literature written by Hasanzadeh and Urbanova group (Hasanzadeh et al. 2015; Urbanova et al. 2014). Bank's group developed disposable screen printed electrodes modified with iron oxide nanocubes for meclizine, antihistamine (Khorshed et al. 2019). Iron and associated nanomaterials are known to exhibit electrocatalytic ability toward a wide range of analytes including hydrogen peroxide ( $\text{H}_2\text{O}_2$ ) (Comba et al. 2010), sulfide (S) (Sun et al. 2005), nitrite ( $\text{NO}_2$ ) (Bharath et al. 2015; Xia et al. 2012), phenyl hydrazine (Hwang et al. 2014), and hydrazine (Benvidi et al. 2015; Mehta et al. 2011). Šljukić et al. 2006 demonstrated that Fe-oxide particles existed at the multiwalled carbon nanotube were responsible for electrocatalytic detection of  $\text{H}_2\text{O}_2$  (Šljukić et al. 2006). Some examples for the Iron (Fe) electrode-based sensors are listed in Table 7.4.

### 7.2.5 Cobalt (Co)

Cobalt is a relatively rare magnetic element with properties similar to iron and nickel (Barceloux and Barceloux 1999a). Cobalt oxide ( $\text{Co}_3\text{O}_4$ ) nanowires exhibited glucose oxidase-like enzymatic activity. Chemical vapor deposition (CVD) method was employed to synthesize  $\text{Co}_3\text{O}_4$  nanowires and subsequently used for enzymeless glucose sensor application (Fig. 7.6) (Dong et al. 2012; Wang et al. 2012). Reports have shown that Co and associated nanomaterials display high sensitivity and selectivity toward phosphate ion (Chen et al. 1997), and electrocatalytic ability

Table 7.3 List of Manganese (Mn) electrode-based sensors

Electrode material	Detection method	Analyte	Electrolyte	Linear range	Detection limit	Reference
MnO <sub>2</sub> /Chit/GC	Amperometry	Cysteine	pH 7.8 BBS	0.5–630 μM	70 nM	Bai et al. (2009)
MnO <sub>2</sub> -C/chit/GC	Chronoamperometry	Cysteine	pH 7.8, BBS	0.5–680 μM	22 nM	Xiao et al. (2011)
MnO <sub>2</sub> -SPC	Voltammetry	Ascorbic acid	pH 7, PB	20–100 μM	2.8 μM	Šjukić et al. (2011)
MnO <sub>2</sub> -SPC	LSV	Nitrite	HClO <sub>4</sub> + NaClO <sub>4</sub>	20–200 μM	2.5 μM	Šjukić et al. (2011)
MnO <sub>2</sub> /nafion/Pt	Chronoamperometry	H <sub>2</sub> O <sub>2</sub>	NaOH	1–5 mM	–	Chinnasamy et al. (2015)
MnO <sub>2</sub> NPs	Amperometry	H <sub>2</sub> O <sub>2</sub>	pH 7.4, KCl	78 nM –0.78 mM	78 nM	Dontsova et al. (2008)
Au-MnO <sub>2</sub> -rGO/GCE	Amperometry	H <sub>2</sub> O <sub>2</sub>	pH 7, PBS	0.1 μM–12.6 mM	50 nM	Wang et al. (2013)
MnO <sub>2</sub> nanosheet	Amperometry	H <sub>2</sub> O <sub>2</sub>	pH 7, PBS	5 μM–3.5 mM	1.5 μM	Zhang et al. (2014)
MnO <sub>2</sub> /QPOE composite electrodes	Amperometry	Nitrite	HClO <sub>4</sub> + NaClO <sub>4</sub>	0.5 μM–3 mM	0.36 μM	Xia et al. (2009)
α-MnO <sub>2</sub> /GCE	Amperometry	H <sub>2</sub> O <sub>2</sub>	KCl	0.67–20 μM	0.175 μM	Revathi and Kumar (2017)

*MnO<sub>2</sub>/Chit/GC* manganese dioxide nanowires and chitosan modified glassy carbon electrode, *MnO<sub>2</sub>-SPC* manganese oxide screen printed electrodes, *MnO<sub>2</sub>/nafion/Pt* manganese oxide and nafion modified platinum electrode, *MnO<sub>2</sub>NPs* manganese oxide nanoparticles, *Au-MnO<sub>2</sub>-rGO/GCE* manganese oxide-reduced graphene oxide modified glassy carbon electrode, *BBS* Borate buffered saline, *PB* phosphate buffer, *PBS* phosphate buffer saline, *H<sub>2</sub>O<sub>2</sub>* hydrogen peroxide, *HClO<sub>4</sub>* perchloric acid, *NaClO<sub>4</sub>* sodium perchlorate, *LSV* linear sweep voltammetry, *KCl* potassium chloride

**Table 7.4** List of Iron (Fe) electrode-based sensors

Electrode material	Detection method	Analyte	Electrolyte	Linear range	Detection limit	Reference
Fe <sub>3</sub> O <sub>3</sub> NCs-SPEs	DPV	Mecizine	Sulfuric acid	6.6–196 μM	1.6 μM	Khorshed et al. (2019)
FeNPs	Amperometry	Hydrogen peroxide	pH 7, PBS	Up to 20 mM	0.2 mM	Comba et al. (2010)
α-Fe <sub>2</sub> O <sub>3</sub>	Chemiluminescence	Sulfide	–	–	10 ppm	Sun et al. (2005)
Fe <sub>3</sub> O <sub>4</sub> -rGO	DPV	Nitrite	pH 4, PBS	0.5 μM–9.5 mM	30 nM	Bharath et al. (2015)
Fe <sub>2</sub> O <sub>3</sub>	Amperometry	Nitrite	pH 7.5, PBS	9 μM – 3 mM	2.6 μM	Xia et al. (2012)
α-Fe <sub>2</sub> O <sub>3</sub>	I-V	Phenyl hydrazine	pH 7, PBS	97 μM–1.56 mM	97 μM	Hwang et al. (2014)
Fe <sub>3</sub> O <sub>4</sub> NP <sub>8</sub>	DPV	Hydrazine	pH 7, PBS	0.12–0.6 μM	40 nM	Benvidi et al. (2015)
α-Fe <sub>2</sub> O <sub>3</sub>	Amperometry	Hydrazine	pH 7, PBS	–	3.84 μM	Mehta et al. (2011)
Iron oxide	CV	Hydrogen peroxide	pH 7.4, PBS	–	–	Šjukić et al. (2006)

Fe<sub>2</sub>O<sub>3</sub> NCs-SPEs screen-printed carbon electrode modified with uniform iron oxide nanocubes, FeNPs iron nanoparticles, α-Fe<sub>2</sub>O<sub>3</sub> iron oxide, rGO reduced graphene oxide, PBS phosphate buffer saline, DPV differential pulse voltammetry, CV cyclic voltammetry

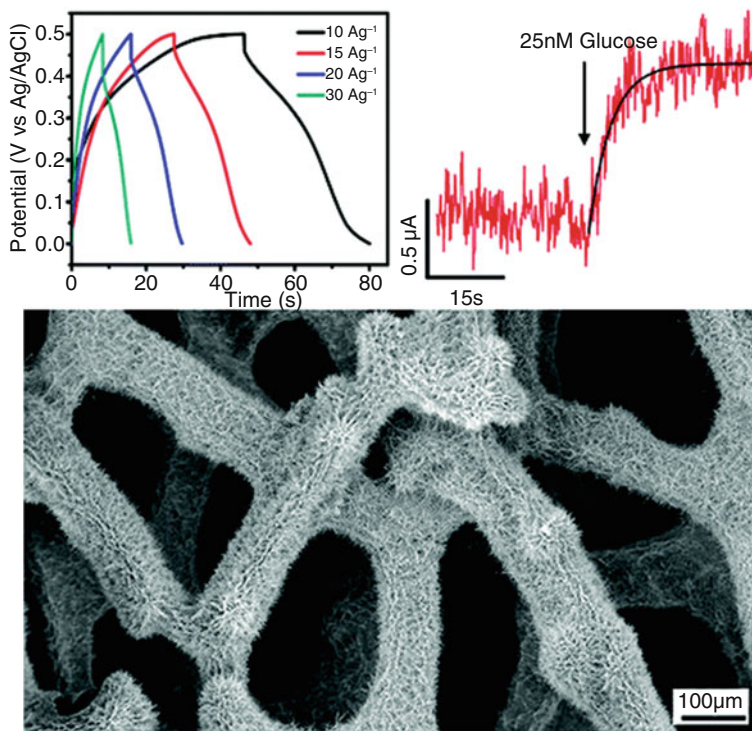


**Fig. 7.6** Electro catalytic detection of glucose on cobalt oxide modified electrode. (Reproduced with permission from (Dong et al. 2012)

toward hydrogen peroxide (Salimi et al. 2007). Furthermore, numerous enzyme-free sensors are configured using various cobalt nanomaterials such as nanorod, nanosheet, and nanoparticles (George et al. 2018). Some examples for the Cobalt (Co) electrode-based sensors are listed in Table 7.5.

### 7.2.6 Nickel (Ni)

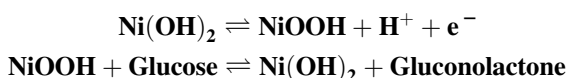
Nickel is an important metal and a possible alternative to the noble metals. Nickel and its composites are most active catalyst for glucose oxidation process in alkaline medium (Yuan et al. 2013). Nickel nanomaterials have been widely used for broad range of sensor applications. The Ni nanomaterials are pH dependent, and redox active in the alkaline environment; therefore, they are suitable for sensing glucose in alkaline pH. The previously published articles indicated that nickel oxide modified electrodes were capable of catalyzing the glucose oxidation reaction, as shown below:



**Table 7.5** List of Cobalt (Co) electrode-based sensors

Electrode material	Detection method	Analyte	Electrolyte	Linear range	Detection limit	References
Co <sub>3</sub> O <sub>4</sub>	Amperometry	Glucose	KOH	20–80 μM	100 nM	Dong et al. (2012)
Graphene/Co <sub>3</sub> O <sub>4</sub>	Amperometry	Glucose	NaOH	50–300 μM	10 μM	Wang et al. (2012)
Cobalt wire	Potentiometry	Phosphate	pH 5, potassium acid phthalate	50 μM–5 mM	1 μM	Chen et al. (1997)
Cobalt oxide/GC	Amperometry	H <sub>2</sub> O <sub>2</sub>	pH 7, PBS	4–80 nM	0.4 nM	Salimi et al. (2007)

Co<sub>3</sub>O<sub>4</sub> cobalt oxide, GC glassy carbon



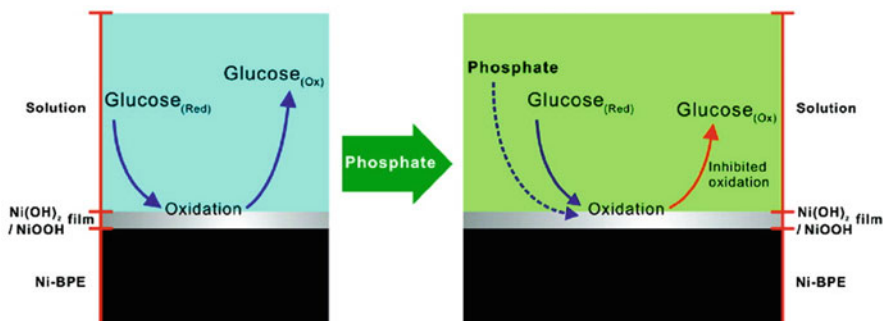
Yuan et al. (2013) electrochemically synthesized 3D nickel oxide nanoparticles (NiONPs) onto the surface of graphene oxide (GO) modified glassy carbon (GC), resulted in the development of the nonenzymatic glucose sensor and supercapacitor (Yuan et al. 2013). The catalytic ability of nickel electrode toward glucose was also useful for indirect detection of phosphate, as indicated in Fig. 7.7 (Cheng et al. 2010), Cheng et al. (2010) used activated nickel electrode to develop enzyme-free method for the detection of phosphate (PO<sub>4</sub><sup>3-</sup>) anion with flow injection analysis (FIA) (Cheng et al. 2010). In this system, the activation of barrel plated nickel electrode (NiBPE) was found to initiate the adsorption of PO<sub>4</sub><sup>3-</sup> anion at the nickel electrode, which suppressed glucose oxidation current at the NiBPE in 0.1 M, NaOH solution induced by adsorption of phosphate.

Zen's group constructed an electrochemical cell coupled with flow injection analytical system (FIA) using disposable NiBPE for the analysis of trivalent chromium (Cr<sup>III</sup>), as illustrated in Fig. 7.8 (Sue et al. 2008). Some examples for the Nickel (Ni) electrode-based sensors are listed in Table 7.6.

### 7.2.7 Molybdenum (Mo)

Both Molybdenum sulfide (MoS<sub>2</sub>) and Molybdenum oxide (MoO) were widely known as semiconductors, which are mostly utilized as electrode for energy generations. Experimental and theoretical studies have confirmed the catalytic activity of MoS<sub>2</sub> (Lee et al. 2010). Structural diversity of 2D/3D molybdenum disulfide (MoS<sub>2</sub>) rendered them first choice for electrochemical sensors and biosensor applications

(A)



(B)

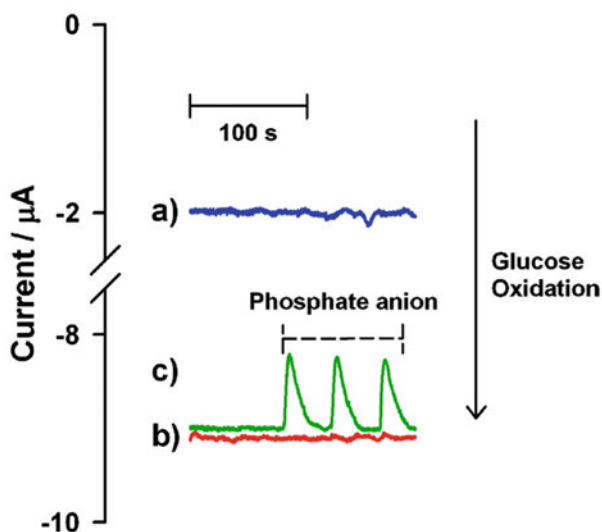


**Fig. 7.7** (a) Detection scheme of the proposed system mentioned in Cheng et al. (2010). (b) FIA responses of the activated Ni-barrel plating electrode in 0.1 M NaOH (a), in 0.1 M NaOH with 25  $\mu\text{M}$  glucose (b), and sequential injection of 500  $\mu\text{M}$   $\text{PO}_4^{3-}$  in 0.1 M NaOH with 25  $\mu\text{M}$  glucose as carrier solution (c) at  $E_{\text{app}} = +0.55$  V vs Ag/AgCl. (Reproduced with permission from (Cheng et al. 2010))

than MoO (Figs. 7.9 and 7.10). In fact, MoO has not been explored much for sensor applications (Vilian et al. 2019).

Ezhil Vilian et al. (2019) have done an extensive review on  $\text{MoS}_2$  based electrochemical sensors (Vilian et al. 2019). Mani and colleagues synthesized  $\text{MoS}_2$  nanoflowers onto the CNTs decorated-graphene nanosheet (GNS) through hydrothermal method, followed by the utilization in developing an electrochemical sensor,

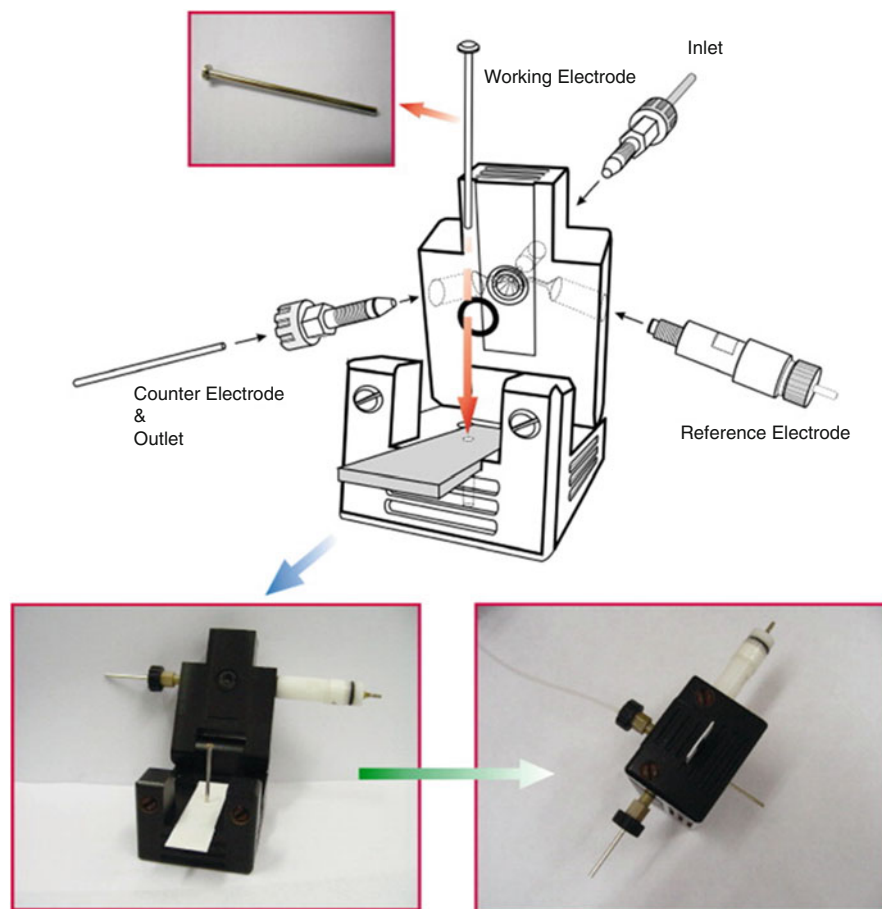


**Fig. 7.8** Proposed flow injection electrochemical detector setup. (Reproduced with permission from Sue et al. 2008)

**Table 7.6** List of Nickel (Ni) electrode-based sensors

Electrode material	Detection method	Analyte	Electrolyte	Linear range	Detection limit	Reference
NiONPs/GO/GC	Amperometry	Glucose	NaOH	3.13 $\mu\text{M}$ –3.05 mM	1 $\mu\text{M}$	Yuan et al. (2013)
Ni-BPE	FIA	Phosphate	NaOH	25 $\mu\text{M}$ –1 mM	0.3 $\mu\text{M}$	Cheng et al. (2010)
Ni-BPE	FIA	$\text{Cr}^{\text{III}}$	NaOH	Up to 1 mM	0.3 $\mu\text{M}$	Sue et al. (2008)

*NiONPs/GO/GC* nickel oxide nanoparticles-graphene oxide modified glassy carbon electrode, *Ni-BPE* Ni-barrel plating electrode, *FIA* flow injection analysis, *NaOH* sodium hydroxide

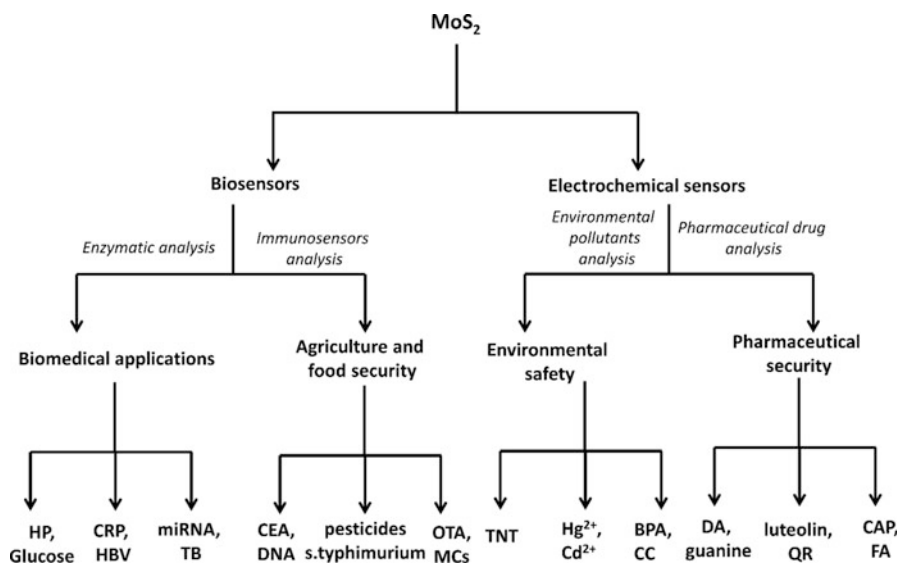


**Fig. 7.9** Schematic illustration of the electrochemical sensing and biosensing applications of MoS<sub>2</sub>-based detection devices.

MoS<sub>2</sub> molybdenum sulfide, *HP* hydrogen peroxide, *CRP* C-Reactive Protein, *HBV* Hepatitis B virus, *miRNA* micro RNA, *TB* tuberculosis, *CEA* carcinoembryonic antigen, *DNA* deoxyribonucleic acid, *OTA* Ochratoxin A, *MCs* microcystins, *TNT* trinitrotoluene, *BPA* Bisphenol A, *CC* Catechol, *DA* dopamine, *QR* quercetin, *CAP* Chloramphenicol, *FA* folic acid. (Reproduced with permission from Vilian et al. 2019)

which showed feasibility in detecting nanomolar level of dopamine (DA) in rat brain and serum samples, as illustrated in Fig. 7.11 (Mani et al. 2016). In addition, MoS<sub>2</sub> was also used to develop an electrochemiluminescence-sandwich type sensor for concanavalin A (Con A) (Fig. 7.12) (Ou et al. 2016).

## 7.2.8 Copper (Cu)

The redox chemistry of copper is interesting, and it has been involved in various biological and chemical processes (Lewis and Tolman 2004). Copper is an attractive material for sensing application, which was employed in the electrochemical analysis of o-diphenols, glucose, amino acids, and oxygen. Sivasankar et al. 2018 constructed a glucose sensor based on copper nanoparticles-decorated, nitrogen doped graphite oxide (NGO) (Sivasankar et al. 2018). In addition to sugar detection, Cu nanomaterials (both CuO and CuS) were also used as an electrocatalyst in the H<sub>2</sub>O<sub>2</sub> sensor (Dutta et al. 2014; Gu et al. 2010; Wang et al. 2008). Baskar et al. (2013) reported the complex forming ability of free amine group of poly(melamine) with Cu to enhance the electrocatalytic behavior of poly(melamine)-Cu nanoclusters

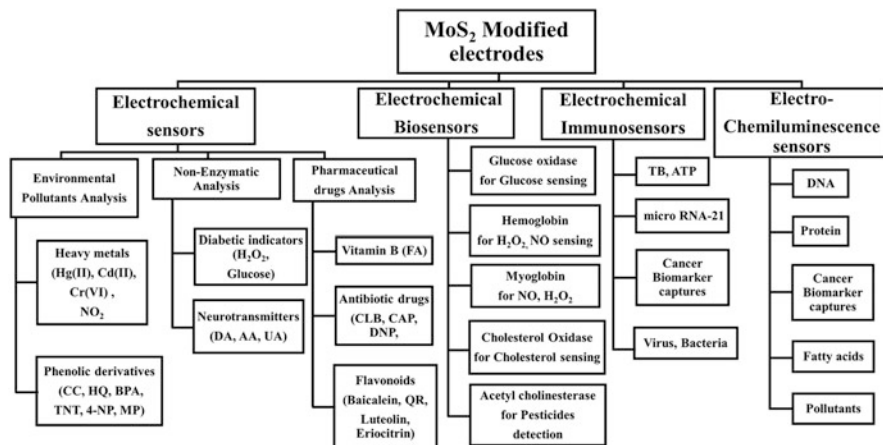


**Fig. 7.10** Flowchart representing the applications of MoS<sub>2</sub>-based modified electrodes toward their sensors and biosensors applications

MoS<sub>2</sub> molybdenum sulfide, H<sub>2</sub>O<sub>2</sub> hydrogen peroxide, NO<sub>2</sub> nitrite, HQ hydroquinone, BPA Bisphenol A, TNT trinitrotoluene, NP nitrophenol, MP metaphenol, CC Catechol, DA dopamine, AA ascorbic acid, UA uric acid, CLB Clenbuterol, CAP Chloramphenicol, DNP diamond nanoparticles, QR quercetin, TB tuberculosis, ATP Adenosine triphosphate, DNA deoxyribonucleic acid. (Reproduced with permission from (Vilian et al. 2019))

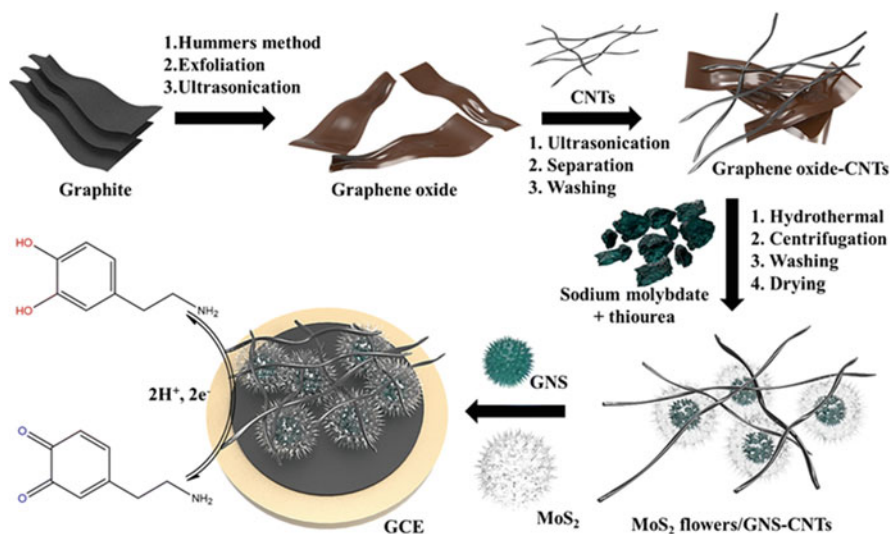


**Fig. 7.11** Fabrication of a GNS-CNT/MoS<sub>2</sub> hybrid nanostructure, and its application in the electrochemical sensing of dopamine for biological and pharmaceutical samples (CNTs carbon nanotubes, GCE glassy carbon electrode, GNS graphene nanosheet. (Reproduced with permission from Mani et al. 2016))

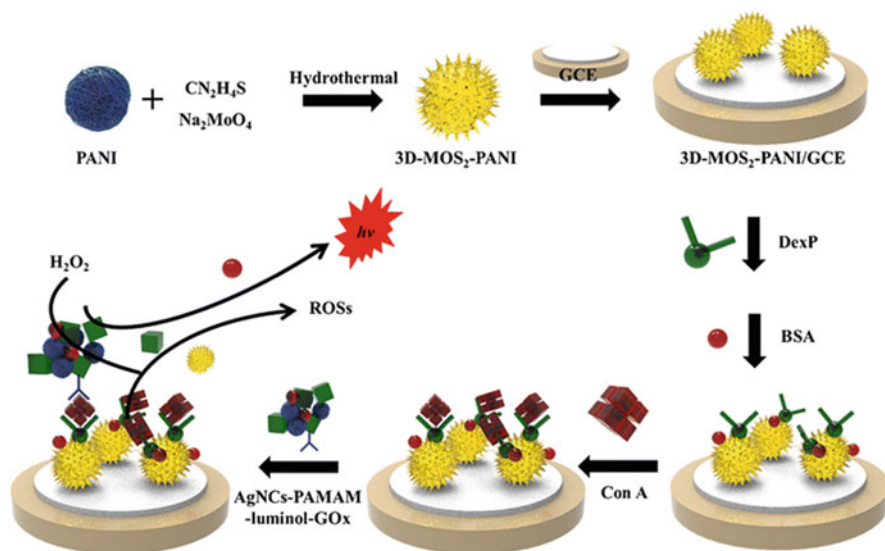


**Fig. 7.12** 3D-MoS<sub>2</sub>-PANI-based ECL biosensor (PANI polyaniline, BSA bovine serum albumin, GCE glassy carbon electrode, ECL electrochemiluminescence, Con A concanavalin A, H<sub>2</sub>O<sub>2</sub> hydron peroxide). (Reproduced with permission from Ou et al. 2016))

that was efficient for H<sub>2</sub>O<sub>2</sub> sensing, and the system showed excellent stability (Baskar et al. 2013). In addition, Cu nanoparticle-plated disposable electrodes were also utilized for amino acid detection (Zen et al. 2004).

Ling et al. (2018) reported a novel method to prepare 3D porous Cu@Cu<sub>2</sub>O aerogel networks by self-assembling method. The resultant Cu@Cu<sub>2</sub>O aerogel networks displayed excellent electrocatalytic activity toward glucose oxidation at a low onset potential. The Cu@Cu<sub>2</sub>O aerogels were found to be electroactive, pH dependent, and stable, possess horseradish peroxidase (HRP)-like and NADH peroxidase-like enzymatic activities, demonstrating sufficient electro/photo catalytic activities toward the oxidation of dopamine (DA), o-phenylenediamine (OPD), 3,3,5,5-tetramethylbenzidine (TMB), and dihydronicotinamide adenine dinucleotide (NADH) in the presence of H<sub>2</sub>O<sub>2</sub> (Fig. 7.13) (Ling et al. 2018).

Copper-plated electrodes were capable of selectively detecting the O-diphenols, such as catechol (CA), dopamine (DA), and pyrogallol (PY), in the presence of the other interfering species, including diphenol and ascorbic acid, for clinical and biochemical examination (Zen et al. 2002a). The o-diphenols have been detected amperometrically through electrochemical oxidation, of which the possible mechanism and detection signal were shown in Fig. 7.14. Zen's group also developed photoelectrocatalytic based o-diphenol sensor, its reaction mechanism and amperometric signal were shown in Fig. 7.15 (Zen et al. 2003a). Some examples for the Copper (Cu) electrode-based sensors are listed in Table 7.7.

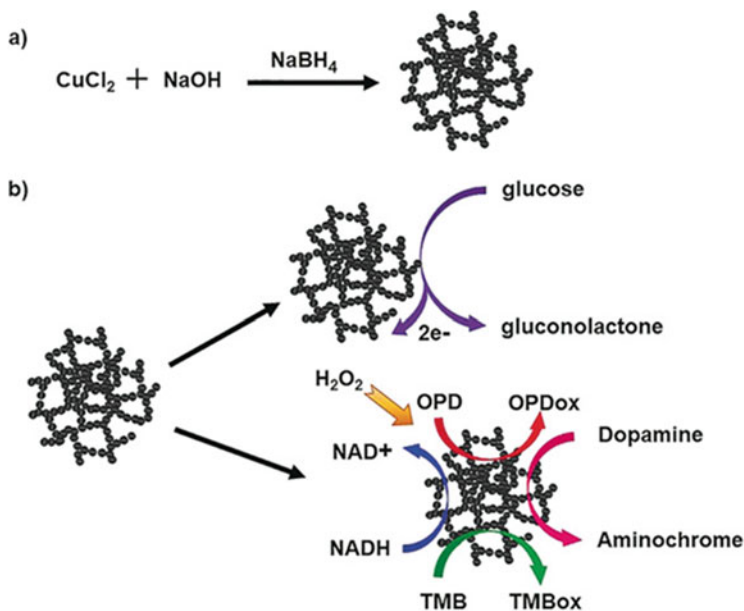


**Fig. 7.13** Illustration of (a) the preparation and (b) versatile biomimetic catalytic properties of 3D Cu@Cu<sub>2</sub>O aerogel networks. (Reproduced with permission from Ling et al. 2018)

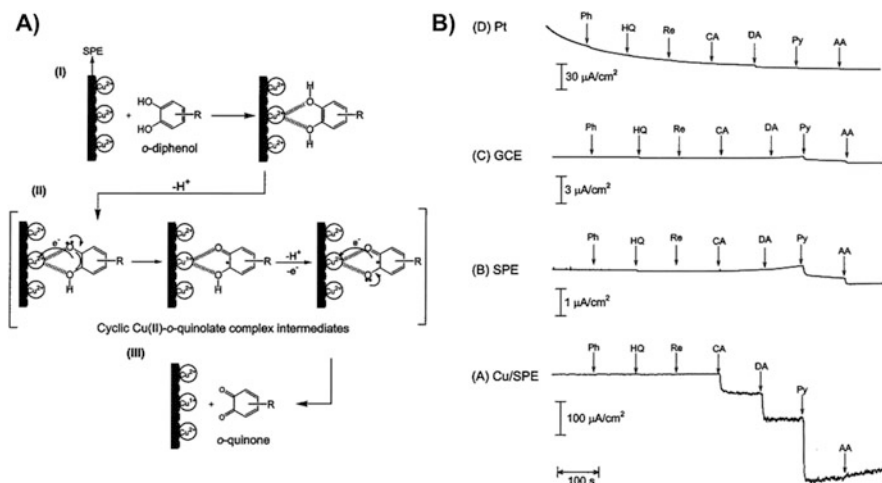


**Fig. 7.14** (a) Reaction mechanism for the selective oxidation of o-diphenol on the screen printed electrode. (b) Typical amperometric hydrodynamic response for the copper screen printed electrode (a), screen printed electrode (b), glassy carbon electrode (c), and Pt electrode (d) with a spike of 2 mM various phenolic and o-diphenol derivatives in pH 7.4 PBS at an applied potential of  $-0.05$  V (vs Ag/AgCl). (Reproduced with permission from Zen et al. 2002a)

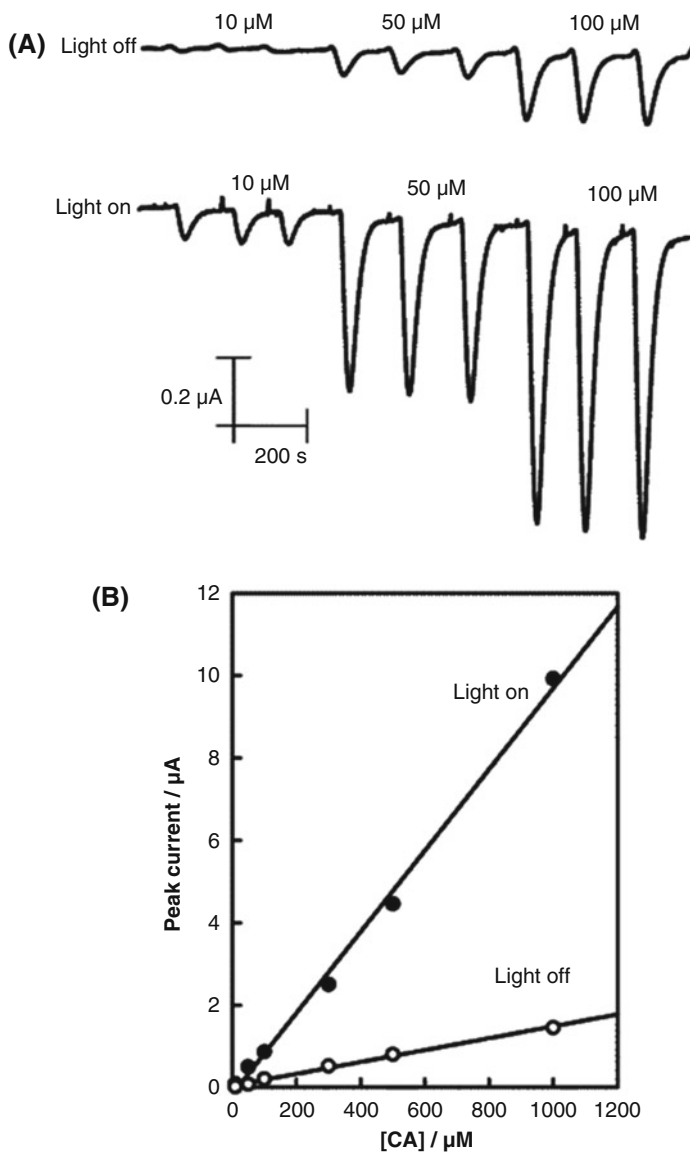


**Fig. 7.15** (a) Amperometric responses for the analyses of 10, 50, and 100 μM Catechol (CA). (b) Calibration curve for CA. Experimental conditions: flow rate 100 mL/min,  $E_p = -0.1$  V (vs Ag/AgCl), and light power 120 W. (Reproduced with permission from Zen et al. 2003a)



**Table 7.7** List of Copper (Cu) electrode-based sensors

Electrode material	Detection method	Analyte	Electrolyte	Linear range	Detection limit	References
CuNPs/NGO	Amperometry	Glucose	NaOH	1–1803 $\mu\text{M}$	0.44 $\mu\text{M}$	Sivasankar et al. (2018)
CuS/GCE	Amperometry	H <sub>2</sub> O <sub>2</sub>	pH 7.4, PBS	10–1900 $\mu\text{M}$	1.1 $\mu\text{M}$	Dutta et al. (2014)
CuO/Au	Amperometry	H <sub>2</sub> O <sub>2</sub>	pH 7.2, PBS	50–750 $\mu\text{M}$	5 $\mu\text{M}$	Gu et al. (2010)
Cu/CHIT/CNT/GC	Amperometry	H <sub>2</sub> O <sub>2</sub>	pH 7, PBS	0.05–12 mM	0.02 mM	Wang et al. (2008)
Cu/poly(melamine)-SPCE*	FIA	H <sub>2</sub> O <sub>2</sub>	pH 7, PBS	1 $\mu\text{M}$ –10 mM	0.21 $\mu\text{M}$	Baskar et al. (2013)
Cu <sup>n</sup> -SPE <sub>100-nm</sub>	FIA	Amino acids	pH 8, PBS	5–500 $\mu\text{M}$	24 nM–2.7 $\mu\text{M}$	Zen et al. (2004)
Cu@Cu <sub>2</sub> O	Amperometry	Glucose	NaOH	50 $\mu\text{M}$ to 8 mM	15 $\mu\text{M}$	Ling et al. (2018)
CuSPEs	FIA	Catechol	pH 7.4, PBS	10–200 $\mu\text{M}$	3 $\mu\text{M}$	Zen et al. (2002a)
CuSPEs	FIA	Dopamine	pH 7.4, PBS	10–300 $\mu\text{M}$	5 $\mu\text{M}$	Zen et al. (2002a)
CuSPEs	FIA	o-diphenols	pH 8, PBS	10–100 $\mu\text{M}$	0.84 $\mu\text{M}$	Zen et al. (2003a)

*CuNPs/NGO* copper nanoparticles/nitrogen doped graphene oxide, *CuS/GCE* copper sulfide modified glassy carbon electrode, *CuO/Au* copper oxide modified gold, *Cu/CHIT/CNT/GC* copper chitosan carbon nanotube modified glassy carbon electrode, *Cu/poly(melamine)-SPCE\** copper polymelamine modified preanodized screen printed carbon electrode, *Cu<sup>n</sup>-SPE<sub>100-nm</sub>* copper modified screen printed electrode, *Cu@Cu<sub>2</sub>O* copper oxide modified on copper, *CuSPEs* copper screen printed electrodes, *FIA* flow injection analysis H<sub>2</sub>O<sub>2</sub>-hydrogen peroxide, *NaOH* sodium hydroxide, *PBS* phosphate buffer solution

## 7.3 Precious/Noble Metal Electrodes (Pd, Ag, Au, Pt)

### 7.3.1 Palladium (Pd)

Palladium metal has properties similar to those of platinum (Campbell and Compton 2010). Determination of dissolved dioxygen (O<sub>2</sub>) through electrocatalytic oxygen reduction reaction at a preanodized screen-printed carbon electrode (SPCE\*) modified with Pd nanoparticles (PdNPs) was explored by Zen and his co-workers (Yang et al. 2006). They also electrochemically deposited copper–palladium alloy nanoparticle onto the screen-printed carbon electrodes (SPE/Cu–Pd) for the electrocatalytic hydrazine (NH<sub>2</sub>-NH<sub>2</sub>) sensor (Yang et al. 2005). Gupta and Prakash 2014a developed a method that took only 90 seconds to prepare uniform sized of Pd nanocubes electrochemically without using template (Gupta and Prakash 2014a). Electrochemically synthesized palladium nanocubes were used for

chronoamperometric detection of cefotaxime drug. It was also confirmed that PdNPs can be utilized as highly efficient catalyst toward the reduction of hydrogen peroxide ( $\text{H}_2\text{O}_2$ ) (Ning et al. 2017). Some examples for the Palladium (Pd) electrode-based sensors are listed in Table 7.8.

### 7.3.2 Silver (Ag)

Silver is a relatively abundant metal that is less expensive than gold and platinum. Silver oxide electrodes have been used for detection of halides in the field of biomedical, food, and environment samples. Zen's group developed a single strip three-electrode configuration using silver working, auxiliary, and reference electrodes, and that was used for simultaneous determination of halides, such as chloride, bromide, and iodide in aqueous solutions (Chiu et al. 2009). Moreover, the same group also developed a powerful tool based on Ag electrodes for the measurement of trace levels of heavy metals, such as, lead ion ( $\text{Pb}^{2+}$ ) (Zen et al. 2002b), mercury (Hg) (Chiu et al. 2008), and  $\text{H}_2\text{O}_2$  (Chiu et al. 2011). Silver metal possesses the highest electrical conductivity but is susceptible to oxidation. The stability of silver across a range of pH and potentials is outlined in Fig. 7.16.

Therefore, capping agents/stabilizing ligands were largely used to improve the stability of the AgNPs. For example,  $\text{SiO}_2$  was functionalized with two different carboxylate ligands to stabilize silver nanoparticles, and used as electrochemical sensors for non-enzymatic  $\text{H}_2\text{O}_2$  and glucose detection (Ensafi et al. 2016). Raymundo-Pereira et al. (2016) prepared nano-carbons-silver nanoparticle composites for sensitive estimation of antioxidant activity (Raymundo-Pereira et al. 2016). Silver oxides in silver-reduced graphene oxide (Ag-rGO) nanocomposites showed an electrocatalytic and electroensing activity for hydroquinone ( $\text{H}_2\text{Q}$ ) and ascorbic acid (AA) (Bhat et al. 2015). AgO was also employed for detection of cefotaxime (Gupta and Prakash 2014c) and nitrite (Gupta and Prakash 2014b). Some examples for the Silver (Ag) electrode-based sensors are listed in Table 7.9.

### 7.3.3 Gold (Au)

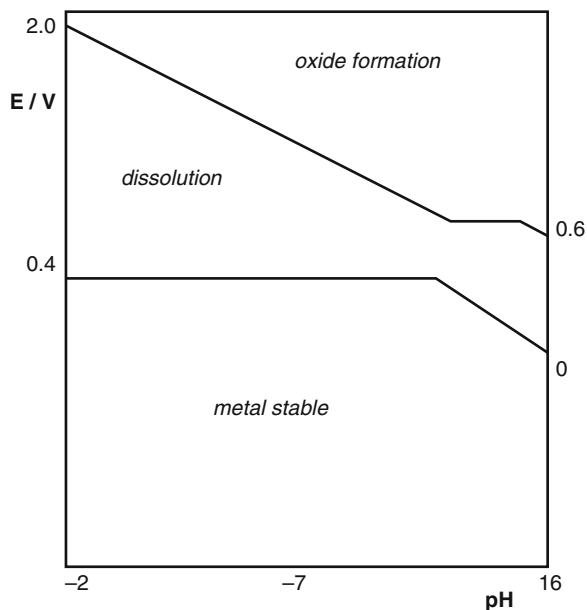
Gold is also an efficient electricity conductor and is known for its biological applications. Due to the good conductivity and chemical inertness, gold electrode becomes an attractive material in electrochemical analysis. Many publications revealed that the electrocatalytic ability of gold is dramatically increased with the decreasing particle size (Burke and Nugent 1998). Thus, AuNPs-modified electrode led to many developments in the enzyme-based biosensors, DNA sensors, and immunosensors. The flat gold electrode is one of the favorable characters to develop the immunosensor; since thiol, pyridine, and amine groups are relatively easy to be modified onto the surface of gold.

**Table 7.8** List of Palladium (Pd) electrode-based sensors

Electrode material	Detection method	Analyte	Electrolyte	Linear range	Detection limit	References
SPE*/Pd	CV	O <sub>2</sub>	pH 7.4, PBS	1–8 ppm	–	Yang et al. (2006)
SPE/Cu–Pd	FIA	Hydrazine	pH 7.4, PBS	2–100 μM	270 nM	Yang et al. (2005)
ITO/Pd nanocubes	Chronoamperometry	Cefotaxime	pH 7.2, Tris buffer	0.1–0.7 μM	0.062 μM	Gupta and Prakash (2014a)
Pd/ZnFe <sub>2</sub> O <sub>4</sub> /rGO	Amperometry	H <sub>2</sub> O <sub>2</sub>	pH 7, PBS	25 μM – 10.2 mM	2.12 μM	Ning et al. (2017)

SPE\*/Pd palladium modified preanodized screen printed carbon electrode, SPE/Cu–Pd copper–palladium alloy nanoparticle onto the screen-printed carbon electrodes, ITO indium tin oxide, Pd/ZnFe<sub>2</sub>O<sub>4</sub>/rGO palladium, zinc-iron oxide-reduced graphene oxide

**Fig. 7.16** Silver metal stability reported across a range of pH and potential values. (Reproduced with permission from Campbell and Compton 2010)



Our group utilized Au-S binding for the development of various biochemical sensors including a rapid electrochemical assay for L-dopa in urine samples (Viswanathan et al. 2007), a DNA electrochemical sensor for the detection of *Escherichia coli* O157 (Fig. 7.17) (Liao and Ho 2009), a rapid and sensitive diagnostic method for human lung cancer marker enolase 1 (ENO1) (Figs. 7.18 and 7.19) (Ho et al. 2010a), a biotin sensor (Ho et al. 2010b), a formaldehyde and glucose sensor (Tanwar et al. 2012), a Cu ion and  $\text{H}_2\text{O}_2$  sensor (Tanwar et al. 2013), a nonenzymatic detection of  $\text{H}_2\text{O}_2$  and glucose (Jou et al. 2014), and Tyramine sensor (Li et al. 2017).

To date, many commercial disposable screen-printed gold electrodes are available for electroanalysis. As a typical example, a highly toxic heavy metal ion chemical sensor, based on poly(L-lactide) stabilized gold nanoparticle (PLA-AuNP), was developed for the detection of As(III) by differential pulse anodic stripping voltammetry (Song et al. 2006).

Kesavan et al. (2012) synthesized  $\beta$ -D-Glucose capped gold nanoparticles (Glu-AuNPs) on an aminophenyl grafted GC electrode for the selective determination of norepinephrine (NEP) in the presence of uric acid (UA). The schematic representation of the interactions between NEP and Glu was shown in Fig. 7.20 (Kesavan et al. 2012). Huang's group also developed a highly sensitive detection method for copper using nanoporous gold electrode via mercury-free anodic stripping voltammetry (ASV) (Huang and Lin 2009). Some examples for the gold (Au) electrode-based sensors are listed in Table 7.10.

**Table 7.9** List of Silver (Ag) electrode-based sensors

Electrode material	Detection method	Analyte	Electrolyte	Linear range	Detection limit	References
Screen-printed silver strip	LSV	Chloride	pH 6, PBS	0.1–20 mM	18.83 $\mu$ M	Chiu et al. (2009)
Screen-printed silver strip	LSV	Bromide	pH 6, PBS	0.01–20 mM	2.95 $\mu$ M	Chiu et al. (2009)
Screen-printed silver strip	LSV	Iodide	pH 6, PBS	0.01–20 mM	3.05 $\mu$ M	Chiu et al. (2009)
AgSPE	SWV	Pb <sup>2+</sup>	pH 3, KNO <sub>3</sub> /HNO <sub>3</sub>	5–80 ppb	0.46 ppb	Zen et al. (2002b)
AgSPE	LSV	Hg	H <sub>2</sub> SO <sub>4</sub>	500–4500 ppb	98 ppb	Chiu et al. (2008)
SPAgE-Bi <sup>nano</sup>	CV	H <sub>2</sub> O <sub>2</sub>	pH 7, PBS	100 $\mu$ M–5 mM	56.59 $\mu$ M	Chiu et al. (2011)
AgNPs-Higand 1	Amperometry	H <sub>2</sub> O <sub>2</sub>	pH 7, PBS	3.6–1460 $\mu$ M	0.28 $\mu$ M	Ensafi et al. (2016)
AgNPs-Higand 2	Amperometry	H <sub>2</sub> O <sub>2</sub>	pH 7, PBS	1.0–1618 $\mu$ M	0.094 $\mu$ M	Ensafi et al. (2016)
AgNPs-Higand 1	Amperometry	Glucose	NaOH	4.28–5492 $\mu$ M	0.62 $\mu$ M	Ensafi et al. (2016)
AgNPs-Higand 2	Amperometry	Glucose	NaOH	1.43–3202 $\mu$ M	0.33 $\mu$ M	Ensafi et al. (2016)
GC/PC-Ag	DPV	Gallic acid	pH 7, PBS	0.5–8.5 $\mu$ M	63.3 nM	Raymundo-Pereira et al. (2016)
Ag/Ag <sub>2</sub> O+rGO/GCE	CV	Hydroquinone	pH 7, PBS	–	–	Bhat et al. (2015)
Ag/Ag <sub>2</sub> O+rGO/GCE	DPV	Ascorbic acid	pH 7, PBS	–	–	Bhat et al. (2015)
Ag-DTZH	Chronoamperometry	Cefotaxime	pH 7.2, Tris buffer	0.1–0.8 $\mu$ M	15.32 nM	Gupta and Prakash (2014c)
Ag-PTZH	Amperometry	Nitrite	pH 7.2, Tris buffer	5–45 nM	2.3 nM	Gupta and Prakash (2014b)

AgSPE silver screen printed electrode, SPAgE-Bimano Screen printed silver-nano bismuth electrode, AgNPs silver nanoparticles, GC glassy carbon, GCE glassy carbon electrode, Ag/Ag<sub>2</sub>O+rGO/GCE silver, silver oxide-reduced graphene oxide modified glassy carbon electrode, Ag-DTZH silver colloids dithizone (DTZ)/its oxidation products (DTZH), Ag-PTZH nanoscale silver capped with phenothiazine and its oxidation product (PTZH), CV cyclic voltammetry, LSV linear sweep voltammetry, SWV square wave voltammetry, and DPV differential pulse voltammetry

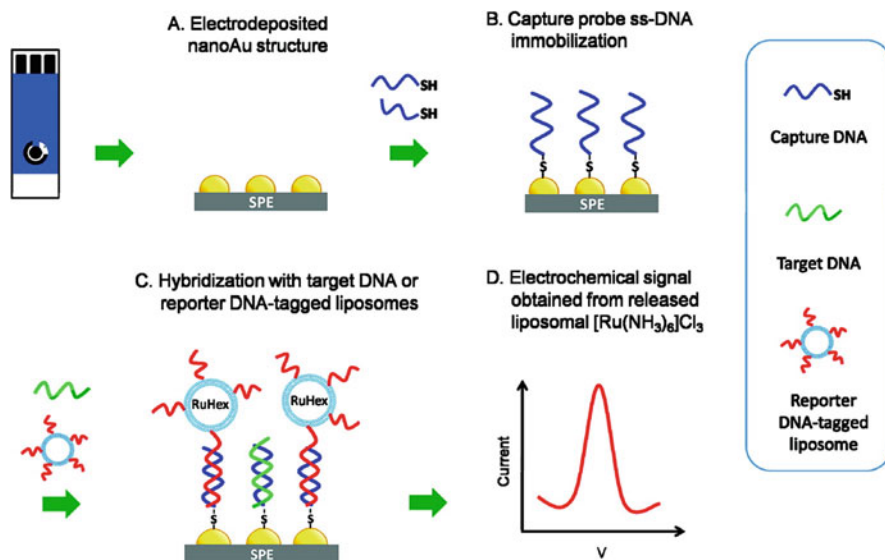


Fig. 7.17 Flow diagram displaying the concept behind the competitive assay-based performance of the developed genosensor. (Reproduced with permission from Liao and Ho 2009)

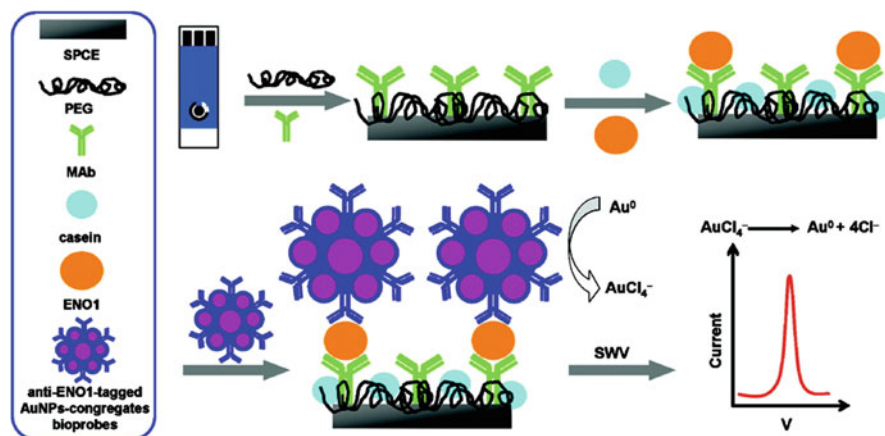
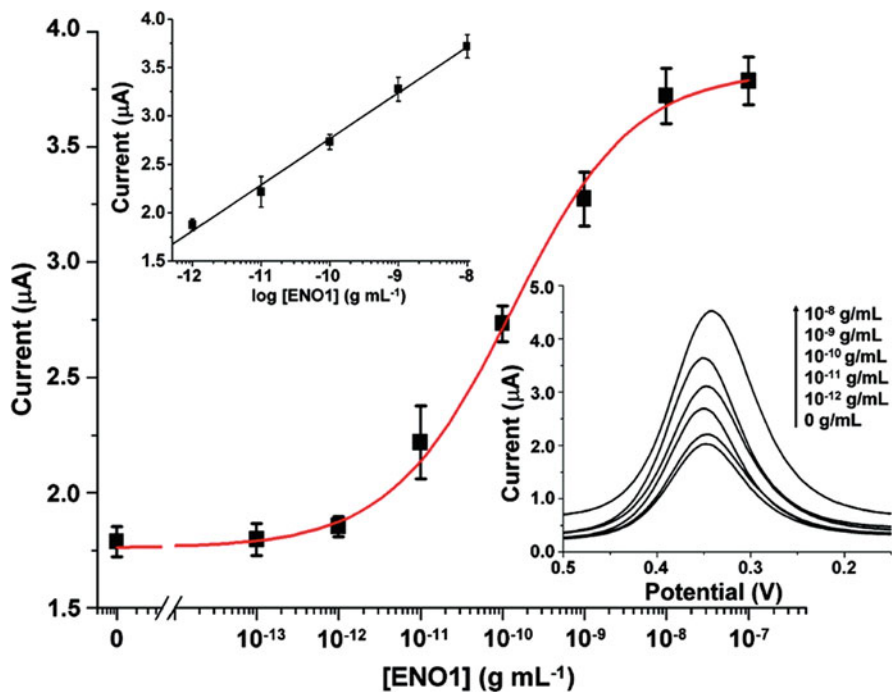


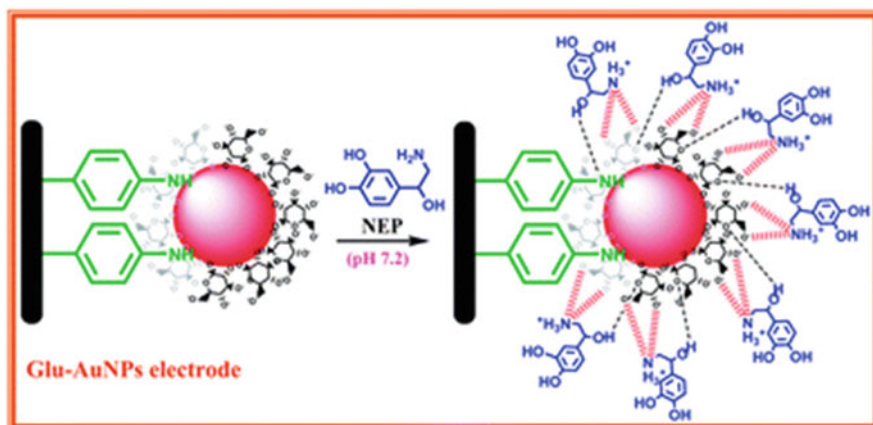
Fig. 7.18 Operation of the electrochemical immunosensor for the detection of enolase I. (Reproduced with permission from Ho et al. 2010a)

### 7.3.4 Platinum (Pt)

Platinum is more expensive than both silver and gold. Platinum wires are often employed in electroanalysis owing to their excellent stability, chemical inertness, and high conductivity (Campbell and Compton 2010). Pt electrodes have been long



**Fig. 7.19** Dose-response curve for the enolase 1 target using the PEG-modified SPCE. Insets: (lower right) Square wave voltammograms for the electrochemical detection of enolase 1 upon serial dilutions of the enolase 1 stock from  $10^{-8}$  to  $10^{-12}$  g/mL; (upper left) linear fit to the central data of main curve. (Reproduced with permission from Ho et al. 2010a)



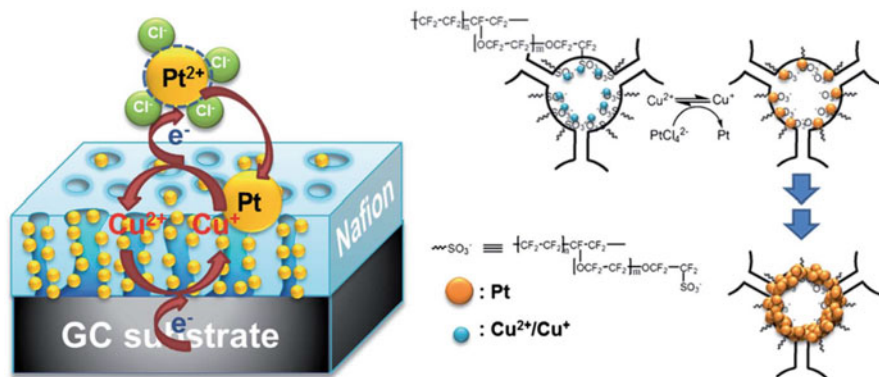
**Fig. 7.20** Interactions between norepinephrine and Glu-AuNPs electrode. (Reproduced with permission from Kesavan et al. 2012)

Table 7.10 List of gold (Au) electrode-based sensors

Electrode material	Detection method	Analyte	Electrolyte	Linear range	Detection limit	References
GNEE	FIA	L-dopa	pH 7, PBS	5–300 ng/mL	3 ng/mL	Viswanathan et al. (2007)
Nano Au/SPE	SWV	E-coli O157	Tris-HCl, pH 7.4	1–106 fM	0.75 aM	Liao and Ho (2009)
AuNP	SWV	Enolase 1	HCl	$10^{-8}$ – $10^{-12}$ g/mL	2.38 pg/mL	Ho et al. (2010a)
AuNP/SPGE	SWV	Biotin	$K_4Fe(CN)_6$ - $K_4Ru(CN)_6$	$1 \times 10^{-3}$ – $1 \times 10^{-10}$ M	$1.6 \times 10^{-10}$ M	Ho et al. (2010b)
Au-calix-PPY	LSV	Formaldehyde	NaOH	–	–	Tanwar et al. (2012)
Au-calix-PPY	LSV	Glucose	NaOH	–	–	Tanwar et al. (2012)
Au-PANI-calix	SWV	$Cu^{2+}$	pH 7.12, PBS	1 $\mu$ M–5 mM	10 nM	Tanwar et al. (2013)
Au-PANI-calix	Amperometry	$H_2O_2$	pH 7, PBS	5–50 $\mu$ M	1 $\mu$ M	Tanwar et al. (2013)
CNT@GNB	Amperometry	Glucose	NaOH	1–10 mM	0.07 mM	Jou et al. (2014)
CNT@GNB	CV	$H_2O_2$	pH 7.2, PBS	1–100 $\mu$ M	0.8 $\mu$ M	Jou et al. (2014)
SPCE/PEDOT: PSS/AuNP/1-m-4-MP	DPV	Tyramine	NaOH	5–100 nM	2.31 nM	Li et al. (2017)
PLA-AuNP/SPE	DPSV	$As^{3+}$	HCl	0–4 ppm	0.09 ppb	Song et al. (2006)
Glu-AuNPs/GCE	Amperometry	Norepinephrine	pH 7.2, PBS	30 nM–0.1 mM	0.147 nM	Kesavan et al. (2012)
Nanoporous gold	ASV	$Cu^{2+}$	$NaNO_3$	0.1–5 $\mu$ g $L^{-1}$	0.002 $\mu$ g $L^{-1}$	Huang and Lin (2009)

GNEE gold nanoelectrode ensembles, Nano Au/SPE nanogold screen printed electrode, AuNP gold nanoparticles, AuNP/SPGE gold nanoparticles screen printed graphite electrode, Au-Calix-PPY gold calix polypropylene, PANI polyaniline, CNT@GNB Gold nanobone/carbon nanotube hybrids, SPCE/PEDOT: PSS/AuNP/1-m-4-MP-PEDOT: PSS/AuNPs/1-methyl-4-mercaptopyridine modified screen-printed carbon electrode with molecularly imprinted polymer, PLA-AuNP/SPE PLA capped gold nanoparticle modified screen printed electrode, Glu-AuNPs/GCE glucose capped gold nanoparticle modified screen printed electrode, CV cyclic voltammetry, LSV linear sweep voltammetry, SWV square wave voltammetry, and DPV differential pulse voltammetry





**Fig. 7.21** Schematics of the process for  $\text{Cu}^+$  assisted formation and self-assembly of Pt nanoparticles in the micro-framework of Nafion. (Reproduced with permission from Huang 2014)

used as a working electrode in energy generation field, such as methanol oxidation, oxygen reduction, and hydrogen evolution. Jing-Fang Huang (2008) developed a simple and effective way to prepare a highly stable mesoporous platinum electrode with large surface area, the as-prepared PtNPs were utilized for developing non-enzymatic glucose sensors (Huang 2008).

A facile electrochemical followed by chemical (EC) catalytic process, involving a  $\text{Cu}^+$  mediated Pt reduction (CMPR), was developed by Huang et al. (Huang 2014). The proton conducting polymer nafion's porosity was utilized as a template for preparation of nanostructured mesoporous platinum composites for non-enzymatic determination of glucose (Fig. 7.21). Pt electrode has also used in gas sensor. Zen's group developed formaldehyde gas sensor based on platinum working electrode, screen printed edge band micro carbon electrodes were used for deposition of homogeneous PtNPs, and Nafion polymer was used as a solid electrolyte. The sensor setup was shown in Fig. 7.22. The results suggested that it is possible to monitor gaseous formaldehyde continuously down to the ppb level with the present approach (Chou et al. 2010). Some examples for the Platinum (Pt) electrode-based sensors are listed in Table 7.11.

## 7.4 Conclusion

Metals, metal oxides, and metal sulfides have been used for construction of various chemically modified electrodes for the use of developing electrochemical sensors or biosensors. With this chapter, we provide a summary on several electrochemical sensing processes with many types of analytes. All the aforementioned sensors prove the ideality and benefit of metal nanomaterials. However, designing and developing new types of metal nanoparticles (MNPs) for electrochemical-sensor applications with good stability and selectivity remains a challenge. Electrochemical application

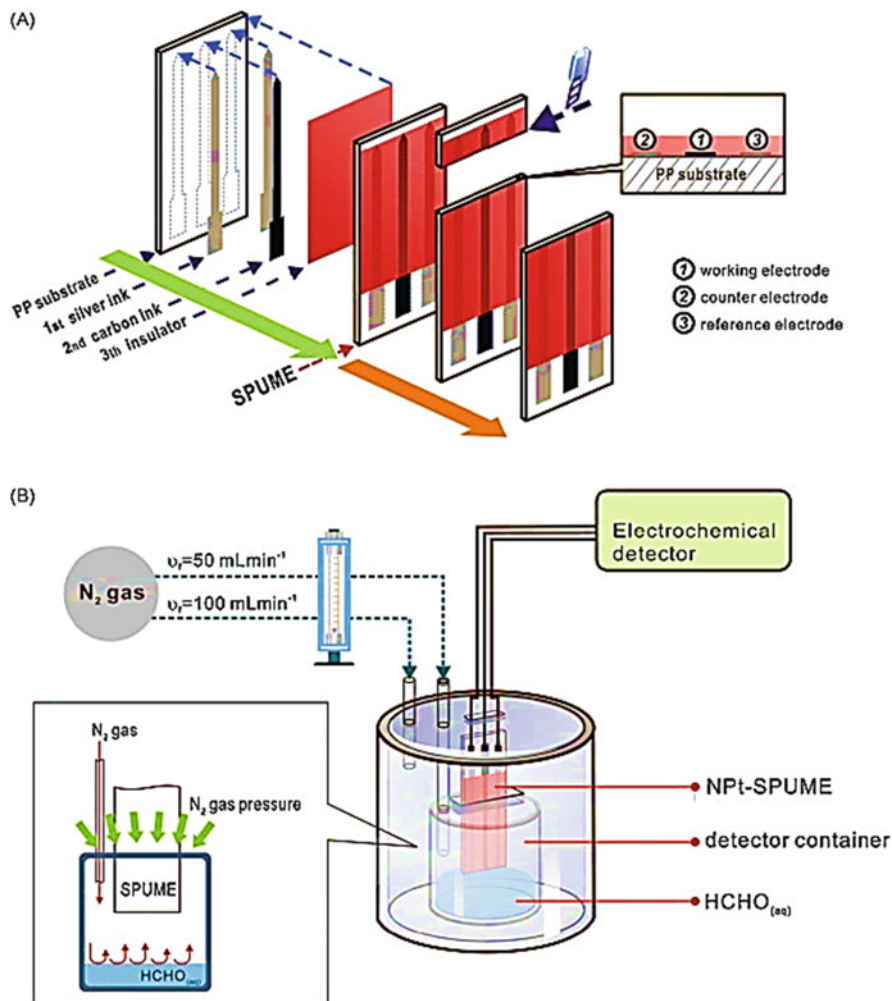


**Fig. 7.22** (a) The structure of the SPUME assembly with a built-in three-electrode configuration and (b) schematic representation of the detecting system. (Reproduced with permission from Chou et al. 2010)

**Table 7.11** List of Platinum (Pt) electrode-based sensors

Electrode material	Detection method	Analyte	Electrolyte	Linear range	Detection limit	References
PtNPs	Amperometry	Glucose	pH 7.4, PBS	0.1–1.5 mM	–	Huang (2008)
NF( $Pt_{nano}$ )/GC	Amperometry	Glucose	pH 7.4, PBS	0.1–20 mM	–	Huang (2014)
NPt-SPUME	SWV	Formaldehyde	Gas phase	0–5.1 ppm	80 ppb	Chou et al. (2010)

*PtNPs* Platinum nanoparticles, *NF( $Pt_{nano}$ )/GC* Pt–nanoparticle-embedded Nafion composites modified glassy carbon, *NPt-SPUME* platinum-deposited screen-printed edge band ultramicroelectrode, *SWV* square wave voltammetry

of metal nanomaterials in environmental and biological/biomedical monitoring are still evolving. Numerous efforts are required to design many other new MNPs, such as highly stable nanostructured copper material, metal organic frame work (MOF), or metal based covalent organic frame work, to be employed in the development of various biosensors that function efficiently at biological pH 7.4 and physiological condition. The application of these materials should enable strong driving forces for the development of more advanced electrochemical-sensor systems. At last, we must be aware that the renovation of lab sensor to an integrated self-powered portable or wearable device is in high demand, a robust chemically modified electrodes therefore become indispensable.

**Acknowledgments** The authors gratefully acknowledge financial support provided by the Taiwan Ministry of Science and Technology (MOST) under grant Nos. 98-2113-M-002-025-MY3, 101-2113-M-002-003-MY3, 102-2628-M-002-004-MY4, 106-2113-M-002-014-MY3, and 107-2811-M-002-026.

## References

- Alves AK, Berutti FA, Sánchez FAL (2011) Nanomaterials and catalysis. In: Bergmann CP, de Andrade MJ (eds) Nanostructured materials for engineering applications. Springer Berlin Heidelberg, Berlin/Heidelberg, pp 93–117. [https://doi.org/10.1007/978-3-642-19131-2\\_7](https://doi.org/10.1007/978-3-642-19131-2_7)
- Anderson DL (1989) Theory of the earth. Blackwell scientific publications
- Bai Y-H, Xu J-J, Chen H-Y (2009) Selective sensing of cysteine on manganese dioxide nanowires and chitosan modified glassy carbon electrodes. *Biosens Bioelectron* 24(10):2985–2990. <https://doi.org/10.1016/j.bios.2009.03.008>
- Barceloux DG, Barceloux D (1999a) Cobalt. *J Toxicol Clin Toxicol* 37(2):201–216. <https://doi.org/10.1081/CLT-100102420>
- Barceloux DG, Barceloux D (1999b) Vanadium. *J Toxicol Clin Toxicol* 37(2):265–278. <https://doi.org/10.1081/CLT-100102425>
- Baskar S, Chang J-L, Zen J-M (2013) Extremely stable copper–Polymelamine composite material for Amperometric hydrogen peroxide sensing. *J Polym Sci B Polym Phys* 51(22):1639–1646. <https://doi.org/10.1002/polb.23378>
- Benvidi A, Jahanbani S, Akbari A, Zare HR (2015) Simultaneous determination of hydrazine and hydroxylamine on a magnetic bar carbon paste electrode modified with reduced graphene oxide/ Fe<sub>3</sub>O<sub>4</sub> nanoparticles and a heterogeneous mediator. *J Electroanal Chem* 758:68–77. <https://doi.org/10.1016/j.jelechem.2015.10.008>
- Bharath G, Madhu R, Chen S-M, Veeramani V, Mangalaraj D, Ponpandian N (2015) Solvent-free mechanochemical synthesis of graphene oxide and Fe<sub>3</sub>O<sub>4</sub>-reduced graphene oxide nanocomposites for sensitive detection of nitrite. *J Mater Chem A* 3(30):15529–15539. <https://doi.org/10.1039/C5TA03179F>
- Bhat SA, Rather MA, Pandit SA, Ingole PP, Bhat MA (2015) Oxides in silver–graphene nanocomposites: electrochemical signatures and electrocatalytic implications. *Analyst* 140(16):5601–5608. <https://doi.org/10.1039/C5AN00740B>
- Bukhtigar SD, Shetti NP, Kulkarni RM, Halbhavi SB, Wasim M, Mylar M, Durgi PS, Chirmure SS (2016) Electrochemical oxidation of nimesulide in aqueous acid solutions based on TiO<sub>2</sub> nanostructure modified electrode as a sensor. *J Electroanal Chem* 778:103–109. <https://doi.org/10.1016/j.jelechem.2016.08.024>

- Burke LD, Nugent PF (1998) The electrochemistry of gold: II the electrocatalytic behaviour of the metal in aqueous media. *Gold Bull* 31(2):39–50. <https://doi.org/10.1007/bf03214760>
- Campbell FW, Compton RG (2010) The use of nanoparticles in electroanalysis: an updated review. *Anal Bioanal Chem* 396(1):241–259. <https://doi.org/10.1007/s00216-009-3063-7>
- Chen Z, De Marco R, Alexander PW (1997) Flow-injection potentiometric detection of phosphates using a metallic cobalt wire ion-selective electrode. *Anal Commun* 34(3):93–95. <https://doi.org/10.1039/A700771J>
- Cheng W-L, Sue J-W, Chen W-C, Chang J-L, Zen J-M (2010) Activated nickel platform for electrochemical sensing of phosphate. *Anal Chem* 82(3):1157–1161. <https://doi.org/10.1021/ac9025253>
- Chinnasamy R, Mohan Rao G, Rajendra Kumar RT (2015) Synthesis and electrocatalytic properties of manganese dioxide for non-enzymatic hydrogen peroxide sensing. *Mater Sci Semicond Process* 31:709–714. <https://doi.org/10.1016/j.mssp.2014.12.054>
- Chiu M-H, Zen J-M, Kumar AS, Vasu D, Shih Y (2008) Selective cosmetic mercury analysis using a silver ink screen-printed electrode with potassium iodide solution. *Electroanalysis* 20(20):2265–2270. <https://doi.org/10.1002/elan.200804307>
- Chiu M-H, Cheng W-L, Muthuraman G, Hsu C-T, Chung H-H, Zen J-M (2009) A disposable screen-printed silver strip sensor for single drop analysis of halide in biological samples. *Biosens Bioelectron* 24(10):3008–3013. <https://doi.org/10.1016/j.bios.2009.03.004>
- Chiu M-H, Kumar AS, Somambikai S, Chen P-Y, Shih Y, Zen J-M (2011) Cosmetic hydrogen peroxide detection using nano bismuth species deposited built-in three-in-one screen-printed silver electrode. *Int J Electrochem Sci* 6(7):2352–2365
- Chou C-H, Chang J-L, Zen J-M (2010) Effective analysis of gaseous formaldehyde based on a platinum-deposited screen-printed edge band ultramicroelectrode coated with Nafion as solid polymer electrolyte. *Sens Actuators B Chem* 147(2):669–675. <https://doi.org/10.1016/j.snb.2010.03.090>
- Comba FN, Rubianes MD, Herrasti P, Rivas GA (2010) Glucose biosensing at carbon paste electrodes containing iron nanoparticles. *Sens Actuators B Chem* 149(1):306–309. <https://doi.org/10.1016/j.snb.2010.06.020>
- Devi S, Tharmaraj V (2019) Nanomaterials for advanced analytical applications in chemo- and biosensors. In: Naushad M, Rajendran S, Gracia F (eds) *Advanced nanostructured materials for environmental remediation*. Springer, Cham, pp 91–110. [https://doi.org/10.1007/978-3-030-04477-0\\_4](https://doi.org/10.1007/978-3-030-04477-0_4)
- Dong X-C, Xu H, Wang X-W, Huang Y-X, Chan-Park MB, Zhang H, Wang L-H, Huang W, Chen P (2012) 3D graphene–cobalt oxide electrode for high-performance supercapacitor and Enzymeless glucose detection. *ACS Nano* 6(4):3206–3213. <https://doi.org/10.1021/nn300097q>
- Dontsova EA, Budashov IA, Eremenko AV, Kurochkin IN (2008) Hydrogen peroxide-sensitive amperometric sensor based on manganese dioxide nanoparticles. *Nanotechnol Russ* 3(7):510–520. <https://doi.org/10.1134/s199507800807015x>
- Dutta AK, Das S, Samanta PK, Roy S, Adhikary B, Biswas P (2014) Non-enzymatic amperometric sensing of hydrogen peroxide at a CuS modified electrode for the determination of urine H<sub>2</sub>O<sub>2</sub>. *Electrochim Acta* 144:282–287. <https://doi.org/10.1016/j.electacta.2014.08.051>
- Ensafi AA, Zandi-Atashbar N, Rezaei B, Ghiaci M, Taghizadeh M (2016) Silver nanoparticles decorated carboxylate functionalized SiO<sub>2</sub>, new nanocomposites for non-enzymatic detection of glucose and hydrogen peroxide. *Electrochim Acta* 214:208–216. <https://doi.org/10.1016/j.electacta.2016.08.047>
- Eremenko AV, Dontsova EA, Nazarov AP, Evtushenko EG, Amitonov SV, Savilov SV, Martynova LF, Lunin VV, Kurochkin IN (2012) Manganese dioxide nanostructures as a novel electrochemical mediator for thiol sensors. *Electroanalysis* 24(3):573–580. <https://doi.org/10.1002/elan.201100535>
- Gates BC (1993) Metal oxide and metal sulfide catalysts. *Inorg React Methods*. <https://doi.org/10.1002/9780470145319.ch15>

- George JM, Antony A, Mathew B (2018) Metal oxide nanoparticles in electrochemical sensing and biosensing: a review. *Microchim Acta* 185(7):358. <https://doi.org/10.1007/s00604-018-2894-3>
- Gooding JJ (2008) Advances in interfacial design for electrochemical biosensors and sensors: aryl Diazonium salts for modifying carbon and metal electrodes. *Electroanalysis* 20(6):573–582. <https://doi.org/10.1002/elan.200704124>
- Gu A, Wang G, Zhang X, Fang B (2010) Synthesis of CuO nanoflower and its application as a H<sub>2</sub>O<sub>2</sub> sensor. *Bull Mater Sci* 33(1):17–20. <https://doi.org/10.1007/s12034-010-0002-3>
- Gupta S, Prakash R (2014a) Ninety second Electrosynthesis of palladium Nanocubes on ITO surface and its application in Electroensing of cefotaxime. *Electroanalysis* 26 (11):2337–2341. <https://doi.org/10.1002/elan.201400200>
- Gupta S, Prakash R (2014b) Photochemical assisted formation of silver nano dendrites and their application in amperometric sensing of nitrite. *RSC Adv* 4(15):7521–7527. <https://doi.org/10.1039/C3RA45360J>
- Gupta S, Prakash R (2014c) Photochemically assisted formation of silver nanoparticles by dithizone, and its application in amperometric sensing of cefotaxime. *J Mater Chem C* 2 (33):6859–6866. <https://doi.org/10.1039/C4TC01090F>
- Hasanzadeh M, Shadjou N, de la Guardia M (2015) Iron and iron-oxide magnetic nanoparticles as signal-amplification elements in electrochemical biosensing. *TrAC Trends Anal Chem* 72:1–9. <https://doi.org/10.1016/j.trac.2015.03.016>
- Ho J-A, Chang H-C, Shih N-Y, Wu L-C, Chang Y-F, Chen C-C, Chou C (2010a) Diagnostic detection of human lung Cancer-associated antigen using a gold nanoparticle-based electrochemical Immunosensor. *Anal Chem* 82(14):5944–5950. <https://doi.org/10.1021/ac1001959>
- Ho J-A, Hsu W-L, Liao W-C, Chiu J-K, Chen M-L, Chang H-C, Li C-C (2010b) Ultrasensitive electrochemical detection of biotin using electrically addressable site-oriented antibody immobilization approach via aminophenyl boronic acid. *Biosens Bioelectron* 26(3):1021–1027. <https://doi.org/10.1016/j.bios.2010.08.048>
- Huang J-F (2008) 3-D Nanoporous Pt electrode prepared by a 2-D UPD monolayer process. *Electroanalysis* 20(20):2229–2234. <https://doi.org/10.1002/elan.200804306>
- Huang J-F (2014) Cu<sup>+</sup> assisted preparation of mesoporous Pt-organic composites for highly selective and sensitive non-enzymatic glucose sensing. *J Mater Chem B* 2(10):1354–1361. <https://doi.org/10.1039/C3TB21688H>
- Huang J-F, Lin B-T (2009) Application of a nanoporous gold electrode for the sensitive detection of copper/mercury-free anodic stripping voltammetry. *Analyst* 134(11):2306–2313. <https://doi.org/10.1039/B910282E>
- Huang K-J, Liu Y-J, Shi G-W, Yang X-R, Liu Y-M (2014) Label-free aptamer sensor for 17-β-estradiol based on vanadium disulfide nanoflowers and Au nanoparticles. *Sens. Actuators. B Chem* 201:579–585. <https://doi.org/10.1016/j.snb.2014.05.055>
- Hwang SW, Umar A, Dar GN, Kim SH, Badran RI (2014) Synthesis and characterization of Iron oxide nanoparticles for phenyl hydrazine sensor applications. *Sens Lett* 12(1):97–101. <https://doi.org/10.1166/sl.2014.3224>
- Jou AF-J, Tai N-H, Ho J-aA (2014) Gold Nanobone/carbon nanotube hybrids for the efficient nonenzymatic detection of H<sub>2</sub>O<sub>2</sub> and glucose. *Electroanalysis* 26(8):1816–1823. <https://doi.org/10.1002/elan.201400140>
- Kang Q, Yang L, Cai Q (2008) An electro-catalytic biosensor fabricated with Pt–Au nanoparticle-decorated titania nanotube array. *Bioelectrochemistry* 74(1):62–65. <https://doi.org/10.1016/j.bioelechem.2008.06.004>
- Kesavan S, Revin SB, John SA (2012) Fabrication, characterization and application of a grafting based gold nanoparticles electrode for the selective determination of an important neurotransmitter. *J Mater Chem* 22(34):17560–17567. <https://doi.org/10.1039/C2JM33013J>
- Khorshed AA, Khairy M, Elsafty SA, Banks CE (2019) Disposable screen-printed electrodes modified with uniform iron oxide nanocubes for the simple electrochemical determination of meclizine, an antihistamine drug. *Anal Methods* 11(3):282–287. <https://doi.org/10.1039/C8AY02405G>

- Kubota LT, Gouvea F, Andrade AN, Milagres BG, De Oliveira Neto G (1996) Electrochemical sensor for NADH based on Meldola's blue immobilized on silica gel modified with titanium phosphate. *Electrochim Acta* 41(9):1465–1469. [https://doi.org/10.1016/0013-4686\(95\)00395-9](https://doi.org/10.1016/0013-4686(95)00395-9)
- Lane RF, Hubbard AT (1973) Electrochemistry of chemisorbed molecules. I. Reactants connected to electrodes through olefinic substituents. *J Phys Chem* 77(11):1401–1410. <https://doi.org/10.1021/j100630a018>
- Lee C, Yan H, Brus LE, Heinz TF, Hone J, Ryu S (2010) Anomalous lattice vibrations of single- and few-layer MoS<sub>2</sub>. *ACS Nano* 4(5):2695–2700. <https://doi.org/10.1021/nn1003937>
- Lewis EA, Tolman WB (2004) Reactivity of dioxygen–copper systems. *Chem Rev* 104(2):1047–1076. <https://doi.org/10.1021/cr020633r>
- Li X, Shen J, Li N, Ye M (2015) Fabrication of  $\gamma$ -MnS/rGO composite by facile one-pot solvothermal approach for supercapacitor applications. *J Power Sources* 282:194–201. <https://doi.org/10.1016/j.jpowsour.2015.02.057>
- Li Y, Hsieh C-H, Lai C-W, Chang Y-F, Chan H-Y, Tsai C-F, Ho J-aA, L-c W (2017) Tyramine detection using PEDOT:PSS/AuNPs/1-methyl-4-mercaptopyridine modified screen-printed carbon electrode with molecularly imprinted polymer solid phase extraction. *Biosens Bioelectron* 87:142–149. <https://doi.org/10.1016/j.bios.2016.08.006>
- Liao W-C, Ho J-aA (2009) Attomole DNA electrochemical sensor for the detection of Escherichia coli O157. *Anal Chem* 81(7):2470–2476. <https://doi.org/10.1021/ac8020517>
- Ling P, Zhang Q, Cao T, Gao F (2018) Versatile three-dimensional porous Cu@Cu<sub>2</sub>O aerogel networks as Electrocatalysts and mimicking peroxidases. *Angew Chem* 130(23):6935–6940. <https://doi.org/10.1002/ange.201801369>
- Mani V, Govindasamy M, Chen S-M, Karthik R, Huang S-T (2016) Determination of dopamine using a glassy carbon electrode modified with a graphene and carbon nanotube hybrid decorated with molybdenum disulfide flowers. *Microchim Acta* 183(7):2267–2275. <https://doi.org/10.1007/s00604-016-1864-x>
- Mehta S, Singh K, Umar A, Chaudhary G, Singh S (2011) Well-crystalline  $\alpha$ -Fe<sub>2</sub>O<sub>3</sub> nanoparticles for hydrazine chemical sensor application. *Sci Adv Mater* 3(6):962–967. <https://doi.org/10.1166/sam.2011.1244>
- Murray RW (1980) Chemically modified electrodes. *Acc Chem Res* 13(5):135–141. <https://doi.org/10.1021/ar50149a002>
- Ning L, Liu Y, Ma J, Fan X, Zhang G, Zhang F, Peng W, Li Y (2017) Synthesis of palladium, ZnFe<sub>2</sub>O<sub>4</sub> functionalized reduced graphene oxide nanocomposites as H<sub>2</sub>O<sub>2</sub> detector. *Ind Eng Chem Res* 56(15):4327–4333. <https://doi.org/10.1021/acs.iecr.6b04964>
- Ou X, Fang C, Fan Y, Chen H, Chen S, Wei S (2016) Sandwich-configuration electrochemiluminescence biosensor based on ag nanocubes–polyamidoamine dendrimer–luminol nanocomposite for on a detection. *Sens Actuators B Chem* 228:625–633. <https://doi.org/10.1016/j.snb.2016.01.083>
- Privman M, Hepel T (1995) Electrochemistry of vanadium electrodes part 1. Cyclic voltammetry in aqueous solutions. *J Electroanal Chem* 382(1):137–144. [https://doi.org/10.1016/0022-0728\(94\)03633-E](https://doi.org/10.1016/0022-0728(94)03633-E)
- Raymundo-Pereira PA, Campos AM, Prado TM, Furini LN, Boas NV, Calegari ML, Machado SAS (2016) Synergy between Printex nano-carbons and silver nanoparticles for sensitive estimation of antioxidant activity. *Anal Chim Acta* 926:88–98. <https://doi.org/10.1016/j.aca.2016.04.036>
- Revathi C, Kumar RTR (2017) Electro catalytic properties of  $\alpha$ ,  $\beta$ ,  $\gamma$ ,  $\epsilon$  – MnO<sub>2</sub> and  $\gamma$  – MnOOH nanoparticles: role of polymorphs on enzyme free H<sub>2</sub>O<sub>2</sub> sensing. *Electroanalysis* 29(5):1481–1489. <https://doi.org/10.1002/elan.201600608>
- Salimi A, Hallaj R, Soltanian S, Mamkhezri H (2007) Nanomolar detection of hydrogen peroxide on glassy carbon electrode modified with electrodeposited cobalt oxide nanoparticles. *Anal Chim Acta* 594(1):24–31. <https://doi.org/10.1016/j.aca.2007.05.010>

- Sivasankar K, Rani KK, Wang S-F, Devasenathipathy R, Lin C-H (2018) Copper nanoparticle and nitrogen doped graphite oxide based biosensor for the sensitive determination of glucose. *Nano* 8(6):429. <https://doi.org/10.3390/nano8060429>
- Šljukić B, Banks CE, Compton RG (2006) Iron oxide particles are the active sites for hydrogen peroxide sensing at multiwalled carbon nanotube modified electrodes. *Nano Lett* 6(7):1556–1558. <https://doi.org/10.1021/nl060366v>
- Šljukić BR, Kadara RO, Banks CE (2011) Disposable manganese oxide screen printed electrodes for electroanalytical sensing. *Anal Methods* 3(1):105–109. <https://doi.org/10.1039/C0AY00444H>
- Song Y-S, Muthuraman G, Chen Y-Z, Lin C-C, Zen J-M (2006) Screen printed carbon electrode modified with poly(L-Lactide) stabilized gold nanoparticles for sensitive as(III) detection. *Electroanalysis* 18(18):1763–1770. <https://doi.org/10.1002/elan.200603634>
- Sue J-W, Tai C-Y, Cheng W-L, Zen J-M (2008) Disposable barrel plating nickel electrodes for use in flow injection analysis of trivalent chromium. *Electrochem Commun* 10(2):277–282. <https://doi.org/10.1016/j.elecom.2007.12.008>
- Sun Z, Yuan H, Liu Z, Han B, Zhang X (2005) A highly efficient chemical sensor material for H<sub>2</sub>S:  $\alpha$ -Fe<sub>2</sub>O<sub>3</sub> nanotubes fabricated using carbon nanotube templates. *Adv Mater* 17(24):2993–2997. <https://doi.org/10.1002/adma.200501562>
- Tanwar S, Chuang M-C, Prasad KS, Ho J-aA (2012) Template-free synthesis of an electroactive aulcalix-PPY nanocomposite for electrochemical sensor applications. *Green Chem* 14(3):799–808. <https://doi.org/10.1039/C2GC16232F>
- Tanwar S, J-a AH, Magi E (2013) Green synthesis and characterization of novel gold nanocomposites for electrochemical sensing applications. *Talanta* 117:352–358. <https://doi.org/10.1016/j.talanta.2013.09.011>
- Thiruppathi M, Thiyagarajan N, Gopinathan M, Zen J-M (2016) Role of defect sites and oxygen functionalities on preanodized screen printed carbon electrode for adsorption and oxidation of polyaromatic hydrocarbons. *Electrochem Commun* 69:15–18. <https://doi.org/10.1016/j.elecom.2016.05.015>
- Thiruppathi M, Thiyagarajan N, Gopinathan M, Chang J-L, Zen J-M (2017) A dually functional 4-aminophenylboronic acid dimer for voltammetric detection of hypochlorite, glucose and fructose. *Microchim Acta* 184(10):4073–4080. <https://doi.org/10.1007/s00604-017-2440-8>
- Thiruppathi M, Lin P-Y, Chou Y-T, Ho H-Y, L-c W, Ho J-aA (2019) Simple aminophenol-based electrochemical probes for non-enzymatic, dual amperometric detection of NADH and hydrogen peroxide. *Talanta* 200:450–457. <https://doi.org/10.1016/j.talanta.2019.03.083>
- Thiyagarajan N, Chang J-L, Senthilkumar K, Zen J-M (2014) Disposable electrochemical sensors: a mini review. *Electrochem Commun* 38:86–90. <https://doi.org/10.1016/j.elecom.2013.11.016>
- Tian L, Chen L, Liu L, Lu N, Song W, Xu H (2006) Electrochemical determination of ascorbic acid in fruits on a vanadium oxide polypropylene carbonate modified electrode. *Sens. Actuators. B Chem* 113(1):150–155. <https://doi.org/10.1016/j.snb.2005.02.041>
- Tsiafoulis CG, Trikalitis PN, Prodromidis MI (2005) Synthesis, characterization and performance of vanadium hexacyanoferrate as electrocatalyst of H<sub>2</sub>O<sub>2</sub>. *Electrochem Commun* 7(12):1398–1404. <https://doi.org/10.1016/j.elecom.2005.10.001>
- Urbanova V, Magro M, Gedanken A, Baratella D, Vianello F, Zboril R (2014) Nanocrystalline Iron oxides, composites, and related materials as a platform for electrochemical, magnetic, and chemical biosensors. *Chem Mater* 26(23):6653–6673. <https://doi.org/10.1021/cm500364x>
- Velmurugan R, Incharoensakdi A (2018) Chapter 18 – Nanoparticles and organic matter: process and impact. In: Tripathi DK, Ahmad P, Sharma S, Chauhan DK, Dubey NK (eds) *Nanomaterials in plants, algae, and microorganisms*. Academic Press, pp 407–428. <https://doi.org/10.1016/B978-0-12-811487-2.00018-9>
- Vilian ATE, Dinesh B, Kang S-M, Krishnan UM, Huh YS, Han Y-K (2019) Recent advances in molybdenum disulfide-based electrode materials for electroanalytical applications. *Microchim Acta* 186(3):203. <https://doi.org/10.1007/s00604-019-3287-y>
- Viswanathan S, Liao W-C, Huang C-C, Hsu W-L, Ho J-aA (2007) Rapid analysis of l-dopa in urine samples using gold nanoelectrode ensembles. *Talanta* 74(2):229–234. <https://doi.org/10.1016/j.talanta.2007.05.056>

- Wang Y, Wei W, Zeng J, Liu X, Zeng X (2008) Fabrication of a copper nanoparticle/chitosan/carbon nanotube-modified glassy carbon electrode for electrochemical sensing of hydrogen peroxide and glucose. *Microchim Acta* 160(1):253–260. <https://doi.org/10.1007/s00604-007-0844-6>
- Wang X, Dong X, Wen Y, Li C, Xiong Q, Chen P (2012) A graphene–cobalt oxide based needle electrode for non-enzymatic glucose detection in micro-droplets. *Chem Commun* 48(52):6490–6492. <https://doi.org/10.1039/C2CC32674D>
- Wang L, Deng M, Ding G, Chen S, Xu F (2013) Manganese dioxide based ternary nanocomposite for catalytic reduction and nonenzymatic sensing of hydrogen peroxide. *Electrochim Acta* 114:416–423. <https://doi.org/10.1016/j.electacta.2013.10.074>
- Xia C, Ning W, Lin G (2009) Facile synthesis of novel MnO<sub>2</sub> hierarchical nanostructures and their application to nitrite sensing. *Sens Actuators B Chem* 137(2):710–714. <https://doi.org/10.1016/j.snb.2008.11.023>
- Xia C, Yanjun X, Ning W (2012) Hollow Fe<sub>2</sub>O<sub>3</sub> polyhedrons: one-pot synthesis and their use as electrochemical material for nitrite sensing. *Electrochim Acta* 59:81–85. <https://doi.org/10.1016/j.electacta.2011.10.039>
- Xiao C, Chen J, Liu B, Chu X, Wu L, Yao S (2011) Sensitive and selective electrochemical sensing of l-cysteine based on a caterpillar-like manganese dioxide–carbon nanocomposite. *PCCP* 13(4):1568–1574. <https://doi.org/10.1039/C0CP00980F>
- Yang C-C, Kumar AS, Kuo M-C, Chien S-H, Zen J-M (2005) Copper–palladium alloy nanoparticle plated electrodes for the electrocatalytic determination of hydrazine. *Anal Chim Acta* 554(1):66–73. <https://doi.org/10.1016/j.aca.2005.08.027>
- Yang C-C, Kumar AS, Zen J-M (2006) Electrocatalytic reduction and determination of dissolved oxygen at a Preanodized screen-printed carbon electrode modified with palladium nanoparticles. *Electroanalysis* 18(1):64–69. <https://doi.org/10.1002/elan.200503374>
- Yi Q, Yu W (2009) Nanoporous gold particles modified titanium electrode for hydrazine oxidation. *J Electroanal Chem* 633(1):159–164. <https://doi.org/10.1016/j.jelechem.2009.05.008>
- Yi Q, Li L, Yu W, Zhou Z, Xu G (2008) A novel titanium-supported ag/Ti electrode for the electro-oxidation of hydrazine. *J Mol Catal A Chem* 295(1):34–38. <https://doi.org/10.1016/j.molcata.2008.08.013>
- Yuan B, Xu C, Deng D, Xing Y, Liu L, Pang H, Zhang D (2013) Graphene oxide/nickel oxide modified glassy carbon electrode for supercapacitor and nonenzymatic glucose sensor. *Electrochim Acta* 88:708–712. <https://doi.org/10.1016/j.electacta.2012.10.102>
- Zen J-M, Chung H-H, Kumar AS (2002a) Selective detection of o-Diphenols on copper-plated screen-printed electrodes. *Anal Chem* 74(5):1202–1206. <https://doi.org/10.1021/ac0110121>
- Zen J-M, Yang C-C, Kumar AS (2002b) Voltammetric behavior and trace determination of Pb<sup>2+</sup> at a mercury-free screen-printed silver electrode. *Anal Chim Acta* 464(2):229–235. [https://doi.org/10.1016/S0003-2670\(02\)00472-5](https://doi.org/10.1016/S0003-2670(02)00472-5)
- Zen J-M, Chung H-H, Yang H-H, Chiu M-H, Sue J-W (2003a) Photoelectrocatalytic oxidation of o-phenols on copper-plated screen-printed electrodes. *Anal Chem* 75(24):7020–7025. <https://doi.org/10.1021/ac030183i>
- Zen J-M, Senthil Kumar A, Tsai D-M (2003b) Recent updates of chemically modified electrodes in analytical chemistry. *Electroanalysis* 15(13):1073–1087. <https://doi.org/10.1002/elan.200390130>
- Zen J-M, Hsu C-T, Senthil Kumar A, Lyuu H-J, Lin K-Y (2004) Amino acid analysis using disposable copper nanoparticle plated electrodes. *Analyst* 129(9):841–845. <https://doi.org/10.1039/B401573H>
- Zhang N, Yi R, Wang Z, Shi R, Wang H, Qiu G, Liu X (2008) Hydrothermal synthesis and electrochemical properties of alpha-manganese sulfide submicrocrystals as an attractive electrode material for lithium-ion batteries. *Mater Chem Phys* 111(1):13–16. <https://doi.org/10.1016/j.matchemphys.2008.03.040>
- Zhang P, Guo D, Li Q (2014) Manganese oxide ultrathin nanosheets sensors for non-enzymatic detection of H<sub>2</sub>O<sub>2</sub>. *Mater Lett* 125:202–205. <https://doi.org/10.1016/j.matlet.2014.03.172>



# Chapter 8

## Developing Trends in DNA Biosensor and Their Applications



Chandrasekar Selvaraj, Srinivas B.T.V, and Hai Xiong

### Contents

8.1	Introduction .....	246
8.2	DNA Biosensor Construction .....	247
8.2.1	Colorimetric and Fluorescent Nucleic Acids .....	247
8.2.2	The Label-Free Luminescent Probes .....	253
8.3	Biosensor Applications in Detection of Metal Ion .....	255
8.3.1	Functional Nucleic Acids as Recognition Probes .....	255
8.3.2	Aptamer-Assembled Nanomaterials for Biosensing .....	264
8.4	Biosensor Applications in Detection of Biomolecules and Cellular Bioimaging .....	271
8.4.1	Detection of DNA or RNA .....	271
8.4.2	Detection of Protein or Enzyme .....	272
8.4.3	Immunosensors .....	273
8.4.4	Detection in Cancer Diagnosis and Therapy .....	275
8.5	Conclusions .....	275
	References .....	276

**Abstract** DNA-based biosensor strategy has been pursued due to their mounting applications in the fields of bio-analysis, clinical diagnosis, and forensic sciences. DNA's chemical structure is well suitable for sensing metals and bio-molecules through the backbone of phosphate and nucleobases. Numerous secondary structures like G-quadruplexes, *i*-motifs, triplexes, DNazymes, and aptamers were prepared or/and used for target detection, and their signal transduction mechanisms such as colorimetry, fluorescence, and electrochemical methods were studied. The major challenge associated with the DNA biosensors is to construct the conjugated structures manageable small in order to prevent the perturbation of the DNA.

---

Chandrasekar Selvaraj and Srinivas B. T. V. contributed equally with all other contributors.

---

C. Selvaraj · S. B.T.V · H. Xiong (✉)  
Institute for Advanced Study, Shenzhen University, Shenzhen, China  
e-mail: [hai.xiong@szu.edu.cn](mailto:hai.xiong@szu.edu.cn)

© The Editor(s) (if applicable) and The Author(s), under exclusive licence to Springer Nature Switzerland AG 2021

245

S. Rajendran et al. (eds.), *Metal, Metal-Oxides and Metal Sulfides for Batteries, Fuel Cells, Solar Cells, Photocatalysis and Health Sensors*, Environmental Chemistry for a Sustainable World 62, [https://doi.org/10.1007/978-3-030-63791-0\\_8](https://doi.org/10.1007/978-3-030-63791-0_8)

Additionally, pure synthetic methods are simple to produce short DNAs and RNAs, which restrict their application in the synthesis of larger DNAs and RNAs.

The natural nucleic acids are generally non-fluorescent. Studies employing the manipulation of natural nucleic acids to produce fluorescent analogues have demonstrated that even a subtle change in their structure is ample enough to promote their use as prominent tools in biosensors. We reviewed various modifications of purine and pyrimidine scaffolds, sugar moieties, and phosphate backbone in a precise manner in the early sections. For metal sensing, two primary classes of functional DNAs have been developed: aptamers and DNazymes. Some metal-binding aptamers are well studied because of their unique 3-dimensional structure, which makes them to selectively recognize a target or a family of targets. On the other side, DNazymes were chosen based on their strong metal sensitivity and catalytic activity. More recently, a lot of *in vitro* studies have been emerging in this direction to frame the best DNA sensors. This chapter is not aimed to be comprehensive, but rather focuses precisely on the various trends in DNA biosensors, and their applications in detection of various biomolecules and clinical diagnosis.

**Keywords** DNA biosensor · G-quadruplex · Aptamers · DNazymes

## 8.1 Introduction

Biosensors built with nucleic acids are powerful analytical devices that convert a biological response into an electrical signal. Different biosensors have been developed for detecting various metal ions, deoxyribonucleic acids, proteins, cells, and small molecules. Apart from these, biosensors play a critical role in many fields like environmental monitoring, food control, disease progression, forensics, drug discovery, and biomedical research. In 1962, Clark and Lyons invented the first biosensor to measure glucose level in biological samples utilized for the electrochemical detection of hydrogen peroxide or oxygen (Clark and Lyons 1962). Biosensors of nucleic acid are of great interest due to their wide range of chemical, physical, biological properties, and their ability to obtain the specific-sequence information in a faster way. Nucleic acids are extensively modified by replacing the existing base, phosphodiester, and sugar groups with cationic, anionic, and neutral structures. So, in this chapter, we present many of these modified oligonucleotides that exhibit enhanced properties including faster recognition and binding to RNA, duplex DNA, and proteins. DNA-based biosensors in combination with polymerase chain reaction methods can be more sensitive and specific. The functional nucleic acids including DNA/RNA aptamers and DNazymes/ribozymes are emerging as molecular tools for different applications. In particular, the large area-to-volume ratio of nanomaterials can afford efficient aptamers. In this chapter, we

will discuss recent strategies of DNA biosensor construction, and their applications in detection of metal ions, biomolecules, and clinical diagnosis.

## 8.2 DNA Biosensor Construction

DNA-based biosensors are called genosensors. The hybridization property of the nucleic acid strands is the main principle for DNA sensor detection. Numerous methods were developed for this purpose, such as polymerase chain reaction, flow cytometry, and other amplification methods.

### 8.2.1 Colorimetric and Fluorescent Nucleic Acids

DNA/RNA basically consists of three components: a nitrogenous base with purine and pyrimidine, sugar, and a backbone with phosphodiester. The current studies show that the chemical modification of DNA can lead to various discoveries of new drugs and biosensors. There has been renewed interest in these three sections containing such oligoribonucleotides modifications, leading to the formation of colorimetric and fluorescent nucleic acids. First, we will discuss the nitrogenous base moieties modification with designed functional groups.

#### Substituted Purine and Pyrimidine Analogues

With careful design, fluorescent nucleobases can be crafted to retain some or most of these properties: hydrogen-bonded base pairing, enzyme and protein recognition, and purine/pyrimidine pairing architecture. Considering the size, electronic distribution, tautomerism, and  $pK_a$  values of functional groups, we reasoned that even a subtle change in the analogue can have a drastic effect in interpreting the results obtained with base analogues. The N7 in purine is situated in significant groove of B-form DNA and it can act in the recognition processes as a potential hydrogen bond acceptor. 7-Deazapurine nucleoside derivatives can be readily integrated into oligonucleotides either through enzymatic or automated solid phase synthesis. 8-Aza-7-deazapurine coumarin and pyrene dye conjugates (Fig. 8.1a) exhibit fluorescence emission much higher than that of 7-deazapurine derivatives (Fig. 8.1b). They are quenched by intramolecular charge transfer between the nucleobase and the dye synthesized by “click” reaction (Seela et al. 2009).

G-rich sequences have a strong tendency to form quadruplex through hydrogen bonding between guanine  $N-2$  hydrogen and another's  $N-7$  nitrogen, and the tetraplex formation was confirmed by gel electrophoretic mobility shift experiments. Purine  $N-3$  nitrogen is situated in DNA's minor groove and is not

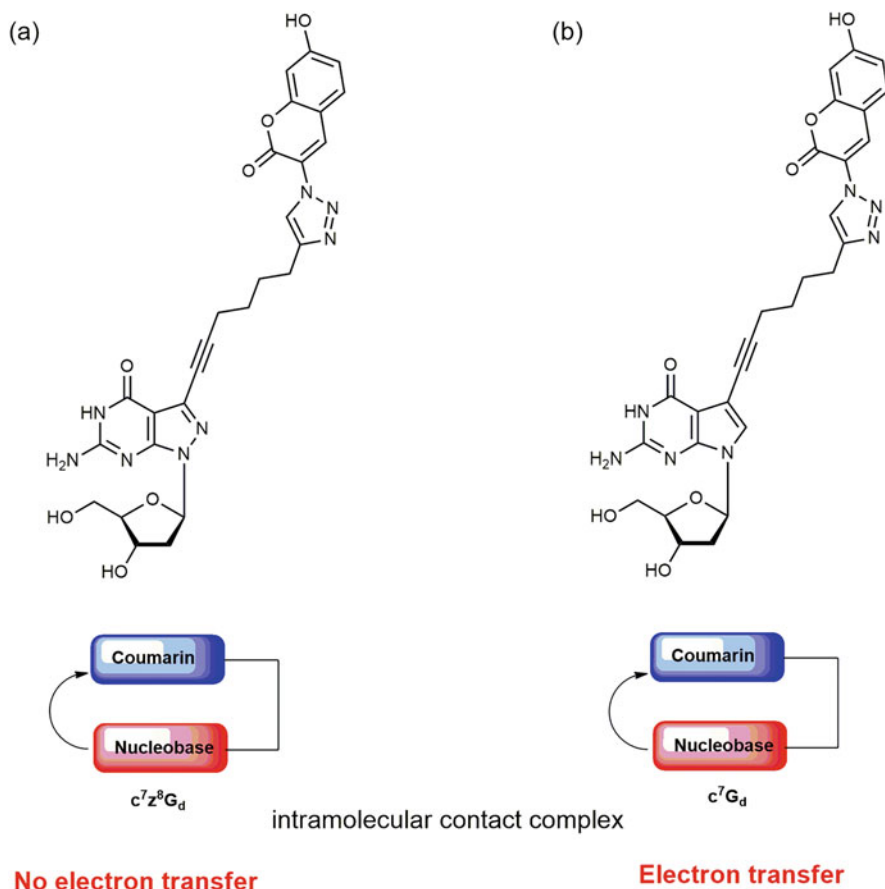


**Fig. 8.1** Intramolecular and intermolecular contact complexes within nucleoside dye conjugates. 8-Aza-7-deazapurine coumarin and pyrene dye conjugates (a) exhibit fluorescence emission much higher than that of 7-deazapurine derivatives (b). This is because in the first case no electron transfer takes place, whereas in the second case electron transfer does take place. Reprinted with permission of Copyright 2009 Royal Society of Chemistry from reference Seela et al. (2009)

directly involved in the base pairing through hydrogen bond formation. However, the replacement of 3-deazaadenosine from ribozyme significantly decreases its catalytic efficacy indicating a momentous role of the *N*-3 nitrogen atom. Other analogues such as isoguanine, thioguanine, 2,6-diaminopurine, and hypoxanthine were also used as probes to recognize purine nucleosides in protein-DNA interactions. Furthermore, 8-Aza-2'-deoxyisoguanosine is the first fluorescent-shaped mimic of 2'-deoxyisoguanosine, its fluorescence is stronger in alkaline medium than under neutral conditions (Seela et al. 2009).

In 2003, Saito and co-workers developed benzopyridopyrimidine containing oligodeoxynucleotide which is used as effective reporter probe for typing of the

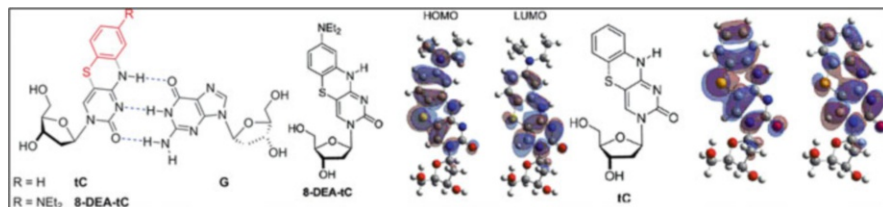


**Fig. 8.2** Watson-crick base pair and molecular orbital calculations comparing HOMO and LUMO orbitals of tricyclic cytidine and tC nucleosides. Tricyclic cytidine was used for fluorescence turn on and the fluorescent quantum yield increases up to 20-fold when compared to the free nucleoside. *HOMO* highest occupied molecular orbital, *LUMO* lowest unoccupied molecular orbital. Reprinted with permission of Copyright 2017 American Chemical Society from reference Purse et al. (2017)

A/G single-nucleotide polymorphism (Okamoto et al. 2003). In 2017, Purse and co-workers developed a new tricyclic cytidine analogue for fluorescence turn on DNA duplex formation, and the fluorescent quantum yield increases up to 20-fold when compared to the free nucleoside. The duplex protects tricyclic cytidine against quenching by excited state proton transfer using deuterated buffer, and this experimental result was supported by density-functional theory calculations (Fig. 8.2). In 2018, Harki et al. developed incorporation of 4-cyanoindole-2'-deoxyribonucleoside into DNA and obtained quantum yields >0.90 in water.

A variety of pyrimidine modifications at the fifth position is known as of today. DNA difunctionalization of both terminal triple bonds in 5-triisopropylamine-2'-deoxyuridine generated by double “click” reaction shows a strongly fluorescent with bis-dye conjugate, and forms stable base pairs with the “clickable” moieties protruding into the major groove of duplex DNA (Seela et al. 2009).

The variation of functional groups on the pyrimidine nucleoside, specifically, H versus OH at the 2'-position, NH<sub>2</sub> versus OH at the fourth position, and H versus CH<sub>3</sub> at the 5-position, results in eight species of pyrimidine nucleosides. The number of chemical species dramatically increases when 5-modifications other than methyl groups are admitted into this perusal. It is well known that thymine exist as a 5-methylated pyrimidine nucleobase. However, recent research has shown that the 5-methyl group was subsequently oxidised into various products such as 5-formyl and 5-hydroxymethyl derivatives. The existence of 5-hydroxymethylcytidine in eukaryotes is a more recent discovery in chemical biology.

On the other hand, non-canonical nucleobases are emerging as alternatives to natural nucleobases. The fluorescent nucleobases are not necessarily purines or pyrimidines, but rather have more greatly varied structure since they are not constrained in their architecture or base-pairing abilities. However, these non-canonical nucleobases are too bulky to fit into dsDNAs, which restricts their applications in polymerase enzymes.

## Sugar Modifications

Several sugar modifications, primarily at the 2'-position, have been described to generate nuclease-resistant RNA aptamers and ribozymes. For example, there are moieties of fluoro, amino, methoxy, allyloxy, and 2'-C-allyl substituents. 2'-Deoxy or 2'-O-methyl sugar modifications were introduced to identify the positions of 2'-hydroxyl groups necessary for the hairpin ribozyme activity. 2-Fluoro and 2'-difluoro-2'-deoxyuridine containing oligonucleotides have been widely used to investigate the mechanism of human G and T glycosylase. Another interesting sugar modification involves the replacement of O-4' furanose ring oxygen with a methylene group, resulting in a carbocyclic analogue. Such sugar modified analogues of thymidine and 5-methyl-2'-deoxycytidine have been incorporated in oligodeoxynucleotides to allow the triplex formation. The O-4' ring oxygen can also be substituted by sulfur to 4'-thiofuranose modification, and this kind of modified oligonucleotide was used for detection of DNA-protein interactions, for example, methylase system and EcoRV restriction endonucleases. The introduction of a single alkyne-modified oligonucleotide could be exploited to generate bottle brush-DNA.

Synthetic genetic polymers consisting of sugar modifications such as polyamide nucleic acid, locked nucleic acid, 1,5-anhydrohexitol nucleic acids, and threose nucleic acid are often referred to as xenobiotic nucleic acids (Fig. 8.3). 1,5-Anhydrohexitol nucleic acids represent a rather drastic sugar modification since the deoxyribose is substituted by a six-membered hexitol moiety. 1,5-Anhydrohexitol nucleic acids form more stable duplexes with complementary 1,5-anhydrohexitol nucleic acids and it is resistant to nuclease degradation.

Nielsen and co-workers developed an artificial polyamide nucleic acid based on the aminoethylglycyl backbone connected to each repeating unit with nucleobases (Nielsen et al. 1991). Mixtures of DNA and polyamide nucleic acid can form DNA-polyamide nucleic acid duplexes, polyamide nucleic acid<sub>2</sub>-DNA triplexes, and polyamide nucleic acid<sub>2</sub>-DNA<sub>2</sub> quadruplexes; the resulting secondary structures are more stable than the corresponding pure DNA. It has been shown that the

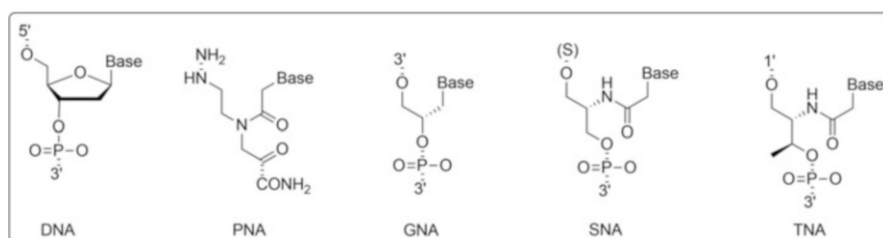


**Fig. 8.3** Structures of some xenobiotic nucleic acids. *PNA* polyamide nucleic acid, *GNA* glycol nucleic acid, *SNA* serinol nucleic acid, *TNA* threoinol nucleic acid

stability of polyamide nucleic acid-DNA complexes considerably improves the incorporation of a positively charged polyamide nucleic acid in the triangular DNA origami structures. This is feasible at low cation level concentrations where the DNA–DNA duplex is less stabilized by DNA–DNA duplex invasion using a DNA origami framework that switched from a closed to an open conformation after sequence-specific polyamide nucleic acid invasion.

Imanishi and co-workers developed the first locked nucleic acid, and studied their interaction with DNA and RNA. The sugar moiety's 2'-O and 4'-C are connected through a methylene group; it offers more stable locked nucleic acid-RNA and locked nucleic acid-DNA duplexes compared to the duplexes of DNA-DNA and DNA-RNA. Algar et al. demonstrated locked nucleic acid nucleotides were used to increase the thermal stability of the photonic wires to explore a time-consuming cascade energy transfer configuration based on four types of fluorophores hybridized with oligonucleotides.

Acyclic nucleic acids are a versatile class of compounds that are used extensively as synthetically important intermediates for the formation of stable duplex, homoduplex, and heteroduplex with DNA. Ramasamy et al. first reported the amino acid nucleic acid synthesized from L-serine but it doesn't show the hybridization with polyd(A) (Ramasamy and Seifert 1996). In 2005, Meggers and co-workers demonstrated the formation of stable homoduplex by using an acyclic glycol scaffold with phosphodiester linkages. Recently, Asanuma et al. reported D-threoninol (Asanuma et al. 2010) and L-serinol nucleic acids, which exhibited more stable homoduplex formation. Work by Asanuma has also shown that high stability of  $\alpha$  threoninol nucleic acids can be compared with serinol nucleic acids to afford more stable homoduplexes due to the less flexibility of additional methyl group in  $\alpha$  threoninol. In addition, the same group developed hexaplex formation using D-threoninol artificial nucleic acids in aqueous solution. Kurt's group has investigated the formation of *i*-motifs from acyclic (L)-threoninol nucleic acids at lower pH value.

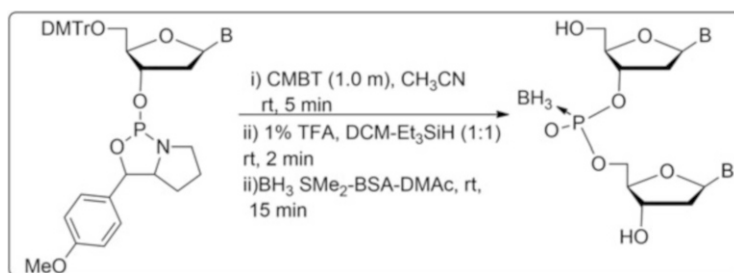
## Phosphate Modifications

Chemical changes in the phosphate backbone are not as varied as nucleobase and sugar units. Chemical synthesis of DNA using phosphoramidite chemistry is generally achieved from 3' to 5' end, opposite to the direction of DNA synthesis by polymerases. Stetsenko and co-workers developed phosphoryl guanidine nucleic acid derivative with oxidation of polymer-supported dinucleoside 2-cyanoethyl phosphite by iodine. It can bind to their complementary DNA or RNA strands with similar to natural oligodeoxyribonucleotides. In addition, the same group has developed novel *N*-(methanesulfonyl)-phosphoramidate oligonucleotide derivatives using an automated DNA synthesizer with the Staudinger reaction. Rosenberg et al.

developed the solid phase synthesis of 5-O-phosphonomethyl-deoxyribosyl oligonucleotides through phosphotriester method. This phosphonate can form triplex with natural counterparts, and exhibits higher stability against nucleases of L1210 cell free extract. In another approach, oligothymidylates with different phosphodiester and isopolar ratios of 5'-hydroxyphosphonate, 5'-O-methylphosphonate, and 3'-O-methylphosphonate internucleotide linkages were found to have the ability to induce RNA cleavage by ribonuclease H.

Click chemistry has been successfully applied to ligation, bioconjugation, fluorophore labeling of DNA, modified nucleoside synthesis, PNA-DNA chimeras (Kumar et al. 2007), DNA-carbohydrate dendrimers, and monolayer coupling of oligonucleotides. In particular, post-synthetic functionalization of DNA using alkyne modified dU phosphoramidites in the presence of Cu-AAC catalyst has found wide applications in modern bio-chemistry. Seela et al. reported phosphoramidites from alkyne-labeled 7-deazapurines, pyrimidines (Seela and Sirivolu 2006), and O-alkynyl-modified sugars. They observed single TP modification at 3' and 5'-ends that was approximately 30 times more stable than native DNA towards SVPDE digestion exhibiting 40-fold increase in nuclease resistance to CSPDE.

Another promising phosphorus modification was made by using boranophosphate. The first boranophosphate DNA was introduced by Shaw et al. by replacing one of the non-bridging oxygen atoms with a borane group. Caruthers and co-workers developed the synthesis of boranophosphate-modified homo-T oligomers via H-boranophosphonate and boranophosphotriester methods. All these synthetic techniques are non-stereocontrolled boranophosphate-DNAs and provide 2n stereoisomers similar to thiophosphate oligonucleotide's old-time synthesis. Wada et al. developed the first stereocontrolled synthesis of boranophosphate via an oxazaphospholidine approach with an acid-labile protecting group (Scheme 8.1). They introduced 4-methoxybenzyloxycarbonyl protecting group on nucleobases



**Scheme 8.1** Synthesis of boranophosphate using oxazaphospholidine. *CMPT* N-cyanomethylpyrrolidinium triflate, *CH<sub>3</sub>CN* acetonitrile, *TFA* trifluoro acetic acid, *DCM* dichloro methane, *Et<sub>3</sub>SiH* triethyl silane, *BH<sub>3</sub>·SMe<sub>2</sub>* borane dimethylsulfide, *NH<sub>3</sub>* ammonia. Modified after reference Wada et al. (2019)



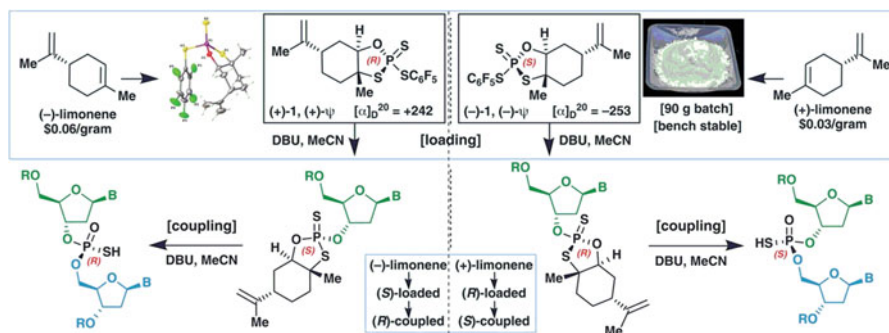
rather than trityl-type groups that were anticipated to be less sterically hindered than the trityl group, and cleaved under acidic circumstances.

### Thio-Modified DNA

Thiophosphate modifications are those in which one of the non-bridging oxygen atoms of a phosphodiester bond is replaced by a sulfur atom. psDNA is considerably more stable towards nucleases than the simple DNA. The P-atom-modified nucleic acids have stereogenic P centers resulting in two diastereomers *Sp* and *Rp*. The oxidation of phosphoramidite to phosphorothioate oligonucleotide was attempted using Beaucage's reagent for sulfurization exchange. Recently, the construction of stereo-regular PSDNA backbone has been reported by Baran et al. using P(V)-based reagents that were different from standard phosphoramidite chemistry. The P(III)-based reagents are useful for stereo-controlled synthesis of several nucleotidic architectures through a simple, inexpensive, and operationally simple protocol (Scheme 8.2). Neutral hydrophobic backbones of lipid bilayers were synthesized from alkylation of the phosphorothioate group using alkylhalides. These lipid bilayers are used in DNA nanopores. Phosphorothioate alkylation is also used to functionalize DNA nanostructures with proteins and metal nanoparticles.

### 8.2.2 The Label-Free Luminescent Probes

Luminophores are normally achieved by non-covalent binding methods such as groove binding, intercalation, electrostatic interactions, and end stacking. In aqueous solution, the luminescent molecules that are used in label-free DNA probes are generally emissive or non-emissive due to solvent interactions quenching the excited



**Scheme 8.2** Synthesis of chiral phosphorothioate using P(V) reagents. *DBU* 1,8-diazabicyclo [5.4.0]undec-7-ene, *MeCN* acetonitrile. Reprinted with permission of Copyright 2018 The American Association for the Advancement of Science from reference Baran et al. (2018)

state. However, they showed enhanced luminescence when binding to a specific DNA structure owing to the protection of their excited states within the oligonucleotide's hydrophobic interior. Luminescent DNA molecules can usually be categorized into two types: organic dyes and transition metal complexes.

## Organic Dyes

In 1856, William et al. developed the first human-made organic dye called mauveine. Most of the natural dyes were prepared from plant sources: berries, roots, leaves, wood, bark, insects, and lichens in Fig. 8.4. Organic dyes have been widely used in supramolecular chemistry as a probe and also used as fluorescent tracer in medicinal and biological applications. A large number of organic reactions are usually carried out by using organic dyes as photoredox catalysts. For example, the Scaiano group recently developed photocatalytic hydroxylation of boronic acids using methylene blue as a photosensitizer under aerobic conditions. In addition, the selective oxidation of benzene to phenol was carried out in the presence of a photocatalyst (3-Cyano-1-methylquinolinium ion) under homogeneous and ambient conditions.

Organic dyes are used in various studies to explore new photosensitizers for the development of dye-sensitized solar cells. For instance, Tian et al. developed new phenothiazine organic dyes as sensitizers for their application in dye-sensitized solar cells. Dye-sensitized solar cells have emerged as one of the most promising renewable photovoltaic cells alternative to solid-state cells due to the characteristics like low price, compatibility, and simple manufacturing methods. In recent years, metal-free organic dyes have been widely used to enhance the photovoltaic efficiency of dye-sensitized solar cells (Błaszczuk 2018).

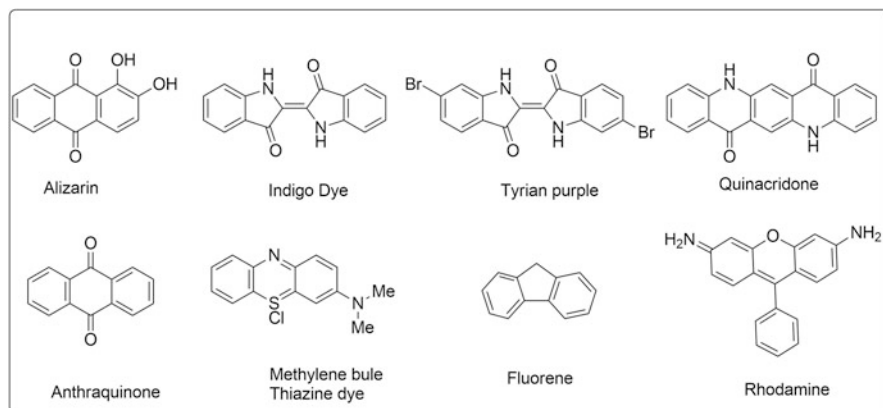


**Fig. 8.4** Some of natural and synthetic dyes

## Transition Metal Complexes

In 2009, Ma and co-workers have developed mismatch of thymine-Hg<sup>2+</sup>-thymine to design a label-free mercury ion-based DNA assay using luminescent platinum (II) metallo intercalator. The polythymine oligonucleotide 5-T33-3 occurs as a random coil in the absence of Hg<sup>2+</sup> ions, showing selectivity for Hg<sup>2+</sup> over a fivefold excess of other metal cations. The same complex was recently used as a luminescent probe in an “OR” DNA logic device to detect Ag<sup>+</sup> and H<sup>+</sup> (Leung et al. 2015). In recent years, several mononuclear Ir(III) complexes were developed as G-quadruplex-selective probes for label-free luminescent biosensors. This mononuclear Ir(III) complex potentially interacts with the loop of G-quadruplex through noncovalent interactions. Chang et al. developed a carbazole derivative fluorescent G-quadruplex ligand using 3,6-bis(1-methyl-4-vinylpyridinium)carbazole diiodide to monitor the cellular uptake and localization of guanine-rich oligonucleotides. Squarine dye STQ1 G-quadruplex binding properties demonstrated a strong luminescence (up to 70-fold) in the presence of G-quadruplex DNA, but the same system failed to show luminescence with dsDNA and ssDNA (Chen et al. 2014). A low luminescence signal was observed because of weak interaction between duplex DNA and Ir(III) complex. The same group also developed a luminescent iridium (III) complex [Ir(ppy)<sub>2</sub>(bcp)]<sup>+</sup> for the detection of a pyrimidinic endonuclease activity. This endonuclease IV is used as a model enzyme. Certain examples of luminescent metal complexes which are used as DNA probes for the construction of oligonucleotides are described in Table 8.1.

## 8.3 Biosensor Applications in Detection of Metal Ion

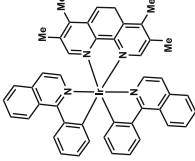
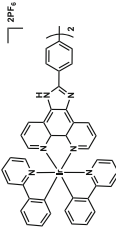
This is one of the hot topics of analytical chemistry. Only a small number of metal ion sensors are available for practical use because the design of the chemosensor is often a trial and error process.

### 8.3.1 Functional Nucleic Acids as Recognition Probes

Functional nucleic acids are short RNA/DNA oligonucleotides capable to bind to target molecules, and mediate enzyme catalysis in nucleic acids resulting in aptazymes. There are several reports on the use of FNAs as molecular recognition probes.

**Table 8.1** Examples of luminescent metal complexes used as DNA probes for the construction of oligonucleotide-based detection methods and their corresponding target analytes and detection limits

Name	Structure	DNA target	Assay analyte	Detection limit	References
$[\text{Ir}(\text{Phen})_2(\text{dppz})]^{2+}$		dsDNA	Hg K	0.35–5 nM 50 nM	Zhang et al. (2010)
$[\text{Ir}(\text{bpy})_2(\text{biq})]^+$		G-quadruplex	Nucleic acids Sr Pb	50 nM 13 nM 600pM	Ma et al. (2012)
$[\text{Ir}_2(\text{Br-ppy})_4\text{Cl}_2]$		G-quadruplex	Lysozyme	2 nM	
$[\text{Ir}(\text{phq})_2(\text{phen})]\text{PF}_6$		G-quadruplex	Hepatitis C virus NS3 helicase	NA	Leung et al. (2015)

[Ir(piq) <sub>2</sub> (tmphen)]		dsDNA ssDNA G-quadruplex	Ochratoxin A (OTA)	5 nM	
4,4'-di(1H-imidazo[4,5-f][1,10]phenanthroline-2-yl)biphenyl		G-quadruplex	Pesticides	0.37 μg/L	Liu et al. (2016)

## DNAzyme-Based Sensing Strategies

DNAzyme-based fluorescent biosensors are called catalytic beacons because of the catalytic reactions involved in the sensing process. Recent investigations have shown various signal transduction mechanisms such as colorimetry, fluorescence, and electrochemical. DNAzymes are one of the catalytic nucleic acids depending on cofactors, and serve equally diverse functions including enzymatic turnover properties and as outstanding signal amplifiers. DNAzymes consist of an enzyme chain and a substrate chain. In the presence of cofactor, the substrate strand cleaves into two parts, which makes them very attractive to design different kinds of biosensors that respond to the cofactor. The cleavage process leads to an increase in the fluorescent signal, when the substrate strand and enzyme strand are functionalized with a fluorophore and a quencher, respectively.

The most common way to design a fluorescent probe RNA-cleaving DNAzyme is to add a fluorophore-quencher (F-Q) pair that would release the fluorophore and offer a signal after the cleavage of the substrate (Gong et al. 2015). The F and Q pairs are carefully placed so that they are near to each other before catalytic cleavage. The F and Q's precise positions have many choices as shown in Fig. 8.5. Several modifications were made to design F and Qs to reduce the background. They were initially located on the two ends of the substrate strands (Fig. 8.5a). They may also be situated either at the end of the binding arms or near the cleavage site (Fig. 8.5b). To shorten the distance they could be set on the same side but on different strands (Fig. 8.5c). Other choices consist of using an extended enzyme part to place the Q close to the F (Fig. 8.5d), introducing a second Q on the other end of the substrate (Fig. 8.5e) and using some nanoparticles as quenchers (Fig. 8.5f). The first fluorescent catalytic beacon was developed by Lu et al. based on the 8–17 DNAzyme for  $Pb^{2+}$ . In the presence of  $Pb^{2+}$ , the fluorophore-labeled substrate increases the fluorescence by ~300%. However, the sensor efficiency reduces significantly if the temperature is brought to room temperature due to high background fluorescence. Zhang and Lu proposed a general catalytic and molecular beacon approach by combining the high quenching effectiveness of catalytic beacon with molecular beacons for multiple enzymatic turnover properties (Fig. 8.5g). Gianneschi and coworkers reported a novel fluorogenic substrate consisting of cooperatively assembled DNA-nanoparticle micelles. They served as supramolecular fluorogenic substrates by assembling dye-labeled DNA-brush copolymer surfactants to overcome the inhibition limitation of ordinary ssDNA substrates (Fig. 8.5h). The Li et al. conducted several in vitro selections to obtain such fluorescent DNAzyme probes that could detect a specific bacterium *E. Coli*, and proved that a single live cell can be detected by this probe (Fig. 8.5i) (Li et al. 2012).

### DNAzyme-Functionalized Gold Nanoparticles

In 1996, DNA-functionalized gold nanoparticles were first discovered to assemble complementary DNA strands via DNA hybridization. The method involves the attachment of non-complementary DNA oligonucleotides with thiol groups, which

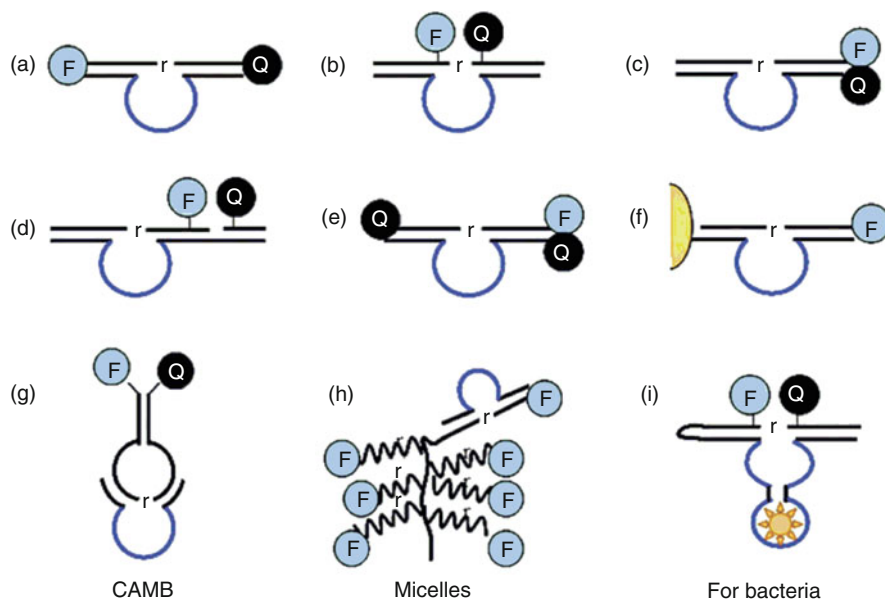


**Fig. 8.5** DNAzyme arrangement of fluorophore-quencher pairs. (a) F and Q were placed at the two ends of the substrate strands. (b) F and Q were placed next to the cleavage site flanking the cleavage site. (c) F and Q were placed on the same side but on different strands. (d) Use an extended enzyme part acting as a template to place the Q close to the F. (e) A second Q was introduced on the other end of the substrate. (f) Nanoparticles as quencher. (g) F and Q were placed at the two ends of a hairpin-shaped molecular beacon, which was called the catalytic and molecular beacon. (h) Using DNA–nanoparticle micelles as supramolecular fluorogenic substrates. (i) Fluorogenic DNAzyme probes for bacteria. Reprinted with permission of Copyright 2015 Royal Society of Chemistry from reference Gong et al. (2015)

further can bind to gold nanoparticles. Recently, Lu et al. have fabricated colorimetric lead biosensors based on DNAzyme-directed assembly of gold nanoparticles. This strategy is useful for the transformation of inactive DNAzymes to activated DNAzymes, allowing the cleavage of substrate strand to disassemble the gold nanoparticles, further resulting in a blue to red color change. In addition, DNAzyme-functionalized gold nanoparticles are useful for specific detection of  $Mg^{2+}$ ,  $Zn^{2+}$ ,  $Pb^{2+}$ ,  $Cu^{2+}$ ,  $Co^{2+}$ ,  $Hg^{2+}$ , and  $UO_2^{2+}$ . Moreover, the biosensor applications also included DNAzyme-functionalized gold nanoparticles with electrochemically active substances. Electrochemical sensors for  $Pb^{2+}$  have been demonstrated by using 8–17 DNAzymes. The authors investigated that  $Pb^{2+}$  cleave the nucleic acid substrates on gold nanoparticles to be detached onto a DNA-coated electrode. The DNA on gold nanoparticles allows big quantities of electrochemically active metal complexes to be attached, thus giving a large signal improvement on the electrode in the presence of  $Pb^{2+}$ . Graphene sheets decorated with DNAzyme-functionalized gold nanoparticles were also used as cofactors for DNAzymes, for example, L-histidine (Liang et al. 2011) and  $Pb^{2+}$  (Chen et al. 2014). In 2018, Ling

et al. reported a colorimetric sensing phenomenon to detect the acetyl-cholinesterase based on  $\text{Cu}^{2+}$ -specific DNAzyme.

### Triplex DNA-Based Strategies

In 2011, for the first time, Tan and co-workers reported the fluorescent aptasensors–based triplehelix molecular switch. It consists of a central target-specific aptamer sequence, two arm fragments, and a dual-labeled oligonucleotide. Dual-labeled oligonucleotide is used as a signal transduction probe triplehelix molecular switch that could complement the arm fragment sequence (Fig. 8.6). The signal transduction probe is doubly labeled with pyrene at both the 5′- and 3′-end.

Binding the two arm segments of the aptamer with the STP loop sequence makes creating an “open” configuration. The aptamer complex led to the discharge of the STP as well as fresh signal measurements. This methodology has consensus for a wide scope of analysis by simply changing the aptamer sequence, and remains the same with the triple-helix structure. Moreover, the added advantages of these triplehelix molecular switch are: (1) no labeling is required for the original aptamer, and (2) both the binding affinity and specificity of the aptamer are improved. Another novel aptasensor for protein detection was identified, and amplification properties of PCR combined with the sequence-specific identification capacity of triplex formation for DNA duplex. However, the two DNA probes were hybridized with each other after introduction of thrombin, which was expanded when Klenow fragment polymerase and dNTPs were present. The PCR amplification began with addition of Taq DNA polymerase and two primers, accompanied by product

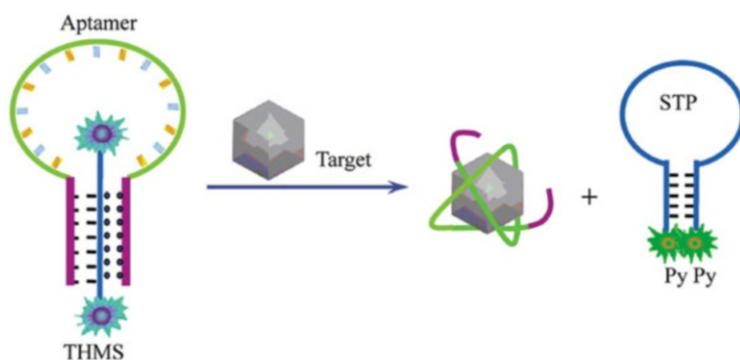


**Fig. 8.6** The fluorescent aptasensor–based triplehelix molecular switch. After the introduction of a specific target, aptamertarget binding results in the formation of a structured aptamer/target complex, which disassembles the triplehelix molecular switch and releases the signal transduction probe. Once this process is finished, then the configuration of signal transduction probe changes from open to close, leading to new signal readout. *THMS* triplehelix molecular switch, *STP* signal transduction probe, *Py* pyrene. Reprinted with permission of Copyright 2011 American Chemical Society from reference Tan et al. (2011)



recognition by molecular beacon through triplex formation. The most important requirement is to remove non-specific amplification and DNA contamination.

### **G-Quadruplex-Enabled Detection Platforms**

The G-quadruplex is a non-canonical structure, strongly organized framework of nucleic acid with stacked planar G-tetrads. Over the years, G-quadruplex structures provide an important regulatory role in the detection of metal ions.

#### **Detection of K<sup>+</sup>**

G-quadruplexes can be used for potassium detectors using triphenylmethane fluorescent dye crystal violet. Kong et al. developed G-quadruplex complexes for assaying the presence of K<sup>+</sup> or Na<sup>+</sup>, and the fluorescence changes with K<sup>+</sup> concentration variability. Two K<sup>+</sup> detection modes were developed depending on the type of the fluorescence shift in crystal violet as a function of ionic condition. A label-free detection of K<sup>+</sup> was developed by Qin et al. using G-quadruplex DNA (c-Myc), which further enhanced the fluorescence of tetrakis (diisopropylguanidino) zinc phthalocyanine (Wang et al. 2009). Another novel detection of K<sup>+</sup> was achieved by utilizing a K<sup>+</sup>-sensitive G-quadruplex DNA named PS5. Quadruplex structure is capable of binding hemin to adopt a hemin-G-quadruplex DNAzyme that catalyzes the conversion of colourless 3,3',5,5'-tetramethylbenzidine to blue product in the presence of H<sub>2</sub>O<sub>2</sub> oxidation.

#### **Detection of Ag<sup>+</sup>**

Zhou et al. developed the G-quadruplex-hemin DNAzyme-amplified Ag<sup>+</sup>-sensing method based on the capacity of Ag<sup>+</sup> to stabilize C–C mismatches by forming C–Ag<sup>+</sup>–C base pairs. In this method, an intramolecular duplex was formed by the oligonucleotide strand in the absence of Ag<sup>+</sup> (Fig. 8.7). The addition of Ag<sup>+</sup> allows the formation of another intramolecular duplex in which C–C mismatches were stabilized by base pairs of C–Ag<sup>+</sup>–C, resulting in the release of the G-rich sequence that can be folded to form a catalytically active G-quadruplex-hemin DNAzyme (Zhou et al. 2010).

Additionally, Kong et al. developed two different length oligonucleotide chains for the detection of Ag<sup>+</sup>. Cysteine broke C–Ag<sup>+</sup>–C bonds leading to reformation of the DNA duplex and reduced catalytic activity of the system (Kong et al. 2010). Furthermore, Seela et al. have identified silver-mediated base pairs in DNA-incorporating purines such as 7-deazapurines and 8-aza-7-deazapurines and further studied their impact of reduced nucleobase binding sites on glycosylation positions.

#### **Detection of Cu<sup>+</sup>/Cu<sup>2+</sup>**

Zeng et al. developed an effective G-quadruplex sequence using copper (I) catalyzed click chemistry between azide and alkyne to generate G-rich sequences. The G-quadruplex and hemin system had mimic-horseradish peroxidase activity with

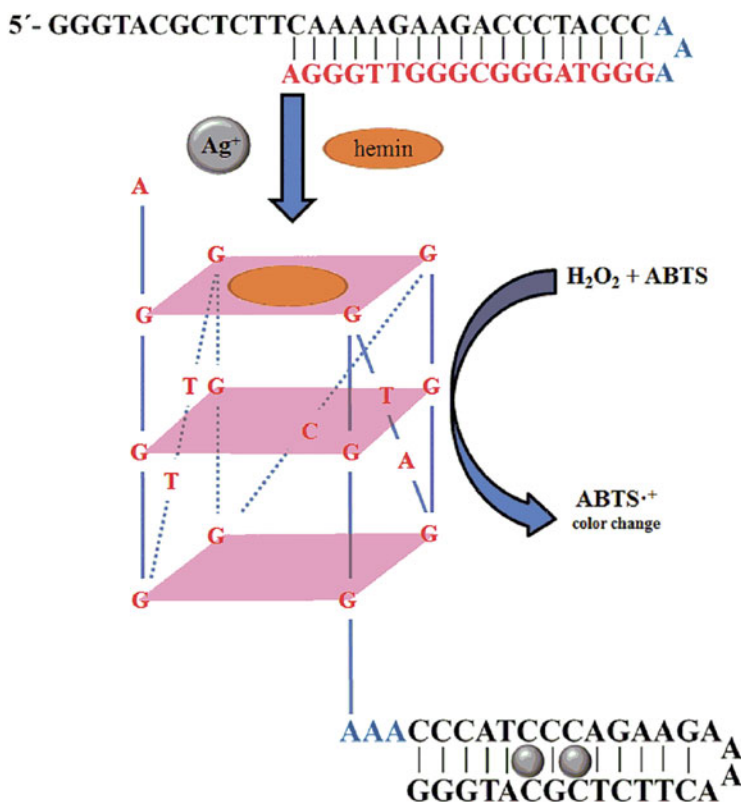


**Fig. 8.7** The G-quadruplex-hemin DNAzyme amplified Ag<sup>+</sup>-sensing method. Duplexes formed before addition of Ag<sup>+</sup> does not enhance the catalytic activity of hemin due to formation of intramolecular duplex that could not completely prohibit the G-quadruplex formation. The addition of Ag<sup>+</sup> to the hemin/oligonucleotides mixture could further enhance the catalytic activity of hemin, suggesting that the presence of Ag<sup>+</sup> changed the equilibration between Form A and Form AA, and more Form AA was produced. Reprinted with permission of Copyright 2010 Elsevier from reference Zhou et al. (2010)

the assistance of hemin and K<sup>+</sup>, catalyzing tetramethyl benzidine into a green color material. The fluorescence strength of the resulting green material was observed at optical density 450 nm reflects the quantity of Cu<sup>+</sup> and DNAzyme attached to protoporphyrin IX. However, when Cu<sup>2+</sup> was brought into the lighting scheme, the fluorescence was selectively quenched due to the powerful metallization of protoporphyrin IX induced by Cu<sup>2+</sup>. In 2014, Li et al. developed a DNA-based mimic-HRP interaction between Cu<sup>2+</sup> and GC-rich dsDNA. Cu<sup>2+</sup> catalyzes the accumulation of tetramethyl benzidine in the presence of H<sub>2</sub>O<sub>2</sub>, which can be seen with naked eye. Furthermore, GpG-duplex DNA picked out and applied to detect Cu<sup>2+</sup> in aqueous solution with a detection limit of 1.2 nM.

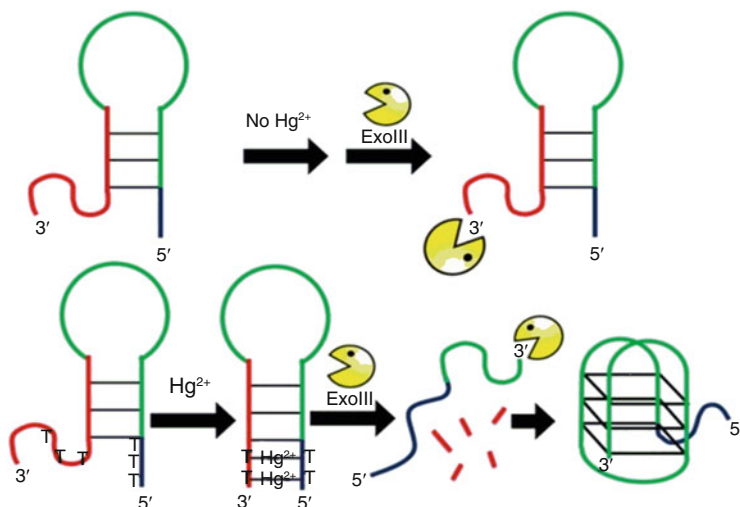


**Fig. 8.8** The label-free G-quadruplex-based sensor for Hg<sup>2+</sup>. Reprinted from reference Wang et al. (2015)

**Detection of Hg<sup>2+</sup>** Hg<sup>2+</sup> is one of the heavy metals that cause public health hazards. Mirkin et al. developed DNA-functionalized gold nanoparticles for the detection of Hg<sup>2+</sup>. The thiol DNA-based detection system is well known for thymidine-Hg<sup>2+</sup>-thymidine (T-Hg<sup>2+</sup>-T) base pairs. Hg<sup>2+</sup> was detected using selective iridium (III) complex and Exo III (Fig. 8.8) (Wang et al. 2015).

In 2009, Wang et al. developed a highly selective colorimetric biosensor for Hg<sup>2+</sup> detection using thymine-rich proteins in one strand of FNA with guanine-rich sequences. The designed FNA forms a G-quadruplex DNAzyme with the stable of K<sup>+</sup> and hemin creating a green color when the target ion is blank or contrast ions (Wang et al. 2009). The DNA strand creates an intra-molecular hairpin G-quadruplex DNAzyme, which imitates HRP activity, producing a green color for naked-eye testing. In addition, Dong et al. reported a visual detection of Hg<sup>2+</sup> in the TMB-H<sub>2</sub>O<sub>2</sub> reaction system with high selectivity and sensitivity. The Chen et al. demonstrated colorimetric detection of Hg<sup>2+</sup> using hybridization chain reaction and T-Hg<sup>2+</sup>-T base pairs (Chen et al. 2014). In 2017, Seela et al. studied the duplex stability of mercury ion-mediated dU-Hg<sup>2+</sup>-dU pair depending on substituents introduced at the 5-position of the pyrimidine moiety.

### ***i*-Motif or Mismatched DNA Base Pair-Mediated Assays**

*i*-Motif has gained a specific attention among the various secondary structures of DNA. Gehring et al. developed the first *i*-motif DNA for the hexamer sequence d

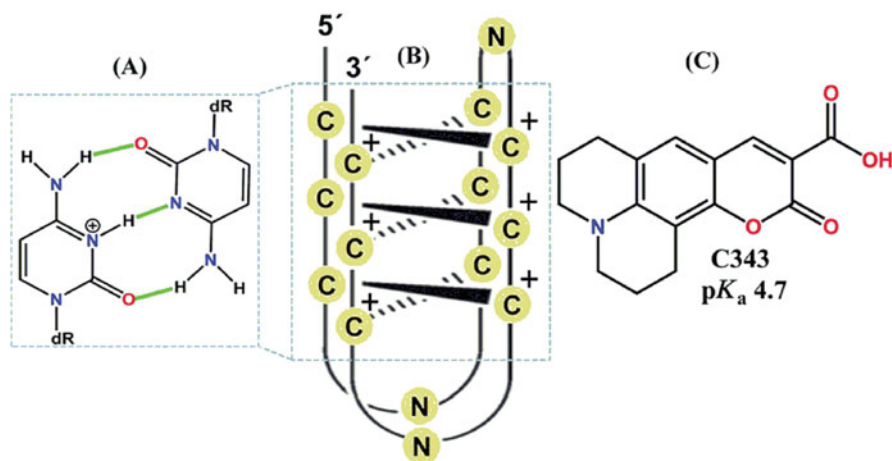


**Fig. 8.9** (a) Hemi-protonated cytosine-cytosine Hoogsteen base pairing in *i*-motif DNA. (b) Chemical structure of *i*-motif DNA and (c) Coumarin 343. Reprinted with permission of Copyright 2019 Royal Society of Chemistry from reference Hazra et al. (2019)

(TCCCCC), forming an intercalated tetramolecular quadruple helical structure under acidic circumstances. Cytosine-rich sequences create *i*-motif DNA at slightly acidic pH (4.0–6.0) through Hoogsteen hydrogen bonding between hemi-protonated cytosine-cytosine base pairs, resulting in the structure of two parallel duplexes intercalated in an antiparallel way (Fig. 8.9). These *i*-motif DNA structures become volatile in neutral and alkaline media owing to the deprotonation of cytosine bases, thus forming a single-stranded DNA (Nesterova and Nesterov 2014). Therefore, a label-free strategy with a specific noncovalent-centered fluorescent antibody is preferable for targeting *i*-motif DNA. Shi et al. developed a novel selective sensor for  $\text{Ag}^+$  based on the mechanism that *i*-motif formation induced by  $\text{Ag}^+$  sensitively recognized by a cyanine as a fluorescence indicator, exhibited over 130–16,000-fold selectivity toward  $\text{Ag}^+$  than other metal ions (Tang et al. 2015).

### 8.3.2 Aptamer-Assembled Nanomaterials for Biosensing

Aptamers are cost-effective, animal-friendly, reproducible, and easily functionalized with nanomaterials for specific detection. Furthermore, the negatively charged aptamers can adsorb on the surface of nanomaterials by electrostatic adsorption mechanism.

## Metallic Nanoparticles

Unique physical properties of metal nanoparticles like size, composition, shape, surface function, and spacing distance make them prominent tools in biosensors.

### Gold Nanoparticles–Assisted Methods

Gold nanoparticle–based colorimetric sensing for metal ions usually requires the incorporation of chelating agents on the nanoparticle surface. The presence of an analyte ion induces the nanoparticle aggregation by forming multidentate interparticle complexes with the chelating ligand. 15-Crown-5 functionalized aqueous matrix gold nanoparticles containing physiologically important cations such as  $\text{Li}^+$ ,  $\text{Cs}^+$ ,  $\text{NH}_4^+$ ,  $\text{Mg}^{2+}$ ,  $\text{Ca}^{2+}$ , and  $\text{Na}^+$  were used for the detection of alkali and alkaline earth metal ions. Liu et al. developed gold nanoparticles functionalized quaternary ammonium group-terminated thiols for colorimetric sensing of  $\text{Hg}^{2+}$  at room temperature. The actual mechanism is the abstraction of thiols by  $\text{Hg}^{2+}$  that led to the aggregation of nanoparticles. Hupp and co-worker demonstrated a straightforward colorimetric method to detect aqueous heavy metal ions like mercury, cadmium, and lead using 11-mercaptoundecanoic acid and 13 nm gold nanoparticles.

Recently, Rajendran and co-workers developed gold nanoparticles–based highly selective detection of heavy metal ions such as  $\text{Cr}^{6+}$ ,  $\text{Hg}^{2+}$ , and  $\text{Pb}^{2+}$  by using phenylalanine conjugated cholic acid for colorimetric titrations in aqueous medium. Chen and group demonstrated a colorimetric sensor for  $\text{Pb}^{2+}$  with a protected AuNP using both carboxylate and 15-crown-5 ethers. Addition of  $\text{Pb}^{2+}$  interferes with the hydrogen-bonded structure by associating with crown ether moiety and producing electrostatic repulsion between gold nanoparticles, resulting in a shift of color change from blue to red. Chang and co-workers improved mercaptopropionic acid-modified gold nanoparticles for highly selective and sensitive detection of  $\text{Hg}^{2+}$  ions in the presence of 2,6-pyridinedicarboxylic acid. The Liu group very recently described detection of arsenite As(III) using gold nanoparticles with DNA oligonucleotide Probes. They used isothermal titration calorimetry experiments for measuring As(III) adsorption by gold nanoparticles and its competition with DNA adsorption. In addition, Diaz et al. demonstrated different sizes of gold nanoparticle synthesis for quenching luminescence. Their strong luminescence quenching was observed from small gold nanoparticles due to resonance energy transfer (Fig. 8.10).

### Silver Nanoparticles-Assisted Methods

There are two primary approaches in silver nanoparticles used colorimetric detection assays: a cross-linking and a non-cross-linking approach. In the cross-linking

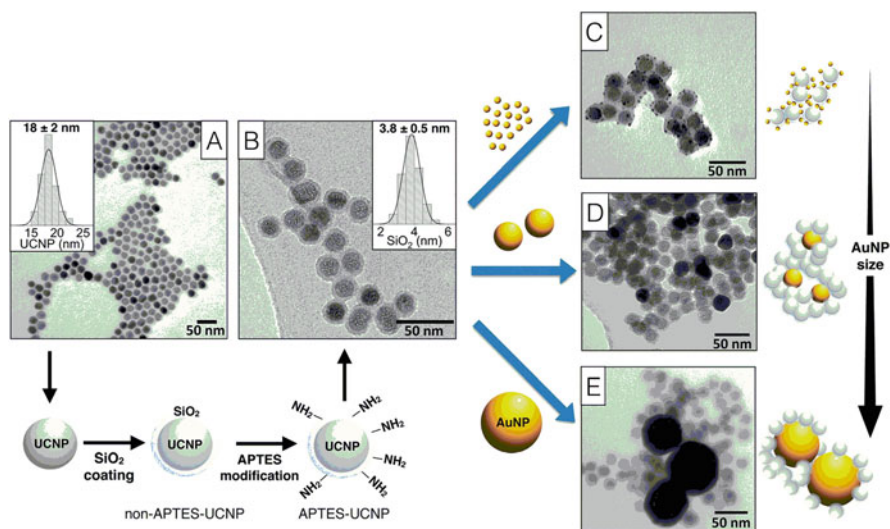


**Fig. 8.10** Luminescence quenching controlled by gold nanoparticle size. (a) TEM image of  $\text{NaYF}_4:\text{Yb,Er}$  UCNPs, (b) TEM image of  $\text{NaYF}_4:\text{Yb,Er}@\text{SiO}_2\text{-NH}_2$  UCNPs, and (c–e) TEM images of  $\text{NaYF}_4:\text{Yb,Er}@\text{SiO}_2\text{-NH}_2$  UCNPs after attaching (c)  $\text{Au}_4$  nm, (d)  $\text{Au}_{21}$  nm, and (e)  $\text{Au}_{66}$  nm nanoparticles. UCNP<sub>s</sub> upconverting nanoparticles, TEM transmission electron microscopy, AuNP gold nanoparticles,  $\text{SiO}_2$  silica, APTES (3-aminopropyl)-triethoxysilane. Reprinted with permission of Copyright 2019 Royal Society of Chemistry from reference Diaz et al. (2019)

approach, aggregation is induced by functionalized silver nanoparticles, which cross-link to target and form plasmonic network centers that are closely spaced. On the other side, the aggregation of non-cross-linking approach depends on the ionic strength of silver nanoparticles medium.

In 2008, Graham et al. developed the synthesis of oligonucleotide silver nanoparticle and beautifully described their use in sandwich assay for target DNA detection. The oligonucleotide silver nanoparticle conjugates have practically identical properties to that of their gold analogues, and due to their greater extinction coefficient both visual and absorption analyses can occur at much lower concentrations. Tan et al. developed silver nanoparticle-dsDNA conjugates for colorimetric sequence-specific DNA-protein binding assay. This assay is a colorimetric assay called “light off” since the existence of the target analyte stabilizes against aggregation nanoparticles. Plasmonic sensor-based detection of heavy metal ions in water using 3-mercapto-1 propanesulfonic acid sodium salt capped with silver nanoparticles. Very recently Zhang et al. developed ultrasensitive detection of DNA in serum samples by dual signal amplification of DNA templated silver nanoparticle and electrochemical atom transfer radical polymerization. This method is useful for detecting gene biomarkers and clinical analysis.

## Carbon Nanomaterials

Carbon nanostructures like fullerenes, carbon nanotubes, carbon nanofibers, and grapheme are confined to  $sp^2$  hybridized orbitals, facilitating zero-gap linear electron momentum dispersion and high electric conductivity.

### Carbon Nanotube-Assisted Methods

They are very attractive nanomaterials for the development of innovative devices like composites and sensors. To improve their solubility and other functional properties, carbon nanotubes need to be functionalized by either covalent or/and non-covalent bonding. For example, the covalent-bonded carbon nanotubes are normally oxidized by an acid such as nitric acid or the mixture of nitric acid and sulfuric acid.

During oxidation, the carboxyl or hydroxyl groups were introduced onto the ends and sidewalls of carbon nanotubes. These groups reduce the vander Waals interactions between carbon nanotubes and further change the structural homogeneity and other properties of carbon nanotubes. Two factors control the chemical reactivity of the sidewalls of carbon nanotubes in non-planar carbon structure: (1) curvature-induced pyramidalization of the individual carbon atoms and (2) mis-alignment of  $\pi$ - $\pi$ -orbital between neighboring carbon atoms. Highly reactive species (such as halogens, radicals, carbenes, or nitrenes) are ideal reagents for covalent functionalization of the sidewall. An efficient electrochemical-based sensor was developed for  $Pb^{2+}$  and  $Cd^{2+}$  ions using functionalized 1,3,6,8-pyrenetetrasulfonic acid sodium salt carbon nanotubes nanocomposites as a sensor material. This method offers detection limits are  $0.8 \mu\text{g L}^{-1}$  for  $Cd^{2+}$  and  $0.02 \mu\text{g L}^{-1}$  for  $Pb^{2+}$  (Jiang et al. 2018). In 2019, Nie and co-workers reported an electrochemiluminescence based detection of  $Hg^{2+}$  using poly(5-formylindole)/reduced graphene oxide to furnish a wide linear response to  $Hg^{2+}$  ranging from 0.01 nM to 100 nM.

### Graphene Oxide-Assisted Methods

Among the current research, the integration of nucleic acids with graphene-based materials or functional grapheme has been substantially advanced over the past few years, achieving the exceptional properties and functions, thereby exhibiting attractive potential applications in biosensing, diagnostics, drug screening, and biomedicine (Dikin et al. 2007; Li et al. 2015). In clinical diagnosis selective and cost-effective detection of biomolecules is very important. Under this method, DNA adsorbed on the graphene oxide surface and its fluorescence is quenched when graphene oxide mixed with a fluorophore-labeled single-stranded DNA probe, and restored the fluorescence signal after forming a double-stranded dsDNA in solution (Wang et al. 2009).

Recently, Zhang et al. reported a novel finding that nucleic acid aggregates self-assembled on graphene oxide nanoplates as a result of DNA rolling circle amplification and a functionalized triple-helix probe in single cells. The functionalized triple-helix probe containing the aptamer region for target recognition and the trigger DNA region for rolling circle amplification was used to activate rolling circle amplification for miRNA imaging. The fluorescent-labeled nucleic acids molecular aggregates were hybridized by both the rolling circle amplification products and FAM-DNA, and could partly self-assemble on graphene oxide nanoplates. Significantly, the nucleic acids molecular aggregates were successfully applied for low-abundance miRNA detection and imaging in single cells (Fig. 8.11) (Zhang et al. 2016).

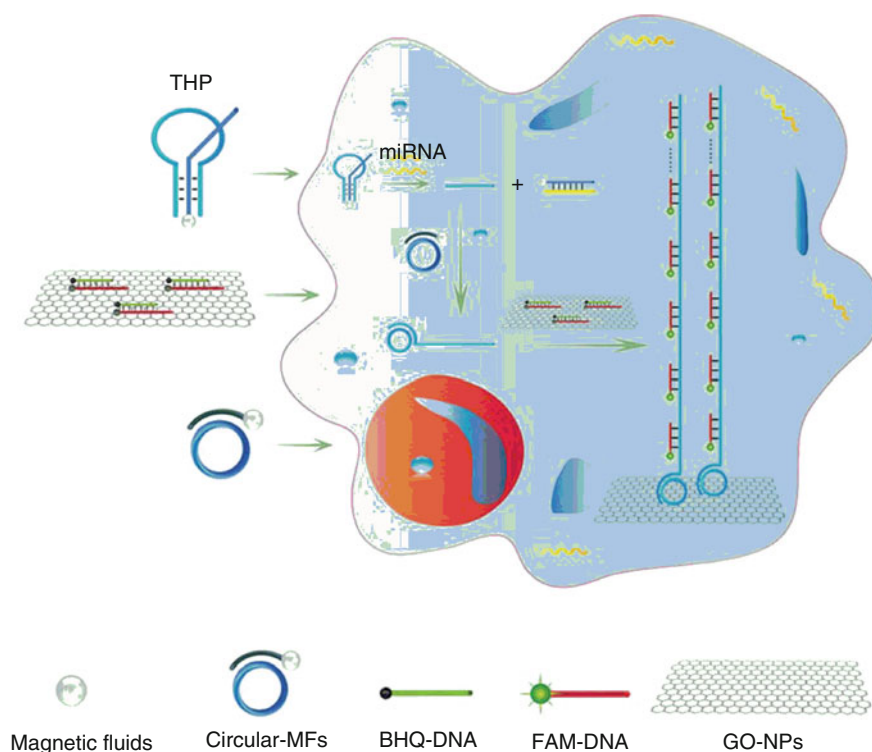


**Fig. 8.11** NAMA-FAM for analyzing target miRNA in single cells based on a functionalized THP probe and RCA. First, the triple-helix probe conjugated onto carboxyl-modified magnetic fluids was ingeniously designed, which could serve as the primer for the rolling circle amplification reaction in single cells. Second, after the THP-CMFs probe entering into cells, miR-21 can combine with the THP-CMFs probe. Meanwhile, the primer DNA1 strands were substituted and released from the triple-helix probe, to activate the intracellular rolling circle amplification reaction at the existence of circular DNA3. Third, GONPs loaded with many fully quenched DHS strands (dsDNA hybridized segmentally by FAM-DNA5 and BHQ-DNA6, abbreviated as DHS) into single cells. *NAMAs* nucleic acids molecular aggregates, *GONPs* graphene oxide nanoplates, *RCA* rolling circle amplification, *THP* triple-helix probe, *CMFs* carboxyl-modified magnetic fluids. Reprinted with permission from reference Zhang et al. (2016)



In addition, Mergeny et al. developed a novel fluorescence biosensing strategy: simple, fast, and sensitive selection of quadruplex-binding ligands result in the formation of an intramolecular G-quadruplex structure that further releases the FAM-labeled signal probe from the surface of graphene oxide, and the fluorescence intensity is recovered.

### Silicon Nanoparticles

Silicon nanoparticles have drawn an excellent attention in recent centuries due to their fascinating physical characteristics, active surface state, unique photoluminescence, and biocompatibility. Fluorescent silicon nanoparticles are having high photoluminescence quantum yield, and low or non-toxicity has pulled an incredible consideration for a heap of optical applications. The use of silicon nanoparticles in sensors benefits from their optical and/or electronic transport characteristics; therefore, controlling the surface chemistry of nanoparticles is a key issue in developing such applications.

Yu and coworkers synthesized highly fluorescent silicon nanoparticles in the presence of sodium citrate by hydrothermal treatment with 3-aminopropyltrimethoxysilane for the detection of mercuric ion. Due to the strong interaction between biothiols and  $\text{Hg}^{2+}$ , only  $\text{Hg}^{2+}$  can clearly quench silicon nanoparticles fluorescence.

Zhao et al. used a label-free silicon quantum dots as new fluorescent probes for copper ions ( $\text{Cu}^{2+}$ ) in a selective and sensitive manner. In their investigation, silicon quantum dots were effectively quenched by  $\text{H}_2\text{O}_2$  from the reaction of ascorbic acid with  $\text{O}_2$ , and hydroxyl radicals from Fenton reaction between  $\text{H}_2\text{O}_2$  and  $\text{Cu}^+$ . The fluorescence is linearly quenched as a function of  $\text{Cu}^{2+}$  concentration ranging from 25 to 600 nM. The detection limit was as low as 8 nM, significantly reduced than that of current approaches (Zhao et al. 2014). The Veinot et al. reported luminescent silicon nanocrystal surface functionalized dodecyl groups with disposable paper-based sensors. This sensor is useful for the detection of nitroaromatic compounds including nitroamine, nitrotoluene, and dinitrotoluene. Paper-based sensors are fabricated in a toluene solution containing silicon nanoparticles through dip-coating filter paper. In 2016, for the determination of Sudan dyes I, a turn-off fluorescent sensor based on hexadecylamine-capped silicon nanoparticles was developed by Girish Kumar et al. The fluorescence of silicon nanoparticles was effectively quenched by Sudan I via an innerfilter effect.

### Nanostructured Polymers

Due to small size and high surface-to-volume ratio, nanostructured polymers have great potential for developing new carriers in drug and gene delivery. The shape, size, assembly, composition, and molecular engineering are key parameters that characterize nanostructured polymers to drive their functions and applications in

different fields. Polymer nanofibers can be produced through various techniques and the most commonly used approach is electrospinning where a charged solution of a polymer when exposed to an opposite high electric field is pulled into long thin nanofibers. A variety of polymer nanofibers have been developed and used for noise and air pollution filtrations. Moreover, polymer nanofibers can also be fabricated with phase change materials that are usually employed for thermal energy storage in construction industry.

However, their potential is still strongly dependent on the development of scaling-up and reliable processing routes. Bottom-up and top-down approaches have been typically reported for material nanotechnologies. A special interest has been focused on the use of amphiphilic block copolymers due to their versatility in allowing different types of nanostructured polymeric materials. A very promising application of polymeric nanostructured materials is in the treatment of several diseases and revolutionizing the diagnosis. These nanomaterials give noteworthy improvement in the nature of human care because of their accuracy and unwavering quality in diagnostics, and improved convenience of frameworks for tissue designing and regenerative drug. In general, polymeric nanostructured materials for biomedical applications ought to have satisfactory properties like huge water solvency or dispersibility to maintain a strategic distance from quick leeway (10–200 nm), and to achieve preferred biodegradability to minimize the side effects.

### **Quantum Dots-Coordinated Metal Ions**

Quantum dots are tiny particles or nanocrystals in the range of 2–10 nm (10–50 atoms) and they exhibit controllable luminescent properties of a semiconducting material. They were found in 1980s for the first time. Quantum dots are highly fluorescent typically consisting of an inorganic semi-conductor core and a shell, as well as a passive layer of organic ligands. Quantum dots have drawn considerable attention due to their super fluorescence characteristics, and different quantum dots have been developed, such as CdTe, CdZnSe, PbS, CdSe/ZnS, and ZnS-SiO<sub>2</sub>.

Recently, DNAzyme-functionalized Quantum dot biosensors are widely used for the determination of Pb<sup>2+</sup> assays, which displayed elevated sensitivity and even reached a detection limit of 7.8 pM (Zhang et al. 2013). The DNAzyme could be activated in the presence of Pb<sup>2+</sup> to cleave the substrate strand into two DNA fragments. Further, the rolling circle amplification generated a lengthy single-stranded DNA with repeating sequence. Similarly, G-quadruplex aptamers have also been used to make quantum dots. Different selective and reproducible G-quadruplex DNAzyme-functionalized quantum dots were developed for the detection of Pb<sup>2+</sup>.

## 8.4 Biosensor Applications in Detection of Biomolecules and Cellular Bioimaging

DNA-based biosensors can be used effectively to provide some genetic, cancer, and infectious diseases with easy, rapid, cost-effective, sensitive, and specific detection. Additionally, they can be used as a platform for diagnosing immune deficiency and for neurological and other diseases.

### 8.4.1 Detection of DNA or RNA

The specific detection of DNA and RNA sequences is pivotal to disease diagnosis and genetic profiling because of their vital role in hybridization reactions and/or signal amplification strategies. Over the years, various methods have been developed for the detection of the specific DNA sequences including luminescence sensing (Chen et al. 2014), optical, mass-sensitive (Yang et al. 2017), and electrochemical methods. Among all the methods, electrochemical methods have attracted a significant attention due to their simple operation, high sensitivity, and cost-efficiency. DNA detection can be directly achieved without PCR protocols using an ultrasensitive DNA assay at low attomol concentrations. In addition, an oligonucleotide-functionalized silver nanoparticle has been developed for the ultrasensitive electrochemical detection of DNA. Hepatitis B virus sequence was used as a sample model for the ultrasensitive detection of DNA, and obtained a detection limit of 5 nM. Moreover, array chips functionalized with Epstein-Barr virus, cytomegalovirus, and Herpes simplex virus have also been used to detect multiplexed DNA. A simple label-free and sensitive protocol was previously employed for the detection of a specific mutation of the COL4A5 gene correlated Alport syndrome, and a single stranded oligonucleotide probe was immobilized by disposable electrochemical printed electrodes.

The development of label-free method for target DNA sequences generally uses non-canonical DNA secondary structures, for example, G-quadruplex-specific luminescent probe with G-quadruplex in conjunction molecule. Wang et al. developed a G-quadruplex-mediated fluorescence for DNA detection using two fluorescent probes porphyrin-*N*-methylmesoporphyrinIX and tetrakis(dicyclohexylguanidino)-zinc-phthalocyanine. The method is capable to detect low concentration ( $3.2 \text{ nmol L}^{-1}$ ) of target DNA and serum-containing samples used for analysis (Fig. 8.12). In addition, Ma et al. demonstrated G-quadruplex-based detection of gene deletion using a cyclometallated iridium(III) complex. This method is based on the formation of a split G-quadruplex from the two split G-quadruplex-forming sequences, and their response for the luminescence emission of the iridium(III) complex (Ma et al. 2012).

In 1996, the first classical “molecular beacon”-based strategy has been reported for the doubly labeled oligonucleotides that become fluorescent upon hybridization

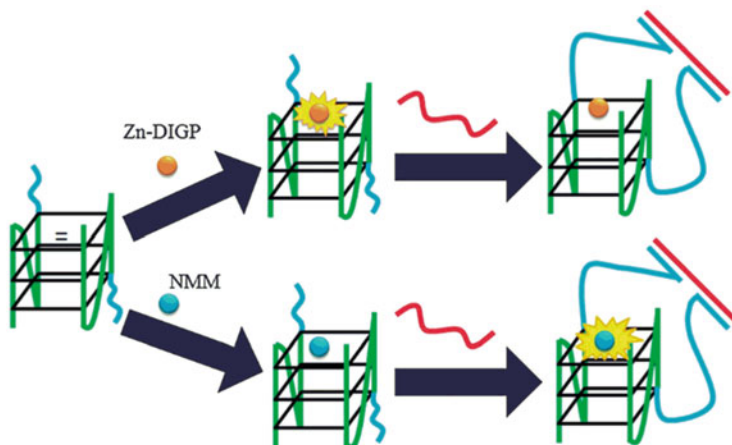


**Fig. 8.12** ssDNA with switch-off/on detection modes using G-quadruplex platform. In the presence of  $K^+$ , a split cMyc forms an associated G-quadruplex-fluorescent dye complex. Sequence-specific DNA hybridization results in reduced fluorescence from Zn-DIGP (pathway A) or increased fluorescence from NMM (pathway B). Zn-DIGP tetrakis(diisopropylguanidino)-zinc-phthalocyanine, NMM N-methylmesoporphyrin IX. Reprinted with permission of Copyright 2011 Springer Nature from reference Wang et al. (2011)

to detect target sequences. Colorimetric-based single strand oligonucleotide modified gold nanoparticles were developed for highly sensitive detection of DNA at lower concentrations (0.086 fM). Gold nanoparticles exhibit long-term stability, when the density of single-stranded DNA on the gold nanoparticle surface is higher than  $34 \text{ pmol cm}^{-2}$  and gives a red color upon high salt concentration.

#### 8.4.2 Detection of Protein or Enzyme

Protein/enzyme detection plays an important role in the biomedical and clinical diagnostic studies. Current protein assays are mostly based on the use of antibodies that are not well suited to fast, sensitive proteins detection and it is not suitable for the amplifying signal. In order to achieve molecular signal amplification, heterogeneous antibody-based assays have been developed by Li et al. (2015).

Aptamer-based protein detection has been demonstrated through several methods using fluorescence, colorimetry, conjugation with electrochemistry, and chemiluminescent techniques. Colorimetric-based simple and cost-effective detection of protein has been developed using target-triggered activation of aptazyme and gold nanoparticles. This strategy was able to detect vascular endothelial growth factor, and the spanning detection is in the range of three orders of

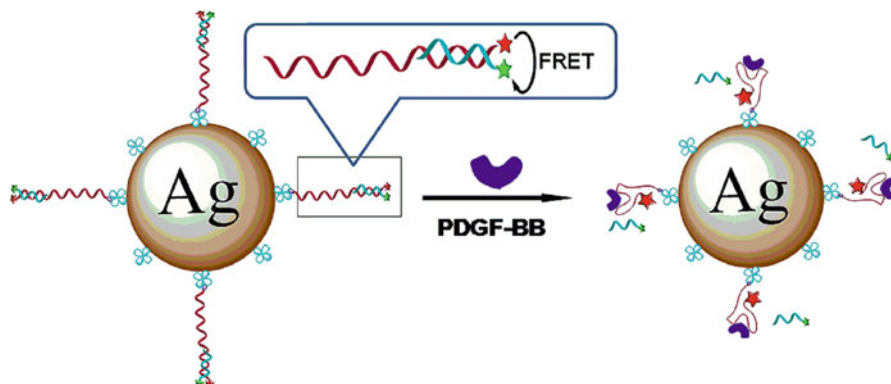


**Fig. 8.13** The detection of Human PDGF-BB. Upon the addition of PDGF-BB, the quencher-carrying strands of the duplex are displaced leading to the disruption of the fluorescence resonance energy transfer effect. As a result, the fluorescent intensity of the fluorophore-aptamer within the proximity of the silver nanoparticle is increased. *PDGF-BB* platelet-derived growth factor-BB, *FRET* fluorescence resonance energy transfer. Reprinted with permission of Copyright 2013 American Chemical Society from reference Xu et al. (2017)

magnitude. The use of gold nanoparticle provides a simple “mix-and-detect” assay for visual detection of target.

In 2013, silver nanoparticle-coupled fluorescence resonance energy transfer sensor has been developed for the detection of human platelet-derived growth factor-BB. Silver nanoparticle-enhanced fluorescence resonance energy transfer sensor, which was synthesized from streptavidin with fluorophore, modified aptamers. Xu et al. was pleased to find that silver nanoparticle-based fluorescence resonance energy transfer sensor provided high fluorescence, sensitivity, and target specificity when compared with that of the gold nanoparticles (Fig. 8.13) (Xu et al. 2017).

Surface Plasmon Resonance is also one of the most powerful tools for the detection of protein. In 2018, functionalized graphene oxide-based immunosensor has been developed for the detection of non-small cell lung carcinoma using cytokeratin 19 in spiked human plasma. This carboxylic acid functionalized graphene oxide surface plasmon resonance sensor is highly sensitive for the detection of CK19 protein. The target protein induces the fluorescence changes through DNA conformational changes using isothermal amplification reactions.

### 8.4.3 Immunosensors

Immunosensors are powerful tools in solid state devices because of their wide applications in environmental monitoring, clinical diagnostics, and food safety.

Immunosensors incorporate into immunochemical reactions with optical, microgravimetric, and electrochemical transducers.

An ultrasensitive label-free electrochemical immunosensor was developed by using nitrogen-doped graphene quantum dots for the detection of carcinoembryonic antigen. The bimetallic nanoparticles Pt-Pd-supported nitrogen-based quantum dots (PtPd/*N*-GQDs) were synthesized by green hydrothermal procedure. In addition, a nitrogen-doped graphene quantum dots (PtPd/*N*-GQDs)-functionalized gold nanoparticles (PtPd/*N*-GQDs@Au) were successfully synthesized through self-assembly approach. These novel nanocomposites have excellent features such as large surface area, conductivity, and good biocompatibility, reflecting their successful application as transducing materials to amplify electrochemical signals.

A novel electrochemical immunosensor using concave gold nanocuboids was used for the detection of antigen-antibody interactions. The redox current response was observed by cyclic voltammetry studies. The formation of antigen-antibody complex between the antibody on the concave gold nanocuboids and IgG antigen leads to decrease in the anodic peak current when model IgG antigens were introduced into the system (Fig. 8.14).

A multiplex surface plasmon resonance-based immunosensor was developed for the detection of paralytic shellfish poisoning, domoic acid, and okadaic acid. The developed surface plasmon resonance immunosensors detected domoic acid and okadaic acid within 13 min, and they can be used as tools for monitoring seawater samples. The superiority of the surface plasmon resonance immunosensor was compared with a traditional indirect enzyme-linked immunosorbent assay in terms of LOD, analysis time, reagent consumption, and operation automation. In 2014, Ying and co-workers developed an optical immunosensor for the detection of aflatoxin B1 at very low concentrations in food materials. Gold nanorods were used as sensing agents in this study which further showed high stability without any stabilizing agent.

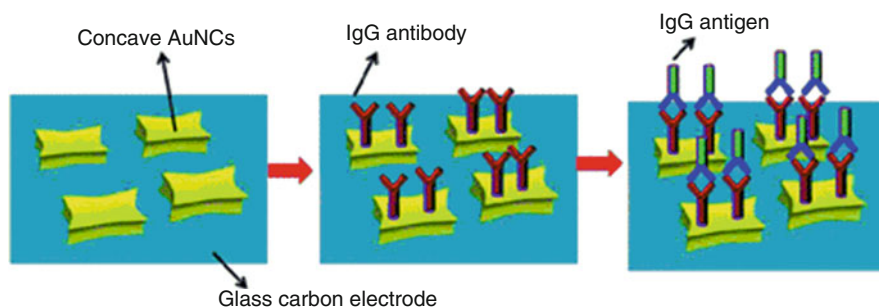


**Fig. 8.14** The formation of antigen-antibody complex between the antibody on the concave gold nanocuboids. Herein, a sandwich-type immunobiosensing approach was adopted. *AuNCs* gold nanocuboids. Reprinted with permission of Copyright 2015 Royal Society of Chemistry from reference Kim et al. (2015)

Zourob et al. in 2018 have reported carbon nanofiber voltammetric immunosensor for sensitive detection of SMN protein. The voltammetric immunosensor utilizes carbon nanofiber-modified screen-printed electrodes functionalized with 4-carboxyphenyl group covalently. Subsequently, SMN antibodies surface were immobilized through carbodiimide hydrochloride /*N*-hydroxysuccinimide.

#### ***8.4.4 Detection in Cancer Diagnosis and Therapy***

The sensitive detection of cancer biomarkers plays an important role in the early diagnosis of cancer, disease stage forecasting, and cancer metastasis. However, these methods required cancer cells lysis with polymerase chain reaction process, which in turn is expensive, difficult, and not suitable for point of care detection. To overcome this polymerase chain reaction process and lysis step, Pang et al. developed a simple and effective method for detecting circulating tumor cells using magnetic nanospheres. The magnetic nanospheres were fabricated by LBL assembly method and further magnetic nanosphere was nano-sized by fast magnetic response. The bio-inspired multivalent DNA was synthesized by a microfluidic surface by rolling circle amplification method. This multivalent DNA efficiently captures the lymphoblast CCRF-CEM cells over monovalent aptamers. Recently, aptamer-modified hydrogel and restriction endonuclease was developed by Wang et al. for the cell catch and release of cancer cells with over the density 1000 cells/mm<sup>2</sup> and hydrogel binding with nonspecific cells. In 2019, Li et al. developed a DNA-oriented shaping strategy to convert the metastasis-associated circulation tumor cells into a dominant signature. Biotin-14-dATP is incorporated into the DNA polymers which in turn are grafted into the CTC subset that over expresses folate receptors, and the linear detection ranges from 5 to 320 cells/cm<sup>2</sup> (Fig. 8.15).

### **8.5 Conclusions**

The biosensor field has undergone rapid growth because of its quick, reliable, mobile, low-cost, highly sensitive, and selective properties. The phosphoramidite method has been illustrated for automated DNA sequencing, allowing the formation of colorimetric and fluorescent nucleic acids. Further, research has begun to extend the fluorescent nucleic acid applications on the living cells. Many functional nucleic acids have attracted considerable attention due to their prevalent molecular recognition for small molecule targets. The negatively charged nucleotides act as substrates for the detection of metal ions. Finally, we discussed the applications of these DNA sensors in detection of various biomolecules, and highlighted a short emphasis on their applications in clinical diagnosis and therapy. Understanding of the

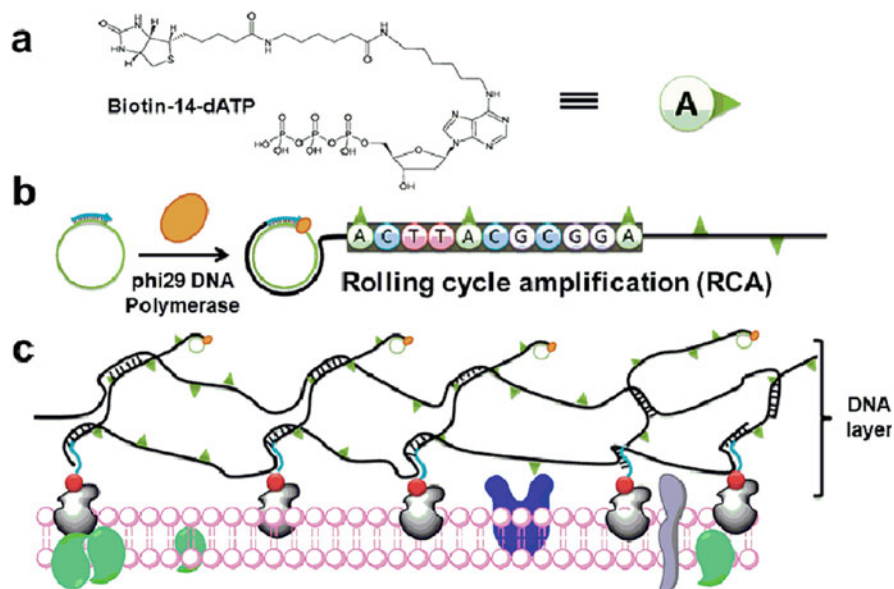


**Fig. 8.15** DNA-oriented shaping to dominate the cell-surface feature. (a) Chemical structure of the biotin-labeled deoxyadenosine triphosphate. (b) Schematic illustration of the DNA rolling cycle amplification, in order to incorporate biotin labels into DNA polymers. (c) Schematic illustration of the rolling cycle amplification at cell surface to synthesize biotin-labeled DNA polymers, thus converting the cell-surface feature into the biotin-DNA signature. Reprinted with permission of Copyright 2019 American Chemical Society from reference Li et al. (2019)

electronic interaction will definitely lead to the construction of effective biosensors that can be used in sensing and imaging. Future research will be directed towards the construction of new conjugated structures that are highly specific to recognized sites.

**Acknowledgements** This work is supported by the Science and Technology Innovation Commission of Shenzhen (JCYJ20170818143131729) and (KQJSCX20180328095517269).

## References

- Adams CJ, Murray JB, Farrow MA, Arnold JRP, Stockley PG (1995) Incorporation of 6-thioguanosine into oligoribonucleotides. *Tetrahedron Lett* 36(30):5421–5424. [https://doi.org/10.1016/0040-4039\(95\)00995-O](https://doi.org/10.1016/0040-4039(95)00995-O)
- Ali MM, Aguirre SD, Lazim H, Li Y (2011) Fluorogenic DNAzyme probes as bacterial indicators. *Angew Chem Int Ed* 50(16):3751–3754, S3751/3751-S3751/3759. <https://doi.org/10.1002/anie.201100477>
- Asanuma H, Toda T, Murayama K, Liang X, Kashida H (2010) Unexpectedly stable artificial duplex from flexible acyclic threoninol. *J Am Chem Soc* 132(42):14702–14703. <https://doi.org/10.1021/ja105539u>



- Berndl S, Herzig N, Kele P, Lachmann D, Li X, Wolfbeis OS, Wagenknecht H-A (2009) Comparison of a nucleosidic vs. non-nucleosidic postsynthetic “click” modification of DNA with base-labile fluorescent probes. *Bioconjug Chem* 20(3):558–564. <https://doi.org/10.1021/bc8004864>
- Blaszczyk A (2018) Strategies to improve the performance of metal-free dye-sensitized solar cells. *Dyes Pigments* 149:707–718. <https://doi.org/10.1016/j.dyepig.2017.11.045>
- Bonanni A, Pumera M, Miyahara Y (2010) Rapid, sensitive, and label-free impedimetric detection of a single-nucleotide polymorphism correlated to kidney disease. *Anal Chem* 82(9):3772–3779. <https://doi.org/10.1021/ac100165q>
- Burns DD, Teppang KL, Lee RW, Lokensgard ME, Purse BW (2017) Fluorescence turn-on sensing of DNA duplex formation by a tricyclic cytidine analogue. *J Am Chem Soc* 139(4):1372–1375. <https://doi.org/10.1021/jacs.6b10410>
- Carella A, Borbone F, Centore R (2018) Research progress on photosensitizers for DSSC. *Front Chem* 6:481. <https://doi.org/10.3389/fchem.2018.00481>
- Chen Y, Yan S, Yuan L, Zhou Y, Song Y, Xiao H, Weng X, Zhou X (2014) Nonlinear optical dye TSQ1 as an efficiently selective fluorescent probe for G-quadruplex DNA. *Org Chem Front* 1(3):267–270. <https://doi.org/10.1039/c3qo00048f>
- Chien M-P, Thompson MP, Gianneschi NC (2011) DNA-nanoparticle micelles as supramolecular fluorogenic substrates enabling catalytic signal amplification and detection by DNzyme probes. *Chem Commun* 47(1):167–169. <https://doi.org/10.1039/C0CC02291H>
- Chiu N-F, Lin T-L, Kuo C-T (2018) Highly sensitive carboxyl-graphene oxide-based surface plasmon resonance immunosensor for the detection of lung cancer for cytokeratin 19 biomarker in human plasma. *Sensors Actuators B Chem* 265:264–272. <https://doi.org/10.1016/j.snb.2018.03.070>
- Clark LC Jr, Lyons C (1962) Electrode systems for continuous monitoring in cardiovascular surgery. *Ann NY Acad Sci* 102(Art 1):29–45. <https://doi.org/10.1111/j.1749-6632.1962.tb13623.x>
- Colas F, Crassous M-P, Laurent S, Litaker RW, Rinnert E, Le Gall E, Lunven M, Delauney L, Compere C (2016) A surface plasmon resonance system for the underwater detection of domoic acid. *Limnol Oceanogr Methods* 14(7):456–465. <https://doi.org/10.1002/lom3.10104>
- Cutler JJ, Zheng D, Xu X, Giljohann DA, Mirkin CA (2010) Polyvalent oligonucleotide iron oxide nanoparticle “click” conjugates. *Nano Lett* 10(4):1477–1480. <https://doi.org/10.1021/nl100477m>
- Day HA, Pavlou P, Waller ZAE (2014) *i*-motif DNA: structure, stability and targeting with ligands. *Bioorg Med Chem* 22(16):4407–4418. <https://doi.org/10.1016/j.bmc.2014.05.047>
- Dikin DA, Stankovich S, Zimney EJ, Piner RD, Dommett GHB, Evmenenko G, Nguyen ST, Ruoff RS (2007) Preparation and characterization of graphene oxide paper. *Nature* 448(7152):457–460. <https://doi.org/10.1038/nature06016>
- Eissa S, Alshehri N, Abdel Rahman AM, Dasouki M, Abu Salah KM, Zourob M (2018) Electrochemical immunosensors for the detection of survival motor neuron (SMN) protein using different carbon nanomaterials-modified electrodes. *Biosens Bioelectron* 101:282–289. <https://doi.org/10.1016/j.bios.2017.10.015>
- Ellington AD, Szostak JW (1990) In vitro selection of RNA molecules that bind specific ligands. *Nature* 346(6287):818–822. <https://doi.org/10.1038/346818a0>
- El-Sagheer AH, Brown T (2010) Click chemistry with DNA. *Chem Soc Rev* 39(4):1388–1405. <https://doi.org/10.1039/b901971p>
- Fouz MF, Mukumoto K, Averick S, Molinar O, McCartney BM, Matyjaszewski K, Armitage BA, Das SR (2015) Bright fluorescent Nanotags from bottlebrush polymers with DNA-tipped bristles. *ACS Cent Sci* 1(8):431–438. <https://doi.org/10.1021/acscentsci.5b00259>
- Fratoddi I, Bearzotti A, Venditti I, Cametti C, Russo MV (2016) Role of nanostructured polymers on the improvement of electrical response-based relative humidity sensors. *Sensors Actuators B Chem* 225:96–108. <https://doi.org/10.1016/j.snb.2015.11.001>

- Froehler BC, Ricca DJ (1992) Triple-helix formation by oligodeoxynucleotides containing the carbocyclic analogues of thymidine and 5-methyl-2'-deoxycytidine. *J Am Chem Soc* 114 (21):8320–8322. <https://doi.org/10.1021/ja00047a071>
- Gao T, Li L, Chen T, Shi L, Yang Y, Li G (2019) DNA-oriented shaping of cell features for the detection of rare disseminated tumor cells. *Anal Chem* 91(1):1126–1132. <https://doi.org/10.1021/acs.analchem.8b04783>
- Gierlich J, Burley GA, Gramlich PME, Hammond DM, Carell T (2006) Click chemistry as a reliable method for the high-density postsynthetic functionalization of alkyne-modified DNA. *Org Lett* 8(17):3639–3642. <https://doi.org/10.1021/ol0610946>
- Gogoi K, Mane MV, Kunte SS, Kumar VA (2007) A versatile method for the preparation of conjugates of peptides with DNA/PNA/analog by employing chemo-selective click reaction in water. *Nucleic Acids Res* 35(21):e139/131–e139/137. <https://doi.org/10.1093/nar/gkm935>
- Gokarna A, Jin L-H, Hwang JS, Cho Y-H, Lim YT, Chung BH, Youn SH, Choi DS, Lim JH (2008) Quantum dot-based protein micro- and nanoarrays for detection of prostate cancer biomarkers. *Proteomics* 8(9):1809–1818. <https://doi.org/10.1002/pmic.200701072>
- Gong L, Zhao Z, Lv Y-F, Huan S-Y, Fu T, Zhang X-B, Shen G-L, Yu R-Q (2015) DNAzyme-based biosensors and nanodevices. *Chem Commun* 51(6):979–995. <https://doi.org/10.1039/C4CC06855F>
- Griffith MC, Risen LM, Greig MJ, Lesnik EA, Sprankle KG, Griffey RH, Kiely JS, Freier SM (1995) Single and Bis peptide nucleic acids as Triplexing agents: binding and stoichiometry. *J Am Chem Soc* 117(2):831–832. <https://doi.org/10.1021/ja00107a033>
- Guo J-H, Kong D-M, Shen H-X (2010) Design of a fluorescent DNA IMPLICATION logic gate and detection of Ag<sup>+</sup> and cysteine with triphenylmethane dye/G-quadruplex complexes. *Biosens Bioelectron* 26(2):327–332. <https://doi.org/10.1016/j.bios.2010.08.020>
- Guo X, Ingale SA, Yang H, He Y, Seela F (2017) MercuryII-mediated base pairs in DNA: unexpected behavior in metal ion binding and duplex stability induced by 2'-deoxyuridine 5-substituents. *Org Biomol Chem* 15(4):870–883. <https://doi.org/10.1039/C6OB02560A>
- Gutsmiedl K, Fazio D, Carell T (2010) High-density DNA functionalization by a combination of Cu-catalyzed and Cu-free click chemistry. *Chem Eur J* 16(23):6877–6883. <https://doi.org/10.1002/chem.201000363>
- Hancock EL, Connolly BA, Walker RT (1993) Synthesis and properties of oligodeoxyribonucleotides containing the analog 2'-deoxy-4'-thiothymidine. *Nucleic Acids Res* 21(15):3485–3491. <https://doi.org/10.1093/nar/21.15.3485>
- Hao Y, Guo Q, Wu H, Guo L, Zhong L, Wang J, Lin T, Fu F, Chen G (2014) Amplified colorimetric detection of mercuric ions through autonomous assembly of G-quadruplex DNAzyme nanowires. *Biosens Bioelectron* 52:261–264. <https://doi.org/10.1016/j.bios.2013.08.034>
- Hara RI, Saito T, Kogure T, Hamamura Y, Uchiyama N, Nukaga Y, Iwamoto N, Wada T (2019) Stereocontrolled synthesis of Boranophosphate DNA by an Oxazaphospholidine approach and evaluation of its properties. *J Org Chem* 84(12):7971–7983. <https://doi.org/10.1021/acs.joc.9b00658>
- He H-Z, Chan DS-H, Leung C-H, Ma D-L (2012) A highly selective G-quadruplex-based luminescent switch-on probe for the detection of gene deletion. *Chem Commun* 48(76):9462–9464. <https://doi.org/10.1039/c2cc32253f>
- He H-Z, Leung K-H, Yang H, Chan S-HD, Leung C-H, Zhou J, Bourdoncle A, Mergny J-L, Ma D-L (2013) Label-free detection of sub-nanomolar lead(II) ions in aqueous solution using a metal-based luminescent switch-on probe. *Biosens Bioelectron* 41:871–874. <https://doi.org/10.1016/j.bios.2012.08.060>
- Hendrix C, Rosemeyer H, Verheggen I, Seela F, Van Aerschot A, Herdewijn P (1997) 1',5'-Anhydrohexitol oligonucleotides: synthesis, base pairing and recognition by regular oligodeoxyribonucleotides and oligoribonucleotides. *Chem Eur J* 3(1):110–120. <https://doi.org/10.1002/chem.19970030118>

- Huang C-C, Chang H-T (2007) Parameters for selective colorimetric sensing of mercury(II) in aqueous solutions using mercaptopropionic acid-modified gold nanoparticles. *Chem Commun* 12:1215–1217. <https://doi.org/10.1039/B615383F>
- Huang Y, Kannan P, Zhang L, Chen T, Kim D-H (2015) Concave gold nanoparticle-based highly sensitive electrochemical IgG immunobiosensor for the detection of antibody-antigen interactions. *RSC Adv* 5(72):58478–58484. <https://doi.org/10.1039/C5RA10990F>
- Iwamoto N, Butler DCD, Svrikapa N, Mohapatra S, Zlatev I, Sah DWY, Meena, Standley SM, Lu G, Apponi LH, Frank-Kamenetsky M, Zhang JJ, Vargeese C, Verdine GL (2017) Control of phosphorothioate stereochemistry substantially increases the efficacy of antisense oligonucleotides. *Nat Biotechnol* 35(9):845–851. <https://doi.org/10.1038/nbt.3948>
- Jarvis TC, Wincott FE, Alby LJ, McSwiggen JA, Beigelman L, Gustofson J, DiRenzo A, Levy K, Arthur M (1996) Optimizing the cell efficacy of synthetic ribozymes. Site selection and chemical modifications of ribozymes targeting the proto-oncogene c-myc. *J Biol Chem* 271(46):29107–29112. <https://doi.org/10.1074/jbc.271.46.29107>
- Jiang R, Liu N, Gao S, Mamat X, Su Y, Wagberg T, Li Y, Hu X, Hu G (2018) A facile electrochemical sensor based on PyTS-CNTs for simultaneous determination of cadmium and lead ions. *Sensors* 18(5):1567/1561–1567/1513. <https://doi.org/10.3390/s18051567>
- Jose AR, Sivasankaran U, Menon S, Kumar KG (2016) A silicon nanoparticle based turn off fluorescent sensor for Sudan I. *Anal Methods* 8(28):5701–5706. <https://doi.org/10.1039/C6AY01125J>
- Kashida H, Murayama K, Toda T, Asanuma H (2011) Control of the chirality and helicity of oligomers of serinol nucleic acid (SNA) by sequence design. *Angew Chem Int Ed* 50(6):1285–1288, S1285/1281–S1285/1211. <https://doi.org/10.1002/anie.201006498>
- Kashida H, Hattori Y, Tazoe K, Inoue T, Nishikawa K, Ishii K, Uchiyama S, Yamashita H, Abe M, Kamiya Y, Asanuma H (2018) Bifacial Nucleobases for Hexaplex formation in aqueous solution. *J Am Chem Soc* 140(27):8456–8462. <https://doi.org/10.1021/jacs.8b02807>
- Kim Y, Johnson RC, Hupp JT (2001) Gold nanoparticle-based sensing of “Spectroscopically silent” heavy metal ions. *Nano Lett* 1(4):165–167. <https://doi.org/10.1021/nl0100116>
- Knouse KW, deGruyter JN, Schmidt MA, Zheng B, Vantourout JC, Kingston C, Mercer SE, McDonald IM, Olson RE, Zhu Y, Hang C, Zhu J, Yuan C, Wang Q, Park P, Eastgate MD, Baran PS (2018) Unlocking P(V): reagents for chiral phosphorothioate synthesis. *Science* 361(6408):1234–1238. <https://doi.org/10.1126/science.aau3369>
- Kong D-M, Guo J-H, Yang W, Ma Y-E, Shen H-X (2009) Crystal violet-G-quadruplex complexes as fluorescent sensors for homogeneous detection of potassium ion. *Biosens Bioelectron* 25(1):88–93. <https://doi.org/10.1016/j.bios.2009.06.002>
- Kong D-M, Cai L-L, Shen H-X (2010) Quantitative detection of Ag<sup>+</sup> and cysteine using G-quadruplex-hemin DNAszymes. *Analyst* 135(6):1253–1258. <https://doi.org/10.1039/b925168e>
- Kool ET (2002) Active site tightness and substrate fit in DNA replication. *Annu Rev Biochem* 71:191–219. <https://doi.org/10.1146/annurev.biochem.71.110601.135453>
- Krishna H, Caruthers MH (2012) Alkynyl Phosphonate DNA: a versatile clickable backbone for DNA-based biological applications. *J Am Chem Soc* 134(28):11618–11631. <https://doi.org/10.1021/ja3026714>
- Kumar R, El-Sagheer A, Tumpance J, Lincoln P, Wilhelmsson LM, Brown T (2007) Template-directed oligonucleotide strand ligation, covalent intramolecular DNA circularization and catenation using click chemistry. *J Am Chem Soc* 129(21):6859–6864. <https://doi.org/10.1021/ja070273v>
- Kupryushkin MS, Pyshnyi DV, Stetsenko DA (2014) Phosphoryl guanidines: a new type of nucleic acid analogues. *Acta Nat* 6(4):116–118
- Lan X, Masala S, Sargent EH (2014) Charge-extraction strategies for colloidal quantum dot photovoltaics. *Nat Mater* 13(3):233–240. <https://doi.org/10.1038/nmat3816>
- Laura P, Debora P, Luigi T, Luca V, José MK (2014) Processing of nanostructured polymers and advanced polymeric based nanocomposites. *Mater Sci Eng R Rep* 85:1–46. <https://doi.org/10.1016/j.mser.2014.08.002>

- Leung K-H, He H-Z, He B, Zhong H-J, Lin S, Wang Y-T, Ma D-L, Leung C-H (2015) Label-free luminescence switch-on detection of hepatitis C virus NS3 helicase activity using a G-quadruplex-selective probe. *Chem Sci* 6(4):2166–2171. <https://doi.org/10.1039/C4SC03319A>
- Levina AS, Repkova MN, Chelobanov BP, Stetsenko DA, Zarytova VF, Levina AS, Repkova MN, Chelobanov BP, Zarytova VF, Bessudnova EV, Mazurkova NA (2017) Impact of delivery method on antiviral activity of Phosphodiester, Phosphorothioate, and Phosphoryl guanidine oligonucleotides in MDCK cells infected with H5N1 bird flu virus. *Mol Biol (Mosk)* 51(4):717–723
- Li J, Lu Y (2000) A highly sensitive and selective catalytic DNA biosensor for lead ions. *J Am Chem Soc* 122(42):10466–10467. <https://doi.org/10.1021/ja0021316>
- Li T, Dong S, Wang E (2009) Label-free colorimetric detection of aqueous mercury ion ( $Hg^{2+}$ ) using  $Hg^{2+}$ -modulated G-quadruplex-based DNAzymes. *Anal Chem* 81(6):2144–2149. <https://doi.org/10.1021/ac900188y>
- Li H, Sun Z, Zhong W, Hao N, Xu D, Chen H-Y (2010) Ultrasensitive electrochemical detection for DNA arrays based on silver nanoparticle aggregates. *Anal Chem* 82(13):5477–5483. <https://doi.org/10.1021/ac101193e>
- Li J, Fu H-E, Wu L-J, Zheng A-X, Chen G-N, Yang H-H (2012) General colorimetric detection of proteins and small molecules based on cyclic enzymatic signal amplification and hairpin aptamer probe. *Anal Chem* 84(12):5309–5315. <https://doi.org/10.1021/ac3006186>
- Li H, Wang M, Wang C, Li W, Qiang W, Xu D (2013) Silver nanoparticle-enhanced fluorescence resonance energy transfer sensor for human platelet-derived growth factor-BB detection. *Anal Chem* 85(9):4492–4499. <https://doi.org/10.1021/ac400047d>
- Li Y, Miao X, Ling L (2015) Triplex DNA: a new platform for polymerase chain reaction - based biosensor. *Sci Rep* 5:13010. <https://doi.org/10.1038/srep13010>
- Liang J, Chen Z, Guo L, Li L (2011) Electrochemical sensing of L-histidine based on structure-switching DNAzymes and gold nanoparticle-graphene nanosheet composites. *Chem Commun* 47(19):5476–5478. <https://doi.org/10.1039/c1cc10965k>
- Limauro S, Benseler F, McLaughlin LW (1994) 1-Methylguanosine substitutions of the conserved guanosine residues inactivate the hammerhead ribozyme. *Bioorg Med Chem Lett* 4(18):2189–2192. [https://doi.org/10.1016/S0960-894X\(00\)80069-4](https://doi.org/10.1016/S0960-894X(00)80069-4)
- Lin S-Y, Wu S-H, Chen C-H (2006) A simple strategy for prompt visual sensing by gold nanoparticles: general applications of interparticle hydrogen bonds. *Angew Chem Int Ed* 45(30):4948–4951. <https://doi.org/10.1002/anie.200600771>
- Liu J, Lu Y (2003) A colorimetric lead biosensor using DNAzyme-directed assembly of gold nanoparticles. *J Am Chem Soc* 125(22):6642–6643. <https://doi.org/10.1021/ja034775u>
- Liu J, Lu Y (2005) Stimuli-responsive disassembly of nanoparticle aggregates for light-up colorimetric sensing. *J Am Chem Soc* 127(36):12677–12683. <https://doi.org/10.1021/ja053567u>
- Liu J, Rinzler AG, Dai H, Hafner JH, Bradley RK, Boul PJ, Lu A, Iverson T, Shelimov K, Huffman CB, Rodriguez-Macias F, Shon Y-S, Lee TR, Colbert DT, Smalley RE (1998) Fullerene pipes. *Science* 280(5367):1253–1256. <https://doi.org/10.1126/science.280.5367.1253>
- Liu C, Dumbre SG, Pannecouque C, Huang C, Ptak RG, Murray MG, De Jonghe S, Herdewijn P (2016) Amidate Prodrugs of Deoxythreosyl nucleoside Phosphonates as dual inhibitors of HIV and HBV replication. *J Med Chem* 59(20):9513–9531. <https://doi.org/10.1021/acs.jmedchem.6b01260>
- Lu L, Shiu-Hin Chan D, Kwong DWJ, He H-Z, Leung C-H, Ma D-L (2014) Detection of nicking endonuclease activity using a G-quadruplex-selective luminescent switch-on probe. *Chem Sci* 5(12):4561–4568. <https://doi.org/10.1039/C4SC02032D>
- Lu L, Wang M, Ma D-L, Liu L-J, Leung C-H, Ma D-L (2015) Label-free luminescent switch-on probe for Ochratoxin A detection using a G-Quadruplex-selective iridium(III) complex. *ACS Appl Mater Interfaces* 7(15):8313–8318
- Lu L, Wang W, Wang M, Kang T-S, Lu J-J, Chen X-P, Han Q-B, Leung C-H, Ma D-L (2016) A luminescent G-quadruplex-selective iridium(III) complex for the label-free detection of lysozyme. *J Mater Chem B* 4(14):2407–2411. <https://doi.org/10.1039/C6TB00426A>

- Lu L, Su H, Li F, Liu Q (2018) Development of a luminescent DinuclearIr(III) complex for ultrasensitive determination of pesticides. *Anal Chem* 90(19):11716–11722
- Ma D-L, He H-Z, Ma VP-Y, Chan DS-H, Leung K-H, Zhong H-J, Lu L, Mergny J-L, Leung C-H (2012) Label-free sensing of pH and silver nanoparticles using an “OR” logic gate. *Anal Chim Acta* 733:78–83. <https://doi.org/10.1016/j.aca.2012.04.041>
- Magerusan L, Socaci C, Coros M, Pogacean F, Rosu MC, Gergely S, Pruneanu S, Leostean C, Pana IO (2017) Electrochemical platform based on nitrogen-doped graphene/chitosan nanocomposite for selective Pb<sup>2+</sup> detection. *Nanotechnology* 28(11):114001/114001–114001/114012. <https://doi.org/10.1088/1361-6528/aa56cb>
- Massey M, Ancona MG, Medintz IL, Algar WR (2015) Time-gated DNA photonic wires with forster resonance energy transfer cascades initiated by a luminescent terbium donor. *ACS Photonics* 2(5):639–652. <https://doi.org/10.1021/acsp Photonics.5b00052>
- Mendez-Gonzalez D, Laurenti M, Lopez-Cabarcos E, Rubio-Retama J, Melle S, Calderon OG, Cabrera-Granado E, Egatz-Gomez A, Diaz E (2019) Control of upconversion luminescence by gold nanoparticle size: from quenching to enhancement. *Nanoscale* 11(29):13832–13844
- Michalet X, Pinaud FF, Bentolila LA, Tsay JM, Doose S, Li JJ, Sundaresan G, Wu AM, Gambhir SS, Weiss S (2005) Quantum dots for live cells, in vivo imaging, and diagnostics. *Science* 307(5709):538–544. <https://doi.org/10.1126/science.1104274>
- Mirkin CA, Letsinger RL, Mucic RC, Storhoff JJ (1996) A DNA-based method for rationally assembling nanoparticles into macroscopic materials. *Nature* 382(6592):607–609. <https://doi.org/10.1038/382607a0>
- Mochi F, Burratti L, Fratoddi I, Venditti I, Battocchio C, Carlini L, Iucci G, Casalboni M, De Matteis F, Casciardi S, Nappini S, Pis I, Proposito P (2018) Plasmonic sensor based on interaction between silver nanoparticles and Ni<sup>2+</sup> or Co<sup>2+</sup> in water. *Nano* 8(7):488/481–488/414. <https://doi.org/10.3390/nano8070488>
- Mohammed M-I, Desmulliez M (2011) Lab-on-a-chip based immunosensor principles and technologies for the detection of cardiac biomarkers: a review. *Lab Chip* 11(4):569–595. <https://doi.org/10.1039/C0LC00204F>
- Murchie A, Lilley D (1994) Tetraplex folding of telomere sequences and the inclusion of adenine bases. *EMBO J* 13(4):993–1001. <https://doi.org/10.1002/j.1460-2075.1994.tb06344.x>
- Nagrath S, Sequist LV, Maheswaran S, Bell DW, Irimia D, Ullkus L, Smith MR, Kwak EL, Digumarthy S, Muzikansky A, Ryan P, Balis UJ, Tompkins RG, Haber DA, Toner M (2007) Isolation of rare circulating tumour cells in cancer patients by microchip technology. *Nature* 450(7173):1235–1239. <https://doi.org/10.1038/nature06385>
- Nesterova IV, Nesterov EE (2014) Rational design of highly responsive pH sensors based on DNA *i*-Motif. *J Am Chem Soc* 136(25):8843–8846. <https://doi.org/10.1021/ja501859w>
- Nicewicz DA, Nguyen TM (2014) Recent applications of organic dyes as photoredox catalysts in organic synthesis. *ACS Catal* 4(1):355–360. <https://doi.org/10.1021/cs400956a>
- Nielsen PE, Egholm M, Berg RH, Buchardt O (1991) Sequence-selective recognition of DNA by strand displacement with a thymine-substituted polyamide. *Science* 254(5037):1497–1500. <https://doi.org/10.1126/science.1962210>
- Obika S, Nanbu D, Hari Y, Morio K-I, In Y, Ishida T, Imanishi T (1997) Synthesis of 2'-O,4'-C-methyleneuridine and -cytidine. Novel bicyclic nucleosides having a fixed C3'-endo sugar puckering. *Tetrahedron Lett* 38(50):8735–8738. [https://doi.org/10.1016/S0040-4039\(97\)10322-7](https://doi.org/10.1016/S0040-4039(97)10322-7)
- Oh BN, Park S, Ren J, Jang YJ, Kim SK, Kim J (2011) Label-free emission assay of mercuric ions using DNA duplexes of poly(dT). *Dalton Trans* 40(24):6494–6499. <https://doi.org/10.1039/c1dt10083a>
- Okamoto A, Tainaka K, Saito I (2003) Clear distinction of purine bases on the complementary strand by a fluorescence change of a novel fluorescent nucleoside. *J Am Chem Soc* 125(17):4972–4973. <https://doi.org/10.1021/ja034090u>

- Olsen DB, Benseler F, Aurup H, Pieken WA, Eckstein F (1991) Study of a hammerhead ribozyme containing 2'-modified adenosine residues. *Biochemistry* 30(40):9735–9741. <https://doi.org/10.1021/bi00104a024>
- Paolella G, Sproat BS, Lamond AI (1992) Nuclease resistant ribozymes with high catalytic activity. *EMBO J* 11(5):1913–1919. <https://doi.org/10.1002/j.1460-2075.1992.tb05244.x>
- Passow KT, Harki DA (2018) 4-Cyanoindole-2'-deoxyribonucleoside (4CIN): a universal fluorescent nucleoside analogue. *Org Lett* 20(14):4310–4313. <https://doi.org/10.1021/acs.orglett.8b01746>
- Pieken WA, Olsen DB, Benseler F, Aurup H, Eckstein F (1991) Kinetic characterization of ribonuclease-resistant 2'-modified hammerhead ribozymes. *Science* 253(5017):314–317. <https://doi.org/10.1126/science.1857967>
- Pitre SP, McTiernan CD, Ismaili H, Scaiano JC (2013) Mechanistic insights and kinetic analysis for the oxidative hydroxylation of arylboronic acids by visible light photoredox catalysis: a metal-free alternative. *J Am Chem Soc* 135(36):13286–13289. <https://doi.org/10.1021/ja406311g>
- Qin H, Ren J, Wang J, Luedtke NW, Wang E (2010a) G-Quadruplex-modulated fluorescence detection of potassium in the presence of a 3500-fold excess of sodium ions. *Anal Chem* 82(19):8356–8360. <https://doi.org/10.1021/ac101894b>
- Qin WJ, Yim OS, Lai PS, Yung L-YL (2010) Dimeric gold nanoparticle assembly for detection and discrimination of single nucleotide mutation in Duchenne muscular dystrophy. *Biosens Bioelectron* 25(9):2021–2025. <https://doi.org/10.1016/j.bios.2010.01.028>
- Ramasamy KS, Seifert W (1996) Amino acid nucleic acids: synthesis and hybridization properties of a novel class of antisense oligonucleotides. *Bioorg Med Chem Lett* 6(15):1799–1804. [https://doi.org/10.1016/0960-894X\(96\)00320-4](https://doi.org/10.1016/0960-894X(96)00320-4)
- Rejman D, Snasel J, Liboska R, Tocik Z, Paces O, Kralikova S, Rinnova M, Kois P, Rosenberg I (2001) Oligonucleotides with isopolar phosphonate internucleotide linkage: a new perspective for antisense compounds? *Nucleosides Nucleotides Nucleic Acids* 20(4–7):819–823. <https://doi.org/10.1081/NCN-100002437>
- Ren J, Qin H, Wang J, Luedtke NW, Wang E, Wang J (2011) Label-free detection of nucleic acids by turn-on and turn-off G-quadruplex-mediated fluorescence. *Anal Bioanal Chem* 399(8):2763–2770. <https://doi.org/10.1007/s00216-011-4669-0>
- Satpathi S, Sappati S, Das K, Hazra P (2019) Structural characteristics requisite for the ligand-based selective detection of i-motif DNA. *Org Biomol Chem* 17(21):5392–5399. <https://doi.org/10.1039/c9ob01020c>
- Scharer OD, Kawate T, Gallinari P, Jiricny J, Verdine GL (1997) Investigation of the mechanisms of DNA binding of the human G/T glycosylase using designed inhibitors. *Proc Natl Acad Sci* 94(10):4878–4883. <https://doi.org/10.1073/pnas.94.10.4878>
- Schroeder AS, Steinbacher J, Steigenberger B, Gnerlich FA, Schiesser S, Pfaffeneder T, Carell T (2014) Synthesis of a DNA promoter segment containing all four epigenetic nucleosides: 5-methyl-, 5-hydroxymethyl-, 5-formyl-, and 5-carboxy-2'-deoxycytidine. *Angew Chem Int Ed* 53(1):315–318. <https://doi.org/10.1002/anie.201308469>
- Seela F, Kehne A (1985) Oligomers with alternating thymidine and 2'-deoxytubercidin: duplex stabilization by a 7-deazapurine base. *Biochemistry* 24(26):7556–7561. <https://doi.org/10.1021/bi00347a008>
- Seela F, Sirivolu VR (2006) DNA containing side chains with terminal triple bonds: base-pair stability and functionalization of alkynylated pyrimidines and 7-deazapurines. *Chem Biodivers* 3(5):509–514. <https://doi.org/10.1002/cbdv.200690054>
- Seela F, Xiong H, Leonard P, Budow S (2009) 8-Aza-7-deazaguanine nucleosides and oligonucleotides with octadiynyl side chains: synthesis, functionalization by the azide-alkyne 'click' reaction and nucleobase specific fluorescence quenching of coumarin dye conjugates. *Org Biomol Chem* 7(7):1374–1387. <https://doi.org/10.1039/b822041g>
- Sergueev DS, Shaw BR (1998) H-Phosphonate approach for solid-phase synthesis of Oligodeoxyribonucleoside Boranophosphates and their characterization. *J Am Chem Soc* 120(37):9417–9427. <https://doi.org/10.1021/JA9814927>

- Sheng W, Chen T, Tan W, Fan ZH (2013) Multivalent DNA nanospheres for enhanced capture of cancer cells in microfluidic devices. *ACS Nano* 7(8):7067–7076. <https://doi.org/10.1021/nn4023747>
- Shi Y, Sun H, Xiang J, Yu L, Yang Q, Li Q, Guan A, Tang Y (2015) *i*-Motif-modulated fluorescence detection of silver(I) with an ultrahigh specificity. *Anal Chim Acta* 857:79–84. <https://doi.org/10.1016/j.aca.2014.12.002>
- Si H, Sheng R, Li Q, Feng J, Li L, Tang B (2018) Highly sensitive fluorescence imaging of Zn<sup>2+</sup> and Cu<sup>2+</sup> in living cells with signal amplification based on functional DNA self-assembly. *Anal Chem* 90(15):8785–8792. <https://doi.org/10.1021/acs.analchem.7b05268>
- Song J, Li Z, Cheng Y, Liu C (2010) Self-aggregation of oligonucleotide-functionalized gold nanoparticles and its applications for highly sensitive detection of DNA. *Chem Commun* 46(30):5548–5550. <https://doi.org/10.1039/c0cc00308e>
- Stasiak N, Kukula-Koch W, Glowniak K (2014) Modern industrial and pharmacological applications of indigo dye and its derivatives – a review. *Acta Pol Pharm* 71(2):215–221. 217 pp
- Sun HB, Kang JM, Wang QW, Liu QR, Zhang XJ (2019) Dual signal amplification by eATRP and DNA templated silver nanoparticles for ultrasensitive electrochemical detection of nucleic Acids. *ACS Appl Mater Interfaces*. Just Accepted Manuscript. <https://doi.org/10.1021/acsami.9b08037>
- Tang S, Tong P, Li H, Tang J, Zhang L (2013) Ultrasensitive electrochemical detection of Pb<sup>2+</sup> based on rolling circle amplification and quantum dots tagging. *Biosens Bioelectron* 42:608–611. <https://doi.org/10.1016/j.bios.2012.10.073>
- Tang L, Wang Y, Li J (2015) The graphene/nucleic acid nanobiointerface. *Chem Soc Rev* 44(19):6954–6980. <https://doi.org/10.1039/C4CS00519H>
- Tang Y, Li J, Guo Q, Nie G (2019) An ultrasensitive electrochemiluminescence assay for Hg<sup>2+</sup> through graphene quantum dots and poly(5-formylindole) nanocomposite. *Sensors Actuators B Chem* 282:824–830. <https://doi.org/10.1016/j.snb.2018.11.151>
- Thompson DG, Enright A, Faulds K, Smith WE, Graham D (2008) Ultrasensitive DNA detection using oligonucleotide-silver nanoparticle conjugates. *Anal Chem* 80(8):2805–2810. <https://doi.org/10.1021/ac702403w>
- Tyagi S, Kramer FR (1996) Molecular beacons: probes that fluoresce upon hybridization. *Nat Biotechnol* 14(3):303–308. <https://doi.org/10.1038/nbt0396-303>
- Vipin K, Thuy JD, A Johan P, Kurt VG (2019) Formation of *i*-motifs from acyclic (L)-threoninol nucleic acids. *Org Biomol Chem*. <https://doi.org/10.1039/C9OB01220F>
- Walling MA, Novak JA, Shepard JRE (2009) Quantum dots for live cell and in vivo imaging. *Int J Mol Sci* 10(2):441–491. <https://doi.org/10.3390/ijms10020441>
- Wang Z, Zhou X, Zhang J, Boey F, Zhang H (2009) Direct electrochemical reduction of single-layer Graphene oxide and subsequent functionalization with glucose oxidase. *J Phys Chem C* 113(32):14071–14075. <https://doi.org/10.1021/jp906348x>
- Wang W, Kang T-S, Lu J-J, Chen X-P, Leung C-H, Chan PWH, Ma D-L (2015) A label-free G-quadruplex-based mercury detection assay employing the exonuclease III-mediated cleavage of T-Hg(2+)-T mismatched DNA. *Sci Technol Adv Mater* 16(6):065004. <https://doi.org/10.1088/1468-6996/16/6/065004>
- Warner JH, Hoshino A, Yamamoto K, Tilley RD (2005) Water-soluble photoluminescent silicon quantum dots. *Angew Chem Int Ed* 44(29):4550–4554. <https://doi.org/10.1002/anie.200501256>
- Wei L, Wang X, Wu D, Li C, Yin Y, Li G (2016) Proximity ligation-induced assembly of DNazymes for simple and cost-effective colourimetric detection of proteins with high sensitivity. *Chem Commun* 52(32):5633–5636. <https://doi.org/10.1039/C6CC00205F>
- Wen Y, Li FY, Dong X, Zhang J, Xiong Q, Chen P (2013) The electrical detection of Lead ions using gold-nanoparticle- and DNazyme-functionalized Graphene device. *Adv Healthc Mater* 2(2):271–274. <https://doi.org/10.1002/adhm.201200220>
- Wen C-Y, Wu L-L, Zhang Z-L, Liu Y-L, Wei S-Z, Hu J, Tang M, Sun E-Z, Gong Y-P, Yu J, Pang D-W (2014) Quick-response magnetic nanospheres for rapid, efficient capture and sensitive detection of circulating tumor cells. *ACS Nano* 8(1):941–949. <https://doi.org/10.1021/nn405744f>

- Xu W, Chan KM, Kool ET (2017) Fluorescent nucleobases as tools for studying DNA and RNA. *Nat Chem* 9(11):1043–1055. <https://doi.org/10.1038/nchem.2859>
- Yamazaki T, Aiba Y, Yasuda K, Sakai Y, Yamanaka Y, Kuzuya A, Ohya Y, Komiyama M (2012) Clear-cut observation of PNA invasion using nanomechanical DNA origami devices. *Chem Commun* 48(92):11361–11363. <https://doi.org/10.1039/c2cc36358e>
- Yang Y, Liu Q, Liu Y, Cui J, Liu H, Wang P, Li Y, Chen L, Zhao Z, Dong Y (2017) A novel label-free electrochemical immunosensor based on functionalized nitrogen-doped graphene quantum dots for carcinoembryonic antigen detection. *Biosens Bioelectron* 90:31–38. <https://doi.org/10.1016/j.bios.2016.11.029>
- Zhang J, Yu S-H (2014) Highly photoluminescent silicon nanocrystals for rapid, label-free and recyclable detection of mercuric ions. *Nanoscale* 6(8):4096–4101. <https://doi.org/10.1039/c3nr05896d>
- Zhang L, Peritz A, Meggers E (2005) A simple glycol nucleic acid. *J Am Chem Soc* 127(12):4174–4175. <https://doi.org/10.1021/ja042564z>
- Zhang X, Li Y, Su H, Zhang S (2010) Highly sensitive and selective detection of Hg<sup>2+</sup> using mismatched DNA and a molecular light switch complex in aqueous solution. *Biosens Bioelectron* 25(6):1338–1343. <https://doi.org/10.1016/j.bios.2009.10.023>
- Zhang L, Zhu J, Ai J, Zhou Z, Jia X, Wang E (2013) Label-free G-quadruplex-specific fluorescent probe for sensitive detection of copper(II) ion. *Biosens Bioelectron* 39(1):268–273. <https://doi.org/10.1016/j.bios.2012.07.058>
- Zhang Z, Wang Y, Zhang N, Zhang S (2016) Self-assembly of nucleic acid molecular aggregates catalyzed by a triple-helix probe for miRNA detection and single cell imaging. *Chem Sci* 7(7):4184–4189. <https://doi.org/10.1039/C6SC00694A>
- Zhao J, Deng J, Yi Y, Li H, Zhang Y, Yao S (2014) Label-free silicon quantum dots as fluorescent probe for selective and sensitive detection of copper ions. *Talanta* 125:372–377. <https://doi.org/10.1016/j.talanta.2014.03.031>
- Zhao H, Leonard P, Guo X, Yang H, Seela F (2017) Silver-mediated base pairs in DNA incorporating purines, 7-Deazapurines, and 8-Aza-7-deazapurines: impact of reduced Nucleobase binding sites and an altered glycosylation position. *Chem Eur J* 23(23):5529–5540. <https://doi.org/10.1002/chem.201605982>
- Zheng J, Li J, Jiang Y, Jin J, Wang K, Yang R, Tan W (2011) Design of aptamer-based sensing platform using triple-helix molecular switch. *Anal Chem* 83(17):6586–6592. <https://doi.org/10.1021/ac201314y>
- Zhou X-H, Kong D-M, Shen H-X (2010) G-quadruplex-hemin DNAzyme-amplified colorimetric detection of Ag<sup>+</sup> ion. *Anal Chim Acta* 678(1):124–127. <https://doi.org/10.1016/j.aca.2010.08.025>
- Zong C, Zhang Z, Liu B, Liu J (2019) Adsorption of Arsenite on gold nanoparticles studied with DNA oligonucleotide probes. *Langmuir* 35(22):7304–7311. <https://doi.org/10.1021/acs.langmuir.9b01161>



# Chapter 9

## Electrochemical Sensors Based on Metal Oxide and Sulfide Nanostructures



R. Suresh, Claudio Sandoval, Eimmy Ramirez, K. Giribabu,  
R. V. Mangalaraja, and Jorge Yáñez

### Contents

9.1	Introduction .....	286
9.2	Metal Oxides–Based Electrochemical Sensors .....	289
9.2.1	Pure Metal Oxides .....	289
9.2.2	Surface Functionalization .....	294
9.2.3	Metal Ion Doping Process .....	294
9.2.4	Fabrication of Composites .....	295
9.3	Metal Sulfides–Based Electrochemical Sensor .....	295
9.3.1	Pure Metal Sulfides .....	297
9.3.2	Doped Metal Sulfides .....	299
9.3.3	Composites .....	300
9.4	Conclusion .....	300
	References .....	303

**Abstract** Electrochemical sensors are widely used in air and water quality testing, agricultural activities, medical diagnosis, food industries, defense, and forensic science. This is because of their fast response, portability, easy testing procedure,

---

R. Suresh (✉)

Department of Chemistry, Easwari Engineering College (Autonomous), Chennai, India

C. Sandoval · E. Ramirez · J. Yáñez (✉)

Department of Analytical and Inorganic Chemistry, Faculty of Chemical Sciences, University of Concepción, Concepción, Chile

e-mail: [jyanez@udec.cl](mailto:jyanez@udec.cl)

K. Giribabu

Electrodics and Electrocatalysis Division, Council of Scientific & Industrial Research-Central Electrochemical Research Institute, Karaikudi, India

R. V. Mangalaraja

Department of Materials Engineering, Faculty of Engineering, University of Concepción, Concepción, Chile

Technological Development Unit (UDT), University of Concepción, Coronel Industrial Park, Coronel, Chile

© The Editor(s) (if applicable) and The Author(s), under exclusive licence to Springer Nature Switzerland AG 2021

285

S. Rajendran et al. (eds.), *Metal, Metal-Oxides and Metal Sulfides for Batteries, Fuel Cells, Solar Cells, Photocatalysis and Health Sensors*, Environmental Chemistry for a Sustainable World 62, [https://doi.org/10.1007/978-3-030-63791-0\\_9](https://doi.org/10.1007/978-3-030-63791-0_9)

low cost, and considerable sensitivity. However, due to lack of selectivity and sensitivity, pristine electrodes used in electrochemical sensors are not suitable for accurate detection of analytes in real samples. But, the fast growing nanotechnology eliminates the existing practical issues and significantly facilitates the development of highly selective and sensitive electrochemical sensors for many kinds of analytes, including organic molecules and inorganic species in liquid and gas medium. Nanomaterials such as metals, metallic compounds, and carbon-based materials have been widely utilized as electrode materials in electrochemical sensor. In this chapter, we particularly focus on metal oxide and metal sulfide-based electrochemical sensors applied in techniques such as cyclic voltammetry, amperometry, differential pulse voltammetry (DPV), and square wave voltammetry (SWV). The development of metal oxides and metal sulfides-based electrochemical sensors are separately outlined. Initially, reasons for enhanced catalytic current response and better redox potentials of analytes at pure metal oxide/sulfide modified electrodes than pristine electrodes have been described. Then, the existing issues (low selectivity and instability) in pure metal oxide/sulfide modified electrodes have been addressed. Finally, improvement strategies including metal ion doping, surface functionalization, and composite formation in metal oxide/sulfide modified electrodes are described.

**Keywords** Metal oxide · Metal sulfide · Food safety · Defense · Electrochemistry · Sensor · Pollutant · Detection limit · Composites · Nanostructures

## 9.1 Introduction

The pollutants are toxic or poisonous chemical substances which cause undesirable changes in air, water, and soil environment (Sharavanan et al. 2020). Due to population growth, industrialization, urbanization, and modern life styles, pollutants include organic, inorganic, and organometallic compounds and are discharged into environment (Leclerc et al. 2019). For example, sulfur dioxide, carbon monoxide, and nitrogen oxides are emitted from vehicles and industries (Tsang et al. 2019). The chromium, cadmium, lead, selenium, cobalt, nickel, arsenic, and iron ions are discharged into environment through tanning industries (Lofrano et al. 2014). The volatile organic compounds such as alcohol, formaldehyde, acetone, methyl chloride, and xylene are emitted by household products like paints, varnishes, cosmetics, hobby products, and cleaning agents (Gennaro et al. 2014). In modern agricultural practices, fertilizers, fungicides, pesticides, and herbicides are directly applied to crop fields and plants (Malyan et al. 2019). They contaminate aquatic environment through surface run-off process (Gregoire et al. 2009). Owing to leaking pipes and accidents, pollutants are also released into environment (Bubbico and Mazzarotta 2008). The harmful organometallic compounds are also discharged into environment

by various ways. For instance, organotin compounds are released from antifouling paints, wood preservatives, and biocide products (Haydee and Dalma 2017). From chlorine alkali plastic industry and coal power station, organo mercurial compounds are discharged into the environment (Haydee and Dalma 2017). From petroleum industry and automobiles, organo lead (tetramethyl lead and alkyl lead) compounds are emitted (Haydee and Dalma 2017). These pollutants persist in environment and cause serious health related issues to humans and aquatic living things. Hence, monitoring of environmental pollutants is essential to protect the human beings and our mother nature from their adverse effects. Furthermore, detection of target analytes in the field of food safety (Khansili et al. 2018; Srivastava et al. 2018), clinical diagnosis (Singh et al. 2014), forensic detection (Ferreira et al. 2019), and defense activities (Li et al. 2019a) are also essential.

In order to detect targeted analytes, numerous analytical techniques have been developed by the scientific community so far. Their details with possible applications as sensing methods are given in Table 9.1.

Some of these methods have shown high sensitivity and selectivity toward certain kinds of analytes. For example, inductively coupled plasma optical emission spectrometry, flame atomic absorption spectrometry, and laser-induced breakdown spectroscopy are exclusively used for detection of metal ions in aqueous phase while FTIR spectroscopy and ultrahigh performance liquid chromatography tandem mass spectrometry are used for sensing of organic molecules. Nevertheless, they have some disadvantages which are as follows: (a) high instrument cost and maintenance cost, (b) time-consuming analytical procedure, (c) need of special operational condition, and (d) unsuitability for on-site analysis. Therefore, inexpensive, portable, and efficient analytical techniques are needed to be developing for detection of targeted analytes.

In this regard, electroanalytical techniques such as amperometry, differential pulse voltammetry (DPV), and cyclic voltammetry methods have considerable attention in the field of sensors. The electrochemical sensors are portable, selective, sensitive, and relatively low cost. It is also active in wide analytes concentration range and simple to use. Besides, nanomaterials-based electrochemical sensors further offer the benefits of reliability, improved sensitivity, and selectivity due to the unique structure, high surface area, and notable electrocatalytic activity of nanomaterials. So far, nanomaterials including metals, metallic compounds, and carbon-based materials are used to amplify the current response and thus have achieved high performance electrochemical sensor for the determination of analytes at trace level (Maduraiveeran et al. 2019; Thiyagarajan et al. 2014).

In this chapter, we reviewed recent developments on metal oxide and metal sulfide modified electrodes as sensors in the detection of environmental pollutants, food contaminants, and biologically important molecules. Basically an ideal electrocatalytic material should fulfill three features for sensing applications. They should have (a) good electrical conductivity for fast electron transport, (b) rich exposed catalytic sites, and (c) easy accessibility to target molecules. These features

**Table 9.1** Analytical techniques for detection of analytes

S. no.	Analytical techniques	Application	References
1	Laser-induced breakdown spectroscopy (LIBS)	Detection of heavy metals	Fu et al. (2018)
2	Atomic fluorescence spectroscopy (AFS)	Detection of heavy metals and metalloids	Rodas et al. (2010)
3	Fluorescence spectroscopy	Quantification of organic and inorganic species	Fu et al. (2019)
4	Ultra violet-visible absorption spectroscopy	Quantification of organic and inorganic species	Shi et al. (2019)
5	<sup>a</sup> FTIR spectroscopy	Determination of organic molecules	Nieuwoudt et al. (2004)
6	Quadrupole ion trap mass spectrometer	Determination of dry microparticles	Özdemir et al. (2019)
7	Raman spectroscopy	Organic and inorganic species	Shende et al. (2019)
8	Capillary electrophoresis	<sup>b</sup> DNA analysis	Liu et al. (2001)
9	Field effect transistors	Biological molecules	Syu et al. (2018)
10	Bio-imaging	Inorganic species within biological system	Wang et al. (2019)
11	Inductively coupled plasma mass spectrometry (ICPMS)	Inorganic species and isotopes	Rojano et al. (2019)
12	Inductively coupled plasma optical emission spectrometry (ICPOES)	Metal ions	Sneddon et al. (2017)
13	Flame atomic absorption spectrometry (FAAS)	Metal ions	Habila et al. (2019)
14	External cavity-quantum cascade laser spectroscopy	Determination of biological molecules	Montemurro et al. (2019)
15	Laser desorption ionization mass spectrometry imaging	Metabolite detection	Mourroux et al. (2019)
16	High pressure liquid chromatography-mass spectrometry (HPLC-MS)	Organic molecules and metal ions	You et al. (2019)
17	Ultrahigh performance liquid chromatography tandem mass spectrometry	Organic molecules	Du et al. (2019)

<sup>a</sup>FTIR Fourier transform infrared, <sup>b</sup>DNA deoxyribonucleic acid

included in one material are difficult to obtain. Thus, new materials using mixtures of metal oxides and metal sulfides and surface functionalization are developed for inducing a synergistic effect. The adaptation of these improvement strategies in metal oxide and metal sulfide-based sensors are also described.

## 9.2 Metal Oxides–Based Electrochemical Sensors

The nanostructured metal oxides have larger surface area and unique morphology. Hence, their functions as electrode material in electrochemical sensors will strengthen the conductive sensing interface (George et al. 2018), i.e., nanomaterials exhibit fast electron transfer ability between the analytes and electrode. The surface modification of working electrode by metal oxide nanostructures can also be easily achieved by drop casting (Suresh et al. 2014a) and deposition methods (Dhungel and Park 2010). Therefore, a great attention has been paid by the worldwide researchers for the evaluation of electrochemical sensing properties of transition and inner transition metal oxides such as oxides of iron, copper, manganese, cobalt, nickel, titanium, silver, cadmium, tin, zinc, and cerium.

### 9.2.1 Pure Metal Oxides

In recent decades, the metal oxide modified electrodes have been used for sensing of various analytes in solution as well as in gas phase. Few important metal oxide nanostructures modified electrodes with their sensing performances have been given in Table 9.2. It can be seen that pure  $\text{Fe}_2\text{O}_3$ ,  $\text{CuO}$ ,  $\text{Co}_3\text{O}_4$ ,  $\text{ZnO}$ ,  $\text{SnO}_2$ ,  $\text{CeO}_2$ , and  $\text{TiO}_2$  showed good electrochemical sensing performances toward selected analytes. The plausible reasons behind their enhanced electrochemical sensing behaviors are explained in the following way.

#### (a) The high surface area

In general, electrode with larger electroactive surface area shows relatively high current response even at very low concentration of analyte. The metal oxide nanostructures also have greater electroactive surface area and thus act as better electrochemical sensor. For example,  $\text{CdO}$  (cadmium oxide) modified screen-printed carbon electrode performs as excellent ascorbic acid sensor in phosphate buffer saline electrolyte (Gopalakrishnan et al. 2018) than the bare screen-printed carbon electrode. The obtained sensitivity and detection limit of  $\text{CdO}$  modified electrode are  $0.42 \text{ A M}^{-1} \text{ cm}^{-2}$  and  $53.5 \text{ nM}$ , respectively.

#### (b) Surface hydroxyl group

The presence of surface hydroxyl group on metal oxide plays a vital role in their electrochemical sensing performances (Fig. 9.1). For example,  $\text{Fe}_2\text{O}_3$  modified glassy carbon electrode exhibited greater anodic peak current response than the bare glassy carbon electrode in the presence of  $0.5 \text{ mM}$  pyrocatechol at  $50 \text{ mVs}^{-1}$ . The surface hydroxyl groups on  $\text{Fe}_2\text{O}_3$  nanoparticles could interact with hydroxyl group of pyrocatechol through hydrogen bonding which facilitates electron transfer efficiently from pyrocatechol to the electrode surface (Suresh et al. 2013).

**Table 9.2** List of some metal oxide-based electrochemical sensors

Metal oxide-based sensor	Analyte	Method	Linear range	Detection limit	References
$\alpha$ -Fe <sub>2</sub> O <sub>3</sub> nanofiber/GCE <sup>a</sup>	Folic acid	Amperometry	60–60,000 nM	60 nM	Maiyalagan et al. (2013)
CuO/CPE <sup>b</sup>	Paracetamol and D-glucose	Cyclic voltammetry	1–5 mM	–	Avinash et al. (2019)
ZnO/CPE	Sudan II and Sudan III	<sup>§</sup> DPV	0.05–0.7 and 0.7–20.0 $\mu$ M & 0.05–0.6 and 0.6–15.0 $\mu$ M	1.87 and 2.62 nM	Heydari et al. (2019)
MnO <sub>2</sub>	Nitrite	DPV	10–800 $\mu$ M	0.5 $\mu$ M	Dai et al. (2019)
SnO <sub>2</sub> nanofiber	Atrazine	DPV	1 zM to 1 $\mu$ M	0.9 zM	Supraja et al. (2019)
Co <sub>3</sub> O <sub>4</sub> /FTO <sup>c</sup>	Benzobicyclon	<sup>h</sup> SWV	10.00–582.96 $\mu$ mol L <sup>-1</sup>	0.38 $\mu$ mol L <sup>-1</sup>	Puangjan and Chaiyasith (2018)
CeO <sub>2</sub>	<sup>d</sup> DNA	DPV	0 to 100 nM	–	Kim et al. (2019)
NiO nanorods/GCE	Hydroxide ion	Cyclic voltammetry	100 $\mu$ M ~ 5 mM	22 $\mu$ M	Khairy and El-Safy (2014)
TiO <sub>2</sub> /GSE <sup>e</sup>	Arsenic(III)	<sup>i</sup> LSV	10–80 mg L <sup>-1</sup>	10 $\mu$ g L <sup>-1</sup>	Zhang et al. (2016a)
CdO/SPCE <sup>f</sup>	Ascorbic acid	DPV	5–150 $\mu$ M	53.5 nM	Gopalakrishnan et al. (2018)
Ag <sub>2</sub> O/GCE	Nebivolol	Current voltage	5.46 nM ~ 99.3 $\mu$ M	0.91 nM	Rahman et al. (2013)

<sup>a</sup>GCE glassy carbon electrode, <sup>b</sup>CPE carbon paste electrode, <sup>c</sup>FTO fluorine doped tin oxide, <sup>d</sup>DNA deoxyribo nucleic acid, <sup>e</sup>GSE gold strip electrode, <sup>f</sup>SPCE screen printed carbon electrode, <sup>g</sup>DPV differential pulse voltammetry, <sup>h</sup>SWV square wave voltammetry, <sup>i</sup>LSV linear sweep voltammetry

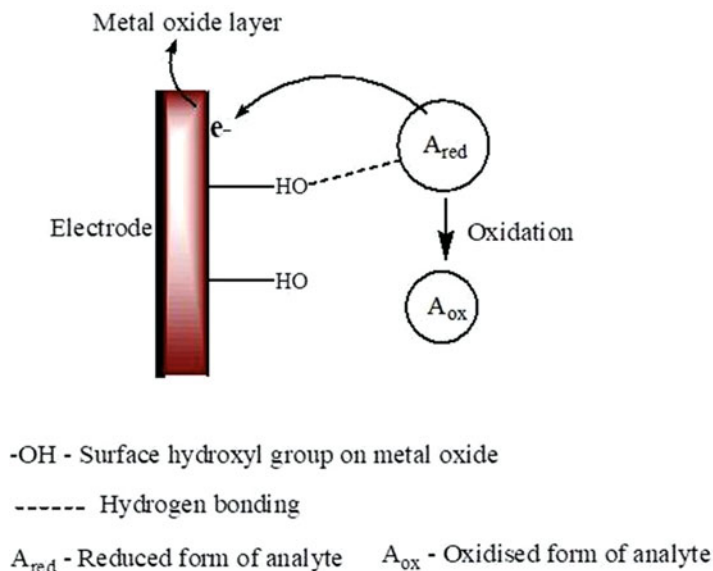


**Fig. 9.1** Role of surface hydroxyl group on metal oxide nanoparticles modified electrode as sensor: the analyte molecule interacts with electrode material through hydrogen bonding and subsequently transfer electrons

### (c) Defective surface

In general, the electrochemical active sites will be more if the electrode material has more defective surface. For example, Cai et al. (2019) have fabricated discal shaped  $Fe_2O_3$ /graphene oxide hybrid modified glassy carbon electrode and used as sensor for dopamine and uric acid. The sensor exhibited detection limit of 3.2 and 2.5 nM for dopamine and uric acid, respectively. They reported that the observed remarkable activity is due to the availability of greater defective surface in  $Fe_2O_3$ /graphene oxide hybrid.

### (d) The unique morphology

Electrochemical sensing property is dependent on morphology of nanomaterials that have been modified on the surface of the electrode (Venkadesh et al. 2017). Eremenko et al. (2012) have reported that the material with wire-like morphology could be one of the best strategies to improve electrocatalytic activity of that material. Because the nanowires have higher specific surface area and better electron transport property than the nanoparticles. Ahmed et al. (2020) have fabricated ZnO microparticles, ZnO cones, and ZnO nanotablet modified glassy carbon electrode and utilized for the determination of ammonia and dimethylamine. They found that ZnO microplates and ZnO cones modified electrodes selectively detect trimethylamine while ZnO nanotablet modified electrode shows highly selective and sensitive detection of ammonia in solution.

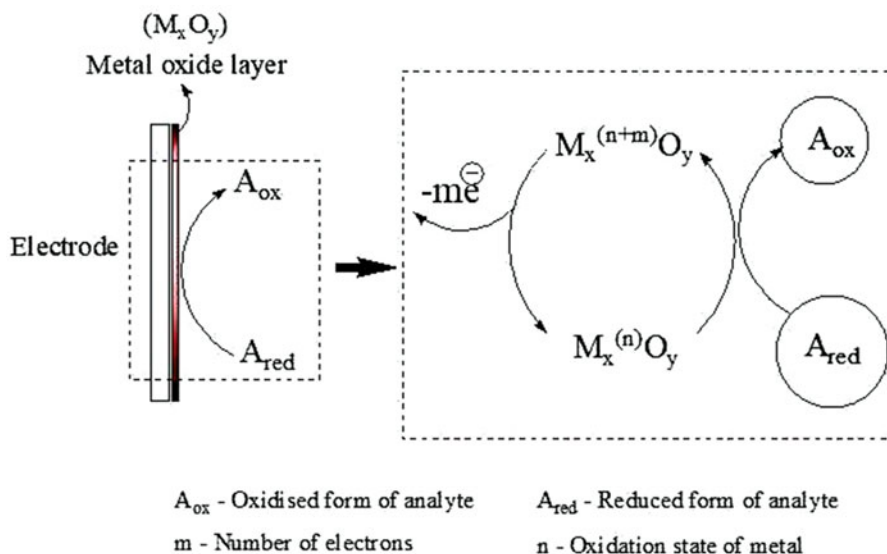


**Fig. 9.2** Electron transfer from analyte to metal oxide modified electrode through redox couple

(e) Inherent electrochemical behavior

Transition metal oxides such as  $Fe_2O_3$ ,  $CuO$ ,  $V_2O_5$ , and  $Co_3O_4$  inherently have excellent redox mediating property due to existence of metal center with variable oxidation states (Fig. 9.2). For example,  $V_2O_5$  has V(IV)/V(V) redox couple, which acts as an electrochemical redox mediator in number of electrocatalytic reactions. The  $d^0$  electronic configuration of V(V) ions facilitates active sites for analyte molecules (George et al. 2018). Similarly, Fe(II)/Fe(III) redox couple in iron oxide-based electrodes effectively mediates electrocatalytic oxidation of uric acid (Suresh et al. 2014b), folic acid (Maiyalagan et al. 2013), and dopamine (Wang et al. 2018a).

(f) Bio-compatibility

The metal oxides like  $Fe_3O_4$ ,  $CuO$ ,  $ZnO$  are generally non-toxic and biocompatible in nature (Melnyk et al. 2019). Therefore, they are used extensively in electrochemical sensing devices for determination of biomolecules such as enzyme, DNA, and bacteria (Cesewski and Johnson 2020).

(g) Availability of different phases

The electrocatalytic property is dependent on the phases of metal oxide. For example, iron(III) oxide commonly exhibits two stable phases namely,  $\alpha$ - $Fe_2O_3$  (hematite) and  $\gamma$ - $Fe_2O_3$  (maghemite). Among them,  $\gamma$ - $Fe_2O_3$  nanofibers modified glassy carbon electrode showed oxidation peak at  $-0.06$  V with larger current in phosphate buffer electrolytic solution containing 1 mM ascorbic acid. While bare



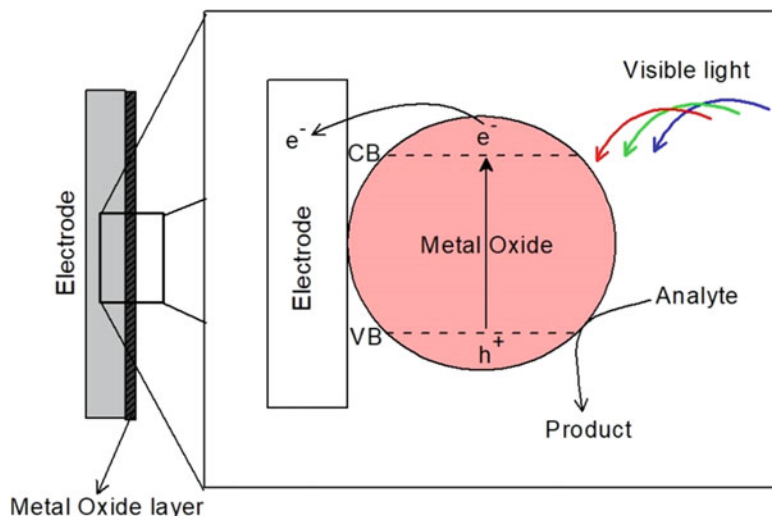


**Fig. 9.3** Photoelectrochemical oxidation of analyte at metal oxide electrode modified electrode. VB valence band, CB conduction band

and  $\alpha$ - $\text{Fe}_2\text{O}_3$  nanofibers modified glassy carbon electrode showed large overpotential with broad peak current for 1 mM ascorbic acid (Wang et al. 2018a). It suggests that  $\gamma$ - $\text{Fe}_2\text{O}_3$  is superior electrocatalyst than  $\alpha$ - $\text{Fe}_2\text{O}_3$  material. The  $\text{WO}_3$  exhibits monoclinic and orthorhombic phases. Among them, monoclinic structured  $\text{WO}_3$  showed an improved electrochemical performance toward the oxidation of dopamine in the presence of ascorbic acid (pH 7.0) than that of orthorhombic  $\text{WO}_3$  (Anithaa et al. 2015).

#### (h) Light harvesting capacity

Metal oxides, like  $\text{Fe}_2\text{O}_3$ ,  $\text{V}_2\text{O}_5$ ,  $\text{Cu}_2\text{O}$  among others, absorb visible light efficiently while  $\text{ZnO}$  and  $\text{TiO}_2$  absorb ultraviolet light in solar energy. This property is used in electrochemical sensing applications (Zhang et al. 2014). That is, during irradiation of suitable light on metal oxide modified electrode, the electrons in valence band are excited to their conduction band and leave holes at valence band. The analyte undergoes oxidation at valence band while excited electrons are transferred to the electrode (Fig. 9.3). The measured photocurrent is directly proportional to the concentration of analyte.

As discussed above, pure form of metal oxides is more useful in the development of electrochemical sensors for many analytes. However, there are some disadvantages of metal oxides as electrode materials. Because (i) some metal oxides are insulators or exhibit poor electron transport behavior, (ii) fouling of oxidized/reduced products occurs at electrode surface, (iii) high agglomeration during electrochemical process, and (iv) limited availability of selective binding sites for analytes. To overcome these shortcomings, the following improvement strategies were developed.

## 9.2.2 Surface Functionalization

Functionalization of suitable functional groups on the surface of metal oxides has considerable interest. For example, polyamidoamine dendrimer functionalized  $\text{Fe}_3\text{O}_4$  nanoparticles (Fig. 9.4) were synthesized and used for the determination of  $\text{Pb}^{2+}$  and  $\text{Cd}^{2+}$  ions in environmental water samples (Maleki et al. 2019). This sensor showed linear response to  $\text{Pb}^{2+}$  and  $\text{Cd}^{2+}$  ions over a range from 0.5 to  $80 \text{ ng mL}^{-1}$ . The obtained low detection limits are  $0.17 \text{ ng mL}^{-1}$  for  $\text{Pb}^{2+}$  and  $0.21 \text{ ng mL}^{-1}$  for  $\text{Cd}^{2+}$ .

## 9.2.3 Metal Ion Doping Process

The material with good electrical conductivity can be used as electrode material in an electrochemical sensor. The metal ion doping is a rational method to increase the electrical conductivity of metal oxides. Generally, transition and inner-transition elements are used as dopants in metal oxides. In this view, metal ion doped metal oxides have been used as electrode surface modifying layer and applied as sensor for various analytes. For instance, the  $\text{Co}^{2+}$  doped hematite nanospheres modified glassy carbon electrode showed greater anodic peak current with lower oxidation potential toward oxidation of uric acid than the bare and pure hematite modified electrode (Suresh et al. 2012). Subsequently, 7%  $\text{Ni}^{2+}$ -doped  $\text{V}_2\text{O}_5$  nanoparticles modified glassy carbon electrode showed greater peak current ( $\sim 22.5 \mu\text{A}$ ) with lower potential for oxidation of dopamine (0.1 mM) in phosphate buffer solution than ( $\sim 12.5 \mu\text{A}$ ) bare and ( $\sim 13.5 \mu\text{A}$ ) pure  $\text{V}_2\text{O}_5$  modified electrode (Suresh et al. 2014a). The  $\text{La}^{3+}$  doped  $\text{Co}_3\text{O}_4$  nanocubes-based screen-printed electrode exhibited peak current enhancement and the low oxidation overpotential for Sudan I than undoped  $\text{Co}_3\text{O}_4$

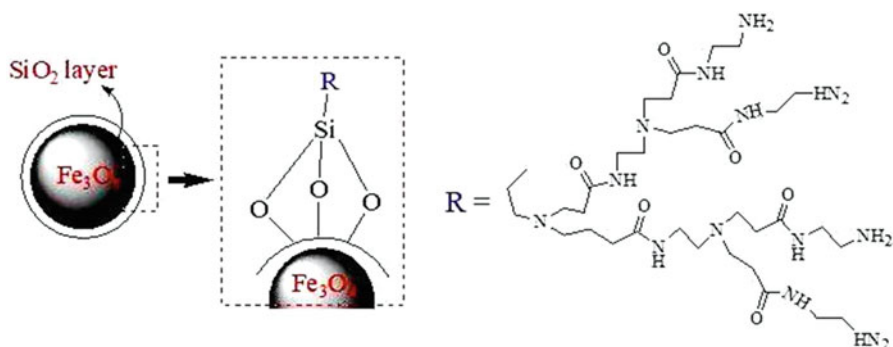


**Fig. 9.4** The structure of polyamidoamine dendrimer functionalized  $\text{Fe}_3\text{O}_4$  nanocomposite that was used for electrochemical detection of  $\text{Pb}^{2+}$  and  $\text{Cd}^{2+}$  ions in solution. The  $\text{SiO}_2$  layer acts as a linker between  $\text{Fe}_3\text{O}_4$  and dendrimer molecule. The structure was redrawn with modification from Maleki et al. (2019)

modified screen printed electrode. This sensor showed detection limit of  $0.05\mu\text{M}$ . Further, it was used as Sudan I sensor in chili powder, tomato paste, and ketchup sauce (Moghaddam and Tajik 2019). The Cu doped ZnO nanoparticles modified indium tin oxide electrode was used as sensor for detection of glucose in alkaline. When compared to pure ZnO modified electrode, Cu doped ZnO modified electrode showed greater current response with detection limit of  $10^{-9}$  M (Mahmoud et al. 2019).

### 9.2.4 Fabrication of Composites

The coupling of metal oxide nanoparticles with metal compounds or metals or carbon materials or polymers will afford material with superior properties. This approach is also adopted in the field of sensor for the development of electrode materials. Table 9.3 shows few metal oxides-based binary composites with their electrochemical sensing properties.

For betterment, metal oxide-based ternary composite electrode materials with good electrochemical sensing behaviors have also been constructed. For instance, Pd@CeO<sub>2</sub>-SnO<sub>2</sub> modified glassy carbon electrode was effectively used for quantification of H<sub>2</sub>O<sub>2</sub> in solution as well as in vegetable samples. The linear range and detection limit were found to be 0.15–1920  $\mu\text{mol L}^{-1}$  and 44  $\text{nmol L}^{-1}$ , respectively (Ensafi et al. 2019). The Bi<sub>2</sub>O<sub>3</sub>/Fe<sub>2</sub>O<sub>3</sub> decorated graphene oxide modified pencil graphite electrode (Das and Sharma 2019) was reported for selective determination of cadmium ions with low detection limit (1.85  $\text{ng L}^{-1}$ ) and high sensitivity (2034.2  $\text{A cm}^{-2}\text{g}^{-1}\text{L}$ ). The CuO/C<sub>3</sub>N<sub>4</sub>/reduced graphene oxide modified glassy carbon electrode was reported (Li et al. 2019b) for detection of nitrite ions. The sensor showed detection limit of  $0.025\mu\text{M}$  with wide linear response range (0.2–110  $\mu\text{M}$ ) and high sensitivity ( $0.093\mu\text{A}\mu\text{M}^{-1}$ ).

## 9.3 Metal Sulfides-Based Electrochemical Sensor

Metal sulfides nanostructures are widely utilized as electrochemical sensor material for various kinds of pollutants present in air, water, land, and biologically important molecules in biological samples (Samadi et al. 2018). This is because of their excellent redox behavior and superior electrical conductivity. Also, they are vastly abundant and cheap materials, since they usually exist in nature as minerals such as pyrite (FeS<sub>2</sub>), chalcocite (Cu<sub>2</sub>S), heazlewoodite (Ni<sub>3</sub>S<sub>2</sub>), molybdenite (MoS<sub>2</sub>), cinnabar (HgS), acanthite (Ag<sub>2</sub>S), sphalerite (ZnS), galena (PbS), and orpiment (As<sub>2</sub>S<sub>3</sub>). Moreover, metal sulfide nanoparticles also synthesized and explored their properties in detail (Shen and Wang 2013; Roberts and Williams 1975).

**Table 9.3** Metal oxide-based binary composites as electrochemical sensors

Binary composites as sensor	Analyte	Method	Linear range	Detection limit	References
Ag/CuO	Levodopa and ascorbic acid	<sup>b</sup> DPV	0.1–20.0 $\mu\text{g mL}^{-1}$ and 0.01–2.0 $\mu\text{g mL}^{-1}$	0.034 $\mu\text{g mL}^{-1}$ and 0.014 $\mu\text{g mL}^{-1}$	Ahirwar et al. (2019)
Au/Fe <sub>2</sub> O <sub>3</sub>	Nitrite	Amperometry	1–1000 $\mu\text{M}$	0.07 $\mu\text{M}$	Kang et al. (2019)
Fe <sub>2</sub> O <sub>3</sub> –CoO	Nitrite	Amperometry	0.2–16.2 mM	0.1 $\mu\text{M}$	Wang et al. (2014)
CeO <sub>2</sub> –SnO <sub>2</sub>	L-cysteine	Amperometry	0.016 $\times 10^{-3}$ M to 2 $\times 10^{-3}$ M	0.016 $\times 10^{-3}$ M	Manibalan et al. (2019)
Fe <sub>2</sub> O <sub>3</sub> /CeO <sub>2</sub>	Hydrazine	Current-voltage	0.02 $\mu\text{M}$ to $\sim 0.02$ M	0.22 $\pm 0.01$ $\mu\text{M}$	Rahman et al. (2018)
FeWO <sub>4</sub> /SnO <sub>2</sub>	Hydroquinone	DPV	0.01 $\mu\text{M}$ to 50 $\mu\text{M}$	0.0013 $\mu\text{M}$	Karthika et al. (2019)
V <sub>2</sub> O <sub>5</sub> @polyaniline	Dopamine	Chronoamperometry	6.6 $\times 10^{-6}$ M to 1.1 $\times 10^{-4}$ M	3.9 $\times 10^{-5}$ M	Suresh et al. (2014c)
Polyaniline/SnO <sub>2</sub>	Nitrite	Amperometry	0.12 $\mu\text{M}$ to 7.8 mM	0.04 $\mu\text{M}$	Duan and Zheng (2019)
CuO/polyaniline	H <sub>2</sub> O <sub>2</sub>	Amperometry	0.005–9.255 mM	0.11 $\mu\text{M}$	Liu et al. (2019)
$\alpha$ -Fe <sub>2</sub> O <sub>3</sub> /MWCNT <sup>a</sup>	Levodopa	Amperometry	5.0 $\times 10^{-8}$ to 3.8 $\times 10^{-6}$ M	30 nM	Sumathi et al. (2014)
Iron oxide /graphene sheets	Dopamine	DPV	0.006 to 635 $\mu\text{M}$	0.004 $\mu\text{M}$	Kokulnathan et al. (2018)

<sup>a</sup>MWCNT multi-walled carbon nanotube, <sup>b</sup>DPV differential pulse voltammetry

### 9.3.1 Pure Metal Sulfides

The nanostructured transition metal sulfides have been synthesized by various methods such as precipitation, hydrothermal, sonochemical, thermal decomposition, electrochemical, microwave assisted method, and vapor phase sulfurization approach, and they are used as electrode material for the detection of analytes. Some important metal sulfide nanostructures modified electrodes with their sensing performances are given in Table 9.4.

From the Table 9.4, it can be said that pure CuS, CoS, ZnS, and FeS showed good electrochemical sensing performances toward targeted analytes. The plausible reasons behind their electrocatalytic activity are explained subsequently.

#### (a) The largest available electroactive surface area

Like metal oxides, metal sulfides also exhibit largest electroactive surface area and thus show good electrochemical sensing performances toward analytes. For example, Li et al. (2019c) have determined the electroactive surface of CuS nanoflower modified glassy carbon electrode by using Anson equation. Since the estimated electroactive surface area of CuS modified electrode ( $0.258 \text{ cm}^2$ ) is more than that of bare electrode ( $0.0709 \text{ cm}^2$ ), its sensing behaviors toward tartrazine (sensitivity –  $1.733 \text{ A M}^{-1}$ , detection limit –  $0.012 \mu\text{M}$ ) and sunset yellow (sensitivity –  $0.226 \text{ A M}^{-1}$ , detection limit –  $0.006 \mu\text{M}$ ) are also superior.

#### (b) The morphology

The sensing property of metal sulfides is also dependent on shape of the particles (Venkadesh et al. 2017). For instance, CuS with different morphologies such as microspheres, hexagonal microsheets, sandwich-like plates, interlaced nanosheets, and nanoflowers have been prepared by simple solvothermal method (Li et al. 2019c). These CuS nanostructures modified glassy carbon electrodes were used to determine tartrazine and sunset in phosphate buffer solution. Among other morphologies, CuS nanoflower showed excellent sensing behavior (detection limit  $0.006 \mu\text{M}$ ) owing to its unique three-dimensional hierarchical porous nanostructures. This morphology preserves larger active surfaces and provides channels for the transport of analyte molecules. Therefore, analyte molecules are enabled to contact with active sites of CuS nanoflowers. On the other hand, PbS dendrites and nanocubes were synthesized by thermal decomposition method and applied as sensor for dopamine in solution (Gaur 2020). When compared to PbS nanocubes modified electrode, PbS dendrites modified electrode showed enhanced redox current and reduced peaks potential.

#### (c) Good electrochemical behavior of metal sulfides

Specifically, sulfides of iron, copper, cobalt, and molybdenum are having good electron transfer capability due to their variable oxidation states. For example, FeS modified fluorine doped indium tin oxide electrode (Show et al. 2017) showed enhanced electrocatalytic activity toward reduction of  $\text{H}_2\text{O}_2$  which was due to

**Table 9.4** List of some metal sulfides-based electrochemical sensors

Metal sulfide as sensor	Analyte	Method	Linear range	Detection limit	References
CoS nanorods / nafion/GCE <sup>a</sup>	Vanillin	<sup>e</sup> DPV	0.5–56 $\mu$ M	0.07 $\mu$ M	Sivakumar et al. (2017)
CuS Nanoflowers /GCE	Tartrazine/sunset yellow	DPV	0.4–100/0.1–700 $\mu$ M	0.012/0.006 $\mu$ M	Li et al. (2019c)
Cu <sub>2</sub> S nanoplates/ GCE	H <sub>2</sub> O <sub>2</sub> /glucose	Amperometry	10 mM to 3.75 mM/ 10 mM to 3.1 mM	1.1 $\mu$ M/1.3 $\mu$ M	Maji et al. (2013)
FeS nanospheres/ FTO <sup>b</sup>	H <sub>2</sub> O <sub>2</sub>	Amperometry	10–700 $\mu$ M	2.699 $\mu$ M	Show et al. (2017)
FeS <sub>2</sub> /ITO <sup>c</sup>	H <sub>2</sub> O <sub>2</sub>	Amperometry	10 M to 1.9 mM	4.00 $\mu$ M	Chakraborty et al. (2013)
Ni <sub>7</sub> S <sub>6</sub> /GCE	H <sub>2</sub> O <sub>2</sub> /Glucose	Amperometry	0.005–20.5 mM/0.005–3.7 mM	0.15 $\mu$ M/0.15 $\mu$ M	Wu et al. (2016)
Ni <sub>3</sub> S <sub>2</sub> /Ni foam	Glucose	Amperometry	0.0005–3 mM	0.82 $\mu$ M	Kim et al. (2016)
MoS <sub>2</sub> /GCE	4-Aminophenol	DPV	0.04–17 $\mu$ M	0.03 ( $\pm$ 0.008) $\mu$ M	Kumar et al. (2016)
ZnS/CPE <sup>d</sup>	Acetaminophen, guanine and adenine	DPV	1–15 $\mu$ M and 15–120 $\mu$ M	0.041, 0.036, and 0.031 $\mu$ M	Mahanthappa et al. (2018)
Ag <sub>2</sub> S quantum dots	Glucose	Photoelectro chemical method	0.1–12.2 mM	$3.2 \times 10^{-5}$ M	Zhang et al. (2014)
Pyrite/chalcopyrite	H <sub>2</sub> O <sub>2</sub>	Amperometry	$1.0 \times 10^{-5}$ M to $1.0 \times 10^{-2}$ M/ $1.0 \times 10^{-4}$ M to 3.0 $\times 10^{-2}$ M	$8.6 \times 10^{-6}$ M/ $5.2 \times 10^{-5}$ M	Wang et al. (2018b)

<sup>a</sup>GCE glassy carbon electrode, <sup>b</sup>FTO fluorine doped tin oxide, <sup>c</sup>ITO indium doped tin oxide, <sup>d</sup>CPE carbon paste electrode, <sup>e</sup>DPV differential pulse voltammetry

electron transfer property of FeS through Fe(III)/Fe(II) redox couple. On the other hand, CuS dendrite modified Ni foam electrode showed sharp redox peaks due to Cu(0)/Cu(I), Cu(0)/Cu(II), Cu(I)/Cu(II), and Cu(II)/Cu(III) couples. Due to this best electrochemical behavior, CuS dendrite exhibited superior sensing behavior toward glucose (Kim et al. 2016).

#### (d) Non-toxicity

Many sulfide minerals are abundant in the earth crust. They are mostly non-toxic to living things (Figueroa et al. 2017). Especially pyrite (FeS) and chalcopyrite (CuFeS<sub>2</sub>), sulfide ores of iron, and copper are widespread sulfide minerals in nature. Also, they are all good electroactive materials. Interestingly, their semiconducting behavior makes them as potential electrochemical sensor materials for quantification of analytes. For example, natural pyrite and chalcopyrite sample (Wang et al. 2018b; Shen and Wang 2013) was used as electrode for detection of H<sub>2</sub>O<sub>2</sub> in solution. The pyrite and chalcopyrite electrodes showed detection limit of 8.6 and 52 Mm, respectively. These sensors also showed great sensitivity and repeatability.

#### (e) Availability of different phases

Different phases of a particular metal sulfide have different electrochemical sensing properties. For example, nickel sulfide has sulfur-rich and nickel-rich phases such as NiS, Ni<sub>3</sub>S<sub>2</sub>, Ni<sub>3</sub>S<sub>4</sub>, Ni<sub>7</sub>S<sub>6</sub>, and Ni<sub>9</sub>S<sub>8</sub>. The Ni<sub>7</sub>S<sub>6</sub>-based sensor detects H<sub>2</sub>O<sub>2</sub> and glucose with sensitivities of 37.77 and 271.80 μA mM<sup>-1</sup> cm<sup>-2</sup>, respectively. Whereas, the Ni<sub>3</sub>S<sub>2</sub> modified Ni foam electrode (Kim et al. 2016) efficiently detects glucose with a greater sensitivity of 16,460 μA mM<sup>-1</sup> cm<sup>-2</sup>.

#### (f) Light absorption property

The metal sulfides have narrow band gap and thus played important role in photoelectrochemical sensor for detection of analytes in real samples. For example, CdS nanostructures were effectively used as electrode materials in photoelectrochemical sensing devices for determination of various analytes (Ibrahim et al. 2018).

Besides their application of pure metal sulfides, they also have disadvantages in using sensitive sensor in real samples due to their poor ion transport kinetics, low selectivity, and sensitivity. These disadvantages can be overcome by the following methods.

### 9.3.2 Doped Metal Sulfides

Like metal oxides, the sensing property of metal sulfides are also tuned by doping process with appropriate dopants. For example, nickel-doped FeS<sub>2</sub> nanoparticles-based electrode has been used as non-enzymatic glucose sensor with linear ranges of 2–12, 0.1–10 mM and sensitivity of 60.04, 240.13 μA mM cm<sup>-2</sup>, respectively (Li et al. 2017). The Ni-doped MoS<sub>2</sub>/reduced graphene oxide modified electrode

has also been used for determination of glucose. The linear detection range and catalytic rate constant was found to be 0.005–8.2 mM and  $6.26 \times 10^5 \text{ cm}^3 \text{ mol}^{-1} \text{ s}^{-1}$ , respectively (Geng et al. 2017).

### 9.3.3 Composites

Several metal sulfides–based binary composites such as metal sulfide/metals compounds, metal sulfide/metals, metal sulfide/carbon materials, and metal sulfide/polymers were fabricated and examined for their electrochemical sensing properties. Some of the important metal sulfide-based composite electrochemical sensors with their sensing performances are listed in Table 9.5.

A focus on ternary composites of metal sulfides has also been given by the researchers. For example,  $\text{VS}_2\text{-SnS}_2$ /multi-walled carbon nanotube–based electrode has been reported for the selective detection of dopamine in solution as well as in human serum and rat brain samples (Sakthivel et al. 2019). This sensor exhibits its activity in the concentration range from 0.025 to 1017  $\mu\text{M}$  with detection limit of 0.008  $\mu\text{M}$ .

## 9.4 Conclusion

The applications of oxides and sulfides of metals in electrochemical sensing devices are pronounced. The major reasons are (a) larger surface area, (b) surface functional group, (c) morphology, (d) porosity, (e) non-toxicity and biocompatibility, (f) different phases, (g) light harvesting capacity, and (h) good redox behaviors.

At the same time, there are some disadvantages to use pure form of metal oxides and metal sulfides as electrode material. They are (a) electrode fouling, (b) higher agglomeration during electrochemical process, and (c) few metal oxides/sulfides act as insulators. These shortcomings were overcome by the following ways.

- (i) The conductivity of metal oxides and metal sulfides can be enhanced by doping with transition and inner transition metal ions.
- (ii) Functionalization of metal oxides and sulfides with suitable functional groups.
- (iii) The metal oxides and sulfides are composited with metals, metal compounds, carbon-based materials, and polymers. There are many binary and ternary composites–based electrochemical sensors that were developed.

Besides their applications, some electrode preparations are time consuming, costly, and sometimes repeatability may be affected. However, these materials significantly improve the sensing performances and this makes impact on the detection of hazardous pollutants, food contaminants, and biologically important



**Table 9.5** Metal sulfides–based binary composite sensors

Sensors	Analyte	Method	Sensing performances		References
			Linear range	Detection limit	
Metal/metal sulfide					
Ag/Ag <sub>2</sub> S/ITO <sup>a</sup>	Dopamine	<sup>b</sup> DPV	1.0–10, and 10–100 $\mu$ M	1.0 $\mu$ M	Li et al. (2011)
Metal compounds/metal sulfide					
Bi <sub>2</sub> S <sub>3</sub> @ZnS/ITO	Cu <sup>2+</sup> ions	<sup>c</sup> OCV	0.003–30.0 $\mu$ M	0.001 $\mu$ M	Xi et al. (2019)
ZnS:Ni/ZnS/ cysteine/GCE <sup>d</sup>	Catechol	Cyclic voltammetry	0.5–100 $\mu$ M	32 nM	Qu et al. (2014)
SnO <sub>2</sub> –SnS <sub>2</sub> /GCE	Serotonin and tryptophan	<sup>e</sup> SWV	0.1–700 $\mu$ M and 0.1–800 $\mu$ M	45 and 59 nM	Lavanya and Sekar (2019)
ZnO/CdS	Cu <sup>2+</sup> ions	Photoelectro chemical method	0.02–40.0 $\mu$ M	0.01 $\mu$ M	Shen et al. (2011)
Polymers/metal sulfide					
CdS/porous silicon	Glucose	Chronoamperometry	10–100 mM	610 $\mu$ M	Rathimamala et al. (2019)
Chitosan/CdS	Urea	DPV	5.0 $\times 10^{-12}$ to 4.0 $\times 10^{-10}$ M and 5.0 $\times 10^{-10}$ to 7.0 $\times 10^{-8}$ M	1.0 $\times 10^{-12}$ M	Lian et al. (2012)
Organic polymer dots and CdS	$\alpha$ -Solanine	Photoelectro chemical method	0.01–1000 ng mL <sup>-1</sup>	6.5 pg mL <sup>-1</sup>	Mao et al. (2019)

(continued)

Table 9.5 (continued)

Sensors	Analyte	Method	Sensing performances		References
			Linear range	Detection limit	
Carbon-based materials/metal sulfide					
Graphene-SnS	Copper ion	$i_{LSV}$	1.5–36.0 $\mu\text{M}$	0.02 $\mu\text{M}$	Lu et al. (2016)
CuS/reduced graphene oxide	Hydrogen peroxide	Amperometry	3–1215 $\mu\text{mol/L}$	0.18 $\mu\text{mol/L}$	Liu et al. (2017)
Graphene-doped $\text{Bi}_2\text{S}_3$	Sulfadimethoxine	Photoelectrochemical method	1.0–100 nM	0.55 nM	Okoth et al. (2016)
CuS-MWCNTs <sup>g</sup>	Nitrite	Amperometry	1.0 $\mu\text{M}$ –8.1 mM	0.33 $\mu\text{M}$	Zhang et al. (2016b)

<sup>a</sup>*ITO* indium tin oxide, <sup>b</sup>*DPV* differential pulse voltammetry, <sup>c</sup>*VOC* open-circuit voltage, <sup>d</sup>*GCE* glassy carbon electrode, <sup>e</sup>*SWV* square wave voltammetry, <sup>f</sup>*LSV* linear sweep voltammetry, <sup>g</sup>*MWCNTs* multi-walled carbon nanotubes

molecules. Hopefully, researchers will produce cheaper and greener composite materials for electrochemical sensing applications.

**Acknowledgments** Authors acknowledge the National Commission for Scientific and Technological Research (CONICYT), Santiago, Chile, for the financial assistance in the form of FONDECYT Post-Doctoral projects No. 3160499, 3190534, FONDECYT project: 1191572 and CONICYT Doctoral Fellowship 21180934.

## References

- Ahirwar D, Bano M, Khan I, Gound SS, Sheikh MUD, Mondal R, Khan F (2019) Facile synthesis of macroporous Ag and CuO monoliths as an efficient nonenzymatic electrochemical sensor and antimicrobial agent. *J Solid State Chem* 273:233–242. <https://doi.org/10.1016/j.jssc.2019.03.002>
- Ahmed M, Zhao R, Hayytov B, Shang Y, Li J, Du J (2020) Morphology evolution of ZnO by controlling solvent and electrochemical sensing of hexagonal nanotablets toward amines. *Chinese Chem Lett*. <https://doi.org/10.1016/j.ccllet.2020.01.014>
- Anithaa AC, Lavanya N, Asokan K, Sekar C (2015) WO<sub>3</sub> nanoparticles based direct electrochemical dopamine sensor in the presence of ascorbic acid. *Electrochim Acta* 167:294–302. <https://doi.org/10.1016/j.electacta.2015.03.160>
- Avinash B, Ravikumar CR, Anil Kumar MR, Nagaswarupa HP, Santosh MS, Bhatt AS, Kuznetsov D (2019) Nano CuO: electrochemical sensor for the determination of paracetamol and D-glucose. *J Phys Chem Solids* 134:193–200. <https://doi.org/10.1016/j.jpcs.2019.06.012>
- Bubbico R, Mazzarotta B (2008) Accidental release of toxic chemicals: influence of the main input parameters on consequence calculation. *J Hazard Mater* 151:394–406. <https://doi.org/10.1016/j.jhazmat.2007.06.002>
- Cai Z, Ye Y, Wan X, Liu J, Yang S, Xia Y, Li G, He Q (2019) Morphology-dependent electrochemical sensing properties of iron oxide-graphene oxide nanohybrids for dopamine and uric acid. *Nano* 9:835 (19 p). doi:<https://doi.org/10.3390/nano9060835>
- Cesewski E, Johnson BN (2020) Electrochemical biosensors for pathogen detection. *Biosens Bioelectron* 159:112214. <https://doi.org/10.1016/j.bios.2020.112214>
- Chakraborty B, Show B, Jana S, Mitra BC, Maji SK, Adhikary B, Mukherjee N, Mondal A (2013) Cathodic and anodic deposition of FeS<sub>2</sub> thin films and their application in electrochemical reduction and amperometric sensing of H<sub>2</sub>O<sub>2</sub>. *Electrochim Acta* 94:7–15. <https://doi.org/10.1016/j.electacta.2012.12.018>
- Dai Y, Huang J, Zhang H, Liu CC (2019) Highly sensitive electrochemical analysis of tunnel structured MnO<sub>2</sub> nanoparticle-based sensors on the oxidation of nitrite. *Sensor Actuat B Chem* 281:746–750. <https://doi.org/10.1016/j.snb.2018.11.014>
- Das TR, Sharma PK (2019) Sensitive and selective electrochemical detection of Cd<sup>2+</sup> by using bimetal oxide decorated graphene oxide (Bi<sub>2</sub>O<sub>3</sub>/Fe<sub>2</sub>O<sub>3</sub>@GO) electrode. *Microchem J* 147:1203–1214. <https://doi.org/10.1016/j.microc.2019.04.001>
- Dhungle SK, Park JG (2010) Optimization of paste formulation for TiO<sub>2</sub> nanoparticles with wide range of size distribution for its application in dye sensitized solar cells. *Renew Energy* 35:2776–2780. <https://doi.org/10.1016/j.renene.2010.04.031>
- Du P, Guan Y, An Z, Li P, Liu L (2019) A selective and robust UPLC-MS/MS method for the simultaneous quantitative determination of anlotinib, ceritinib and ibrutinib in rat plasma and its application to a pharmacokinetic study. *Analyst Adv*. <https://doi.org/10.1039/C9AN00861F>
- Duan C, Zheng J (2019) Porous coralloid polyaniline/SnO<sub>2</sub>-based enzyme-free sensor for sensitive and selective detection of nitrite. *Colloids Surf A Physicochem Eng Asp* 567:271–277. <https://doi.org/10.1016/j.colsurfa.2019.01.063>

- Ensafi AA, Mahmoodi A, Rezaei B (2019) Pd@CeO<sub>2</sub>-SnO<sub>2</sub> nanocomposite, a highly selective and sensitive hydrogen peroxide electrochemical sensor. *Sensor Actuat B Chem* 296:126683. <https://doi.org/10.1016/j.snb.2019.126683>
- Eremenko AV, Dontsova EA, Nazarov AP, Evtushenko EG, Amitonov SV, Savilov SV, Martynova LF, Lunin VV, Kurochkin IN (2012) Manganese dioxide nanostructures as a novel electrochemical mediator for thiol sensors. *Electroanalysis* 24:573–580. <https://doi.org/10.1002/elan.201100535>
- Ferreira PC, Ataíde VN, Chagas CLS, Angnes L, Coltro WKT, Paixão TRLC, de Araujo WR (2019) Wearable electrochemical sensors for forensic and clinical applications. *TrAC Trend Anal Chem* 119:115622. <https://doi.org/10.1016/j.trac.2019.115622>
- Figueroa LA, Alvarez OM, Cruz JS, Contreras RG, Torres LSA, Hernández JF, Arrocena MCA (2017) Nanomaterials made of non-toxic metallic sulfides: a systematic review of their potential biomedical applications. *Mater Sci Eng* 76:1305–1315. <https://doi.org/10.1016/j.msec.2017.02.120>
- Fu X, Li G, Tian H, Dong D (2018) Detection of cadmium in soils using laser-induced breakdown spectroscopy combined with spatial confinement and resin enrichment. *RSC Adv* 8:39635–39640. <https://doi.org/10.1039/c8ra07799a>
- Fu J, Chang Y, Li B, Mei H, Yang L, Xu K (2019) A novel fluorescent-colorimetric probe for Al<sup>3+</sup> and Zn<sup>2+</sup> ion detection with different response and applications in F<sup>-</sup> detection and cell imaging. *Analyst Adv*. <https://doi.org/10.1039/C9AN01295H>
- Gaur R (2020) Morphology dependent activity of PbS nanostructures for electrochemical sensing of dopamine. *Mater Lett* 264:127333. <https://doi.org/10.1016/j.matlet.2020.127333>
- Geng D, Bo X, Guo L (2017) Ni-doped molybdenum disulfide nanoparticles anchored on reduced graphene oxide as novel electroactive material for a non-enzymatic glucose sensor. *Sensor Actuat B Chem* 244:131–141. <https://doi.org/10.1016/j.snb.2016.12.122>
- Gennaro GD, Dambruoso PR, Loiotile AD, Gilio AD, Giungato P, Tutino M, Marzocca A, Mazzone A, Palmisani J, Porcelli F (2014) Indoor air quality in schools. *Environ Chem Lett* 12:467–482. <https://doi.org/10.1007/s10311-014-0470-6>
- George JM, Antony A, Mathew B (2018) Metal oxide nanoparticles in electrochemical sensing and biosensing: a review. *Microchim Acta* 185:358. <https://doi.org/10.1007/s00604-018-2894-3>
- Gopalakrishnan A, Sha R, Vishnu N, Kumar R, Badhulika S (2018) Disposable, efficient and highly selective electrochemical sensor based on cadmium oxide nanoparticles decorated screen-printed carbon electrode for ascorbic acid determination in fruit juices. *Nano-Struct Nano-Objects* 16:96–103. <https://doi.org/10.1016/j.nanoso.2018.05.004>
- Gregoire C, Elsaesser D, Huguenot D, Lange J, Lebeau T, Merli A, Mose R, Passeport E, Payraudeau S, Schütz T, Schulz R, Padilla GT, Tournèbize J, Trevisan M, Wanko A (2009) Mitigation of agricultural nonpoint-source pesticide pollution in artificial wetland ecosystems. *Environ Chem Lett* 7:205–231. <https://doi.org/10.1007/s10311-008-0167-9>
- Habila MA, AL Othman ZA, Yilmaz E, Alabdulkarem EA, Soylyak M (2019) A new amine based microextraction of lead (II) in real water samples using flame atomic absorption spectrometry. *Microchem J* 148:214–219. <https://doi.org/10.1016/j.microc.2019.04.078>
- Haydee KM, Dalma KE (2017) Concerning organometallic compounds in environment: occurrence, fate, and impact, recent progress in organometallic chemistry. Edited by Mohammed Muzibur Rahman and Abdullah Mohamed Asiri. *IntechOpen*. <https://doi.org/10.5772/67755>
- Heydari M, Ghoreishi SM, Khoobi A (2019) Chemometrics-assisted determination of Sudan dyes using zinc oxide nanoparticle-based electrochemical sensor. *Food Chem* 283:68–72. <https://doi.org/10.1016/j.foodchem.2018.12.132>
- Ibrahim I, Lim HN, Zawawi RM, Tajudin AA, Ng YH, Guo H, Huang NM (2018) A review on visible-light induced photoelectrochemical sensors based on CdS nanoparticles. *J Mater Chem B* 6:4551–4568. <https://doi.org/10.1039/C8TB00924D>
- Kang S, Zhang H, Wang G, Zhang Y, Zhao H, Zhou H, Cai W (2019) Highly sensitive detection of nitrite by using gold nanoparticles-decorated  $\alpha$ -Fe<sub>2</sub>O<sub>3</sub> nanorod arrays as self-supporting photoelectrodes. *Inorg Chem Front*. <https://doi.org/10.1039/C9QI00176J>

- Karthika A, Raja VR, Karuppasamy P, Suganthi A, Rajarajan M (2019) A novel electrochemical sensor for determination of hydroquinone in water using FeWO<sub>4</sub>/SnO<sub>2</sub> nanocomposite immobilized modified glassy carbon electrode. *Arab J Chem*. <https://doi.org/10.1016/j.arabjc.2019.06.008>
- Khairy M, El-safty SA (2014) Nanosized rambutan-like nickel oxides as electrochemical sensor and pseudocapacitor. *Sensor Actuat B Chem* 193:644–652. <https://doi.org/10.1016/j.snb.2013.11.113>
- Khansili N, Rattu G, Krishna PM (2018) Label-free optical biosensors for food and biological sensor applications. *Sensor Actuat B Chem* 265:35–49. <https://doi.org/10.1016/j.snb.2018.03.004>
- Kim S, Lee SH, Cho M, Lee Y (2016) Solvent-assisted morphology confinement of a nickel sulfide nanostructure and its application for non-enzymatic glucose sensor. *Biosens Bioelectron* 85:587–595. <https://doi.org/10.1016/j.bios.2016.05.062>
- Kim HY, Ahn JK, Kim MI, Park KS, Park HG (2019) Rapid and label-free, electrochemical DNA detection utilizing the oxidase-mimicking activity of cerium oxide nanoparticles. *Electrochem Commun* 99:5–10. <https://doi.org/10.1016/j.elecom.2018.12.008>
- Kokulnathan T, Allen JA, Chen SM, Viswanathan C, Krishna K (2018) Trace level electrochemical determination of neurotransmitter dopamine in biological samples based on iron oxide nanoparticles decorated graphene sheets. *Inorg Chem Front* 5:705–718. <https://doi.org/10.1039/C7QI00716G>
- Kumar JV, Karthik R, Chen SM, Saravanakumar K, Mani G, Muthuraj V (2016) Novel hydrothermal synthesis of MoS<sub>2</sub> nanoclusters structure for sensitive electrochemical detection of human and environmental hazardous pollutant 4-aminophenol. *RSC Adv* 6:40399–40407
- Lavanya N, Sekar C (2019) SnO<sub>2</sub>-SnS<sub>2</sub> nanocomposite as electrocatalyst for simultaneous determination of depression biomarkers serotonin and tryptophan. *J Electroanal Chem* 840:1–9. <https://doi.org/10.1016/j.jelechem.2019.03.046>
- Leclerc A, Sala S, Secchi M, Laurent A (2019) Building national emission inventories of toxic pollutants in Europe. *Environ Int* 130:104785. <https://doi.org/10.1016/j.envint.2019.03.077>
- Li CY, Cai YJ, Yang CH, Wu CH, We Y, Wen TC, Wang TL, Shieh YT, Lin WC, Chen WJ (2011) Highly sensitive and selective electrochemical determination of dopamine and ascorbic acid at Ag/Ag<sub>2</sub>S modified electrode. *Electrochim Acta* 56:1955–1959. <https://doi.org/10.1016/j.electacta.2010.11.091>
- Li Y, Xiao Q, Huang S (2017) Highly active nickel-doped FeS<sub>2</sub> nanoparticles trigger non-enzymatic glucose detection. *Mat Chem Phy* 193:311–315. <https://doi.org/10.1016/j.matchemphys.2017.02.051>
- Li P, Li X, Chen W (2019a) Recent advances in electrochemical sensors for the detection of 2,4,6-trinitrotoluene. *Curr Opin Electrochem* 17:16–22. <https://doi.org/10.1016/j.coelec.2019.04.013>
- Li Y, Cheng C, Yang YP, Dun XJ, Gao J, Jin XJ (2019b) A novel electrochemical sensor based on CuO/H-C<sub>3</sub>N<sub>4</sub>/rGO nanocomposite for efficient electrochemical sensing nitrite. *J Alloys Compd* 798:764–772. <https://doi.org/10.1016/j.jallcom.2019.05.137>
- Li J, Liu M, Jiang J, Liu B, Tong H, Xu Z, Yang C, Qian D (2019c) Morphology-controlled electrochemical sensing properties of CuS crystals for tartrazine and sunset yellow. *Sensor Actuat B Chem* 288:552–563. <https://doi.org/10.1016/j.snb.2019.03.028>
- Lian HT, Liu B, Chen YP, Sun X (2012) A urea electrochemical sensor based on molecularly imprinted chitosan film doping with CdS quantum dots. *Anal Biochem* 426:40–46. <https://doi.org/10.1016/j.ab.2012.03.024>
- Liu Y et al (2001) Polycarbonate-based capillary electrophoresis devices for DNA analysis. In: Obermeier E (ed) *Transducers '01 Eurosensors XV*. Springer, Berlin/Heidelberg. [https://doi.org/10.1007/978-3-642-59497-7\\_270](https://doi.org/10.1007/978-3-642-59497-7_270)
- Liu W, Lei C, Zhang H, Wu X, Jia Q, He D, Yang B, Li Z, Hou Y, Lei L, Zhang X (2017) CuS/RGO hybrid by one-pot hydrothermal method for efficient electrochemical sensing of hydrogen peroxide. *Chin Chem Lett* 28:1306–1311. <https://doi.org/10.1016/j.ccllet.2017.04.032>

- Liu T, Guo Y, Zhang Z, Miao Z, Zhang X, Su Z (2019) Fabrication of hollow CuO/PANI hybrid nanofibers for nonenzymatic electrochemical detection of  $H_2O_2$  and glucose. *Sensor Actuat B Chem* 286:370–376. <https://doi.org/10.1016/j.snb.2019.02.006>
- Lofrano G, Carotenuto M, Gautam RK, Chattopadhyaya MC (2014) Chapter 12: Heavy metals in tannery wastewater and sludge: environmental concerns, and future challenges. In: Sharma SK (ed) *Heavy metals in water: presence, removal and safety*. Print ISBN:978-1-84973-885-9. PDF eISBN:978-1-78262-017-4. <https://doi.org/10.1039/9781782620174>
- Lu J, Zhang X, Liu N, Zhang X, Yu Z, Duan T (2016) Electrochemical detection of Cu using graphene–SnS nanocomposite modified electrode. *J Electroanal Chem* 769:21–27. <https://doi.org/10.1016/j.jelechem.2016.03.009>
- Maduraiveeran G, Sasidharan M, Jin W (2019) Earth-abundant transition metal and metal oxide nanomaterials: synthesis and electrochemical applications. *Prog Mater Sci* 100574. <https://doi.org/10.1016/j.pmatsci.2019.100574>
- Mahanthappa M, Kottam N, Yellappa S (2018) Electrocatalytic performance of a zinc sulphide nanoparticles modified carbon paste electrode for the simultaneous determination of acetaminophen, guanidine and adenine. *Anal Methods*. <https://doi.org/10.1039/C8AY00007G>
- Mahmoud A, Echabaane M, Omri K, Mir LE, Chaabane RB (2019) Development of an impedimetric non enzymatic sensor based on ZnO and Cu doped ZnO nanoparticles for the detection of glucose. *J Alloys Compd* 786:960–968. <https://doi.org/10.1016/j.jallcom.2019.02.060>
- Maiyalagan T, Sundaramurthy J, Suresh Kumar P, Kannan P, Opallo M, Ramakrishna S (2013) Nanostructured  $\alpha\text{-Fe}_2\text{O}_3$  platform for the electrochemical sensing of folic acid. *Analyst* 138:1779–1786. <https://doi.org/10.1039/c3an00070b>
- Maji SK, Dutta AK, Bhadu GR, Paul P, Mondal A, Adhikary B (2013) A novel amperometric biosensor for hydrogen peroxide and glucose based on cuprous sulfide nanoplates. *J Mater Chem B* 1:4127–4134. <https://doi.org/10.1039/c3tb20846j>
- Maleki B, Baghayeri M, Motlagh MG, Zonoz FM, Amiri A, Hajizadeh F, Hosseini AR, Esmailnezhad E (2019) Polyamidoamine dendrimer functionalized iron oxide nanoparticles for simultaneous electrochemical detection of Pb and Cd ions in environmental waters. *Measurement* 140:81–88. <https://doi.org/10.1016/j.measurement.2019.03.052>
- Malyan SK, Singh R, Rawat M, Kumar M, Pugazhendhi A, Kumar A, Kumar V, Kumar SS (2019) An overview of carcinogenic pollutants in groundwater of India. *Biocatal Agric Biotechnol* 21:101288. <https://doi.org/10.1016/j.bcab.2019.101288>
- Manibalan G, Murugadoss G, Thangamuthu R, Kumar MR, Kumar RM (2019) Facile synthesis of  $\text{CeO}_2\text{-SnO}_2$  nanocomposite for electrochemical determination of L-cysteine. *J Alloys Compd* 792:1150–1161. <https://doi.org/10.1016/j.jallcom.2019.04.127>
- Mao L, Gao M, Xue X, Yao L, Wen W, Zhang X, Wang S (2019) Organic-inorganic nanoparticles molecularly imprinted photoelectrochemical sensor for  $\alpha$ -solanine based on p-type polymer dots and n-CdS heterojunction. *Anal Chim Acta* 1059:94–102. <https://doi.org/10.1016/j.aca.2019.01.039>
- Melnyk I, Vaclavikova M, Seisenbaeva G, Kessler V (eds) (2019) *Biocompatible hybrid oxide nanoparticles for human health*, 1st edn, Elsevier, p 288. Paperback ISBN: 9780128158753, eBook ISBN: 9780128161883
- Moghaddam HM, Tajik S (2019) Beitollahi H, Highly sensitive electrochemical sensor based on La-doped  $\text{Co}_3\text{O}_4$  nanocubes for determination of Sudan I content in food samples. *Food Chem* 286:191–196. <https://doi.org/10.1016/j.foodchem.2019.01.143>
- Montemurro M, Schwaighofer A, Schmidt A, Culzoni MJ, Mayer HK, Lendl B (2019) High-throughput quantitation of bovine milk proteins and discrimination of commercial milk types by external cavity-quantum cascade laser spectroscopy and chemometrics. *Analyst Adv*. <https://doi.org/10.1039/c9an00746f>
- Mouroux MRE, Emans PJ, Zautsen RRM, Boonen A, Heeren RMA, Pastor BC (2019) Spatially resolved endogenous improved metabolite detection in human osteoarthritis cartilage by matrix assisted laser desorption ionization mass spectrometry imaging. *Analyst Adv*. <https://doi.org/10.1039/C9AN00944B>

- Nieuwoudt HH, Prior BA, Pretorius IS, Manley M, Bauer FF (2004) Principal component analysis applied to Fourier transform infrared spectroscopy for the design of calibration sets for glycerol prediction models in wine and for the detection and classification of outlier samples. *J Agric Food Chem* 52:3726–3735. <https://doi.org/10.1021/jf035431q>
- Okoth OK, Yan K, Liu Y, Zhang J (2016) Graphene-doped Bi<sub>2</sub>S<sub>3</sub> nanorods as visible-light photoelectrochemical aptasensing platform for sulfadimethoxine detection. *Biosens Bioelectron* 86:636–642. <https://doi.org/10.1016/j.bios.2016.07.037>
- Özdemir A, Lin JL, Gülfen M, Hsiao CJ, Chen CH (2019) A quadrupole ion trap mass spectrometer for dry microparticle analysis. *Analyst Adv*. <https://doi.org/10.1039/C9AN01431D>
- Puangjan A, Chaiyasith S (2018) A Co<sub>3</sub>O<sub>4</sub> nano-octahedron modified fluorine doped tin oxide electrochemical sensor for detection of benzocyclon. *J Electroanal Chem* 813:20–30. <https://doi.org/10.1016/j.jelechem.2018.02.008>
- Qu J, Wang Y, Dong Y, Zhu Z, Xing H (2014) Sensitive determination of catechol using a glassy carbon electrode modified with L-cysteine and ZnS:Ni/ZnS quantum dots. *Anal Methods*. <https://doi.org/10.1039/C4AY02199A>
- Rahman MM, Khan SB, Asiri AM et al (2013) Detection of nebigolol drug based on as-grown un-doped silver oxide nanoparticles prepared by a wet-chemical method. *Int J ElectrochemSci* 8:323–335
- Rahman MM, Alam MM, Asiri AM (2018) Selective hydrazine sensor fabrication with facile low-dimensional Fe<sub>2</sub>O<sub>3</sub>/CeO<sub>2</sub> nanocubes. *New J Chem*. <https://doi.org/10.1039/C8NJ01750F>
- Rathinamala I, Jeyakumaran N, Prithivikumaran N (2019) Sol-gel assisted spin coated CdS/PS electrode based glucose biosensor. *Vacuum* 161:291–296. <https://doi.org/10.1016/j.vacuum.2018.12.045>
- Roberts DB, Williams DJ (1975) Large scale synthesis of chalcopyrite and other sulphides in the laboratory. *Mat Res Bull* 10:163–168. [https://doi.org/10.1016/0025-5408\(75\)90150-6](https://doi.org/10.1016/0025-5408(75)90150-6)
- Rodas DS, Corns WT, Chen B, Stockwell PB (2010) Atomic fluorescence spectrometry: a suitable detection technique in speciation studies for arsenic, selenium, antimony and mercury. *J Anal At Spectrom* 25:933–946. <https://doi.org/10.1039/B917755H>
- Rojano WJS, Anjos T, Duyck CB, Saint’Pierre TD (2019) Determination of rare earth elements in environmental samples with high concentrations of barium by quadrupole inductively coupled plasma mass spectrometry. *Microchem J* 149:104026. <https://doi.org/10.1016/j.microc.2019.104026>
- Sakthivel R, Kubendhiran S, Chen SM, Kumar JV (2019) Rational design and facile synthesis of binary metal sulfides VS<sub>2</sub>-SnS<sub>2</sub> hybrid with functionalized multiwalled carbon nanotube for the selective detection of neurotransmitter dopamine. *Anal Chim Acta* 1071:98–108. <https://doi.org/10.1016/j.aca.2019.04.058>
- Samadi M, Sarikhani N, Zirak M, Zhang H, Zhang HL, Moshfegh AZ (2018) Group 6 transition metal dichalcogenide nanomaterials: synthesis, applications and future perspectives. *Nanoscale Horiz* 3:90–204. <https://doi.org/10.1039/c7nh00137a>
- Sharavanan VJ, Sivaramakrishnan M, Sivarajasekar N, Senthilrani N, Kothandan R, Dhakal N, Sivamani S, Show PL, Awwal MR, Naushad M (2020) Pollutants inducing epigenetic changes and diseases. *Environ Chem Lett* 18:325–343. <https://doi.org/10.1007/s10311-019-00944-3>
- Shen S, Wang Q (2013) Rational tuning the optical properties of metal sulfide nanocrystals and their applications. *Chem Mater* 25:1166–1178. <https://doi.org/10.1021/cm302482d>
- Shen Q, Zhao X, Zhou S, Hou W, Zhu JJ (2011) ZnO/CdS hierarchical nanospheres for photoelectrochemical sensing of Cu<sup>2+</sup>. *J Phys Chem C* 115:17958–17964. [dx.doi.org. https://doi.org/10.1021/jp203868t](https://doi.org/10.1021/jp203868t)
- Shende C, Brouillette C, Farquharson S (2019) Detection of codeine and fentanyl in saliva, blood plasma and whole blood in 5-minutes using a SERS flow-separation strip. *Analyst Adv*. <https://doi.org/10.1039/C9AN01087D>
- Shi W, Shuang E, Wang MM, Li TZ, Yang T, Liu SR, Chen ML, Wang JH (2019) Facile synthesis of metal-organic framework-derived SiW<sub>12</sub>@Co<sub>3</sub>O<sub>4</sub> and its peroxidase-like activity in colorimetric assay. *Analyst Adv*. <https://doi.org/10.1039/C9AN01262A>

- Show B, Mukherjee N, Mondal A (2017) Reusable iron sulfide nanospheres towards promoted photocatalytic and electrocatalytic activities. *New J Chem* 41:10083–10095. <https://doi.org/10.1039/C7NJ02018J>
- Singh R, Mukherjee MD, Sumana G, Gupta RK, Sood S, Malhotra BD (2014) Biosensors for pathogen detection: a smart approach towards clinical diagnosis. *Sensor Actuat B Chem* 197:385–404. <https://doi.org/10.1016/j.snb.2014.03.005>
- Sivakumar M, Sakthivel M, Chen SM (2017) Simple synthesis of cobalt sulfide nanorods for efficient electrocatalytic oxidation of vanillin in food samples. *J Colloid Interf Sci* 490:719–726. <https://doi.org/10.1016/j.jcis.2016.11.094>
- Sneddon EJ, Hardaway CJ, Sneddon J, Boggavarapu K, Tate AS, Tidwell SL, Gary DP, Douvris C (2017) Determination of selected metals in rice and cereal by inductively coupled plasma-optical emission spectrometry (ICP-OES). *Microchem J* 134:9–12. <https://doi.org/10.1016/j.microc.2017.04.009>
- Srivastava AK, Dev A, Karmakar S (2018) Nanosensors and nanobiosensors in food and agriculture. *Environ Chem Lett* 16:161–182. <https://doi.org/10.1007/s10311-017-0674-7>
- Sumathi C, Muthukumar P, Radhakrishnan S, Wilson J, Umar A (2014) Controlled growth of single-crystalline nanostructured dendrites of  $\alpha$ - $\text{Fe}_2\text{O}_3$  blended with MWCNT: a systematic investigation of highly selective determination of L-dopa. *RSC Adv* 4:23050–23057. <https://doi.org/10.1039/c4ra01451k>
- Supraja P, Tripathy S, Vanjari SRK, Singh V, Singh SG (2019) Electrospun tin (IV) oxide nanofiber based electrochemical sensor for ultra-sensitive and selective detection of atrazine in water at trace levels. *Biosens Bioelectron* 141:111441. <https://doi.org/10.1016/j.bios.2019.111441>
- Suresh R, Prabu R, Vijayaraj A, Giribabu K, Stephen A, Narayanan V (2012) Facile synthesis of cobalt doped hematite nanospheres: magnetic and their electrochemical sensing properties. *Mat Chem Phys* 134:590–596. <https://doi.org/10.1016/j.matchemphys.2012.03.034>
- Suresh R, Vijayaraj A, Giribabu K, Manigandan R, Prabu R, Stephen A, Thirumal E, Narayanan V (2013) Fabrication of iron oxide nanoparticles: magnetic and electrochemical sensing property. *J Mater Sci Mater Electron* 24:1256–1263. <https://doi.org/10.1007/s10854-012-0916-1>
- Suresh R, Giribabu K, Manigandan R, Praveen Kumar S, Munusamy S, Muthamizh S, Stephen A, Narayanan V (2014a) New electrochemical sensor based on Ni-doped  $\text{V}_2\text{O}_5$  nanoplates modified glassy carbon electrode for selective determination of dopamine at nanomolar level. *Sensor Actuat B Chem* 202:440–447. <https://doi.org/10.1016/j.snb.2014.05.095>
- Suresh R, Giribabu K, Manigandan R, Vijayaraj A, Prabu R, Stephen A, Narayanan V (2014b)  $\alpha$ - $\text{Fe}_2\text{O}_3$  nanoflowers: synthesis, characterization, electrochemical sensing and photocatalytic property. *J Iran Chem Soc* 11:645–652. <https://doi.org/10.1007/s13738-013-0335-0>
- Suresh R, Giribabu K, Manigandan R, Praveen Kumar S, Munusamy S, Muthamizh S, Narayanan V (2014c) Characterization and dopamine sensing property of  $\text{V}_2\text{O}_5$ @polyaniline nanohybrid. *Synth Met* 196:151–157. <https://doi.org/10.1016/j.synthmet.2014.07.025>
- Syu YC, Hsu WE, Lin CT (2018) Review-field-effect transistor biosensing: devices and clinical applications. *ECS J Solid State Sci and Technol* 7(7):Q3196–Q3207. <https://doi.org/10.1149/2.0291807jss>
- Thiyagarajan N, Chang JL, Senthilkumar K, Zen JM (2014) Disposable electrochemical sensors: a mini review. *Electrochem Commun* 38:86–90. <https://doi.org/10.1016/j.elecom.2013.11.016>
- Tsang CHA, Li K, Zeng Y, Zhao W, Zhang T, Zhan Y, Xie R, Leung DYC, Huang H (2019) Titanium oxide based photocatalytic materials development and their role of in the air pollutants degradation: overview and forecast. *Environ Int* 125:200–228. <https://doi.org/10.1016/j.envint.2019.01.015>
- Venkadesh A, Radhakrishnan S, Mathiyarasu J (2017) Eco-friendly synthesis and morphology-dependent superior electrocatalytic properties of CuS nanostructures. *Electrochim Acta* 246:544–552. <https://doi.org/10.1016/j.electacta.2017.06.077>
- Wang J, Zhao D, Zhang Y, Li J, Xu C (2014) A highly sensitive sensor for the detection of nitrite based on a nanoporous  $\text{Fe}_2\text{O}_3$ -CoO composite. *Anal Methods* 6:3147–3151. <https://doi.org/10.1039/c4ay00171k>



- Wang Q, Liu S, Fu L, Cao Z, Ye W, Li H, Guo P, Zhao XS (2018a) Electrospun  $\gamma$ -Fe<sub>2</sub>O<sub>3</sub> nanofibers as bioelectrochemical sensors for simultaneous determination of small biomolecules. *Anal Chim Acta* 1026:125–132. <https://doi.org/10.1016/j.aca.2018.04.010>
- Wang Y, Zhao KJ, Tao DP, Zhai FG, Yang HB, Zhang Z (2018b) Application of pyrite and chalcopyrite as sensor electrode for amperometric detection and measurement of hydrogen peroxide. *RSC Adv* 8:5013–5019. <https://doi.org/10.1039/c7ra13628e>
- Wang X, Zuo Y, Zhang Y, Yang T, Lin W (2019) Triphenylamine Schiff base as a lipid droplet-targeted fluorescent probe using Si–O–Si as a bridge for the detection of Cr<sup>6+</sup> applied in bio-imaging. *Analyst Adv.* <https://doi.org/10.1039/C9AN01174A>
- Wu W, Yu B, Jin J, Wu H, Wang S, Xia Q (2016) A novel nonenzymatic electrochemical sensor based on 3D flower-like Ni<sub>7</sub>S<sub>6</sub> for hydrogen peroxide and glucose. *Sensor Actuat B Chem.* <https://doi.org/10.1016/j.snb.2016.04.006>
- Xi J, Wang H, Zhang B, Hu X, Zhao F, Zeng B (2019) Type I Bi<sub>2</sub>S<sub>3</sub>@ZnS core-shell structured photocatalyst for the selective photoelectrochemical sensing of Cu<sup>2+</sup>. *Anal Methods.* <https://doi.org/10.1039/C9AY00591A>
- You J, Shi Y, Li J, Yang X, Liu Z, Zhu W, Wu Z, Xiong J (2019) Rapid quantification of human urinary estrogens and estrogen metabolites by HPLC mass spectrometry. *Microchem J* 147:157–162. <https://doi.org/10.1016/j.microc.2019.03.008>
- Zhang X, Liu M, Liu H, Zhang S (2014) Low-toxic Ag<sub>2</sub>S quantum dots for photoelectrochemical detection glucose and cancer cells. *Biosens Bioelectron* 56:307–312. <https://doi.org/10.1016/j.bios.2014.01.033>
- Zhang X, Zeng T, Hu C et al (2016a) Studies on fabrication and application of arsenic electrochemical sensors based on titanium dioxide nanoparticle modified gold strip electrodes. *Anal Methods* 8:1162–1169. <https://doi.org/10.1039/C5AY02397A>
- Zhang S, Li B, Sheng Q, Zheng J (2016b) Electrochemical sensor for sensitive determination of nitrite based on the CuS-MWCNTs nanocomposites. *J Electroanal Chem.* <https://doi.org/10.1016/j.jelechem.2016.03.025>

# Chapter 10

## Biosensor Devices Based on Metal Oxide Materials



Selvaraj Devi and Vairaperumal Tharmaraj

### Contents

10.1	Introduction .....	312
10.2	Methods of Synthesis in Metal Oxide Nanostructured Materials .....	313
10.3	Properties of Metal Oxide Nanomaterials .....	315
10.4	Fabrication of Metal Oxide-Based Biosensor Devices .....	316
10.5	Optical Waveguide-Based Metal Oxide Biosensor Devices .....	317
10.5.1	Fluorescence-Based Waveguide Biosensor Devices .....	317
10.5.2	TriPLeX™ Waveguide Chip .....	317
10.5.3	Nanoporous Optical Waveguide Sensor Device .....	318
10.6	Surface Enhanced Raman Spectroscopy Based Optofluidic Biosensors Devices .....	319
10.7	Electrochemical Biosensor Devices .....	321
10.7.1	Electrochemical Sensors for Metal-Oxide-Metal Sensor Devices .....	323
10.7.2	Metal Oxide Nanowire Mat Based Biosensing Devices .....	325
10.7.3	Lab-on-a-Chip Flexible Electrochemical Biosensors Devices .....	326
10.7.4	Three-Dimensional Origami Devices for Biosensing .....	327
10.8	Conclusion .....	327
	References .....	329

**Abstract** Biosensor is a device that detects biological signals by converting biological signals into detectable electronic signals. Biosensor involves the combination of bioreceptors like proteins/enzymes, DNA, and RNA that interact with some specific bioanalytes like antibody–antigen and a transducer that converts the interaction into a useful analytical signal. Several types of biosensor devices have been successfully developed and utilized in the field of biomedical, food industries, and environment. The conventional biosensor devices have some limitations such as poor selectivity, low sensitivity, and expensive fabrication. Therefore, the

---

S. Devi

Department of Inorganic Chemistry, University of Madras, Chennai, Tamil Nadu, India

V. Tharmaraj (✉)

Department of Analytical Chemistry, National Chung-Hsing University, Taichung, Taiwan

© The Editor(s) (if applicable) and The Author(s), under exclusive licence to Springer Nature Switzerland AG 2021

311

S. Rajendran et al. (eds.), *Metal, Metal-Oxides and Metal Sulfides for Batteries, Fuel Cells, Solar Cells, Photocatalysis and Health Sensors*, Environmental Chemistry for a Sustainable World 62, [https://doi.org/10.1007/978-3-030-63791-0\\_10](https://doi.org/10.1007/978-3-030-63791-0_10)

development of a wide range of detection purposes, nontoxic, highly stable and biocompatible with low cost biosensing devices, is still crucial and challenging.

The diverse chemical and physical properties including larger active surface area, easier functionality, high adsorption capability, and fast electron-transfer capability of metal oxide materials make them essential and cost-effective resources for the fabrication of biosensing devices. The additional advantages of scalability and tunable bandgap features in hybrid metal oxide materials make them suitable alternative biocompatible devices.

This chapter addresses recent advancement in the fabrication of various types of metal oxide-based biosensors devices including optical waveguides sensor devices, optofluidic biosensors devices, and electrochemical sensor devices. Finally, this chapter concludes with some interesting results, challenging innovative methods for the development of new biosensors device, and future perspective on the fabrications of metal oxide-based sensors devices.

**Keywords** Biosensing devices · Metal oxide · Materials · Optical waveguides · Optofluidic · Electrochemical · Biomolecules · Spectroscopy

## Abbreviations

DNA	deoxyribonucleic acid
HQ-PA	4-(1,4-dihydroxybenzene)butyl phosphonic acid
HS- DNA	thiol-terminated DNA
pH	hydrogen ion concentration
Q-PA	4-(1,4-diketobenzene)butyl phosphonic acid
SEM	scanning electron microscopy
SERS	surface enhanced Raman spectroscopy
TEM	transmission electron microscopy

## 10.1 Introduction

The efforts of device fabrication engineers and material researchers mainly focus on metal oxide materials due to the abundance, cheap, easy fabrication, and high performances of metal oxide materials. Recently, biosensor devices are developed by using metal oxide nanostructured materials because of high sensitivity, long reliability, and high surface-to-volume ratio of metal oxide nanostructured materials (Caruso 2001; Tenne 2006; Doong and Shih 2010; Gupta and Gupta 2005; Pandey et al. 2008; Chen et al. 2005). Silicon, zinc, iron, cerium, tin, zirconium, titanium, and magnesium-based metal oxide nanostructured materials have various morphologies, functional biocompatible, nontoxic, and enhanced electron transfer properties. Metal oxide nanomaterials have significant enhancement in sensing properties for successfully demonstrating biosensor devices (Yamazoe 1991).

The commonly used biosensing devices are targeting physical and chemical (Burke et al. 2006), or biological information (Reverté et al. 2017) of analyte by detecting changes in fluorescence intensity (Kondo et al. 2017), refractive index (Escorihuela et al. 2014), or spectroscopic shifts (Puyol et al. 1999; Lavers et al. 2000;). Various transducers have been used in sensing devices such as waveguide sensors (Mukundan et al. 2009; Tokel et al. 2015), total internal reflection fluorescence spectroscopy, dual polarization interferometry (Roy et al. 2008; Swann et al. 2004), and electrochemical sensors (Ansari et al. 2010).

The biosensor devices are needed to improve versatile design with low cost fabrication and enhance the output signals when the sensing molecules binding to the receptors (Yoon and Kim 2012; Luchansky and Bailey 2011). In some cases, reversibility of the recognition is limited due to the strong binding of biomolecules with receptors. However, different types of binding receptors have ideal signaling mechanisms such as electrostatic interactions, affinity-based binding, electron transfer, energy transfer, and complex formation. Especially, nanostructured materials surface functionalized with binding receptors layer have increased sensitivity response due to the high surface area of nanomaterials (Hennemann et al. 2013; Balamurugan and Spivak 2011; Flavin and Resmini 2010; Xu et al. 2011).

Device-based biosensors are mainly utilized as optical and electrochemical transducers because of the flexible design and easy to handle. Optical waveguide-based device has lots of attention due to the flexibility with high configuration and less optical loss (Duer et al. 2010; Prak et al. 2011). Electrochemical devices are very easy to fabricate handheld devices (Kumar et al. 2017), and screen-printing electrodes are very cost-effective technology to fabricate the devices with innovative design (Sun et al. 2017).

This chapter deals with the synthesis and properties of metal oxide materials, fabrication of metal oxide-based biosensor devices, and focusing on optical (Raman/fluorescent) and electrochemical transducer-based biosensing devices. Finally, conclude this chapter with future perspective of fabrications of metal oxide-based sensors devices.

## 10.2 Methods of Synthesis in Metal Oxide Nanostructured Materials

Synthesis of metal oxide nanostructured materials has mainly involved either direct physical or chemical deposition techniques. Physical deposition is “top-down” approach without the involvement of chemical reactions such as thermal evaporation (Pan et al. 2001), molecular beam epitaxial (Mia and Chang 2009), sputtering (Zheng et al. 2008), laser ablation (Nagashima et al. 2007), and confinement growth (Liang et al. 2010; Choi et al. 2006). Chemical deposition method is a “bottom-up” approach, usually involving chemical reactions during the synthesis through chemical vapor deposition (Park et al. 2002), hot-filament metal oxide vapor deposition

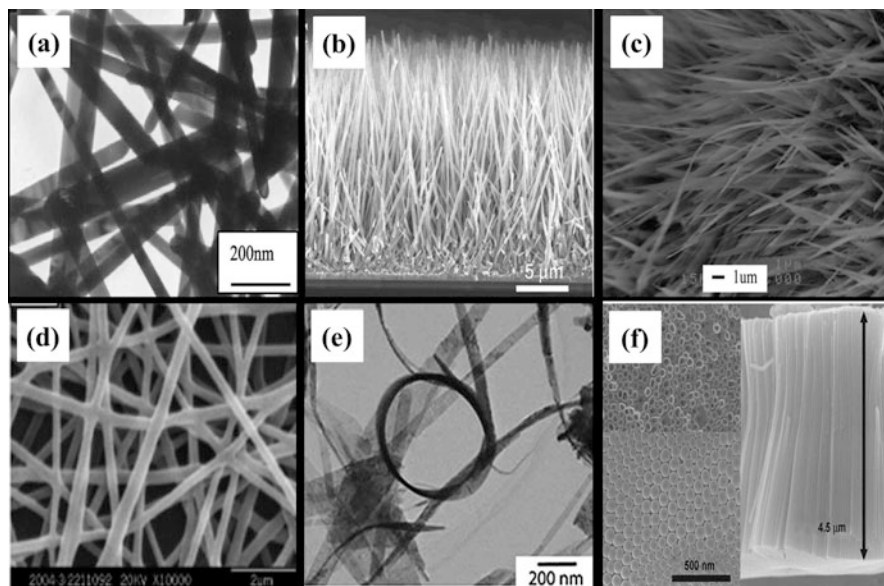


**Fig. 10.1** (a) Transmission electron microscopy (TEM) image of nickel oxide nanorods. (b) Scanning electron microscopy (SEM) cross-section image of zinc oxide nanowire. (c) SEM images of zinc oxide nanobelts. (d) SEM image of zinc oxide nanofibers. (e) TEM image of copper oxide nanoribbons. (f) SEM image of titanium oxide nanotube. Inset: top and bottom views of nanotube structures; *nm*, nanometer;  $\mu\text{m}$ , micrometer; *kV*, beam accelerating voltage or electron volt. (Reprinted with permission of Elsevier from Wang et al. *Chem. Phys. Lett.* **2002**; ACS from Lori E. Greene et al. *Inorg. Chem.* **2006**; ACS from Wen et al. *J. Phys. Chem. B*, **2005**; John Wiley and sons from Pan et al. *J. American Ceramic Society*, 2005; RSC from Gou et al. *J. Mater. Chem.* **2008**; John Wiley and sons from Schmuki et al. *small*. **2007**)

(Kumari et al. **2007**; Devan et al. **2010**), thermal oxidation (Sedach et al. **2010**), solvothermal (Sun et al. **2005**; Su et al. **2011**), and sol-gel syntheses (Limmer and Cao **2003**).

Metal oxide nanostructured materials have been used for the fabrication of nanosensing devices because researchers have believed the uniform size and shape of nanostructured materials with well crystalline structure and a consistent chemical composition with verity of morphology. The structural morphology of metal oxide nanostructured materials is related with the concentrations of metal oxide precursor, diffusion rate, temperature, and reaction time. Figure 10.1 shows the various morphologies of metal oxide nanostructured materials such as nanorods (Wang et al. **2002**), nanowires (Greene et al. **2006**), nanobelts (Wen et al. **2005**), nanofibers (Wu and Pan **2006**), nanoribbons (Gou et al. **2008**), and nanotubes (Macak et al. **2007**).

### 10.3 Properties of Metal Oxide Nanomaterials

Zinc oxide (ZnO), nickel oxide (NiO), titanium oxide (TiO<sub>2</sub>), silicon oxide (SiO<sub>2</sub>), iron oxide (Fe<sub>2</sub>O<sub>3</sub>), and zirconium oxide (ZrO<sub>2</sub>) based metal oxide nanostructured materials (Gooding 2006; Rosenholm et al. 2009; Bavykin et al. 2004; Forzani et al. 2004; Wang et al. 2006; Liu et al. 2005) are widely used for fabricating various biosensing devices.

Metal oxide nanomaterials have unique physical and chemical properties, including wide bandgaps (Emeline et al. 2005; Kroger et al. 2009), good electrical (Mavrou et al. 2008; Lee et al. 2009), optical (Su et al. 2006), high dielectric constants (Gutowski et al. 2002; Rignanese 2005; Robertson 2006), reactive electronic transitions (Chen et al. 2002; Sysoev et al. 2006), electrochromic characteristics (Rosseinsky and Mortimer 2001; Granqvist 2008), and superconductivity (Takada et al. 2003). In addition, metal oxide nanomaterials are biocompatible, nontoxic, larger surface area with tunable transition state, and thermally stable. The hybrid of metal oxide nanomaterials-based biocomposites is currently used as promising materials for designing new biosensor devices applications. Some examples of metal oxide nanomaterials used for biosensors applications are shown in Table 10.1 (Malhotra et al. 2012).

**Table 10.1** The properties of various metal oxide nanomaterials such as zinc oxide, nickel oxide, titanium oxide, silicon oxide, iron oxide, zirconium oxide, and cerium oxide

Metal oxides	Properties	Analyte	References
Zinc oxide (ZnO)	Structural morphology, fast electron transfer, and biocompatibility	Cholesterol oxidase (ChOx), DNA, glucose oxidase (GOx), horseradish peroxidase (HRP), and immunoglobulin G (IgG)	Gooding (2006)
Nickel oxide (NiO)	Fast electron transfer and high adsorption	Cholesterol oxidase (ChOx), DNA, glucose oxidase (GOx), lipase, and immunoglobulin G (IgG)	Rosenholm et al. (2009)
Titanium oxide (TiO <sub>2</sub> )	Photocatalysis, wide bandgap, and biocompatibility	Cholesterol oxidase (ChOx), DNA, glucose oxidase (GOx), horseradish peroxidase (HRP), lipase, and immunoglobulin G (IgG)	Bavykin et al. (2004)
Silicon dioxide (SiO <sub>2</sub> )	Structural morphology, surface functionalization, and biocompatibility	Cholesterol oxidase (ChOx), DNA, glucose oxidase (GOx), lipase, and immunoglobulin G (IgG)	Forzani et al. (2004)
Iron oxide (Fe <sub>2</sub> O <sub>3</sub> )	Super paramagnetism and affinity with oxygen atom of proteins	Cholesterol oxidase (ChOx), DNA, glucose oxidase (GOx), and immunoglobulin G (IgG)	Wang et al. (2006)
Zirconium oxide (ZrO <sub>2</sub> )	Biocompatibility and binding with phosphorus atom of DNA	Cholesterol oxidase (ChOx), DNA, glucose oxidase (GOx), horseradish peroxidase (HRP), lipase, and immunoglobulin G (IgG)	Liu et al. (2005)

The use of metal oxide nanomaterials in biosensor devices for analyzing bioanalytes such as DNA, cholesterol oxidase.

## 10.4 Fabrication of Metal Oxide-Based Biosensor Devices

A sensor device can sense the measured information into an electrical or other analytically useful signal using specific receptors molecules. The signal intensity is related to the concentration of target biomolecule to be detected (McQuade et al. 2000; Dzyadevych et al. 2007). Fabrication of biosensors devices mainly focused on selectivity, sensitivity, flexibility, and low cost. The metal oxide-based sensing devices overcome the limitations of conventional methods such as incapability of precise control of the transducer. Metal oxide-based biosensor devices are constructed by specific biorecognition subunit (ligand) layer decorated with a transducer surface (metal oxide) through spacer (monolayer) as shown in Fig. 10.2. Sensor devices generated the signals from analyte concentration and evaluated with physicochemical transducers mainly as optical or electrochemical. Hence, metal oxides have hope for fabricating biosensors devices with flexible and handhold with low cost.

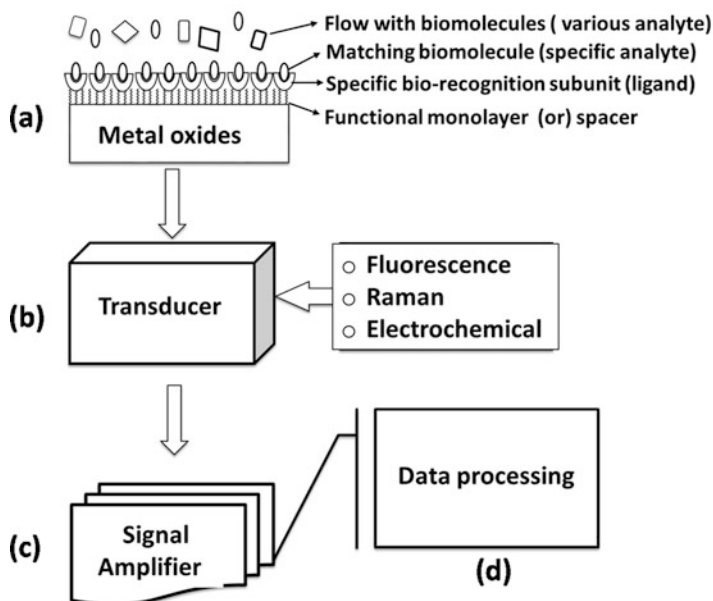


**Fig. 10.2** The component involves in the fabrication of metal oxide-based biosensor device. **(a)** Receptors: the surface functionalization of metal oxide to achieve a targeted interaction with the analytes. **(b)** Transducer analyzes the valuable analytical signals from receptors as electrical energy. **(c)** Signal amplifier further amplified the electrical signal to processor. **(d)** Finally, the data processed in an electronic form

## 10.5 Optical Waveguide-Based Metal Oxide Biosensor Devices

An optical waveguide is a device that guides waves; electromagnetic waves pass through the analyte molecules in direct or indirect methods (Girard et al. 2000). Waveguide-based sensing devices can offer a label-free detection of biomolecules with high selectivity and sensitivity in real-time analysis (Lukosz 1995; McDonagh et al. 2008).

### 10.5.1 Fluorescence-Based Waveguide Biosensor Devices

Fluorescence-based waveguide biosensor devices have much attention in the field of biomedical and materials researcher due to the high sensitivity, easy to handle, interpretation, fast analysis in real samples, and portability with moderate cost (Leung et al. 2007; Wang and Wolfeis 2013). The major advantage of fluorescence-based waveguide biosensor devices is that the lower concentration of analyte can be detected with high sensitivity because of the waveguide chip that is always away from the detection region (Farré et al. 2009; Golden et al. 1992; Wadkins et al. 1998).

### 10.5.2 TriPleX™ Waveguide Chip

Liu et al. (2018) fabricated a TriPleX™ waveguide chip on glass substrate for the simultaneous detection of 32 analytes. TriPleX™ waveguide sensing chip consisted of 32 separated sensors patches with 3 Y-junctions splitters in four equal rows and eight excitation windows in parallel as shown in Fig. 10.3a. The layout of TriPleX™ waveguide chip shows that the chip contains the multilayer stacking of silicon nitride and silicon oxide in the area of 65 mm × 20 mm and 1 mm in depth for distributing laser light into 32 separated sensing windows. The cross-section of TriPleX™ waveguide chip single stripe is shown in Fig. 10.3b and c. Figure 10.3d shows the fluorescence collection of integrated flow cell with polymer fiber. The waveguide chip successfully applied for the detection of environmental contamination in water samples with higher sensitivity. The detection limit as low as 0.22 μgL<sup>-1</sup> for microcystin-laboratory reagent (LR), 1.18 μgL<sup>-1</sup> for 2, 4-dichlorophenoxyacetic acid, 0.2 μgL<sup>-1</sup> for atrazine, and 0.06 μgL<sup>-1</sup> for bisphenol-A in real water samples.

Similar kind of waveguide was developed by Liu et al. (2017) for the detection of microcystin-LR in lake water samples with high sensitivity using integrated optical waveguide. Multichannel waveguide chip is constructed by using 5 mW at 635 nm semiconductor light source coupled with multichannel ion exchange waveguide. One end of optical fiber is located under the sensor surface and another end is chip



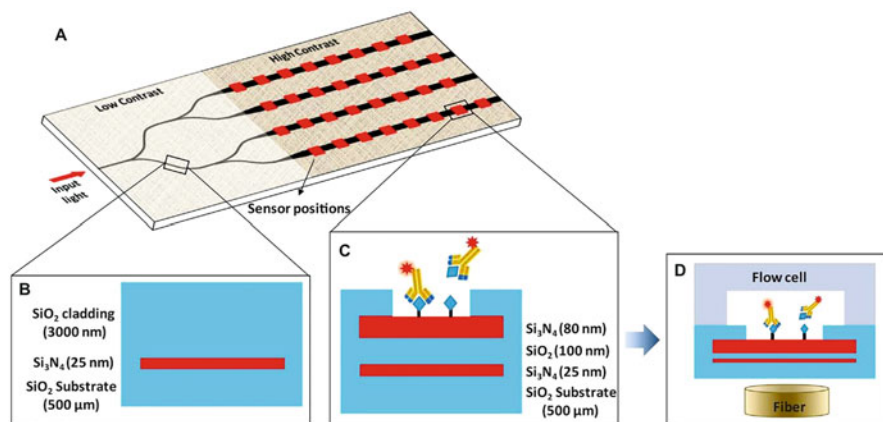


**Fig. 10.3** (a) TriPleX™ waveguide chip layout. (b) Cross-section of TriPleX™ waveguide chip single-stripe. (c) Cross-section of TriPleX™ waveguide double-stripe waveguide structure and sensing windows. (d) Integration of flow cell and polymer fiber for fluorescence collection; SiO<sub>2</sub>, silicon dioxide; Si<sub>3</sub>N<sub>4</sub>, silicon nitride; nm, nanometer; μm, micrometer. (Reprinted with the permission of Elsevier from Liu et al. *Biosensors and Bioelectronics*, 2019)

surface. The flow injection system is comprised by a syringe pump connected to six-way injection valve with preincubation loop and sonication valve of flow cell. All the data acquisition is fully automated by using computer and the whole diagram of the integrated optical fluorescence multichannel biosensor is shown in Fig. 10.4.

The waveguide chip was designed as shown in Fig. 10.5a and the cross-sectional view along one of the sensing patches can be seen in Fig. 10.5b. A photographic image of light propagation along the waveguide chip is shown in Fig. 10.5c. The fabrication of fluorescence waveguide decorated with monolayer of (3-mercaptopropyl) trimethoxysilane and N-(4-maleimidobutyryloxy) succinimide for immobilization of bovine serum albumin-microcystin-LR conjugate was confirmed by atomic force microscopy. The beam transmission model simulated broadcast of light throughout the waveguide chip that allowed the optimization of waveguides for immune sensing applications. The waveguide chip was successfully applied in real water samples for the detection of microcystin-LR in the range of submicrogram (e.g. 0.5 μg L<sup>-1</sup>) per liter with recovery rates between 84% and 108%.

### 10.5.3 Nanoporous Optical Waveguide Sensor Device

Nanoporous optical waveguide devices also have much attention for label-free biosensing applications. Hotta et al. (2012) have developed on optical waveguide for label-free biosensing of bovine serum albumin. The fabrication of nanoporous optical waveguide device is composed by porous anodic alumina film wrapped with aluminum film on glass substrate as shown in Fig. 10.6a. The incident light reflection

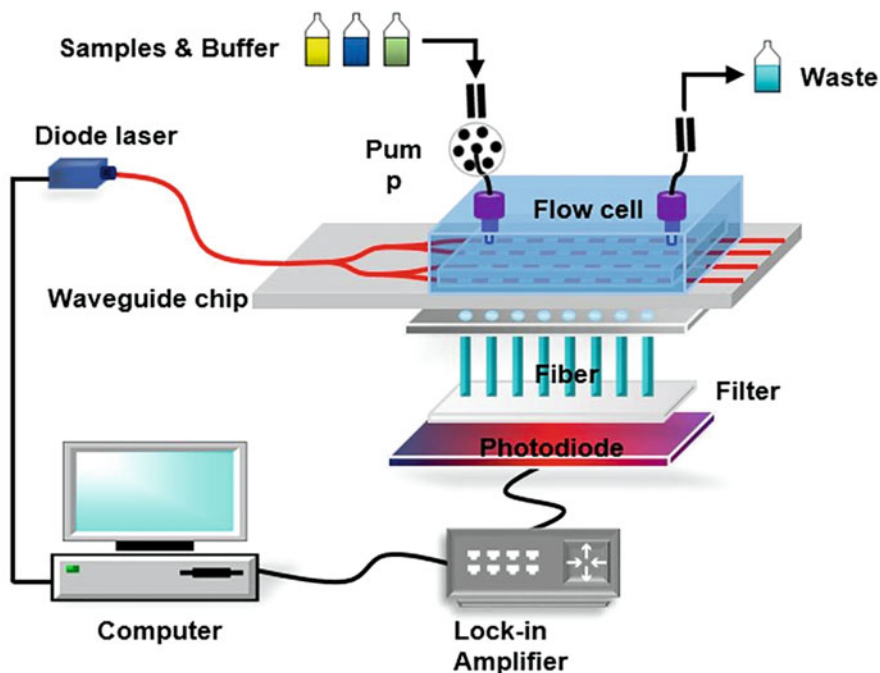


**Fig. 10.4** Integrated optical fluorescence multichannel biosensor. (Reprinted with the permission of Springer Nature from Lanhua Liu et al. *Scientific Reports*. 2017)

spectrum of porous anodic alumina wrapped with aluminum multilayer and electric field distribution of different orders are shown in Fig. 10.6b and c. Nanoporous optical waveguide has been successfully utilized bioaffinity interaction between biotin and streptavidin at different pH. The sensitivity of porous anodic alumina was 20-fold higher than that of conventional surface plasmon resonance sensors, and the detection limit was as low as  $5.7 \text{ pg}(\text{mm}^2)^{-1}$  for bovine serum albumin.

## 10.6 Surface Enhanced Raman Spectroscopy Based Optofluidic Biosensors Devices

Titanium oxide nanotubes coated with silver nanoparticles array-based optofluidic device have been developed for the detection of alkylthiol-capped deoxy ribonucleic acid (DNA) oligo strand using surface-enhanced Raman spectroscopy (SERS) (Lamberti et al. 2015). Titanium oxide nanotubes and silver nanoparticles have the potential to enhance the electromagnetic enhancement and charge transfer mechanism because the high surface area of titanium oxide nanotubes will increase the amount of adsorbed molecules as shown in Fig. 10.7.

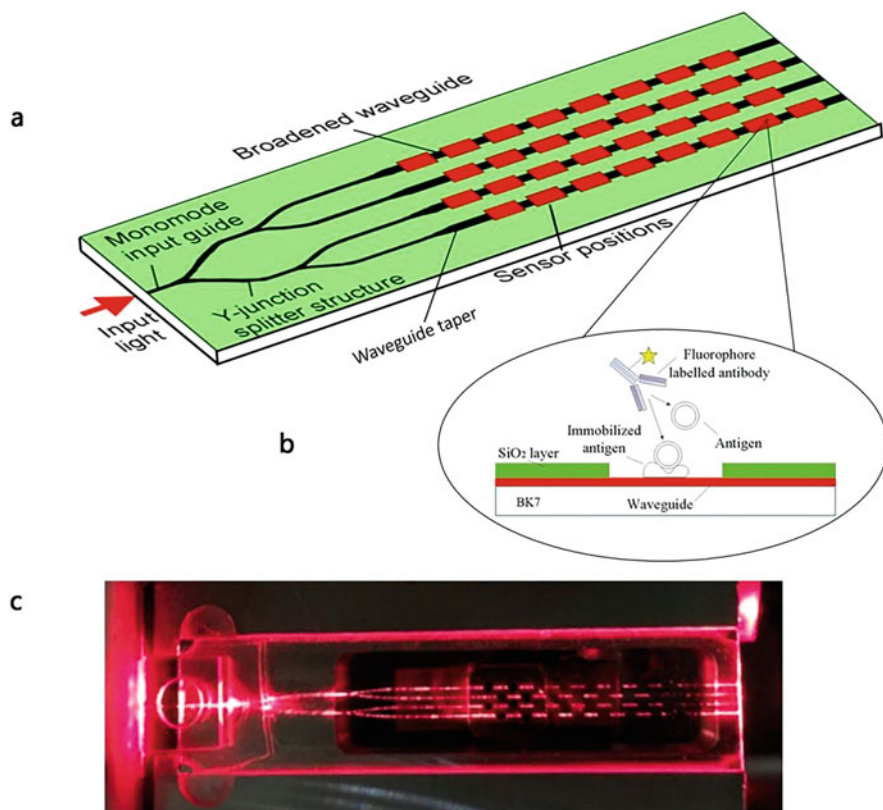


**Fig. 10.5** (a) Sensor layout; (b) a cross-sectional view along one of the sensing patches, showing the waveguide, isolation layer, and location of the surface chemistry; (c) a photographic image of light propagation along the waveguide chip (SiO<sub>2</sub>- silicon dioxide; BK7- 7th borosilicate crown glass; a junction divide a single input waveguide into two output waveguides with a geometry similar to the letter Y is called as Y- junction splitter). (Reprinted with the permission of springer nature from Lanhua Liu et al. Scientific Reports. 2017)

The array-based devices have good uniformity of Raman signals as shown in Fig. 10.8a, and the SERS spectrum of rhodamine 6G injected into the channel with 30 s patterned is shown in Fig. 10.8b. The performance of silver/titanium oxide nanotubes optofluidic device was obtained by measuring the Raman intensity at  $1610\text{ cm}^{-1}$  for free surface of silver with titanium oxide nanotubes and also the SERS detection of an alkylthiol-capped DNA oligo strand (SH-C6-AAAAAA, polyA-SH).

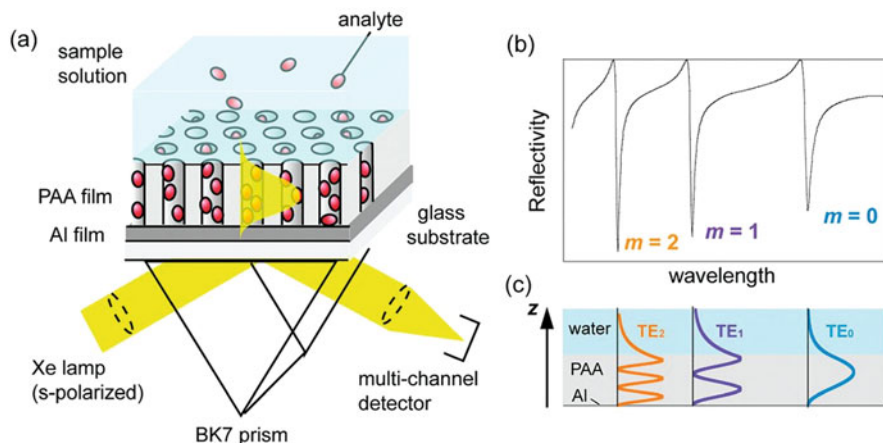
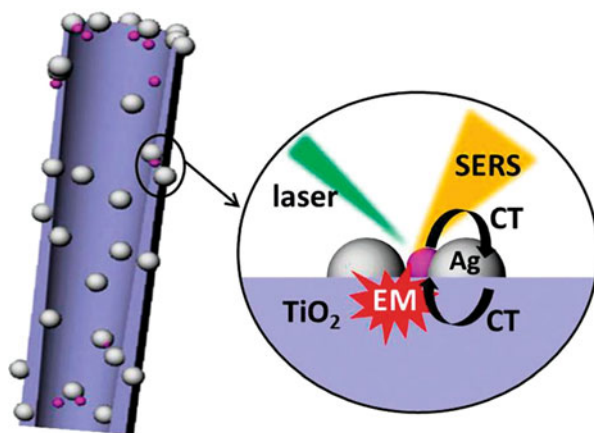


**Fig. 10.6** (a) Nanoporous optical waveguide platform with porous anodic alumina/aluminum multilayer film. (b) Reflection spectrum of porous anodic alumina/aluminum multilayer film measured in the Kretschmann configuration. (c) Electric field distributions of TE waveguide modes with different mode orders ( $m$ );  $TE$ , transverse electric;  $BK7-th$ , borosilicate crown glass;  $Al$ , aluminum;  $PAA$ , porous anodic alumina;  $Xe$ , xenon;  $m$ , mode order;  $s$ , polarized-German senkrecht polarized (the polarization of light electric field occur perpendicularly to the plane of incidence). (Reprinted with the permission of ACS from Hotta et al. *ACS Nano* 2012)

**Fig. 10.7** Three-dimensional design of  $TiO_2$  nanotubes coated with silver nanoparticles with mechanism of electromagnetic (EM) enhancements and charge transfer (CT);  $Ag$ , silver;  $SERS$ , surface enhanced Raman spectroscopy;  $TiO_2$ , titanium oxide. (Reprinted with the permission of RSC from Lamberti et al. *J. Mater. Chem. C* 2015)



## 10.7 Electrochemical Biosensor Devices

The fabrication of modified electrodes has very important role in electrochemical biosensor for the detection of biomolecules. The electrode surface should be modified with suitable binding receptors of biological molecule with good uniformity for increasing the selectivity and sensitivity of biosensor devices.

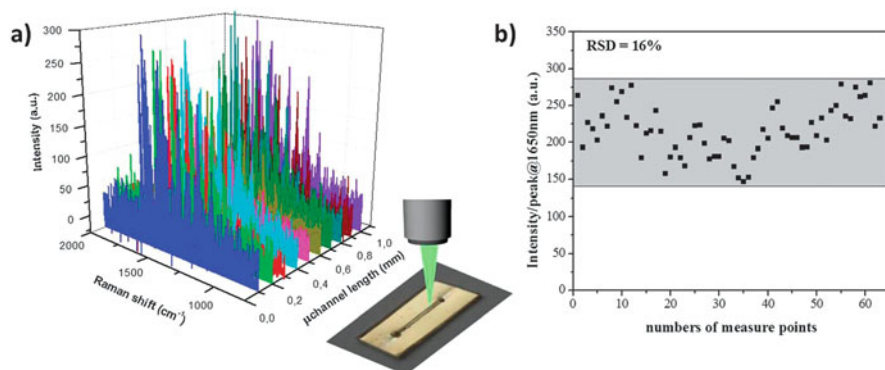


**Fig. 10.8** SERS spectra of rhodamine 6G at  $10^{-6}$  molar concentration (a) and peak intensity at  $1650 \text{ cm}^{-1}$  of rhodamine 6G along the microfluidic channel (b); *RSD*, relative standard deviation; *a. u.*, arbitrary unit; *mm*, millimeter;  $\text{cm}^{-1}$ , centimeter inverse. (Reprinted with the permission of RSC from Lamberti et al. *J. Mater. Chem. C*. 2015)

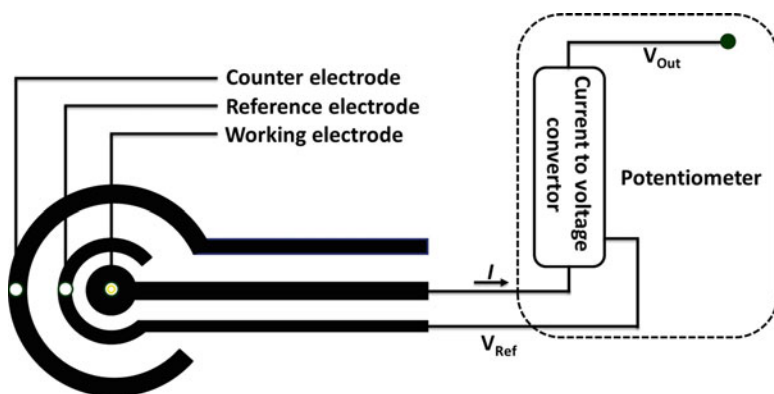


**Fig. 10.9** Parts of the component mainly involving in the electrochemical sensors device; *I*, current;  $V_{\text{Ref}}$ , reference voltage;  $V_{\text{out}}$ , output current

The arrangement of three electrodes test strip was comprised of three electrodes. The working electrode was coated with biorecognizing molecules. The reference electrode keeps the current of working electrode during the chemical reaction, and the counter electrode supplied the optimal current into the working electrode and the whole process of electrochemical sensors device is shown in Fig. 10.9.

### 10.7.1 Electrochemical Sensors for Metal-Oxide-Metal Sensor Devices

A simple and low cost glucose sensors device was fabricated by using platinum/copper oxide/platinum metal-oxide-metal. Standard photolithography process has been used to fabricate the device with high uniform arrangements for providing a larger surface area that acts as a nonenzymatic reservoir for glucose oxidation. The unique property of metal-oxide-metal sensor devices was to detect the glucose levels at neutral pH and perform copper oxide based nonenzymatic electrochemical sensors in alkaline medium (Abunahla et al. 2019).

The fabrication process of metal-oxide-metal sense devices (Fig. 10.10) involves the formation of copper oxide layer on a hot plate by heating the wafer at 500 °C followed by lithography step. The photoresist layer was patterned on the wafer by using ultraviolet exposure system and an appropriate developer. The final wafer was obtained by lifting the photoresist layer after sputtering the platinum layer on the wafer devices.

The fabricated metal-oxide-metal sensor devices on glass wafer are seen in Fig. 10.11a that show the planar structure of the devices consisting of CuO layer and Pt electrodes. Copper oxide layer was separated by platinum electrodes as shown in Fig. 10.12b. The SEM cross-sectional view of metal oxide metal device shows that the formation of CuO with thickness of 26.7 nm and 20.8 nm Pt layer (Fig. 10.11c).

#### Electrochemical Glucose Oxidation in Copper Oxide System

Electrochemical glucose oxidation was achieved in aqueous medium by using copper oxide as catalyst with the formation of various oxidized/hydroxylated species at all pH range. A plausible mechanism for the electrochemical glucose oxidation into gluconolactone in the presence of redox active couple  $\text{Cu}^{2+}/\text{Cu}^{3+}$  in alkaline pH is as follows:

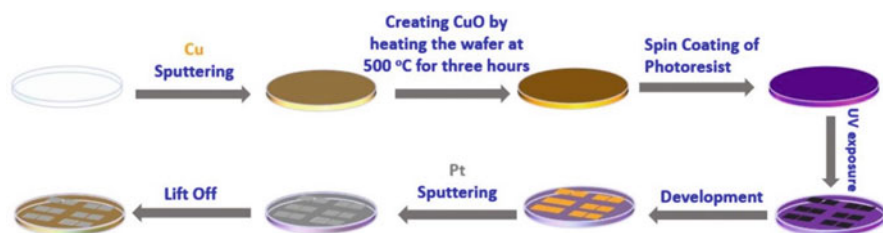


**Fig. 10.10** The fabrication process of metal-oxide-metal sensor devices; *Cu*, copper; *CuO*, copper oxide; *Pt*, platinum; *UV*, ultraviolet. (Reprinted with the permission of springer nature from Heba Abunahla et al. Scientific reports, 2019)

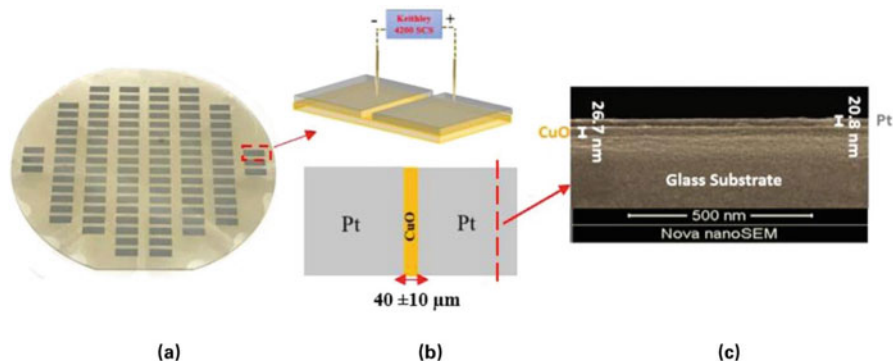


**Fig. 10.11** (a) The fabricated metal-oxide-metal sense device on a glass wafer. (b) Planar Pt/CuO/Pt device. (c) SEM cross-sectional view of metal-oxide-metal sense device; *CuO*, copper oxide; *Pt*, platinum; *SEM*, scanning electron microscopy; *nm*, nanometer;  $\mu\text{m}$ , micrometer; *SCS*, semiconductor characterization system. (Reprinted with the permission of springer nature from Heba Abunahla et al. Scientific reports, 2019)

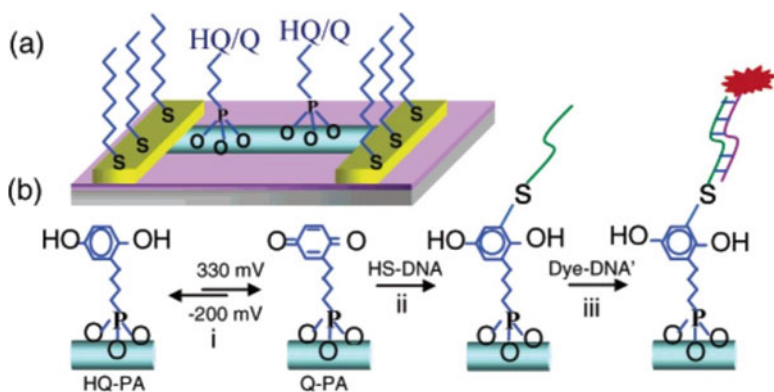
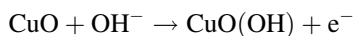


**Fig. 10.12** (a) Indium oxide nanowire mat device. (b) The DNA detection process of electrochemical cell; *HQ*, hydroquinone; *Q*, quinone or diketobenzene; *HQ-PA*, 4-(1,4-dihydroxybenzene) butyl phosphonic acid; *Q-PA*, 4-(1,4-diketobenzene)butyl phosphonic acid; *HS-DNA*, thiol-terminated DNA; *Mv* millivolt. (Reprinted with the permission of ACS from Curreli et al. JACS, 2005)

Step (i): Oxidation reaction of  $\text{Cu}^{2+}$  to  $\text{Cu}^{3+}$



Step (ii): Formed  $\text{Cu}^{\text{III}}$  oxyhydroxide species can adsorb glucose.



### 10.7.2 Metal Oxide Nanowire Mat Based Biosensing Devices

The indium oxide nanowires array based electrochemical biosensing devices was successfully fabricated for the detection of single-strand DNA (Curreli et al. 2005). Indium oxide nanowires mat biosensing devices were contained two gold electrodes that protected by a self-assembled monolayer of dodecane-1-thiol and nanowire (between the two electrodes) followed by functionalization with 4-(1,4-dihydroxybenzene)butyl phosphonic acid (HQ-PA) as shown in Fig. 10.12a. The formed monolayer of HQ-PA on indium oxide nanowire was reversibly oxidized into Q-PA that was attached with thiol-terminated DNA (HS-DNA) followed by the attachment of complementary DNA strand (dye-DNA') as seen in Fig. 10.12b.

The selective functionalization array of indium oxide nanowire-based device was shown in Fig. 10.13a by using two groups of electrodes. The upper electrodes converted the formed HQ-PA layer into Q-PA on the surface of indium oxide nanowires. SEM images before the surface functionalization of indium oxide nanowires at different magnification were shown in Fig. 10.13b and c. The higher magnified SEM images clearly show that the gold electrodes cover the nanowire mat at brighter strip. Figure 10.14d shows the fluorescence image of indium oxide nanowires device of Q-PA attached with fluorescent dye labeled DNA stand. The dark lines are gold electrodes whereas DNA binding with Q-PA mat device appears as the bright network. Figure 10.13e. is not showing any fluorescence because there was no DNA binding to the nanowires with HQ-PA.

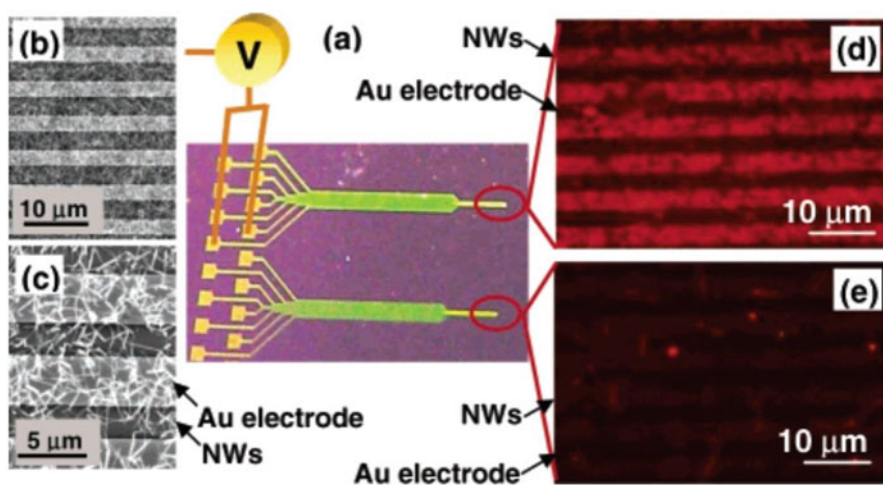


**Fig. 10.13** (a) Photograph of an electrode array on indium oxide nanowire mat device. (b and c) Scanning electron microscopy images of indium oxide nanowire mat. Fluorescence image of indium oxide nanowire mat device (d) with thiol terminated DNA to 4-(1,4-diketobenzene)butyl phosphonic acid, and (e) with dye-DNA' attached to the probe DNA; NW, nanowire; Au, gold; V, volt;  $\mu\text{m}$ , micrometer. (Reprinted with the permission of ACS from Curreli et al. JACS. 2005)



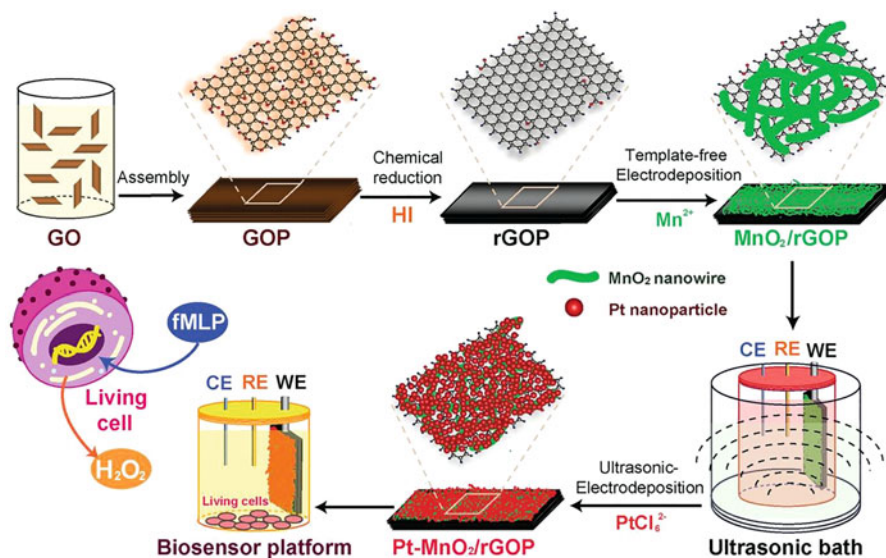


**Fig. 10.14** Fabrication process of flexible electrodes for biosensors platform; *fMLP*, *N*-formyl-methionyl-leucyl-phenylalanine; *Rgop*, reduced graphene oxide paper; *CE*, counter electrode; *WE*, working electrode; *RE*, reference electrode;  $H_2O_2$ , hydrogen peroxide; *GO*, graphene oxide; *GOP*, graphene oxide paper; *rGOP*, reduced GOP; *HI*, hydrogen iodide;  $MnO_2$ , manganese oxide;  $PtCl_6^{2-}$ , platinum hexachloride. (Reprinted with the permission of John Wiley and Sons from Xiao et al. *Adv. Funct. Mater.* 2012)

### 10.7.3 Lab-on-a-Chip Flexible Electrochemical Biosensors Devices

A novel flexible electrochemical biosensor device was fabricated by using platinum-manganese oxide with graphene paper triple component for the detection of hydrogen peroxide and successfully applied for real-time sensing of hydrogen peroxide in live cells (Xiao et al. 2012). Graphene oxide nanosheets were used as a model object for fabricating the biosensor devices through the formation of reduced graphene oxide paper by chemical reduction method. Further three-dimensional reduced graphene oxide paper substrate with large surface areas is produced from template-free electrodeposition of manganese oxide nanowire. The flexible platinum-manganese oxide graphene paper formed by mold casting and electrodeposition provides great flexibility for scaling-up in practical applications without limiting the size of platinum nanoparticles (Fig. 10.14). The platinum-manganese oxide with reduced graphene oxide paper device was successfully applied for the real-time detection of hydrogen peroxide in live cells.

### 10.7.4 Three-Dimensional Origami Devices for Biosensing

Paper-based 3D origami electrochemical devices are fabricated by using gold nanoparticles and manganese oxide nanowire networks for the detection of prostate protein antigen in real human serum assay (Li et al. 2014). Three-dimensional origami device is comprised by an equal size of auxiliary pad and sample tab on the wax-penetrated paper sheet as a screen-printed electrode as shown in Fig. 10.15a. Screen-printed electrodes array was constructed by silver/ silver chloride as a reference electrode in paper auxiliary zone and carbon as counter electrode on the paper sample zone. Sheet-A was used to print on electrode and cut into individual 3D origami device as shown in Fig. 10.15b and c, respectively. Finally, the individual 3D origami device was further modified for detecting bovine serum albumin, as seen in Fig. 10.15d. Bovine serum albumin sensing mechanism is shown in Fig.10.15e.

Paper-based electrochemical analytical device has fabricated by the growth of silver nanoparticles layer on the surface of cellulose fibers that was enhanced the surface area of bare paper working electrode and binding with target prostate protein antigen as shown in Fig. 10.16.

## 10.8 Conclusion

Novel approach for the fabrication of metal oxide-based biosensor devices with enhanced selectivity and sensitivity was reported. Silicon oxide with silicon nitride TriPleX™ waveguide-based sensing devices shows the excellent selectivity and

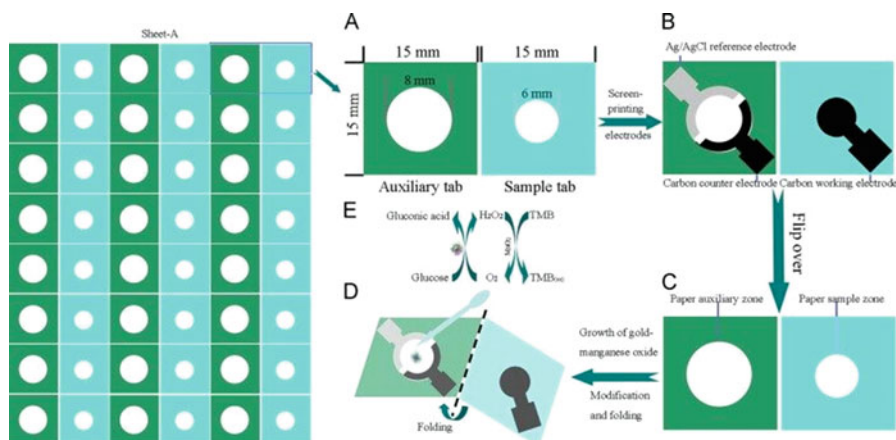
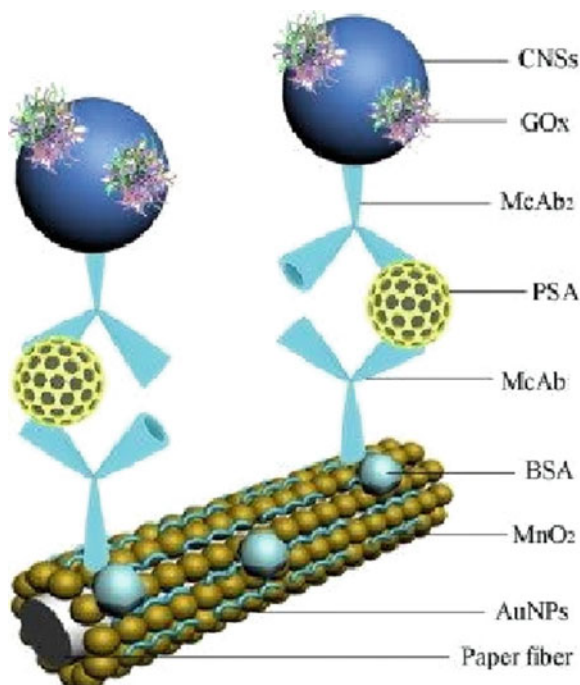


**Fig. 10.15** Fabrication of 3D origami device; *TMB*, 3,3,5,5-tetramethylbenzidine; *mm*, millimeter; *H<sub>2</sub>O<sub>2</sub>*, hydrogen peroxide; *O<sub>2</sub>*, oxygen molecule; *MnO<sub>2</sub>*, manganese oxide; *Ag/AgCl*, silver/silver chloride; *TMB<sub>OX</sub>*, oxidized form of TMB. (Reprinted with permission of Elsevier from Li et al. *Biosensors and Bioelectronics*. 2014)

**Fig. 10.16** Fabrication of electrochemical paper-based analytical device including the sequential growth of gold nanoparticles (AuNPs) and electrodeposition of manganese oxide ( $\text{MnO}_2$ ) nanowires, and application for detection of prostate protein antigen (PSA); *McAb*<sub>1</sub>, monoclonal capture anti-PSA; *McAb*<sub>2</sub>, signal anti-PSA; *BSA*, bovine serum albumin; *GOx*, glucose oxidase; *CNS* carbon nanosphere. (Reprinted with permission of Elsevier from Li et al. Biosensors and Bioelectronics. 2014)



high sensitivity with multiple contaminants detection in water samples and simultaneous determination of 32 different pollutants. Nanoporous label-free optical waveguide devices have 20-fold highly sensitive than conventional surface plasmon resonance sensor devices. In addition, the device allows enhancing the sensitivity when tuning the optical properties of porous anodic alumina film. Titanium oxide nanotube/silver nanoparticle-based optofluidic devices are promising for the detection of DNA oligo stand in surface enhanced Raman spectroscopy. Metal-oxide-metal sensors like copper/copper oxide/copper-based electrochemical devices have achieved for the detection of blood glucose level in human in the detection range of 2.2–10 mM. Indium oxide nanowire array based electrochemical mat devices show an excellent selectivity of single-strand DNA. Many of the metal oxide-based biomolecules sensing devices can achieve in real-time and continuous monitoring of biomolecules sensing response. The challenge of innovative methods for the fabrication of metal oxide-based sensing devices is still demanded. The future investigations will be going on novel approach for the fabrication of metal oxide-based biosensor device with highly simple method. Also, the surface functionalized bioreceptor molecule can simultaneously be detected with various biomolecules on the closely packed 1D biosensing devices.

## References

- Abunahla H, Mohammad B, Alazzam A, Jaoud MA, Al-Qutayri M, Hadi SA, Al-sarawi SF (2019) MoMsense: metal-oxide-metal elementary glucose sensor. *Sci Rep* 9:5524. <https://doi.org/10.1038/s41598-019-41892-w>
- Ansari AA, Alhoshan M, Alsalthi MS, Aldwayyan AS (2010) Nanostructured metal oxides based enzymatic electrochemical biosensors. INTECH, Rijeka, p 302. ISBN 978-953-7619-99-2
- Balamurugan S, Spivak DA (2011) Molecular imprinting in monolayer surfaces. *J Mol Recognit* 24:915–929. <https://doi.org/10.1002/jmr.1150>
- Bavykin DV, Parmon VN, Lapkin AA, Walsh FC (2004) The effect of hydrothermal conditions on the mesoporous structure of TiO<sub>2</sub> nanotubes. *J Mater Chem* 14:3370–3377. <https://doi.org/10.1039/B406378C>
- Burke CS, Markey A, Nooney RI, Byrne B, McDonagh C (2006) Development of an optical sensor probe for the detection of dissolved carbon dioxide. *Sensors Actuators B Chem* 119:288–294. <https://doi.org/10.1016/j.snb.2005.12.022>
- Caruso F (2001) Nanoengineering of particle surfaces. *Adv Mater* 13:11–22. [https://doi.org/10.1002/1521-4095\(200101\)13:1<11:AID-ADMA11>3.0.CO;2-N](https://doi.org/10.1002/1521-4095(200101)13:1<11:AID-ADMA11>3.0.CO;2-N)
- Chen K, Bell AT, Iglesia E (2002) The relationship between the electronic and redox properties of dispersed metal oxides and their turnover rates in oxidative dehydrogenation reactions. *J Catal* 209:35–42. <https://doi.org/10.1006/jcat.2002.3620>
- Chen Z, Appenzeller J, Knoch J, Lin YM, Avouris P (2005) The role of metal-nanotube contact in the performance of carbon nanotube field-effect transistors. *Nano Lett* 5(7):1497–1502. <https://doi.org/10.1021/NI0508624>
- Choi YC, Kim J, Bu SD (2006) Template-directed formation of functional complex metal-oxide nanostructures by combination of sol–gel processing and spin coating. *Mater Sci Eng B* 133:245–249. <https://doi.org/10.1016/j.mseb.2006.06.034>
- Curreli M, Li C, Sun Y, Lei B, Gundersen MA, Thompson ME, Zhou C (2005) Selective functionalization of In<sub>2</sub>O<sub>3</sub> nanowire mat devices for biosensing applications. *J Am Chem Soc* 127:6922–6923. <https://doi.org/10.1021/ja0503478>
- Devan RS, Ho WD, Wu SY, Ma YR (2010) Low-temperature phase transformation and phonon confinement in one-dimensional Ta<sub>2</sub>O<sub>5</sub> nanorods. *J Appl Cryst* 43:498–503. <https://doi.org/10.1107/S002188981000796X>
- Doong R, Shih H (2010) Array-based titanium dioxide biosensors for ratiometric determination of glucose, glutamate and urea. *Biosens Bioelectron* 25:1439–1446. <https://doi.org/10.1016/j.bios.2009.10.044>
- Duer R, Lund R, Tanaka R, Christensen DA, Herron JN (2010) In-plane parallel scanning: a microarray technology for point-of-care testing. *Anal Chem* 82(21):8856–8865. <https://doi.org/10.1021/ac101571b>
- Dzyadevych SV, Arkhypova VN, Soldatkin AP, El'skaya AV, Martelet C, Jaffrezic-Renault N (2007) Amperometric enzyme biosensors: past, present and future. *IRBM* 29:171–180. <https://doi.org/10.1016/j.rbmret.2007.11.007>
- Emeline AV, Kataeva GV, Panasuk AV, Ryabchuk VK, Sheremetyeva NV, Serpone N (2005) Effect of surface photoreactions on the photocoloration of a wide band gap metal oxide: probing whether surface reactions are photocatalytic. *J Phys Chem B* 109:5175–5185M. <https://doi.org/10.1021/jp0452047>
- Escorihuela J, González-Martínez MA, López-Paz JL, Puchades R, Maquieira A, Gimenez-Romero D (2014) Dual-polarization interferometry: a novel technique to light up the nanomolecular world. *Chem Rev* 115:265–294. <https://doi.org/10.1021/cr5002063>
- Farré M, Rodríguez-Mozas S, Alda ML, Barceló D, Hansen PD (2009) Biosensors for environmental monitoring at global scale and the EU level. In: Barceló D, Hansen PD (eds) *Biosensors for environmental monitoring of aquatic systems. The handbook of environmental chemistry*, vol 5J. Springer, Berlin/Heidelberg, pp 1–32. [https://doi.org/10.1007/978-3-540-36253-1\\_1](https://doi.org/10.1007/978-3-540-36253-1_1)

- Flavin K, Resmini M (2010) Molecular imprinting with nanomaterials. In: Geckeler KE, Nishide H (eds) *Advanced nanomaterials*. Wiley-VCH Verlag, Weinheim, pp 651–675
- Forzani ES, Zhang HQ, Nagahara LA, Amlani I, Tsui R, Tao NJ (2004) A conducting polymer nanojunction sensor for glucose detection. *Nano Lett* 4:1785–1788. <https://doi.org/10.1021/nl049080l>
- Girard C, Joachim C, Gauthier S (2000) The physics of the near-field. *Rep Prog Phys* 3:893. <https://doi.org/10.1088/0034-4885/63/6/202>
- Golden JP, Shriver-Lake LC, Anderson GP, Thompson RB, Ligler FS (1992) Fluorometer and tapered fiber optic probes for sensing in the evanescent wave. *Opt Eng* 31:1458–1462. <https://doi.org/10.1117/12.58764>
- Gooding JJ (2006) Nanoscale biosensors: significant advantages over larger devices? *Small* 2:313–315. <https://doi.org/10.1002/smll.200500477>
- Gou X, Wang G, Yang J, Park J, Wexler D (2008) Chemical synthesis, characterisation and gas sensing performance of copper oxide nanoribbons. *J Mater Chem* 18:965–969. <https://doi.org/10.1039/b716745h>
- Granqvist CG (2008) Oxide electrochromics: why, how, and whither. *Sol Energy Mater Sol Cells* 92:203–208. <https://doi.org/10.1016/j.solmat.2006.10.027>
- Greene LE, Yuhas BD, Law M, Zitoun D, Yang P (2006) Solution-grown zinc oxide nanowires. *Inorg Chem* 45:7535. <https://doi.org/10.1021/ic0601900>
- Gupta AK, Gupta M (2005) Synthesis and surface engineering of iron oxide nanoparticles for biomedical applications. *Biomaterials* 26:3995–4021. <https://doi.org/10.1016/j.biomaterials.2004.10.012>
- Gutowski M, Jaffe JE, Liu CL, Stoker M, Hegde RI, Rai RS, Tobin PJ (2002) Thermodynamic stability of high-K dielectric metal oxides  $ZrO_2$  and  $HfO_2$  in contact with Si and  $SiO_2$ . *Appl Phys Lett* 80:1897–1899. <https://doi.org/10.1063/1.1458692>
- Hennemann J, Kohl CD, Reisert S, Kirchner P, Schoning MJ (2013) Copper oxide nanofibers for detection of hydrogen peroxide vapour at high concentrations. *Phys Status Solid A* 210:859–863. <https://doi.org/10.1002/pssa.201200775>
- Hotta K, Yamaguchi A, Teramae N (2012) Nanoporous waveguide sensor with optimized nanoarchitectures for highly sensitive label-free biosensing. *ACS Nano* 6:1541–1547. <https://doi.org/10.1021/nn204494z>
- Kondo T, Chen WJ, Schlau-Cohen GS (2017) Single-molecule fluorescence spectroscopy of photosynthetic systems. *Chem Rev* 117:860–898. <https://doi.org/10.1021/acs.chemrev.6b00195>
- Kroger HS, Meyer J, Riedl T, Kowalsky W, Kahn A (2009) P-type doping of organic wide band gap materials by transition metal oxides: a case-study on molybdenum trioxide. *Org Electron* 10:932–938. <https://doi.org/10.1016/j.orgel.2009.05.007>
- Kumar V, Guleria P, Mehta SK (2017) Nanosensors for food quality and safety assessment. *Environ Chem Lett* 15:165–177. <https://doi.org/10.1007/s10311-017-0616-4>
- Kumari L, Lin JH, Ma YR (2007) Synthesis of bismuth oxide nanostructures by an oxidative metal vapour phase deposition technique. *Nanotechnology* 18:295605. <https://doi.org/10.1088/0957-4484/18/29/295605>
- Lamberti A, Virga A, Chiado A, Chiodoni A, Bejtka K, Rivolo P, Giorgis F (2015) Ultrasensitive Ag-coated  $TiO_2$  nanotube arrays for flexible SERS-based optofluidic devices. *J Mater Chem C* 3:6868–6875. <https://doi.org/10.1039/c5tc01154j>
- Lavers C, Itoh K, Wu S, Murabayashi M, Mauchline I, Stewart G, Stout T (2000) Planar optical waveguides for sensing applications. *Sensors Actuators B Chem* 69:85–95. [https://doi.org/10.1016/S0925-4005\(00\)00412-3](https://doi.org/10.1016/S0925-4005(00)00412-3)
- Lee MJ, Han S, Jeon SH, Park BH, Kang BS, Ahn SE, Kim KH, Lee CB, Kim CJ, Yoo IK, Seo DH, Li XS, Park JB, Lee JH, Park Y (2009) Electrical manipulation of nanofilaments in transition-metal oxides for resistance-based memory. *Nano Lett* 9:1476–1481. <https://doi.org/10.1021/nl803387q>

- Leung A, Shankar PM, Mutharasan RA (2007) Review of fiber-optic biosensors. *Sensor Actuat B Chem* 125:688–703. <https://doi.org/10.1016/j.snb.2007.03.010>
- Li L, Xu J, Zheng X, Ma C, Song X, Ge S, Yu S, Yan M (2014) Growth of gold-manganese oxide nanostructures on a 3D origami device for glucose-oxidase label based electrochemical immunosensor. *Biosens Bioelectron* 61:76–82. <https://doi.org/10.1016/j.bios.2014.05.012>
- Liang HW, Liu S, Yu SH (2010) Controlled synthesis of one-dimensional inorganic nanostructures using pre-existing one-dimensional nanostructures as templates. *Adv Mater* 22:3925–3937. <https://doi.org/10.1002/adma.200904391>
- Limmer SJ, Cao G (2003) Sol-gel electrophoretic deposition for the growth of oxide nanorods. *Adv Mater* 15:427–431. <https://doi.org/10.1002/adma.200390099>
- Liu Z, Liu Y, Yang H, Yang Y, Shen G, Yu R (2005) A mediator-free tyrosinase biosensor based on ZnO sol-gel matrix. *Electroanalysis* 17:1065–1070. <https://doi.org/10.1002/elan.200403215>
- Liu L, Zhou X, Wilkinson JS, Hua P, Song B, Shi H (2017) Integrated optical waveguide based fluorescent immunosensor for fast and sensitive detection of microcystin-LR in lakes: optimization and analysis. *Sci Rep* 7:3655. <https://doi.org/10.1038/s41598-017-03939-8>
- Liu L, Shan D, Zhou X, Shi H, Song B, Falke F, Leinse A, Heideman R (2018) TriPleX™ waveguide-based fluorescence biosensor for multichannel environmental contaminants detection. *Biosens Bioelectron* 106:117–121. <https://doi.org/10.1016/j.bios.2018.01.066>
- Luchansky MS, Bailey RC (2011) High-Q optical sensors for chemical and biological analysis. *Anal Chem* 84:793–821. <https://doi.org/10.1021/ac2029024>
- Lukosz W (1995) Integrated optical chemical and direct biochemical sensors. *Sens Actuat B* 29:37–50. [https://doi.org/10.1016/0925-4005\(95\)01661-9](https://doi.org/10.1016/0925-4005(95)01661-9)
- Macak M, Zlamal M, Krysa J, Schmuki P (2007) Self-organized TiO<sub>2</sub> nanotube layers as highly efficient photocatalysts. *Small* 3:300–304. <https://doi.org/10.1002/smll.200600426>
- Malhotra BD, Das M, Solanki PR (2012) Opportunities in nano-structured metal oxides based biosensors. *J Phys Conf Ser* 358:012007. <https://doi.org/10.1088/1742-6596/358/1/012007>
- Mavrou G, Galata G, Tsipas P, Sotiropoulos A, Panayiotatos Y, Dimoulas A, Evangelou AK, Seo JW, Dieker C (2008) Electrical properties of La<sub>2</sub>O<sub>3</sub> and HfO<sub>2</sub>/La<sub>2</sub>O<sub>3</sub> gate dielectrics for germanium metal-oxide-semiconductor devices. *J Appl Phys* 103:014506. <https://doi.org/10.1063/1.2827499>
- McDonagh C, Burke CS, MacCraith BD (2008) Optical chemical sensors. *Chem Rev* 108:400–422. <https://doi.org/10.1021/cr068102g>
- McQuade DT, Pullen AE, Swager TM (2000) Conjugated polymer-based chemical sensors. *Chem Rev* 100:2537–2574. <https://doi.org/10.1021/cr9801014>
- Mia Z, Chang YL (2009) III-V compound semiconductor nanostructures on silicon: epitaxial growth, properties, and applications in light emitting diodes and lasers. *J Nanophotonics* 3:031602. <https://doi.org/10.1117/1.3081051>
- Mukundan H, Anderson AS, Grace WK, Grace KM, Hartman N, Martinez JS, Swanson BI (2009) Waveguide-based biosensors for pathogen detection. *Sensors* 9:5783–5809. <https://doi.org/10.3390/s90705783>
- Nagashima K, Yanagida T, Tanaka H, Kawai T (2007) Epitaxial growth of MgO nanowires by pulsed laser deposition. *J Appl Phys* 101:124304. <https://doi.org/10.1063/1.2748625>
- Pan ZW, Dai ZR, Wang ZL (2001) Nanobelts of semiconducting oxides. *Science* 291:1947–1949. <https://doi.org/10.1126/science.1058120>
- Pandey P, Datta M, Malhotra BD (2008) Prospects of nanomaterials in biosensors. *Anal Lett* 41:159–209. <https://doi.org/10.1080/00032710701792620>
- Park WI, Kim HD, Jung SW, Yi GC (2002) Metalorganic vapor-phase epitaxial growth of vertically well-aligned ZnO nanorods. *Appl Phys Lett* 80:4232–4234. <https://doi.org/10.1063/1.1482800>
- Prak A, Leeuwis H, Heideman R, Leinse A, Borst G (2011) Integration of optical waveguides and microfluidics in a miniaturized antibody micro-array system for life detection in the NASA/ESA ExoMars mission. *Proc SPIE* 7928:79280L–79281L. <https://doi.org/10.1117/12.879309>

- Puyol M, Valle M, Garcés I, Villuendas F, Domínguez C, Alonso J (1999) Integrated waveguide absorbance optode for chemical sensing. *Anal Chem* 71:5037–5044. <https://doi.org/10.1021/ac9901561>
- Reverté L, Campàs M, Yakes BJ, Deeds JR, Katikou P, Kawatsu K, Lochhead M, Elliott CT, Campbell K (2017) Tetrodotoxin detection in puffer fish by a sensitive planar waveguide immunosensor. *Sensors Actuators B Chem* 253:967–976. <https://doi.org/10.1016/j.snb.2017.06.181>
- Rignanese GM (2005) Dielectric properties of crystalline and amorphous transition metal oxides and silicates as potential high- $\kappa$  candidates: the contribution of density-functional theory. *J Phys Condens Matter* 17:R357–R379. <https://doi.org/10.1088/0953-8984/17/7/R03>
- Robertson J (2006) High dielectric constant gate oxides for metal oxide Si transistors. *Rep Prog Phys* 69:327–396. <https://doi.org/10.1088/0034-4885/69/2/R02>
- Rosenholm JM, Meinander A, Peuhu E, Niemi R, Eriksson JE, Sahlgren C, Linden M (2009) Targeting of porous hybrid silica nanoparticles to cancer cells. *ACS Nano* 3:197–206. <https://doi.org/10.1021/nn800781r>
- Rosseinsky DR, Mortimer RJ (2001) Electrochromic systems and the prospects for devices. *Adv Mater* 13:783–793. [https://doi.org/10.1002/1521-4095\(200106\)13:11<783:AID-ADMA783>3.CO;2-D](https://doi.org/10.1002/1521-4095(200106)13:11<783:AID-ADMA783>3.CO;2-D)
- Roy R, Hohng S, Ha T (2008) A practical guide to single-molecule FRET. *Nat Methods* 5:507–516. <https://doi.org/10.1038/nmeth.1208>
- Sedach PA, Gordon TJ, Sayed SY, Furstenhaupt T, Sui RH, Baumgartner T, Berlinguette CP (2010) Solution growth of anatase TiO<sub>2</sub> nanowires from transparent conducting glass substrates. *J Mater Chem* 20:5063–5069. <https://doi.org/10.1039/C0JM00266F>
- Su X, Zhang Z, Zhu M (2006) Melting and optical properties of ZnO nanorods. *Appl Phys Lett* 88:061913. <https://doi.org/10.1063/1.2172716>
- Su JZ, Feng XJ, Sloppy JD, Guo LJ, Grimes CA (2011) Vertically aligned WO<sub>3</sub> nanowire arrays grown directly on transparent conducting oxide coated glass: synthesis and photoelectrochemical properties. *Nano Lett* 11:203–208. <https://doi.org/10.1021/nl1034573>
- Sun CW, Li H, Zhang HR, Wang ZX, Chen LQ (2005) Controlled synthesis of CeO<sub>2</sub> nanorods by a solvothermal method. *Nanotechnology* 16:1454–1463. <https://doi.org/10.1088/0957-4484/16/9/006>
- Sun AL, Zhang YF, Sun GP, Wang XN, Tang D (2017) Homogeneous electrochemical detection of ochratoxin A in foodstuff using aptamer–graphene oxide nanosheets and DNase I-based target recycling reaction. *Biosens Bioelectron* 89:659–665. <https://doi.org/10.1016/j.bios.2015.12.032>
- Swann MJ, Peel LL, Carrington S, Freeman NJ (2004) Dual-polarization interferometry: an analytical technique to measure changes in protein structure in real time, to determine the stoichiometry of binding events, and to differentiate between specific and nonspecific interactions. *Anal Biochem* 329:190–198. <https://doi.org/10.1016/j.ab.2004.02.019>
- Sysoev VV, Button BK, Wepsiec K, Dmitriev S, Kolmakov A (2006) Toward the nanoscopic “electronic nose”: hydrogen vs carbon monoxide discrimination with an array of individual metal oxide nano- and mesowire sensors. *Nano Lett* 6:1584–1588. <https://doi.org/10.1021/nl060185t>
- Takada K, Sakurai H, Muromachi ET, Izumi F, Dilanian RA, Sasaki T (2003) Superconductivity in two-dimensional CoO<sub>2</sub> layers. *Nature* 422:53–55. <https://doi.org/10.1038/nature01450>
- Tenne R (2006) Inorganic nanotubes and fullerene-like nanoparticles. *Nat Nanotechnol* 1:103–111. <https://doi.org/10.1038/nnano.2006.62>
- Tokel O, Yildiz UH, Inci F, Durmus NG, Ekiz OO, Turker B, Cetin C, Rao S, Sridhar K, Natarajan N, Shafiee H, Dana A, Demirci U (2015) Portable microfluidic integrated plasmonic platform for pathogen detection. *Sci Rep* 5:9152. <https://doi.org/10.1038/srep09152>
- Wadkins RM, Vladu B, Tung CS (1998) Actinomycin D binds to metastable hairpins in single-stranded DNA. *Biochemistry* 37:11915–11923. <https://doi.org/10.1021/bi9809730>
- Wang XD, Wolfes OS (2013) Fiber-optic chemical sensors and biosensors (2008–2012). *Anal Chem* 85:487–508. <https://doi.org/10.1021/ac303159b>

- Wang W, Liu Y, Xu C, Zheng C, Wang G (2002) Synthesis of NiO nanorods by a novel simple precursor thermal decomposition approach. *Chem Phys Lett* 362:119–122. [https://doi.org/10.1016/S0009-2614\(02\)00996-X](https://doi.org/10.1016/S0009-2614(02)00996-X)
- Wang JX, Sun XW, Wei A, Lei Y, Cai XP, Li CM, Dong ZL (2006) Zinc oxide nanocomb biosensor for glucose detection. *Appl Phys Lett* 88:233106. <https://doi.org/10.1063/1.2210078>
- Wen X, Fang Y, Pang Q, Yang C, Wang J, Ge W, Wong KS, Yang S (2005) ZnO nanobelt arrays grown directly from and on zinc substrates: synthesis, characterization, and applications. *J Phys Chem B* 109:15303–15308. <https://doi.org/10.1021/jp052466f>
- Wu H, Pan W (2006) Preparation of zinc oxide nanofibers by electrospinning. *J Am Ceram Soc* 89:699–701. <https://doi.org/10.1111/j.1551-2916.2005.00735.x>
- Xiao F, Li Y, Zan X, Liao K, Xu R, Duan H (2012) Growth of metal–metal oxide nanostructures on freestanding graphene paper for flexible biosensors. *Adv Funct Mater* 22:2487–2494. <https://doi.org/10.1002/adfm.201200191>
- Xu Z, Gao H, Zhang L, Chen X, Qiao X (2011) The biomimetic immunoassay based on molecularly imprinted polymer: a comprehensive review of recent progress and future prospects. *J Food Sci* 76:R69–R75. <https://doi.org/10.1111/j.1750-3841.2010.02020.x>
- Yamazoe N (1991) New approaches for improving semiconductor gas sensors. *Sensors Actuators B Chem* 5:7–19. [https://doi.org/10.1016/0925-4005\(91\)80213-4](https://doi.org/10.1016/0925-4005(91)80213-4)
- Yoon JY, Kim B (2012) Lab-on-a-chip pathogen sensors for food safety. *Sensors* 12:10713–10741. <https://doi.org/10.3390/s120810713>
- Zheng H, Zhong J, Wang W, Zheng Y, Ma C (2008) A method to fabricate nanorod films on aluminum lattice membrane by magnetron sputtering. *Thin Solid Films* 516:4983–4987. <https://doi.org/10.1016/j.tsf.2007.10.005>



# Index

## A

Abe, M., 10  
Ahirwar, D., 296  
Ahmed, M., 291  
Ahn, J.-H., 38–66  
Alam, M.M., 296  
Alinia, R., 7  
Alkaline fuel cells (AFC), 117, 122  
Amatucci, G.G., 83, 92, 94  
Ansari, A.A., 195  
Aptamers, 194, 246, 250, 260, 264, 268, 270, 273, 275  
Armand, 43  
Arun, N., 94  
Asanuma, H., 251  
Asiri, A.M., 296  
Ay, H., 116–139

## B

Babu, B., 94  
Babu, K.J., 190, 192  
Baby, T.T., 195  
Bai, Y.-H., 216, 218  
Balakrishnan, N.T.M., 38–66  
Baran, P.S., 253  
Baskar, S., 224, 229  
Bavykin, D.V., 315  
Benedek, P., 42  
Benvidi, A., 219  
Bharath, G., 219  
Bhat, S.A., 233  
Bi, H., 62

Biomolecules, 170, 171, 193, 194, 196, 247, 267, 271–275, 292, 313, 317, 321, 328  
Biosensing devices, 313, 325, 328  
Biosensors, 170–175, 177–179, 183, 192, 194–196, 198, 216, 217, 221, 225, 226, 230, 237, 239, 246, 247, 255–276, 311–329

Bo, X., 176  
Brouillette, C., 288  
Bukkitgar, S.D., 214, 215

## C

Cai, Z., 291  
Cao, M., 175  
Cao, X., 190  
Caravaca, A., 17  
Carbon nanotubes (CNTs), 37, 43, 48–52, 55, 77, 85–88, 90, 92, 93, 95, 97, 100, 104, 105, 182, 183, 189, 222, 225, 267, 302  
Caruthers, M.H., 252  
Cathode materials, 39–41, 49, 56, 59, 62, 65, 104  
Cellulose II, 3–5, 8–14, 23–26  
Cellulose photocatalysis, 2–26  
Chaiyasith, S., 290  
Chakraborty, B., 298  
Chandrasekar, S., 246  
Chang, C., 24  
Chang, H.-T., 255, 265  
Charge discharge (CD), 51, 64, 85–87  
Chen, C.-H., 265  
Chen, G., 7

- Chen, S.M., 298  
Chen, Y., 263  
Chen, Z., 97, 221  
Cheng, G., 10  
Cheng, W.-L., 221–223  
Chinnasamy, R., 218  
Chiu, M.-H., 233  
Chou, C.-H., 238  
Clark, L.C., 246  
Comba, F.N., 219  
Composites, 23, 42, 44–46, 48–63, 77, 86, 87, 93, 104, 128, 130–135, 137, 139, 183, 189, 192, 194, 198, 218, 220, 230, 237, 238, 267, 295, 296, 300, 301, 303, 315  
Croce, F., 65  
Cross, C.F., 10  
Cycling stability, 47, 52, 55, 56, 60–62, 92
- D**  
da Costa Sousa, L., 7  
Dai, C., 105  
Dai, H., 190  
Dai, Y., 290  
Dai, Z., 191  
Das, A., 38–66  
David, S.P., 148–164  
David, T.M., 76–107  
Defense, 287  
Deng, Y., 10  
Detection limits, 176–178, 182, 186, 189, 190, 192, 195, 198, 215, 216, 218, 219, 221, 223, 229, 231, 233, 236, 238, 256, 262, 267, 269–271, 289–291, 294–300, 302, 317, 319  
Devi, S., 312–327  
Dhindsa, K.S., 60  
Diaz, E., 265  
Ding, J., 97  
Ding, R., 97  
Ding, Y., 59, 61  
DNA biosensors, 245–276  
DNAzymes, 246, 258–263, 270  
Dong, S., 263  
Dong, X., 221  
Dontsova, E.A., 218  
Du, P., 288  
Du, X., 186, 187  
Duan, C., 296  
Dubal, D.P., 88  
Dutta, A.K., 229
- E**  
Ebrahimi, A., 191  
Efficiencies, 6, 15, 18, 38, 48, 50, 51, 61, 62, 98, 117, 118, 120–123, 132, 133, 148, 150, 154–156, 159, 161, 164, 254, 258  
Electrochemical, 6, 41–45, 47, 49–52, 54, 55, 57–63, 65, 66, 85–87, 89, 91, 93, 96, 98, 101, 104, 107, 118, 120, 130, 136, 170–172, 177, 178, 181, 183, 185, 189, 194, 196, 198, 210, 211, 214, 216, 217, 221, 223–226, 230, 232, 234, 235, 237, 246, 258, 266, 267, 271, 274, 289, 291–295, 297, 299, 300, 303, 313, 316, 321–328  
Electrochemical sensors, 183, 186, 190, 198, 210, 211, 213, 216, 217, 221, 222, 230, 232, 237, 239, 259, 286–300, 313, 322, 323  
Electrochemistry, 120, 135, 198, 272  
El-safty, S.A., 290  
Ensafi, A.A., 233  
Eremenko, A.V., 291
- F**  
Fan, L., 96, 99  
Fan, L.T., 7  
Fan, Q., 94  
Fang, L., 186  
Farquharson, S., 288  
Food safety, 273, 287  
Forzani, E.S., 315  
Fu, D., 14  
Fu, J., 288  
Fu, X., 288  
Fuel cells, 38, 49, 77, 78, 116–124, 127–134, 139  
Fujishima, A., 15
- G**  
Gamble, F.R., 39  
Gao, M., 7  
Gao, Z., 191  
Geng, D., 186  
Gianneschi, N.C., 258  
Giribabu, K., 286–300  
Glucose, 3, 8, 17–19, 23, 44, 170, 171, 173–188, 190, 192–195, 198, 210, 217, 220–224, 226, 229, 230, 232, 233, 236–238, 246, 295, 298–301, 315, 323–324, 328

- Gong, L., 259  
 Goodenough, J.B., 39, 40  
 Gooding, J.J., 315  
 Gopalakrishnan, A., 290  
 G-quadruplex, 255–257, 261–263, 269–272  
 Graham, D., 266  
 Graphene, 37, 43, 48, 49, 51, 55, 58–62, 77, 87,  
 90, 92, 94, 95, 97, 104, 105, 137, 172,  
 176, 177, 182, 183, 187, 189, 191, 218,  
 219, 221, 225, 229–231, 233, 259,  
 267–269, 273, 274, 291, 295, 296, 299,  
 302, 326  
 Gu, A., 229  
 Gupta, S., 231, 233
- H**  
 Habila, M.A., 288  
 Hao, H., 17  
 Hazra, P., 264  
 Herle, P.S., 47  
 Hiden, A., 7  
 Ho, J.-aA., 210–239  
 Honda, K., 15  
 Hotta, K., 318  
 Hsu, W.E., 288  
 Hsu, Y.W., 195  
 Huang, J., 186  
 Huang, J.-F., 216, 236–238  
 Huang, K.-J., 216, 232, 237, 238  
 Huo, H., 182  
 Hupp, J.-T., 265  
 Hwang, S.W., 219
- I**  
 Imanishi, T., 251
- J**  
 Jabeen Fatima, M.J., 38–66  
 Jang, H.D., 195  
 Jeong, J.M., 186  
 Ji, J., 105  
 Jia, X., 10  
 Jiang, L.C., 195  
 Jiang, W., 195  
 Joshi, N., 170–198  
 Jou, A.F.-J., 236
- K**  
 Kang, Q., 214, 215  
 Kang, S., 296  
 Kannan, P., 182  
 Kannan, P.K., 180, 182  
 Karikalan, N., 175, 177  
 Karthika, A., 296  
 Kasap, H., 17  
 Kawai, T., 17, 18  
 Kesavan, S., 232, 236  
 Khairi, M., 290  
 Khorshed, A.A., 219  
 Kim, H.Y., 290, 298  
 Kim, S., 175, 177, 182  
 Klemm, D., 10  
 Kokulnathan, T., 296  
 Kolathodi, M.S., 105  
 Komaba, S., 99  
 Kottam, N., 298  
 Krishnan, M.A., 38–66  
 Kubendhiran, S., 182, 191  
 Kubota, L.T., 214, 215  
 Kumar, J.V., 298  
 Kumar, K.G., 269  
 Kumar, R., 7  
 Kumar, R.T.R., 217, 218  
 Kurt, V.G., 251
- L**  
 Lang, J.-W., 105  
 Lawton, L., 2–26  
 Lee, H., 176  
 Lee, J.E., 89, 90  
 Leung, K.-H., 256  
 Li, H., 97  
 Li, J., 258, 276, 298  
 Li, K., 100  
 Li, L., 195  
 Li, P., 297  
 Li, X., 97, 186, 187, 195  
 Li, Y., 7, 236, 262, 272  
 Li, Z., 100  
 Liao, W.-C., 236  
 Lim, E., 97  
 Lin, B.-T., 236  
 Lin, C.T., 288  
 Lin, T.W., 182, 183  
 Lin, X., 186, 187  
 Ling, L., 260  
 Ling, P., 226, 229  
 Lithium ion batteries (LIB), 37–41  
 Lithium iron phosphate (LIP), 37, 40, 66  
 Liu, B., 265  
 Liu, C., 94, 256  
 Liu, G., 26  
 Liu, J., 90, 265  
 Liu, L., 317, 319  
 Liu, M., 296

- Liu, T., 288  
 Liu, Z., 315  
 Lu, Y., 258  
 Lukatskaya, M.R., 102  
 Luo, J.-Y., 94  
 Lyons, C., 246
- M**  
 Ma, D.-L., 255, 256  
 Ma, H., 14, 90  
 Ma, K., 186  
 Mahanthappa, M., 298  
 Maji, S.K., 176, 178, 191, 298  
 Mangalaraja, R.V., 286–300  
 Manibalan, G., 296  
 Materials, 3, 4, 7, 15, 19–23, 25, 26, 39–41, 43, 45, 47–50, 52, 56–59, 61, 62, 65, 66, 76, 79, 80, 82–87, 89, 91–93, 98, 104, 118–121, 124, 125, 127, 134, 136, 137, 148, 149, 151, 157, 159, 163, 171–173, 177, 181, 183, 189, 192, 198, 211, 214–216, 218, 219, 221, 223, 224, 229–231, 233, 236, 238, 239, 262, 267, 270, 274, 287–289, 291, 293–295, 297, 299, 300, 302, 303, 312–315, 317  
 Mathews, T., 76–107  
 Mazza, G., 14  
 Mehta, S., 219  
 Mercer, J., 10  
 Mergeny, M.J., 269  
 Mesopores, 149  
 Metal oxides, 39, 49, 55, 58, 59, 82, 87, 89, 92, 93, 98, 121, 125, 127, 128, 130, 133, 139, 151, 159, 164, 172, 194, 196, 198, 210–213, 237, 286–300, 312–328  
 Metals, 13, 15, 18, 39, 43, 45, 65, 87, 93, 96, 98, 115–139, 151, 161, 169–199, 210–214, 216, 220, 229, 230, 232, 237, 239, 246, 247, 253–270, 275, 287–301, 312–328  
 Metal sulfides, 136–139, 210, 212, 213, 237, 287, 288, 295, 297–301  
 Mhamane, D., 94  
 Miao, Z., 7  
 Mittal, A., 14  
 Miyazaki, C.M., 170–198  
 Mizushima, K., 39  
 Mondal, A., 298  
 Montemuro, M., 288  
 Mourroux, M.R.E., 288
- Mukherjee, N., 298  
 Mutyala, S., 187
- N**  
 Nagarajan, S., 2–26  
 Nanomaterials, 151, 183, 193, 212, 214, 216, 217, 220, 224, 237, 239, 246, 264–271, 287, 289, 291, 312, 313, 315  
 Nanostructures, 44, 59, 137, 192, 194–196, 198, 225, 253, 267, 285–303  
 Ni, J., 103  
 Nielsen, P.E., 250  
 Nieuwoudt, H.H., 288  
 Ning, L., 231
- O**  
 Odorico, F.H., 14  
 Oliveira, O.N., 170–198  
 Optical waveguides, 317–319, 321, 328  
 Optofluidic, 319, 320, 328  
 Özdemir, A., 288
- P**  
 Pang, D.-W., 275  
 Parlak, O., 186  
 Patil, D., 195  
 Patil, S.S., 88  
 Paul, A., 38–66  
 Pena, C.A., 14  
 Peng, H., 90  
 Peng, S., 105  
 Perovskite solar cells, 157, 164  
 Perret, P., 103  
 Photovoltaics (PV), 148–151, 154, 157, 159, 254  
 Pollutants, 6, 16, 117, 183, 286, 287, 295, 300, 328  
 Prakash, R., 231, 233  
 Prasanth, R., 38–66  
 Proton exchange membrane (PEM), 117–119, 121, 127–130, 134, 139  
 Puangjan, A., 290  
 Purushothaman, K.K., 88
- Q**  
 Qian, L., 173, 175, 177  
 Qiao, Y.Q., 55

Qu, P., 190  
 Qu, Q., 97, 99  
 Que, L., 94

**R**

Radhakrishnan, S., 175, 182  
 Rahman, M.M., 290, 296  
 Rajendran, 265  
 Ramaprabhu, S., 195  
 Ramasamy, K.S., 251  
 Ramirez, E., 286–300  
 Raphaez, L.R., 38–66  
 Ray, M.J., 7  
 Raymundo-Pereira, P.A., 230, 233  
 Reitz, E., 195  
 Ren, X., 105  
 Renewable energy, 2–26, 38, 139  
 Revathi, C., 217, 218  
 Robertson, P., 2–26  
 Rodas, D.S., 288  
 Rojano, W.J.S., 288  
 Rosenholm, J.M., 315  
 Rout, C.S., 182

**S**

Saha, B.C., 7  
 Sakata, T., 17, 18  
 Sakthivel, M., 298  
 Sakthivel, T., 148–162  
 Salammal, S.T., 148–164  
 Salimi, A., 221  
 Sambandam, B., 148–164  
 Sandoval, C., 286–300  
 Sarkar, A., 190, 191  
 Sasaki, M., 10  
 Sassner, P., 7  
 Satish, R., 94  
 Scordia, D., 7  
 Seela, F., 248, 252, 263  
 Sen, F., 117–139  
 Sensors, 151, 170–173, 176–178, 180–184,  
 186, 187, 189–191, 194–196, 198,  
 214–226, 229–233, 236–239, 247, 255,  
 258, 263–267, 269, 273, 275, 287–291,  
 294–302, 313, 316, 317, 319, 320, 323,  
 328  
 Shafiei, M., 14  
 Shaw, B.R., 252  
 Shen, L., 256  
 Shende, C., 288  
 Shi, W., 288  
 Shimizu, F.M., 170–198  
 Show, B., 298

Shukla, M., 195  
 Sindhu, R., 7  
 Sivakumar, M., 298  
 Sivaramalingam, A., 148–164  
 Sivasankar, K., 224, 229  
 Skillen, N., 2–26  
 Šljukić, B., 219  
 Šljukić, B.R., 218  
 Sneddon, E.J., 288  
 Song, Y.-S., 236  
 Soosaimanickam, A., 148–164  
 Spectroscopy, 197, 287, 288, 313, 319, 321,  
 328  
 Speltini, A., 17, 20  
 Su, F.Y., 59  
 Su, L., 88  
 Su, S., 186, 189  
 Sue, J.-W., 223  
 Sumathi, C., 296  
 Sun, Z., 219  
 Supraja, P., 290  
 Suresh, R., 286–300  
 Syu, Y.C., 288

**T**

Tamboli, M.S., 105  
 Tan, W., 260, 266  
 Tan, Z., 182  
 Tang, Z., 105  
 Tanwar, S., 236  
 Tharmaraj, V., 312–328  
 Thirupathi, M., 210–239  
 Thiyagarajan, N., 210–239  
 Tian, L., 216  
 Titanium dioxide (TiO<sub>2</sub>), 148–164  
 Toprakci, O., 56  
 Tsiafoulis, C.G., 216

**V**

Vilian, A.T.E., 195, 222  
 Viswanathan, S., 236  
 Vitz, J., 10

**W**

Wada, T., 252  
 Wakerley, D.W., 17, 22  
 Wan, C., 7  
 Wang, B., 97  
 Wang, C., 102  
 Wang, F., 44, 90, 94, 97, 100  
 Wang, H., 105  
 Wang, J., 296

Wang, J.X., 315  
 Wang, K., 271, 272  
 Wang, L., 59, 218  
 Wang, M., 191  
 Wang, P., 94  
 Wang, Q., 298  
 Wang, R., 90, 102  
 Wang, S., 185, 186  
 Wang, T., 187  
 Wang, W., 275  
 Wang, X., 221, 288  
 Wang, Y., 10, 190, 191, 229  
 Wang, Y.-X., 102  
 Wang, Z., 263  
 Watanabe, M., 128  
 Wei, C., 180, 182  
 Wei, W., 10  
 William, D.J., 254  
 Wittingham, M.S., 39  
 Wu, L., 7  
 Wu, W., 182, 190, 298  
 Wyman, C.E., 7

**X**

Xia, C., 218, 219  
 Xia, Y.-Y., 94  
 Xiao, C., 218  
 Xiong, H., 246, 275  
 Xu, D., 63  
 Xu, G.R., 175, 177  
 Xu, R., 26  
 Xu, W., 190, 273  
 Xu, X., 175, 177  
 Xu, Y., 194  
 Xue, Y., 187

**Y**

Yagati, A.K., 195  
 Yan, J., 105  
 Yan, X., 175  
 Yáñez, J., 286–300

Yang, K., 195  
 Yang, L., 7  
 Yang, P., 89, 90  
 Yang, Y.J., 175, 176  
 Yellappa, S., 298  
 Yi, Q., 215  
 Yin, J., 97  
 You, J., 288  
 Yu, L., 10  
 Yu, S.-H., 269  
 Yu, W., 215  
 Yuan, B., 221, 223  
 Yuvaraj, S., 94

**Z**

Zavrel, M., 10  
 Zen, J.-M., 221, 226, 229, 230, 233, 237  
 Zeng, Y., 261  
 Zhai, Y.J., 186  
 Zhang, B., 190, 191  
 Zhang, F., 94  
 Zhang, G., 17, 19, 20, 22, 23  
 Zhang, L., 103  
 Zhang, P., 218  
 Zhang, S., 298  
 Zhang, X., 175, 256, 290  
 Zhang, Z., 266, 268  
 Zhao, H., 10  
 Zhao, J., 269  
 Zhao, M.-Q., 102  
 Zhao, X., 93  
 Zheng, J., 296  
 Zhou, L., 99  
 Zhou, S., 62  
 Zhou, X.-H., 262  
 Zhu, J., 90  
 Zhu, Y., 97  
 Zhuang, Z., 195  
 Zou, J., 17  
 Zourob, M., 275  
 Zuo, W., 94